frontiers | Research Topics

Innovative methods and techniques in new electric power systems

Edited by
David Gao, Chaolong Zhang, Xiao Wang and Tianqiao Zhao

Published in
Frontiers in Energy Research

ISSN 1664-8714
ISBN 978-2-83251-973-8
DOI 10.3389/978-2-83251-973-8

About Frontiers

Frontiers is more than just an open access publisher of scholarly articles: it is a pioneering approach to the world of academia, radically improving the way scholarly research is managed. The grand vision of Frontiers is a world where all people have an equal opportunity to seek, share and generate knowledge. Frontiers provides immediate and permanent online open access to all its publications, but this alone is not enough to realize our grand goals.

Frontiers journal series

The Frontiers journal series is a multi-tier and interdisciplinary set of open-access, online journals, promising a paradigm shift from the current review, selection and dissemination processes in academic publishing. All Frontiers journals are driven by researchers for researchers; therefore, they constitute a service to the scholarly community. At the same time, the *Frontiers journal series* operates on a revolutionary invention, the tiered publishing system, initially addressing specific communities of scholars, and gradually climbing up to broader public understanding, thus serving the interests of the lay society, too.

Dedication to quality

Each Frontiers article is a landmark of the highest quality, thanks to genuinely collaborative interactions between authors and review editors, who include some of the world's best academicians. Research must be certified by peers before entering a stream of knowledge that may eventually reach the public - and shape society; therefore, Frontiers only applies the most rigorous and unbiased reviews. Frontiers revolutionizes research publishing by freely delivering the most outstanding research, evaluated with no bias from both the academic and social point of view. By applying the most advanced information technologies, Frontiers is catapulting scholarly publishing into a new generation.

What are Frontiers Research Topics?

Frontiers Research Topics are very popular trademarks of the *Frontiers journals series*: they are collections of at least ten articles, all centered on a particular subject. With their unique mix of varied contributions from Original Research to Review Articles, Frontiers Research Topics unify the most influential researchers, the latest key findings and historical advances in a hot research area.

Find out more on how to host your own Frontiers Research Topic or contribute to one as an author by contacting the Frontiers editorial office: frontiersin.org/about/contact

Innovative methods and techniques in new electric power systems

Topic editors

David Gao — University of Denver, United States
Chaolong Zhang — Jinling Institute of Technology, China
Xiao Wang — Wuhan University, China
Tianqiao Zhao — Brookhaven National Laboratory (DOE), United States

Citation

Gao, D., Zhang, C., Wang, X., Zhao, T., eds. (2023). *Innovative methods and techniques in new electric power systems*. Lausanne: Frontiers Media SA. doi: 10.3389/978-2-83251-973-8

Table of contents

frontiers | Frontiers in Energy Research

TYPE Editorial
PUBLISHED 07 March 2023
DOI 10.3389/fenrg.2023.1134563

OPEN ACCESS

EDITED AND REVIEWED BY
ZhaoYang Dong,
Nanyang Technological University,
Singapore

*CORRESPONDENCE
Xiao Wang,
xiaowang@whu.edu.cn

SPECIALTY SECTION
This article was submitted to Smart Grids, a section of the journal Frontiers in Energy Research

RECEIVED 30 December 2022
ACCEPTED 03 March 2023
PUBLISHED 07 March 2023

CITATION
Zhang C, Wang X, Zhao T and Gao D (2023), Editorial: Innovative methods and techniques in new electric power systems.
Front. Energy Res. 11:1134563.
doi: 10.3389/fenrg.2023.1134563

Editorial: Innovative methods and techniques in new electric power systems

Chaolong Zhang[1], Xiao Wang[2]*, Tianqiao Zhao[3] and David Gao[4]

[1]College of Intelligent Science and Control Engineering, Jinling Institute of Technology, Nanjing, China, [2]School of Electrical and Automation, Wuhan University, Wuhan, China, [3]Interdisciplinary Science Department, Brookhaven National Laboratory, Upton, NY, United States, [4]Department of Electrical and Computer Engineering, University of Denver, Denver, CO, United States

KEYWORDS

new electric power system, renewable energy, energy storage, power prediction, decentralized and distributed control, virtual storage plant

Editorial on the Research Topic
Innovative methods and techniques in new electric power systems

The digital evolution of the energy industry is increasing in intensity worldwide, among which reform of the electric power system plays a central role. In order to achieve the goals of carbon peaking and carbon neutrality, the construction of a new electric power system (NEPS) with renewable energy as its core is the only viable path (Aslam et al., 2021). In the process of digital transformation of the NEPS, intelligent power equipment, sensor technology and energy storage technology are of strategic significance for enhancing the operational level of the power system, preserving the national energy security, and facilitating the achievement of carbon peaking and carbon neutrality. Wind and solar energy occupy a dominant position in the NEPS (Cameron and Van Der Zwaan, 2015). Renewable generation is projected to account for 25% of total electricity production in 2030% and 60% in 2060. The volatility, intermittency, randomness, and anti-peak shaving characteristics of wind and solar energy will pose new challenges to the capability of NEPS to provide a dependable power supply and maintain a safe and stable operation.

Therefore, innovative methods and techniques including energy storage materials, energy storage management, wind and solar power predictions, decentralized and distributed control, and fault tolerance are researched to manage the low-carbon transformation of power delivery and supply to maximize the cost-effectiveness of generation resources in the NEPS (Zhang et al., 2022; Zhao et al., 2022), which guarantees that the carbon emission targets in the power industry can be achieved.

The Research Topic consists of sixteen highly diverse contributions, which we briefly summarize below.

Firstly, Mao et al. proposes a new integrated energy system based on reversible solid oxide cell (RSOC) for photovoltaic consumption. The integrated electricity-gas system (IEGS) considers the two modes of electrolysis and power generation of RSOC in the model. The model takes the minimum running cost as the objective function to linearize part of the model to generate a mixed integer linearization problem and solve it in general algebraic modeling system. The case study shows that wind power is maximized, and the gas mixture can be transported in natural gas pipelines, improving the economics and stability of IEGS.

Chen et al. deduces the theoretical calculation equation of the quantitative evaluation index of the participation factor. She establishes the small-signal model of the MMC-HVDC transmission system for a wind farm and calculates the dominant oscillation mode of the system and participation factors of 11 oscillation modes of the system. The correlation between the participation factors of each oscillation mode, wind farm, and the MMC system is investigated, which laid a foundation for the formulation of broadband oscillation suppression strategies.

Wind power prediction accuracy is beneficial to the effective utilization of wind energy. Xiong et al. proposes an improved XGBoost algorithm optimized by Bayesian hyperparameter optimization (BH-XGBoost method), and the method is employed to forecast the short-term wind power of wind farms. The proposed BH-XGBoost method can outperforms other commonly used methods including XGBoost, SVM, KELM, and LSTM in all the cases, especially in the cases of wind ramp events caused by extreme weather conditions and low wind speed range.

Wu et al. proposes an adaptive under-frequency load shedding (UFLS) control strategy of power systems with wind turbines and ultra high-voltage DC (UHVDC) participating in frequency regulation. He establishes the simplified frequency response model of the power system considering the participation of wind turbines and UHVDC in frequency regulation, and analyzes the impact of the active power response characteristics of wind turbines and UHVDC participating in frequency regulation on the magnitude of the active power deficiency.

Cai et al. develops a distributed control framework for cost-effective storage coordination in the distribution networks, in which the energy storage units are coordinated to contribute to a given power reference at the aggregated level while regulating the local network voltages in the presence of renewable generations. The salient features of the proposed virtual storage plant (VSP) control roots from the successful employment of an inexact alternating direction method of multiplier (ADMM) algorithm, in which the primal updates have analytical solutions in closed form using proximal operators, which significantly reduces the computation efforts of individual storage agents and renders fast storage dispatch.

Finally, energy storage is very important to the new power system, which has the function of peak cutting and valley filling. Chen et al. proposes a hybrid model for the battery life prediction. The capacity signal is decomposed by the improved complete ensemble empirical mode decomposition with an adaptive noise algorithm to solve the backward problem. Then, the least squares support vector regression algorithm is used to predict each decomposition component separately. A good point set principle and inertia weights are introduced to optimize a sparrow search algorithm. Experimental results confirm that the proposed hybrid prediction model has high accuracy, good stability, and strong robustness.

Overall, recent years have seen great progress in the NEPS. However, this Research Topic could not be finished without the authors' and reviewers' contributions. We hope that this issue sheds light on various frontiers related to the NEPS and adds the credits to the effort in solving the current challenges in the fields.

Author contributions

CZ has written the text, XW has checked the whole paper and all authors listed have made a substantial, direct and intellectual contribution to the work, and approved it for submission.

Funding

This work was supported by the scientific research foundation for high-level personnel in Jinling Institute of Technology under Grant No. jit-rcyj-202202; industry-school cooperative education program of ministry of education under Grant No. 202102355002, and National Science Foundation of China under Grant No. 52207134.

Conflict of interest

The authors declare that the research was conducted in the absence of any commercial or financial relationships that could be construed as a potential conflict of interest.

Publisher's note

References

Aslam, S., Herodotou, H., Mohsin, S. M., Javaid, N., Ashraf, N., and Aslam, S. (2021). A survey on deep learning methods for power load and renewable energy forecasting in smart microgrids. *Renew. Sustain. Energy Rev.* 144, 110992. doi:10.1016/j.rser.2021.110992

Cameron, L., and Van Der Zwaan, B. (2015). Employment factors for wind and solar energy technologies: A literature review. *Renew. Sustain. Energy Rev.* 45, 160–172. doi:10.1016/j.rser.2015.01.001

Zhang, C., Zhao, S., and He, Y. (2022). An integrated method of the future capacity and RUL prediction for lithium-ion battery pack. *IEEE Trans. Veh. Technol.* 71 (3), 2601–2613. doi:10.1109/TVT.2021.3138959

Zhao, S., Zhang, C., and Wang, Y. (2022). Lithium-ion battery capacity and remaining useful life prediction using board learning system and long short-term memory neural network. *J. Energy Storage* 52, 104901. doi:10.1016/j.est.2022.104901

frontiers | Frontiers in Energy Research

METHODS
published: 10 May 2022
doi: 10.3389/fenrg.2022.905155

A Short-Term Wind Power Forecast Method *via* XGBoost Hyper-Parameters Optimization

Xiong Xiong[1], Xiaojie Guo[2], Pingliang Zeng[2], Ruiling Zou[1] and Xiaolong Wang[3]*

[1]*Jiangsu Collaborative Innovation Center of Atmospheric Environment and Equipment Technology, Nanjing University of Information Science and Technology, Nanjing, China,* [2]*School of Automation, Hangzhou Dianzi University, Hangzhou, China,* [3]*Guohua (Hami) New Energy Co., Ltd., Hami, China*

The improvement of wind power prediction accuracy is beneficial to the effective utilization of wind energy. An improved XGBoost algorithm *via* Bayesian hyperparameter optimization (BH-XGBoost method) was proposed in this article, which is employed to forecast the short-term wind power for wind farms. Compared to the XGBoost, SVM, KELM, and LSTM, the results indicate that BH-XGBoost outperforms other methods in all the cases. The BH-XGBoost method could yield a more minor estimated error than the other methods, especially in the cases of wind ramp events caused by extreme weather conditions and low wind speed range. The comparison results led to the recommendation that the BH-XGBoost method is an effective method to forecast the short-term wind power for wind farms.

Keywords: wind power forecasting, Bayesian hyperparameters optimization, Xgboost algorithm, numerical weather prediction, machine learning

OPEN ACCESS

Edited by:
Xiao Wang,
Wuhan University, China

Reviewed by:
Chi Zhou,
Tianjin University of Technology, China
Guanghong Wang,
Jiangsu Normal University, China
Bo Cao,
University of New Brunswick Fredericton, Canada

****Correspondence:***
Xiaojie Guo
gxj_workmail@163.com

Specialty section:
This article was submitted to Smart Grids, a section of the journal Frontiers in Energy Research

Received: *26 March 2022*
Accepted: *13 April 2022*
Published: *10 May 2022*

Citation:
Xiong X, Guo X, Zeng P, Zou R and Wang X (2022) A Short-Term Wind Power Forecast Method via XGBoost Hyper-Parameters Optimization. Front. Energy Res. 10:905155. doi: 10.3389/fenrg.2022.905155

1 INTRODUCTION

In recent years, as the pace of global carbon reduction has accelerated, China's "carbon neutrality" task has clarified the direction of China's energy transition. It is imperative to develop clean and sustainable renewable energy. As an efficient, non-polluting, zero-emission renewable energy source, wind energy has become an important measure to solve the energy crisis. However, wind's intermittent and random nature causes uncertainty and instability in wind power generation, which leads to difficulties in dispatching and low efficiency in grid connection (Quan et al., 2019; Santhosh et al., 2020; Maldonado-Correa et al., 2021). Accurate wind power forecast is beneficial to optimize the operation and dispatch of power systems, develop reasonable control strategies, improve energy storage efficiency and maximize economic benefits (Zhang et al., 2021, 2017). Therefore, timely and accurate wind forecasts are essential for the safe operation of the grid and the planning of electricity market transactions (Wang et al., 2017; Han et al., 2018).

For time scale, wind power forecast includes ultra-short-term, short-term, medium-term and long-term power forecast (Tian, 2021). Ultra-short-term forecast is used to predict power generation in the next few hours based on historical data, which is helpful for controlling the daily operation of wind farm units. Short-term forecast is used to predict in advance for several hours to several days, which is helpful for the rationality of the economic system and maintenance of the wind turbine. The medium-long term forecast is used to predict in advance for several days to several months,which is helpful for making quarterly power generation plans for grid and wind farm construction (Ju et al., 2019; Li L. et al., 2020).

Due to the uncertainty of the wind power system, the time scale of the current wind power prediction results mostly focuses on the short-term forecast (Tian, 2021). The physical, statistical, artificial intelligence and ensemble methods are usually used to forecast short-term wind power (Hanifi et al., 2020). The physical model uses micro-scale meteorology and fluid mechanics to convert the numerical weather forecast (NWP) data into wind speed, and wind direction data at the height of the wind turbine and finally matches the wind turbine power curve. The prediction accuracy of the physical model mainly depends on the accuracy of the numerical weather forecast (NWP) data and the accuracy of the geographical environment around the wind farm (Rodríguez et al., 2020). The statistical method is based on historical wind power data through curve fitting and parameterization methods to predict wind power. Hao (2019) designed an extreme learning machine prediction method based on variational mode decomposition feature extraction. The ELM model is optimized with a multi-objective gray wolf optimizer using historical wind power time series data as input. Finally, a high-precision wind power prediction time series hybrid model is obtained. Zameer et al. (2015) proposed a new short-term wind power prediction method based on the machine learning method (STWP). This method combines machine learning technology with feature selection and regression. The proposed method is a hybrid maximum likelihood model, which uses feature selection through irrelevant and redundant filters, and then uses a support vector regression machine for auxiliary prediction, And finally realizes wind power forecasting. Sideratos and Hatziargyriou (2020) proposed an improved radial basis function neural network for wind power prediction. The method has better results than others, but the iterative convergence process is longer. Liu et al. (2018) proposed a short-term wind speed and wind prediction model based on singular spectrum analysis and Locality-sensitive Hashing (LSH). To deal with the high volatility of the original time series, SSA is used to decompose it into two components. The two components are reconstructed in the phase space to obtain the average trend and fluctuation components. Then, LSH is used to select similar segments of the intermediate trend segment for local prediction, thereby improving the accuracy and efficiency of prediction.

The above methods, mainly from the perspective of clustering, combination, deep neural network, and other considerations, improve wind power prediction accuracy. The choice of hyperparameters in the algorithm is also crucial. The same algorithm with different datasets and different hyperparameters can have additional prediction precision. Therefore, this article proposed a new short-term wind power forecast mehtod named BH-XGBoost, which sets up Hyper-parameter optimization during the model training process to optimize and improve the performance of XGBoost (Yang et al., 2019; Zheng and Wu, 2019). Finally, BH-XGBoost is verified through wind farm turbine data and numerical weather forecast data.

The remainder of this article is arranged as follows. **Section 2** introduced the dataset used in this study. **Section 3** described the method of BH-XGBoost. Results and discussion in **Section 4** and conclusion in **Section 5**.

2 DATA

2.1 Wind Farm Data

In order to verify the effectiveness of the proposed method, the real data of a wind farm is employed to test the BH-XGBoost method. The target wind farm locates on the east coast of Jiangsu province in China (as shown in **Figure 1**). The wind farm data includes the historical wind power of each wind farm and wind speed from SCADA system of the wind turbines, and all the data were subjected to strict quality control. The target wind farm has 100 wind turbines with 2 MW rated power, and the hub height of the wind turbine is 100 m. The frequency of the power and wind data collection is 15 min from October 2020 to December 2021.

2.2 Numerical Weather Forecast Data

In this study, Numerical weather forecasting (NWP) is employed to provide weather data for the next 1–3 days. NWP is based on the actual conditions of the atmosphere. Given initial conditions and boundary conditions, numerical calculations are carried out by large-scale computers, and atmospheric motion equations are solved numerically. The atmospheric state at the initial time is known to predict the initial state of the future moment. The numerical weather prediction system is based on Weather Research and Forecast (WRF), a mesoscale weather model. It mainly realizes a small area weather forecast with a resolution of fewer than 10 km and a time scale of 3 days. The WRF model has advanced data assimilation technology, powerful nesting capabilities, and advanced physical processes. High-quality NWP data can improve the forecast accuracy of the short-term wind power prediction greatly. The NWP data of the target wind farm is from the China Meteorological Administration (CMA), which is updated twice a day with a temporal resolution of 15 min, the spatial resolution is 1.0 km × 1.0 km, and for a predicted length of 144 h. The output of the NWP elements includes wind speed (m/s), temperature (°C), relative humidity (%), and pressure (hPa). **Figure 2** is the basic flow chart of the WRF model for this research.

3 METHODS

3.1 XGBoost Algorithm

The XGBoost algorithm (eXtreme Gradient Boosting) is optimized and improved based on the gradient progressive regression tree algorithm. Once it appeared, it has received widespread attention for its excellent learning effect and efficient training model speed (Kumar et al., 2020; Phan et al., 2020). The algorithm can effectively construct a boosting tree and perform parallel operations while effectively using the multi-threading of the CPU. This algorithm has achieved excellent results in Kaggle's Higgs sub-signal recognition competition and has been widely concerned. Its core is to pre-order all features and enhances classification trees and decision trees. XGBoost is an integrated model consisting of k decision trees, the predicted value is calculated from:

$$\hat{y}_i = \sum_{t=1}^{k} f_t(x_i), \tag{1}$$

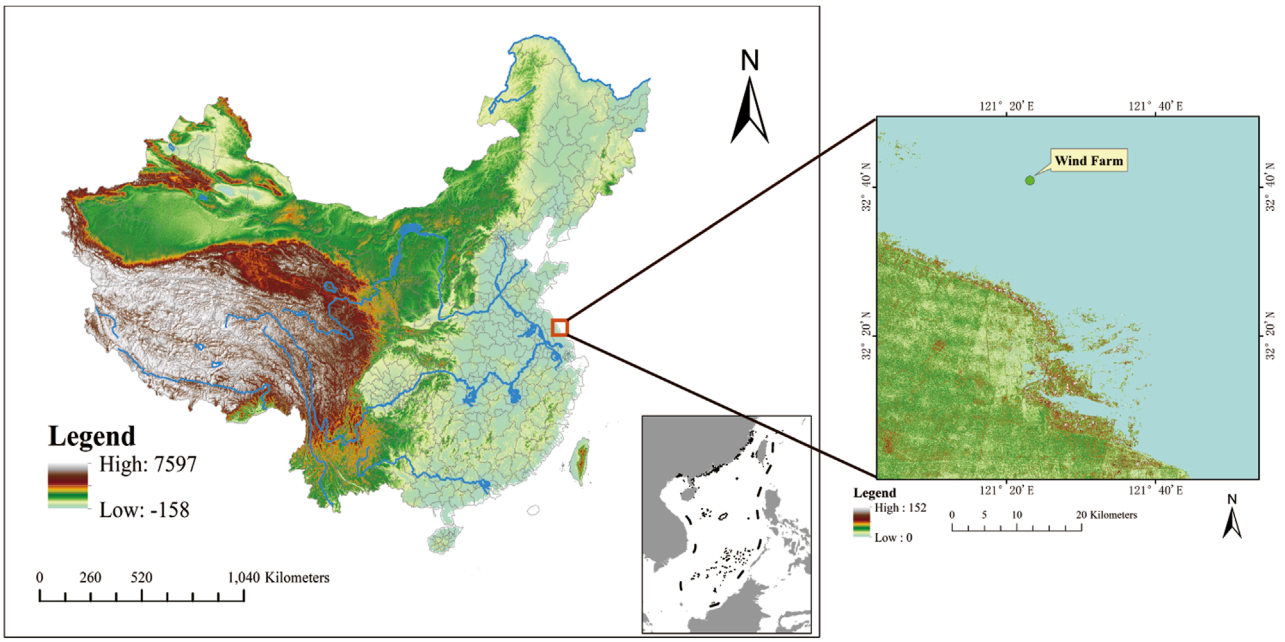

FIGURE 1 | The location of the target wind farm.

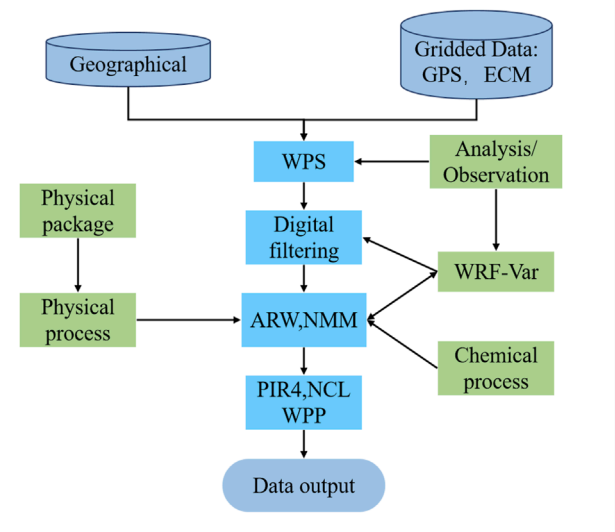

FIGURE 2 | The flow chart of WRF model.

$\hat{y}_i$ is the predicted value of x_i. f_t represents a decision tree, and $f_t(x_i)$ is the predicted value of f_t given x_i. Then the loss function L can be expressed in terms of predicted value $\hat{y}_i$ and true values y_i:

$$L = \sum_{i=1}^{n} l(y_i, \hat{y}_i). \tag{2}$$

To avoid overfitting and improve the model's generalization ability, the regular term Ω is usually added to the equation. The loss function can be rewritten as **Eq. 3**, and the regular term $\Omega(f_t)$ define as **Eq. 4**, where T denotes the number of leaf nodes and $w_j$refers to the weight of the jth leaf node.

$$Obj = \sum_{i=1}^{n} l(\hat{y}_i, y_i) + \sum_{t=1}^{k} \Omega(f_t), \tag{3}$$

$$\Omega(f_t) = \gamma T + \frac{1}{2}\lambda \sum_{j=1}^{T} w_j^2. \tag{4}$$

XGBoost uses a forward addition strategy where each time the model adds a decision tree, it learns a new function and its coefficients to fit the residuals of the last step of the prediction. Therefore, using the model at step t as an example, the prediction for the ith sample x_i is as **Eq. 5** and the object function of step t is as **Eq. 6**.

$$\hat{y}_i^t = \hat{y}_i^{t-1} + f_t(x_i), \tag{5}$$

$$\mathrm{Obj}^{(t)} = \sum_{i=1}^{n} L(y_i, \hat{y}^{t-1} + f_t(x_i)) + \Omega(f_t). \tag{6}$$

Use Taylor expansion to expand the above equation:

$$\mathrm{Obj}^{(t)} \approx \sum_{i=1}^{n} \left[L(y_i, \hat{y}^{t-1}) + g_i f_t(x_i) + \frac{1}{2} h_i f_t^2(x_i) \right] + \Omega(f_t). \tag{7}$$

Among them, g_i represents the first derivative of $L(y_i, \hat{y}^{t-1})$ to $\hat{y}^{t-1}$, and h_i represents the second derivative of $(y_i, \hat{y}^{t-1})$ to $\hat{y}^{t-1}$. In addition, you can merge the same function values on the same leaf node. So the final deduced result is:

$$w_j = -\frac{G_j}{H_j + \lambda}. \tag{8}$$

Therefore, substituting w_j into the objective function is simplified as:

$$\mathrm{Obj}^{(t)} = -\frac{1}{2}\sum_{j=1}^{T}\frac{G_j^2}{H_j+\lambda} + \gamma T + C. \tag{9}$$

The above equation simplifies the objective function. It is evident that XGBoost can customize the objective function, use only the first derivative and the second derivative in the calculation process, and obtain the simplified equation. XGBoost parameter selection is significant. **Table 1** shows the specific parameter types of the XGBoost algorithm (Zheng et al., 2017; Li K. et al., 2020).

The parameters max_depth and learing_rate will determine the performance of the XGBoost algorithm model.

3.2 Hyper-Parameter Principle

Hyper-parameter is the frame parameters in the machine learning model. The hyper-parameters are the number of classes in the clustering method, the number of topics in the topic model, etc. Machine learning algorithms have been widely used in various fields. Its hyper-parameter must be adjusted to adapt the machine learning model to different problems (Zhou et al., 2017; Huang et al., 2021).

In this article, Bayesian hyper-parameter optimization is selected. The goal of network learning is to determine the mapping $y = f(x, \theta)$, y is the output, x is the input vector, and the vector determines the size of the mapping. The main idea of Bayesian optimization is adjusting the hyper-parameter of a given model to establish a probability model of the objective function. Using the acquisition function to perform an effective search before selecting the optimal hyper-parameter set and selecting the optimal hyper-parameter set (Wang et al., 2021). Taking the hyper-parameter θ in GBRT as a point in the multidimensional space for optimization, the hyper-parameter θ that minimizes the loss function value $f(\theta)$ can be found in the set $A \in X^d$, as shown in the following equation:

$$\theta^* = \arg\min_{\theta \in A} f(\theta). \tag{10}$$

There is no prior knowledge about the structure of UNKNOWN, it is assumed that the noise in the observation is:

$$y(\theta) = f(\theta) + \varepsilon, \text{ and } \varepsilon \sim N\left(0, \sigma^2_{\text{noise}}\right). \tag{11}$$

The Bayesian framework includes two basic options. First, a prior function $p(f|D)$ (called a hypothesis function) must be selected to represent the hypothesis of the function to be optimized. Secondly, the posterior model establishes the acquisition function to determine the next test point.

The Bayesian framework uses hypothesis function $p(f|D)$ to build an objective function model based on the observed data sample D. Based on the current $p(f|D)$ model, The model chooses between optimization and development (Kotthoff et al., 2019). The main distinction of the Bayesian optimization model is the difference in surrogate functions, which generally include Tree Parzen Estimator (TPE), Random Forest, and Gaussian Process (Yoo, 2019).

3.3 BH-XGBoost Method

In this study, the hyperparameters of the XGBoost are optimized via Bayesian theory for the short-term wind power forecast. **Figure 3** shows the workflow of the new method (BH-XGBoost). Before training, define the search space of each hyper-parameters based on XGBoost. The init hyper-parameters values from the search space are chosen randomly for the first iteration.

After the first iteration, the metric results, such as MAE, MSRE, etc., will be input to the hyper-parameters algorithm. The bayesian algorithm integrates the history-measured results and searches space, and outputs each hyper-parameters value. The algorithm will kick off a new iteration while receiving the new hyper-parameters values. The algorithm will stop until the validation error is less than the threshold we set.

4 RESULTS AND DISCUSSION

4.1 Hyper-Parameter Optimization

This article defines the four seasons based on month, Jan. for spring, Apr. for summer, Jul. for Autumn, and Oct. for Winter. The data of the first 10 days from each month are selected as the

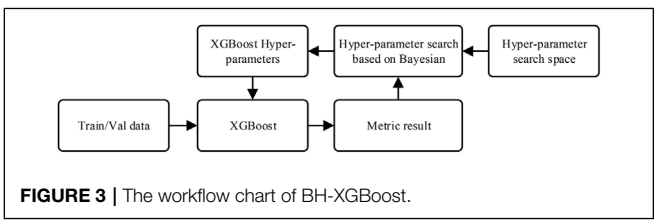

FIGURE 3 | The workflow chart of BH-XGBoost.

TABLE 1 | XGBoost various parameters.

Parameter	Effect	Parameter Value Setting
max_depth	Control overfitting	Given the depth of the tree, the default is 3
learing_rate	Symbolic model generalization ability	The weight/learning rate of the model produced in each iteration. The default is 0.1
n_estimators	Control the scale of random forest algorithm	The number of submodels, the default is 100
n_jobs	Number of CPUs called by the algorithm	Select the number of linear parallel construction Xgboost models, the default is 1
reg_alpha	Convergence rate of control algorithm	L1 is the weight of the regular term, the default is 0
reg_alpha	Convergence rate of control algorithm	L2 is the weight of the regular term, the default is 1

TABLE 2 | XGBoost various parameters.

Hyperparameter	Jan.	Apr.	Jul.	Oct.
max_depth	5	8	7	6
learing_rate	0.153	0.158	0.136	0.174
n_estimators	98	97	96	103
min_child_weight	7.52	8.76	9.43	8.65

test dataset and the remaining data as the training dataset for next month. The Bayesian hyper-parameter optimization method is employed to determine the optimal XGBoost parameters. Different data sets have different selection parameters. XGBoost simplifies the model due to the addition of regularization items. At the same time, it combines the actual situation with proper pruning in the later stage, which further improves the model's efficiency to obtain the best value. While improving the accuracy, XGBoost uses the CPU's multi-threading to carry out parallel calculations during the application process, which significantly reduces the training time. However, the shortcoming of XGBoost is that it must traverse the entire training set in each iteration cycle. In the pre-sorting step, XGBoost retains the eigenvalues of the training dataset while retaining the evaluation results of the eigenvalues. Hyperparameter optimization searches effectively via selecting the optimal hyperparameter set and optimizing the XGBoost algorithm's parameters as points in the multidimensional space to achieve the optimal effect of the model. In this paper, Bayesian hyper-parameter optimization is used to improve XGBoost. The input function is XGBoost hyperparameters, such as max_depth (range from 3 to 30), learing_rate (range from 0.1 to 0.15), and n_estimators (range from 100 to 1,000). The output model uses the root mean square error to solve the objective function and cross-validate. **Table 2** lists the best parameters of the model for each month. The optimized parameters obtained in the default range are also different. The four data sets have no significant differences in sub-models and the maximum depth. There are differences in other model parameters. In addition, due to the various constraints between the hyperparameters, the model error will also increase as the number of adjustment parameters becomes larger. Therefore, the other model hyperparameters are randomly selected in this article.

4.2 Sensitivity Analysis for Different Cases

In order to evaluate the new method, XGBoost, SVM, KELM, ELM, and LSTM are employed to compare the performance of BH-XGBoost. **Table 3** shows the comparison results of different methods. **Table 3** shows that the proposed method is more accurate than other methods. **Table 3** describes the distribution of the three metrics for different methods and months. It illustrates that the root means square error (RMSE) obtained by BH-XGBoost is 21% lower than others for Jan. All the results of RMSE from other methods are around 11.7. Especially in Jul. and Oct., the proposed method is considerably better than the other methods. Also, the same results can be seen from MAE and R-square for all the cases. The results demonstrate that the proposed method is superior to the traditional machine learning methods for all the months.

TABLE 3 | The performance of different methods for three metrics.

Method	Metric	Jan.	Apr.	Jul.	Oct.
BH-XGBoost	RMSE (MW)	9.29	12.45	8.99	8.66
	MAE (MW)	6.52	9.95	9.32	8.06
	R-square	0.64	0.73	0.68	0.80
XGBoost	RMSE (MW)	11.76	15.17	10.01	11.02
	MAE (MW)	8.93	12.66	11.15	10.89
	R-square	0.63	0.54	0.61	0.50
SVM	RMSE (MW)	11.74	17.16	12.51	12.02
	MAE (MW)	9.02	15.22	12.00	11.89
	R-square	0.59	0.42	0.50	0.61
KELM	RMSE (MW)	11.77	17.06	18.75	19.52
	MAE (MW)	9.01	13.99	13.20	12.42
	R-square	0.58	0.46	0.62	0.53
LSTM	RMSE (MW)	11.74	17.09	18.72	16.89
	MAE (MW)	9.02	14.03	15.36	14.95
	R-square	0.58	0.48	0.58	0.62

Figure 4 compares the forecast results of the different methods for different cases. **Figure 4** (a)-(d) show that the BH-XGBoost method obviously outperformance the other methods for all the cases. The forecast results curve of BH-XGBoost is the closest to the observed curve, especially in the highlighted region 1 of the callout. As the highlighted region 2 of **Figure 4** (b),(d) shows, the results demonstrate that the BH-XGBoost method is superior to the other methods when the wind speed changes drastically and significantly. The BH-XGBoost method can be well adapted to both short-term wind power and ramp events caused by extreme weather conditions. Also, in the highlighted region 3 of the callout of **Figure 4** (a),(c), notice that the performance of the BH-XGBoost method is better than the performance of other methods over the low wind speed. Thus, the proposed method can effectively provide wind energy utilization via the results of efficient wind power forecasting for all the cases.

Figure 5 illustrates the regression between observed and forecast power data for two special cases: **Figure 5A** for wind speed changes drastically, **Figure 5B** for low wind speed. Using the proposed method, the slope of the regression line has tiny gaps against the observations, which is better than the other methods (**Figure 5A**). Both in **Figure 5A** and **Figure 5B**, the SVM, ELM and XGBoost methods almost have the same performance. In **Figure 5B**, the slope of the regression for the BH-XGBoost method is not as good as the performance in **Figure 5A**, but considerably better than the other methods. This method is reasonable because the BH-XGBoost method has the advantages of optimal parameters, which can better simulate wind turbines' power generation law.

In this article, the residual boxplot is employed to analyze the center position and degree of dispersion of the residual result obtained by the different methods against the observation. **Figure 6A**-(d) illustrate that the residual box of BH-XGBoost outperforms others, especially in **Figure 6B** while the median line is infinitely close to 0. And the performance of SVM, ELM and XGBoost are similar to each other, which also can be proved

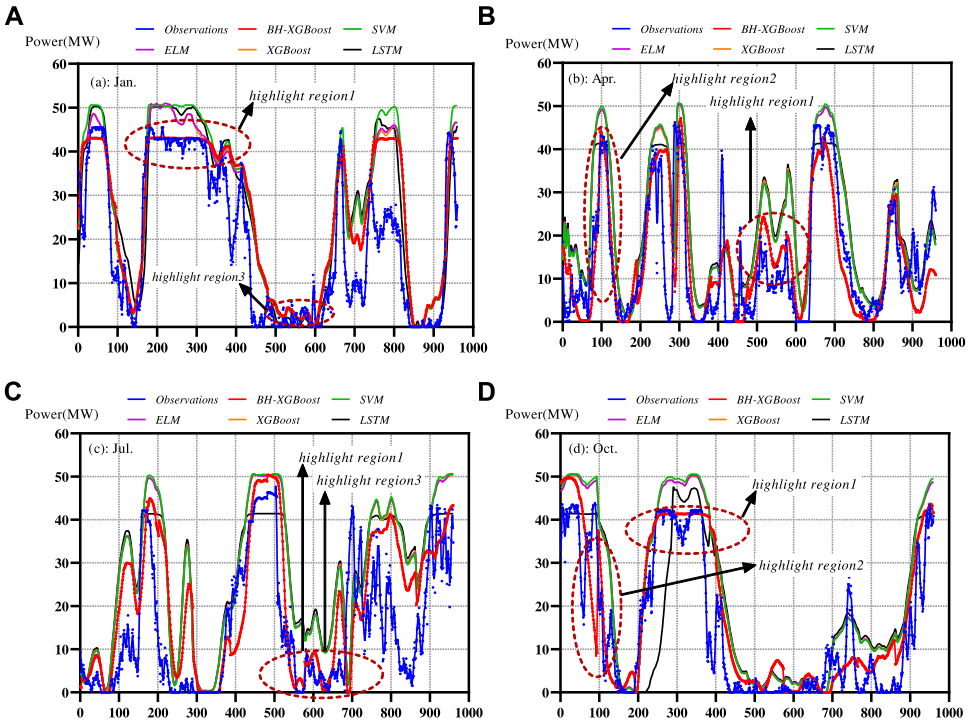

FIGURE 4 | Examples of performance of the different methods for different cases: **(A)** Jan., **(B)** Apr., **(C)** Jul., **(D)** Oct.

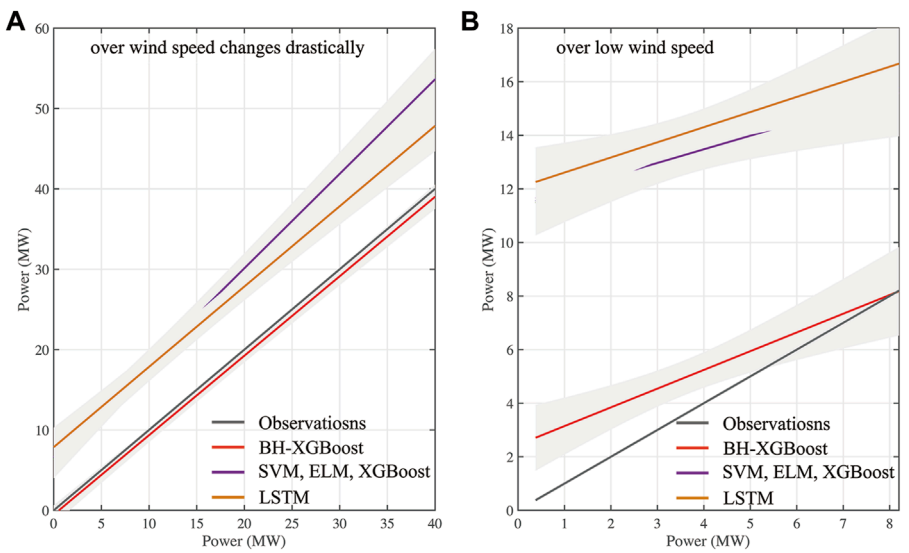

FIGURE 5 | Comparison of observed to forecast power data for different methods over two special cases: **(A)** over wind speed changes drastically, **(B)** over low wind speed.

to form the distribution of outliers in **Figure 6D**. More, the residuals of the proposed method are most concentrated among all the methods as the width of the residual box is the smallest. From **Figure 6A**-(d), the forecast results are generally higher than the observations. The reason is that there are power cuts and maintenance in the actual process of wind farm power generation. From the distribution of outliers, the proposed method also seems to perform better. In **Figure 6A**, (b), (d), the outliers that deviate from the maximum and minimum values are more homogeneous against the other methods. Noticed that all the outliers are below the minimum values in **Figure 6C**. A possible explanation for these is that the target farm is located in

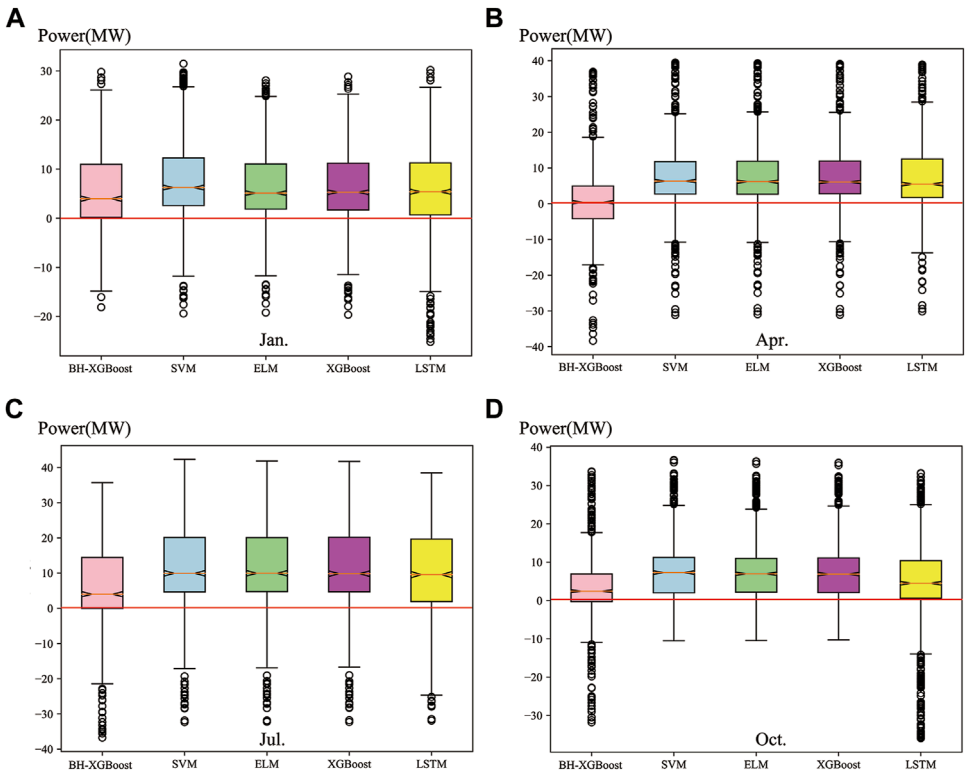

FIGURE 6 | The residual boxplot of the result obtained by the different methods against the observation for different cases: **(A)** Jan., **(B)** Apr., **(C)**Jul., **(D)**Oct.

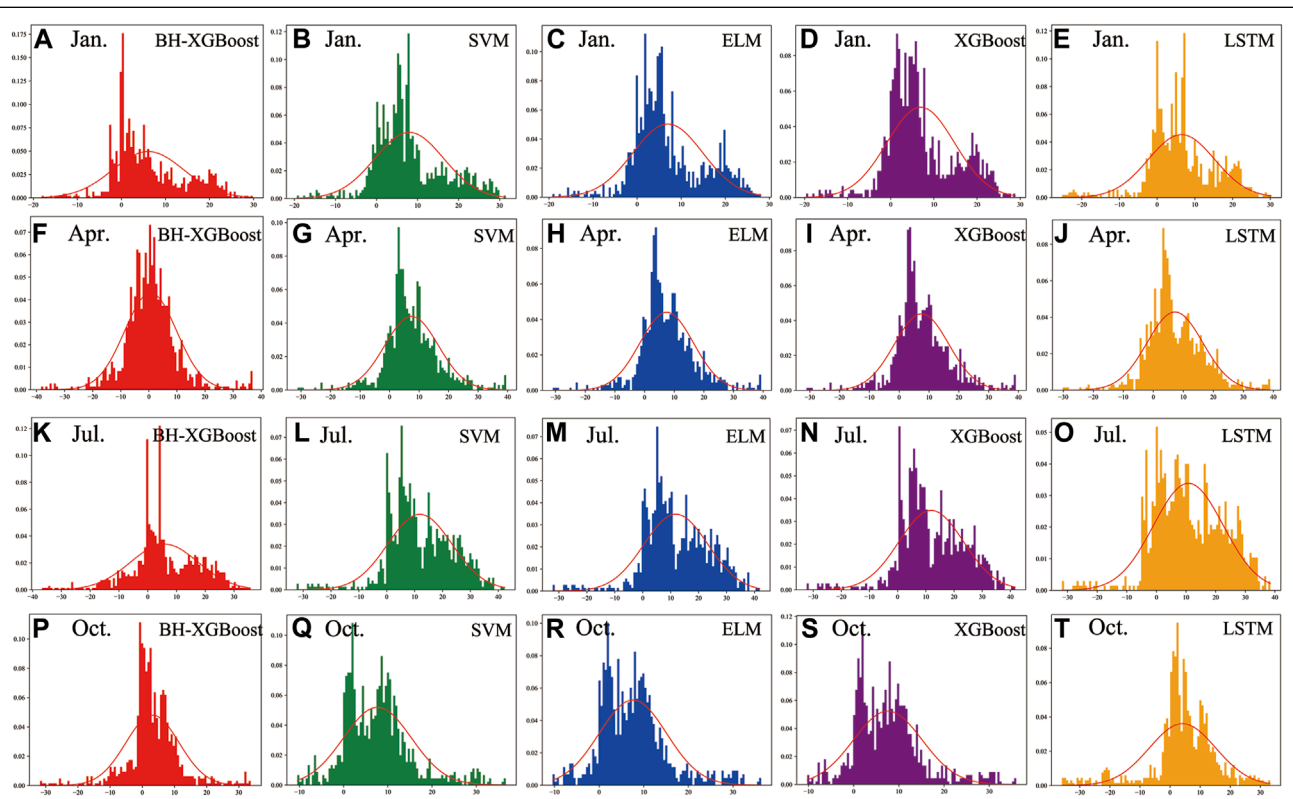

FIGURE 7 | The residual distribution of the different methods for different cases: **(A–E)** for Jan., **(F–J)** for Apr., **(K–O)** for Jul., **(P–T)** for Oct.

the eastern coastal area of Chins, which is affected by the western Pacific Subtropical High in summer. In summer, the wind speed of the wind farm shows irregular and violent changes in the low wind speed range.

In order to verify the advantage of the proposed method, **Figure 7** presents the residual distribution of the different methods for four different months. For all the cases, the kurtosis of the distribution curve for BH-XGBoost is lower than the other curves, and all the skewness of distribution curves is relatively positive. In **Figures 7F,K**, the residual distribution obtained by BH-XGBoost conforms to the normal distribution which means that the proposed algorithm has better robustness.

5 CONCLUSION

A new short-term wind power forecast method based on XGBoost is explored in this article. The proposed method utilizes a Bayesian optimization hyperparameter, which can create the best-fit regression between the wind speed from WRF and the power from the target wind farm. To evaluate the new method, SVM, ELM, XGBoost and LSTM are employed to compare the performance of BH-XGBoost. For the case study results, the BH-XGBoost was significantly better than other methods. This method is reasonable because BH-XGBoost, as hyperparameter optimization based on Bayesian, yields the best-fit regression while other methods do not optimize hyperparameters according to the characteristics of the target wind farm.

Compared with other methods, the proposed method can effectively improve the accuracy of wind power forecasting especially in the cases of wind ramp events caused by extreme weather conditions and low wind speed ranges. For all the cases, the results of the RMSE, MAE and R-square show that the proposed method outperforms other methods. As expected, when the physics are spatially coherent, the methods work well, but when local spatiotemporal scale strong convective weather conditions dominate, the methods do not work. Thus, in future research, we will improve and test the BH-XGBoost method over more data and regions by integrating more meteorological elements, mainly when extreme events occur.

DATA AVAILABILITY STATEMENT

The original contributions presented in the study are included in the article/Supplementary Material, further inquiries can be directed to the corresponding author.

AUTHOR CONTRIBUTIONS

XX and XG contributed to the conception and design of the study. XW and RZ organized the database. PZ performed the statistical analysis. XX wrote the first draft of the manuscript. All authors contributed to manuscript revision, read, and approved the submitted version.

FUNDING

This research was partially supported by the Natural Science Foundation of Jiangsu Province under Grant no. BK20210661; Foundation of Jiangsu Rail Transit Industry Development Collaborative Innovation Base under Grant no. GCXC2105; Foundation of Collaborative Innovation Center on High-speed Rail Safety of Ministry of Education under Grant no. GTAQ2021001.

REFERENCES

Han, L., Romero, C. E., Wang, X., and Shi, L. (2018). Economic Dispatch Considering the Wind Power Forecast Error. *IET Gener. Transm. & Distrib.* 12, 2861–2870. doi:10.1049/iet-gtd.2017.1638

Hanifi, S., Liu, X., Lin, Z., and Lotfian, S. (2020). A Critical Review of Wind Power Forecasting Methods-Past, Present and Future. *Energies* 13, 3764. doi:10.3390/en13153764

Hao, Y., and Tian, C. (2019). A Novel Two-Stage Forecasting Model Based on Error Factor and Ensemble Method for Multi-step Wind Power Forecasting. *Appl. energy* 238, 368–383. doi:10.1016/j.apenergy.2019.01.063

Huang, H., Jia, R., Shi, X., Liang, J., and Dang, J. (2021). Feature Selection and Hyper Parameters Optimization for Short-Term Wind Power Forecast. *Appl. Intell.* 51, 6752–6770. doi:10.1007/s10489-021-02191-y

Ju, Y., Sun, G., Chen, Q., Zhang, M., Zhu, H., and Rehman, M. U. (2019). A Model Combining Convolutional Neural Network and Lightgbm Algorithm for Ultra-short-term Wind Power Forecasting. *Ieee Access* 7, 28309–28318. doi:10.1109/access.2019.2901920

Kotthoff, L., Thornton, C., Hoos, H. H., Hutter, F., and Leyton-Brown, K. (2019). "Auto-weka: Automatic Model Selection and Hyperparameter Optimization in Weka," in *Automated Machine Learning* (Cham: Springer), 81–95. doi:10.1007/978-3-030-05318-5_4

Kumar, D., Abhinav, R., and Pindoriya, N. (2020). "An Ensemble Model for Short-Term Wind Power Forecasting Using Deep Learning and Gradient Boosting Algorithms," in 2020 21st National Power Systems Conference (NPSC) (Gandhinagar, India: IEEE), 1–6. doi:10.1109/npsc49263.2020.9331902

Li, K., Huang, D., Tao, Z., Li, H., Xiong, H., and Du, Y. (2020a). "Short-term Wind Power Prediction Based on Integration of Feature Set Mining and Two-Stage Xgboost," in *The Purple Mountain Forum on Smart Grid Protection and Control* (Berlin, Germany: Springer), 64–81.

Li, L., Li, Y., Zhou, B., Wu, Q., Shen, X., Liu, H., et al. (2020b). An Adaptive Time-Resolution Method for Ultra-short-term Wind Power Prediction. *Int. J. Electr. Power & Energy Syst.* 118, 105814. doi:10.1016/j.ijepes.2019.105814

Liu, L., Ji, T., Li, M., Chen, Z., and Wu, Q. (2018). Short-term Local Prediction of Wind Speed and Wind Power Based on Singular Spectrum Analysis and Locality-Sensitive Hashing. *J. Mod. Power Syst. Clean. Energy* 6, 317–329. doi:10.1007/s40565-018-0398-0

Maldonado-Correa, J., Solano, J., and Rojas-Moncayo, M. (2021). Wind Power Forecasting: A Systematic Literature Review. *Wind Eng.* 45, 413–426. doi:10.1177/0309524x19891672

Phan, Q.-T., Wu, Y.-K., and Phan, Q.-D. (2020). "A Comparative Analysis of Xgboost and Temporal Convolutional Network Models for Wind Power Forecasting," in 2020 International Symposium on Computer, Consumer and Control (IS3C) (Taichung City, Taiwan: IEEE), 416–419. doi:10.1109/is3c50286.2020.00113

Quan, H., Khosravi, A., Yang, D., and Srinivasan, D. (2019). A Survey of Computational Intelligence Techniques for Wind Power Uncertainty Quantification in Smart Grids. *IEEE Trans. neural Netw. Learn. Syst.* 31, 4582–4599.

Rodríguez, F., Florez-Tapia, A. M., Fontán, L., and Galarza, A. (2020). Very Short-Term Wind Power Density Forecasting through Artificial Neural Networks for Microgrid Control. *Renew. energy* 145, 1517–1527.

Santhosh, M., Venkaiah, C., and Vinod Kumar, D. (2020). Current Advances and Approaches in Wind Speed and Wind Power Forecasting for Improved Renewable Energy Integration: A Review. *Eng. Rep.* 2, e12178. doi:10.1002/eng2.12178

Sideratos, G., and Hatziargyriou, N. D. (2020). A Distributed Memory Rbf-Based Model for Variable Generation Forecasting. *Int. J. Electr. Power & Energy Syst.* 120, 106041. doi:10.1016/j.ijepes.2020.106041

Tian, Z. (2021). A State-Of-The-Art Review on Wind Power Deterministic Prediction. *Wind Eng.* 45, 1374–1392. doi:10.1177/0309524x20941203

Wang, C., Wang, H., Zhou, C., and Chen, H. (2021). Experiencethinking: Constrained Hyperparameter Optimization Based on Knowledge and Pruning. *Knowledge-Based Syst.* 223, 106602. doi:10.1016/j.knosys.2020.106602

Wang, Y., Zhou, Z., Botterud, A., and Zhang, K. (2017). Optimal Wind Power Uncertainty Intervals for Electricity Market Operation. *IEEE Trans. Sustain. Energy* 9, 199–210.

Yang, L., Li, Y., and Di, C. (2019). "Application of Xgboost in Identification of Power Quality Disturbance Source of Steady-State Disturbance Events," in 2019 IEEE 9th International Conference on Electronics Information and Emergency Communication (ICEIEC) (Beijing, China: IEEE), 1–6. doi:10.1109/iceiec.2019.8784554

Yoo, Y. (2019). Hyperparameter Optimization of Deep Neural Network Using Univariate Dynamic Encoding Algorithm for Searches. *Knowledge-Based Syst.* 178, 74–83. doi:10.1016/j.knosys.2019.04.019

Zameer, A., Khan, A., and Javed, S. G. (2015). Machine Learning Based Short Term Wind Power Prediction Using a Hybrid Learning Model. *Comput. Electr. Eng.* 45, 122–133.

Zhang, C., He, Y., Yuan, L., and Xiang, S. (2017). Capacity Prognostics of Lithium-Ion Batteries Using Emd Denoising and Multiple Kernel Rvm. *IEEE Access* 5, 12061–12070. doi:10.1109/access.2017.2716353

Zhang, C., Zhao, S., and He, Y. (2021). An Integrated Method of the Future Capacity and Rul Prediction for Lithium-Ion Battery Pack. *IEEE Trans. Veh. Technol.* 71, 2601.

Zheng, H., and Wu, Y. (2019). A Xgboost Model with Weather Similarity Analysis and Feature Engineering for Short-Term Wind Power Forecasting. *Appl. Sci.* 9, 3019. doi:10.3390/app9153019

Zheng, H., Yuan, J., and Chen, L. (2017). Short-term Load Forecasting Using EMD-LSTM Neural Networks with a Xgboost Algorithm for Feature Importance Evaluation. *Energies* 10, 1168. doi:10.3390/en10081168

Zhou, C., Tang, W., Tang, W., and Zhao, R. (2017). Optimal Consumption with Reference-Dependent Preferences in On-The-Job Search and Savings. *J. Industrial Manag. Optim.* 13, 505–529. doi:10.3934/jimo.2016029

Conflict of Interest: Authors XX and RZ are employed by Nanjing University of Information Science and Technology, authors XG and PZ are employed by Hangzhou Dianzi University, author XW is employed by Guohua (Hami) New Energy Co., Ltd.

The remaining authors declare that the research was conducted in the absence of any commercial or financial relationships that could be construed as a potential conflict of interest.

frontiers | Frontiers in Energy Research

ORIGINAL RESEARCH
published: 10 May 2022
doi: 10.3389/fenrg.2022.875785

Adaptive Under-Frequency Load Shedding Control Strategy of Power Systems With Wind Turbines and UHVDC Participating in Frequency Regulation

Xingyang Wu[1], Feng Xue[2], Jianfeng Dai[3] and Yi Tang[4]*

[1]College of Energy and Electrical Engineering, Hohai University, Nanjing, China, [2]NARI Group Corporation (State Grid Electric Power Research Institute), Nanjing, China, [3]College of Automation and College of Artificial Intelligence, Nanjing University of Post and Telecommunication, Nanjing, China, [4]School of Electrical Engineering, Southeast University, Nanjing, China

Represented by wind turbines and ultra high-voltage DC (UHVDC), the power-electronic interfaced power sources participate in fast frequency control, which has a significant impact on the power system frequency. However, the conventional under-frequency load shedding (UFLS) scheme doesn't take into account the impact above, resulting in unreasonable load shedding after a large loss of generation. To this end, this article proposes an adaptive UFLS control strategy of power systems with wind turbines and UHVDC participating in frequency regulation. Firstly, based on the virtual inertia control model and the primary frequency control model of wind turbines and UHVDC, the study establishes the simplified frequency response model of the power system considering the participation of wind turbines and UHVDC in frequency regulation. Furthermore, the impact of the active power response characteristics of wind turbines and UHVDC participating in frequency regulation on the magnitude of the active power deficiency is comprehensively analyzed. Thus the precise estimation of the magnitude of the power deficiency can be achieved, which provides technical guidance for multi-stage UFLS. Finally, simulation results demonstrate that the proposed UFLS strategy is capable of reflecting the power system frequency more objectively after a large loss of generation event. In addition, the proposed UFLS strategy outperforms the conventional UFLS strategy in terms of shedding less amount of load when the same desired effect of frequency recovery is achieved.

Keywords: wind turbines, ultra high-voltage DC, under-frequency load shedding, virtual inertia control, primary frequency control, equivalent inertia constant, actual magnitude of power deficiency

OPEN ACCESS

Edited by:
Xiao Wang,
Wuhan University, China

Reviewed by:
Rafael Mihalič,
University of Ljubljana, Slovenia
Jiejie Huang,
Nantong University, China

****Correspondence:***
Xingyang Wu
wuxingyang@hhu.edu.cn

Specialty section:
This article was submitted to Smart Grids, a section of the journal Frontiers in Energy Research

Received: *14 February 2022*
Accepted: *11 April 2022*
Published: *10 May 2022*

Citation:
Wu X, Xue F, Dai J and Tang Y (2022) Adaptive Under-Frequency Load Shedding Control Strategy of Power Systems With Wind Turbines and UHVDC Participating in Frequency Regulation. Front. Energy Res. 10:875785. doi: 10.3389/fenrg.2022.875785

INTRODUCTION

The global electric power industry has been in a transition towards low-carbon sustainability in recent years. Conventional synchronous generators will be replaced by large-scale renewable energy sources connected to power systems in the future through power electronic devices (Tian et al., 2021). As a significant part of renewable energy generation, the development of wind power presents a large-scale and high-growth trend. By the end of 2020, the global installed capacity of wind power had reached approximately 743 GW, a 53% growth compared to 2019 [Global Wind Energy Council

(GWEC), 2021]. The gradual replacement of the source-side synchronous generators with power electronic devices intensifies the power-electronization of power systems. Considering the characteristics of the reverse space distribution for renewable energy sources and load centers in some countries and regions, it is imperative to develop long-distance and large-capacity transmission technologies (Pérez-Molina et al., 2020). In China, advanced transmission technologies represented by UHVDC have been applied widely to the promotion of renewable energy consumption and the enhancement of the power supply capacity to load centers. The development of UHVDC transmission accelerates the growth of large-capacity grid-side power electronic devices.

The tendency towards the source- and grid-side power-electronization will dramatically decrease the total system inertia. The frequency stability issues existing in the conventional power systems are becoming more prominent, which is corroborated by incidents such as the blackout in South Australia in September 2016 and the power cut in the U.K. in August 2019 (Australian Energy Market Operator, 2016; National Grid ESO, 2019). To arrest cascading failures and blackouts after a large disturbance occurs in the power grid, UFLS is fully used as the last defense line of the frequency stability control. Generally, we can group all the UFLS schemes into three main categories: conventional UFLS, semi-adaptive UFLS, and adaptive UFLS (Kundur, 2001). In the conventional UFLS schemes, the stages of load shedding, the frequency thresholds of the stages, the time delay, and the load shedding amount are all predefined. Once the frequency drops below the frequency threshold, load shedding is implemented after a certain time delay. The settings of the conventional UFLS schemes derive from assorted presumed power grid parameters including the total system inertia (Horowitz and Phadke, 2008). The time-variant characteristics of the power systems, as well as limited stages and discreteness of load shedding, contribute to the inadaptability of the conventional UFLS schemes to all the system operating conditions. Consequently, it is prone to over- or under-shedding (Sigrist et al., 2012; Rudez and Mihalic, 2016).

To surmount the problems above, numerous scholars have been devoted to the research on semi-adaptive and adaptive UFLS schemes. The load to be shed is determined by the frequency deviation and the rate of change of frequency (RoCoF) in the semi-adaptive UFLS schemes (Anderson and Mirheydar, 1992). In the first stage of load shedding, the amount of load to be shed is calculated based on the swing equation. For the subsequent stages, however, the load shedding amount is predefined. Load shedding is triggered according to the frequency deviation. Hence, semi-adaptive UFLS schemes can not be immune to the problem of inappropriate load shedding. To fill the gap, adaptive UFLS schemes are proposed. The progress of widearea monitoring system (WAMS) technology promotes several adaptive UFLS schemes (Terzija, 2006; Abdelwahid et al., 2014; Tofis et al., 2017). The amount of load shedding is determined by taking advantage of the valuable information provided by WAMS. In addition, numerous scholars pay attention to the thorough and often mathematically complex modification of the entire UFLS (Skrjanc et al., 2021). In (Hoseinzadeh et al., 2015), a voltage deviation of load buses is used to determine the threshold of each UFLS relay. On the contrary, a continuous UFLS scheme to shed loads in proportion to the frequency deviation is proposed in (Li et al., 2020).

It can be observed from the summarization of the research results that, although massive remarkable work has been done from various angles, there are scarcely any studies on the actual impact of the power-electronic interfaced power sources represented by wind power and UHVDC participating in fast frequency control (Eriksson et al., 2018) on UFLS. In modern power systems, wind turbines mainly use rotor speed control to improve the inertia and primary frequency regulation ability of the system, while variable pitch angle control and matching energy storage system are adopted to improve the rotating reserve capacity of wind farms participating in the system frequency regulation (Vidyanandan and Senroy, 2013; Van de Vyver et al., 2016; Ye et al., 2016; Lyu et al., 2019). In (Li et al., 2017), the impact of virtual inertia response, as well as the characteristics of the under-frequency protection and the power output on the UFLS scheme, are investigated. The UFLS scheme is optimized according to the dynamic calculation of the magnitude of the power deficiency. As one of the main power supplies in the future power grid, wind turbines are required to take the responsibility for frequency regulation by many power systems operators. A UFLS scheme considering the virtual inertia response and the primary frequency control of doubly fed induction generator (DFIG)-based wind turbines is proposed in (Li et al., 2019), which reflects the frequency characteristics of the power grid more objectively. Moreover, the amount of load to be shed in the scheme is less. For UHVDC transmission systems, the characteristics of large transmission capacity and fast power regulation speed make it possible to participate in frequency regulation, which is of great significance to ensure the frequency safety of the power grid. The frequency regulation mechanism, response characteristics, parameter tuning method and limiting factors are quite different from those of wind power generation systems. In (Prakash et al., 2019), an auxiliary frequency control strategy with additional frequency control and automatic generation control for HVDC transmission is presented. In (Ambia et al., 2021), a novel adaptive droop control strategy is proposed to provide power sharing and frequency regulation in HVDC systems. Though the research results above are of great significance in supporting the system frequency stability, none of them makes an attempt to use UHVDC transmission systems to provide inertia support. To address the issue, the coordinated frequency control proposed in (Shi et al., 2021) is realized by introducing the virtual inertia control on the basis of the frequency droop control.

From the analysis above, it is obvious that the participation of wind turbines and UHVDC in frequency regulation shows a great favorable influence on the frequency characteristics of the power grid. However, none of the existing UFLS schemes take into account the actual effect of frequency regulation with the participation of wind turbines and UHVDC. On one hand, the virtual inertia response of wind turbines and UHVDC leads to the alteration of the equivalent inertia of the power grid, further influencing the calculation of the magnitude of the power

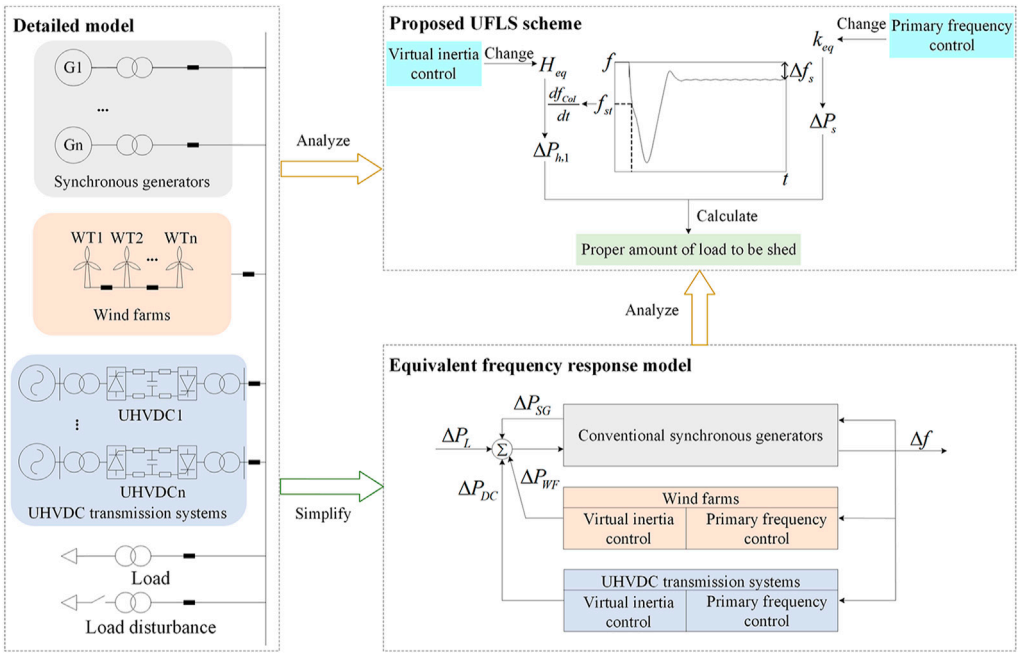

FIGURE 1 | Overall scheme of the proposed UFLS control strategy.

deficiency. On the other hand, the primary frequency control of wind turbines and UHVDC can offset the power deficiency. Ignoring the offset will bring about the problems of over-shedding and economic loss. Therefore, the existing UFLS schemes are not applicable to the modern power system with wind turbines and UHVDC participating in frequency regulation. It is urgent to solve the issue for the sake of the frequency safety of the power grid.

This article proposes an adaptive UFLS control strategy of the power system with wind turbines and UHVDC participating in frequency regulation. Firstly, based on the virtual inertia control model and the primary frequency control model, we establish the simplified frequency response model of the power system considering the participation of wind turbines and UHVDC in frequency regulation. Then the impact of the active power response characteristics of wind turbines and UHVDC participating in frequency regulation on the magnitude of the power deficiency is comprehensively analyzed. Afterward, in light of the estimation result of the magnitude of the power deficiency, the amount of load to be shed in the multi-stage UFLS scheme is determined. Finally, simulation results are presented and discussed to illustrate the outperformance of the proposed UFLS control strategy.

OVERALL SCHEME OF THE PROPOSED UNDER-FREQUENCY LOAD SHEDDING CONTROL STRATEGY

After the integration of a high proportion of wind power and UHVDC, wind turbines and UHVDC participate in frequency regulation by means of virtual inertia control and primary frequency control. However, the existing UFLS schemes do not take into account the situation, which possibly causes frequency trajectory distortion and unreasonable load shedding. To address the issue, this paper proposes an adaptive UFLS control strategy of power systems with wind turbines and UHVDC participating in frequency regulation. The overall scheme of the strategy is shown in **Figure 1**.

It can be seen from **Figure 1** that, this paper firstly simplifies the detailed models of synchronous generators, wind turbines, UHVDC and load. Afterward, the equivalent frequency response model of the power system considering the virtual inertia control and the primary frequency control of the wind turbines and UHVDC is obtained. Based on the detailed models and the equivalent frequency response model, this paper analyzes the two main effects which are brought about by the integration of large-scale wind power and UHVDC on the power grid. For one thing, the virtual inertia control of the wind turbines and UHVDC changes the equivalent inertia constant of the power grid H_{eq}, thus influencing the calculation result of the magnitude of the power deficiency $\Delta P_{h,1}$ when the system frequency reaches the frequency threshold of the first stage f_{st}. For another, after the primary frequency control of the wind turbines and UHVDC is taken into account, ΔP_s refers to the active power provided not only by the primary frequency response of the synchronous generators and the effect of load regulation, but also the primary frequency response of the wind turbines and UHVDC. This impact is reflected in the equivalent power regulation coefficient k_{eq}. This coeffecient k_{eq} includes the unit power regulation of the synchronous generators and the load, as well as the droop control gain of the wind turbines and UHVDC

participating in primary frequency control. Thus ΔP_s needs to be revised when compared to the situation without considering the primary frequency control of the wind turbines and UHVDC. Finally, this paper precisely calculate the amount of load to be shed of UFLS based on $\Delta P_{h,1}$ and ΔP_s to achieve the frequency recovery of the power system.

CONTROL MODELS OF WIND TURBINES AND ULTRA HIGH-VOLTAGE DC PARTICIPATING IN FREQUENCY REGULATION

Control Model of Wind Turbines Participating in Frequency Regulation

Taking DFIG-based wind turbines as an example, the control model of the wind turbines participating in frequency regulation is analyzed and established considering the virtual inertia control and the primary frequency control.

DFIG-based wind turbines lack intrinsic inertia from the system aspect for the reason that their mechanical rotor speed is decoupled with system frequency. However, by introducing an auxiliary virtual inertia control loop in the maximum power tracking loop of the DFIG rotor-side convertor, the wind turbines can also supply the power grid with the virtual inertia response. The rate of change of frequency, i.e. df/dt, is the input of the virtual inertia control. The system frequency drops when the power grid suffers a power deficiency. The virtual inertia control shares part of the power deficiency by rapidly augmenting the active power output of the wind turbines. The active power increment ΔP_{inWF} comes from the released kinetic energy, as expressed in **Eq. 1**. It is conducive to alleviating the sudden change in the frequency of the power grid. The virtual inertia control provides the wind turbines with the ability to support the total system inertia.

$$\Delta P_{inWF} = -k_{inWF}\frac{df}{dt} \tag{1}$$

Where k_{inWF} is the inertia time constant of the wind turbines; f is the system frequency.

Similar to the droop control of synchronous generators, the primary frequency control of the wind turbines is designed in this study. The frequency deviation, i.e. $f - f_{nom}$, is the input of the primary frequency control. When the system frequency drops due to the power deficiency, the active power increment provided by the wind turbines can be expressed as

$$\Delta P_{dWF} = -k_{dWF}\left(f - f_{nom}\right) \tag{2}$$

Where k_{dWF} is the droop control gain of the wind turbines participating in the primary frequency control; f_{nom} is the system nominal frequency.

The control model of the wind turbines participating in frequency regulation combines the virtual inertia control and the primary frequency control holistically. **Figure 2** shows the control block diagram.

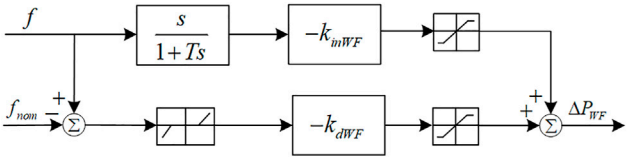

FIGURE 2 | Control block diagram of wind turbines participating in frequency regulation.

In **Figure 2**, T is filter time constant; ΔP_{WF} is the active power increment provided by the control model of wind turbines participating in frequency regulation, as expressed in **Eq. 3**.

$$\Delta P_{WF} = -k_{dWF}\left(f - f_{nom}\right) - k_{inWF}\frac{df}{dt} \tag{3}$$

Control Model of Ultra High-Voltage DC Participating in Frequency Regulation

At present, the participation of UHVDC transmission systems in frequency regulation mainly includes two frequency control modes based on the PI controller and the droop controller, respectively. In this article, the frequency control mode based on the droop controller is used as the primary frequency control of UHVDC. The control block diagram is shown in **Figure 3**.

In **Figure 3**, T_1 and T_2 are filter time constants; k_{dDC} is the proportional coefficient of UHVDC; ΔP_{dDC} is the active power increment of UHVDC participating in primary frequency control.

By introducing the virtual inertia control on the basis of the regular droop control, UHVDC is capable of participating in the process of the system inertia response. It helps to reduce the rate and range of the frequency deviation when the power grid suffers a huge power deficiency. The active power increment ΔP_{DC} provided by UHVDC participating in frequency regulation can be expressed as follows:

$$\Delta P_{DC} = -k_{dDC}\left(f - f_{nom}\right) - k_{inDC}\frac{df}{dt} \tag{4}$$

Where k_{inDC} is the differential coefficient of UHVDC.

Similar to the control model of wind turbines participating in frequency regulation established in Section 3.1, the droop control of UHVDC is mainly in response to the frequency deviation, while the virtual inertia control of UHVDC is mainly in response to the frequency differential quantity. Thus UHVDC can simultaneously participate in the process of the inertia response and the primary frequency control, the same as synchronous generators.

As shown in **Figure 4**, typical HVDC transmission system mainly consists of rectifier station, DC tansmission line and inverter station. In this paper, the virtual inertia control and the primary frequency control of UHVDC can be realized by modifying the UHVDC control systems. P_{DC_ref} is the active power reference value of UHVDC, and P_{DC} is the active power

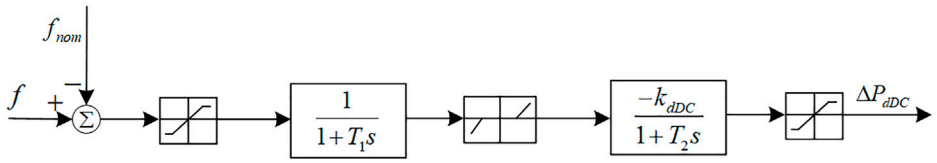

FIGURE 3 | Block diagram of the primary frequency control base on the droop controller of UHVDC.

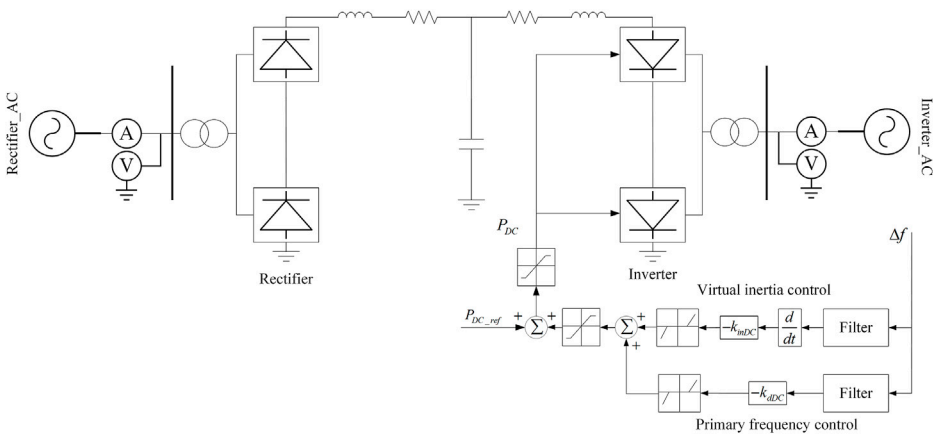

FIGURE 4 | Typical HVDC transmission system with the implementation of virtual inertia control and primary frequency control.

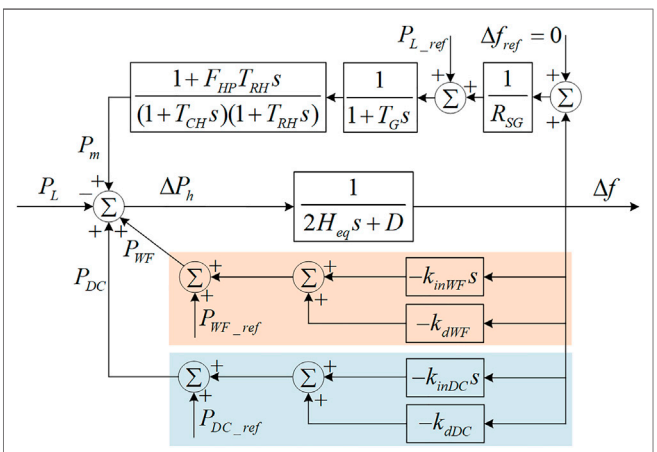

FIGURE 5 | Equivalent frequency response model of the power system.

which needs to be provided by UHVDC. Δf is the system frequency deviation.

The power regulation of UHVDC systems is rapid enough to ensure that the response time is no longer than 150 ms after a power step disturbance occurs. The frequency regulation process of the power system belongs to the electromechanical transient process, of which the timescale is usually second level. Therefore, the regulation process of the UHVDC systems can be neglected in the process of analyzing the UHVDC frequency regulation mechanism, and the UHVDC transmission power strictly tracks the reference command. In addition, the effects of the filtering link, the deadband link, and the power amplitude limiting link are further neglected to simplify the analyzing process.

Based on the analysis above, the equivalent frequency response model of the power system including the virtual inertia control and the primary frequency control of wind turbines and UHVDC is shown in **Figure 5**. Where Δf_{ref} is the system frequency deviation reference value; P_{L_ref} is the load power reference value; R_{SG} is the equivalent droop parameter of the power grid; T_G is the main servo time constant; T_{CH} is the time constant of main inlet volumes and steam chest; T_{RH} is the time constant of reheater; F_{HP} is the fraction of total turbine power generated by high pressure (HP) sections; H_{eq} and D are the inertia constant and the damping coefficient of the equivalent generator of the power grid, respectively; P_m is the mechanical power provided by the synchronous generators in the power grid; P_L is the load power of the power grid; P_{WF_ref} and P_{DC_ref} are the active power reference value of wind power and UHVDC, respectively; P_{WF} and P_{DC} are the active power provided by wind power and UHVDC, respectively; ΔP_h is the actual magnitude of the active power deficiency.

Assume that a sudden increase of load occurs and results in a power deficiency ΔP_{de}. Based on **Figure 5**, the equivalent rotor motion equation of the power system (transferred into the time domain equation) can be represented as

$$2H_{eq}\frac{d\Delta f}{dt} = P_{m0} + \Delta P_m + \Delta P_{WF} + \Delta P_{DC} - P_{e0} - D\Delta f - \Delta P_{de} \tag{5}$$

where P_{m0} and P_{e0} are the initial mechanical power and electromagnetic power of the power system, respectively; ΔP_m is the mechanical power increment provided by the synchronous generators; ΔP_{WF} and ΔP_{DC} are the power increment provided by the wind power and UHVDC, seperately.

ADAPTIVE UNDER-FREQUENCY LOAD SHEDDING CONTROL STRATEGY OF POWER SYSTEMS WITH WIND TURBINES AND ULTRA HIGH-VOLTAGE DC PARTICIPATING IN FREQUENCY REGULATION

The participation of the wind turbines and UHVDC in frequency regulation of the power system affects UFLS mainly from two aspects as follows: 1) The virtual inertia control provides the wind turbines and UHVDC with virtual inertia and changes the equivalent inertia of the power grid, thus influencing the calculation of the magnitude of the power deficiency. 2) The primary frequency control of the wind turbines and UHVDC offsets part of the magnitude of the power deficiency corresponding to the steady-state frequency deviation, which contributes to less amount of load to be shed. In conclusion, both the virtual inertia control and the primary frequency control influence the calculation result of the total amount of load to be shed in the UFLS scheme.

Dynamic Calculation of the Magnitude of the Power Deficiency

When we study the frequency characteristics of the power system integrated with wind power and UHVDC, one of the difficult problems we face with is the calculation of the system equivalent inertia constant H_{eq}. For most situations, the inertia constant of the synchronous generators is a definite number. However, it is hard to analyze and calculate the equivalent inertia constants of the wind turbines and UHVDC. In the adaptive UFLS schemes, the actual magnitude of the power deficiency is commonly calculated as follows

$$\Delta P_h = \frac{2H_{eq}}{f_{nom}}\frac{df_{CoI}}{dt} \tag{6}$$

It is obvious from **Eq. 6** that we can calculate H_{eq} precisely after we obtain the power disturbance variation ΔP around the time when the operating status of the power system changes or the disturbance occurs, as well as the RoCoF of CoI $\frac{df_{CoI}}{dt}$, as expressed in **Eq. 7**.

$$H_{eq} = \frac{\Delta P f_{nom}}{2\dfrac{df_{CoI}}{dt}} \tag{7}$$

Furthermore, in order to reduce the error of calculating the equivalent inertia constant H_{eq}, the study employs the method as follows: by maintaining the current operating state of the power system unchanged and setting L different and known power disturbance variation $\Delta P_{set,l}$, the corresponding RoCoF of CoI $\frac{df_{CoI}}{dt}$ can be calculated. Solve all the values of the equivalent inertia constant $H_{eq,\,l}$ correponding to $\Delta P_{set,l}$ according to **Eq. 7**. Then calculate the mean value of $H_{eq,\,l}$ as the setting value of the equivalent inertia constant of the power system, which can be represented as

$$H_{eq} = \frac{\sum_{l=1}^{L} H_{eq,l}}{L} = \sum_{l=1}^{L}\frac{\Delta P_{set,\,l} f_{nom}}{2L\dfrac{df_{CoI}}{dt}} \tag{8}$$

After the system equivalent inertia constant H_{eq} is obtained, calculate the actual magnitude of the power deficiency $\Delta P_{h,1}$ at the time when the system frequency drops to the frequency threshold in the first stage of UFLS.

Assume that the steady-state frequency after UFLS is f_s. As $f_s < f_{nom}$, the steady-state frequency deviation is $\Delta f_s = f_s - f_{nom}$. Considering the participation of the wind turbines and UHVDC in primary frequency control, ΔP_s refers to the active power provided by the primary frequency control of the synchronous generators, the wind turbines, and UHVDC, together with the effect of load regulation, as expressed in **Eq. 8**.

$$\Delta P_s = -(k_L + k_G + k_{dWF} + k_{dDC})\Delta f_s \tag{9}$$

where k_L and k_G are the unit regulation power of the load and the synchronous generators, respectively.

Then the total amount of load to be shed $P_{shed,\sum}$ can be calculated as (Yang, 2007)

$$\Delta P_{shed,\sum} = \frac{\Delta P_{h,1} - (k_L + k_G + k_{dWF} + k_{dDC})P_{Ls}\Delta f_s^*}{1 - (k_L + k_G + k_{dWF} + k_{dDC})\Delta f_s^*} \tag{10}$$

where P_{Ls} is the load of the power grid in the steady state; Δf_s^* is the per unit steady-state frequency deviation.

Then the total amount of the load will be shed by stages. It is obvious from **Eq. 9** that the primary frequency control of the wind turbines and UHVDC leads to the increase in their active power output in steady state, thus reducing $\Delta P_{h,1}$.

Implementation Strategy of Under-Frequency Load Shedding

Firstly, determine the stages, frequency thresholds, load shedding percentage in each stage, and steady-state recovery frequency in the UFLS control strategy.

In the process of UFLS, the first frequency threshold should not exceed 49.25 Hz to fully use the rotating reserve capacity of the power system. The typical frequency difference between the stages is 0.2~0.25 Hz and 5~8 stages are commonly set. Based on the UFLS schemes of actual power grids, this paper sets four basic stages with the corresponding frequency thresholds of 49.2, 49.0, 48.8, 48.6 Hz, and the time delay of 0.2 s. The load shedding percentages in the basic stages are 20, 25, 25, and 30%, separately.

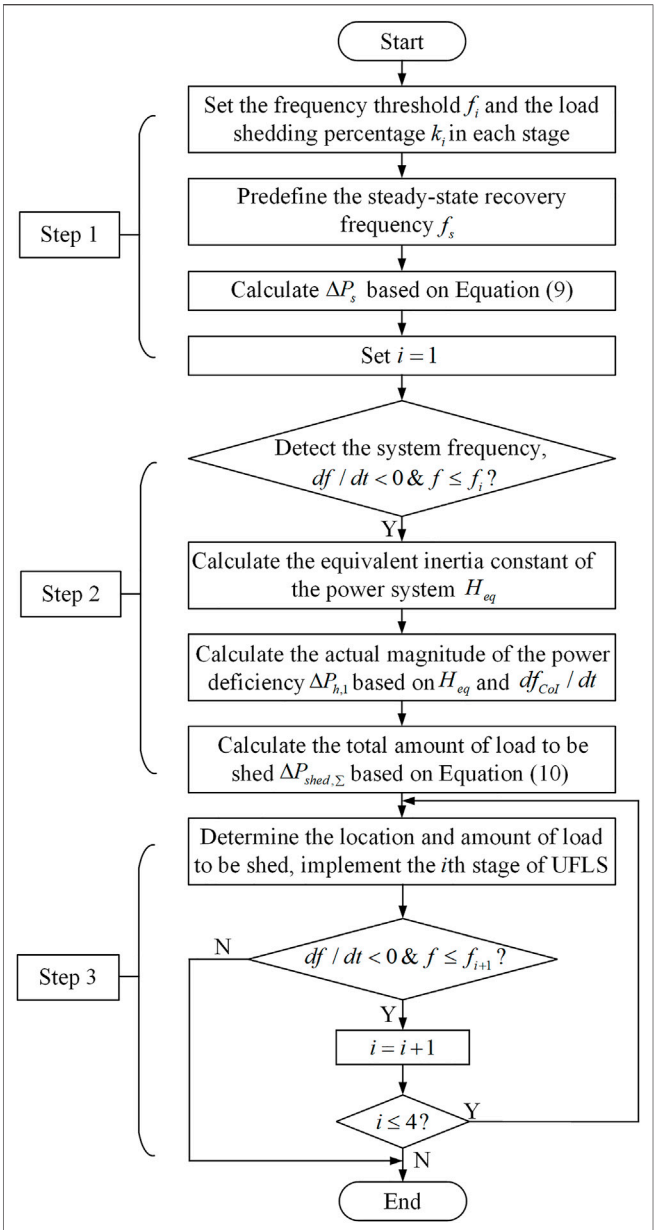

FIGURE 6 | Flowchart of the proposed UFLS control strategy.

Afterward, determine the location and the amount of load to be shed in the UFLS control strategy.

In the actual operation of UFLS, the load of the scattered nodes needs to be shed. The load shedding location can be selected and the load shedding amount can be allocated based on the load shedding sensitivity index (Yang and Cai, 2016). The load shedding amount of the n th node of the power grid $\Delta P_{shed,n}$ can be determined as

$$\Delta P_{shed,n} = \frac{\Delta P_{shed,i}\phi_n}{\sum_{n=1}^{N}\phi_n} \tag{11}$$

where $\Delta P_{shed,i}$ is the total amount of load to be shed in the i th stage; ϕ_n is the load shedding sensitivity of the load node, directly related to the electrical distance from the load node to the disturbance node; N is the total number of the load nodes.

Finally, design the UFLS implementation strategy.

In this study, the UFLS control strategy is implemented as shown in **Figure 6**. The corresponding steps can be described as follows:

1) Set the frequency threshold f_i and the load shedding percentage k_i in each stage. Predefine the steady-state recovery frequency f_s. Calculate ΔP_s according to **Eq. 9**. Set i = 1.
2) Detect the frequency state of the power system. If $\frac{df}{dt}<0$ and $f \le f_i$, then calculate the equivalent inertia constant of the power system H_{eq} by using the method proposed in **Section 4.1**. Then based on H_{eq} and $\frac{df_{CoI}}{dt}$, the actual magnitude of the power deficiency at the time when the system frequency drops to the first frequency threshold $\Delta P_{h,1}$ can be obtained according to **Eq. 6**.
3) On the basis of $\Delta P_{h,1}$ and **Eq. 10**, calculate the total amount of load to be shed $\Delta P_{shed,\sum}$ in the UFLS control strategy.

It can be seen from **Figure 6** that when the system frequency reaches the threshold of the i th stage, i.e. $f \le f_i$, UFLS is started in accordance with the load shedding percentage in each stage k_i. After completing load shedding in the i th stage, detect the system frequency. If $\frac{df}{dt}<0$ and $f \le f_{i+1}$, it is clear that the load shedding amount is not enough to avoid the frequency from declining. Then the next stage of UFLS is triggered. Conversely, it means that load shedding has already restrained the descending of the system frequency. The frequency does not fall below the frequency threshold in the $(i+1)$ th stage. The UFLS process ends.

SIMULATION ANALYSIS

In this section, simulations are carried out on the IEEE 39-bus test system. Power System Analysis Synthesis Program (PSASP) developed by China Electric Power Research Institute is used to conduct the simulation studies. The single-line diagram of this test system is provided in **Figure 7**. Suppose that DFIG-based wind turbines are connected at Bus 34 and Bus 36 replacing the thermal generators with equal active power output. A UHVDC transmission line with a rated active power output of 1000 MW is connected to the system at Bus 18, replacing the thermal generators at Bus 30 and Bus 32. To achieve the power equilibrium, we also reduce the active power output of the thermal generator at Bus 31. Both the wind turbines and UHVDC have the abilities of virtual inertia control and primary frequency control. We set the available capacity of the wind turbines for frequency regulation as 10% of their rated active power (Lyu et al., 2021). The available capacity of UHVDC for frequency regulation is set as 5% of its rated active power (Zhao, 2004).

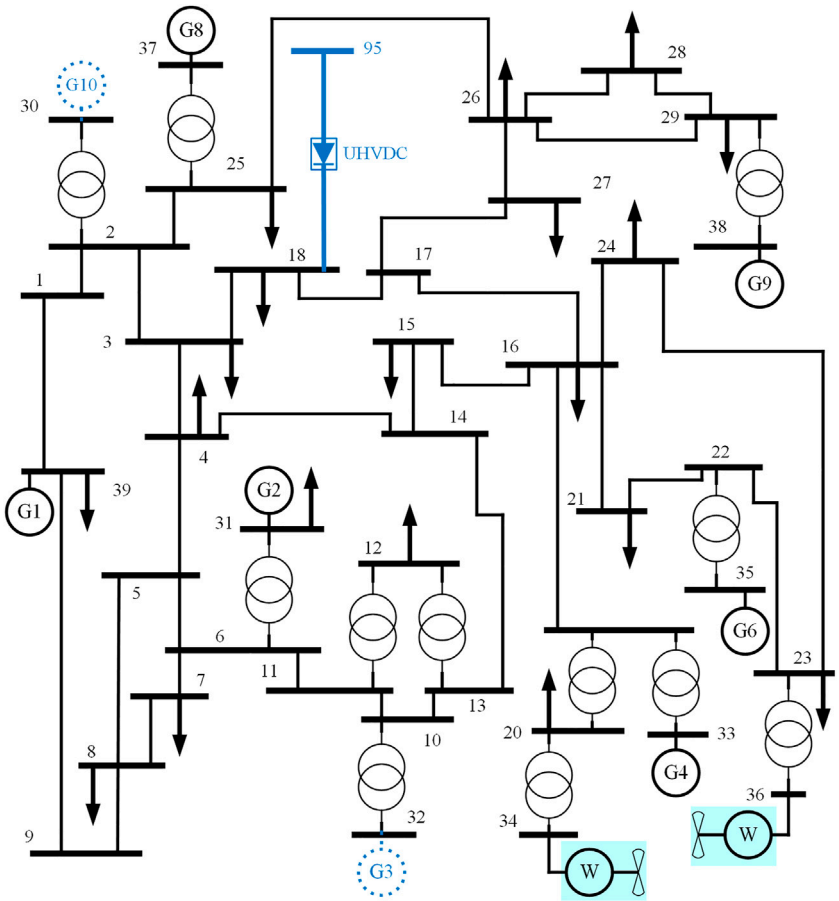

FIGURE 7 | Single-line diagram of the IEEE 39-bus test system with wind turbines and UHVDC.

Impact of Wind Turbines and Ultra High-Voltage DC Participating in Frequency Regulation on Frequency Response

In this case, when $t = 5$ *s*, a 300 MW load surge at Bus 21 occurs. This disturbance is used to imitate the power deficiency caused by new energy or conventional generators off-grid. Simulate and compare the effects of four frequency control modes on the system frequency response after the disturbance: 1) both the wind turbines and UHVDC participate in frequency regulation; 2) only the wind turbines participate in frequency regulation; 3) only UHVDC participates in frequency regulation; 4) neither the wind turbines nor UHVDC participates in frequency regulation. The simulation results are shown in **Figure 8**.

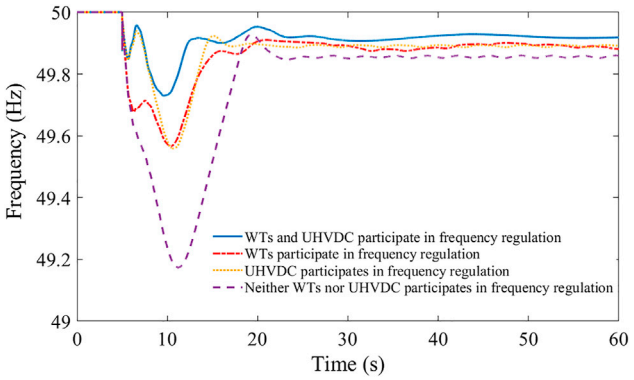

FIGURE 8 | Frequency curves under different frequency control modes.

It is revealed from **Figure 8** that when neither the wind turbines nor UHVDC participates in frequency regulation, the maximum frequency deviation is the largest and the steady-state frequency is the lowest of the four frequency control modes. Besides, the frequency nadir drops below 49.2 Hz, violating the frequency threshold of the first stage. Once the wind turbines or UHVDC participates in frequency regulation, the absolute maximum frequency deviation decreases by 0.4 Hz, and the steady-state frequency is higher. When both the wind turbines and UHVDC participate in frequency regulation, the maximum frequency deviation and the steady-state frequency deviation are the minima. It can be inferred that the participation of the wind turbines and UHVDC in frequency regulation can effectively ameliorate the system frequency characteristics. The combined

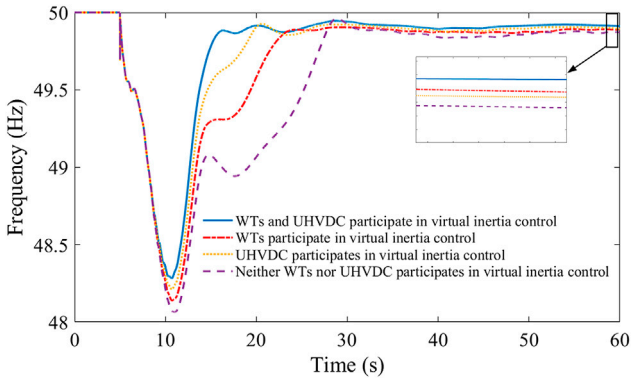

FIGURE 9 | Frequency curves under different UFLS schemes considering different virtual inertia control modes.

action of the virtual inertia control and the primary frequency control significantly decreases the maximum frequency deviation and the steady-state frequency deviation. Thus the dynamic process and the trajectory of the system frequency are notably impacted by the participation of the wind turbines and UHVDC in frequency regulation.

Impact of Virtual Inertia Control of Wind Turbines and Ultra High-Voltage DC on Under-Frequency Load Shedding

For cases in Sections 5.2, 5.3, and 5.4, a 780 MW load surge at Bus 21 at the time $t = 5\ s$ is used as the disturbance to imitate the power deficiency caused by new energy or conventional generators off-grid.

In this case, both the wind turbines and UHVDC in the test system possess the capability of virtual inertia control actually. However, to illustrate the impact of the virtual inertia control of the wind turbines and UHVDC on UFLS, we consider four different situations in the process of formulating four UFLS schemes respectively: 1) both the wind turbines and UHVDC participate in virtual inertia control; 2) only the wind turbines participate in virtual inertia control; 3) only UHVDC participates in virtual inertia control; 4) neither the wind turbines nor UHVDC participates in virtual inertia control. Then the four UFLS schemes are implemented on the same test system in which both the wind turbines and UHVDC participate in virtual inertia control, separately. The simulation results are shown in **Figure 9** and **Table 1**.

It can be seen from **Figure 9** and **Table 1** that, the steady-state recovery frequency in scheme 1 is the highest, followed by scheme 3 and scheme 2, while in scheme 4 is the lowest. The reason is that for one thing, the virtual inertia control of the wind turbines and UHVDC is considered in scheme 1 so that the calculated inertia constant H_{eq} is the largest. However, scheme 2 only accounts for the virtual inertia control of the wind turbines, and scheme 3 only takes the virtual inertia control of UHVDC into account. Thus the calculated H_{eq} in scheme 2 and scheme 3 is less. As scheme 4 does not consider

TABLE 1 | Results of different UFLS schemes considering different virtual inertia control modes.

UFLS scheme	Steady-state frequency (Hz)	Load shedding amount (MW)
1	49.9127	560
2	49.8860	482
3	49.8941	519
4	49.8713	437

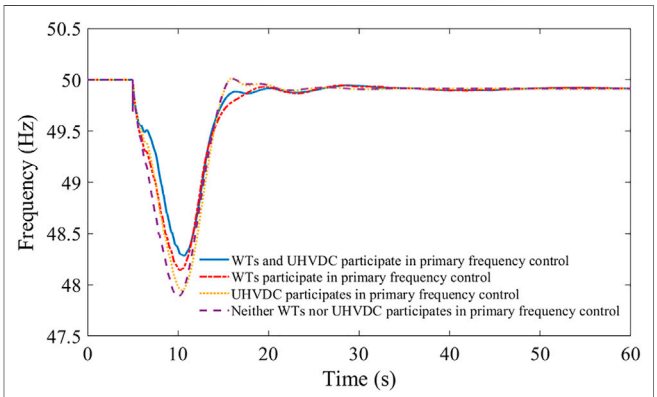

FIGURE 10 | Frequency curves under different UFLS schemes considering different primary frequency control modes.

the virtual inertia control of the wind turbines or UHVDC, the calculated H_{eq} in scheme 4 is the least. For another, it can be inferred from **Eq. 10** that the further calculated total amount of load to be shed $\Delta P_{shed,\sum}$ is the largest in scheme 1, followed by scheme 3 and scheme 2, while in scheme 4 is the least. Thus the steady-state recovery frequency in each scheme has certain differences.

The simulation results in this case also demonstrate that when the virtual inertia control of the wind turbines and UHVDC is taken into consideration, scheme 1 can calculate the actual magnitude of the power deficiency more precisely and reflect the effect of the virtual inertia control on UFLS more objectively. Obviously, the effect is significant.

Impact of Primary Frequency Control of Wind Turbines and Ultra High-Voltage DC on Under-Frequency Load Shedding

In this case, to illustrate the impact of the primary frequency control of the wind turbines and UHVDC on UFLS, design and contrast four different UFLS schemes: 1) UFLS scheme considering the primary frequency control of both the wind turbines and UHVDC; 2) UFLS scheme only considering the primary frequency control of the wind turbines; 3) UFLS scheme only considering the primary frequency control of UHVDC; 4) UFLS scheme without considering the primary frequency control of wind turbines or UHVDC. Then each of the four schemes is implemented on the test system with the primary frequency

TABLE 2 | Results of different UFLS schemes considering different primary frequency control modes.

UFLS scheme	Steady-state frequency (Hz)	Load shedding amount (MW)
1	49.9127	560
2	49.9127	633
3	49.9120	628
4	49.9133	704

control mode corresponding to the scheme itself. The simulation results are shown in **Figure 10** and **Table 2**.

It can be observed from **Figure 10** and **Table 2** that, the steady-state recovery frequency is almost the same in the four schemes. However, the amount of load to be shed $\Delta P_{shed,\sum}$ in scheme 1 is 560 MW, which is 73 MW, 68 MW, and 144 MW less than that in scheme 2, scheme 3, and scheme 4, respectively. This shows that the magnitude of the power deficiency is partly offset by the primary frequency control of the wind turbines and UHVDC in scheme1, resulting in the decrease in the amount of load to be shed by 144 MW compared with scheme 4. Schemes 2 and scheme 3 respectively take into account the primary frequency control of wind turbines and UHVDC. The part of the magnitude of the power deficiency offset by the primary frequency control is less than that in scheme 1. Thus the amount of load to be shed in scheme 2 and scheme 3 is more than that in scheme 1. As neither the primary frequency control of the wind turbines nor of UHVDC is taken into account in scheme 4, more load needs to be shed to maintain the same steady-state recovery frequency as that in scheme 1, scheme 2, and scheme 3. To conclude, the primary frequency control of the wind turbines and UHVDC has a prominent effect on the steady-state recovery results and the amount of load to be shed.

Verification of Adaptive Under-Frequency Load Shedding Control Strategy With Wind Turbines and Ultra High-Voltage DC Participating in Frequency Regulation

In this case, simulations are conducted to compare three different UFLS schemes. Scheme 1 is the scheme proposed in this paper, which is performed according to the implementation strategy of UFLS in **Figure 5**. Scheme 2 is the conventional UFLS scheme in literature (Rudez and Mihalic, 2011). Scheme 3 is the adaptive UFLS scheme in literature (Song et al., 2014) without considering the virtual inertia control and the primary frequency control of the wind turbines and UHVDC. Compare the frequency response curves and the steady-state results of all the schemes in the process of UFLS. The simulation results are shown in **Figure 11** and **Table 3**.

It can be seen from **Figure 11** and **Table 3** that all the schemes complete the action process of UFLS through four stages of load shedding, and the steady-state recovery frequency is close. However, the load shedding amount in scheme 1 is evidently less than that in scheme 2 and scheme 3 in each stage

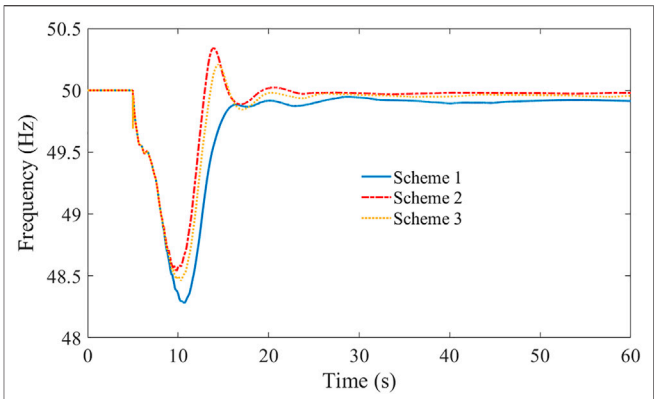

FIGURE 11 | Comparison of different UFLS schemes.

TABLE 3 | Load shedding amount and steady-state frequency of different UFLS schemes.

Load shedding stages	Load shedding amount (MW)		
	Scheme 1	Scheme 2	Scheme 3
First stage	112	156.2	137.6
Second stage	140	195.25	172
Third stage	140	195.25	172
Fourth Stage	168	234.3	206.4
Total	560	781	688
Steady-state frequency (Hz)	49.9127	49.9781	49.9552

and in total. The reasons for the difference in the load shedding amount are as follows. On one hand, the actual magnitude of the power deficiency $\Delta P_{h,1}$ is calculated in scheme 1 considering the virtual inertia control and the primary frequency control of the wind turbines and UHVDC. On the other hand, the total amount of load to be shed $\Delta P_{shed,\sum}$ is calculated in scheme 1 considering the primary frequency control of the wind turbines and UHVDC. Thus the simulation results show that when taking into account the virtual inertia control and the primary frequency control of the wind turbines and UHVDC, the load shedding amount can be significantly reduced on the premise of reaching the steady-state recovery frequency. Thus it is conducive to the improvement of the power supply reliability of the power grid and the reduction of the loss caused by load shedding.

CONCLUSION

This paper proposes an adaptive UFLS control strategy of power systems with wind turbines and UHVDC participating in frequency regulation. The following conclusions are obtained through theoretical research and simulation verification.

1) The virtual inertia control of the wind power and UHVDC has a significant impact on the frequency dynamic process and trajectory, resulting in the obvious differences in the

calculation results of the magnitude of the power deficiency and the amount of load to be shed, which makes the steady-state recovery frequency higher.
2) The primary frequency control of the wind power and UHVDC can effectively offset part of the power deficiency magnitude and reduce the load shedding amount.
3) Compared with the existing typical UFLS strategies, on the premise of reaching the same level of steady-state recovery frequency, the strategy proposed in this paper can shed the least amount of load. Moreover, it can better adapt to the UFLS process of the power grid with the wind turbines and UHVDC participating in frequency regulation.

This paper takes DFIG-based wind turbines and UHVDC as examples to discuss the UFLS control strategy. In the future, we will further study other UFLS improvement strategies considering frequency regulation of other types of renewable energy, flexible DC, and energy storage, so as to provide a better guarantee for the safety and stability of the power grid frequency.

DATA AVAILABILITY STATEMENT

The original contributions presented in the study are included in the article/**Supplementary Material**, further inquiries can be directed to the corresponding author.

AUTHOR CONTRIBUTIONS

XW: Methodology, Software, Validation, Investigation, Data curation, Writing—original draft preparation, Visualization. FX: Methodology, Formal analysis, Supervision. JD: Conceptualization, Validation, Writing—review and editing. YT: Resources, Writing—review and editing.

SUPPLEMENTARY MATERIAL

The Supplementary Material for this article can be found online at: https://www.frontiersin.org/articles/10.3389/fenrg.2022.875785/full#supplementary-material

REFERENCES

Abdelwahid, S., Babiker, A., Eltom, A., and Kobet, G. (2014). Hardware Implementation of an Automatic Adaptive Centralized Underfrequency Load Shedding Scheme. *IEEE Trans. Power Deliv.* 29 (6), 2664–2673. doi:10.1109/TPWRD.2014.2331495

Ambia, M. N., Meng, K., Xiao, W., Al-Durra, A., and Dong, Z. Y. (2021). Adaptive Droop Control of Multi-Terminal HVDC Network for Frequency Regulation and Power Sharing. *IEEE Trans. Power Syst.* 36 (1), 566–578. doi:10.1109/TPWRS.2020.2999443

Anderson, P. M., and Mirheydar, M. (1992). An Adaptive Method for Setting Underfrequency Load Shedding Relays. *IEEE Trans. Power Syst.* 7 (2), 647–655. doi:10.1109/59.141770

Australian Energy Market Operator (2016). *Black System South Australia 28 September 2016—Third Preliminary Report*. Australia: Australian Energy Market Operator Limited.

Eriksson, R., Modig, N., and Elkington, K. (2018). Synthetic Inertia versus Fast Frequency Response: A Definition. *IET Renew. Power Generation* 12 (5), 507–514. doi:10.1049/iet-rpg.2017.0370

Global Wind Energy Council (GWEC) (2021). *Global Wind Report 2021*. Brussels, Belgium: Global Wind Energy Council.

Horowitz, S. H., and Phadke, A. G. (2008). *Power System Relaying*. Hoboken, NJ, USA: Wiley.

Hoseinzadeh, B., da Silva, F. M. F., and Bak, C. L. (2015). Adaptive Tuning of Frequency Thresholds Using Voltage Drop Data in Decentralized Load Shedding. *IEEE Trans. Power Syst.* 30 (4), 2055–2062. doi:10.1109/TPWRS.2014.2351015

Kundur, P. (2001). *Power System Stability and Control*. Beijing: China Electric Power Press.

Li, C., Wu, Y., Sun, Y., Zhang, H., Liu, Y., Liu, Y., et al. (2020). Continuous Underfrequency Load Shedding Scheme for Power System Adaptive Frequency Control. *IEEE Trans. Power Syst.* 35 (2), 950–961. doi:10.1109/TPWRS.2019.2943150

Li, S. C., Lyu, X. S., Zhong, H., Long, Q. W., Xie, W. J., and Shu, Z. Y. (2019). Adaptive Under-frequency Load Shedding Strategy of Power Grid with Large-Scale DFIG Wind Turbines Participating in Frequency Regulation. *Automation Electric Power Syst.* 43 (15), 109–120. doi:10.7500/AEPS2018112800

Li, S., Liao, Q. F., Tang, F., Zhao, H. S., and Shao, Y. G. (2017). Adaptive Underfrequency Load Shedding Strategy Considering High Wind Power Penetration. *Power Syst. Tech.* 41 (4), 1084–1090. doi:10.13335/j.1000-3673.pst.2016.3029

Lyu, X., Jia, Y., and Dong, Z. (2021). Adaptive Frequency Responsive Control for Wind Farm Considering Wake Interaction. *J. Mod. Power Syst. Clean Energ.* 9 (5), 1066–1075. doi:10.35833/MPCE.2020.000237

Lyu, X., Zhao, J., Jia, Y., Xu, Z., and Wong, K. P. (2019). Coordinated Control Strategies of PMSG-Based Wind Turbine for Smoothing Power Fluctuations. *IEEE Trans. Power Syst.* 34 (1), 391–401. doi:10.1109/TPWRS.2018.2866629

National Grid ESO. (2019). Technical Report on the Events of 9 August. Available at: https://www.nationalgrideso.com/document/152346/download (Accessed September 6, 2019).

Pérez-Molina, M. J., Larruskain, D. M., López, P. E., and Buigues, G. (2020). Challenges for Protection of Future HVDC Grids. *Front. Energ. Res.* 8, 33. doi:10.3389/fenrg.2020.00033

Prakash, A., Murali, S., Shankar, R., and Bhushan, R. (2019). HVDC Tie-Link Modeling for Restructured AGC Using a Novel Fractional Order cascade Controller. *Electric Power Syst. Res.* 170, 244–258. doi:10.1016/j.epsr.2019.01.021

Rudez, U., and Mihalic, R. (2011). Monitoring the First Frequency Derivative to Improve Adaptive Underfrequency Load-Shedding Schemes. *IEEE Trans. Power Syst.* 26 (2), 839–846. doi:10.1109/TPWRS.2010.2059715

Rudez, U., and Mihalic, R. (2016). WAMS-based Underfrequency Load Shedding with Short-Term Frequency Prediction. *IEEE Trans. Power Deliv.* 31 (4), 1912–1920. doi:10.1109/TPWRD.2015.2503734

Shi, Q. M., Guo, M. Q., Liu, K., Wang, Y., Zou, X., Zou, Q., et al. (2021). Coordinated Frequency Control for UHVDC Considering Inertia Response. *Power Syst. Tech.* 45 (9), 1084–1090. doi:10.13335/j.1000-3673.pst.2021.0015

Sigrist, L., Egido, I., and Rouco, L. (2012). A Method for the Design of UFLS Schemes of Small Isolated Power Systems. *IEEE Trans. Power Syst.* 27 (2), 951–958. doi:10.1109/TPWRS.2011.2174448

Skrjanc, T., Mihalic, R., and Rudez, U. (2021). A Non-Intrusive Approach for Enhancing Power-System Frequency Stability. *IEEE Trans. Power Syst.*, 1. doi:10.1109/TPWRS.2021.3131098

Song, Z. O., Liu, J. Y., Liu, Y., Masoud, B., and Liang, W. (2014). WAMS-based Adaptive UFLS Considering Dynamic Correction. *Electric Power Automation Equipment* 34 (4), 95–100. doi:10.3969/j.issn.1006-6047.2014.04.017

Terzija, V. V. (2006). Adaptive Underfrequency Load Shedding Based on the Magnitude of the Disturbance Estimation. *IEEE Trans. Power Syst.* 21 (3), 1260–1266. doi:10.1109/TPWRS.2006.879315

Tian, Z., Xiao, Q.-W., and Ren, F.-R. (2021). Assessing the Efficiency and CO2 Reduction Performance of China's Regional Wind Power Industry Using an Epsilon-Based Measure Model. *Front. Energ. Res.* 9, 672183. doi:10.3389/fenrg.2021.672183

Tofis, Y., Timotheou, S., and Kyriakides, E. (2017). Minimal Load Shedding Using the Swing Equation. *IEEE Trans. Power Syst.* 32 (3), 2466–2467. doi:10.1109/TPWRS.2016.2614886

Van de Vyver, J., De Kooning, J. D. M., Meersman, B., Vandevelde, L., and Vandoorn, T. L. (2016). Droop Control as an Alternative Inertial Response Strategy for the Synthetic Inertia on Wind Turbines. *IEEE Trans. Power Syst.* 31 (2), 1129–1138. doi:10.1109/TPWRS.2015.2417758

Vidyanandan, K. V., and Senroy, N. (2013). Primary Frequency Regulation by Deloaded Wind Turbines Using Variable Droop. *IEEE Trans. Power Syst.* 28 (2), 837–846. doi:10.1109/TPWRS.2012.2208233

Yang, D. Y., and Cai, G. W. (2016). The Sensitivity of Load Shedding Control and its Application in Wide-Area Low Frequency Protection. *Electric Power Automation Equipment* 36 (3), 124–128. doi:10.16081/j.issn.1006-6047.2016.03.019

Yang, G. C. (2007). *The Principle of Automatic Power System*. Beijing: China Electric Power Press.

Ye, H., Pei, W., and Qi, Z. (2016). Analytical Modeling of Inertial and Droop Responses from a Wind Farm for Short-Term Frequency Regulation in Power Systems. *IEEE Trans. Power Syst.* 31 (5), 3414–3423. doi:10.1109/TPWRS.2015.2490342

Zhao, W. J. (2004). *Technology for HVDC Transmission Project*. Beijing: China Electric Power Press.

Conflict of Interest: Author FX was employed by the NARI Group Corporation (State Grid Electric Power Research Institute).

The remaining authors declare that the research was conducted in the absence of any commercial or financial relationships that could be construed as a potential conflict of interest.

frontiers | Frontiers in Energy Research

ORIGINAL RESEARCH
published: 26 May 2022
doi: 10.3389/fenrg.2022.902891

Multi-Stage Expansion Planning of Distribution Network Considering Distributed Power Generation

Qingjie Wang[1,2] *and Ma Jing*[1]*

[1]Department of Electric and Electronic Engineering, North China Electric Power University, Beijing, China, [2]State Grid Corporation of China, Beijin, China

With the gradual increase in the penetration rate of distributed power sources, in view of the planning problem of coordinating the location and capacity of distributed power sources with the grid frame and transformers of the distribution network, a distribution network that takes into account distributed power sources is proposed. Aiming at the lowest cost of investment, maintenance, energy production, energy loss, and load loss penalty, and considering the power flow constraints, planning and operation constraints of each planning stage, a multi-stage expansion planning model for the distribution network is established. The mixed-integer linear programming algorithm is used to solve the problem, and the optimal planning scheme at each stage is obtained. The simulation results show that the multi-stage expansion planning method for coordinating distributed power and distribution network proposed in this paper can prevent the problems of isolated nodes and transmission nodes, improve the reliability of the planning scheme, and have good economic benefits.

Keywords: distributed generation, distribution network planning, multi-stage, planning model, planning scheme

OPEN ACCESS

Edited by:
Chaolong Zhang,
Anqing Normal University, China

Reviewed by:
Yin Yao,
Shanghai University of Electric Power, China
Nan Yang,
China Three Gorges University, China

***Correspondence:**
Ma Jing
3466673668@qq.com

Specialty section:
This article was submitted to Smart Grids, a section of the journal Frontiers in Energy Research

Received: *23 March 2022*
Accepted: *12 April 2022*
Published: *26 May 2022*

Citation:
Wang Q and Jing M (2022) Multi-Stage Expansion Planning of Distribution Network Considering Distributed Power Generation. Front. Energy Res. 10:902891. doi: 10.3389/fenrg.2022.902891

1 INTRODUCTION

With the deterioration of the environment and the continuous change of the energy structure (National Development and Reform Commission, 2015; Mansor and Levi, 2018; Nikoobakht et al., 2020), the penetration of Distributed Generation (DG) is gradually increasing (Afraz et al., 2019; Borghei and Ghassemi, 2021). This means that the distribution network structure as well as the power supply mode has changed (Alarcon et al., 2020; Vahidinasab et al., 2020). On the one hand, the planning results of distributed power supply and distribution network will affect each other, and it is difficult to achieve the overall optimum for a single separate planning. This will affect the planning economy and reliability (Cattani et al., 2020; Shahbazi et al., 2021a). On the other hand, for medium-term and long-term distribution network planning, its construction works are often divided into multiple stages, which are reasonably adjusted according to the changes in load. A single-stage planning model makes it difficult to take into account future load changes and the impact of distributed power sources (Franco, 2016). Therefore, it is necessary to coordinate and unify the siting and capacity of distributed power with the planning of the distribution network's grid and transformers. And it is important to study a multi-stage coordinated planning method of distribution network taking into account distributed power sources.

There are a lot of research on distribution network planning problems (Saeed and Mahmud, 2018; Koutsoukis and Georgilakis, 2019; Faria et al., 2020; Delarestaghi et al., 2021; Mojtahedzadeh et al., 2021). The author in Liu et al. (2019) takes into account the volatility of DG output and establishes a

DG siting and capacity model with the minimum risk of distribution network operation as the objective function. Narimani et al. (2018) use Monte Carlo for simulation and introduces delayed option theory for planning the multiple uncertainties of load as well as tariff in incremental distribution network planning. Jooshaki et al. (2020) considers the impact of DG on the distribution network grid structure and optimizes the lines, DG locations, and capacity of the distribution network in the distribution network planning process, but ignores the coordination between DG and the distribution network. In response to the above problems, Akbari and Moghaddam (2020) proposes to construct a fuzzy planning of distribution network grid considering DG output uncertainty. It coordinates the interaction between DG and the distribution network grid. Hemmati et al. (2015) considers the uncertainty of load and price in the electricity market environment. In the paper, a coordination and expansion planning model of distribution network and DG is proposed and the model is solved by particle swarm optimization algorithm. Muoz -Delgado et al. (2014) considered several alternatives for the installation or replacement of DGs, feeders, and transformers, and proposed a joint expansion planning model for DGs and distribution networks. The results show that incorporating distributed generation investments into the distribution network problem can significantly reduce investment costs. However, these models involve only one planning phase. In the actual planning process, construction projects are often divided into multiple stages. If a single-stage planning model is used, it is difficult to take into account future load changes and the impact of distributed power sources, and lacks an integrated layout for long-term investment strategies.

To address the multi-stage planning problem, the Tabares et al. (2015); Xing et al. (2016) considered line, substation, and distributed power supply renewal replacement and proposed a multi-stage planning model of distribution network with mixed integer linear programming. However, relatively little attention has been paid to the issue of joint expansion. The author in Masoumi-Amiri et al. (2021) propose a multi-stage planning model for active distribution networks considering the load level by using a clustering algorithm for multi-stage division of the source-load timing characteristics. And it increases the penetration of distributed power and the reliability of the system. Xiao et al. (2020) proposes an active distribution network multi-stage two-level planning model. The paper presents the boundary conditions for the most multi-stage planning with operationally constrained cases. The model improves the economics of the investment as well as the reliability of the actual operation. Shahbazi et al. (2021b) use the idea of multi-stage planning for the siting of distributed power sources and distribution grids and for the expansion of the grid. The paper improves the convergence speed of model solving by using the improved genetic membrane algorithm. However, it ignores the expansion decision of distributed generation and focuses the study on the impact of distributed power expansion on distribution investment deferral instead of solving the optimization problem of the joint expansion planning model.

To address the problems of existing research, this paper proposes a multi-stage planning method for distribution networks that considers distributed power sources. This paper establishes a multi-stage expansion planning model for distribution networks. The model aims to minimize the cost of investment, maintenance, energy production, energy loss and loss of load penalties and consider the tidal constraints, planning and operational constraints for each planning stage. The model is solved using a mixed integer linear programming algorithm to obtain the optimal planning solution for each stage. At the end of the article, the economics and effectiveness of the proposed method are verified by simulation examples.

2 DISTRIBUTION NETWORK COORDINATION PLANNING MODEL

2.1 Objective Function

The distribution network planning model aims at minimizing the total cost F. The objective function mainly includes investment cost c_t^I, maintenance cost c_t^M, production cost c_t^E, energy loss cost c_t^R and penalty cost c_t^U. The details are as follows:

$$\min F = \sum_{t\in T}\frac{(1+i)^{-t}}{i}c_t^I + \sum_{t\in T}\left[(1+i)^{-t}\left(c_t^M + c_t^E + c_t^R + c_t^U\right)\right] + \frac{(1+i)^{-n_T}}{i}\left(c_{n_T}^M + c_{n_T}^E + c_{n_T}^R + c_{n_T}^U\right) \quad (1)$$

Where, T is the set of planning stages; i is the annual interest rate; n_T is the number of planning stages; c_t^I is the investment cost; $c_t^E, c_t^M, c_t^R, c_t^U$ are the cost of energy production, maintenance, losses and penalties at stage t, respectively; $c_{n_T}^E, c_{n_T}^M, c_{n_T}^R, c_{n_T}^U$ are the cost of energy production, maintenance, losses and penalties for the time planning phase n_T, respectively.

2.1.1 Investment Costs

Investment costs for all stages include replacement and new feeder costs, reinforcement of existing substations and new substation costs, new transformer costs, and distributed power costs. The formula is shown below:

$$c_t^I = \sum_{l\in\{NRF,NAF\}}\left(i(1+i)^{\eta^l}\right)\Big/\left((1+i)^{\eta^l}-1\right)\sum_{k\in K^l}\sum_{(s,r)\in\}Y^l}C_k^{I,l}l_{sr}x_{srkt}^l + \left(i(1+i)^{\eta^{SS}}\right)\Big/\left((1+i)^{\eta^{SS}}-1\right)\sum_{s\in\Omega^{SS}}C_s^{I,SS}x_{st}^{SS} + \left(i(1+i)^{\eta^{NT}}\right)\Big/\left((1+i)^{\eta^{NT}}-1\right)\sum_{k\in K^{NT}}\sum_{s\in\Omega^{SS}}C_k^{I,NT}x_{skt}^{NT} + \sum_{p\in P}\left(i(1+i)^{\eta^p}\right)\Big/\left((1+i)^{\eta^p}-1\right)\sum_{k\in K^p}\sum_{s\in\Omega^p}C_k^{I,p}\lambda\bar{G}_k^p x_{skt}^p \quad (2)$$

Where, K^l, K^{NT}, K^p are the set of new feeders, transformers and distributed power sources that can be constructed, respectively; Ω^{SS}, Ω^p are collection of substations and distributed power supplies; $\}Y^l$ is the set of feeder types l, where feeder type L: $\{EFF, REF, NRF, NAF\}$ represent existing feeders, replaceable

feeders, new replaceable feeders and new feeders; $C_k^{I,l}, C_s^{I,SS}, C_k^{I,NT}, C_k^{I,p}$ are the investment cost factors for feeders, substations, transformers and distributed power sources, respectively; l_{sr} is the length of the feeder *sr*; $x_{srkt}^{l}, x_{st}^{SS}, x_{skt}^{NT}, x_{skt}^{p}$ are 0–1 variables and it is used to indicate whether decision feeders, substations, transformers and distributed power supplies are constructed; λ is the system power factor; $\bar{G}_k^p$ is the rated capacity of generator *k*.

2.1.2 Maintenance Costs

Maintenance costs in all stages include feeder, transformer and generator maintenance costs. This is shown in **Equation 3**

$$c_t^M = \sum_{l\in L}\sum_{k\in K^l}\sum_{(s,r)\in\}\Upsilon^l} C_k^{M,l} y_{srkt}^{l} + \sum_{tr\epsilon TR}\sum_{k\in K^t}\sum_{s\in\Omega^{SS}} C_k^{M,tr} y_{skt}^{tr} + \sum_{p\epsilon P}\sum_{k\epsilon K^p} \times \sum_{s\in\Omega^p} C_k^{M,p} y_{skt}^{p} \tag{3}$$

Where, TR is the transformer type, where $TR = \{ET, NT\}$ represent existing transformers and new transformers respectively; P is the type of generator set, where $P = \{C, W\}$ represent conventional units and distributed wind turbines respectively; $C_k^{M,l}, C_k^{M,tr}, C_k^{M,p}$ are the maintenance cost factors for feeders, generators and transformers; $y_{srkt}^{l}, y_{skt}^{tr}, y_{skt}^{p}$ are 0–1 variables and these variables are used to make decisions about feeder, transformer and generator operating conditions.

2.1.3 Energy Production Costs

Energy production costs for each stage include energy production conversion costs for substations and distributed power sources and determined by **Equation 4**

$$c_t^E = \sum_{b\in B}\Delta_b\lambda\left(\sum_{tr\epsilon TR}\sum_{k\in K^{tr}}\sum_{s\in\Omega^{SS}} C_b^{SS} g_{sktb}^{tr} + \sum_{p\in P}\sum_{k\in K^p}\sum_{s\in\Omega^p} C_k^{E,p} g_{sktb}^{p}\right) \tag{4}$$

Where, B is the set of load levels; Δ_b is the duration of the load level b; $C_b^{SS}, C_k^{E,p}$ are the cost coefficients of energy supply for substations and generating units; $g_{sktb}^{tr}, g_{sktb}^{p}$ are the currents injected into node s by the transformer and generator set, respectively.

2.1.4 Energy Loss Costs

Energy loss costs include energy loss costs for transformers and feeders. The specific calculation of energy loss cost is shown in **Equation 5**

$$c_t^R = \sum_{b\in B}\Delta_b C_b^{SS}\lambda\left[\sum_{tr\epsilon TR}\sum_{k\in K^{tr}}\sum_{s\in\Omega^{SS}} Z_k^{tr}\left(g_{sktb}^{tr}\right)^2 + \sum_{l\in L}\sum_{k\in K^i (s,r)\epsilon\}\Upsilon^l} Z_k^{l} l_{sr}\left(f_{srktb}^{l} + f_{rsktb}^{l}\right)^2\right] \tag{5}$$

Where, C_b^{SS} is the energy loss cost factor of the substation; Z_k^{tr}, Z_k^{l} are the impedance of the transformer and the unit impedance of the feeder; g_{sktb}^{tr} is the current injected into node s by the transformer; f_{srktb}^{l} is the current in the feeder *sr*.

2.1.5 Penalty Costs

Penalty costs include those incurred by generators and substations when they fail to meet load demand. The penalty cost is calculated by **Equation 6**

$$c_t^U = \sum_{b\in B}\sum_{s\in\Omega_t^{LN}}\Delta_b C^U \lambda d_{stb}^{U} \tag{6}$$

Where, C^U is the penalty cost factor and d_{stb}^{U} is the unsatisfied load of node *s*.

2.2 Constraint Conditions

2.2.1 Flow Constraint

The flow constraint is used to constrain the operating state of the system to ensure the normal operation of the system, and the relevant constraint equation is as follows.

1) Node voltage constraints

$$\underline{V} \le v_{stb} \le \bar{V} \quad \forall s \in \Omega^N, \forall t \in T, \forall b \in B \tag{7}$$

Where, a is the voltage of node s at load level b in planning stage t; b, c are the minimum and maximum values of node voltage, respectively.

2) Feeder current constraints

$$\begin{aligned} &0 \le f_{srktb}^{l} \le y_{srkt}^{l}\bar{F}_k^{l} \\ &\forall l \in L, \forall s \in \Omega_r^{l}, \forall r \in \Omega^N, \forall k \in K^l, \forall t \in T, \forall b \in B \end{aligned} \tag{8}$$

Where, $\bar{F}_k^{l}$ is the maximum value of the current flowing through the feeder.

3) Transformer injection current constraints

$$\begin{aligned} &0 \le g_{sktb}^{tr} \le y_{skt}^{tr}\bar{G}_k^{tr} \\ &\forall tr \in TR, \forall s \in \Omega^{SS}, \forall k \in K^{tr}, \forall t \in T, \forall b \in B \end{aligned} \tag{9}$$

Where, $\bar{G}_k^{tr}$ is the maximum value of transformer current injection.

4) Loss of load constraints

$$0 \le d_{stb}^{U} \le \mu_b D_{st} \quad \forall s \in \Omega_t^{LN}, \forall t \in T, \forall b \in B \tag{10}$$

Where, μ_b is the load factor at load level b; D_{st} is the maximum load demand at node *s*.

5) Unit output constraints

$$\begin{aligned} &0 \le g_{sktb}^{W} \le y_{skt}^{W}\bar{G}_{sktb}^{W} \\ &\forall s \in \Omega^W, \forall k \in K^W, \forall t \in T, \forall b \in B \end{aligned} \tag{11}$$

Where, $\bar{G}_{sktb}^{W}$ is the maximum wind speed level.

6) Distributed power penetration constraints

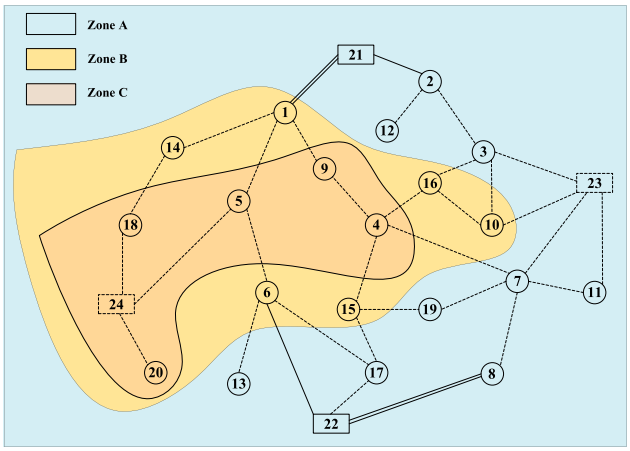

FIGURE 1 | 24 node distribution system.

TABLE 1 | Distribution network node load data.

Node	Stage/MVA			Node	Stage/MVA		
	1	2	3		1	2	3
1	5.13	4.21	6.24	11	0.00	1.53	2.64
2	0.58	0.45	1.21	12	0.00	0.96	1.36
3	2.65	3.74	4.21	13	0.00	1.14	1.87
4	0.38	0.51	2.54	14	0.00	3.09	3.15
5	0.21	0.36	0.46	15	0.00	1.63	1.62
6	1.42	0.69	1.81	16	0.00	2.17	1.24
7	4.32	3.74	4.36	17	0.00	0.00	2.48
8	0.74	0.63	0.96	18	0.00	0.00	2.17
9	1.32	1.24	1.74	19	0.00	0.00	1.82
10	1.52	2.31	2.41	20	0.00	0.00	3.74

$$\sum_{p\in P}\sum_{k\in K^p}\sum_{s\in\Omega^p} g^p_{sktb} \le \xi \sum_{s\in\Omega^{LN}_t} \mu_b D_{st} \quad \forall t \in T, \forall b \in B \tag{12}$$

Where, ξ is the upper limit of penetration of distributed generation.

7) Node current balance constraints

$$\sum_{l\in L}\sum_{k\in K^1}\sum_{r\in\Omega^l_s}\left(f^l_{srktb} - f^l_{rsktb}\right) = \sum_{tr\in TR}\sum_{k\in K^{tr}} g^{tr}_{sktb} + \sum_{p\in P}\sum_{k\in K^p} g^p_{sktb} - \mu_b D_{st} + d^U_{stb} \quad \forall s \in \Omega^N, \forall t \in T, \forall b \in B \tag{13}$$

8) Feeder state constraints

$$y^l_{srkt}\left[Z^l_k l_{sr} f^l_{srktb} - (v_{stb} - v_{rtb})\right] = 0 \quad \forall l \in L, \forall s \in \Omega^l_r, \forall r \in \Omega^N, \forall k \in K^l, \forall t \in T, \forall b \in B \tag{14}$$

Where, v_{stb}, v_{rtb} are the voltage amplitudes at node s and node r, respectively.

TABLE 2 | Branch data.

Branch		l_{sr}/km	Branch		l_{sr}/km	Branch		l_{sr}/km
s	r		s	r		s	r	
1	5	2.64	4	9	1.20	7	23	0.90
1	9	1.25	4	15	1.60	8	22	1.90
1	14	1.25	4	16	1.30	10	16	1.60
1	21	2.64	5	6	2.40	10	23	1.30
2	3	2.00	5	24	0.70	11	23	1.60
2	12	1.10	6	13	1.20	14	18	1.00
2	21	1.70	6	17	2.20	15	17	1.20
3	10	1.10	6	22	2.70	15	19	0.80
3	16	1.20	7	8	2.00	17	22	1.50
3	23	1.20	7	11	1.10	18	24	1.50
4	7	2.60	7	19	1.20	20	24	0.90

TABLE 3 | Wind speed for each area in the three stages.

Zone	Wind speed/(m/s)		
	1	2	3
A	9.44	10.36	11.25
B	5.32	8.47	7.36
C	4.69	6.21	5.97

2.2.2 Planning and Operational Constraints

In this paper, **Eqs. 15–18** are line, substation, transformer, and distributed power supply construction constraints and these constructions allow up to one reinforcement, replacement or new construction; **Eq. 19** is a new transformer constraint to ensure that new transformers can only be added to previously expanded or constructed substations; **Eqs. 20–22** are the constraints on the use of the feeder, which determine the direction of the current; **Eqs. 23**, **24** are the new transformers and distributed generators put into operation constraints; **Eq. 25** is the investment constraint for each stage. The construction program for each stage, the timing as well as the number of lines, substations, transformers, and distributed power sources shall meet the following constraints:

$$\sum_{t\in T}\sum_{k\in K^l} x^l_{srkt} \le 1 \quad \forall l \in \{NRF, NAF\}, \forall (s,r) \in \}\Upsilon^l \tag{15}$$

$$\sum_{t\in T} x^{SS}_{st} \le 1 \quad \forall s \in \Omega^{SS} \tag{16}$$

$$\sum_{t\in T}\sum_{k\in K^{NT}} x^{NT}_{skt} \le 1 \quad \forall s \in \Omega^{SS} \tag{17}$$

$$\sum_{t\in T}\sum_{k\in K^p} x^p_{skt} \le 1 \quad \forall p \in P, \forall s \in \Omega^p \tag{18}$$

$$x^{NT}_{skt} \le \sum_{\tau=1}^{t} x^{SS}_{s\tau} \quad \forall s \in \Omega^{SS}, \forall k \in K^{NT}, \forall t \in T \tag{19}$$

$$y^{EFF}_{srkt} + y^{EFF}_{rskt} \le 1 \quad \forall (s,r) \in \}\Upsilon^{EFF}, \forall k \in K^{EFF}, \forall t \in T \tag{20}$$

TABLE 4 | Related parameters of DG to be selected and conventional units.

	Type	Capacity/MW	Construction costs/(million yuan/MW)	Maintenance costs/(yuan/MWh)
Wind Turbines	1	1	130	300
	2	2	120	280
Conventional Units	1	0.95	1120	50
	2	2.25	1100	50

TABLE 5 | Related parameters for candidate transformers units.

Transformer type	Capacity/MW	Impedance/Ω	Investment costs/million yuan	Maintenance costs/yuan
1	12	0.16	450	1200
2	15	0.13	600	1500

$$y^{l}_{srkt} + y^{l}_{rskt} \le \sum_{\tau=1}^{t} x^{l}_{srk\tau} \quad \forall l \in \{NRF, NAF\}, \forall (s,r) \in \}\Upsilon^{l}, \forall k \in K^{l}, \forall t \in T \tag{21}$$

$$y^{ERF}_{srkt} + y^{ERF}_{rskt} \le 1 - \sum_{\tau=1}^{t} \sum_{\kappa \in K^{NRF}} x^{NRF}_{sr\kappa\tau} \quad \forall (s,r) \in \}\Upsilon^{ERF}, \forall k \in K^{ERF}, \forall t \in T \tag{22}$$

$$y^{NT}_{skt} \le \sum_{\tau=1}^{t} x^{NT}_{sk\tau} \quad \forall s \in \Omega^{SS}, \forall k \in K^{NT}, \forall t \in T \tag{23}$$

$$y^{p}_{skt} \le \sum_{\tau=1}^{t} x^{p}_{sk\tau} \quad \forall p \in P, \forall s \in \Omega^{p}, \forall k \in K^{p}, \forall t \in T \tag{24}$$

$$\sum_{l \in \{NRF, NAF\}} \sum_{k \in K^{l}} \sum_{(s,r) \in \}\Upsilon^{l}} C^{I,l}_{k} l_{sr} x^{l}_{srkt} + \sum_{s \in \Omega^{SS}} C^{I,SS}_{s} x^{SS}_{st} + \sum_{k \in K^{NT}} \times \sum_{s \in \Omega SS} C^{I,NT}_{k} x^{NT}_{skt} + \sum_{p \in P} \sum_{k \in K^{p}} \sum_{s \in \Omega^{p}} C^{I,p}_{k} \lambda \bar{G}^{p}_{k} x^{p}_{skt} \le IB_{t} \tag{25}$$

Where, IB_t is the investment budget for stage t; $\}\Upsilon^{l}$ is the set of feeder types l, where feeder type L: $\{EFF, REF, NRF, NAF\}$ represent existing feeders, replaceable feeders, new replaceable feeders and new feeders; l_{sr} is the length of the feeder sr; $x^{l}_{srkt}, x^{SS}_{st}, x^{NT}_{skt}, x^{p}_{skt}$ are 0–1 variables and it is used to indicate whether decision feeders, substations, transformers and distributed power supplies are constructed.

3 SIMULATION AND ANALYSIS

3.1 Parameter Setting

In this paper, to verify the validity of the proposed methodology, a 3-year phase planning analysis is conducted using the IEEE 24-node power distribution system. The system includes 20 load nodes, 4 substation nodes and 33 feeders, and its topology is shown in **Figure 1**. Where the system voltage level is 20 KV, the upper and lower limits of the node voltage are 0.95–1.05pu of the rated voltage, and the inflation rate is 0.05; the load data for the three stages are shown in **Table 1**, with a load power factor of 0.9 and a load cutting cost of 16 yuan/kwh; line data as shown in **Table 2**, with a feeder life of 30 years; The wind speed data for each region in the three stages are shown in **Table 3**; the parameters related to the DG to be selected and the conventional unit are shown in **Table 4**, where the positions to be selected are {1, 4, 5, 9, 15, 17, 18, 19} for the DG and {2, 3, 7, 13, 15, 16, 17, 20} for the conventional unit; the parameters of the constructed and to-be-constructed substation are shown in **Table 5**, and the cost of purchasing power from the substation is 0.49 yuan/kwh; the relevant parameters of the conductor to be selected are shown in **Table 6**.

The simulation was performed in Win10 environment with Intel(R) Core(TM) i5-7200U CPU @ 2.50GHz, running memory of 8 GB, and simulation software of MATLAB R2016b. Since the model developed is an integer linear programming model, the YALMIP & CPLEX solver is used to solve the model. Two cases are set up for comparative analysis.

Case I. distribution network expansion planning without considering distributed power sources.

Case II. Multi-stage expansion planning of distribution network considering distributed power sources (method in this paper).

3.2 Analysis of Planning Results

As can be seen in **Figure 2**, the two cases have significantly different planning results at each planning stage. The capacity of the feeder and transformer installed without distributed power is greater than the capacity of the feeder and transformer installed with distributed power. It results in larger investment costs in feeders and transformers. In the case of distributed generation, the load pressure can be effectively relieved by installing wind turbines as the load demand gradually increases. On the other hand, more distributed power sources are installed in the C zone, where wind speeds are higher, and conventional generators are mostly installed at load nodes outside the C zone.

TABLE 6 | Related parameters for candidate conductors units.

	Line type	Current limit/MVA	Impedance/(Ω/km)	Investment costs/(million yuan/km)
NRF	1	6.29	0.557	11.5
	2	9.21	0.487	18.2
NAF	1	3.96	0.731	9.1
	2	6.29	0.558	15.3

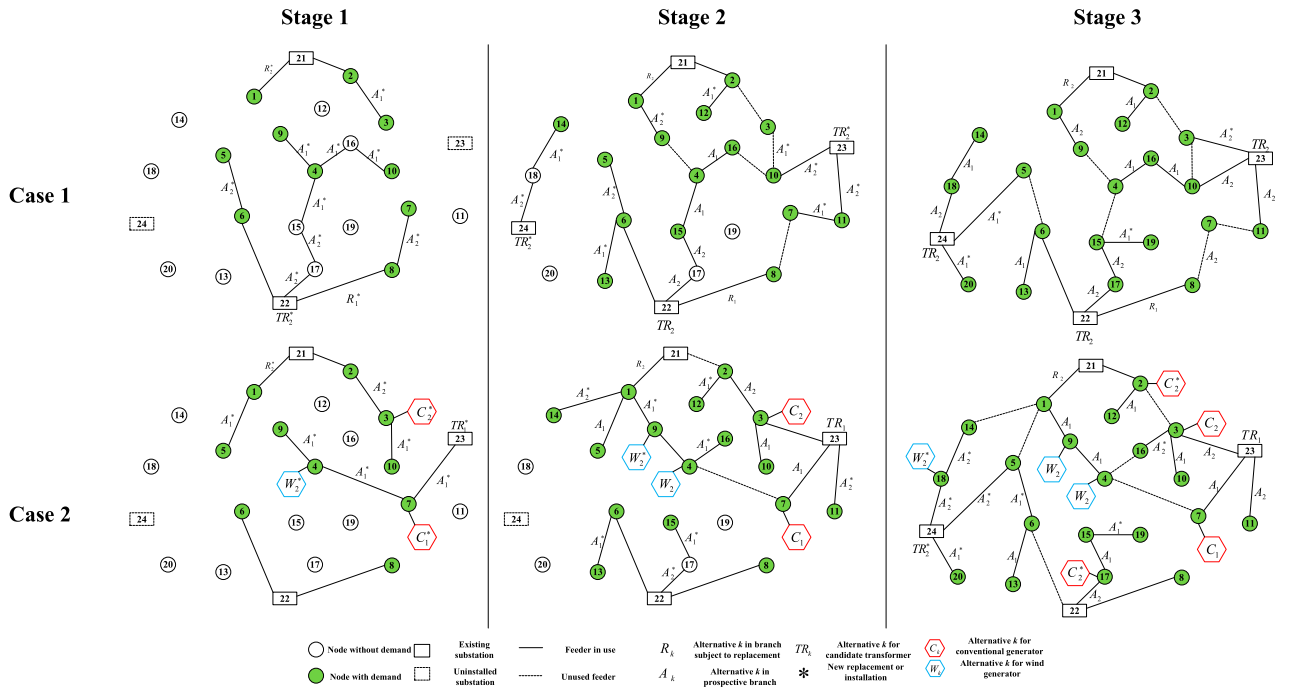

FIGURE 2 | Planning schemes for two cases.

TABLE 7 | Unit output and loss in different cases.

			Stage		
			1	2	3
Without DG	Production	Generators	0.00	0.00	0.00
		Transformers	107.54	187.36	309.97
	Losses	Generators	1.96	2.36	4.65
		Transformers	0.36	0.48	0.84
With DG	Production	Generators	26.47	52.81	76.45
		Transformers	80.54	139.74	228.54
	Losses	Generators	0.74	1.87	2.64
		Transformers	0.24	0.52	0.82

3.3 System Performance Comparison

The unit output as well as loss data for different cases are shown in **Table 7**. As can be seen in **Table 7**, the addition of distributed power sources leads to a significant reduction in the level of energy provided by the transformer located at the substation node. In addition, for Case 2, the energy losses in the feeder and transformer are lower than those in Case 1, except for the energy losses in the transformer in stage 2, which are slightly higher than those in Case 1. In stage 2, the energy provided by the transformer in Case 2 is lower compared to Case 1. However, the overall output is higher due to the distributed power supply.

TABLE 8 | Planning costs in different cases.

		Stage		
		1	2	3
Without DG	Investment cost/million yuan	8.84	16.055	6.11
	Maintenance cost/million yuan	0.065	0.13	0.13
	Production cost/million yuan	48.75	80.795	137.215
	Loss cost/million yuan	0.91	1.235	2.275
	Penalty cost/million yuan	0.00	0.00	0.00
With DG	Investment cost/million yuan	37.83	29.315	36.595
	Maintenance cost/million yuan	1.56	2.73	4.42
	Production cost/million yuan	41.665	68.51	116.675
	Loss cost/million yuan	0.455	1.04	1.495
	Penalty cost/million yuan	0.00	0.00	0.00

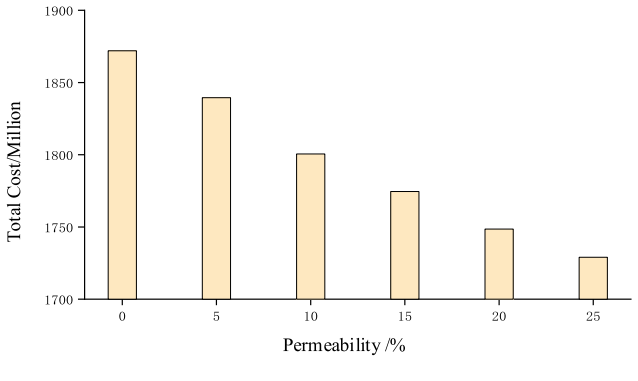

FIGURE 3 | The relationship between distributed power penetration level and total cost.

3.4 Comparison of Planning Economics

A comparison of the planning economics for different cases is shown in **Table 8**. The table shows that for Case 1 the investment cost in stage 2 is higher compared to stage 1 and stage 3. The reason for this is the construction of two new substations at nodes 23 and 24 in phase 2, including the installation of two new transformers at these nodes. But for Case 2, the biggest investment cost is during Stage 1. It is caused by the addition of substations and transformers at candidate node 23 in stage 1 and the installation of three distributed power sources at nodes 3, 4, and 7. In both cases, as load demand increases, O&M costs as well as wear and tear costs are gradually rising. It can be seen that the addition of DG makes Case 2 incur higher investment and maintenance costs compared to Case 1. However, the costs associated with energy production and energy losses are lower, resulting in more significant overall economics. The total cost is reduced by 7.55% relative to Case 1.

3.5 Analysis of Penetration Levels

Figure 3 shows the variation of the total cost for penetration levels between 0% and 25%. It can be seen that the total planning cost decreases significantly as the wind penetration level increases.

4 CONCLUSION

In this paper, the application of distributed power investment decision in multi-stage distribution expansion planning problem is studied, and a multi-stage coordinated planning method for distribution network taking into account distributed power is proposed. Simulation results show that, on the one hand, coordinating the investment decision of distributed power sources with the expansion planning of the distribution network can prevent the problems of isolated and transmission nodes. It also reduces network energy loss, thus improving the reliability of planning results. On the other hand, multi-stage planning can avoid the depreciation cost of equipment generated by overbuilding and equipment redundancy in the early stage of operation. Multi-stage planning is a more rational planning scheme based on the load demand at each planning stage and has good economic benefits.

DATA AVAILABILITY STATEMENT

The raw data supporting the conclusions of this article will be made available by the authors, without undue reservation.

AUTHOR CONTRIBUTIONS

QW: conceptualization, methodology, software, resources, formal analysis, investigation, writing—original draft, writing—review and editing. JM: conceptualization, methodology, software, resources, formal analysis, investigation, writing—review and editing.

REFERENCES

Afraz, A., Rezaeealam, B., Seyedshenava, S., and Doostizadeh, M. (2019). Active Distribution Network Planning Considering Shared Demand Management. *Ifs* 37 (6), 8015–8028. doi:10.3233/jifs-190420

Akbari, T., and Moghaddam, S. Z. (2020). Coordinated Scheme for Expansion Planning of Distribution Networks: A Bilevel Game Approach. *IET Generation, Transm. Distribution* 14 (14), 2839–2846. doi:10.1049/iet-gtd.2019.1924

Alarcon, J. A., Santamaria, F., Al-Sumaiti, A. S., and Rivera, S. (2020). Low-Capacity Exploitation of Distribution Networks and its Effect on the Planning of Distribution Networks[J]. *Energies* 8 (63), 4562–4573. doi:10.3390/en13081920

Borghei, M., and Ghassemi, M. (2021). Optimal Planning of Microgrids for Resilient Distribution Networks. *Int. J. Electr. Power Energ. Syst.* 128 (52), 106682–106693. doi:10.1016/j.ijepes.2020.106682

Cattani, I. B., Chaparro, E., and Barán, B. (2020). Distribution System Operation and Expansion Planning Using Network Reconfiguration[J]. *IEEE Latin America Trans.* 18 (5), 845–852. doi:10.1109/tla.2020.9082912

Delarestaghi, J. M., Arefi, A., Ledwich, G., and Borghetti, A. (2021). A Distribution Network Planning Model Considering Neighborhood Energy Trading. *Electric Power Syst. Res.* 191 (26), 106894. doi:10.1016/j.epsr.2020.106894

Faria, W. R., Martins, D. d. B., Nametala, C. A. L., and Pereira, B. R. (2020). Protection System Planning for Distribution Networks: A Probabilistic Approach. *Electric Power Syst. Res.* 189 (15), 106612–106623. doi:10.1016/j.epsr.2020.106612

Franco, J. F. (2016). Multistage Long-Term Expansion Planning of Electrical Distribution Systems Considering Multiple Alternatives[J]. *IEEE Trans. Power Syst.* 31 (3), 1900–1914. doi:10.1109/tpwrs.2015.2443175

Hemmati, R., Hooshmand, R.-A., and Taheri, N. (2015). Distribution Network Expansion Planning and DG Placement in the Presence of Uncertainties. *Int. J. Electr. Power Energ. Syst.* 73, 665–673. doi:10.1016/j.ijepes.2015.05.024

Jooshaki, M., Farzin, H., Abbaspour, A., Fotuhi-Firuzabad, M., and Lehtonen, M. (2020). A Model for Stochastic Planning of Distribution Network and Autonomous DG Units. *IEEE Trans. Ind. Inf.* 16 (6), 3685–3696. doi:10.1109/tii.2019.2936280

Koutsoukis, N., and Georgilakis, P. (2019). A Chance-Constrained Multistage Planning Method for Active Distribution Networks. *Energies* 12 (21), 4154. doi:10.3390/en12214154

Liu, X., Wang, L., Wu, Y., Wei, B., and Dongyang, Q. (2019). Locating and Sizing Planning of Distributed Generation Power Supply Consid-Ering the Operational Risk Cost of Distribution Network[J]. *Trans-actions China Electrotechnical Soc.* 34 (S1), 264–271. doi:10.19595/j.cnki.1000-6753.tces.181516

Mansor, N. N., and Levi, V. (2018). Operational Planning of Distribution Networks Based on Utility Planning Concepts[J]. *IEEE Trans. Power Syst.* 34 (3), 2114–2127. doi:10.1109/tpwrs.2018.2885275

Masoumi-Amiri, S. M., Shahabi, M., and Barforoushi, T. (2021). Interactive Framework Development for Microgrid Expansion Strategy and Distribution Network Expansion Planning. *Sustainable Energ. Grids Networks* 27 (11), 100512–100526. doi:10.1016/j.segan.2021.100512

Mojtahedzadeh, S., Ravadanegh, S. N., and Haghifam, M. R. (2021). Microgrid-based Resilient Distribution Network Planning for a new town. *IET Renew. Power Gen* 15 (15), 3524–3538. doi:10.1049/rpg2.12241

Muoz-Delgado, G., Contreras, J., and Arroyo, J. M. (2014). Joint Expansion Planning of Distributed Generation and Distribution Networks[J]. *IEEE Trans. Power Syst.* 30 (5), 2579–2590. doi:10.1109/TPWRS.2014.2364960

Narimani, A., Nourbakhsh, G., Arefi, A., Ledwich, G. F., and Walker, G. R. (2018). SAIDI Constrained Economic Planning and Utilization of Central Storage in Rural Distribution Networks[J]. *IEEE Syst. J.* 13 (1), 842–853. doi:10.1109/jsyst.2018.2852630

National Development and Reform Commission (2015). Several Opin-Ions of the central Committee of the Communist Party of China and the State council on Further Deepening the Reform of the Power System (Zhong Fa[2015]No.9) [EB/OL]. Available at : http://tgs.ndrc.gov.cn/zywj/201601/20160129773852.html.

Nikoobakht, A., Aghaei, J., Massrur, H. R., and Hemmati, R. (2020). Decentralized Hybrid Robust/stochastic Expansion Planning in Coordinated Transmission and Active Distribution Networks for Hosting Large-Scale Wind Energy[J]. *IET Generation Transm. Distribution* 14 (5), 797–807. doi:10.1049/iet-gtd.2019.0888

Saeed, H., and Mahmud, F. F. (2018). Integrated Planning for Distribution Automation and Network Capacity Expansion[J]. *IEEE Trans. Smart Grid* 10 (4), 4279–4288. doi:10.1109/TSG.2018.2855218

Shahbazi, A., Aghaei, J., Pirouzi, S., Niknam, T., Shafie-khah, M., and Catalão, J. P. S. (2021). Effects of Resilience-Oriented Design on Distribution Networks Operation Planning. *Electric Power Syst. Res.* 191 (6), 106902–106915. doi:10.1016/j.epsr.2020.106902

Shahbazi, A., Aghaei, J., Pirouzi, S., Niknam, T., Vahidinasab, V., Shafie-khah, M., et al. (2021). Holistic Approach to Resilient Electrical Energy Distribution Network Planning. *Int. J. Electr. Power Energ. Syst.* 132 (5), 107212–107226. doi:10.1016/j.ijepes.2021.107212

Tabares, A., Franco, J. F., Lavorato, M., and Rider, M. J. (2015). Multistage Long-Term Expansion Planning of Electrical Distribution Systems Considering Multiple Alternatives[J]. *IEEE Trans. Power Syst.* 31 (3), 1900–1914. doi:10.1109/tpwrs.2015.2448942

Vahidinasab, V., Tabarzadi, M., Arasteh, H., Alizadeh, M. I., Mohammad Beigi, M., Sheikhzadeh, H. R., et al. (2020). Overview of Electric Energy Distribution Networks Expansion Planning. *IEEE Access* 8 (79), 34750–34769. doi:10.1109/access.2020.2973455

Xiao, X., Wang, F., Shahidehpour, M., Li, Z., and Yan, M. (2020). Coordination of Distribution Network Reinforcement and DER Planning in Competitive Market[J]. *IEEE Trans. Smart Grid* 12 (3), 12261–12271. doi:10.1109/tsg.2020.3026014

Xing, H., Cheng, H., Zhang, Y., and Zeng, P. (2016). Active Distribution Network Expansion Planning Integrating Dispersed Energy Storage Systems. *IET Generation, Transm. Distribution* 10 (3), 638–644. doi:10.1049/iet-gtd.2015.0411

Conflict of Interest: QW is working at State Grid Corporation of China, and at the same time he is a PhD student at NCEPU.

The remaining author declares that the research was conducted in the absence of any commercial or financial relationships that could be construed as a potential conflict of interest.

Publisher's Note: All claims expressed in this article are solely those of the authors and do not necessarily represent those of their affiliated organizations, or those of the publisher, the editors and the reviewers. Any product that may be evaluated in this article, or claim that may be made by its manufacturer, is not guaranteed or endorsed by the publisher.

frontiers | Frontiers in Energy Research

ORIGINAL RESEARCH
published: 30 May 2022
doi: 10.3389/fenrg.2022.899804

Battery Life Prediction Based on a Hybrid Support Vector Regression Model

Yuan Chen[1], *Wenxian Duan*[2]*, *Zhenhuan Ding*[1] and *Yingli Li*[3]

[1]School of Artificial Intelligence, Anhui University, Hefei, China, [2]State Key Laboratory of Automotive Simulation and Control, Jilin University, Changchun, China, [3]School of Mechanical Engineering, Tongji University, Shanghai, China

An accurate state of health and remaining useful life prediction is important to provide effective judgment for the lithium-ion battery and reduce the probability of battery effectiveness. This article proposes a hybrid model for the prediction by combining an improved decomposition algorithm, an improved parameterization algorithm, and a least squares support vector regression algorithm. The capacity signal is decomposed by the improved complete ensemble empirical mode decomposition with an adaptive noise algorithm to solve the backward problem. Then, the least squares support vector regression algorithm is used to predict each decomposition component separately. To obtain better parameters of the prediction model, a good point set principle and inertia weights are introduced to optimize a sparrow search algorithm. Experimental results confirm that the proposed hybrid prediction model has high accuracy, good stability, and strong robustness, which achieves a minimum 0.3% mean absolute error of the B0005 battery. The impact of prediction steps on accuracy is also discussed in this article. The results verified the capacity accuracy of the batteries predicted by eight steps.

Keywords: lithium-ion battery, life prediction, parameterization algorithm, mode decomposition, support vector regression

OPEN ACCESS

Edited by:
Xiao Wang,
Wuhan University, China

Reviewed by:
Jiaqiang Tian,
Xi'an University of Technology, China
Tongmao Zhang,
The University of Manchester, United Kingdom
Yajian Zhang,
Shanghai University, China

***Correspondence:**
Wenxian Duan
dwx342977542@126.com

Specialty section:
This article was submitted to Smart Grids, a section of the journal Frontiers in Energy Research

Received: *19 March 2022*
Accepted: *08 April 2022*
Published: *30 May 2022*

Citation:
Chen Y, Duan W, Ding Z and Li Y (2022) Battery Life Prediction Based on a Hybrid Support Vector Regression Model. Front. Energy Res. 10:899804. doi: 10.3389/fenrg.2022.899804

INTRODUCTION

The lithium-ion battery has been widely used in pure electric or hybrid electric vehicles, satellites, and aircrafts due to its high energy density, long power endurance, satisfying nominal voltage, low self-discharge rate, long cycle, and rare memory effect (Lin et al., 1153; Li et al., 2021). With the increase in charging and discharging times, the chemical reaction inside the battery will become slow, which will eventually lead to the aging of the battery. The aging of the battery makes the actual capacity of the battery far lower than its rated capacity, resulting in a performance of degradation. An aging battery will directly lead to the failure of an automobile or satellite power system, affecting the regular use of the whole machine. In recent years, the prediction of battery state of health (SOH) and remaining useful life (RUL) has become a challenging problem in the field of prognostic and health management (PHM), to reduce some major disasters caused by battery aging. Extensive attention is attracted on the degradation of batteries. The estimation methods can be roughly divided into model-based methods and data-driven methods (Hannan et al., 2017; Kong et al., 2021).

The model-based method mainly uses the empirical degradation model such as the exponential model and polynomial model to describe the trend of battery capacity degradation, and then the method uses a particle filter (PF) to obtain and adjust the parameters of the model to track the aging trend of batteries (Wei et al., 2018). Li and Xu (2015) employed a mixture of Gaussian process (MGP) and a PF algorithm to predict battery SOH under uncertain conditions. Zhang et al. (2017a) developed an improved unscented

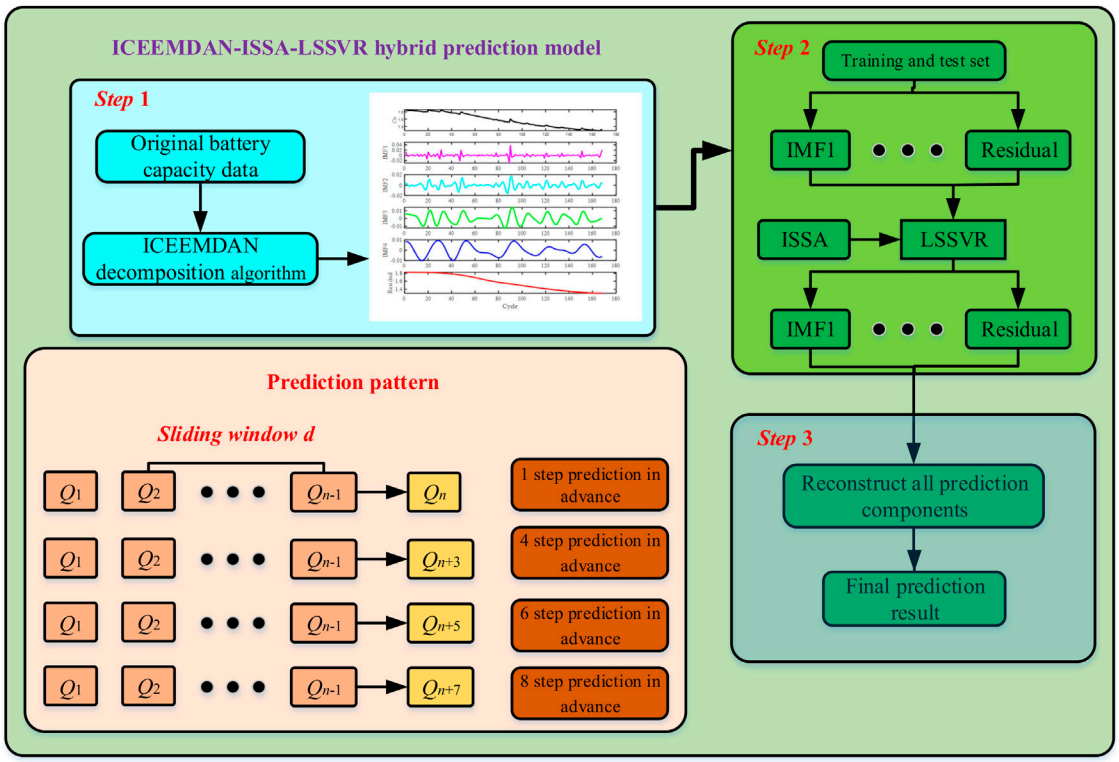

FIGURE 1 | Detailed prediction process.

particle filter (IUPF) method, using an algorithm called Markov chain Monte Carlo, to maintain the diversity of samples to solve the particle degeneracy phenomenon. Based on a double exponential mathematical model, Chen et al. (2020) applied a second-order central differential particle filter method to predict the SOH and RUL more accurately by optimizing the importance probability density function of the PF method. Hu et al. (2018) proposed an SOC and SOH co-estimation scheme based on the fractional-order calculus. The comparative studies show that it improves the modeling accuracy appreciably from its second- and third-order counterparts. The model-based method has succeeded in the PHM prediction of the battery. However, there is no general and accurate mathematical model to describe the degradation of different types of batteries, and the particle degeneracy phenomenon of the PF cannot be completely eliminated. In addition, the results are prone to large deviations due to the noise in the simulation process.

The data-driven approach obtains the battery degradation trend based on historical data without a definite mathematical model, and this approach is more suitable for different types of battery prediction. These methods include artificial neural network (ANN) (Li et al., 2019a; Gong et al., 2021; Yang, 2021), support vector regression (SVR) (Zhang et al., 2016; Feng et al., 2019; Wang et al., 2019; Li et al., 2020), relevance vector machine (RVM) (Cadini et al., 2019; Zhang et al., 2020), and Gaussian process regression (GPR) (Nagulapati et al., 2021; Pang et al., 2021). Deng et al. (2022) extracted the random capacity under different voltage segments from the partial charging process, and the average value and standard deviation of the random capacity were used as the input of the GPR model to estimate the battery SOH. Tang et al. (Tang et al., 2021) reconstructed the voltage curve from the measured data with the changing current and noise, and this article extracted the corresponding health indicators from the IC curve to estimate the SOH of the battery. To predict the SOH and RUL of batteries, Ma and Zhang et al. (Ma et al., 2019) employed a combination neural network composed of long short-term memory neural network (LSTM) and convolutional neural network (CNN) by using the false nearest neighbors method to calculate the size of the input window. The results showed that the proposed approach performs well in improving the accuracy and stability of the prediction. To optimize the extreme learning machine (ELM) model parameters, Zhu et al. (2019) developed an algorithm called the differential evolution gray wolf optimization (DE-GWO). The experiment results demonstrated that the DGWO-ELM method offers reduced errors. Although some deep learning networks such as LSTM and gated recurrent unit (GRU) usually perform well on a large number of datasets, they are weak in learning with small samples, and they consume a lot of computation (Zhao et al., 2018; Ungurean et al., 2020; Liu et al., 2021). SVR not only has the advantages of minimizing structural risks and being suitable for small sample predictions but also can improve the efficiency of regression convergence (Patil et al., 2015; Zhang et al., 2018). To find the optimal parameters of SVR algorithm, Qin et al. (2015) utilized particle swarm optimization (PSO) to find the best coefficient c and kernel radius g in SVR to improve the accuracy and the robustness of battery RUL prediction to a certain extent. However, the PSO algorithm is easy to fall into the

TABLE 1 | Benchmark functions (U, unimodal functions; M, multimodal functions).

Type	Test function	Range	Optimum
U	$F_1(x) = \sum_{i=1}^{n} x_i^2$	[-100,100]	0
	$F_2(x) = \sum_{i=1}^{n} \lvert x_i \rvert + \prod_{i=1}^{n} \lvert x_i \rvert$	[-10,10]	0
	$F_3(x) = \sum_{i=1}^{n-1} [100(x_{i+1} - x_i^2)^2 + (x_i - 1)^2]$	[-30,30]	0
	$F_4(x) = \sum_{i=1}^{n} i x_i^4 + random[0,1)$	[-1.28,1.28]	0
M	$F_5(x) = \sum_{i=1}^{n} -x_i \sin(\sqrt{\lvert x_i \rvert})$	[-500,500]	-418.9829*n*
	$F_6(x) = \frac{1}{4000} \sum_{i=1}^{m} x_i^2 - \prod_{i=1}^{n} \cos(\frac{x_i}{\sqrt{i}}) + 1$	[-600,600]	0

TABLE 2 | Parameter settings of the optimization algorithms.

Algorithm	Parameter
PSO	N = 30, Itermax = 500, c1 = c2 = 1.4944, and w = 0.729
DE	N = 30, Itermax = 500, FDE = 0.5, and CDE = 0.2
GWO	N = 30, Itermax = 500, ã = 2→0, and r1 and r2 ϵrand [0,1]
SSA	N = 30, Itermax = 500, SE = 0.2, SD = 0.1, and ST = 0.8
ISSA	N = 30, Itermax = 500, SE = 0.2, SD = 0.1, and ST = 0.8

TABLE 3 | Optimization results of algorithms (D = 30).

F	Value	PSO	DE	GWO	SSA	ISSA
F_1	Mean	1.86e-02	2.76e-04	1.47e-27	3.65e-63	1.01e-281
	Std	2.80e-02	1.19e-04	2.33e-27	2.47e-62	0
F_2	Mean	8.95e-01	1.88e-03	1.03e-16	5.17e-30	1.29e-140
	Std	6.76e-01	4.87e-04	1.03e-16	3.37e-29	6.43e-140
F_3	Mean	159.54	134.69	26.92	2.25e-04	1.66e-05
	Std	122.50	45.24	7.12e-01	1.28e-03	3.44 e-05
F_4	Mean	1.89e-01	5.21e-02	1.84e-03	1.71e-03	8.56e-04
	Std	8.88e-02	1.21e-02	9.81e-04	1.52e-03	7.81e-04
F_5	Mean	-4,024.68	-9,738.87	-5,871.08	-8,587.26	-9,727.40
	Std	858.26	522.22	970.23	488.62	642.65
F_6	Mean	4.30e-01	3.64e-03	3.72e-03	0	0
	Std	3.87e-01	3.61e-03	9.93e-03	0	0

local optimal value, and the problem of premature convergence exists. Li et al. (2019b) and Wang et al. (2019) designed an improved bird swarm algorithm (IBSA) and an artificial bee colony (ABC) algorithm to obtain the parameters of SVR models for life prediction. The aforementioned two hybrid algorithms can improve the accuracy of parameters and RUL prediction by using the historical capacity data. However, they also have a shortcoming of easily falling into the local optimum and then the global optimal value can hardly be found.

In the practical working process, batteries are easily affected by physical characteristics and the external working environment. There is a short-term capacity regeneration phenomenon of the batteries due to the accompanied noise (Li et al., 2019c; Sui et al., 2020). To reduce the disturbance of the random noise to battery SOH estimation, some signal processing methods have been proposed (Zhang et al., 2017b). Chang et al. (2017) directly used an improved empirical mode decomposition algorithm to decompose the original signal into several components and then employed the hybrid model of UKF and RVM to track the degradation trend of the batteries. On the basis of Ref. 36, Qu et al. (2019) developed the mode decomposition with adaptive noise and then utilized the PSO algorithm to optimize the mixed model for RUL prediction. The methods mentioned previously reduced the instability of time series which have strong nonlinearity, time-varying, and high complexity. However, they have the problems of some "spurious" modes in the early stages of the decomposition.

In order to solve the problems previously mentioned, a combination algorithm of improved CEEMDAN (ICEEMDAN), improved sparrow search algorithm (ISSA), and LSSVR model is proposed in this article. ICEEMDAN is utilized to decompose historical capacity data of batteries, and ISSA is introduced to obtain two important parameters of the LSSVR model to improve the performance of life prediction.

This article is organized as follows: related algorithms used in this work are presented in **Section 2**. **Section 3** mainly describes the experimental data, model evaluation criteria, and prediction process. Experimental results are analyzed and discussed in detail from three aspects with two open source datasets in **Section 4**. Conclusions and future work are presented in **Section 5**.

RELATED TECHNOLOGY AND THEORY

Decomposition Methods in Data Processing

The EMD proposed in 1988 is a time-frequency focusing algorithm with a high signal-to-noise ratio. It is suitable for processing non-stationary and nonlinear signals. According to the data time scale characteristics, complex signals can be decomposed into various intrinsic mode functions (IMFs).

In order to solve the problem of noise residue, modal aliasing, and false modes that appeared early in the EMD method, the ICEEMDAN algorithm is proposed by adding the positive and negative Gaussian white noise and calculating the local mean.

The detailed ICEEMDAN algorithm steps are described as follows:

Step 1:By **Eq. 1**, add noise to the original signal ζ.

$$\begin{aligned} \zeta^{(i)} &= \zeta + \beta_0 E_1(\omega^{(i)}), \\ \beta_0 &= \frac{\varepsilon_0 std(\zeta)}{std(E_1(\omega^{(i)}))}, \end{aligned} \tag{1}$$

where ε_0 is the reciprocal of the expected signal-to-noise ratio and $\omega^{(i)}$ is a Gaussian white noise with zero mean and unit variance.

Step 2: Decompose the noisy signal to obtain the first IMF_1 component and residual component R_1 by EMD algorithm.

$$\begin{aligned} R_1 &= \langle H(\zeta^{(i)}) \rangle, \\ IMF_1 &= \zeta - R_1. \end{aligned} \tag{2}$$

Step 3: The second residual component was calculated by the local mean of $R_1+\beta_1 E_2(\omega^{(i)})$, and then the second IMF_2 is calculated by:

$$IMF_2 = R_1 - \langle H(R_1 + \beta_1 E_2(\omega^{(i)})) \rangle. \tag{3}$$

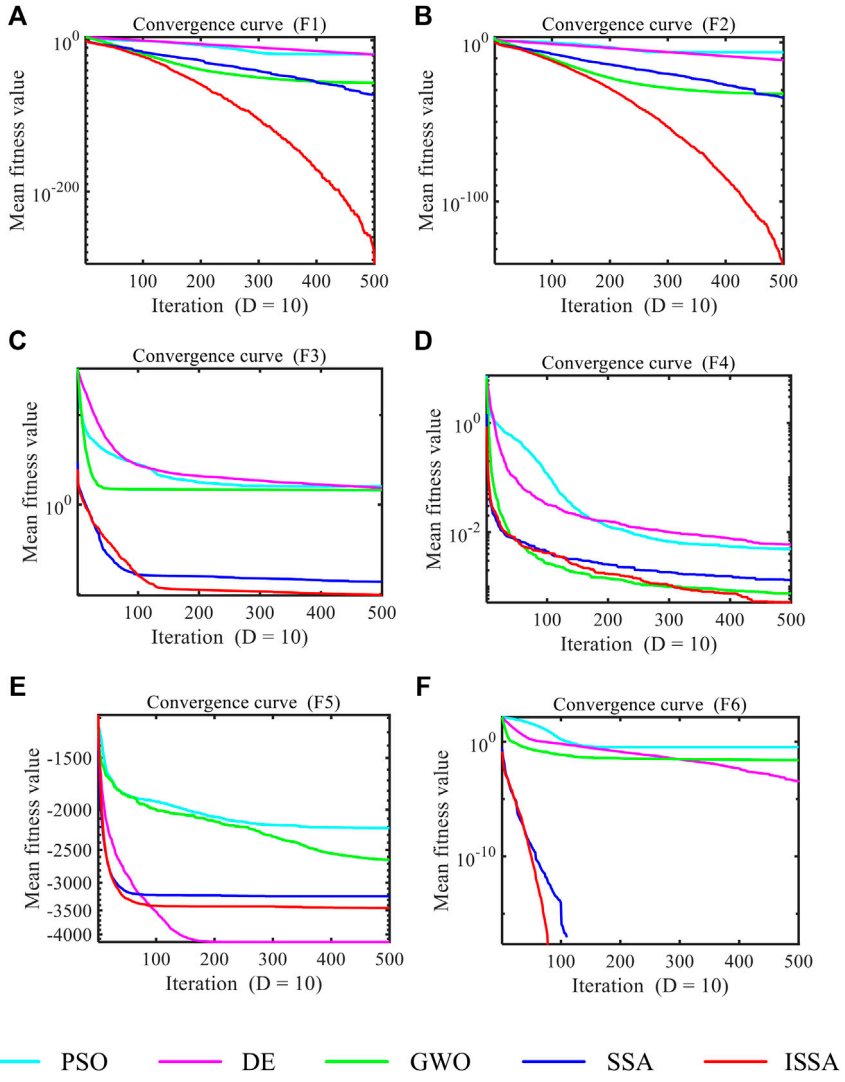

FIGURE 2 | Average fitness curve of the five algorithms **(A)** F1 **(B)** F2 **(C)** F3 **(D)** F4 **(E)** F5 **(F)** F6.

TABLE 4 | Parameter settings of the hybrid model.

Algorithm	Parameter
ISSA	N = 20, Itermax = 20, SE = 0.2, SD = 0.1, and ST = 0.8
ICEEMDAN	K = 500 and E1 (ω(i)) = 0.2
LSSVR	c = 500 and g = 500

Step 4: By **Eq. 4**, calculate the kth residue R_k in turn.

$$R_k = \langle H\left(R_{k-1} + \beta_{k-1} E_k\left(\omega^{(i)}\right)\right)\rangle, \quad k = 3, \ldots, K. \tag{4}$$

Step 5: Calculate the kth IMF_k component

$$IMF_k = R_{k-1} - R_k. \tag{5}$$

Step 6: Repeat steps 4 and 5 to obtain several IMFs and a residual component.

Sparrow Search Algorithm

The sparrow search algorithm (SSA) is a novel swarm intelligence optimization algorithm proposed in 2020, mainly inspired by the behavior of sparrows (Xue and Shen, 2020). Compared with other optimization algorithms such as GWO, DE, and PSO, it has achieved good results in engineering applications for its characteristics of fast convergence, high search accuracy, and strong robustness. The population of the sparrow is grouped into explorers and scroungers. Explorers are responsible for looking for food, and scroungers mainly obtain food following explorers. Each individual will monitor the behavior of other individuals and compete for food.

The sparrow search algorithm is represented as follows:

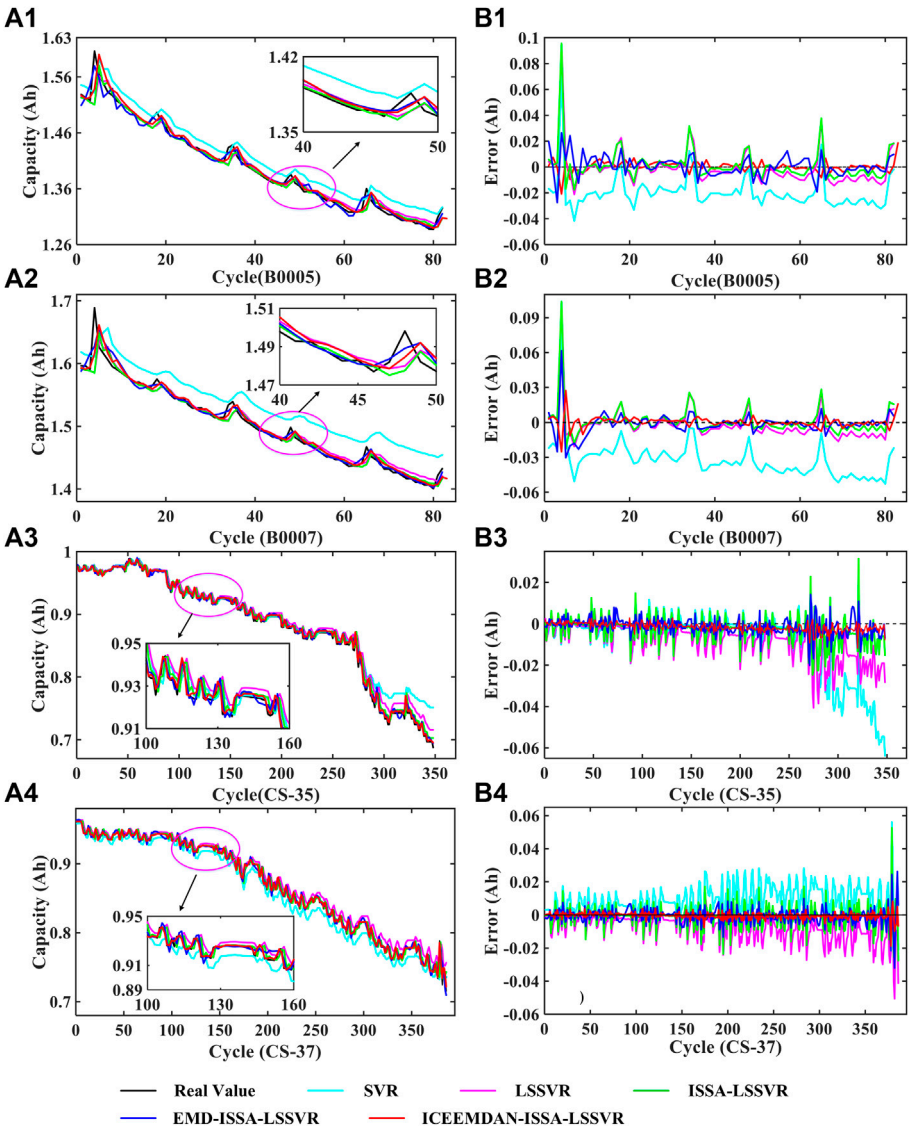

FIGURE 3 | Prediction capacity results and errors of different algorithmss (a1–a4) is the prediction capacity. (b1–b4) is the prediction error.

1) Position and fitness equation of sparrows

The position of sparrows can be described by the following matrix:

$$X = \begin{bmatrix} x_{1,1} & x_{1,2} & \cdots & x_{1,d} \\ x_{2,1} & x_{2,2} & \cdots & x_{2,d} \\ \cdots & \cdots & \cdots & \cdots \\ x_{n,1} & x_{n,2} & \cdots & x_{n,d} \end{bmatrix}, \tag{6}$$

where n is the number of sparrows and d is the dimension of the variable.

The fitness values are defined by the following vectors:

$$F_X = \begin{bmatrix} f([x_{1,1} & x_{1,2} & \cdots & x_{1,d}]) \\ f([x_{2,1} & x_{2,2} & \cdots & x_{1,d}]) \\ & \cdots & & \\ f([x_{n,1} & x_{n,2} & \cdots & x_{n,d}]) \end{bmatrix}. \tag{7}$$

2) Position update:

Explorers have better fitness and a larger range of foraging search than scroungers. Therefore, they can get the food in the search process first and provide the position and direction of food for the whole population.

Explorers' position update is described by **Eq. 8**.

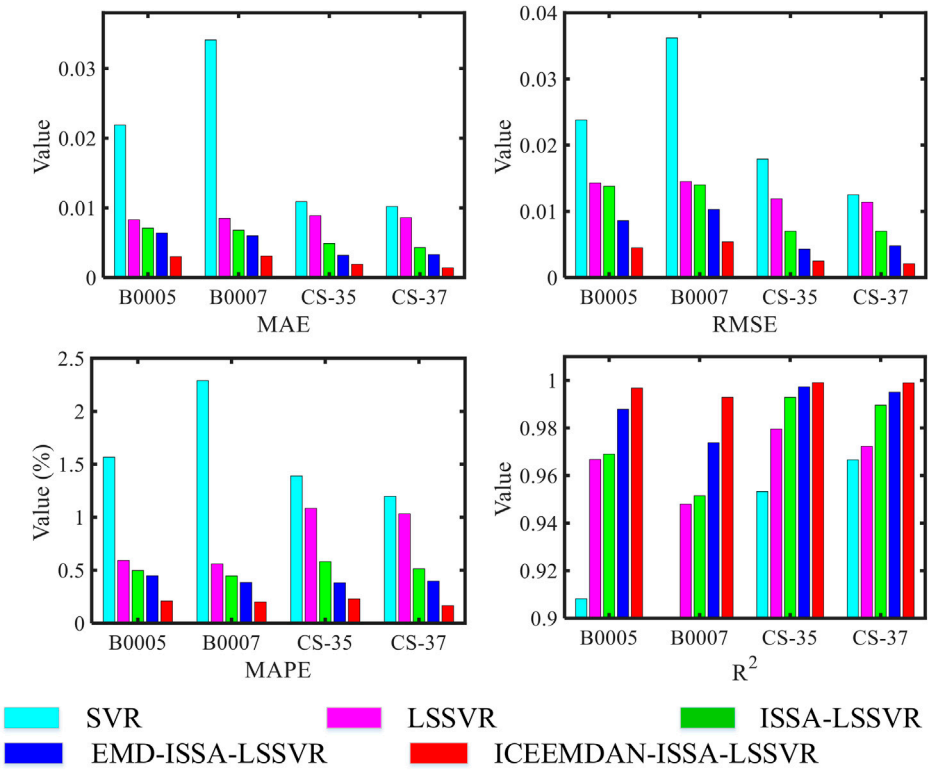

FIGURE 4 | Error metrics of the prediction model.

$$X_{i,j}^{t+1} = \begin{cases} X_{i,j}^{t} \cdot \exp\left(\dfrac{-i}{\alpha_{ssa} \cdot Iter_{\max}}\right), & if \quad AR < ST, \\ X_{i,j}^{t} + Q_{ssa} \cdot L_{ssa}, & if \quad AR \geq ST, \end{cases} \tag{8}$$

where t represents the number of current iterations, α_{ssa} represents a random number between 0 and 1, AR is the alarm value and $AR \in [0,1]$, ST is the safety threshold and $ST \in [0.5, 1]$, Q_{ssa} is the random number with Gaussian distribution, and L is a $1 \times d$ matrix in which each element has a value of 1.

3) Location update:

The location update of scroungers can be calculated by **Eq. 9**.

$$X_{i,j}^{t+1} = \begin{cases} Q_{ssa} \cdot \exp\left(\dfrac{X_{worst}^{t} - X_{i,j}^{t}}{i^2}\right), & if \quad i > N/2, \\ X_{P}^{t+1} + \left|X_{i,j}^{t} - X_{P}^{t+1}\right| \cdot A_{ssa}^{+} \cdot L_{ssa}, & if \quad otherwise, \end{cases} \tag{9}$$

where X_P is the best position occupied by the current explorer, X_{worst} is the worst position in the whole sparrow population, and A_{ssa} is a $1 \times d$ matrix in which each element is randomly assigned 1 or -1 and the condition $A_{ssa}^{+} = A_{ssa}^{\mathrm{T}} (A_{ssa} A_{ssa}^{\mathrm{T}})^{-1}$ is satisfied.

4) Anti-predation behavior:

The sparrow will make anti-predation behavior if they are aware of the danger, and can be calculated by:

$$X_{i,j}^{t+1} = \begin{cases} X_{best}^{t} + \beta_{ssa} \left|X_{i,j}^{t} - X_{best}^{t}\right|, \\ if \; f_i > f_{best}, \\ X_{i,j}^{t} + K_{ssa} \left(\dfrac{\left|X_{i,j}^{t} - X_{worst}^{t}\right|}{(f_i - f_{worst}) + \varepsilon_{ssa}}\right), \\ if \; f_i = f_{best}, \end{cases} \tag{10}$$

where X_{best} is the current global optimal position, β_{ssa} is the control parameter of the step with Gaussian distribution, which is a random number between 0 and 1, K_{ssa} is the step control parameter with the random value between -1 and 1, f_i is the current sparrow's fitness, f_{best} is the best current global fitness, f_{worst} is the worst current global fitness, and ε_{ssa} is the minimum constant to avoid zero denominators.

In the SSA, the population initialization is random, which may cause the population distribution to be far from the actual solution, thus reducing its optimization ability and convergence speed. In order to guarantee the population diversity of SSA, the good point set principle is developed for initialization to make the initial solution evenly distributed in the area of search.

In the H-dimensional euclidean space, there is a unit cube:

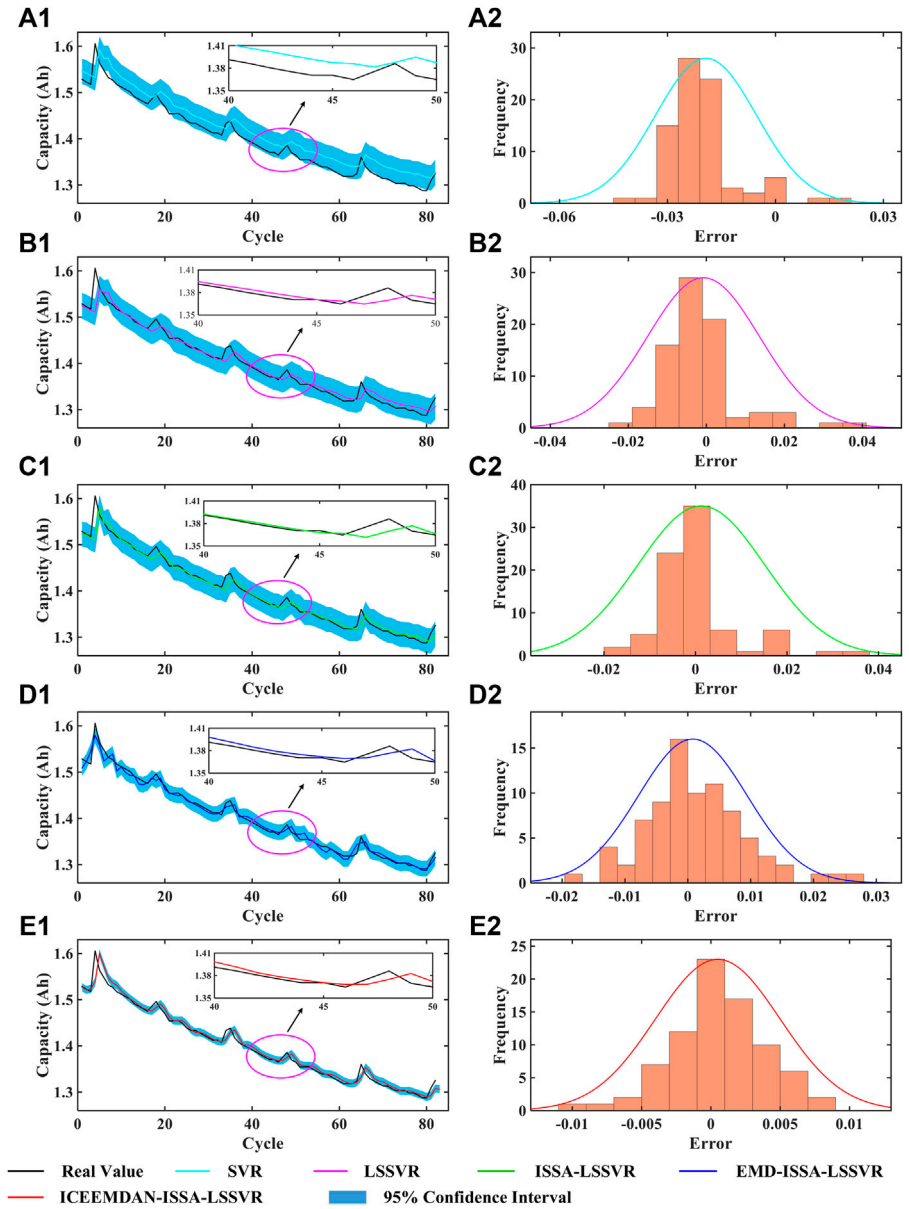

FIGURE 5 | Prediction results of the five algorithms on the B0005 battery. (a1–e1) Prediction capacity. (a2–e2) Probability density curve of the prediction error.

$$P_n(k) = \{((r_1^n \cdot k), \cdots, (r_H^n \cdot k))|1 \le k \le n\}. \tag{11}$$

Here, $P_n(k)$ is the good point set if the deviation satisfies the relationship.

$$\begin{aligned} \varphi(n) &= C(r,\varepsilon)n^{-1+\varepsilon}, \\ r &= 2\cos(2\pi r/p), \end{aligned} \tag{12}$$

where r is the good point, ε is a positive integer, $C(r, \varepsilon)$ is a constant, p is the smallest prime, and $(p\text{-}H/2) \ge H$.

The inertia weight is an important parameter in population optimization which affects the ability and speed of the global and local search. In this article, new adaptive weights are introduced by using adaptive weight coefficients to improve the optimization ability.

The adaptive weight formulas of w_{ssa} and the position update are as follows:

$$w_{ssa} = 1 - \lg((e-1) \cdot n/Iter_{\max} + 1),$$

$$X_{i,j}^{t+1} = \begin{cases} w_{ssa} \cdot \left(X_{i,j}^t \cdot \exp\left(\dfrac{-i}{\alpha_{ssa} \cdot Iter_{\max}} \right) \right), & if\ AR < ST, \\ w_{ssa} \cdot \left(X_{i,j}^t + Q_{ssa} L_{ssa} \right), & if\ AR \ge ST. \end{cases} \tag{13}$$

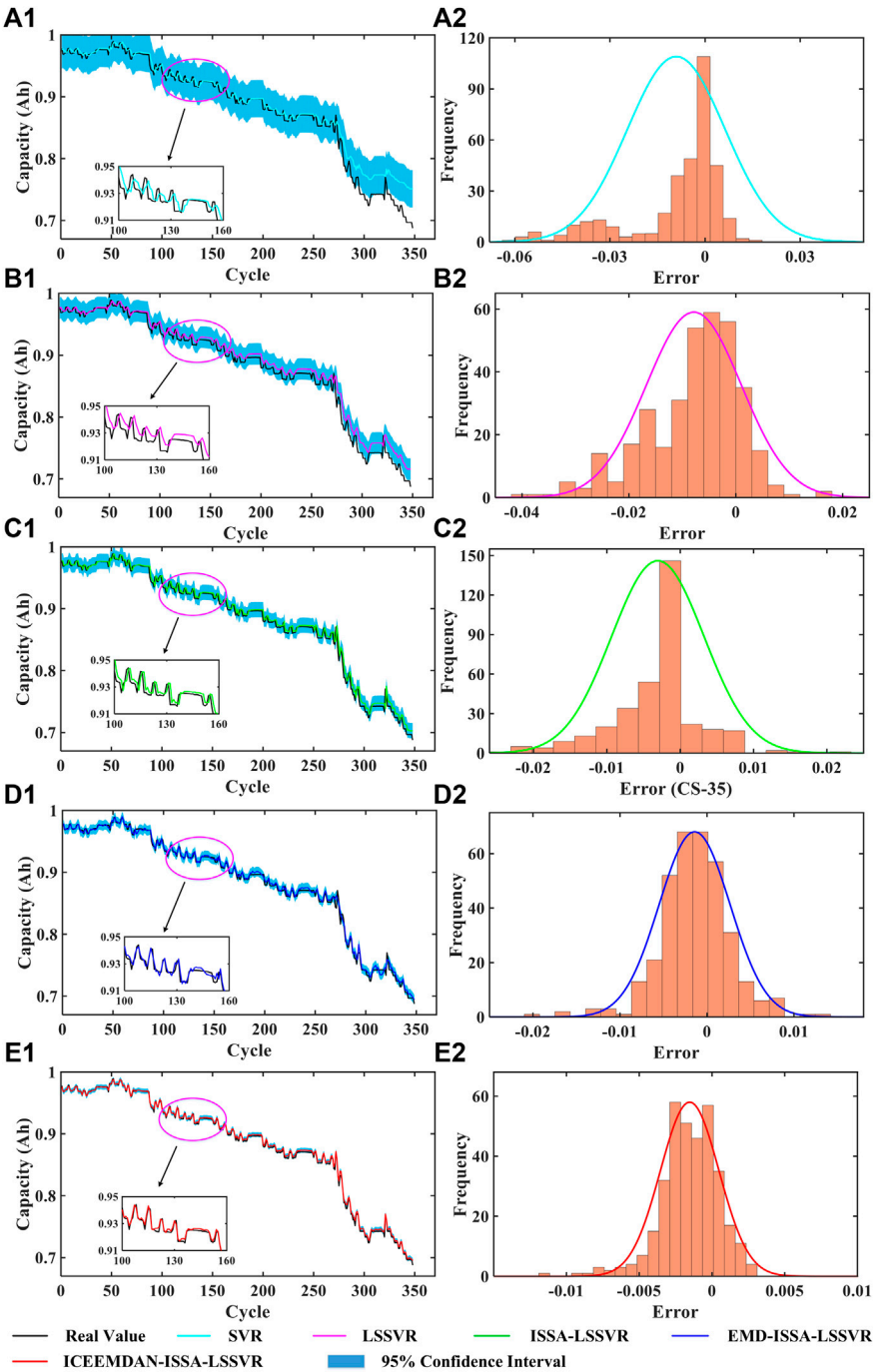

FIGURE 6 | Prediction results of the five algorithms on the CS-35 battery. (a1–e1) Prediction capacity. (a2–e2) Probability density curve of the prediction error.

Least Squares Support Vector Regression

The theory of SVM proposed in 1999 is not only efficient and simple but also has good robustness (Vapnik, 1999). It can be used to solve some classification regression problems with fewer samples. However, when dealing with large samples, the SVM algorithm will become complex with a long training time and low prediction accuracy. LSSVR converts the constraints of SVR into an equation, which has good nonlinear fitting ability and generalization ability. It significantly reduces the amount of calculation and improves the prediction accuracy.

The LSSVR model in a high-dimensional space can be described as:

$$f(x) = w^T \phi(x) + b, \tag{14}$$

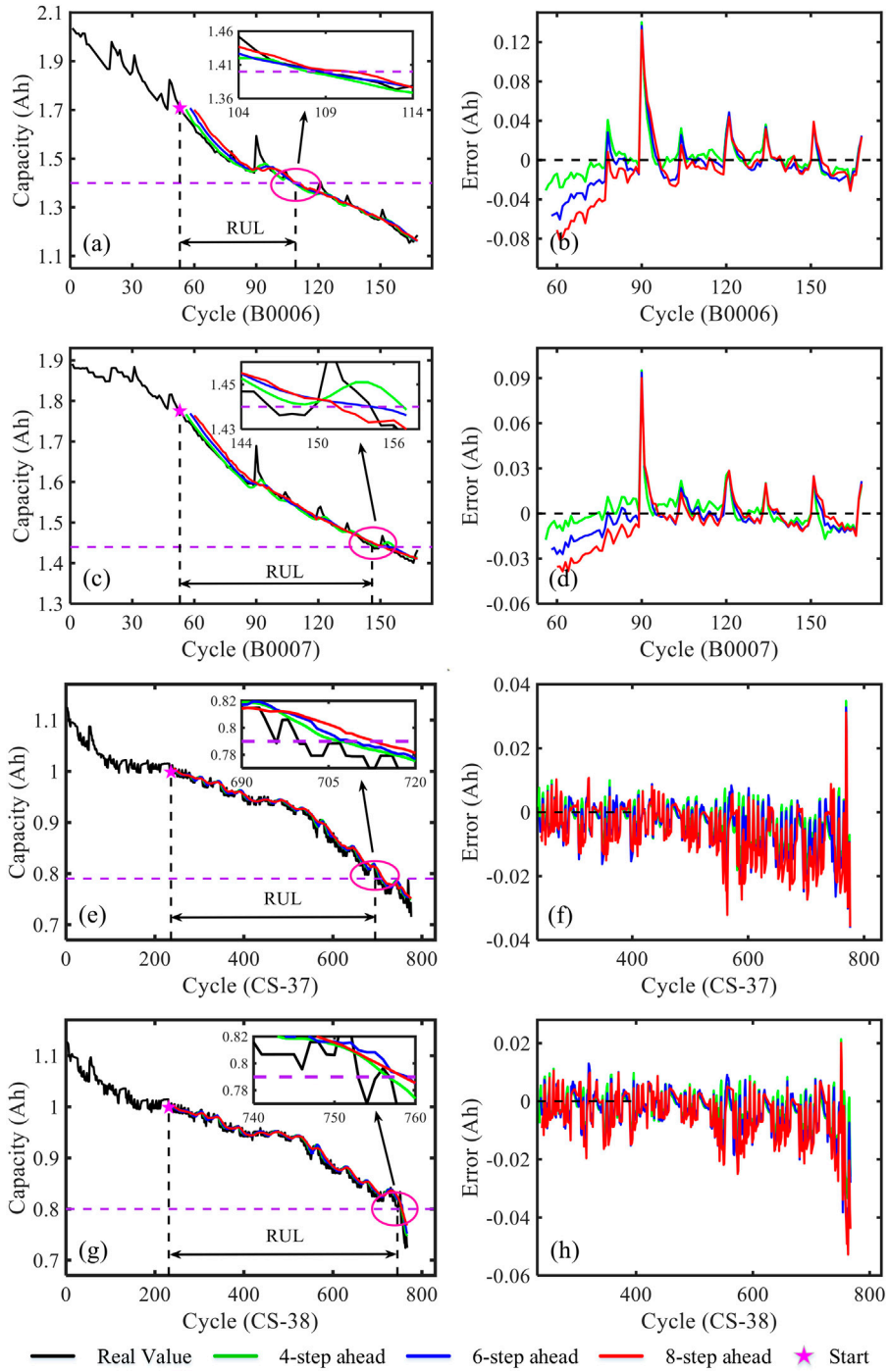

FIGURE 7 | Prediction results on the multi-step prediction in advance. **(A,B)** Capacity and error on B0006. **(C,D)** Capacity and error on B0007. **(E,F)** Capacity and error on CS-37. **(G,H)** Capacity and error on CS-38 of the prediction error.

where $f(x)$ is the output, $\phi(x)$ is a nonlinear mapping function, w is the normal vector, and b is the displacement term.

According to the minimum structural risk theory, the optimization problem of the LSSVR problem can be described by **Eq. 15**:

$$\min_{w,b} J(w,\xi) = \frac{1}{2}w^T w + \frac{\gamma}{2}\sum_{i=1}^{n}\xi_i^2,$$
$$s.t.\ f(x_i) = w^T\phi(x_i) + b + \xi_i, \tag{15}$$

where γ is the penalty constant, which affects the complexity of the model; the larger the value of γ is, the model will become

TABLE 5 | Capacity error statistics of the multi-step prediction.

Battery	Prediction model	MAE	RMSE	MAPE (%)	R^2	NE
B0006	4-step ahead	0.0124	0.0209	0.8641	0.9739	-1
	6-step ahead	0.0179	0.0266	1.2425	0.9552	0
	8-step ahead	0.0219	0.0320	1.5075	0.9306	1
B0007	4-step ahead	0.0077	0.0126	0.4947	0.9829	3
	6-step ahead	0.0097	0.0146	0.6128	0.9756	6
	8-step ahead	0.0122	0.0175	0.7665	0.9620	8
CS-37	4-step ahead	0.0059	0.0078	0.6877	0.9896	12
	6-step ahead	0.0066	0.0089	0.7691	0.9864	14
	8-step ahead	0.0075	0.0103	0.8778	0.9818	18
CS-38	4-step ahead	0.0054	0.0073	0.6092	0.9860	9
	6-step ahead	0.0062	0.0087	0.7017	0.9800	10
	8-step ahead	0.0069	0.0100	0.7910	0.9735	12

more accurate but more complex. The smaller the value of γ is, the larger the deviation between $f(x_i)$ and y_i can be tolerated. ξ_i is the regression error.

Transforming the optimization problem into a maximum value problem of α:

$$L(w, b, \alpha, \xi) = J(w, \xi) - \sum_{i=1}^{n} \alpha_i \left(w^T \phi(x_i) + b + \xi_i - y_i\right), \quad (16)$$

where α is the Lagrange multiplier.

The LSSVR regression model can be finally transformed into:

$$f(x) = \sum_{i=1}^{n} \alpha_i K\left(x_i, x_j\right) + b, \quad (17)$$

where $K(x_i,x_j)$ is the Gaussian radial basis kernel function.

Complete Prediction Process of the Hybrid Model

In this article, a combination algorithm is proposed to improve the performance of life prediction, which is shown in **Figure 1**.

The detailed prediction process is divided into the following steps:

Step 1: Decompose the capacity of batteries into five IMFs and a residual by the ICEEMDAN algorithm.

Step 2: Predict the signal after mode decomposition by the LSSVR model, the parameters of which are optimized by ISSA. The prediction modes are divided into 1-step advance forecast, 4-step advance forecast, 6-step advance forecast, and 8-step advance forecast.

Step 3: After the prediction of each decomposed signal is completed, the prediction results are reconstructed as the final capacity prediction results.

EXPERIMENTAL DATA AND DETAILED PREDICTION PROCESS

Experimental Data

Two open source datasets are applied for battery life prediction: one is from the National Aeronautics and Space Administration (NASA), and the other is from the Center for Advanced Life Cycle Engineering (CALCE) at the University of Maryland (He et al., 2011). In total, six lithium-ion batteries (#5, #6, #7, CS-35, CS-37, and CS-38) are selected from the datasets for algorithm verification. The batteries of NASA are commercially available 18,650 cells with a standard rated capacity of 2Ah, while those of CALCE are square lithium cobalt oxide batteries with a rated capacity of 1.1Ah. The cycle test experiments of the four batteries are all carried out at room temperature, which mainly include three different operational profiles. For NASA batteries, during the charging phase, the three batteries are initially charged in the constant current (CC) mode under a current of 1.5 A until the voltage reaches 4.2V; then, the voltage is kept at 4.2 V until the current drops to 20 mA. In the discharging phase, three batteries are discharged in the CC mode under a suitable current until the respective cut-off voltages are reached. The battery capacity degradation of NASA does not gradually decrease in strict accordance with the increase in the number of cycles, but rises in a small range. The main reason is that the chemical reaction inside the battery is easily interfered by external factors in cyclic charging and discharging. The batteries of CALCE are CS2 with the rated capacity of 1.1Ah. During the charging process, the batteries are charged in the CC mode at a constant current of 0.5C until the charging cut-off voltage reaches 4.2V, and then charged in the constant voltage (CV) mode until the current dropped to 0.05 A. During the discharge process, the batteries are discharged in the CC mode at different constant current until the discharge cut-off voltage reaches 2.7 V.

Model Evaluation Criteria

Four popular metrics are utilized to measure and demonstrate the model which is defined by **Eq. 18**:

$$\begin{aligned} MAE &= \frac{1}{M}\sum_{n=1}^{M}\left|y_n^* - y_n\right|, \\ RMSE &= \sqrt{\frac{1}{M}\sum_{n=1}^{M}\left(y_n^* - y_n\right)^2}, \\ MAPE &= \frac{1}{M}\sum_{n=1}^{M}\left|\frac{y_n^* - y_n}{y_n}\right| \times 100\%, \\ R^2 &= 1 - \frac{\sum_{n=1}^{M}\left(y_n - y_n^*\right)^2}{\sum_{n=1}^{M}\left(y_n - \bar{y}_n\right)^2}, \end{aligned} \quad (18)$$

where MAE represents the mean absolute error, M is the total number of the predicted battery capacity value, y_n* is the predicted battery capacity in the nth cycle, y_n is the actual battery capacity in the nth cycle, RMSE represents the root mean square error, MAPE represents the mean absolute percentage error, R^2 represents the decisive factor, and $\bar{y}_n$ is the average battery capacity.

The 95% confidence interval (CI) of the model is applied for the assessment of the uncertainty, which represents the interval of the prediction error. The equation is as follows:

$$95\%CI = y_n^* \pm 1.96 \times \mathrm{cov}(y_n). \tag{19}$$

A relative error (RE) is defined by **Eq. 20** to evaluate the model accuracy of RUL prediction:

$$RE = RUL_{pre} - RUL_{true}. \tag{20}$$

EXPERIMENTAL RESULTS AND ANALYSIS

In this article, the prediction performance and generalization ability of the proposed combination model is conducted from three aspects to verify the effectiveness.

ISSA Verification

Six classical functions are used including four unimodal functions and two multimodal functions for ISSA verification. The benchmark function is shown in **Table 1**.

To compare the optimization performance with ISSA, PSO, DE, GWO, and SSA algorithms are chosen. The parameter settings of the five optimization algorithms are listed in **Table 2**.

To ensure the robustness of the five algorithms, they are run 50 times for each test function independently, and then the average value (Mean) and the standard deviation (Std) are recorded and listed in **Table 3**. For functions F1 and F2, although the statistical index of ISSA has not been greatly improved, the stability of the algorithm is much higher than that of the other four algorithms. For the multimodal function F5, the ISSA achieves the best performance, and the result is much better than that of PSO, GWO, and SSA algorithms. For the multimodal function F6, the statistical results of ISSA and SSA are almost the same and are much better than the other optimization algorithms.

Figure 2 shows the average fitness curve of the five algorithms in each test function to better reflect the dynamic optimization results. It can be seen intuitively that the convergence speed and optimization ability of ISSA are higher than those of the other four algorithms.

Performance of the Hybrid Model

The superiority of the hybrid model is verified by comparison between SVR-LSSVR, ISSA-LSSVR, EMD-ISSA-LSSVR, and ICEEMDAN-ISSA-LSSVR algorithms on B0005, B0007, CS-35, and CS-37. The parameter settings of the hybrid model are listed in **Table 4**. The first 50% of each battery data is for training, while the left 50% is for test.

As shown in **Figure 3**, there is an obvious lag in the prediction results of SVR, LSSVR, and ISSA-LSSVR models on the four batteries. The prediction performance of LSSVR is better than that of SVR, confirming the superiority of LSSVR algorithm. The parameters of SVR and LSSVR prediction models are given randomly, while ISSA-LSSVR algorithm can automatically find the best parameters of LSSVR in the process of training. The proposed hybrid model achieves a better prediction effect and has a higher degree of fitting with the actual available capacity than EMD-ISSA-LSSVR, indicating that the effect of ICEEMDAN decomposition algorithm is better. **Figure 4** shows the statistical intuitive chart of the prediction error on the four batteries. For the three indexes of MAE, RMSE, and MAPE, the algorithms of SVR, LSSVR, ISSA-LSSVR, EMD-ISSA-LSSVR, and the proposed hybrid model show a decreasing trend, while R^2 shows an increasing trend, indicating that the proposed algorithm has the highest accuracy. Taking the B0007 battery as an example, the MAE, RMSE, and MAPE predicted by the proposed algorithm are 0.0031, 0.0054, and 0.2009, respectively. They are fewer than those of the other four algorithms. The R^2 predicted by the proposed algorithm is 0.9929 which is the largest.

To verify the stability of the algorithm, taking B0005 and CS-35 as examples, the capacity predictions including the confidence interval and the probability density curve are shown in **Figure 5** and **Figure 6**. The narrower 95% ranges indicate the stronger robustness of the prediction models. It can be seen from the figure that 95% IC of the proposed method is the smallest, which confirms that the proposed algorithm can give better performance for capacity prediction.

Performance on Multi-Step Prediction in Advance

Step-by-step prediction is sometimes difficult to ensure the safety and stability of battery long-term operation. To verify the stability of the model, the capacity is predicted in many steps, that is, the actual capacity in the window d is used to predict the capacity in the future $n + l$ secondary charge–discharge cycle, and l is the number of steps in advance. The ability of the proposed combination algorithm in multi-step prediction is tested by four steps in advance, six steps in advance, and eight steps in advance. B0006, B0007, CS-37, and CS-38 batteries are selected as experimental subjects.

The prediction results for the available capacity are shown in **Figure 7**. It is not difficult to see that with the increase of the number of cycles or prediction steps in advance, the error of the combined model will increase accordingly, and the corresponding life error will gradually increase.

Table 5 shows the statistical results of the capacity error of multi-step prediction. The MAE of B0007 obtained by eight steps in advance prediction is 0.0122 Ah, RMSE is 0.0175 Ah, MAPE is 0.7665, R^2 is 0.9620, and the battery life error is 8. The MAE of CS-37 obtained by eight steps prediction is 0.0075 Ah, RMSE is 0.0103 Ah, MAPE is 0.8778, R^2 is 0.9818, and the battery life error is 18. This demonstrates that the proposed hybrid model also has a higher prediction level in the multi-step prediction, which can predict the capacity of the battery in a longer time step and provide a more reliable guarantee for the safety of the battery system.

CONCLUSION

A novel data-driven hybrid model is proposed for SOH and RUL prediction of batteries. The feasibility and superiority of the model are verified from different directions by battery aging datasets from NASA and CALCE. The ISSA plays a significant role in the parameter optimization of LSSVR, which dramatically improves the prediction accuracy of capacity. The ICEEMDAN decomposition algorithm can reduce the random noise interference and solve the backward problem of capacity data. The results of eight steps in advance show that the proposed model can still obtain the accurate

capacity of the battery with a longer time step in the future. It can provide a more reliable guarantee for the safety of the battery system.

DATA AVAILABILITY STATEMENT

The original contributions presented in the study are included in the article/Supplementary Material, Further inquiries can be directed to the corresponding author.

AUTHOR CONTRIBUTIONS

WD, ZD, and YL: for critically reading the manuscript and helpful discussions; YC and WD: conceptualization; YC: methodology; YC and WD: software; YC and WD: validation; YC: formal analysis; YC: data curation; YC: writing–original draft preparation; YC and ZD: writing–review and editing; ZD and YL: supervision.

REFERENCES

Cadini, F., Sbarufatti, C., Cancelliere, F., and Giglio, M. (2019). State-of-life Prognosis and Diagnosis of Lithium-Ion Batteries by Data-Driven Particle Filters. *Appl. Energ.* 235, 661–672. doi:10.1016/j.apenergy.2018.10.095

Chang, Y., Fang, H., and Zhang, Y. (2017). A New Hybrid Method for the Prediction of the Remaining Useful Life of a Lithium-Ion Battery. *Appl. Energ.* 206, 1564–1578. doi:10.1016/j.apenergy.2017.09.106

Chen, Y., He, Y., Li, Z., Chen, L., and Zhang, C. (2020). Remaining Useful Life Prediction and State of Health Diagnosis of Lithium-Ion Battery Based on Second-Order Central Difference Particle Filter. *IEEE Access* 8, 37305–37313. doi:10.1109/access.2020.2974401

Deng, Z., Hu, X., Li, P., Lin, X., and Bian, X. (2022). Data-Driven Battery State of Health Estimation Based on Random Partial Charging Data. *IEEE Trans. Power Electron.* 37 (5), 5021–5031. doi:10.1109/tpel.2021.3134701

Feng, X., Weng, C., He, X., Han, X., Lu, L., Ren, D., et al. (2019). Online State-Of-Health Estimation for Li-Ion Battery Using Partial Charging Segment Based on Support Vector Machine. *IEEE Trans. Veh. Technol.* 68 (9), 8583–8592. doi:10.1109/tvt.2019.2927120

Gong, C., Xwa, B., and Yha, B. (2021). Remaining Useful Life and State of Health Prediction for Lithium Batteries Based on Empirical Mode Decomposition and a Long and Short Memory Neural Network[J]. *Energy* 232, 116812.

Hannan, M. A., Lipu, M. S. H., Hussain, A., and Mohamed, A. (2017). A Review of Lithium-Ion Battery State of Charge Estimation and Management System in Electric Vehicle Applications: Challenges and Recommendations. *Renew. Sust. Energ. Rev.* 78, 834–854. doi:10.1016/j.rser.2017.05.001

He, W., Williard, N., Osterman, M., and Pecht, M. (2011). Prognostics of Lithium-Ion Batteries Based on Dempster-Shafer Theory and the Bayesian Monte Carlo Method. *J. Power Sourc.* 196 (23), 10314–10321. doi:10.1016/j.jpowsour.2011.08.040

Hu, X., Yuan, H., Zou, C., Li, Z., and Zhang, L. (2018). Co-Estimation of State of Charge and State of Health for Lithium-Ion Batteries Based on Fractional-Order Calculus. *IEEE Trans. Veh. Technol.* 67 (11), 10319–10329. doi:10.1109/tvt.2018.2865664

Kong, J.-z., Yang, F., Zhang, X., Pan, E., Peng, Z., and Wang, D. (2021). Voltage-temperature Health Feature Extraction to Improve Prognostics and Health Management of Lithium-Ion Batteries. *Energy* 223 (6), 120114. doi:10.1016/j.energy.2021.120114

Li, F., and Xu, J. (2015). A New Prognostics Method for State of Health Estimation of Lithium-Ion Batteries Based on a Mixture of Gaussian Process Models and Particle Filter. *Microelectronics Reliability* 55 (7), 1035–1045. doi:10.1016/j.microrel.2015.02.025

Li, L.-L., Liu, Z.-F., Tseng, M.-L., and Chiu, A. S. F. (2019). Enhancing the Lithium-Ion Battery Life Predictability Using a Hybrid Method. *Appl. Soft Comput.* 74, 110–121. doi:10.1016/j.asoc.2018.10.014

Li, W., Jiao, Z., Du, L., Fan, W., and Zhu, Y. (2019). An Indirect RUL Prognosis for Lithium-Ion Battery under Vibration Stress Using Elman Neural Network. *Int. J. Hydrogen Energ.* 44 (23), 12270–12276. doi:10.1016/j.ijhydene.2019.03.101

Li, X., Yuan, C., and Wang, Z. (2020). State of Health Estimation for Li-Ion Battery via Partial Incremental Capacity Analysis Based on Support Vector Regression. *Energy* 203, 117852. doi:10.1016/j.energy.2020.117852

Li, X., Zhang, L., Wang, Z., and Dong, P. (2019). Remaining Useful Life Prediction for Lithium-Ion Batteries Based on a Hybrid Model Combining the Long Short-Term Memory and Elman Neural Networks. *J. Energ. Storage* 21, 510–518. doi:10.1016/j.est.2018.12.011

Li, Y., Gao, D. W., Gao, W., Zhang, H., and Zhou, J. (2021). A Distributed Double-Newton Descent Algorithm for Cooperative Energy Management of Multiple Energy Bodies in Energy Internet. *IEEE Trans. Ind. Inf.* 17 (9), 5993–6003. doi:10.1109/tii.2020.3029974

Lin, C. P., Cabrera, J., Yang, F., Ling, M. H., Tsui, K. L., and Bae, S. J. Battery State of Health Modeling and Remaining Useful Life Prediction through Time Series Model[J]. *Appl. Energ.* 275, 115338.

Liu, K., Shang, Y., Ouyang, Q., and Widanage, W. D. (2021). A Data-Driven Approach with Uncertainty Quantification for Predicting Future Capacities and Remaining Useful Life of Lithium-Ion Battery. *IEEE Trans. Ind. Electron.* 68 (4), 3170–3180. doi:10.1109/tie.2020.2973876

Ma, G., Zhang, Y., Cheng, C., Zhou, B., Hu, P., and Yuan, Y. (2019). Remaining Useful Life Prediction of Lithium-Ion Batteries Based on False Nearest Neighbors and a Hybrid Neural Network. *Appl. Energ.* 253, 113626. doi:10.1016/j.apenergy.2019.113626

Nagulapati, V. M., Lee, H., Jung, D., Brigljevic, B., Choi, Y., and Lim, H. (2021). Capacity Estimation of Batteries: Influence of Training Dataset Size and Diversity on Data Driven Prognostic Models, *Reliability Eng. Syst. Saf.* 216. 108048. doi:10.1016/j.ress.2021.108048

Pang, X., Liu, X., Jia, J., Wen, J., Shi, Y., Zeng, J., et al. (2021). A Lithium-Ion Battery Remaining Useful Life Prediction Method Based on the Incremental Capacity Analysis and Gaussian Process Regression. *Microelectronics Reliability* 127, 114405. doi:10.1016/j.microrel.2021.114405

Patil, M. A., Tagade, P., Hariharan, K. S., Kolake, S. M., Song, T., Yeo, T., et al. (2015). A Novel Multistage Support Vector Machine Based Approach for Li Ion Battery Remaining Useful Life Estimation. *Appl. Energ.* 159, 285–297. doi:10.1016/j.apenergy.2015.08.119

Qin, T., Zeng, S., and Guo, J. (2015). Robust Prognostics for State of Health Estimation of Lithium-Ion Batteries Based on an Improved PSO–SVR Model [J]. *Microelectronics and Reliability* 55 (9-10), 1280–1284. doi:10.1016/j.microrel.2015.06.133

Qu, J., Liu, F., Ma, Y., and Fan, J. (2019). A Neural-Network-Based Method for RUL Prediction and SOH Monitoring of Lithium-Ion Battery. *IEEE Access* 7 (99), 87178–87191. doi:10.1109/access.2019.2925468

Sui, X., He, S., Stroe, D. I., and Teodorescu, R. (2020). in Lithium-ion Battery State of Health Estimation Using Empirical Mode Decomposition Sample Entropy and Support Vector machine[C]//2020 IEEE Applied Power Electronics Conference and Exposition (APEC) (IEEE), 3424–3429.

Tang, X., Wang, Y., Liu, Q., and Gao, F., (2021). Reconstruction of the Incremental Capacity Trajectories from Current-Varying Profiles for Lithium-Ion Batteries [J]. *ISCIENCE* 24 (10), 103103. doi:10.1016/j.isci.2021.103103

Ungurean, L., Micea, M. V., and Cârstoiu, G. (2020). Online State of Health Prediction Method for Lithium-ion Batteries, Based on Gated Recurrent Unit Neural Networks. *Int. J. Energ. Res* 44 (8), 6767–6777. doi:10.1002/er.5413

Vapnik, V. N. (1999). An Overview of Statistical Learning Theory. *IEEE Trans. Neural Netw.* 10 (5), 988–999. doi:10.1109/72.788640

Wang, Y., Ni, Y., Lu, S., Wang, J., and Zhang, X. (2019). Remaining Useful Life Prediction of Lithium-Ion Batteries Using Support Vector Regression Optimized by Artificial Bee colony. *IEEE Trans. Veh. Technol.* 68 (10), 9543–9553. doi:10.1109/tvt.2019.2932605

Wei, J., Dong, G., and Chen, Z. (2018). Remaining Useful Life Prediction and State of Health Diagnosis for Lithium-Ion Batteries Using Particle Filter and Support

Vector Regression. *IEEE Trans. Ind. Electron.* 65 (7), 5634–5643. doi:10.1109/tie.2017.2782224

Xue, J., and Shen, B. (2020). A Novel Swarm Intelligence Optimization Approach: Sparrow Search Algorithm. *Syst. Sci. Control. Eng.* 8 (1), 22–34. doi:10.1080/21642583.2019.1708830

Yang, Y. (2021). A Machine-Learning Prediction Method of Lithium-Ion Battery Life Based on Charge Process for Different Applications. *Appl. Energ.* 292 (5), 116897. doi:10.1016/j.apenergy.2021.116897

Zhang, C., He, Y., Du, B., Yuan, L., Li, B., and Jiang, S. (2020). Transformer Fault Diagnosis Method Using IoT Based Monitoring System and Ensemble Machine Learning. *Future Generation Comp. Syst.* 108, 533–545. doi:10.1016/j.future.2020.03.008

Zhang, C., He, Y., Yuan, L., He, W., Xiang, S., and Li, Z. (2016). A Novel Approach for Diagnosis of Analog Circuit Fault by Using GMKL-SVM and PSO. *J. Electron. Test.* 32 (5), 531–540. doi:10.1007/s10836-016-5616-y

Zhang, C., He, Y., Yuan, L., and Xiang, S. (2017). Capacity Prognostics of Lithium-Ion Batteries Using EMD Denoising and Multiple Kernel RVM. *IEEE Access* 5, 12061–12070. doi:10.1109/access.2017.2716353

Zhang, X., Miao, Q., and Liu, Z. (2017). Remaining Useful Life Prediction of Lithium-Ion Battery Using an Improved UPF Method Based on MCMC. *Microelectronics Reliability* 75, 288–295. doi:10.1016/j.microrel.2017.02.012

Zhang, Y., Xiong, R., He, H., and Pecht, M. G. (2018). Long Short-Term Memory Recurrent Neural Network for Remaining Useful Life Prediction of Lithium-Ion Batteries. *IEEE Trans. Veh. Technol.* 67 (7), 5695–5705. doi:10.1109/tvt.2018.2805189

Zhao, Q., Qin, X., Zhao, H., and Feng, W. (2018). A Novel Prediction Method Based on the Support Vector Regression for the Remaining Useful Life of Lithium-Ion Batteries. *Microelectronics Reliability* 85, 99–108. doi:10.1016/j.microrel.2018.04.007

Zhu, J., Tan, T., Wu, L., and Yuan, H. (2019). RUL Prediction of Lithium-Ion Battery Based on Improved DGWO-ELM Method in a Random Discharge Rates Environment. *IEEE Access* 7, 125176–125187. doi:10.1109/access.2019.2936822

Conflict of Interest: The authors declare that the research was conducted in the absence of any commercial or financial relationships that could be construed as a potential conflict of interest.

Publisher's Note: All claims expressed in this article are solely those of the authors and do not necessarily represent those of their affiliated organizations, or those of the publisher, the editors, and the reviewers. Any product that may be evaluated in this article, or claim that may be made by its manufacturer, is not guaranteed or endorsed by the publisher.

frontiers | Frontiers in Energy Research

ORIGINAL RESEARCH
published: 28 June 2022
doi: 10.3389/fenrg.2022.886845

Optimal Dispatch of a Virtual Storage Plant Using Inexact ADMM

Defu Cai[1], Zuowei Wang[1], Xiao Wang[2], Yang Wang[3], Wenna Wang[1], Kunpeng Zhou[1] and Dehua Yu[4]*

[1]State Grid Hubei Electric Power Research Institute, Wuhan, China, [2]School of Electrical Engineering and Automation, Wuhan University, Wuhan, China, [3]School of Automation, Wuhan University of Technology, Wuhan, China, [4]State Grid Hubei Electric Power Co., Ltd., Wuhan, China

A virtual storage plant (VSP) is identified as an effective approach to aggregating distributed storage devices participating in power network supports with similar capability as bulk storage systems. In this study, we develop a distributed control framework for cost-effective storage coordination in the distribution networks, in which the energy storage units are coordinated to contribute to a given power reference at the aggregated level while regulating the local network voltages in the presence of renewable generations. The salient features of the proposed VSP control roots from the successful employment of an inexact alternating direction method of multiplier (ADMM) algorithm, in which the primal updates have analytical solutions in closed form using proximal operators, which significantly reduces the computation efforts of individual storage agents, and renders fast storage dispatch. The proposed control is favorable for near real-time storage dispatch in an optimal manner, and its effectiveness is demonstrated using realistic distributed networks in the simulations.

Keywords: energy storage, virtual storage plant, ADMM, proximal operator, power system

OPEN ACCESS

Edited by:
Xingshuo Li,
Nanjing Normal University, China

Reviewed by:
Tianqiao Zhao,
Brookhaven National Laboratory (DOE), United States
Yushuai Li,
University of Oslo, Norway
Haoji Liu,
The University of Manchester, United Kingdom
Zhai Mingda,
National University of Defense Technology, China

****Correspondence:***
Xiao Wang
xiaowang@whu.edu.cn

Specialty section:
This article was submitted to Smart Grids, a section of the journal Frontiers in Energy Research

Received: *01 March 2022*
Accepted: *09 May 2022*
Published: *28 June 2022*

Citation:
Cai D, Wang Z, Wang X, Wang Y, Wang W, Zhou K and Yu D (2022) Optimal Dispatch of a Virtual Storage Plant Using Inexact ADMM. Front. Energy Res. 10:886845. doi: 10.3389/fenrg.2022.886845

INTRODUCTION

Distributed energy resources (DERs) transform the conventional role of passive distribution networks in modern power grids. These DERs include dispatchable units, such as diesel generators, energy storage systems, and nondispatchable units, for example, rooftop PV and small wind turbine systems. Although the deployment of renewable energy significantly helps with reduced carbon emissions, with their increased penetration, new network regulation issues appear. Distributed energy storage devices, located closed to the end-users and covering wide geographical areas, are identified as an effective measure to accommodate the intermittency of renewables without compromising the quality of power delivery (Morstyn et al., 2016).

Energy storage systems are widely available at different levels of a power system. As utility-scale storage systems, pumped-hydro storage, compressed-air energy storage, etc., have a long history of participating in energy markets and providing ancillary services to the transmission levels. In the near decades, distributed storage devices are integrated with smaller capacities but larger unit numbers. By the end of 2019, the residential energy storage systems coupled with rooftop PVs reached 2GW, representing a 57% annual increase in Europe; electrical vehicles, whose batteries can potentially contribute to grid supports, attained a 184% annual increase by September 2020 in the United Kingdom (Energy Storage News, 2019). The aggregation of distributed storage devices has a competitive capacity and presents more benefits over bulk storage. Such aggregated storage system is

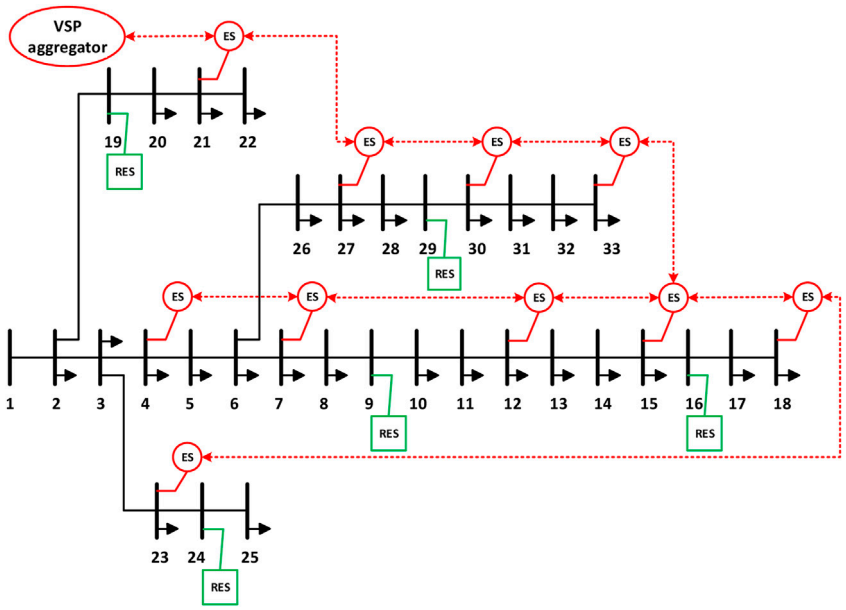

FIGURE 1 | Diagram of the IEEE 33-bus system with distributed energy storage systems aggregated as a VSP (black solid line: distribution lines; red dashed line: communication lines).

designed as a virtual storage plant (VSP), which seeks to use available storage resources providing flexibility to the large network interconnections.

The coordination of storage devices in a VSP relies on the cyber network for storage communications. This coincides with the concept of virtual power plants (VPPs) for the integration of general DERs (Kim et al., 2019; Cheng et al., 2017). The typical centralized control, in which a control center has access to every storage unit, will soon become inadequate regarding the expansions of the scales of storage in future distribution levels. On the other hand, distributed control collaborates individual agents to settle a given target based on neighboring communication, not only reducing the required bandwidth of the cyber layers but also enhancing robustness against failures and noises of the integrated systems (Olfati-Saber et al., 2007). Existing literature studies on distributed controls of power networks can be categorized into consensus-based controls (Wang et al., 2018,2019; Li et al., 2017) and optimization-based distributed controls (Yang et al., 2013a; Dall'Anese et al., 2018; Sulc et al., 2014; Tang et al., 2019; Li et al., 2019). Compared to the consensus controls, distributed optimization can generally achieve more sophisticated objectives, although deriving distributed solutions are not straightforward as that in a centralized setup. Yang et al. (2013b) and Xu et al. (2015) exploited the summation invariant of agent states under special cyber topologies, such that all agents are aggregated to provide a fixed amount of power and meanwhile minimize the overall cost; a similar method is employed for optimal VPP dispatch considering cyber attack in Li et al. (2018). Although these consensus controls are simple and effective in synchronizing agent states, system constraints cannot be easily handled by

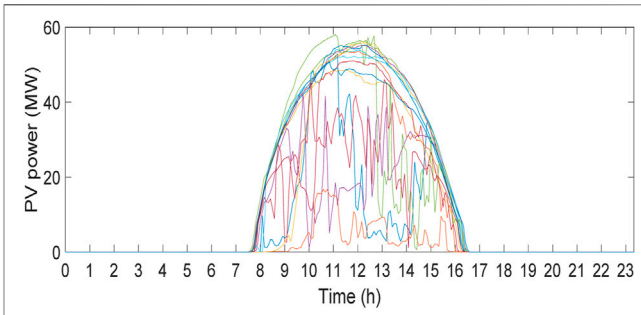

FIGURE 2 | Realistic generation profiles for 25 PV systems in 24 h.

purely consensus-based methods. The power limits of DERs are enforced in Yang et al. (2013b), and then the algorithm stability is established by generalizing the unconstrained consensus cases. In addition, the optimal VSP operation should account for local voltage variations due to storage dispatch and load variations in the distribution level, but most of the studies (Yang et al., 2013a; Wang et al., 2019; Li et al., 2018; Zheng et al., 2018) were only concerned with the cyber layer and ignored the physical grid that holds the controllable units.

Distributed optimization, on the counterpart, can realize optimal storage dispatch and respect device and network constraints in a systematic manner Zhao and Ding, (2021). Primal-dual algorithms are usually used to derive distributed solutions for a centralized optimization problem by exploring the sparsity in the problem setup. For example, Mallada et al. (2017) developed the optimal frequency control in multi-area power networks in which the proposed control keeps the

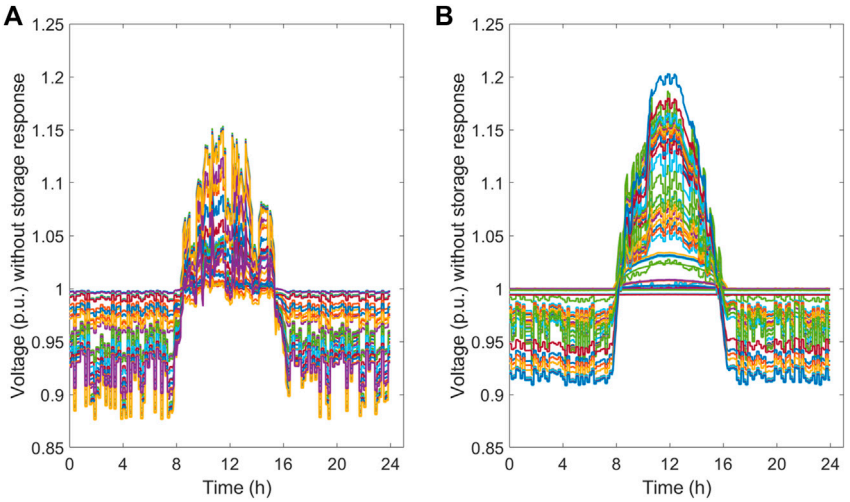

FIGURE 3 | System voltage profiles under no storage response: **(A)** IEEE 33-bus system and **(B)** IEEE 69-bus system.

TABLE 1 | Parameters of the storage assets in the VSP.

	IEEE 33 bus system	IEEE 69 bus system	119 Bus system
No. of storage	20	30	40
No. of PVs	4	7	19
Control parameters	$\sigma = 0.01$ $\tau = 0.05$, $\beta = 2e3$	$\sigma = 1e-3$ $\tau = 0.1$ $\beta = 1e3$	
Storage costs		$\alpha_i^P = 1e2 - 3e2$, $\gamma_i^P = 1e1 - 3e1$ $\alpha_i^Q = 5e1 - 1e2$, $\gamma_i^Q = 5 - 1e1$	
Storage power rating		0.5–1 MW	

distributed structure of the typical automatic generation control (AGC) and incorporates frequency dynamics as part of the primal updates. For voltage control in distribution networks, Zhu and Liu (2016) modified the primal updates by a positive definite matrix, which maintains the direction of primal descent and leads to decentralized computation in radial networks. Tang et al. (2019) further employed the dual ascent by minimizing primal variables in each iteration for accelerated convergence but assumptions are made for homogeneous line parameters and 2-hop neighboring communications. A more relevant study by Dall'Anese et al. (2018) investigated optimal operations of a distribution network feeder as a VPP; the local voltage variations are considered, and the primal-dual algorithm is derived for the regularized Lagrangian showing better convergence. Dall'Anese et al. (2018), Zhu and Liu (2016), and Tang et al. (2019) used gradient-based methods for variable updates, whose slow converging rates are undesirable in time-critical and real-time applications. Combining the features of dual decomposition and the method of the multiplier, the alternating direction method of multiplier (ADMM) improves algorithm robustness and significantly reduces the needed number of iterations for convergence (Boyd et al., 2010; Feijer and Paganini, 1974). Distributed voltage regulation using ADMM is investigated in Sulc et al. (2014), in which the optimization is formulated in a consensus form with copied variables for fully distributed implementation. Similar concepts are employed for area voltage regulations of a partitioned distribution network (Xu and Wu, 2020), in which the dual update is accelerated to outperform the convergence of the original ADMM.

In Sulc et al. (2014), Xu and Wu (2020), and Zheng et al. (2018), the primal updates of ADMM were to find the minimizer of a constrained optimization problem. This process can be computational-intensive for high-dimensional problems. This disadvantage is first tackled for the linear regression issues in Mateos et al. (2010) using a consensus ADMM, which is further extended in Chang et al. (2015) and Chang (2016) considering coupled constraints by optimizing the dual problems based on inexact ADMM. In this investigation, a VSP is controlled to deliver the requested amount of power at the aggregated level by cost-effective storage coordination. This aggregated power reference can either follow an AGC signal or sustain for a specified amount and duration, for example, in the fast frequency reserve (FFR) defined by the National Grid in the United Kingdom (Zhao et al., 2020). In this study, the concerned VSP dispatch is formulated as an optimization problem considering both storage charging and discharging. We use voltage feedback and represent the formulation in an incremental form that accounts for voltage variations against storage dispatch and renewable generations. A proximal dual-consensus ADMM algorithm (PDC-ADMM) (Chang et al., 2015; Chang, 2016) is employed to solve the problem in a distributed manner, whose benefit is that the

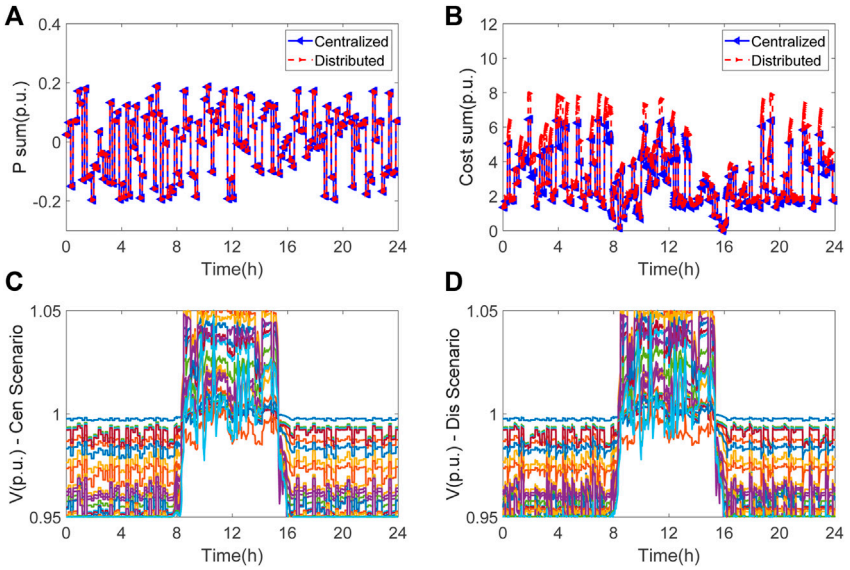

FIGURE 4 | Case I: comparative results of VSP dispatch using a centralized optimization and the proposed distributed control: **(A)** VSP power outputs; **(B)** storage costs in the VSP; **(C)** voltage profile under the centralized control scenario; and **(D)** voltage profile under the distributed control scenario.

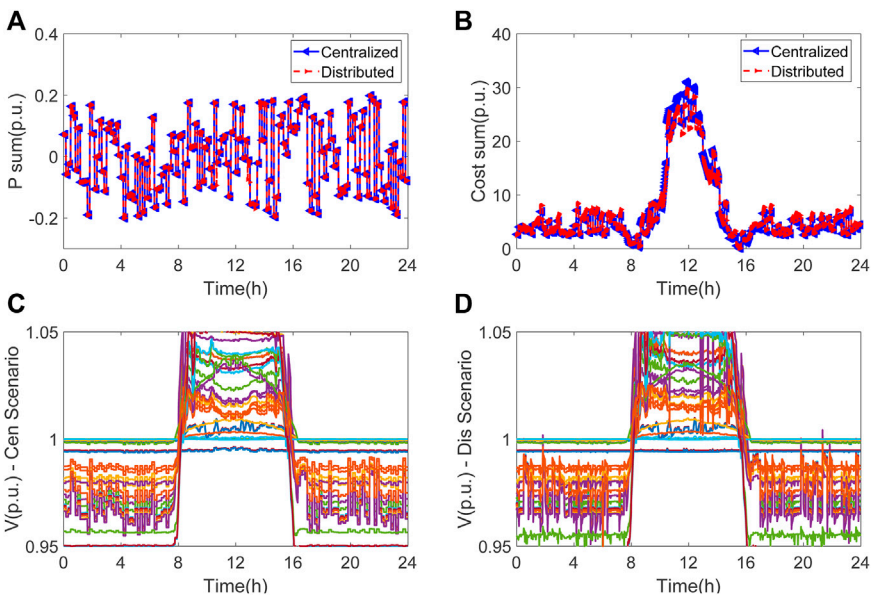

FIGURE 5 | Case II: comparative results of VSP dispatch using a centralized optimization and the proposed distributed control: **(A)** VSP power outputs; **(B)** storage costs in the VSP; **(C)** voltage profile under the centralized control scenario; **(D)** voltage profile under the distributed control scenario.

minimizer of the primal variables can be represented in a closed-form under coupled affine constraints. This results in a low-complexity algorithm that reduces the overall computation cost of ADMM. A similar problem setup appears in Chen and Li (2018), in which the primal update still depends on effective solvers to minimize a constrained optimization problem, and the impact of undispatchable units on network operation is ignored. The contribution of this study is that we develop a distributed control framework for optimal storage cooperation through VSP, considering local voltage regulations during storage dispatch based on the inexact PDC-ADMM, in which the variable update is accomplished by per-agent estimates and enjoy analytical forms that reduce the overall computation efforts.

The rest of the study is organized as follows: the *System Modeling and Problem Formulation* section describes the modeling of the cyber-physical systems involving the

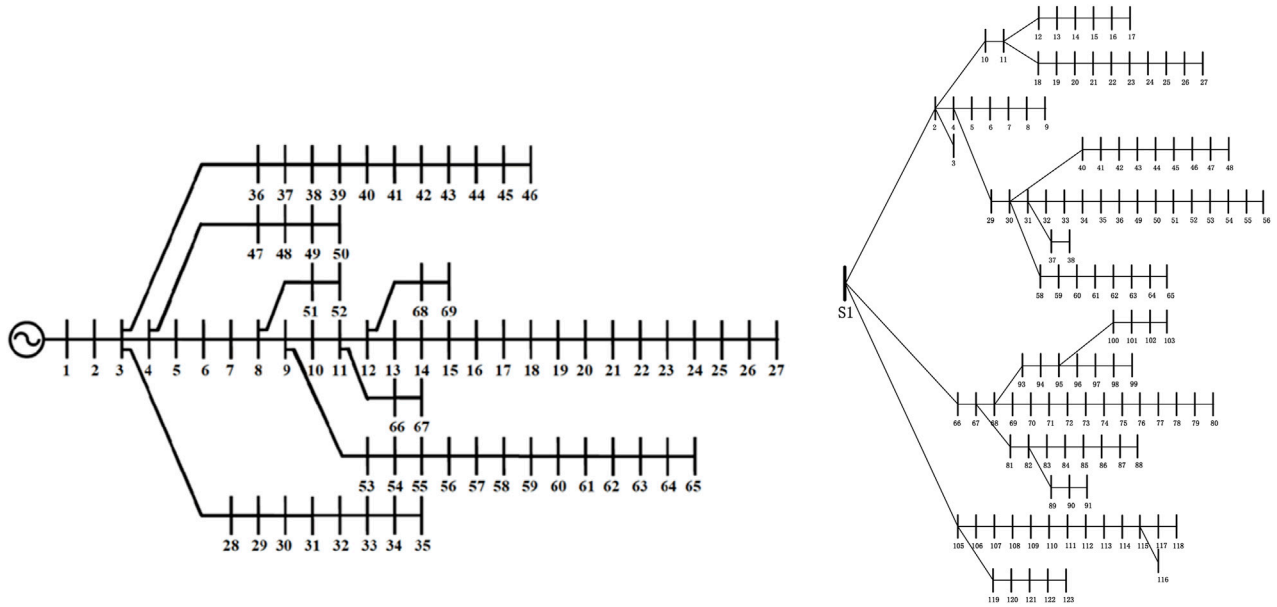

FIGURE 6 | Diagram of the 69 and 119-bus systems.

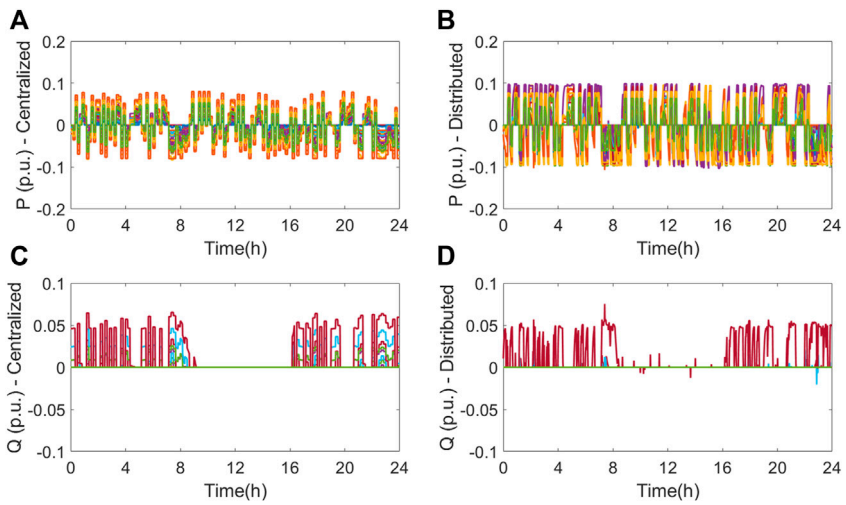

FIGURE 7 | Case III: comparative results of VSP dispatch using a centralized optimization and the proposed distributed control: **(A,B)** active power outputs of individual storage devices; and **(C,D)** reactive power outputs of individual storage devices.

communication and distribution networks and formulates the optimization problem for VSP dispatch; the *Inexact ADMM* section illustrates the classical ADMM and the inexact variant of the ADMM algorithms using the proximal operators; *Case Study* discusses simulation results showing promising performance of the proposed approach in realistic distribution networks with real PV generation data; Conclusions are given in *Data Availability Statement* at the end.

SYSTEM MODELING AND PROBLEM FORMULATION

In this section, models of the considered cyber-physical system are presented. We assume that the distribution network has a radial topology as for most real-world distribution networks. The consequent DistFlow model is linear with small approximation errors from the nonlinear power flow models (Zhu and Liu, 2016). If more general networks with meshed topologies are

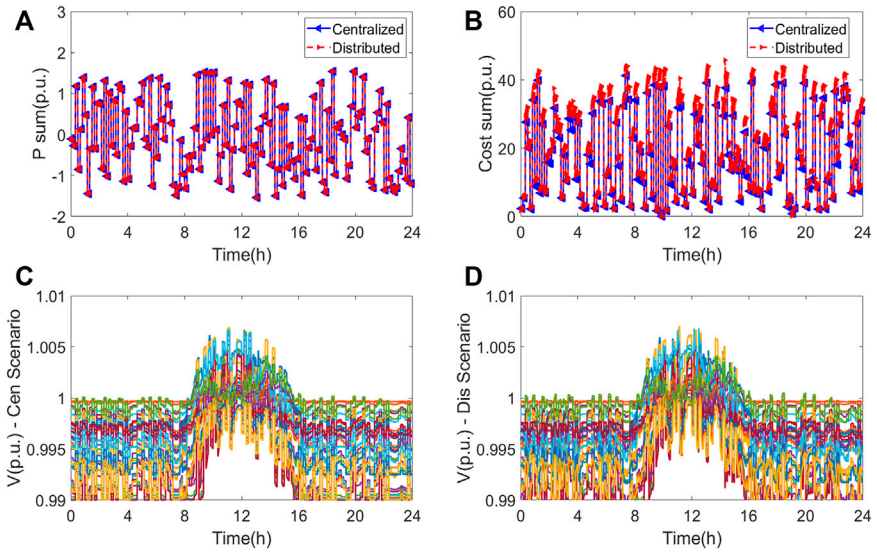

FIGURE 8 | Case III: comparative results of VSP dispatch using a centralized optimization and the proposed distributed control: **(A,B)** active power outputs of individual storage devices; and **(C,D)** reactive power outputs of individual storage devices.

considered, linear approximations can be obtained as well (Dall'Anese et al., 2018).

DistFlow Model for Radial Distribution Networks

A radial distribution network is represented by a directed graph $\mathcal{G}_p$. Except for the substation node having a constant voltage, buses in the distribution networks are denoted by the set $\mathcal{N}$, among which the buses with storage are collected in the set $\mathcal{S}$, while all the other buses are collected in the set $\mathcal{L} = \mathcal{N}\backslash\mathcal{S}$. Note that the buses in $\mathcal{L}$ involve loads and renewables. The set of line segments connecting buses in $\mathcal{N}$ are denoted by the edge set $\mathrm{E}_p = \{(i, j) \subset \mathcal{N} \times \mathcal{N}\}$. For every line segment $(i, j) \in \mathrm{E}_p$, the DistFlow model is established as follows:

$$P_{ij} - \sum_{k\in\mathcal{N}_j} P_{jk} = -P_j^n, \tag{1a}$$

$$Q_{ij} - \sum_{k\in\mathcal{N}_j} Q_{jk} = -Q_j^n, \tag{1b}$$

$$V_i - V_j = r_{ij}^l P_{ij} + x_{ij}^l Q_{ij}, \tag{1c}$$

where P_{ij}, Q_{ij} denote the active and reactive power flows on line (i, j); the net injections of the bus j are $P_j^n = P_j^g - P_j^l$, $Q_j^n = Q_j^g - Q_j^l$, where P_j^g, Q_j^g denote active/reactive powers from DERs and P_j^l, Q_j^l denote the powers of load consumptions. The power flows from the substation to the end buses lead to voltage drops as $V_i - V_j$ described in **(1c)**, where r_{ij}^l, x_{ij}^l are resistance and reactance of the distribution lines, $\mathcal{N}_j$ denotes the set of neighbors of note j. The DistFlow model in **(1)** can be represented in a more compact form as (Zhu and Liu, 2016) follows:

$$V = R^l P^n + X^l Q^n + V_0, \tag{2a}$$

$$R^l = M^{-T} D_r M^{-1},\ X^l = M^{-T} D_x M^{-1}. \tag{2b}$$

In Equation 2, V is the vector of bus voltages and denoted as $V = (V_j)_{j\in\mathcal{N}}$; similarly, $P^n = (P_j)_{j\in\mathcal{N}}$, $Q^n = (Q_j)_{j\in\mathcal{N}}$ are vectors of net bus injections, and $V_0 = v_0 1_{|\mathcal{N}|}$ where v_0 is the voltage magnitude of node 0 and $1_{|\mathcal{N}|}$ denotes a vector of all one with dimension $|\mathcal{N}|$, where $|\mathcal{N}|$ is the cardinality of $\mathcal{N}$. The matrix M is the incidence matrix of the graph $(\mathcal{N}, \mathcal{E}_p)$, and $D_r = \mathrm{diag}(r_{ij}^l)_{ij\in\mathcal{E}_p}$, $D_x = \mathrm{diag}(x_{ij}^l)_{ij\in\mathcal{E}_p}$ are diagonal matrices of the line parameters.

Cyber Network

The cyber network communicating distributed storage devices are represented as a graph $\mathcal{G}_c = \{\mathcal{S}, \mathcal{E}_c\}$ in this study, where the graph edges in $\mathcal{E}_c$ represent the communication lines among storage agents in $\mathcal{S}$. The connectivity of the graph is described by the adjacency matrix $\mathcal{A}_c = (a_{ij})_{i,j\in\mathcal{S}}$ where $a_{ij} = 1$ for all $j \in \mathcal{S}_i$ and 0 otherwise, where $\mathcal{S}_i$ is the neighboring set of node i. We assume that the cyber graph is undirected and connected.

Problem Formulation

The optimization problem is formulated for the optimal storage coordination of a VSP located in a radial distribution network. The VSP is controlled to deliver a given amount of active power while regulating the local network voltage using its reactive power control capability. Considering every time slot t in a time horizon $\mathcal{T}$ and $\forall i \in \mathcal{S}$, we have

$$\min_{\left(P_{i,t}^b, Q_{i,t}^b\right)} \sum_{i=1}^{|\mathcal{S}|} \left\{ \alpha_{i,t}^P \left(P_i^b\right)^2 + \gamma_{i,t}^P \left|P_i^b\right| + \alpha_{i,t}^Q \left(Q_i^b\right)^2 + \gamma_{i,t}^Q \left|Q_i^b\right| \right\}, \tag{3a}$$

$$V_{min}1_{|\mathcal{S}|} \le \sum_{i=1}^{|\mathcal{S}|}\left\{R_i^l\left(P_{i,t}^b + P_{i,t}^l\right) + X_i^l\left(Q_{i,t}^b + Q_{i,t}^l\right)\right\} + \sum_{j=1}^{|\mathcal{L}|}\left\{R_j^l P_{j,t}^n + X_j^l Q_{j,t}^n\right\} + V_0 \le V_{max}1_{|\mathcal{S}|}, \tag{3b}$$

$$\sum_{i=1}^{|\mathcal{S}|} P_{i,t}^b = P_t^A, \tag{3c}$$

$$\left(P_{i,t}^b\right)^2 + \left(Q_{i,t}^b\right)^2 \le \left(S_i^b\right)^2, \tag{3d}$$

$$P_i^{b,min} \le P_{i,t}^b \le P_i^{b,max}, \tag{3e}$$

$$SoC_{min} \le SoC_{i,t}^b = SoC_{i,t-1}^b + \frac{\eta P_{i,t}^b}{CA_i^b} \le SoC_{max}, \quad \forall i \in \mathcal{S}. \tag{3f}$$

In the optimization problem **(3)**, $P_{i,t}^b, Q_{i,t}^b$ are active and reactive power outputs of the ith storage unit at the current time step. We assign a quadratic cost for every storage unit that is described by the parameters $\alpha_{i,t}^P$, $\gamma_{i,t}^P$, $\alpha_{i,t}^Q$, $\gamma_{i,t}^Q$ as in (**Eq. 3a**), and the absolute values indicate that both charging and discharging yield costs are related to storage usage. In (**Eq. 3b**), $R_i^l = (R_{ij}^l)_{j\in\mathcal{S}}$, $X_i^l = (X_{ij}^l)_{j\in\mathcal{S}} \in R^{|\mathcal{S}|}$ are column vectors of R^l, X^l corresponding to the ith storage response on other storage buses, which can be understood as the bus voltage sensitivities with respect to the power injections at the ith buses. Here, we separately represent the power injections on the storage buses and load buses in $\mathcal{L}$, whose net powers $P_{j,t}^n$, $Q_{j,t}^n$ combine the effects of renewables and loads as in (**Eq. 3b**); V_{min}, V_{max} are the bus voltage limits. The VSP is optimized to provide the aggregated power P_t^A as in (**Eq. 3c**). We mainly focus on inverter-based storage technologies, and the local constraints (3d)—(3e) characterize the limits of storage power capacity where S_i^b is the apparent power limit of the power converter. **Eq. 3f** imposes the limits on storage energy capacity based on a general storage model, in which η is the coefficient for charging/discharging, and CA_i^b is the storage energy capacity. Note that (**Eq. 3f**) can be incorporated into (**Eq. 3e**) with time-varying power limits depending on the storage SoC (Dall'Anese et al., 2018); for example, storage with a full charge has $P_{i,t}^{b,max} = 0$ and $P_{i,t}^{b,min} = -S_i^b$. To facilitate the algorithm implementation, the quadratic constraint (3d) is further linearized as follows:

$$-S_i^b \le \cos\left(\tau\frac{\pi}{\kappa}\right)P_{i,t}^b + \sin\left(\tau\frac{\pi}{\kappa}\right)Q_{i,t}^b \le S_i^b, \quad \tau = 1, \ldots, \kappa, \tag{4}$$

where the accuracy loss is 1.5% when $\kappa = 8$ (Jabr, 2017). Moreover, considering that only the power injections on storage buses are known by agents, the network voltage constraint (3b) is rewritten in an increment form of storage power, as follows:

$$V_{min}1_{|\mathcal{S}|} \le \sum_{i=1}^{|\mathcal{S}|}\left\{R_i^l\left(P_{i,t-1}^b + \Delta P_{i,t}^b + P_{i,t}^l\right) + X_i^l\left(Q_{i,t-1}^b + \Delta Q_{i,t}^b + Q_{i,t}^l\right)\right\} + \sum_{j=1}^{|\mathcal{L}|}\left\{R_j^l P_{j,t}^n + X_j^l Q_{j,t}^n\right\} + V_0 \le V_{max}1_{|\mathcal{S}|}. \tag{5}$$

It is assumed that the algorithm is fast enough such that the powers of loads and renewables are nearly constant within each time slot. From (**Eq. 5**) we denote

$$\tilde{V}_t = \sum_{i=1}^{|\mathcal{S}|}\left\{R_i^l\left(P_{i,t-1}^b + P_{i,t}^l\right) + X_i^l\left(Q_{i,t-1}^b + Q_{i,t}^l\right)\right\} + \sum_{j=1}^{|\mathcal{L}|}\left\{R_j^l P_{j,t}^n + X_j^l Q_{j,t}^n\right\} + V_0, \tag{6}$$

which is the vector of voltage magnitudes of storage buses before the agent actions and can be measured at the beginning of the current time step t. We denote $x_{i,t} = (P_{i,t}^b, Q_{i,t}^b)^T = x_{i,t-1} + x_{i,t}$, and then the optimization problem **(3)** is arranged in the canonical form with the incremental variables $x_{i,t}$, considering storage outputs at $t-1$ are known by each agent.

$$\min_{\substack{\Delta x_{i,t}, \Delta r_{i,t} \ge 0 \\ \forall i \in S}} \sum_{i=1}^{|S|}\left\{\Delta x_{i,t}^T \Omega_{i,0}\Delta x_{i,t} + \Omega_{i,t-1}\Delta x_{i,t} + \left\|\Gamma_i \Delta x_{i,t} + \Gamma_i x_{i,t-1}\right\|\right\}, \tag{7a}$$

$$\sum_{i=1}^{|\mathcal{S}|}\left(\begin{bmatrix} A_i \\ E \end{bmatrix}\Delta x_{i,t} + \begin{bmatrix} b_{i,t-1} \\ e_{i,t-1} \end{bmatrix} - \begin{bmatrix} b_0/|\mathcal{S}| \\ e_0/|\mathcal{S}| \end{bmatrix}\right) \le 0, \tag{7b}$$

$$C\Delta x_{i,t} + \Delta r_{i,t} - d_i = 0, \quad \forall i \in \mathcal{S}, \tag{7c}$$

where

$$\Omega_{i,0} = \mathrm{diag}\left(\alpha_{i,t}^P, \alpha_{i,t}^Q\right),\ \Omega_{i,t-1} = 2x_{i,t-1}^T\Omega_{i,0},\ \Gamma_i = \mathrm{diag}\left(\gamma_{i,t}^P, \gamma_{i,t}^Q\right),$$

$$A_i = \begin{bmatrix} R_i^l, X_i^l \\ -R_i^l, -X_i^l \end{bmatrix},\ b_{i,t-1} = \begin{bmatrix} \tilde{V}_{i,t}1_i \\ -\tilde{V}_{i,t}1_i \end{bmatrix},\ b_0 = \begin{bmatrix} V_{max}1_{|\mathcal{S}|} \\ -V_{min}1_{|\mathcal{S}|} \end{bmatrix},$$

$$E = \begin{bmatrix} 1 & 0 \\ -1 & 0 \end{bmatrix},\ e_{i,t-1} = \begin{bmatrix} Ex_{i,t-1} \\ -Ex_{i,t-1} \end{bmatrix},\ e_0 = \begin{bmatrix} P_t^A \\ -P_t^A \end{bmatrix},$$

$$C^s = \begin{bmatrix} \cos\left(1\frac{\pi}{\kappa}\right) & \sin\left(1\frac{\pi}{\kappa}\right) \\ \cos\left(2\frac{\pi}{\kappa}\right) & \sin\left(2\frac{\pi}{\kappa}\right) \\ \vdots & \vdots \\ \cos\left(\kappa\frac{\pi}{\kappa}\right) & \sin\left(\kappa\frac{\pi}{\kappa}\right) \end{bmatrix}, C^p = [1, 0], C = \begin{bmatrix} C^s \\ -C^s \\ C^p \\ -C^p \end{bmatrix},$$

$$d_i = \begin{bmatrix} S_i^b 1_\kappa - C^s x_{i,t-1} \\ S_i^b 1_\kappa + C^s x_{i,t-1} \\ P_{i,t}^{\max} - C^p x_{i,t-1} \\ -P_{i,t}^{\min} + C^p x_{i,t-1} \end{bmatrix}.$$

The vector 1_i has the ith entity equal to 1 and 0 for the others. The 1-norm $\|\blacksquare\|_1$ in the objective function (7a) accounts for storage costs in both charging and discharging modes; the coupled equality constraints 3(c) are represented in inequality, which with (**Eq. 3b**) is incorporated into (7b); (7c) are local constraints for storage capacity limits while $\Delta r_{i,t} \ge 0$ is a slake variable.

INEXACT ADMM

In this section, we introduce the basic principle of ADMM, based on which a proximal dual consensus ADMM is presented to solve convex optimization problem with coupled constraints. The inexact ADMM has the closed form for primal updates and thus reduces computational overheads of individual agents (Chang et al., 2015).

Alternating Direction Method of Multiplier

Consider the following optimization problem:

$$\min_{x,r} . h(x) + g(r), \tag{8a}$$

$$Ax + Br = c. \tag{8b}$$

For the augmented Lagrangian of **(8)**, as $L_\rho(x, r, y) = h(x) + g(r) + y^T(Ax + Br - c) + (\rho/2)||Ax + Br - c_2^2$, ADMM consists of the following iterations:

$$x^{k+1} = \arg\min_x . L_\rho\left(x, r^k, y^k\right), \tag{9a}$$

$$r^{k+1} = \arg\min_r . L_\rho\left(x^{k+1}, r, y^k\right), \tag{9b}$$

$$y^{k+1} = y^k + \rho\left(Ax^{k+1} + Br^{k+1} - c\right). \tag{9c}$$

The updates of the primal variables are carried out jointly with respect to the augmented Lagrangian in a sequential fashion, while the dual update takes on a gradient step with coefficient ρ. ADMM brings robustness and yields convergence without the restrictive assumptions for primal-dual and dual ascent algorithms (Boyd et al., 2010).

Inexact ADMM

In the classical ADMM, a central coordinator is usually needed to collect the primal variables in (**Eq. 9c**), and then the updated dual variable is broadcasted to every agent. To make the ADMM completely distributed, a consensus ADMM is proposed by Mateos et al. (2010), which is further developed to solve the problem with coupled constraints via its Lagrange dual problem (Chang et al., 2015;Chang, 2016). For an optimization problem in the form of (7), in which we make the generalization that $\Delta x_{i,t} \in R^n$, $\Delta r_{i,t} \in R^m$ and the other matrices have compatible sizes. The objection function of (7) can be separated for individual agents and denoted as $f_{i,t}(\Delta x_{i,t}) = g_{i,t}(\Delta x_{i,t}) + h_{i,t}(\Delta x_{i,t})$, where $g_{i,t}(\Delta x_{i,t})$ and $h_{i,t}(\Delta x_{i,t})$ are the smooth and non-smooth parts, respectively. The Lagrange dual problem of (7) is considered and arranged in a consensus form, as follows:

$$\min_{y_{i,t}\geq 0, z_{i,t}} . \max_{\substack{\Delta x_{i,t}, \Delta r_i \geq 0 \\ i\in S}} . \sum_{i=1}^{\mathcal{S}} \left\{ - f_i(\Delta x_{i,t}) - y_{i,t}^T \left(\begin{bmatrix} A_i \\ E \end{bmatrix} \Delta x_{i,t} + \begin{bmatrix} b_{i,t-1} \\ e_{i,t-1} \end{bmatrix} - \begin{bmatrix} b_0/|\mathcal{S}| \\ e_0/|\mathcal{S}| \end{bmatrix} \right) - z_{i,t}^T \left(C\Delta x_{i,t} + \Delta r_{i,t} - d_i \right) \right\}, \tag{10a}$$

$$y_{i,t} = t_{ij}, y_{j,t} = t_{ij}, \forall j \in \mathcal{S}_i, \tag{10b}$$

$$z_{i,t} = l_i, i\varepsilon\mathcal{S}. \tag{10c}$$

where $y_{i,t}$, $z_{i,t}$ are dual variables associated with the coupled constraints and local constraints. Since the dual variables of the coupled constraints are kept by individual agents, constraint (10b) imposes their consensus, in which t_{ij} is an auxiliary variable. Constraint (10c) is a dummy constraint to make a strongly convex subproblem facilitating the following derivation (Chang, 2016). The augmented Lagrangian of (10) is as follows:

$$\begin{aligned} L_c\left(y_i, z_i, \lambda_{+,ij}, \lambda_{-,ij}, \nu_i\right) = \sum_{i=1}^{\mathcal{S}} \Bigg\{ & \varphi_i(y_i, z_i) + \frac{1}{|\mathcal{S}|} y_i^T \left(\begin{bmatrix} b_{i,t-1} \\ e_{i,t-1} \end{bmatrix} - \begin{bmatrix} b_0/|\mathcal{S}| \\ e_0/|\mathcal{S}| \end{bmatrix} \right) + z_i^T d_i \\ & + \sum_{j\in\mathcal{S}_i} \left[\lambda_{+,ij}^T \left(y_i - t_{ij}\right) + \lambda_{-,ij}^T \left(y_j - t_{ij}\right) \right] \\ & + \nu_i^T (z_i - l_i) + \frac{\tau}{2} \|z_i - l_i\|_2^2 \\ & + \frac{\sigma}{2} \sum_{j\in\mathcal{S}_i} \left(\left\|y_i - t_{ij}\right\|_2^2 + \left\|y_j - t_{ij}\right\|_2^2 \right) \Bigg\}. \end{aligned} \tag{11}$$

where we drop the time stamp t to simplify notions, and $\varphi_i(y_i, z_i) = \max_{\Delta x_i, \Delta r_i \geq 0} . \Big\{ - f_i(\Delta x_i) - y_i^T \begin{bmatrix} A_i \\ E \end{bmatrix} x_{i,t} - z_i^T (C_i \Delta x_i + \Delta r_i) \Big\}$, and $\lambda_{+,ij}^T$, $\lambda_{-,ij}^T, \nu_i$ are dual variables associated with the consensus and dummy constraints, τ, σ are positive coefficients of the Lagrange multipliers. Applying the ADMM procedure for (11), we have

$$\begin{aligned} (y_i, z_i) = \arg\min_{y_i \geq 0, z_i} . \Bigg\{ & \varphi_i(y_i, z_i) + \frac{1}{|\mathcal{S}|} y_i^T \left(\begin{bmatrix} b_{i,t-1} \\ e_{i,t-1} \end{bmatrix} - \begin{bmatrix} b_0/|\mathcal{S}| \\ e_0/|\mathcal{S}| \end{bmatrix} \right) \\ & + z_i^T d_i + \sum_{j\in\mathcal{S}_i} \left[\lambda_{+,ij}^T \left(y_i - t_{ij}\right) + \lambda_{-,ij}^T \left(y_j - t_{ij}\right) \right] \\ & + \frac{\sigma}{2} \sum_{j\in\mathcal{S}_i} \left(\left\|y_i - t_{ij}\right\|_2^2 + \left\|y_j - t_{ij}\right\|_2^2 \right) \\ & + \frac{\tau}{2} \left\| z_i - l_i^{k-1} + \frac{\nu_i^{k-1}}{\tau} \right\|_2^2 \Bigg\}, \end{aligned} \tag{12a}$$

$$t_{ij}^k = \arg\min_{t_{ij}} . \left\{ \sum_{j\in\mathcal{S}_i} \left(\left\| y_i^k - t_{ij} + \frac{\lambda_{+,ij}^{k-1}}{\sigma_1} \right\|_2^2 + \left\| y_j^k - t_{ij} + \frac{\lambda_{-,ij}^{k-1}}{\sigma_1} \right\|_2^2 \right) \right\}, \tag{12b}$$

$$l_i^k = \arg\min_{l_i} . \left\{ \left\| z_i^k - l_i + \frac{\nu_i^{k-1}}{\tau} \right\|_2^2 \right\}, \tag{12c}$$

$$\nu_i^k = \nu_i^{k-1} + \tau\left(z_i^k - l_i^k\right), \tag{12d}$$

$$\lambda_{+,ij}^k = \lambda_{+,ij}^{k-1} + \sigma_1\left(y_i^k - t_{ij}^k\right), \quad \lambda_{-,ji}^k = \lambda_{-,ji}^{k-1} + \sigma_1\left(y_i^k - t_{ji}^k\right). \tag{12e}$$

Deriving solutions of (12a)–(12c) and combining with (12d)–(12e) gives $t_{ij}^k = t_{ji}^k = (y_i^k + y_j^k)/2$, $z_i^k = l_i^k$, $\gamma_i^k = 0$. So, (12) can be simplified as follows:

$$\begin{aligned}(y_i, z_i) \quad &= \arg\min_{y_i \geq 0, z_i} \Bigg\{ \varphi_i(y_i, z_i) + \frac{1}{|\mathcal{S}|} y_i^T \left(\begin{bmatrix} b_{i,t-1} \\ e_{i,t-1} \end{bmatrix} - \begin{bmatrix} b_0/|\mathcal{S}| \\ e_0/|\mathcal{S}| \end{bmatrix} \right) \\ &\quad + z_i^T d_i + y_i^T \sum_{j \in \mathcal{S}_i} \left(\lambda_{+,ij}^{k-1} + \lambda_{-,ij}^{k-1} \right) \\ &\quad + \sum_{j \in \mathcal{S}_i} \left(\sigma \left\| y_i - \frac{y_i^{k-1} + y_j^{k-1}}{2} \right\|_2^2 \right) + \frac{\tau}{2} \left\| z_i - z_i^{k-1} \right\|_2^2 \Bigg\}, \end{aligned} \tag{13a}$$

$$\lambda_{+,ij}^k = \lambda_{+,ij}^{k-1} + \sigma \left(y_i^k - \frac{y_i^k + y_j^k}{2} \right), \ \lambda_{-,ji}^k = \lambda_{-,ji}^{k-1} + \sigma \left(y_i^k - \frac{y_i^k + y_j^k}{2} \right). \tag{13b}$$

Using the minmax theorem and the strong convexity of (13a) (Chang, 2016), y_i, z_i can be conveniently obtained by expanding φ_i and combining the linear and quadratic terms, which gives

$$\begin{aligned} &\left(\Delta x_{i,t}^k, \Delta r_{i,t}^k \right) = \arg \min_{\Delta x_{i,t}, \Delta r_{i,t} \geq 0} \\ &\Bigg\{ f_{i,t}(\Delta x_{i,t}) + \frac{\sigma}{4|\mathcal{S}_i|} \left\| \frac{1}{\sigma} \left(\begin{bmatrix} A_i \\ E \end{bmatrix} \Delta x_{i,t} + \begin{bmatrix} b_{i,t-1} \\ e_{i,t-1} \end{bmatrix} - \begin{bmatrix} b_0/|\mathcal{S}| \\ e_0/|\mathcal{S}| \end{bmatrix} \right) \right. \\ &\left. - \frac{p_{i,t}^{k-1}}{\sigma} + \sum_{j \in \mathcal{S}_i} \left(y_{i,t}^{k-1} + y_{j,t}^{k-1} \right) \right\|_2^2 + \frac{1}{2\tau} \left\| C \Delta x_{i,t} + \Delta r_{i,t} - d_i + \tau z_{i,t}^{k-1} \right\|_2^2 \Bigg\}, \end{aligned} \tag{14a}$$

$$y_{i,t}^k = \frac{1}{2|\mathcal{S}_i|} \left[\sum_{j \in \mathcal{S}_i} \left(y_i^{k-1} + y_j^{k-1} \right) - \frac{1}{\sigma} p_{i,t}^{k-1} + \frac{1}{\sigma} \left(\begin{bmatrix} A_i \\ E \end{bmatrix} \Delta x_{i,t} + \begin{bmatrix} b_{i,t-1} \\ e_{i,t-1} \end{bmatrix} - \begin{bmatrix} b_0/|\mathcal{S}| \\ e_0/|\mathcal{S}| \end{bmatrix} \right) \right]^+, \tag{14b}$$

$$z_{i,t}^k = z_{i,t}^{k-1} + \frac{1}{\tau} \left(C \Delta x_{i,t}^k + \Delta r_{i,t}^k - d_i \right), \tag{14c}$$

$$p_{i,t}^k = p_{i,t}^{k-1} + c \sum_{j \in \mathcal{S}_i} \left(y_{i,t}^k + y_{j,t}^k \right), \tag{14d}$$

where $p_i^k = \sum_{j \in \mathcal{S}_i} (\lambda_{+,ij}^k + \lambda_{-,ji}^k)$ and $[\blacksquare]^+ = \max(0, \blacksquare)$. The iterative minimization of primal variables in (14a) does not need to be very accurate since it is an intermediate step in ADMM procedures (Mateos et al., 2010). In this regard, the inexact ADMM approximates (14a) by its first-order Taylor expansion at $(\Delta x_{i,t}^{k-1}, \Delta r_{i,t}^{k-1})$ (Chang, 2016). Denote the smooth part of (14a) as follows:

$$\begin{aligned} \tilde{g}_{i,t}(\Delta x_{i,t}) &= \Delta x_{i,t}^T \Omega_{i,0} \Delta x_{i,t} + \Omega_{i,t-1} \Delta x_{i,t} \\ &\quad + \frac{\sigma}{4|\mathcal{S}_i|} \left\| \frac{1}{\sigma} \left(\begin{bmatrix} A_i \\ E \end{bmatrix} \Delta x_{i,t} + \begin{bmatrix} b_{i,t-1} \\ e_{i,t-1} \end{bmatrix} - \begin{bmatrix} b_0/|\mathcal{S}| \\ e_0/|\mathcal{S}| \end{bmatrix} \right) \right. \\ &\quad \left. - \frac{1}{\sigma} p_{i,t}^{k-1} + \sum_{j \in \mathcal{S}_i} \left(y_{i,t}^{k-1} + y_{j,t}^{k-1} \right) \right\|_2^2 + \frac{1}{2\tau} \left\| C \Delta x_{i,t} + \Delta r_{i,t} - d_i + \tau z_{i,t}^{k-1} \right\|_2^2. \end{aligned} \tag{15}$$

To derive an analytical solution, (14a) is simplified as follows:

$$\begin{aligned} \left(\Delta x_{i,t}^k, \Delta r_{i,t}^k \right) = \arg \min_{\Delta x_{i,t}, \Delta r_{i,t} \geq 0} \Big\{ & h_{i,t}(\Delta x_{i,t}) + \left(\nabla_x \tilde{g}_{i,t}^{k-1} \right)^T \left(\Delta x_{i,t} - \Delta x_{i,t}^{k-1} \right) \\ & + \left(\nabla_r \tilde{g}_{i,t}^{k-1} \right)^T \left(\Delta r_{i,t} - \Delta r_{i,t}^{k-1} \right) \\ & + \frac{\beta_i}{2} \left\| \Delta x_{i,t} - \Delta x_{i,t}^{k-1} \right\|_2^2 + \frac{\beta_i}{2} \left\| \Delta r_{i,t} - \Delta r_{i,t}^{k-1} \right\|_2^2 \Big\}, \end{aligned} \tag{16}$$

where $\beta_i > 0$ is some penalty coefficient. Expanding the gradients $\nabla_x \tilde{g}_{i,t}^{k-1}$ and $\nabla_r \tilde{g}_{i,t}^{k-1}$ gives

$$\begin{aligned} \Delta x_{i,t}^k = \arg \min_{\Delta x_{i,t}} \Bigg\{ & \left\| \Gamma_i \Delta x_{i,t} + \Gamma_i x_{i,t-1} \right\|_1 \\ & + \frac{\beta_i}{2} \left\| \Delta x_{i,t} - \left(\Delta x_{i,t}^{k-1} - \frac{1}{\beta_i} \nabla_x \tilde{g}_{i,t}^{k-1} \right) \right\|_2^2 \Bigg\}, \end{aligned} \tag{17a}$$

$$\Delta r_{i,t}^k = \left[\left(1 - \frac{1}{\beta_i \tau} \right) \Delta r_{i,t}^{k-1} + \frac{1}{\beta_i \tau} \left(d_i - C \Delta x_{i,t}^{k-1} - \tau z_{i,t}^{k-1} \right) \right]^+. \tag{17b}$$

To solve (17a) with non-smooth 1-norm terms, we employ the proximal operator for each coordinate of $\Delta x_{i,t}$. Denoting the jth component of $\Delta x_{i,t}^k$ as $\Delta x_{i,t}^k(j)$, we have

$$\begin{aligned} \Delta x_{i,t}^k(j) = \arg \min_{\Delta x_{i,t}(j)} \Bigg\{ & \left| \Gamma_i(j) \Delta x_{i,t}(j) + \Gamma_i(j) x_{i,t-1}(j) \right| \\ & + \frac{\beta_i}{2} \left[\Delta x_{i,t}(j) - \left(\Delta x_{i,t}^{k-1}(j) - \frac{1}{\beta_i} \nabla_x \tilde{g}_{i,t}^{k-1}(j) \right) \right]^2 \Bigg\}, \end{aligned} \tag{18}$$

where $\Gamma_i(j)$ is the jth diagonal element of Γ_i and $\nabla_x \tilde{g}_{i,t}^{k-1}(j)$ is the jth component of the gradient vector. Since $h_{i,t}(\Delta x_{i,t}) = \sum_{j=1}^n h_{i,t}^j(\Delta x_{i,t}(j)) = \sum_{j=1}^n |\Gamma_i(j) \Delta x_{i,t}(j) + \Gamma_i(j) x_{i,t-1}(j)|$ is separatable, and notice that (**Eq. 18**) is a proximal operator for a scaler function $h_{i,t}^j(\Delta x_{i,t}(j))$, which is precomposed by an affined form. Thus, we rearrange (18) as follows:

$$\begin{aligned} \Delta x_{i,t}^k(j) \quad &= \arg \min_{\Delta x_{i,t}(j)} \left\{ h_{i,t}^j(\Delta x_{i,t}(j)) \right. \\ &\quad \left. + \left[\Delta x_{i,t}(j) - \left(\Delta x_{i,t}^{k-1}(j) - \frac{1}{\beta_i} \nabla_x \tilde{g}_{i,t}^{k-1}(j) \right) \right]^2 \right\} \\ &= \text{prox.}_{h_{i,t}^j / \beta_i} \left(\Delta x_{i,t}^{k-1}(j) - \frac{1}{\beta_i} \nabla_x \tilde{g}_{i,t}^{k-1}(j) \right) \\ &= \frac{1}{\Gamma_i(j)} \left\{ \text{prox}_{\Gamma_i^2(j) |\blacksquare| / \beta_i} \left[\Gamma_i(j) \left(\Delta x_{i,t}^{k-1}(j) \right. \right. \right. \\ &\quad \left. \left. \left. - \frac{1}{\beta_i} \nabla_x \tilde{g}_{i,t}^{k-1}(j) \right) + \Gamma_i(j) x_{i,t-1}(j) \right] - \Gamma_i(j) x_{i,t-1}(j) \right\}, \end{aligned} \tag{19}$$

where the last equation uses the scaling and translation property of the proximal operator (denoted as prox.) for scalar functions (Beck, 2017). The proximal operator of the absolute value is called soft thresholding (Boyd et al., 2010), and thus, (19) can be computed analytically as follows:

$$\Delta x_{i,t}^{k}(j)=\frac{1}{\Gamma_i(j)}\left\{\left[\Gamma_i(j)\left(\Delta x_{i,t}^{k-1}(j)-\frac{\nabla_x \tilde{g}_{i,t}^{k-1}(j)}{\beta_i}\right)+\Gamma_i(j)x_{i,t-1}(j)-\frac{\Gamma_i^2(j)}{\beta_i}\right]^{+}-\left[-\Gamma_i(j)\left(\Delta x_{i,t}^{k-1}(j)-\frac{1}{\beta_i}\nabla_x \tilde{g}_{i,t}^{k-1}(j)\right)-\Gamma_i(j)x_{i,t-1}(j)-\frac{\Gamma_i^2(j)}{\beta_i}\right]^{+}-\Gamma_i(j)x_{i,t-1}(j)\right\}. \tag{20}$$

From (**Eq. 20**), we recover the optimal VSP control as defined in the *System Modeling and Problem Formulation* section. This gives the control commands for storage agents:

$$\Delta P_{i,t}^{k}=\frac{1}{\gamma_{i,t}^{P}}\left\{\left[\gamma_{i,t}^{P}\left(\Delta P_{i,t}^{k-1}-\frac{1}{\beta_i}\nabla_P \tilde{g}_{i,t}^{k-1}\right)+\gamma_{i,t}^{P}P_{i,t-1}-\frac{\gamma_{i,t}^{P\,2}}{\beta_i}\right]^{+}-\left[-\gamma_{i,t}^{P}\left(\Delta P_{i,t}^{k-1}-\frac{1}{\beta_i}\nabla_P \tilde{g}_{i,t}^{k-1}\right)-\gamma_{i,t}^{P}P_{i,t-1}-\frac{\gamma_{i,t}^{P\,2}}{\beta_i}\right]^{+}-\gamma_{i,t}^{P}P_{i,t-1}\right\}, \tag{21a}$$

$$\Delta Q_{i,t}^{k}=\frac{1}{\gamma_{i,t}^{Q}}\left\{\left[\gamma_{i,t}^{Q}\left(\Delta Q_{i,t}^{k-1}-\frac{1}{\beta_i}\nabla_Q \tilde{g}_{i,t}^{k-1}\right)+\gamma_{i,t}^{Q}Q_{i,t-1}-\frac{\gamma_{i,t}^{Q\,2}}{\beta_i}\right]^{+}-\left[-\gamma_{i,t}^{Q}\left(\Delta Q_{i,t}^{k-1}-\frac{1}{\beta_i}\nabla_Q \tilde{g}_{i,t}^{k-1}\right)-\gamma_{i,t}^{Q}Q_{i,t-1}-\frac{\gamma_{i,t}^{Q\,2}}{\beta_i}\right]^{+}-\gamma_{i,t}^{Q}Q_{i,t-1}\right\}. \tag{21b}$$

Combining (21) with the primal and dual updates in (17b), (14b)–(14d) makes up the control law of storage devices in a VSP. Assuming a zero-duality gap, and the primal and dual optimal is attainable, the only requirement for the algorithm convergence is that the penalty coefficient β_i should be larger than some constant determined by the modulus and Lipschitz constant of the smooth part of the objection function $g_{i,t}$ (Chang, 2016).

CASE STUDY

The performance of the proposed method in optimal storage dispatch is demonstrated in this section. A VSP has an aggregator which receives high-level power reference for participating in transmission-level operations. Note that individual storage agents need to know this VSP power reference P_t^A, which can be either estimated by a first-order consensus algorithm or broadcasted by the VSP aggregator with low communication costs. We consider three study cases in the simulations, i.e., the IEEE 33-bus system, IEEE-68 bus system (Schneider et al., 2017), and a 199-bus system originally presented in Zhang et al. (2007). All the three distribution networks have radial topology, but the proposed algorithm can be employed for general network scenarios using linear approximation or voltage sensitivity matrix derived in fast-decoupled power flow. The diagram of the IEEE 33-bus system is shown in **Figure 1** with an illustration of the VSP concept.

Simulation Setup

The simulations use real PV generation data sampled at 5 min, which are collected from a 75 MW solar power plant in Colorado, United States (Solar Power Data for Integration). The PV generation data from different days are used (Solar Power Data for Integration Studies, 2006) for 25 PV systems covering 24 h, and their profiles are shown in **Figure 2**. The PV powers are scaled-down by 150 times to suit the capacities of the distribution networks. The buses where the storage and PVs are located are randomly selected, while the loads are assumed to be constant in the simulations. The VSP dispatch commands are each randomly generated in 10 min. The voltage limits for cases 1 and 2 are 0.95–1.05 p.u., and 0.99–1.01 p.u. for case 3. **Figure 3** shows the voltage profile of the IEEE 33 and IEEE 69 bus systems with integrated PV systems. This indicates that without storage response, a significant voltage increase is observed during peak PV generation hours.

Table 1 gives the storage and control parameters in the simulations. The storage agents are labeled by the same bus number where they are located. We assume a ring topology for storage communication in the VSP cyber network, that id each storage agent communicates to its 2 most adjacent neighbors in the undirect graph. The sampling time of the algorithm is set to 1 min, which gives enough time for algorithm convergence at each time step. The storage power capacities and costs are randomly selected from the ranges provided in **Table 1**. We assume that all the storages have enough energy in the considered duration. The condition for algorithm termination is the accuracy of the objection function $(\text{obj}^k-\text{obj}^*)/\text{obj}^*\le 1e^{-5}$, where obj^* is the cost of a centralized optimization for the same problem.

Simulation Results

Case I: The IEEE 33-bus system is rated at 12.7 kV with 3.75 MW/2.3MVar loads in total. The PV generations are selected from the data profile and integrated into the network at random buses. **Figures 4A, B** compares the VSP aggregated powers and costs under the proposed distributed control and a centralized optimization using YALMIP. This illustrates that the proposed VSP control can track the given power reference in a timely fashion and yield almost identical storage costs with respect to a centralized optimization result. The voltage profiles of the system are given in **Figures 4C,D**. Again, the proposed distributed control, i.e., **Figure 4D** generates similar results as the centralized scenario in **Figure 4C**, both of which successfully restrict the voltage within 0.95–1.01p.u., compared to the significant voltage variation observed in **Figure 2A**. Generally, the computational time of the distributed approach scales linearly with respect to the dimension of the decision variables, while the centralized approach has a high-order polynomial relation between the computational time and the dimension.

Case II: The IEEE 69 bus system is used in this study case. The radial distribution network is rated at 12.7 kV. The total loads are 3.8 MW and 2.7 MVar. Again, the simulation results in **Figure 5** indicate that the proposed distributed control accomplishes nearly identical results as a centralized optimization in VSP dispatch and voltage regulations, while the distributed control

has fewer requirements on the communication capability of the cyber network.

Case III: The data of the 119-bus system is obtained from Zhang et al. (2007) and the diagram is shown in **Figure 6**. The nominal voltage of the system is 11 kV, and all the initial tie switches are open to making a radial distribution network. The total power loads are 22.7 MW and 17.0 MVar. In **Figure 7**, we present the active powers and reactive powers of the total 40 storage units in the VSP. The first column gives the results from a centralized optimization using CPLEX, while the second column is the result using the proposed PDC-ADMM method. It can be observed that the centralized control maintains the storage power references in each dispatch duration, while the proposed distributed control can gradually approach the optimal dispatch using feedback from the previous time step. **Figure 8** validates the performance of the proposed VSP control in terms of the power reference tracking and voltage regulations similar to the results in IEEE 33-bus and IEEE 69-bus systems. Note that the proposed control framework generalizes the functionalities of storage solely by providing voltage supports in distribution networks.

The centralized optimization can provide the global optimal regarding the storage dispatch in the convexified optimization problem. It provides a lower bound on the cost of storage coordination. The proposed distributed control framework uses an inexact approach to reduce the computational efforts of each storage agent. So, the accuracy of the optimization is compromised in exchange for the speed of storage dispatch. In addition, for the sake of practical implementation, we set a fixed value for the maximum number of iterations. So, the distributed control approach might output the calculated storage setpoints even when a suboptimal solution is obtained. These are the reasons that cause slight differences in the cost and storage dispatch between the centralized and distributed approach, but the control performance regarding the reference tracking and voltage regulation is almost in the two control scenarios.

CONCLUSION

This study presents a distributed control framework for the optimal coordination of distributed energy storage devices providing active power at the aggregated level in response to the request from system operators. The proposed control also covers the functionality of local voltage regulation that is widely defined by grid codes in the distribution networks. An improved ADMM algorithm is employed to solve the formulated optimization problem considering storage charging/discharging and its active/reactive power control capabilities. This leads to a fully distributed storage dispatch with analytical control laws based on the inexactness of intermediate ADMM calculations. The closed-form solution significantly reduces the computation overhead in algorithm iterations. The simulation results using MATLAB validate that the proposed VSP control can track the given power reference in a cost-effective manner while maintaining a flat voltage profile against renewable variations. In future work, the proposed control framework will be extended to a robust optimization framework that can handle uncertainties from the renewables and loads.

DATA AVAILABILITY STATEMENT

The raw data supporting the conclusion of this article will be made available by the authors, without undue reservation.

AUTHOR CONTRIBUTIONS

DC: algorithm, mathematical formulation, draft preparation; ZW: algorithm and modeling; XW: idea and supervision; YW: manuscript writing and proofreading; WW: review and editing; KZ: data provision and figure plot; DY: proofreading.

REFERENCES

Beck, A. (2017). *First-order Methods in Optimization*. Society for Industrial and Applied Mathematics.

Boyd, S., Parikh, N., and Chu, E. (2010). Distributed Optimization and Statistical Learning via the Alternating Direction Method of Multipliers. *FNT Mach. Learn.* 3 (1), 1–122. doi:10.1561/2200000016

Chang, T.-H., Hong, M., and Wang, X. (2015). Multi-Agent Distributed Optimization via Inexact Consensus ADMM. *IEEE Trans. Signal Process.* 63 (2), 482–497. Jan.15. doi:10.1109/tsp.2014.2367458

Chang, T. (2016). A Proximal Dual Consensus ADMM Method for Multi-Agent Constrained Optimization. *IEEE Trans. Signal Process.* 64 (14), 3719. doi:10.1109/TSP.2016.2544743

Chen, G., and Li, J. (2018). A Fully Distributed ADMM-Based Dispatch Approach for Virtual Power Plant Problems. *Appl. Math. Model.* 58, 300–312. doi:10.1016/j.apm.2017.06.010

Cheng, M., Sami, S., and Wu, J. (2017). Benefits of Using Virtual Energy Storage System for Power System Frequency Response. *Appl. Energy* 194, 378–385. doi:10.1016/j.apenergy.2016.06.113

Dall'Anese, E., Guggilam, S. S., Simonetto, A., Chen, Y. C., and Dhople, S. V. (2018). Optimal Regulation of Virtual Power Plants. *IEEE Trans. Power Syst.* 33 (2), 1868. doi:10.1109/TPWRS.2017.2741920

Energy Storage News (2019). Europe's Residential Market Installed 745MWh of Battery Storage in 2019: SolarPower Europe. Available: https://www.energy-storage.news/news/europes-residential-market-installed-745mwh-of-battery-storage-in-2019-sola.

Feijer, D., and Paganini, F. (1974). Stability of Primal–Dual Gradient Dynamics and Applications to Network Optimization. *Automatica* 46 (12).

Jabr, R. A. (2017). Linear Decision Rules for Control of Reactive Power by Distributed Photovoltaic Generators. *IEEE Trans. Power Syst.* 33 (2), 2165. doi:10.1109/TPWRS.2017.2734694

Kim, J., Muljadi, E., Gevorgian, V., Mohanpurkar, M., Luo, Y., Hovsapian, R., et al. (2019). Capability-coordinated Frequency Control Scheme of a Virtual Power Plant with Renewable Energy Sources. *IET Gener. Transm. Distrib* 13, 3642–3648. doi:10.1049/iet-gtd.2018.5828

Li, C., Coelho, E. A. A., Dragicevic, T., Guerrero, J. M., and Vasquez, J. C. (2017). Multiagent-Based Distributed State of Charge Balancing Control for Distributed Energy Storage Units in AC Microgrids. *IEEE Trans. Ind. Appl.* 53 (3), 2369–2381. doi:10.1109/tia.2016.2645888

Li, P., Liu, Y., Xin, H., and Jiang, X. (2018). A Robust Distributed Economic Dispatch Strategy of Virtual Power Plant under Cyber-Attacks. *IEEE Trans. Ind. Inf.* 14 (10), 4343–4352. doi:10.1109/tii.2017.2788868

Li, Q., Gao, D. W., Zhang, H., Wu, Z., and Wang, F.-y. (2019). Consensus-Based Distributed Economic Dispatch Control Method in Power Systems. *IEEE Trans. Smart Grid* 10 (1), 941–954. doi:10.1109/tsg.2017.2756041

Mallada, E., Zhao, C., and Low, S. (2017). Optimal Load-Side Control for Frequency Regulation in Smart Grids. *IEEE Trans. Autom. Contr.* 62 (12), 6294–6309. doi:10.1109/tac.2017.2713529

Mateos, G., Bazerque, J. A., and Giannakis, G. B. (2010). Distributed Sparse Linear Regression. *IEEE Trans. Signal Process.* 58 (10), 5262–5276. doi:10.1109/tsp.2010.2055862

Morstyn, T., Hredzak, B., and Agelidis, V. G. (2016). Control Strategies for Microgrids with Distributed Energy Storage Systems: An Overview. *IEEE Trans. Smart Grid* 9 (4), 3652. doi:10.1109/TSG.2016.2637958

Olfati-Saber, R., Fax, J. A., and Murray, R. M. (2007). Consensus and Cooperation in Networked Multi-Agent Systems. *Proc. IEEE* 95 (1), 215–233. doi:10.1109/jproc.2006.887293

Schneider, K. P., Mather, B. A., and Pal, B. C. (2017). Analytic Considerations and Design Basis for the IEEE Distribution Test Feeders. *IEEE Trans. Power Syst.* 99, 1. doi:10.1109/TPWRS.2017.2760011

Solar Power Data for Integration Studies (2006). NREL. Available at: https://www.nrel.gov/grid/solar-power-data.html.

Sulc, P., Backhaus, S., and Chertkov, M. (2014). Optimal Distributed Control of Reactive Power via the Alternating Direction Method of Multipliers. *IEEE Trans. Energy Convers.* 29 (4), 968–977. doi:10.1109/tec.2014.2363196

Tang, Z., Hill, D. J., and Liu, T. (2019). Fast Distributed Reactive Power Control for Voltage Regulation in Distribution Networks. *IEEE Trans. Power Syst.* 34 (1), 802–805. doi:10.1109/tpwrd.2018.2868158

Wang, D., Meng, K., Gao, X., Qiu, J., Lai, L. L., and Dong, Z. Y. (2018). Coordinated Dispatch of Virtual Energy Storage Systems in LV Grids for Voltage Regulation. *IEEE Trans. Ind. Inf.* 14 (6), 2452–2462. doi:10.1109/tii.2017.2769452

Wang, Y., Xu, Y., Tang, Y., Liao, K., Syed, M. H., Guillo-Sansano, E., et al. (2019). Aggregated Energy Storage for Power System Frequency Control: A Finite-Time Consensus Approach. *IEEE Trans. Smart Grid* 10 (4), 3675–3686. doi:10.1109/tsg.2018.2833877

Xu, T., and Wu, W. (2020). Accelerated ADMM-Based Fully Distributed Inverter-Based Volt/Var Control Strategy for Active Distribution Networks. *IEEE Trans. Ind. Inf.* 16 (12), 7532–7543. doi:10.1109/tii.2020.2966713

Xu, Y., Zhang, W., Hug, G., Kar, S., and Li, Z. (2015). Cooperative Control of Distributed Energy Storage Systems in a Microgrid. *IEEE Trans. Smart Grid* 6 (1), 238–248. doi:10.1109/tsg.2014.2354033

Yang, H., Yi, D., Zhao, J., and Dong, Z. (2013). Distributed Optimal Dispatch of Virtual Power Plant via Limited Communication. *IEEE Trans. Power Syst.* 28 (3), 3511–3512. doi:10.1109/tpwrs.2013.2242702

Yang, S., Tan, S., and Xu, J.-X. (2013). Consensus Based Approach for Economic Dispatch Problem in a Smart Grid. *IEEE Trans. Power Syst.* 28 (4), 4416–4426. doi:10.1109/tpwrs.2013.2271640

Zhang, D., Fu, Z., and Zhang, L. (2007). An Improved TS Algorithm for Loss-Minimum Reconfiguration in Large-Scale Distribution Systems. *Electr. Power Syst. Res.* 77, 685–694. doi:10.1016/j.epsr.2006.06.005

Zhao, T., and Ding, Z. (2021). Cooperative Optimal Control of Battery Energy Storage System under Wind Uncertainties in a Microgrid. *IEEE Trans. Power Syst.* 33 (2), 2292. doi:10.1109/TPWRS.2017.2741672

Zhao, T., Parisio, A., and Milanovic, J. V. (2020). Distributed Control of Battery Energy Storage Systems for Improved Frequency Regulation. *IEEE Trans. Power Syst.* 35 (5), 3729–3738. doi:10.1109/tpwrs.2020.2974026

Zheng, Y., Song, Y., Hill, D. J., and Zhang, Y. (2018). Multiagent System Based Microgrid Energy Management via Asynchronous Consensus ADMM. *IEEE Trans. Energy Convers.* 33 (2), 886–888. doi:10.1109/tec.2018.2799482

Zhu, H., and Liu, H. J. (2016). Fast Local Voltage Control under Limited Reactive Power: Optimality and Stability Analysis. *IEEE Trans. Power Syst.* 31 (5), 3794–3803. doi:10.1109/tpwrs.2015.2504419

Conflict of Interest: DY is employed by the State Grid Hubei Electric Power Co., Ltd.

The remaining authors declare that the research was conducted in the absence of any commercial or financial relationships that could be construed as a potential conflict of interest.

The reviewer TZ is currently organizing a Research Topic with the author(s) XW.

frontiers | Frontiers in Energy Research

ORIGINAL RESEARCH
published: 29 June 2022
doi: 10.3389/fenrg.2022.915763

A Novel Grid-Forming Strategy for Voltage-Source Controlled PV Under Nearly 100% Renewable Electricity

Pan Hu[1], Kezhen Jiang[1], Xiaotong Ji[2], Daojun Tan[1], Dan Liu[1], Kan Cao[1] and Wei Wang[2]*

[1]State Grid Hubei Electric Power Research Institute, Wuhan, China, [2]State Grid Hubei Electric Power Company Limited, Wuhan, China

The demand for decarbonization calls for nearly 100% renewable electricity rising as the dominant power resource. The foregoing paradigm shifts require proactive voltage and frequency controllers for the converter-based renewable energy. This article proposed a novel grid-forming technique for voltage-source controlled photovoltaic (PV) operating in 100% renewable power systems. The proposed idea was to design a DC voltage collapse-prevention controller in conjunction with a simplified frequency and inertia controller, thereby smart capturing and releasing PV energy to achieve improvements in dynamic performance and efficiency. By setting the two-phase operation scheme, the model initiatively considers the conflict between frequency regulation and maximum power point tracking (MPPT) curve control. The preferred controls are validated using extensive simulation and experimental findings based on a semi-physical platform and a practical photovoltaic demonstration project. The proposed controller outperforms the standard PV current controller over a much larger range of weak grid situations, according to the experimental and engineering operational data. Results demonstrated the effectiveness of the presented method in applying to the future 100% renewable power system.

Keywords: grid-forming, voltage-source, controlled PV, 100% renewable electricity, DC voltage collapse-prevention controller

OPEN ACCESS

Edited by:
Tianqiao Zhao,
Brookhaven National Laboratory (DOE), United States

Reviewed by:
Ming Wang,
Shandong Jianzhu University, China
Linfei Yin,
Guangxi University, China
Juan Wei,
Hunan University, China

****Correspondence:***
Pan Hu
hupaninwh@whu.edu.cn

Specialty section:
This article was submitted to Smart Grids, a section of the journal Frontiers in Energy Research

Received: *08 April 2022*
Accepted: *10 May 2022*
Published: *29 June 2022*

Citation:
Hu P, Jiang K, Ji X, Tan D, Liu D, Cao K and Wang W (2022) A Novel Grid-Forming Strategy for Voltage-Source Controlled PV Under Nearly 100% Renewable Electricity. Front. Energy Res. 10:915763. doi: 10.3389/fenrg.2022.915763

1 INTRODUCTION

Growing promises to reduce greenhouse gas emissions, as well as ambitious endeavors to minimize global average temperature rise, have driven efforts to decarbonize electricity, with a special emphasis on the use of renewable energy resources (Wu et al., 2021). The climate action plan necessitates the development of a nearly 100% renewable energy system and hence focuses on meeting the operation challenge of the uncertain nature of resources, primarily wind and solar PV. With RE becoming a prominent source in the system, the inverter-based or non-synchronous interface with the grid requires a proactive control strategy undertaking voltage and frequency regulation and support. Furthermore, grid-forming resources need to be widely used to improve synchronization stability in 100% renewable systems or weak grids (Blakers et al., 2019).

There, so far, mainly exists two types of inverter-based resources, i.e., the controlled current (CC) and the controlled voltage (CV) renewable sources (Fu et al., 2021). The CC type uses a phase-locked loop (PLL) to track the voltage and frequency at the point of common coupling (PCC) (Li et al., 2018; Zhou et al., 2018). Moreover, the CC interface often introduces voltage feed-forward (VFF) control to achieve improvement in dynamic response and harmonics suppression, which is particularly

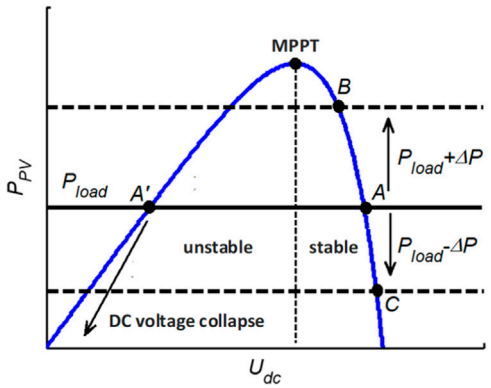

FIGURE 1 | P-V curves of the photovoltaic array.

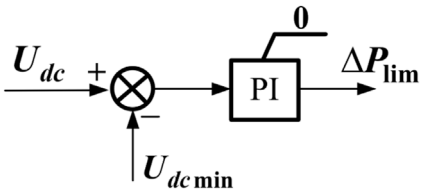

FIGURE 2 | DC voltage collapse-prevention controller.

appropriate for connecting to a strong grid. But at high penetration of RE, i.e., weak grid conditions, the CC controller also causes wide-frequency oscillation, causing harmonic resonance and system instability (Dong et al., 2015). With grid impedance fluctuation, the use of a VFF controller led to the positive feedback of grid impedance, resulting in injecting the harmonic current into weak grids and triggering a tendency toward progressive system instability. In addition, the PLL controller negatively affects the stability of CC inverters under weak grids. Xu et al. (2019) point out that the time delay in PLL brings a negative damping phenomenon, resulting in inverter oscillation. Meanwhile, in weak grids, the PLL bandwidth causes harmonic resonance. With the increase in bandwidth, the damping of the inverter impedance in the low-frequency band deteriorated (Silwal et al., 2019). Through the introduction of improved controllers, for example, time-delay compensation (Zhang et al., 2018), impedance reshaping (Fang et al., 2018a), and adaptive gain scheme (Xu et al., 2017), mitigates the preceding concerns; the dynamic performance of the CC interface is debased. In case of large transient disturbances, some CC renewable sources lose stable equilibrium points and synchronization stability (He et al., 2020). In light of the aforementioned drawbacks, CC resources are better suited for use in strong power systems.

For weak grids, especially under nearly 100% renewable electricity, the CV interface is proven to be a better solution than the CC interface. As a typical grid-forming resource, the CV types achieve power output directly by controlling the voltage vector phase and amplitude, enabling CV to be inherently synchronized with the grid without applying PLL (Yuan et al., 2009). CV resources proactively provide frequency and voltage modulation and moment of inertia if a virtual synchronous generator (VSG) is introduced (Zhong and Weiss, 2011). Furthermore, grid damping and impedance characteristics are increased without compromising CV interface dynamic performance under a lower short current ratio (SCR) (Wu et al., 2019). Therefore, the CV resources are thought to be an efficient solution and a significant component in the configuration of 100 percent renewable systems (Wang et al., 2020; Sang et al., 2022). To satisfy the CV interface requirement, renewable resources typically add energy storage equipment into their DC side to counteract energy absorption or release in the dynamic regulation process, i.e., the unpredictability of wind and solar power (Liu et al., 2021). The energy storage handles the fast-varying power generated by inertia simulation through VSG control, whereas PV implements the portions of frequency regulation and adjusts for relatively long-term power variations with sluggish dynamics. As a result, the VSG provides a better dynamic frequency response during power fluctuations (Fang et al., 2018b; Debnath et al., 2021). To manage PV and energy storage resources, the integrated development combines enhanced control methods to offer inertial and main frequency response, reactive power support, and transient stability (Zhong and Weiss, 2011; Liu et al., 2021). However, virtual synchronous control often treats the DC side as the ideal source and ignores the energy storage limitation; it is difficult to apply it directly to RE's self-synchronous voltage source control. Moreover, because of the energy storage (ES), the traditional VSG technique is difficult to apply in a practical wind turbine and PV unit. ES increases the operation and maintenance workload after installation. The occupied space, geographical location, and machine requirements in the primary component of the original CC equipment restrict the application of ES and hence increase the potential challenges of CV sources used for wind turbines and PV (Imai et al., 2018). Therefore, a proposal for a grid-forming plan for each RE unit without the addition of energy storage is both promising and necessary. However, not much work deals with the above-mentioned relevant issues. This is mostly due to a clash between the uncertainty of RE output and the need for constant frequency support. The MPPT approach, for instance, is responsible for the output of PV arrays. The MPPT controller in the PV needs to be changed to set commands that absorb or release energy in accordance with the primary frequency control requirement. Therefore, the CV interface has the potential to cause PV DC voltage collapse, posing a threat to the PV safety and stability (Hua et al., 2017).

Inspiring by the aforementioned works, this article strived to carry out a novel grid-forming strategy for voltage-source controlled PV without adding energy storage. Thus, the proposed planning model provides a novel perspective of flexibility to operate with nearly 100% renewable electricity. The main contribution and novelty of our works settle in:

1) The article developed a DC voltage collapse-prevention controller that works in tandem with a simpler frequency

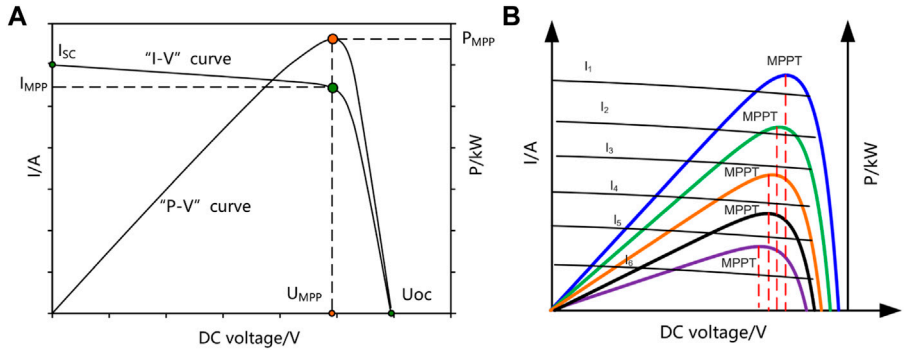

FIGURE 3 | Characteristic of multiple MPPT curves: **(A)** Typical P-V and I-V curves. **(B)** Multiple P-V curves of *PV*.

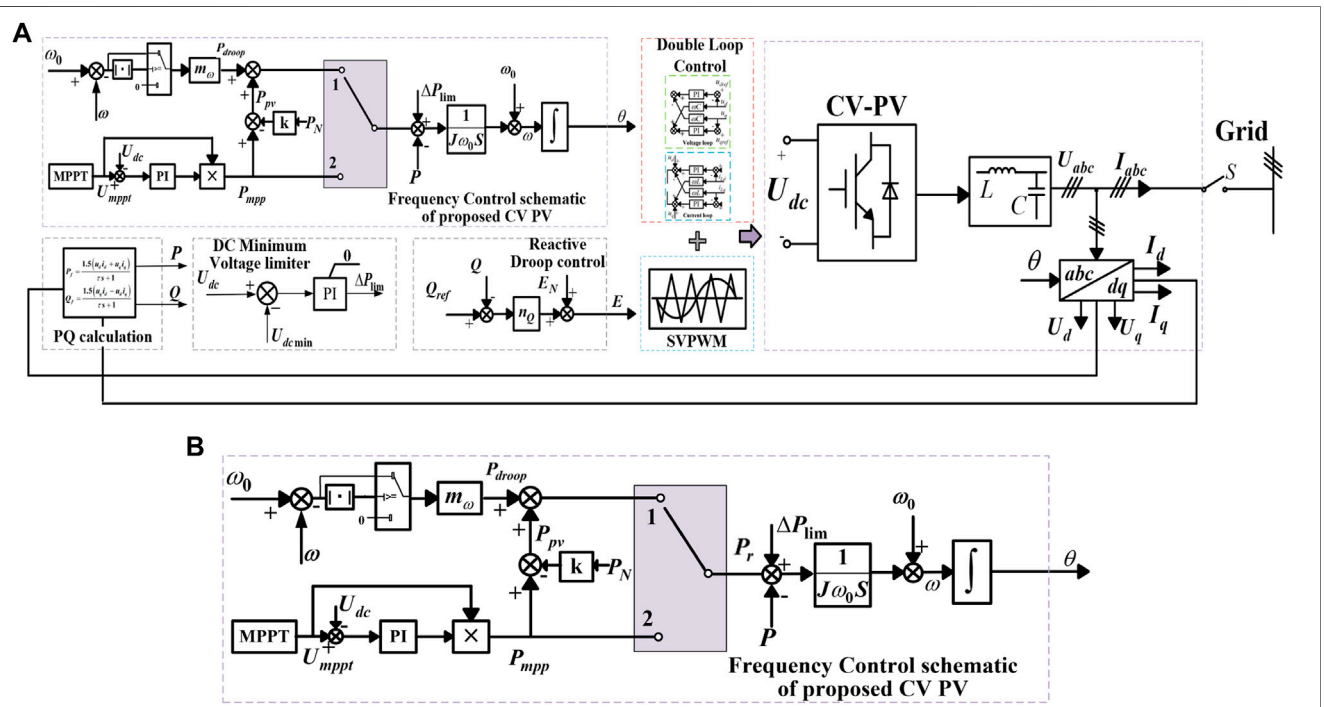

FIGURE 4 | Structure of the grid-forming controller with the DC voltage collapse-prevention controller. **(A)** Overall schematic controller of proposed CV-PV; **(B)** proposed frequency controller combined with DC voltage collapse-prevention controller.

and inertia controller to capture and release PV energy intelligently. The model resolves the issue between frequency regulation and the MPPT approach by establishing the time accounting-storage strategy. The suggested control algorithm can offer adequate actual and reactive power services, as well as ensure PV DC voltage stability, under dynamic system operation and atmospheric circumstances, according to simulation findings obtained during system disruptions and rapid solar irradiation variations.

2) A CV interface and controller framework for the PV is proposed without including energy storage, combined with the proposed model established by the DC voltage collapse-prevention controller and time accounting-storage method. By offering voltage and frequency control and supporting a weak grid, the unique grid-forming technique provides a perspective of flexibility to function in nearly 100% renewable electricity and an ability to design a weak grid.

The article is organized in the manner as follows. **Section 2** theoretically presents the main idea of DC voltage collapse prevention and gives the controller model. Subsequently, the CV interface and controller framework are put forward in **Section 3**. **Section 4** is devoted to the simulation and

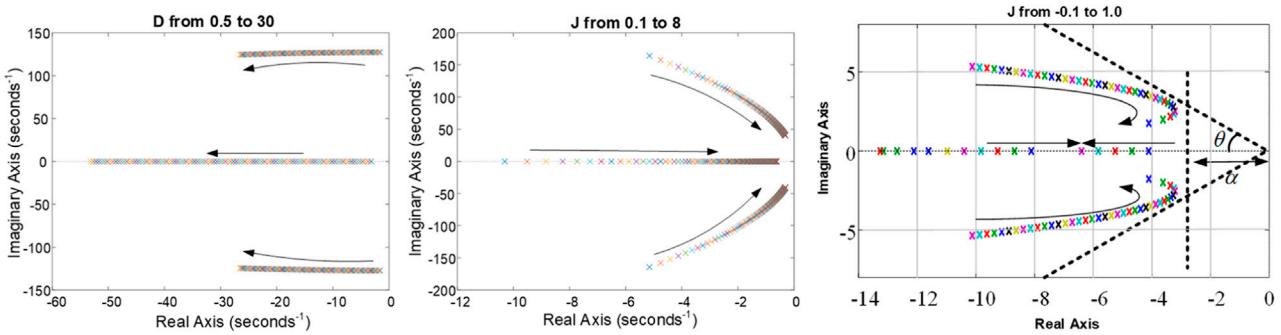

FIGURE 5 | Characteristic root and eigenvalue curves of the CV-PV controller.

hardware-in-the-loop (HIL) experiments and practical engineering verification. Conclusions and future works are summarized in **section 5**.

2 CONTROL STRATEGY AND SYSTEM DESIGN

2.1 Stable Operation Area of MPPT

To clearly analyze the stable operation area of MPPT and DC voltage stability, the following assumptions are put forward:

Assumption 1. The load is less than the PV array's maximum output power.

Assumption 2. The modulation ratio m of the PV inverter is sufficient.

As shown in **Figure 1**, the *P-V* curves indicate the following: 1) when U_{dc} is less than the MPPT *DC* voltage, the PV array's output P_{pv} grows as U_{dc} increases; 2) when U_{dc} is greater than the MPPT *DC* voltage, the P_{pv} declines as U_{dc} increases. Assuming P_{load} as the load power, U_{dc} corresponds to point *A* or *A′* in **Figure 1**.

Due to voltage and frequency regulation requirements, if the load grows by ΔP while U_{dc} is at point *A*, the *PV* unit is required to produce additional energy to match the load. As a result, the extra power is provided by discharging the DC capacitor, and this results in a drop in U_{dc}. The drop in U_{dc} will cause P_{pv} to increase, according to the PV array's P-V characteristics. When P_{pv} equals $P_{load} + \Delta P$, U_{dc} shifts from point *A* to point *B*. U_{dc} is steady at operating point A, as can be shown. When the *PV* power supply is in this operating range, U_{dc} also exhibits a generator-like feature. When the load is increased or decreased, the DC voltage can be automatically discharged or charged, allowing the system to automatically undergo transition to the new balance point and maintain voltage and frequency stability without the need for further controls. When U_{dc} arrives at point A′, however, the situation is inverted. The DC capacitor discharges if the load increases by ΔP, and the fall of U_{dc} further reduces P_{pv} due to the PV array's P-V characteristics, exacerbating the imbalance between the PV output and the load r, eventually leading to the DC bus voltage collapse phenomenon. Furthermore, the inverter is considered to have a sufficient modulation ratio to create the rated AC voltage in the preceding study. In practice, when U_{dc} falls below a particular threshold, m rises to 1. As U_{dc} falls, the AC output voltage falls as well, posing a major threat to the PV power supply system's safe and stable functioning. If the load is reduced by ΔP when U_{dc} is at point A′, the PV array charged the capacitor, increasing P_{pv} and accelerating the charging of the capacitor until U_{dc} passes the MPPT point and enters the stable region. The final operating point transits from point A′ to point C and lets the capacitor overvoltage. It is obvious that point A′ is the unstable operating point.

2.2 DC Voltage Collapse-Prevention Controller

Based on previous analysis, the DC voltage crosses the MPPT point into the unstable region, causing the DC bus voltage to collapse when the PV unit is overloaded. Affected by the variation in the luminous intensity, the maximum DC voltage and MPPT points vary simultaneously. The evolving MPPT curve makes determining the maximum P_{max} in time difficult, and if P_{max} exceeds the MPPT maximum power point, a DC voltage collapse occurs. If the DC voltage can be regulated directly during PV overload, it is envisaged that DC voltage collapse can be prevented.

The diagram of the DC voltage collapse-prevention controller is given in the **Figure 2** a follows:

The controller is a PI controller with an upper limit of 0. U_{dcmin} is the reference input signal, and ΔP_{lim} is the active power increment signal. The MPPT provides the U_{dcmin} command, which is the minimum MPPT voltage, as well as the minimum DC voltage at which the PV power supply can run at a steady state. The controller output is 0 when U_{dc} is greater than U_{dcmin}, and the PV operates in a droop state. Once U_{dc} falls below U_{dcmin}, this controller swiftly reduces the active power, bringing U_{dc} back to U_{dcmin}. ΔP_{lim} is presented as

$$\Delta \boldsymbol{P}_{\mathbf{lim}} = \boldsymbol{k}_{\mathrm{p}}\left(\boldsymbol{U}_{\mathbf{dc}} - \boldsymbol{U}_{\mathbf{dcmin}}\right) + \boldsymbol{k}_{\mathrm{i}} \int \left(\boldsymbol{U}_{\mathbf{dc}} - \boldsymbol{U}_{\mathbf{dcmin}}\right)\mathbf{d}_{\mathrm{t}}. \quad (1)$$

The principal frequency and inertia response can be met by reserving MPPT power, according to the aforementioned DC voltage collapse-prevention controller. However, due to the photoperiodic effect and the uncertainty of solar radiation, multiple MPPT curves exist, shown as in **Figure 3**. As a result,

TABLE 1 | Case scenario description.

Main electrocircuit parameter	Parameter value	Main electrocircuit parameter	Parameter value
AC rated voltage U_N/V	315	Rotational inertia	5
Maximum DC source voltage U_{dc}/V	1,000	Minimum DC source voltage U_{dc}/V	650
Filter inductor L/mH	18.4	Frequency droop coefficient	160
Filter capacitance C/μF	10	Voltage droop coefficient	0.01

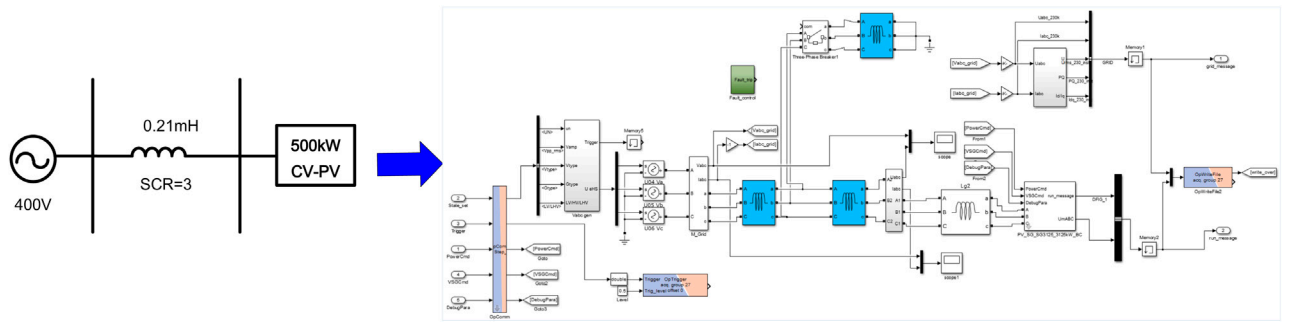

FIGURE 6 | Test platform of the CV-PV controller under RT-LAB/Simulink.

as solar radiation changes, the maximum power and lowest U_{dc} points fluctuate. This fact indicates that the DC voltage collapse-prevention controller has to set a bigger U_{dcmin} to prevent PV from running in the left area of P-V MPPT, resulting in more power loss. The constant DC voltage reduces the MPPT's operation margin, increasing the probability of a PV outage. To solve the aforementioned issue, a responding scheme is put forward.

This article designed a two-phase operation scheme for CV PV sources: the start-up phase and the frequency regulation phase.

Start-up phase: After reaching the maximum power point, the controller enters the MPPT state first, starts the MPPT algorithm, and records the power and DC voltage.

Frequency regulation (FM) phase: The PV seamlessly switches from the MPPT state to FM state and closes the MPPT at the same time. After leaving the maximum power with a specified reserve k, i.e., generally 10 percent of the maximum PV power, the PV begins to participate in primary FM. The FM power is superimposed on the power command once it enters the steady state, and the output power is limited to the maximum PV power. PV uses the set modulation coefficient to calculate the primary FM power. The output active power is the sum of the specified power value after backup and the primary FM's steady-state power, shown in **Figure 4A**. When the FM power surpasses the reserved PV FM interval in the FM process, the PV operates at the maximum power of the MPPT point. The MPPT curve is refreshed every 500 ms. When MPPT point falls below 20% of the rated power, PV departs the FM mode.

2.3 Grid-forming Strategy for Voltage-Source Controlled PV

To clearly illustrate the main controller of the CV-PV, the overall schematic is shown in **Figure 4A**. Frequency and reactive controller, double loop and PWM module and power calculation, electrical measurement, and transformation module are the four basic components. The overall schematic controller takes advantage of the aforementioned technique paired with the proposed DC voltage collapse prevention by using a typical double closed-loop structure (Sun et al., 2021), P/f and Q/V droop management (Awal et al., 2020), and virtual rotor motion equations (Yuan et al., 2009). **Figure 4B** depicts the suggested frequency controller. A switcher in **Figure 4B** is designed to flexibly switch different frequency control modes. The P_{ref} in virtual rotor motion equations is the algebraic calculation of ΔP_{lim}, output active power P and P_r. When it switches to button 1, the CV-PV operates in the FM mode. In this mode, P_r is combined with P_{pv} and droop power P_{droop}. Moreover, P_{pv} is the sum of $k \times P_N$, i.e., power reservation of frequency regulation and MPPT power P_{mpp}. The incremental conductance algorithm (INC) (Liu et al., 2008) can be used to calculate the MPPT power P_{mpp} for a PV. The frequency and inertia-supporting ability of CV-PV is met in this FM mode by power reservation through $k \times P_N$. P_N is the rated power of CV-PV, and k is set to be 10%. To set an acceptable FM dead zone to prevent needless movement, the absolute value and comparison module are employed. To be noted, it causes electricity and energy loss during the FM mode, resulting in lowering the earnings of generation owners. Therefore, we put forward a switcher. When in button 2, P_r equals to P_{mpp}, i.e., close to the MPPT power. Furthermore, U_{mppt} is chosen to be 5–10 V bigger than the minimum DC voltage point from the MPPT curves, which is extremely close to the MPPT point, to improve the reliability of the proposed technique and provide an extra inertia energy source in this mode. The CV-PV does not engage in frequency control in this mode, but it does supply inertia and acts as a CV source to keep voltage and frequency stability in weak grids. The proposed schematic controller enhances the

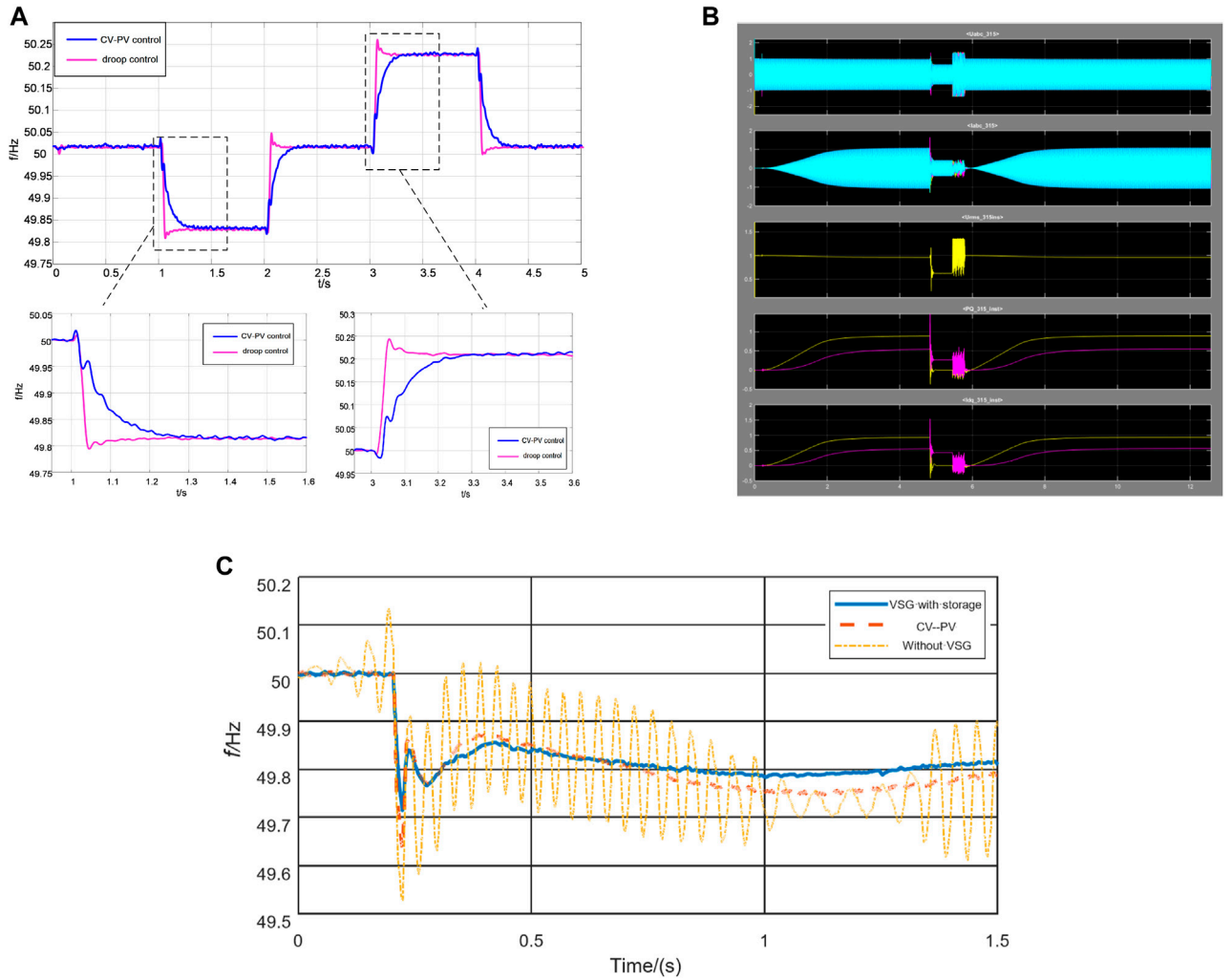

FIGURE 7 | Simulation results of the CV-PV controller. **(A)** Dynamic response curves of frequency under unexpected load changes, **(B)** LVRT test on voltage source inverter, and **(C)** dynamic comparison of the traditional CC controller, VSG with energy storage, and proposed CV-PV.

economy of CV-PV. Moreover, in the transient process, the controller still employs the original CC low-voltage ride-through (LVRT) algorithm, i.e., the controller switches back to the CC mode during the fault period and changes back to CV control after the transient period is finished. Buraimoh et al. (2021) contains the transient controller strategy.

To test the proposed approach and calculate the PI and inertia parameters, Fu et al. (2021) introduced a small signal stability model. This is a summary of our earlier grid-forming controller work. The approach for detailed modeling can be found in the corresponding article. **Figure 5** shows the model's main parameters and the model findings, i.e., characteristic root and eigenvalue curves.

3 CASE STUDY AND ANALYSIS

Three scenarios, based on a semi-physical platform and a practical photovoltaic demonstration project, are used to validate the suggested technique through comprehensive simulation and experimental data. The first example is an RT-LAB-based PV station simulation in Hubei, China. The purpose of this case was to analyze the controller's validity and dynamic characteristics for a PV station, as well as to optimize the parameters of these units under various circumstances. The PV station's hardware in-the-loop (HIL) tests with a CV-PV controller are then carried out in Case 2. As shown in the following figure, the EMT Hardware Solver (eHS) circuit of this PV is constructed in the RT-LAB platform, and the control component is accomplished by using a realistic DSP digital controller of SG500MX-V6, i.e., a 500 kW PV from Sungrow Company. The dynamic frequency response and voltage supporting findings are presented to illustrate the differences between the prior and optimal strategies for improving the PV's operation characteristics and resilience. The recording data and construction information of an actual PV engineering project are provided in Case 3. This project is the power side construction part of the 100% renewable energy

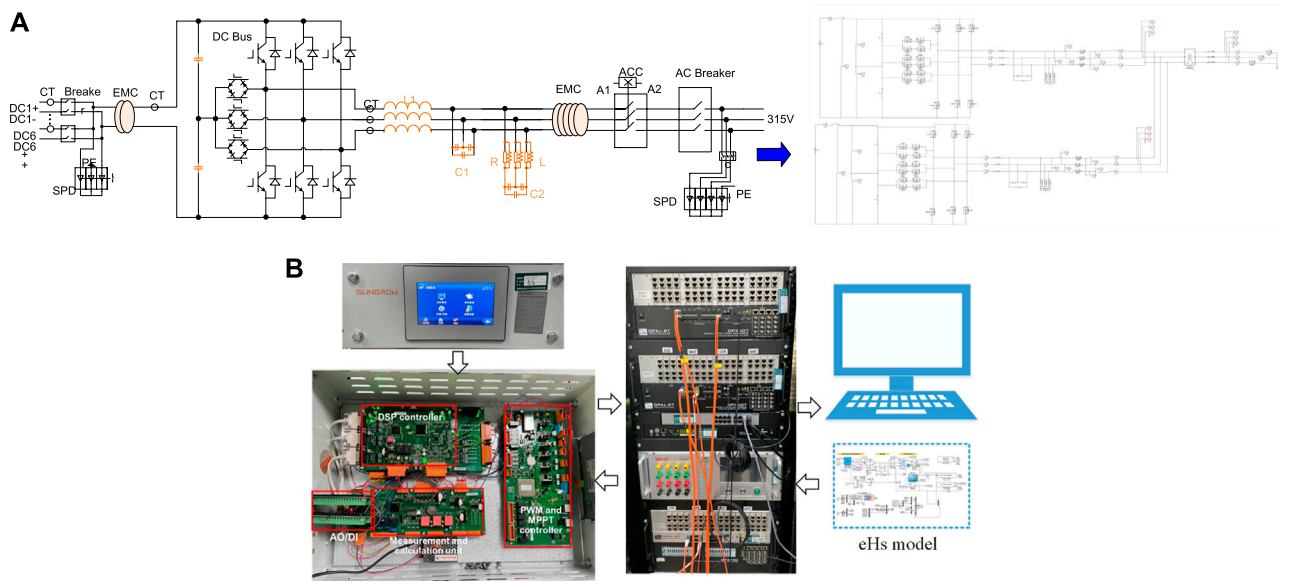

FIGURE 8 | HIL test of the CV-PV controller: **(A)** eHS model of CV-PV; **(B)** HIL test platform.

TABLE 2 | Case 2 scenario description.

No.	Test depicts	Scenario set and purpose
1	Active power control	From 0.1 to 0.8 p.u to test CV-PV control accuracy
2	MPPT control	MPPT test of power reserve response from 200 to 1000 rads
3	LVRT and HVRT test	Voltage from 1.0 to 0.3 p.u. and from 0.3 to 1.275 p.u.
4	Frequency droop test	Frequency varies from 50.5 to 49.5 Hz
5	Inertial test	Test power response when frequency varies within ±0.2 Hz

demonstration project in Suizhou, Hubei Province, China. About 32 MW PV will be updated and reformed to CV-PV. The findings of this study have already been implemented in engineering practice. The engineering data's detailed results demonstrated the practicality of the proposed solution in a large-scale renewable project. In all cases, the CV-PV controller's stability and dependability validated the proposed strategy.

3.1 Case 1

An independent grid simulation model consisting of CV-PV is developed in RT-LAB/Simulink to verify the effectiveness of the controller technique, as shown in **Figure 6**. The parameters of this controller are given in the following **Table 1**. This test is a stand-alone system that consists of three parts: the grid part, the equivalent transmission line, and the tested equipment, of which

1) The grid part is built with the ideal voltage source model, and the power disturbance and fault ride-through configuration are completed by directly scaling the voltage source.
2) The analogous transmission line is designed inductively, with inductance used to represent the transformer and other equipment in the transmission line above the equipment under test, and the short-circuit ratio is set to 1.5.
3) The proposed CV-PV inverter is used in the test equipment. Its dynamic characteristics of transient and steady response are used to determine the effectiveness of the control strategy.

The simulation timer is set to 5 sec. The initial local load is P_L = 400 kW and Q_L = 20 kVar; the load is increased to P_L = 420 kW and Q_L = 25 kVar at 1 s and returns to the initial value at 2 s; the load is reduced to P_L = 380 kW and Q_L = 10 kVar at 3 s and returns to the initial value at 4 s; the load is reduced to PL = 380 kW and QL = 10 kVar at 3 s and returns. **Figure 7A** shows how the virtual proposed control approach compares to the traditional droop control strategy in terms of dynamic response curves of frequency under unexpected load changes. Low-voltage ride-through (LVRT) testing is performed on the voltage source inverter, in which the fault ride-through mimics balanced and unbalanced tests under 20% voltage dips. The inverter's steady-state working condition is set to 100% P_n for the duration of the test. **Figure 7B** shows the simulation results.

In **Figure 7C**, the comparison of the traditional CC controller, VSG with energy storage, and proposed CV-PV in frequency

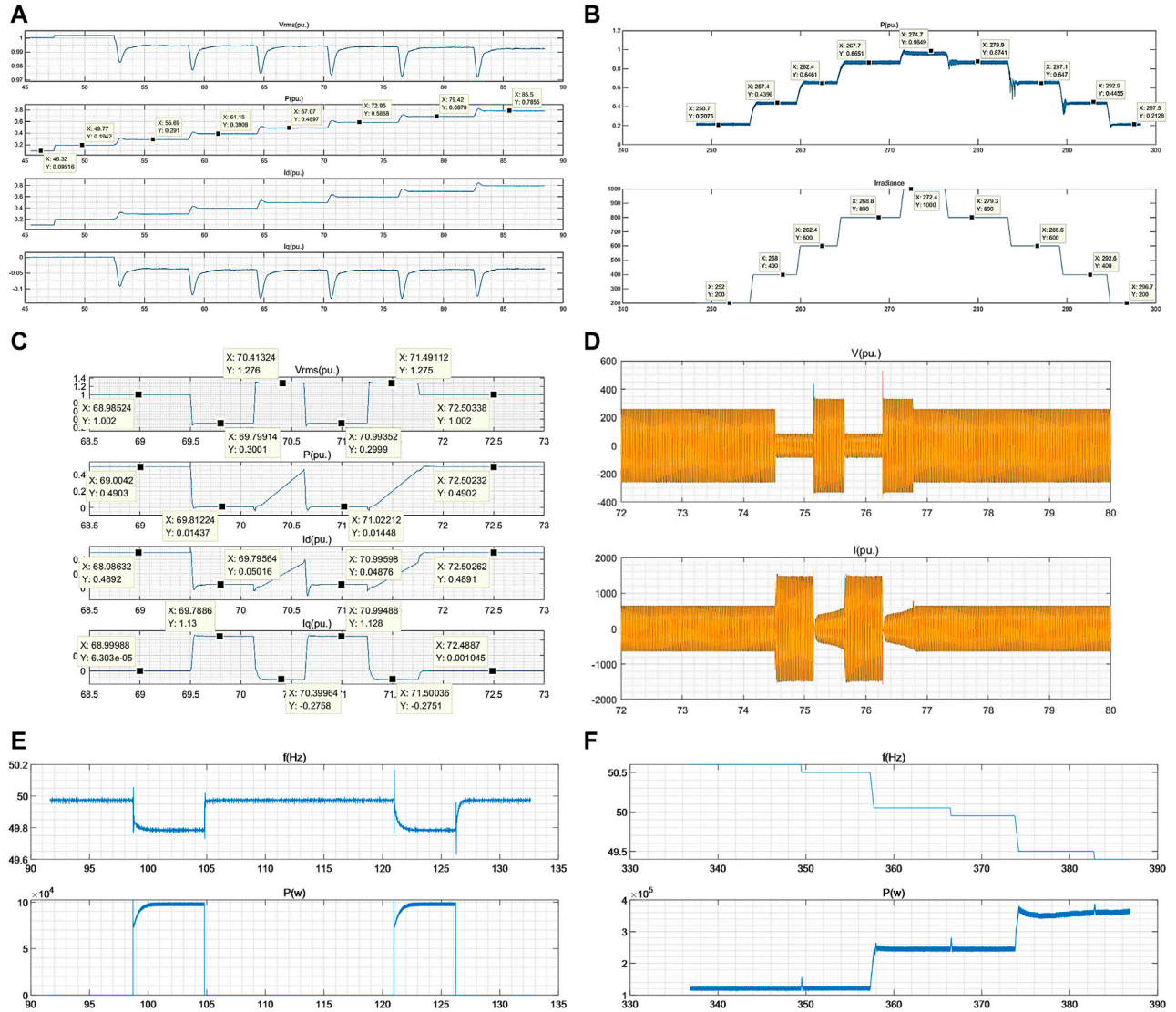

FIGURE 9 | HIL test results of CV-PV: **(A)** active power control from 0.1 to 0.8 p.u., **(B)** MPPT control test from 200 to 1000 radiation, **(C)** and **(D)** LVRT and HVRT test under 0.5 p.u. of rated power from 0.2 to 1.3 p.u. of rated voltage, **(E)** frequency droop test, and **(F)** inertial test.

dynamic response is given. The setting of the simulation condition is the same as in Figure 7A, i.e., 20 kW active power disturbance is introduced. The results revealed that the proposed controller has a good behavior as traditional VSG with energy storage. As displayed in **Figure 7**, the system state does not lose stability in both power disturbance and transient periods. Obviously, the simulation results revealed that compared to the droop control, the control algorithm described in this research has a smoother frequency control impact, and its inertia features save time for future frequency regulation.

3.2 Case 2

In this scenario, HIL tests using grid-connected CV-PV are carried out. In **Figure 8A**, the controller circuit and the eHS model of the primary hardware element of the 500 kW PV are shown, respectively. Two 500 kW PVs comprise a 1 MVA generation unit, as shown in **Figure 8A**, and power is transferred between them *via* a boosting transformer with split winding. The circulation current between CV-PV is generally limited due to the high impedance between split windings, especially when using the virtual impedance technique. The HIL experiments are carried out using this practical unit, and its platform is depicted in **Figure 8B**. The inverter control section of the DSP control board is primarily responsible for the output control signal. The metering board is primarily in charge of communicating with the touch screen. The transmission of trigger signals is handled by PWM and MPPT controllers. Operators can send power scheduling instructions, low penetration strategy coefficients, and key FM and inertia parameters using the parameter setting interface. To test the

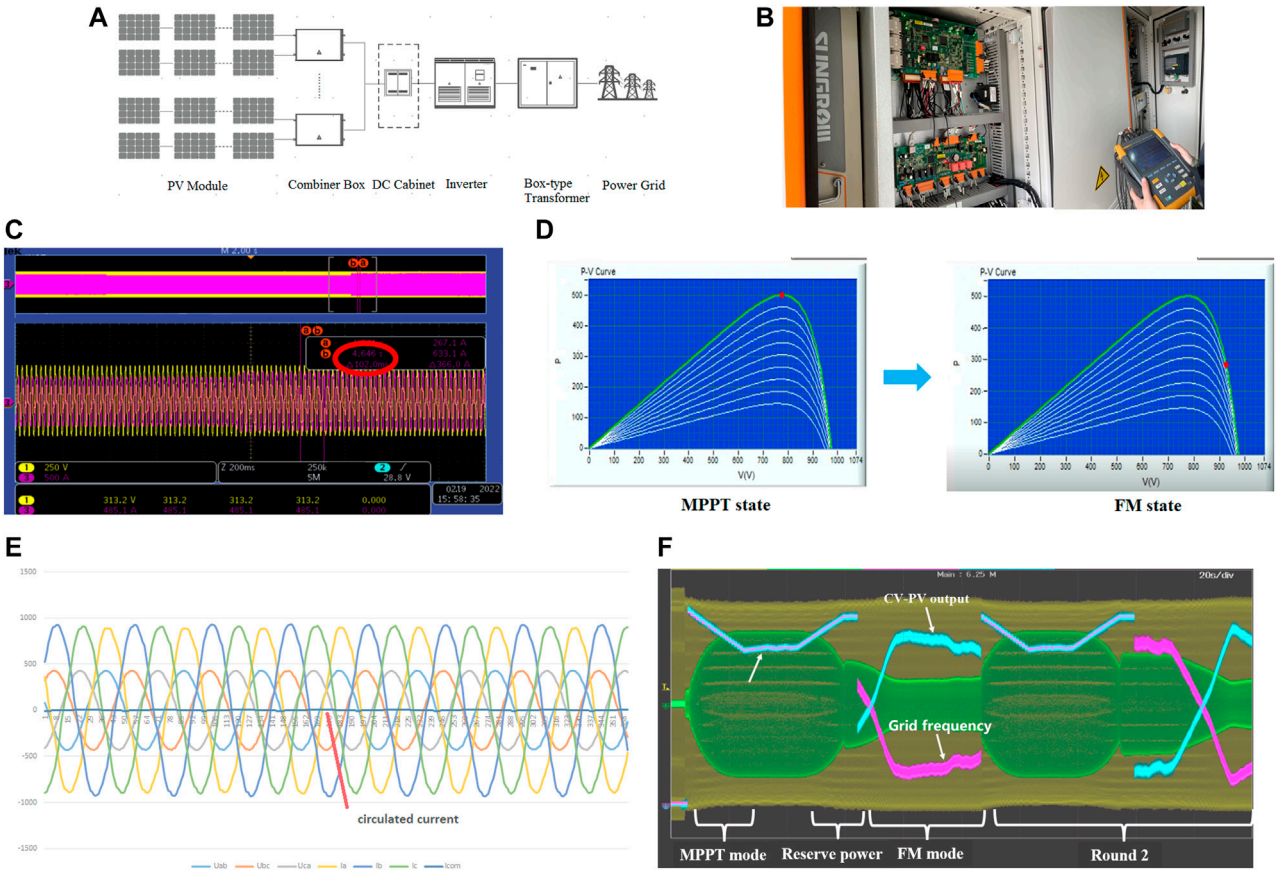

FIGURE 10 | CV-PV controller performance test based on a demonstration project: **(A)** structure of the PV generation system, **(B)** project reconstruction point of the controller, **(C)** switching control results from CC-PV to CV-PV, **(D)** mode switch test from the MPPT mode to FM mode, **(E)** parallel test of two CV-PV units, and **(F)** frequency dynamic response test.

dynamic response of this controller, a series of severity abnormal conditions are introduced and chosen to check the power disturbances and fault ride-through capabilities. The set of tests is depicted in **Table 2**, and the results are shown in **Figure 9**. Clearly, the experimental findings support the effectiveness of the controller's algorithm.

The active power of the CV-PV unit can be flexibly controlled, and the reaction time is less than 5 ms, indicating a quick control accuracy, as shown in **Figures 9A,B**. Based on the results in **Figures 9C,D**, the controller's transient behaviors are compatible with the original CC-PV (d). Moreover, in **Figures 10E,F**, the simulation results clearly illustrate that the frequency and inertia characteristics have an influence on the controller's output. The HIL test verifies the proposed controller's validity and benefits.

3.3 Case 3

A demonstration project is introduced here to verify the validity of the grid-forming strategy. The hybrid renewable station which consists of wind and solar energy is located in the middle of Hubei province, China. The capacity of permanent magnet direct-drive wind is 41.6 MW, while the rated photovoltaic is about 50 MW. Considering the economic and construction aspects, about 60% of PV units are upgraded as voltage-source by utilizing the same CV-PV controller in Case 2. The technical transformation enables the CV-PV to achieve the following functions, especially including the droop and inertia control mode, PQ control mode, seamless switching between them, and provision of reactive voltage support.

Several frequency disturbances are exerted on the secondary windings of the current transformer. The PV responses and its inner MPPT control results are shown in **Figure 10**. For instance, the switching time in **Figure 10C** is approximately 102 ms, and the circulation current between two CV-PV is nearly 0. In **Figure 10F**, the frequency response and its inner power reservation results are present. According to the process of dynamic response, the effectiveness and correctness of the proposed algorithm in a real engineering project are tested.

4 CONCLUSION

This work introduced a unique grid-forming CV-PV controller that can be used to establish a nearly 100% renewable electricity system without the need for energy storage on the DC side. Under dynamic system operation and atmospheric conditions, the

proposed control algorithm provides acceptable actual and reactive power services, as well as PV DC voltage stability. Based on a semi-physical platform and a practical photovoltaic demonstration project, the major conclusions include the following:

1) To intelligently capture and release PV energy, the study built a DC voltage collapse-prevention controller that worked in combination with a simpler frequency and inertia controller. The experimental findings based on a semi-physical platform and a realistic DSP digital controller confirmed that the controller has high dynamic performance and stability.
2) With the suggested model built by the time accounting-storage approach, the CV interface and controller framework for PVs are proposed without integrating energy storage. The model anticipated the conflict between frequency regulation and curve control using the MPPT. The outcomes of the demonstration project attested to the method's efficacy.

Admittedly, concerning the proposed planning model, a few aspects can be enriched, such as the reduction of reserved power and the consideration of the supportability of transient reactive power.

DATA AVAILABILITY STATEMENT

The original contributions presented in the study are included in the article/Supplementary Material; further inquiries can be directed to the corresponding author.

AUTHOR CONTRIBUTIONS

PH selected and studied the sources, designed the structure of the manuscript, and wrote the first draft of the manuscript. KJ and XJ contributed with supervision over the study of the literature and the writing of the manuscript. KC and DL modified the topology of this manuscript. DT designed the HIL test platform. All authors contributed to manuscript revision, read, and approved the submitted version.

FUNDING

This research received funding from the science and technology project of the State Grid Corporation of China, project number: 4000-202222070A-1-1-ZN.

REFERENCES

Awal, M. A., Yu, H., Lukic, S., and Husain, I. (2020). Droop and Oscillator Based Grid-Forming Converter Controls: A Comparative Performance Analysis. *Front. Energy Res.* 8, 3–6. doi:10.3389/fenrg.2020.00168

Blakers, A., Stocks, M., Lu, B., Cheng, C., and Stocks, R. (2019). Pathway to 100% Renewable Electricity. *IEEE J. Photovoltaics* 9 (6), 1828–1833. doi:10.1109/JPHOTOV.2019.2938882

Buraimoh, E., Davidson, I. E., and Martinez-Rodrigo, F. (2021). Decentralized Fast Delayed Signal Cancelation Secondary Control for Low Voltage Ride-Through Application in Grid Supporting Grid Feeding Microgrid. *Front. Energy Res.* 9, 4–8. doi:10.3389/fenrg.2021.643920

Debnath, S., Marthi, P. R. V., Xia, Q., Pan, J., Saeedifard, M., Vipin, V. N., et al. (2021). Renewable Integration in Hybrid AC/DC Systems Using a Multi-Port Autonomous Reconfigurable Solar Power Plant (MARS). *IEEE Trans. Power Syst.* 36 (1), 603–612. Jan. 2021. doi:10.1109/TPWRS.2020.3037520

Dong, D., Wen, B., Boroyevich, D., Mattavelli, P., and Xue, Y. (2015). Analysis of Phase-Locked Loop Low-Frequency Stability in Three-phase Grid-Connected Power Converters Considering Impedance Interactions. *IEEE Trans. Ind. Electron.* 62 (1), 310–321. doi:10.1109/tie.2014.2334665

Fang, J., Li, X., Li, H., and Tang, Y. (2018a). Stability Improvement for Three-phase Grid-Connected Converters through Impedance Reshaping in Quadrature-Axis. *IEEE Trans. Power Electron.* 33 (10), 8365–8375. doi:10.1109/tpel.2017.2777972

Fang, J., Tang, Y., Li, H., and Li, X. (2018b). A Battery/Ultracapacitor Hybrid Energy Storage System for Implementing the Power Management of Virtual Synchronous Generators. *IEEE Trans. Power Electron.* 33 (4), 2820–2824. doi:10.1109/TPEL.2017.2759256

Liu, F., Duan, S., Liu, F., Kang, B., and Kang, Y. (2008). A Variable Step Size INC MPPT Method for PV Systems. *IEEE Trans. Ind. Electron.* 55 (7), 2622–2628. doi:10.1109/TIE.2008.920550

Fu, X., Sun, J., Huang, M., Tian, Z., Yan, H., Iu, H. H.-C., et al. (2021). Large-Signal Stability of Grid-Forming and Grid-Following Controls in Voltage Source Converter: A Comparative Study. *IEEE Trans. Power Electron.* 36 (7), 7832–7840. doi:10.1109/TPEL.2020.3047480

He, X., Geng, H., Li, R., and Pal, B. C. (2020). Transient Stability Analysis and Enhancement of Renewable Energy Conversion System during LVRT. *IEEE Trans. Sustain. Energy* 11 (3), 1612–1623. doi:10.1109/tste.2019.2932613

Hua, T., Yan, X., and Fan, W. (2017). "Research on Power Point Tracking Algorithm Considered Spinning Reserve Capacity in Gird-Connected Photovoltaic System Based on VSG Control Strategy," in *IEEE 3rd International Future Energy Electronics Conference and ECCE Asia (IFEEC 2017 - ECCE Asia)*, 2059–2063. doi:10.1109/IFEEC.2017.7992368

Imai, H., Orihara, D., Iioka, D., and Saitoh, H. (2018). A Novel Virtual Synchronous Generator Control of PMSG-Based Wind Generation System to Enhance Transient Stability of Power System," in *IEEE Electronic Power Grid eGrid*, 1–6. doi:10.1109/eGRID.2018.8598690

Li, M., Zhang, X., and Zhao, W. (2018). A Novel Stability Improvement Strategy for a Multi-Inverter System in a Weak Grid Utilizing Dual-Mode Control. *Energies* 11 (8), 2144. doi:10.3390/en11082144

Liu, J., Golpira, H., Bevrani, H., and Ise, T. (2021). Grid Integration Evaluation of Virtual Synchronous Generators Using a Disturbance-Oriented Unified Modeling Approach. *IEEE Trans. Power Syst.* 36 (5), 4660–4671. doi:10.1109/tpwrs.2021.3061615

Sang, S., Zhang, C., Zhang, J., Shi, G, and Deng, F (2022). Analysis and Stabilization Control of a Voltage Source Controlled Wind Farm under Weak Grid Conditions. *Front. Energy* 2095–1698, 3–8. doi:10.1007/s11708-021-0793-5

Silwal, S., Taghizadeh, S., Karimi-Ghartemani, M., Hossain, M. J., and Davari, M. (2019). An Enhanced Control System for Single-phase Inverters Interfaced with Weak and Distorted Grids. *IEEE Trans. Power Electron.* 34 (12), 12538–12551. doi:10.1109/tpel.2019.2909532

Sun, Z., Zhu, F., and Cao, X. (2021). Study on a Frequency Fluctuation Attenuation Method for the Parallel Multi-VSG System. *Front. Energy Res.* 9 , 4–6. doi:10.3389/fenrg.2021.693878

Wang, X., Taul, M. G., Wu, H., Liao, Y., Blaabjerg, F., and Harnefors, L. (2020). Grid-Synchronization Stability of Converter-Based Resources-An Overview. *IEEE Open J. Ind. Appl.* 1, 115–134. doi:10.1109/ojia.2020.3020392

Wu, C., Zhang, X. -P., and Sterling, M. J. H. (2021). Global Electricity Interconnection with 100% Renewable Energy Generation. *IEEE Access* 9, 113169–113186. doi:10.1109/ACCESS.2021.3104167

Wu, W., Zhou, L., Chen, Y., Luo, A., Dong, Y., Zhou, X., et al. (2019). Sequence-Impedance-Based Stability Comparison between VSGs and Traditional Grid-

Connected Inverters. *IEEE Trans. Power Electron.* 34 (1), 46–52. doi:10.1109/tpel.2018.2841371

Yuan, X. B., Wang, F., Boroyevich, D., Yongdong, L., and Burgos, R. (2009). DC-link Voltage Control of a Full Power Converter for Wind Generator Operating in Weak-Grid Systems. *IEEE Trans. Power Electron.* 24 (9), 2178–2192. doi:10.1109/tpel.2009.2022082

Xu, J., Qian, Q., Zhang, B., and Xie, S. (2019). Harmonics and Stability Analysis of Single-phase Grid-Connected Inverters in Distributed Power Generation Systems Considering Phase-Locked Loop Impact. *IEEE Trans. Sustain. Energy* 10 (3), 1470–1480. doi:10.1109/tste.2019.2893679

Xu, J., Xie, S., Qian, Q., and Zhang, B. (2017). Adaptive Feedforward Algorithm without Grid Impedance Estimation for Inverters to Suppress Grid Current Instabilities and Harmonics Due to Grid Impedance and Grid Voltage Distortion. *IEEE Trans. Ind. Electron.* 64 (9), 7574–7586. doi:10.1109/tie.2017.2711523

Zhang, X., Xia, D., Fu, Z., Wang, G., and Xu, D. (2018). An Improved Feedforward Control Method Considering PLL Dynamics to Improve Weak Grid Stability of Grid-Connected Inverters. *IEEE Trans. Ind. Appl.* 54 (5), 5143–5151. doi:10.1109/tia.2018.2811718

Zhong, Q.-C., and Weiss, G. (2011). Synchronverters: Inverters that Mimic Synchronous Generators. *IEEE Trans. Ind. Electron.* 58 (4), 1259–1267. doi:10.1109/tie.2010.2048839

Zhou, S., Zou, X., Zhu, D., Tong, L., Zhao, Y., Kang, Y., et al. (2018). An Improved Design of Current Controller for LCL-type Grid-Connected Converter to Reduce Negative Effect of PLL in Weak Grid. *IEEE J. Emerg. Sel. Top. Power Electron.* 6 (2), 648–663. doi:10.1109/jestpe.2017.2780918

Conflict of Interest: Authors PH, KJ, XJ, DT, DL, KC and WW were employed by State Grid Hubei Electric Power Company Limited.

frontiers | Frontiers in Energy Research

ORIGINAL RESEARCH
published: 08 July 2022
doi: 10.3389/fenrg.2022.923292

Blockchain Based Peer-To-Peer Energy Trading Between Wind Power Producer and Prosumers in Short-Term Market

Pengbo Du[1], Ziming Liu[1], Bonan Huang[1], Guoxiu Jing[1], Lihong Feng[1] and Chao Yang[2]*

[1]College of Information Science and Engineering, Northeastern University, Shenyang, China, [2]State Grid Liaoning Electric Power Company Limited, Shenyang, China

With the increase of wind power penetration, the deviation caused by its volatility and intermittency poses a growing threat to the grid. Energy trading in short-term markets for wind power and backup storage helps compensate for the deviations. Furthermore, the introduction of peer-to-peer (P2P) energy trading can effectively reduce the risk of centralized market management. However, the higher cost of energy storage are not conducive to wind power producers (WPPs). And P2P trading also suffers from trust and efficiency problems. This paper provides a blockchain based short-term energy trading market, which resolves generation deviations through efficient and trusted real-time transactions between WPP and prosumers. The blockchain-based energy trading market is a trustless P2P structure, and the trading is triggered by smart contracts to ensure efficiency. Furthermore, a reputation mechanism is designed to incentivize WPP's generation forecasts to be accurate and prosumers to participate in the market. A bilevel optimization method is designed to increase the revenue of WPP and reduce the costs of prosumers. The market can effectively balance the deviation of wind power generation, increase the revenue of WPP by 9.55%, and reduce the costs for consumers by 5.6%.

Keywords: wind power producer, blockchain, bilevel, energy trading, short-term market

OPEN ACCESS

Edited by:
Xiao Wang,
Wuhan University, China

Reviewed by:
Qihe Shan,
Dalian Maritime University, China
Dawei Gong,
University of Electronic Science and Technology of China, China
Ruizhuo Song,
University of Science and Technology Beijing, China

****Correspondence:***
Bonan Huang
Huangbonan@ise.neu.edu.cn

Specialty section:
This article was submitted to Smart Grids, a section of the journal Frontiers in Energy Research

Received: *19 April 2022*
Accepted: *19 May 2022*
Published: *08 July 2022*

Citation:
Du P, Liu Z, Huang B, Jing G, Feng L and Yang C (2022) Blockchain Based Peer-To-Peer Energy Trading Between Wind Power Producer and Prosumers in Short-Term Market. Front. Energy Res. 10:923292. doi: 10.3389/fenrg.2022.923292

1 INTRODUCTION

With the increasing penetration of wind power, its volatility make the impact on power quality and grid stability more critical (Shin et al., 2018). Wind power producers (WPPs) should take measures to ensure the stability of wind power generation to avoid power generation deviation between the actual and the forecasted caused by the above conditions. Researchers believe that WPP's participation in the electricity market is one of the effective ways to address wind power deviation and promote wind power consumption (Skajaa et al., 2015).

Electricity markets in many countries have established the short-term market. For example, the European short-term market determines the energy clearing price based on the positive or negative energy adjustment. Many researchers focus on WPPs for electricity energy trading on the short-term market trading floor including day-ahead (DA) and real-time (RT) markets. The RT market has attracted the growing attention of researchers, which may provide possible solutions addressing the above challenges because it can compensate for the high uncertainty of generation forecasts in DA markets (Homa et al., 2017). The independent system operator (ISO) is responsible for regulating the energy for the deviating wind producers, ISO imposes

penalties on WPP when it fails to deliver power as promised. H. Shin et al. (Shin et al., 2018) built an advanced offer curve that considers correlations between wind power and RT price under the hypothesis that the wind power and RT price follow the bivariate normal distribution. Compared with the typical offering curve, this curve can slightly increase the expected profit. Although the offering curve can increase the expected profit of WPP, penalties for mispredicted wind power producers are expensive in RT markets (Fabbri et al., 2005). The centralized power transaction conducted by the system operator has disadvantages such as high information management cost, insufficient communication transmission capacity, and single point of failure when dealing with the above scenarios.

In addition, researchers propose to combine wind energy with other power generation methods to solve the volatility of wind energy. On the one hand, reserves are provided by the supply side, these power generation methods are pumped-storage hydroplanes, thermal energy, compressed air energy storage (Al-Awami and El-Sharkawi 2011; Sánchez de la Nieta et al., 2013; Cheng et al., 2019). However, some thermal units have high generation costs which reduce the revenue of WPP. Moreover, purchasing reserves from the demand side can also balance the deviation of wind power. Demand response (DR) and electric vehicle (EV) were proposed by relevant researchers as more economical reserve energy. In the face of the intermittent wind energy, N. Mohammad et al. (Mohammad and Mishra 2018) aimed to design a plan in which market operators seek suitable DR as reserve energy to cope with the deviation of wind power. EV aggregators are applied as entities to balance the deviation from the uncertainty of renewable energy (Cheng et al., 2019). However, the greater deviation of wind power consumption in RT markets, the more prominent the problems caused by the high adjustment cost. Consequently, higher frequency transactions help balance wind power generation deviation better.

Two-way information flow and peer-to-peer (P2P) mechanisms of the distributed system contribute to the development of energy trading. In the P2P energy trading mechanism, operators do not need to play the role of energy dispatching, a win-win result with direct electricity trading between consumers (Zhou et al., 2018). E. Sorin et al. (Sorin et al., 2018) introduced the variable economic dispatch to build a P2P energy trading market and proposed a method that considers Consensus and Innovation to address the problems in the market in a distributed manner. This plan shared the power trading information well handled and improved social welfare and user satisfaction. C. Zhang et al. (Zhang C. et al., 2018) proposed a hierarchical system architecture model to identify the relevant content involved in P2P energy trading and simulated P2P energy trading using game theory. Experimental tests showed that P2P energy trading can promote consumption balance. H. Rashidizadeh-Kermani et al. (Rashidizadeh-Kermani et al., 2021) considered a P2P transaction framework in which WPP can conduct P2P transactions with the main grid and rival load-serving entities. Through P2P direct transactions, WPP can offset part of the energy deviation and maximize its interests. H. Rashidizadeh-Kermani et al. (Rashidizadeh-Kermani et al., 2020) explored that WPP purchased reserves from energy storage aggregators on the P2P trading floor to compensate for the volatility of wind power, and at the same time introduced conditional value at risk (CVaR) to hedge the randomness of wind energy. Previous work has shown that prosumers take crucial roles in P2P trading. A prosumer is a flexible role that can consume and generate electricity in the meantime (Luo et al., 2019). As shown is **Figure 1**, in conventional models of power systems, only energy consumers existed. However, renewable energy generation technologies are developing rapidly. Its construction cost and equipment size are gradually decreasing and coming into homes (Li et al., 2021). For example, in recent years, solar panels have been installed on the roof of a building and supply it with electricity. Because of the small capacity and fast regulation of prosumers, they are suitable for small-scale regulation of electricity in decentralized mechanism. As a result, WPP can engage in P2P transactions with prosumers to better cover their uncertainty due to their responsiveness and flexibility, but their data on the transaction process lack a transparent management method.

In recent years, blockchain has been proposed as a distributed ledger technology, and its characteristics of trustlessness, traceability, transparency, and irreversibility make it widely used in the energy trading field (Li et al., 2017). Energy trading based on blockchain is not similar to the traditional centralized power trading mechanism with poor information trading. More specifically, blockchain technology can realize the decentralization of electricity (Zhang T. et al., 2018). Each user can realize distributed automatic verification, transmission, and management of transaction information, so as to quickly respond to market information and formulate the most excellent bidding strategy to promote P2P trading of electric energy (Cui et al., 2020).

In summary, we propose a blockchain-based P2P energy trading short-term market between the WPP and prosumers. The market includes the DA market, RT market, and balancing (BL)

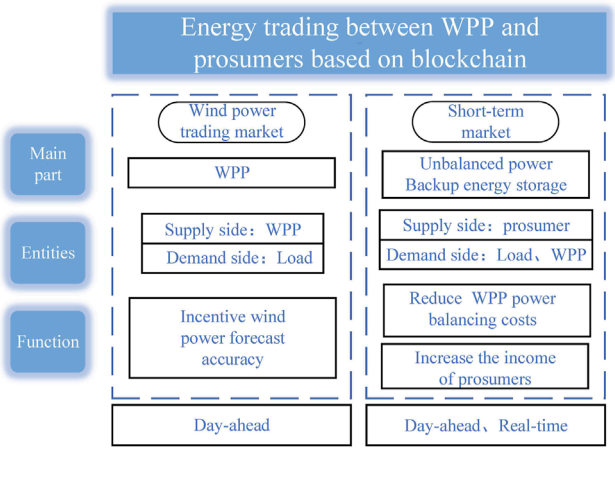

FIGURE 1 | Energy trading between WPP and prosumers.

market. Prosumers regulate deviations in the RT market. The BL market is responsible for regulating the remaining energy after the RT market transaction. The blockchain-based wind energy trading market can realize the decentralization of transactions and ensure data transparency and information security, so it does not require the management of a third-party trust mechanism and reduces the cost of adjusting the market. In addition, we introduce the concept of prosumers into the system, which can directly trade with the WPP when there is a deviation, balancing the real-time power of the system. When there is a deviation in WPP power generation, the smart contract on the blockchain is triggered. After that, the smart contract will arrange for prosumers with high reputation value to give priority to energy trading and publish preferential balancing price to WPP with high reputation value (Huang et al., 2022a). Given that fact, the behavior of prosumers affects the stability of power system. To ensure the accuracy of the real-time transaction balance between prosumers with WPP, we design a reputation mechanism for prosumers and WPP to regulate their trading behavior, respectively.

The main contributions and organization are given as follows:

- A blockchain-based energy trading market is established, which supports real-time direct transactions between WPP and prosumers without a central authority or third parties. It reduces transaction costs and increases the effectiveness of power balancing. Furthermore, blockchain guarantees trustworthiness, transparency, and traceability in the transaction process.
- The reputation mechanism is proposed. The mechanism allows prosumers who actively participate in the transaction to obtain more profits in the RT market, and reward accurate forecasted WPP in the BL market. It facilitates real-time wind energy trading in the market and rationalizes costs.
- A bilevel optimization method is used to maximize WPP revenue and prosumer gains. WPP manages the uncertainty of wind energy by buying and selling electricity to prosumers. In the process, WPP lowers the cost of direct transactions from the BL market while prosumers also get relatively low energy prices.

The rest of our article is organized as follows. **Section 2** describes the mathematical model of trading entities in the market. In **section 3**, a bilevel stochastic problem is proposed to construct optimal trading strategies (Yang et al., 2019). **Section 4** gives the result of the digital simulation. Finally, **section 5** summarizes the main work of this article.

2 SYSTEM FRAMEWORK

In this section, we model the relevant entities in P2P power trading in a bilevel framework.

2.1 Wind Power Producer

Wind power generation is subject to the uncertainty of wind energy and therefore is greatly affected by environmental factors (Wang et al., 2018). WPP makes a profit by selling the total electricity generated by the turbines in their jurisdiction. And from the viewpoint of the understudy WPP, it participates in the market to maximize its own interests. Let $J_i \in \mathcal{J}$ denote the ith WPP. The trading volume of wind power is described as

$$P_t^{\mathrm{W}} - P_t^{DA} - \sum_{K_i \in \mathcal{K}} \left(P_{t,K_i}^{Sell} - P_{t,K_i}^{Buy}\right) - P_t^{B+} + P_t^{B-} = P_t^{DR} + \sum_{K_i \in \mathcal{K}} P_{t,K_i} \tag{1}$$

where P_t^{W} represents wind power generation. P_t^{DA} is the amount of power generation determined by DA market. The P_{t,K_i}^{Sell} and P_{t,K_i}^{Buy} denote WPP sells (buys) energy to (from) prosumers in order to compensate for generation deviations. P_t^{B+} and P_t^{B-} are positive (negative) BL market energy. $P_{t,DR}$ is total demand of loads. P_{t,K_i} presents demand of prosumers.

WPP's trading volume range in DA and RT markets is given by

$$0 < P_t^{DA} \le P_{lim}^{DA} \tag{2}$$

$$0 \le P_t^{B+} \le P_{lim}^{B+} \tag{3}$$

$$0 \le P_t^{B-} \le P_{lim}^{B-} \tag{4}$$

2.2 Prosumer

The prosumers are the integration of producer and consumer. They play the role of consumers when buying electric energy, and they become producers when selling electricity. Taking our model as an example, users make themselves a prosumer by installing solar power on top of the house, home energy storage and other facilities. Let $K_i \in \mathcal{K} = \{K_1, \ldots, K_m\}$ denote the prosumer node of the distribution system. If there is excess power after the power generation of the prosumer in the distributed network meets its demand, its PV power will connect to the grid, and if the power generation of the consumer cannot meet its demand, it needs to buy energy from the producer (Huang et al., 2022b).

$$P_{t,K_i}^{Sell} = 0, P_{t,K_i}^{Buy} \ne 0, if P_{pre} > P_{act} \tag{5}$$

$$P_{t,K_i}^{Sell} \ne 0, P_{t,K_i}^{Buy} = 0, if P_{act} > P_{pre} \tag{6}$$

$$P_{t,K_i}^{Sell} = P_{t,K_i}^{Buy} = 0, if P_{act} = P_{pre} \tag{7}$$

$$P_{lim} \le P_{t,k_i} \le P_{max} \tag{8}$$

where, P_{t,K_i}^{Sell} and P_{t,K_i}^{Buy} are the power generations that WPP sells (buys) to (from) prosumers, respectively. λ_{t,K_i}^{Sell} and λ_{t,K_i}^{Buy} are prices that WPP sells (buys) to (from) prosumers. when the system imbalance is positive (excess of generation), then WPP can sell the power generation to consumers, vice versa.

2.3 Load

Unlike the prosumers, there are many loads that cannot store energy. As a consumer, it purchases energy to provide its own needs. In this paper, this type of load is not the focus of the study, so this part of the load is simplified to data.

2.4 Power System Operator

The operator is the power system dispatcher, which holds and operates the network that delivers electricity. In the traditional model, it implements market trading plans and is responsible for the operational scheduling of the power system and the real-time balancing of the power system to ensure the safe and stable operation of the power system. In this paper, WPP prefers to trade energy under a P2P mechanism, followed by trading in an operator-operated trading floor, due to the high cost of regulation under operator-based scheduling and WPP's loss of profit.

3 DESIGN GOALS OF THE BILEVEL PROBLEM

In this section, we propose a bilevel model (Wang et al., 2022), which can maximize WPP's profits, reduce prosumers' costs, and provide WPP with a reasonable trading strategy.

3.1 Design Goals of the Bilevel Problem

3.1.1 The Objective Function of the Upper-Level Problem

From perspective of WPP, the objective function at this level is to maximize WPP's profit as follows:

$$\begin{aligned}\text{Max} \sum_{\omega\in\Omega}\pi_{\omega}\sum_{t\in T}\left[\begin{array}{c} P_t^{\text{DA,Sell}}\lambda_t^{\text{DA}} \\ +\sum_{K_i\in\mathcal{K}}\left(P_{t,K_i}^{Sell}\lambda_{t,K_i}^{Sell}-P_{t,K_i}^{Buy}\lambda_{t,K_i}^{Buy}\right) \\ +\left(P_t^{B+}\lambda_t^{+}-P_t^{B-}\lambda_t^{-}\right)\end{array}\right] \\ \text{s.t.}\,(1)-(4)\end{aligned} \tag{9}$$

In the above model, the first item represents WPP's revenue from selling energy in DA market. The second item stands for WPP makes profits from selling to prosumers. The third item presents cost from purchasing energy from prosumers. Also, WPP needs to take the cost of penalties in the regulation market.

3.1.2 The Objective Function of the Lower-Level Problem

The objective fuction of lower level is defined as

$$\begin{aligned}\text{Min} \sum_{\omega\in\Omega}\pi_{\omega}\sum_{t\in T}\left[\begin{array}{c} \sum_{K_i\in\mathcal{K}}P_{t,K_i}^{Sell}\lambda_{t,K_i}^{Sell} \\ +\sum_{K_i\in\mathcal{K}}\left(\lambda_{t,K_i}^{m+}R_{t,K_i}^{m+}+\lambda_{t,K_i}^{m-}R_{t,K_i}^{m-}\right) \\ -\sum_{K_i\in\mathcal{K}}P_{t,K_i}^{Buy}\lambda_{t,K_i}^{Buy}\end{array}\right] \\ \text{s.t.}\,(5)-(8)\end{aligned} \tag{10}$$

where, the first item represents the costs of purchasing energy from WPP. The second and third items represent the costs of charging and discharging for prosumers. The last item is the revenue from prosumers selling energy to WPP.

3.1.3 Combination of Upper and Lower Levels

The lower level objective function (10), and constraints (5)-(8) are replaced by their Karush-Kuhn-Tucker (KKT) conditions. The dual theorem of linear programming considers that the objective function of the dual problem is equal to the objective function of the original problem, and the value of this objective function is also optimal (Song et al., 2017). Subject to KKT condition, the upper-layer objective function formula becomes a formula that is linear with respect to the decision variables, and finally, the upper-level optimization process is transformed into the optimal solution problem of solving a single-level mixed integer linear programming.

3.2 Reputation Design

In order to stimulate the accuracy of WPP's forecasted generation and regulate the behavior of the prosumers to participate in the P2P mechanism, we propose their reputation mechanism. The blockchain-based distributed energy trading system has a reputation value for both WPP and prosumers to ensure the proper operation of trading. For WPP, the balancing penalty cost is changed accordingly to its reputation value. For prosumers, the system ranks the prosumers with good reputation value according to the real-time reputation value to motivate them to trade firstly and removes the inactive or malicious prosumers to ensure the regular operation of the distributed energy trading system.

3.2.1 Reputation of Wind Power Producer

The WPP reputation value consists of two parts, one is the generation accuracy and the other is generation efficiency of the wind turbine.

$$R_J=\alpha_1\frac{1}{24}\sum_{t\in T}\frac{\min\left\{P_{pre,t},P_{act,t}\right\}}{\max\left\{P_{pre,t},P_{act,t}\right\}}+\alpha_2\frac{WT_{act}}{WT_{th}} \tag{11}$$

where, $\frac{\min\{P_{pre,t},P_{act,t}\}}{\max\{P_{pre,t},P_{act,t}\}}$ presents the prediction accuracy of WPP at time t, the more accurate the WPP prediction, the closer this term is to 1. $\frac{WT_{act}}{WT_{th}}$ presents the power generation efficiency of the wind turbine during its life cycle. α_1 represents how much RT attaches to the first item, α_2 represents how much RT attaches to the second item, and $\alpha_1+\alpha_2=1$. Note that the reputation value of a WPP the day before a transaction affects the balancing price on the day of the transaction. Therefore, in order to increase the profit of power generation, WPP strives to improve its reputation value.

3.2.2 Reputation of Prosumer

$$R_{K_i,t}=\beta_1\frac{\sum_{t_0}^{t}x_{i,t}}{I_{tot}}+\beta_2\frac{\sum_{t_0}^{t}P_{K_i,t}}{P_{day}} \tag{12}$$

TABLE 1 | Notations.

Notation	Description
$\mathcal{J}$	Set of WPP nodes *j*
$\mathcal{K}$	Set of prosumer nodes *k*
P_t^W	Wind power generation at time *t*
P_t^{DA}	Power generation of DA market at time *t*
$P_{t,K_i}^{Sell/Buy}$	WPP sells/buys energy to/from prosumers at *t*
$P_t^{B+/-}$	Positive/negative balancing energy at *t*
P_t^{DR}	Total demand of loads at *t*
P_{pre}	The forecast power generation
P_{act}	The actual power generation
λ_t^{DA}	Selling DA market price at *t*
λ_{t,K_i}^{Sell}	Offering price by WPP at *t*
λ_{t,K_i}^{Buy}	Offering price by prosumers at *t*
$\lambda_t^{+/-}$	Positive (negative) balancing market price at *t*
$\lambda_{t,K_i}^{m+/-}$	Price of charging and discharging of prosumer at *t*
$R_{t,K_i}^{m+/-}$	Energy of charging and discharging of prosumer at *t*
t(T)	set of time periods
R_J	The reputation value of WPP
R_K	The reputation value of prosumer
$\Delta P^{+/-}$	Positive (negative)generation deviation

$$\Delta R_{K_i} = \beta_1 \frac{x_{i,t+1}}{I_{tot}} + \beta_2 \frac{\Delta P_{i,t+1}}{P_{day}} \tag{13}$$

$$x_{i,t} = \begin{cases} 1 & \text{, transaction completed} \\ 0 & \text{, not completed} \end{cases} \tag{14}$$

$$\alpha_1 + \alpha_2 = 1, \beta_1 + \beta_2 = 1 \tag{15}$$

where, R_{K_i} is reputation value of prosumer, it consists of two parts. The first term $\frac{\sum_{t\in T} I_{i,t}}{I_{tot}}$ expresses the proportion of the number of times the *i*th prosumer participated in transaction from t_0 to t to the total number of times. $x_{i,t}$ as a Boolean variable, when a transaction is completed, $x_{i,t}$ is 1, when a transaction is not completed, $x_{i,t}$ is 0. The second term $\frac{\sum_{t\in T} P_{K_i,t}}{P_{day}}$ is defined as the ratio of the total transaction volume of the *i*th prosumer to the total transaction volume in a day. β_1 and β_2 are reputation weighting factors, which indicate how much RT market attaches importance to $\frac{\sum_{t\in T} I_{i,t}}{I_{tot}}$ and $\frac{\sum_{t\in T} P_{K_i,t}}{P_{day}}$. The sum of the two weightings is 1. Let the reputation value of the consumer is updated once an hour. **Eq. 13** gives the incremental reputation value of the prosumer. $x_{i,t+1}$ represents the prosumer's Boolean function at the next transaction moment. $\Delta P_{i,t+1}$ is the transaction volume of prosumers at the next moment. Specially, when the prosumer does not participate in a transaction at the next moment, the incremental reputation value of the prosumer is zero. **Table 1** lists some important symbols.

4 BLOCKCHAIN NETWORK IMPLEMENTATION

The proposed market consists of four phases: upload initial information, manage real-time information, publish RT market transaction plans and BL market transaction. The frame is shown in **Figure 2**. The figure shows that blockchain is a platform for trading between buyers and sellers, which contains the real-time reputation value of WPP and prosumers, real-time generation, forecasted generation of WPP, and demand of prosumers and loads. Blockchain can realize trustless, decentralized, and efficient P2P transactions between nodes through data encryption, time stamps, and smart contracts (Gong et al., 2020). The blockchain-based real-time trading market supports trustless P2P direct transactions between WPP and prosumers, and the results of the transactions can be published on the chain.

Blockchain acts as a distributed database system that acts as an open ledger to store and manage transactions. It contains the historical records of all transactions (Shan et al., 2019). Before the transaction, the buyer and seller must upload the transaction information to the blockchain. The detail of the algorithm is shown in **Algorithm 1**.

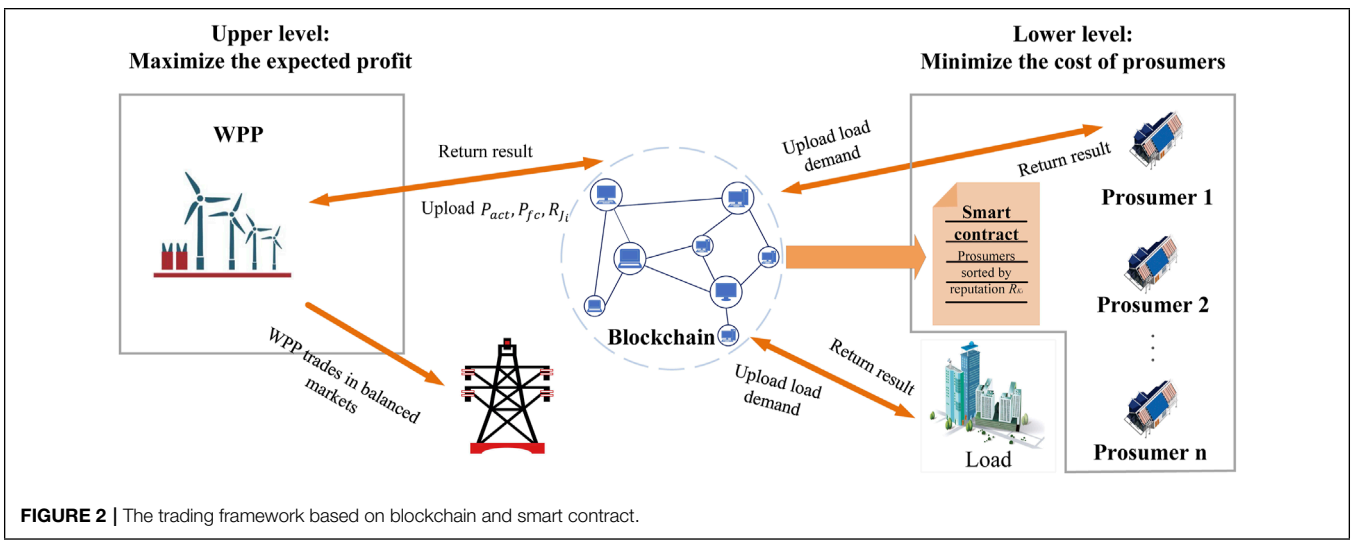

FIGURE 2 | The trading framework based on blockchain and smart contract.

Algorithm 1: Real-time market energy trading algorithms.

Input: $R_{K_1}, ..., R_{K_i}, ..., R_{K_{20}}$; P_{pre}; P_{act}
Output: Real-time market P2P trading plan
P2P transactions of WPP and prosumers according to reputation ;
if $\Delta P^+ = \Delta P^-$ **then**
  Return result
  else if *Remaining deviations from WPP are then traded P2P with prosumers* **then**
    if $\Delta P = \Delta P^+$ **then**
      Sell electricity in the order of reputation value of prosumers
    if $\Delta P = \Delta P^-$ **then**
      Purchase electricity in the order of reputation value of prosumers
if *still energy imbalance* **then**
  WPP sells or buys electricity based on its reputation in BL market
return

- Phase 1: Upload initial information.

Before the DA market opens, WPP uploads its electricity generation forecast data, while the load also uploads the demand forecast information. WPP submits energy bidding on the trading floor of the wholesale market. WPP buys energy at certain times and sells energy at certain times, depending on WPP's forecast accuracy and load demand. After DA market is cleared, the day-ahead prices are uploaded to the blockchain. Finally, the above-mentioned on-chain data are stored and used as the basis for RT market trading.

- Phase 2: Manage real-time information.

At the retail level, WPP trades real-time energy with the electric loads in its jurisdiction. WPP uploads the actual output to the blockchain, and the deviation between the actual generation and the predicted generation will cause a high adjustment price. As a result, WPP has an incentive to participate in a RT market with a P2P mechanism to trade energy with prosumers. Under the P2P trading mechanism, the interaction between WPP and prosumers provides a new solution for the management of renewable energy consumption. Understudy WPP submits energy bid to RT market, let the difference between the actual and forecast generation be the generation deviation (ΔP), which is positive (ΔP^+), and vice versa. According to the positive or negative value of ΔP, WPP will enter the positive or negative RT market under the P2P mechanism, respectively. At this point, WPP uploads the latest reputation value to the blockchain information system, which is determined by the accuracy of WPP's forecasts and the efficiency of its wind turbines. The prosumers upload their real-time power information: up and down reserves, reputation value R_{t,K_i}, Charging and discharging costs to the chain.

- Phase 3: Publish RT market transaction plans.

At the beginning of a period, the smart contract generates specific transaction results for prosumers based on on-chain data and algorithms. Based on the positive/negative deviation of the WPP, the producers or prosumers who need to purchase power/have excess power generation will be ranked from highest to lowest reputation value and will be calculated to match a series of prosumers for WPP. The prosumers will trade in order with the WPP, and the blockchain will then return the scheduling results to the WPP. After the prosumers finish the scheduling task, they update the remaining capacity and reputation value on the chain. If WPP has questions about the scheduling assignment, they can get all the data of that scheduling task from the blockchain.

- Phase 4: BL market transaction.

After completing the RT market tradings, there are still deviated WPPs entering the trading floor managed by BL market to receive punishment. Such punishments are costly. We often hope that minimize the number of penalties to increase WPP's profits. During several of the above tradings, if WPP's reputation value decreases, it will affect the balancing price. For WPP to gain a higher profit, WPP should improve the forecast accuracy and timely attention to the generation efficiency of wind turbines to ensure their proper operation during their life cycle. The updated WPP reputation value will be uploaded to the blockchain after the trading.

5 NUMERICAL RESULTS

5.1 Input Data

The proposed energy market design is implemented based on realistic data to give the optimal bidding strategy of WPP. The predicted wind output power and actual power of WPP are shown in **Figure 3**. Due to changing weather conditions, WPP's forecasts deviation significantly from actual generation during some time periods. Drastic wind speed changes will affect the accuracy of wind power prediction. The generation offset caused by forecast errors impacts the active power balance of the power system. In a power system where wind power is the dominant source of power, the above phenomenon will cause a significant impact on the frequency of the grid and thus affect the stable operation of the system. At 4:00 a.m., 12:00, 1:00 p.m., WPP's actual generation significantly exceeds forecasted generation, When the wind speed fluctuates greatly, the wind turbine will output active power fluctuations. If large-scale electric energy is injected into grid during the wind power generation process, it will not only affect the transient stability of the power grid, but also affect the stability of the power grid frequency. bring serious impact. To solve the above phenomenon, WPP trades with prosumers in RT market to reduce fluctuations on the grid. **Figure 4** shows

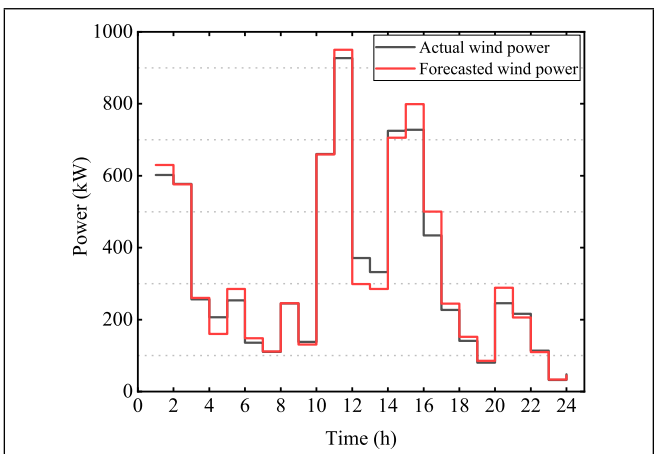

FIGURE 3 | Actual and forecasted wind power.

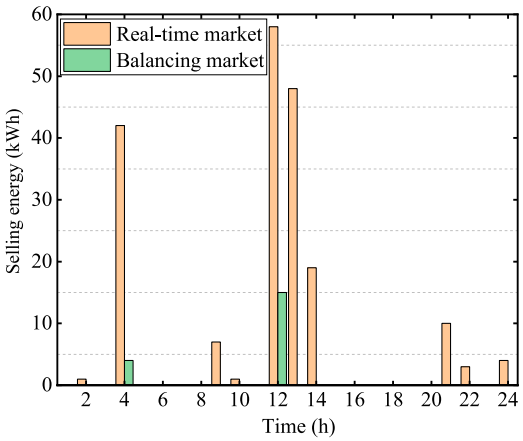

FIGURE 4 | Selling energy to prosumers.

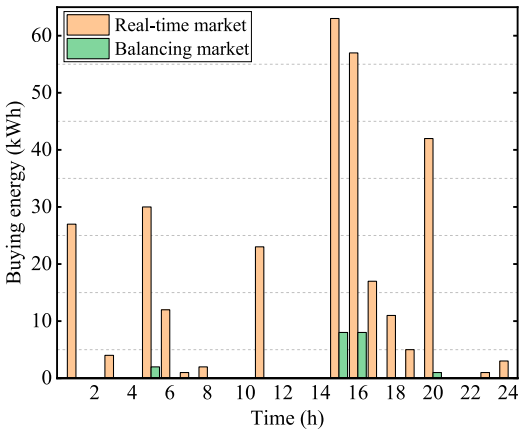

FIGURE 5 | Buying energy from prosumers.

the excess of generation, prosumers and operator use the RT and BL markets to repurchase the energy. **Figure 5** shows the deficit of generation, WPP purchase energy from prosumers and operator. Furthermore, DA and balancing prices are generated according to scenarios. The data mentioned above is uploaded to the blockchain. Simulations were operated with an Intel Core CPU i7-9750H @ 2.6 GHz, 16 GB RAM to verify the performance of model. Also, we use Ethereum Geth client to build a blockchain system to simulate our energy trading system, and calculate the overhead in the chain.

5.2 Results and Discussions

5.2.1 Blockchain Test

Figure 6 shows a prototype of the P2P trading platform implemented using the Ethereum Geth client, which supports direct transactions between prosumers and wind power producers. It also shows the transaction accounts of WPP and prosumers, that is, the Ethereum address. The address is represented by a hash value and has privacy protection. The gas consumption of the operation is also included.

FIGURE 6 | Ethereum test.

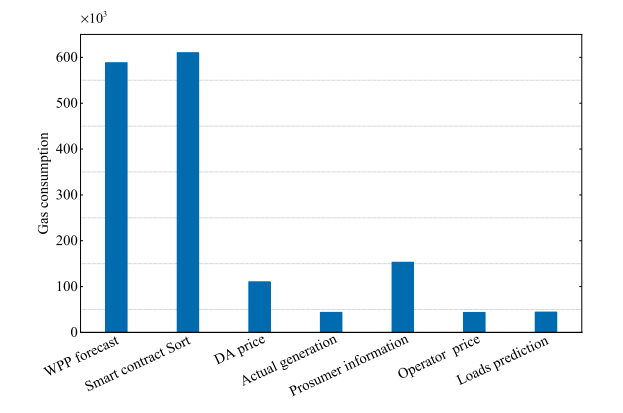

FIGURE 7 | Gas consumption.

In Ethereum's smart contracts, each data transfer requires a certain amount of gas, gas consumption implies the overhead of performing operations on the blockchainLiu et al. (2020) Usually, this is an important criterion for measuring whether a blockchain network design is reasonable. **Figure 7** illustrates the gas overhead for the operation of entities in our framework structure. In the process of energy trading based on blockchain, WPP and prosumers need to upload information and operate on the chain. Moreover, we can see how much gas is mainly consumed by the smart contract by sorting the reputation value of the prosumers. As shown in **Figure 7**, due to the large amount of information that WPP needs to upload, the reputation ranking of prosumers by smart and contract processing information is relatively large, consuming about 600,000 units of gas. The rest of the operations are mainly to store data on the blockchain. Their gas consumption is less than 150,000, which is acceptable to all nodes in the system.

5.2.2 Trading Result

Assuming that a trading cycle T = 24 h, **Figure 3** shows the deviation between the predicted output and the actual output of WPP during some periods (for example during 4 a.m..–6 a.m., 11 a.m..-2 p m. and 7 p.m..–9 p.m.). For mentioned wind forecast errors, WPP conducts P2P tradings with prosumers to decrease the size of the value of Δ_P.

As shown in **Figure 4**, as it can be seen, when wind power production is high, WPP sells surplus energy. At 4 a.m.,

Prosumers consume most of the electricity, and WPP sells a small portion to the operator. At 12:00, WPP tends to sell more energy to prosumers, however, there is a limit to the amount of electricity that can be consumed by prosumers under WPP's jurisdiction. So WPP sells the rest of its energy at a lower price positive BL market. At 2 p.m., there is enough surplus energy in the energy storage of the prosumers, and WPP sells all the surplus energy to the prosumers. In fact, Prosumers make WPP avoid selling all excess energy to BL market. Without using our model, WPP's profits are lower due to the fact that the revenue from selling to consumers is greater than the revenue from selling to the BL market. To be more specific, prosumers promote the consumption of wind power.

As shown in **Figure 5**, in some periods, deviation represents a deficit of production. The producer sells electricity to WPP, and since the amount of electricity sold by the producer is not enough to reach the amount of electricity that WPP wants to buy, WPP buys a small portion of the electricity from the operator at 4 a.m. At 3 p.m. Prosumers' power generations are within a certain range, if prosumers cannot supply WPP, then WPP buys from the BL market at a high price. At 6 p.m., the power generated by the prosumers is sufficient to supply the offset of the WPP, as a result, the WPP purchases all the required power from the prosumers. Generally, the prosumers sell to WPP at a price below the BL market, which reduces WPP's losses.

In our P2P trading mechanism, prosumers cover most of the uncertainty of wind power generation, which not only improves WPP's earnings but also reduces its power purchase costs, thereby reducing the impact of wind power on the grid, ensuring that the stable operation of the power grid.

Table 2 is added to show the profit of WPP and prosumers with and without our model. Compared with the previous trading model, due to the introduction of the real-time market with prosumers, the profit of WPP under our model has increased by 9.55%. In this paper, we consider that the benefits of the prosumers are divided into two aspects, on the one hand, the proceeds from selling to WPP, and on the other hand, the savings from the producer and consumer's direct dealings with WPP, noting that the above earnings minus the discharge costs of the prosumers.

5.2.3 Reputation Experiment

Finally, we test the effect of reputation value about prosumers and WPP. we set 20 prosumers, these prosumers buy and sell electricity in the RT market to compensate for generation deviations, and if the prosumers are unable to cover deviations, then the WPP will trade electricity with the main grid in BL market. For prosumers, We set two scenarios to simulate situation. For WPP, we set two scenarios and three situations to simulate. For WPP, we set up one scenario with three situations.

We track the impact of changes in one prosumer's reputation value on the success rate of a transaction. we set up two scenarios to highlight the influence of the weight factors β_1 and β_2 on the weight terms where they are located. In scenario 1, both β_1 and β_2 are 0.5. In scenario 2, β_1 is 0.8, β_2 is 0.2. In scenario 1, as shown is **Figure 8**, varying the magnitude of the value of the corresponding term of $\sum_{t_0}^{t} x_{i,t}$, specifically, the frequency of the total number of transactions in which the prosumer participates from t_0 to t for low, medium, and high frequencies. The results show that the prosumer with a high number of participations has a higher probability of successful transactions. Similarly, changing the magnitude of the value of the corresponding term of $\sum_{t_0}^{t} P_{K_i,t}$. Specifically, the value of the weight factor and its corresponding reputation item can affect the reputation value. In our experiments, we set three sizes of reputation items from t_0 to t by the prosumer to highlight the influence of reputation item changes on reputation value. In the second scenario, as shown is **Figure 9**, it is obvious that the change in transaction volume has a larger impact on the transaction success rate because

TABLE 2 | Profit of WPP and prosumers.

Entity	With Our Model ($)	Without Our Model ($)	Gain (%)
WPP	4579.63	4180.57	9.55
Prosumers	208.61	—	5.6

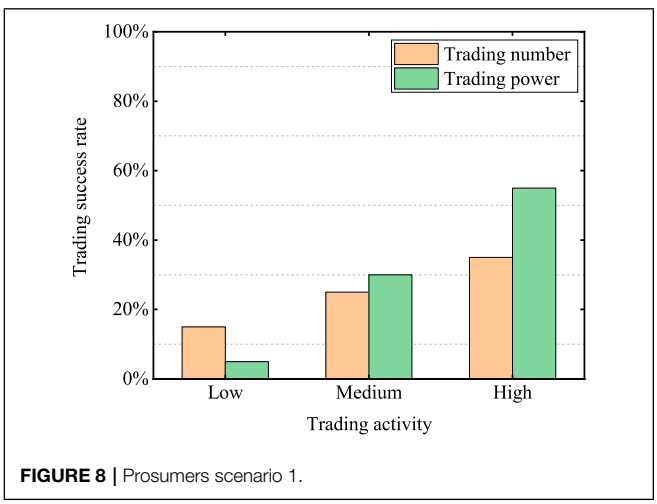

FIGURE 8 | Prosumers scenario 1.

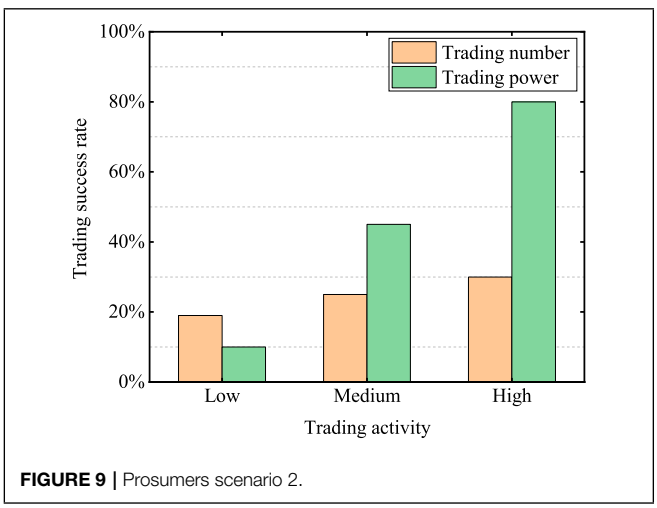

FIGURE 9 | Prosumers scenario 2.

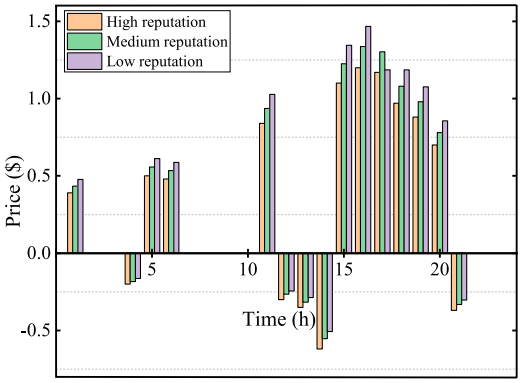

FIGURE 10 | Balancing price of WPP under different reputation values.

we set the weight factor of transaction volume to 0.8. When the transaction increases, the reputation value of the prosumer improves significantly, and then the trading success rate increases significantly.

Figure 10 shows that the price of electricity traded in the BL market differs when the WPP has different reputation values. WPP trades power with the main grid to compensate for generation deviations. We compared WPP's balancing prices at low, medium and high reputation values. The higher the reputation value of WPP, the lower the price of electricity it buys from the main grid in the BL market, the higher the price of electricity it sells, and the higher the profit it earns. Therefore, WPP has to increase the forecast accuracy to increase the reputation value to increase its profit.

6 CONCLUSION AND FUTURE WORK

In this study, a blockchain-based P2P energy trading short-term market is proposed. It supports direct transactions between WPP and prosumers without the third parties or the central agency while ensuring efficient and trustless. In the blockchain-based energy trading market, the participation of prosumers reduces WPP's balancing costs due to generation deviation caused by inaccurate forecasts. At the same time, the benefits of prosumers in the real-time market reduce their electricity purchase costs. In addition, we designed a reputation mechanism to promote more active participation of prosumers in the market and more accurate forecasts of WPP. This mechanism ensures that professional consumers with a high number of participants and a high historical trading capacity will receive more benefits. The pricing of energy transactions is determined by a two-level optimization algorithm, which makes the optimal solution satisfy the maximum WPP revenue and the lowest electricity purchase cost for prosumers. Through numerical simulation experiments, in a given scenario, our scheme can effectively increase the revenue of WPP by 9.55%, reduce its adjustment cost, and increase the profit of prosumers by 5.6%. In the future, we intend to expand the use cases of our solution. On the power generation side, the trading environment of WPPs is complicated, and competition among WPPs is introduced. Seek mutual transactions between WPPs to compensate for power generation deviations and further reduce balancing costs. In addition, we will introduce a variety of renewable energy into the market pricing to promote the consumption of a variety of renewable energy. On the demand side, we will incorporate electric vehicles into our market and participate in transactions to balance wind energy fluctuations.

DATA AVAILABILITY STATEMENT

The original contributions presented in the study are included in the article/supplementary material, further inquiries can be directed to the corresponding author.

AUTHOR CONTRIBUTIONS

Conceptualization, PD, BH and ZL; methodology, PD; software, PD; validation, PD, GJ and LF; formal analysis, PD, ZL and CY; investigation, PD and CY; resources, CY; data curation, PD, GJ and LF; writing—original draft preparation, PD and ZL; writing—review and editing, ZL; visualization, ZL and BH; supervision, BH; project administration, BH and CY; funding acquisition, BH and CY. All authors have read and agreed to the published version of the manuscript.

FUNDING

This work was supported in part by the National Key Technologies Research and Development Program of China (2018YFA0702200) and the Liaoning Revitalization Talents Program of China (XLYC2007181), in part by the Fundamental Research Funds for the Central Universities (N2204010).

REFERENCES

Al-Awami, A. T., and El-Sharkawi, M. A. (2011). Coordinated Trading of Wind and Thermal Energy. *IEEE Trans. Sustain. Energy* 2, 277–287. doi:10.1109/TSTE.2011.2111467

Cheng, J., Li, R., Choobineh, F. F., Hu, Q., and Mei, S. (2019). Dispatchable Generation of a Novel Compressed-Air Assisted Wind Turbine and its Operation Mechanism. *IEEE Trans. Sustain. Energy* 10, 2201–2210. doi:10.1109/tste.2018.2883068

Cui, S., Wang, Y.-W., Li, C., and Xiao, J.-W. (2020). Prosumer Community: A Risk Aversion Energy Sharing Model. *IEEE Trans. Sustain. Energy* 11, 828–838. doi:10.1109/tste.2019.2909301

Fabbri, A., GomezSanRoman, T., RivierAbbad, J., and MendezQuezada, V. H. (2005). Assessment of the Cost Associated with Wind Generation Prediction Errors in a Liberalized Electricity Market. *IEEE Trans. Power Syst.* 20, 1440–1446. doi:10.1109/tpwrs.2005.852148

Gong, D., Song, S., Lopez, M., and Sanchez, E. N. (2020). Synchronous Analysis for Fuzzy Coupled Neural Networks with Column Pinning Controllers. *Theory Appl. Complex Cyber-Physical Interact.* 2020, 1397069. doi:10.1155/2020/1397069

Homa, R. K., Mostafa, V. D., Hamid, N., Amjad, A. M., and Josep, G. (2017). A Stochastic Bi-level Scheduling Approach for the Participation of Ev Aggregators in Competitive Electricity Markets. *Appl. Sci.* 7, 1100.

Huang, B., Li, Y., Zhan, F., Sun, Q., and Zhang, H. (2022a). A Distributed Robust Economic Dispatch Strategy for Integrated Energy System Considering Cyber-Attacks. *IEEE Trans. Ind. Inf.* 18, 880–890. doi:10.1109/TII.2021.3077509

Huang, B., Zheng, S., Wang, R., Wang, H., Xiao, J., and Wang, P. (2022b). Distributed Optimal Control of DC Microgrid Considering Balance of Charge State. *IEEE Trans. Energy Convers* Early Access. doi:10.1109/TEC.2022.3169462

Li, Y., Gao, D. W., Gao, W., Zhang, H., and Zhou, J. (2021). A Distributed Double-Newton Descent Algorithm for Cooperative Energy Management of Multiple Energy Bodies in Energy Internet. *IEEE Trans. Ind. Inf.* 17, 5993–6003. doi:10.1109/TII.2020.3029974

Li, Z., Kang, J., Yu, R., Ye, D., Deng, Q., and Zhang, Y. (2017). Consortium Blockchain for Secure Energy Trading in Industrial Internet of Things. *IEEE Trans. Ind. Inf.* 2017, 2786307. doi:10.1109/tii.2017.2786307

Liu, Z., Wang, D., Wang, J., Wang, X., and Li, H. (2020). A Blockchain-Enabled Secure Power Trading Mechanism for Smart Grid Employing Wireless Networks. *IEEE Access* 8, 177745–177756. doi:10.1109/ACCESS.2020.3027192

Luo, F., Dong, Z. Y., Liang, G., Murata, J., and Xu, Z. (2019). A Distributed Electricity Trading System in Active Distribution Networks Based on Multi-Agent Coalition and Blockchain. *IEEE Trans. Power Syst.* 34, 4097–4108. doi:10.1109/TPWRS.2018.2876612

Mohammad, N., and Mishra, Y. (2018). Coordination of Wind Generation and Demand Response to Minimise Operation Cost in Day-ahead Electricity Markets Using Bi-level Optimisation Framework. *IET Gener. Transm. & Distrib.* 12, 3793–3802. doi:10.1049/iet-gtd.2018.0110

Rashidizadeh-Kermani, H., Vahedipour-Dahraie, M., Shafie-Khah, M., and Catalao, J. (2020). Joint Energy and Reserve Scheduling of a Wind Power Producer in a Peer-To-Peer Mechanism. *IEEE Syst. J.* 15, 1–10.

Rashidizadeh-Kermani, H., Vahedipour-Dahraie, M., Shafie-Khah, M., and Siano, P. (2021). A Peer-To-Peer Energy Trading Framework for Wind Power Producers with Load Serving Entities in Retailing Layer. *IEEE Syst. J.* 16, 1–10.

Sanchez de la Nieta, A. A., Contreras, J., and Munoz, J. I. (2013). Optimal Coordinated Wind-Hydro Bidding Strategies in Day-Ahead Markets. *IEEE Trans. Power Syst.* 28, 798–809. doi:10.1109/TPWRS.2012.2225852

Shan, Q., Chen, Z., Li, T., and Chen, C. (2019). Consensus of Multi-Agent Systems with Impulsive Perturbations and Time-Varying Delays by Dynamic Delay Interval Method. *Commun. Nonlinear Sci. Numer. Simul.* 78, 104890.1–104890.11. doi:10.1016/j.cnsns.2019.104890

Shin, H., Lee, D., and Baldick, R. (2018). An Offer Strategy for Wind Power Producers that Considers the Correlation between Wind Power and Real-Time Electricity Prices. *IEEE Trans. Sustain. Energy* 9, 695–706. doi:10.1109/TSTE.2017.2757501

Skajaa, A., Edlund, K., and Morales, J. M. (2015). Intraday Trading of Wind Energy. *IEEE Trans. Power Syst.* 30, 3181–3189. doi:10.1109/tpwrs.2014.2377219

Song, R., Lewis, F. L., and Wei, Q. (2017). Off-policy Integral Reinforcement Learning Method to Solve Nonlinear Continuous-Time Multiplayer Nonzero-Sum Games. *IEEE Trans. Neural Netw. Learn. Syst.* 28, 704–713. doi:10.1109/tnnls.2016.2582849

Sorin, E., Bobo, L., and Pinson, P. (2018). Consensus-based Approach to Peer-To-Peer Electricity Markets with Product Differentiation. *IEEE Trans. Power Syst.* 34, 994.

Wang, X., Gao, D. W., Wang, J., Yan, W., Gao, W., Muljadi, E., et al. (2018). Implementations and Evaluations of Wind Turbine Inertial Controls with Fast and Digital Real-Time Simulations. *IEEE Trans. Energy Convers.* 33, 1805–1814. doi:10.1109/TEC.2018.2849022

Wang, X., Zhao, T., and Parisio, A. (2022). Frequency Regulation and Congestion Management by Virtual Storage Plants. *Sustain. Energy, Grids Netw.* 29, 100586. doi:10.1016/j.segan.2021.100586

Yang, T., Yi, X., Wu, J., Yuan, Y., Wu, D., Meng, Z., et al. (2019). A Survey of Distributed Optimization. *Annu. Rev. Control* 47, 278–305. doi:10.1016/j.arcontrol.2019.05.006

Zhang, C., Wu, J., Zhou, Y., Cheng, M., and Long, C. (2018a). Peer-to-peer Energy Trading in a Microgrid. *Appl. Energy* 220, 1–12. doi:10.1016/j.apenergy.2018.03.010

Zhang, T., Pota, H., Chu, C.-C., and Gadh, R. (2018b). Real-time Renewable Energy Incentive System for Electric Vehicles Using Prioritization and Cryptocurrency. *Appl. Energy* 226, 582–594. doi:10.1016/j.apenergy.2018.06.025

Zhou, Y., Wu, J., and Long, C. (2018). Evaluation of Peer-To-Peer Energy Sharing Mechanisms Based on a Multiagent Simulation Framework. *Appl. Energy* 222, 993–1022. doi:10.1016/j.apenergy.2018.02.089

Conflict of Interest: Author CY is employed by State Grid Liaoning Electric Power Company Limited. The remaining authors declare that the research was conducted in the absence of any commercial or financial relationships that could be construed as a potential conflict of interest.

Publisher's Note: All claims expressed in this article are solely those of the authors and do not necessarily represent those of their affiliated organizations, or those of the publisher, the editors and the reviewers. Any product that may be evaluated in this article, or claim that may be made by its manufacturer, is not guaranteed or endorsed by the publisher.

frontiers | Frontiers in Energy Research

TYPE Methods
PUBLISHED 12 August 2022
DOI 10.3389/fenrg.2022.969168

OPEN ACCESS

EDITED BY
Xiao Wang,
Wuhan University, China

REVIEWED BY
Ji Wu,
Hefei University of Technology, China
Bolun Du,
China Electric Power Research Institute (CEPRI), China
Jinping Wang,
Hefei University of Technology, China

*CORRESPONDENCE
Wangyang Hu,
huwangyang2011@sina.com
Shaishai Zhao,
zhaoshaishai@126.com

SPECIALTY SECTION
This article was submitted to Smart Grids,
a section of the journal
Frontiers in Energy Research

RECEIVED 14 June 2022
ACCEPTED 01 July 2022
PUBLISHED 12 August 2022

CITATION
Hu W and Zhao S (2022), Remaining useful life prediction of lithium-ion batteries based on wavelet denoising and transformer neural network. *Front. Energy Res.* 10:969168. doi: 10.3389/fenrg.2022.969168

Remaining useful life prediction of lithium-ion batteries based on wavelet denoising and transformer neural network

Wangyang Hu* and Shaishai Zhao*

School of Electronic Engineering and Intelligent Manufacturing, Anqing Normal University, Anqing, China

It is imperative to accurately predict the remaining useful life (RUL) of lithium-ion batteries to ensure the reliability and safety of related industries and facilities. In view of the noise sequence embedded in the measured aging data of lithium-ion batteries and the strong nonlinear characteristics of the aging process, this study proposes a method for predicting lithium-ion batteries' RUL based on the wavelet threshold denoising and transformer model. To specify, firstly, the wavelet threshold denoising method is adopted to preprocess the measured discharging capacity data of lithium-ion batteries to eliminate some noise signals. Second, based on the denoised data, the transformer model output's full connection layer is applied to replace the decoder layer for establishing the RUL prediction model of lithium-ion batteries. Finally, the discharging capacity of each charging–discharging cycle is predicted iteratively, and then the RUL of lithium-ion batteries can be calculated eventually. Two groups of lithium-ion batteries' aging data from the Center for Advanced Life Cycle Engineering (CALCE) at the University of Maryland and the laboratory at Anqing Normal University (AQNU) are employed to verify the proposed method, individually. The experimental results demonstrate that this method can overcome the impacts of data measurement noise, effectively predict the RUL of lithium-ion batteries, and present a sound generalization ability and high accuracy.

KEYWORDS

lithium-ion battery, remaining useful life, wavelet threshold denoising, transformer model, RUL prediction

1 Introduction

Thanks to the advantages of high energy density, long storage life, high safety, and no pollution, lithium-ion batteries are widely applied in the field of electric vehicles (Yuan et al., 2015; Wang et al., 2021). However, with the use of electric vehicles starting, irreversible electrochemical reactions occur in the onboard lithium-ion batteries, which will increase their internal resistance and decrease their maximum available capacity, leading to the attenuation of their remaining useful life (RUL) and a serious reduction of the driving distances of electric vehicles (Guha and Patra., 2018; Ansari et al., 2022). Besides, it is well known that the discharging capacity of lithium-ion batteries is poor in a

low-temperature environment. Consequently, the accurate RUL is difficult to be predicted (Zhang D. et al., 2022). If the lithium-ion battery continues to work even after reaching its failure threshold, it will attenuate drastically, which may result in serious safety accidents (Liu et al., 2020). Therefore, accurate prediction of the battery RUL is of great significance to guarantee the safe and reliable operation of electric vehicles (Murugan et al., 2022).

RUL refers to the quantity of charging–discharging cycles required for the maximum available capacity of the power battery attenuating to the specified failure threshold (Zhao et al., 2022). The RUL prediction is a process of forecasting and calculating the residual power battery's life based on its historical data through certain mathematical approaches (Dong et al., 2020). The existing RUL prediction methods for lithium-ion batteries can mainly divide into model-driven and data-driven (Cadini et al., 2019; Song et al., 2022).

The model-driven method establishes a mathematically physical model by analyzing the battery performance degradation and failure mechanism for better predicting lithium-ion batteries RUL. The commonly-used lithium-ion battery models mainly include the electrochemical model, equivalent circuit model, and empirical degradation model. The electrochemical model primarily follows the internal chemical reaction mechanism of the lithium-ion battery to establish the corresponding algebraic or differential equations for forecasting the RUL. Its accuracy is high, but the model parameters are easily affected by temperature and other factors. Consequently, it is difficult to identify the parameters and the modeling procedure is really complex (Xiong et al., 2018). The equivalent circuit model adopts the traditional circuit elements like resistance, capacitance, and a constant voltage source to constitute a circuit network for describing the externality of the power battery (Guha and Patra, 2018). This model considers the battery degradation mechanism, but its establishment depends on impedance and other data difficult to obtain in practice. Furthermore, the empirical degradation model is mainly based on the exponential model of battery capacity and filtering algorithm to predict RUL (Zhang et al., 2018). Kalman filter (Xiong et al., 2012), sliding mode observer (Liu and Zhang., 2021), and particle filter (Morstyn et al., 2017; Pugalenthi et al., 2018) have all been commonly-applied model methods, which have achieved good research results. However, it has also been quite difficult to establish an accurate and universal mathematically physical model to characterize the attenuation process of lithium-ion battery capacity due to the severe onboard working conditions and the variability of the application environment.

The data-driven approach makes it possible to prognosticate the RUL of lithium-ion batteries by analyzing past data, mining intrinsic principles governing capacity decline, and utilizing mathematical algorithms to analyze, expand, and promote data. This method is simple and does not need to consider the complex mechanism of the power battery. It is suitable for the real vehicle operating environment. Common data-driven methods include the artificial neural network (ANN), (Ansari et al., 2021), support vector regression (SVR) (Xue et al., 2020), relevance vector regression (RVR) (Chen et al., 2021), and gaussian process regression (GPR) (Li et al., 2019). The transformer model, a deep learning neural network, has succeeded in the field of natural language processing and has steadily moved to the field of time-series prediction owing to its unique structure, long-distance modeling capability, and outstanding parallel computing capacity (Tian et al., 2022; Vallés-Pérez et al., 2022).

Considering the capacity regeneration phenomenon in the degradation process of lithium-ion batteries and the noise signal generated by load random interference in the measurement, data preprocessing technology is also widely used to improve the accuracy of RUL prediction, including empirical mode decomposition (EMD) (Zhang et al., 2017), variational modal decomposition (VMD) (Zhang et al., 2021), variational filtering (VF) (Jiao et al., 2020), and particle filter (PF) (Ahwiadi and Wang, 2019), etc. The method employed in this study, based on wavelet threshold denoising (WTD) (Zhang et al., 2015), cannot only effectively filter the noise but also maximize the noise and guarantee that the effective signal is not lost. The combination of a data-driven method and data preprocessing technology can further realize RUL's accurate prediction (Huang et al., 2022).

Based on the above analyses, the key factors affecting the accuracy of RUL prediction are data preprocessing and its modeling methods. In this study, the discharging capacity is selected as the health indicator and a prediction method is proposed. The main contributions are summarized as follows:

The wavelet threshold denoising data preprocessing technology is utilized to eliminate the capacity data noise signals, which not only smooths the capacity data but also retains the original characteristics of the capacity data and avoids the influence of noise components.

With the long-distance modeling ability and the feature representation technique of the series data of the transformer model, the decoder part of the original model is replaced by the output's full connection layer, and the RUL prediction framework of the improved transformer model is established to output the predicted values. The experimental results show that the wavelet denoising and transformer model can be effectively applied to the RUL prediction of the lithium-ion battery.

Two groups of battery capacity data from the Center for Advanced Life Cycle Engineering (CALCE) at the University of Maryland and the laboratory at the Anqing Normal University (AQNU) are applied to separately verify the RUL prediction method proposed in this study. The results exhibit that the performance of this method is superior to the existing prediction methods.

The rest is summarized below. Section 2 introduces the basic principles of wavelet threshold denoising and the transformer

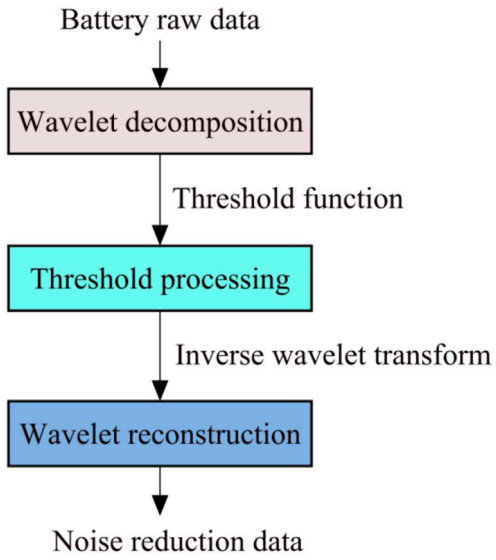

FIGURE 1
Schematic diagram of wavelet threshold denoising.

model. Section 3 specifies the proposed RUL prediction experiment scheme for lithium-ion batteries, including data preprocessing technique, experimental procedures, and evaluation criteria. Section 4 elaborates on the experimental results and compared experiment analyses. Section 5 describes the concluding observations.

2 Theoretical basis for remaining useful life prediction

2.1 Wavelet threshold denoising

Wavelet analysis is based on the characteristic that the original signal is generally concentrated in the low-frequency region. First, a wavelet transform is performed on the high-frequency noisy signal $x(t)$ to obtain a group of wavelet decomposition coefficients $W_{j,k}$ and then a threshold value λ is set for the wavelet coefficients according to the characteristics of the transformed signal. This threshold is the dividing line to process high-frequency wavelet coefficients. For those with amplitudes lower than this threshold, they will be removed directly; for those with amplitudes greater than the threshold, they will be retained. After the wavelet decomposition coefficients are processed by the threshold, the wavelet estimation coefficient $\overline{W_{j,k}}$ is obtained to limit $\|\overline{W_{j,k}} - W_{j,k}\|$ to the minimum. Finally, the estimated wavelet coefficient $\overline{W_{j,k}}$ is used for wavelet reconstruction to acquire the estimation signal $\overline{W_{j,k}}$ as the denoised signal. The principle of this wavelet threshold denoising is shown in Figure 1.

In the process of wavelet threshold denoising, the commonly-used threshold functions mainly include the hard threshold function, soft threshold function, and semi-soft threshold function. Their formulas are as follows:

The expression of the hard threshold function is:

$$\overline{W_{j,k}} = \begin{cases} W_{j,k}, & |W_{j,k}| \geq \lambda \\ 0, & |W_{j,k}| < \lambda \end{cases} \tag{1}$$

The expression of the soft threshold function is:

$$\overline{W_{j,k}} = \begin{cases} \mathrm{sgn}(W_{j,k})(|W_{j,k}| - \lambda), & |W_{j,k}| \geq \lambda \\ 0, & |W_{j,k}| < \lambda \end{cases} \tag{2}$$

The expression of the semi-soft threshold function is:

$$\overline{W_{j,k}} = \begin{cases} \mathrm{sgn}(W_{j,k})|W_{j,k}| - \lambda + \dfrac{2\lambda}{1 + e^{2W_{j,k}/\lambda}}, & |W_{j,k}| \geq \lambda \\ 0, & |W_{j,k}| < \lambda \end{cases} \tag{3}$$

where $W_{j,k}$ represents the wavelet estimation coefficient; $\overline{W_{j,k}}$ is the wavelet decomposition coefficient; sgn () indicates the symbol function, and λ refers to the threshold value.

Wavelet threshold estimation is the optimal threshold obtained under the limitation of minimum and maximum estimation for the joint distribution of multidimensional independent normal variables. The selection formula of this threshold value is:

$$\lambda_j = \sigma\sqrt{2\log(N)} \tag{4}$$

where λ_j is the threshold under the scale j; σ refers to the noise's standard variance, and N represents the signal length. The wavelet denoising method can effectively eliminate or weaken the noise signal in the lithium-ion battery capacity's measured data and restore the raw data.

2.2 Time-series transformer

The transformer model relies on the attention mechanism to draw the global dependency between input and output. Like most neural series transformation models, it has an encoder-decoder structure. The encoder maps the input time-series $X = (X_1, X_2, \cdots, X_n)$ represented by the capacity data to the continuous representation series $Z = (Z_1, Z_2, \cdots, Z_n)$. Under the condition of fixed Z, the decoder generates output time-series $Y = (Y_1, Y_2, \cdots, Y_n)$ from one element at a time. In each step of time-series prediction, the model is automatically regressed, and when generating the output series at the $n + 1$ time, the output series generated at the last n time will be used as an additional input. The transformer time-series model's architecture is shown in Figure 2.

The encoder part selects the original capacity data as the input, while the decoder part replaces the decoder with the full

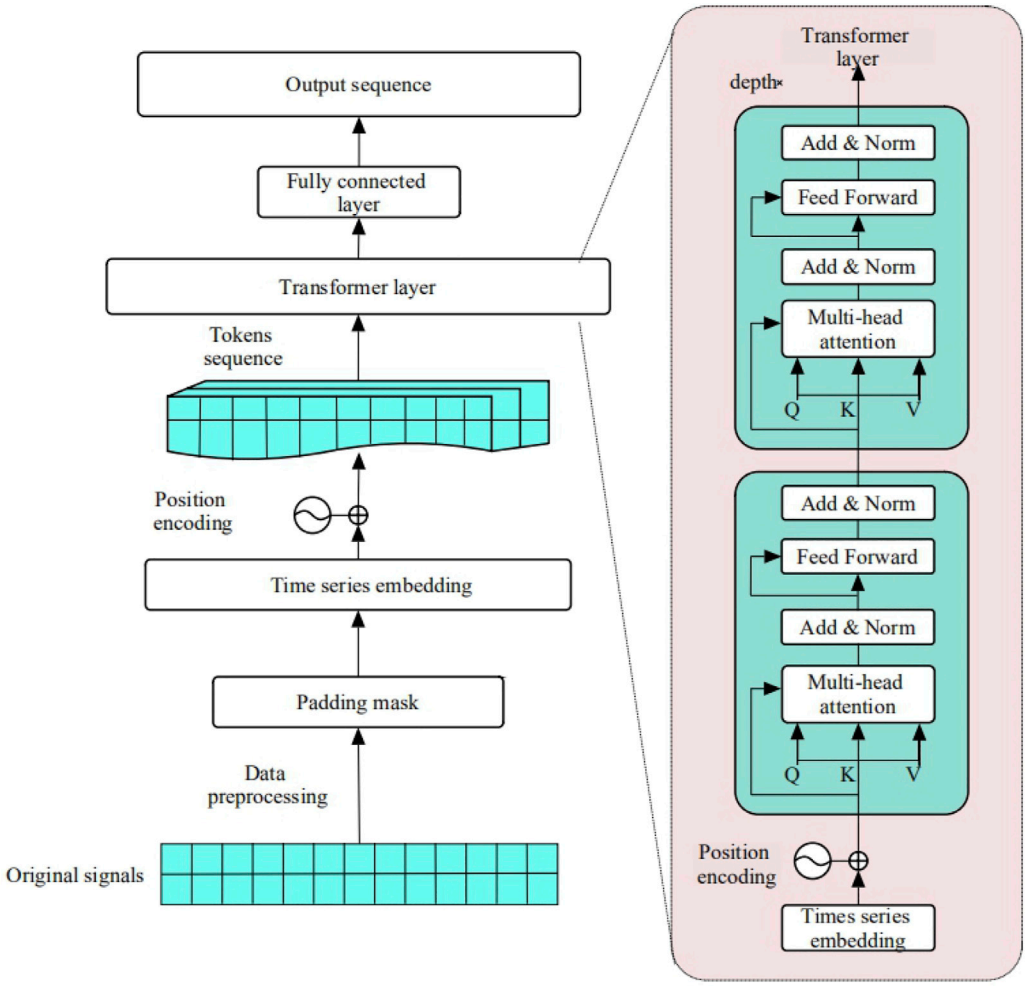

FIGURE 2
Transformer time-series model's architecture.

connection layer to predict the unknown capacity data value by the auto-regressive method (Jin et al., 2022). The decoder uses the attention mechanism to connect with the encoder, and "pays attention" to the most useful part of the input capacity data value before prediction, in which the padding mask part will be input for the mask to avoid gaining future values during training.

In the time-series prediction task, the transformer actually adopts the calculation method of scaled dot product attention, which is also an attention mechanism that links the different positions of a single series to calculate the representation of the series. Its general calculation process is shown in Figure 3.

According to the three variables of query, key, and value gained from the linear mapping of the input series, the attention function is employed to calculate the Q matrix and K matrix for achieving the attention weight matrix. Based on this, the similarity between Q and K is also calculated to obtain the output matrix A. The calculation process is as follows:

$$A = \mathrm{softmax}\left(QK^T / \sqrt{d_h}\right), A \in R^{d\times 3d_h} \tag{5}$$

In the time-series, query, key, value, and output are all vectors. Furthermore, calculate the Value according to A and obtain the weighted sum. The calculation process is as follows:

$$SA(z) = AV \tag{6}$$

In order to improve the diversity of features, a multi-head attention layer is employed to calculate multiple self-attention heads in parallel. Eventually, the final results are obtained by splicing the outputs of all attention heads (Zhang Q. et al., 2022).

Positional encoding is adopted to prevent the loss of position information in the series of input batch capacity data. Its principle is to add sine and cosine data of different frequencies to the input series as position codes so that the

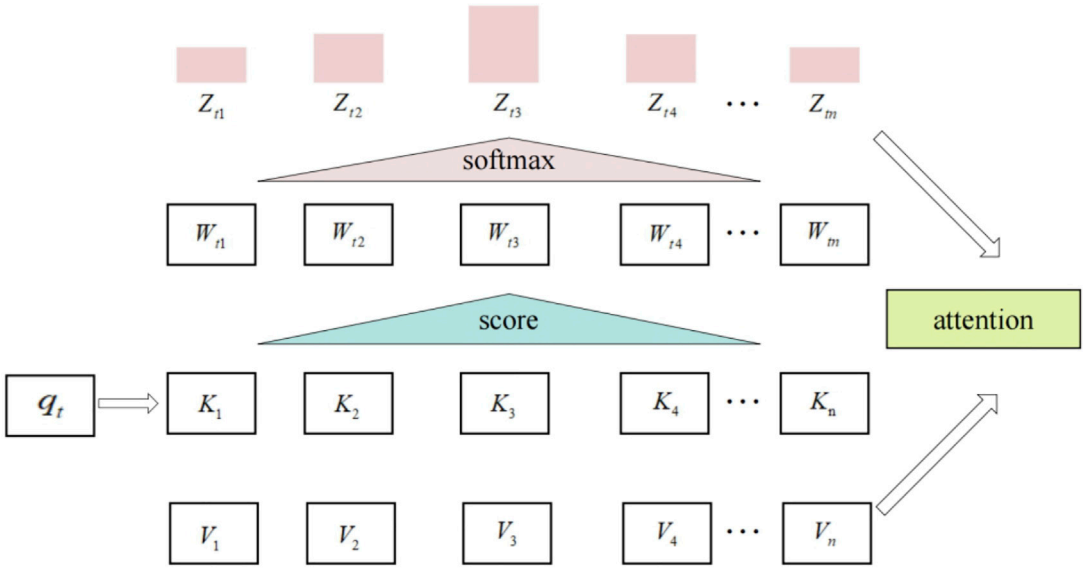

FIGURE 3
General calculation process of attention mechanism.

model can capture the relative position relationship of input variables. The calculation process is expressed in Eqs 7 and 8.

$$PE_{(pos,2i)} = \sin\left(pos \Big/ 10000^{2i/d}\right) \tag{7}$$

$$PE_{(pos,2i+1)} = \cos\left(pos \Big/ 10000^{2i/d}\right) \tag{8}$$

where pos is the position of each capacity value in the whole series; $i \in [0, \cdots, d/2]$ is used to calculate the index of the channel dimension. For the same i, the coding of the $2i + 1$ and the $2i + 1$ positions on the channel is the sine and cosine values with the same angular velocity to ensure that the position-coding can be added to the input embedding.

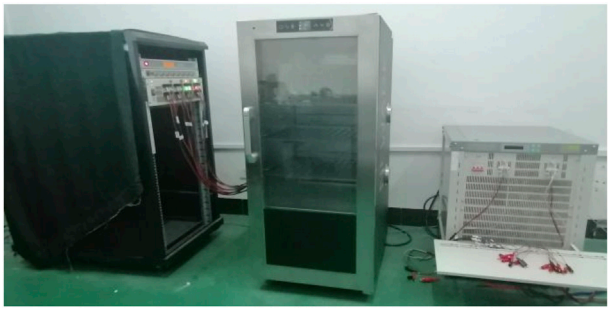

FIGURE 4
Experimental equipment.

3 Remaining useful life prediction's experiment scheme

3.1 Experimental data

Two kinds of lithium-ion battery datasets with different electrode materials and discharge environments are used to verify the performance of the proposed algorithm.

The first group of the battery degradation data is obtained from the University of Maryland's CALCE company. The battery aging test was realized by using the ArbinBT2000 battery test system. In the test, the $LiCoO_2$ battery named CX2-37 accepted

TABLE 1 Specifications of AQ-01 battery.

Cathode	$LiFePO_4$
Anode	Graphite
Rated capacity	2.4 Ah
Normal voltage	3.6 V
Allowed voltage range	3–4.2 V
End-of-charge current	48 mA
Max charge/discharge current	2400 mA/7200 mA

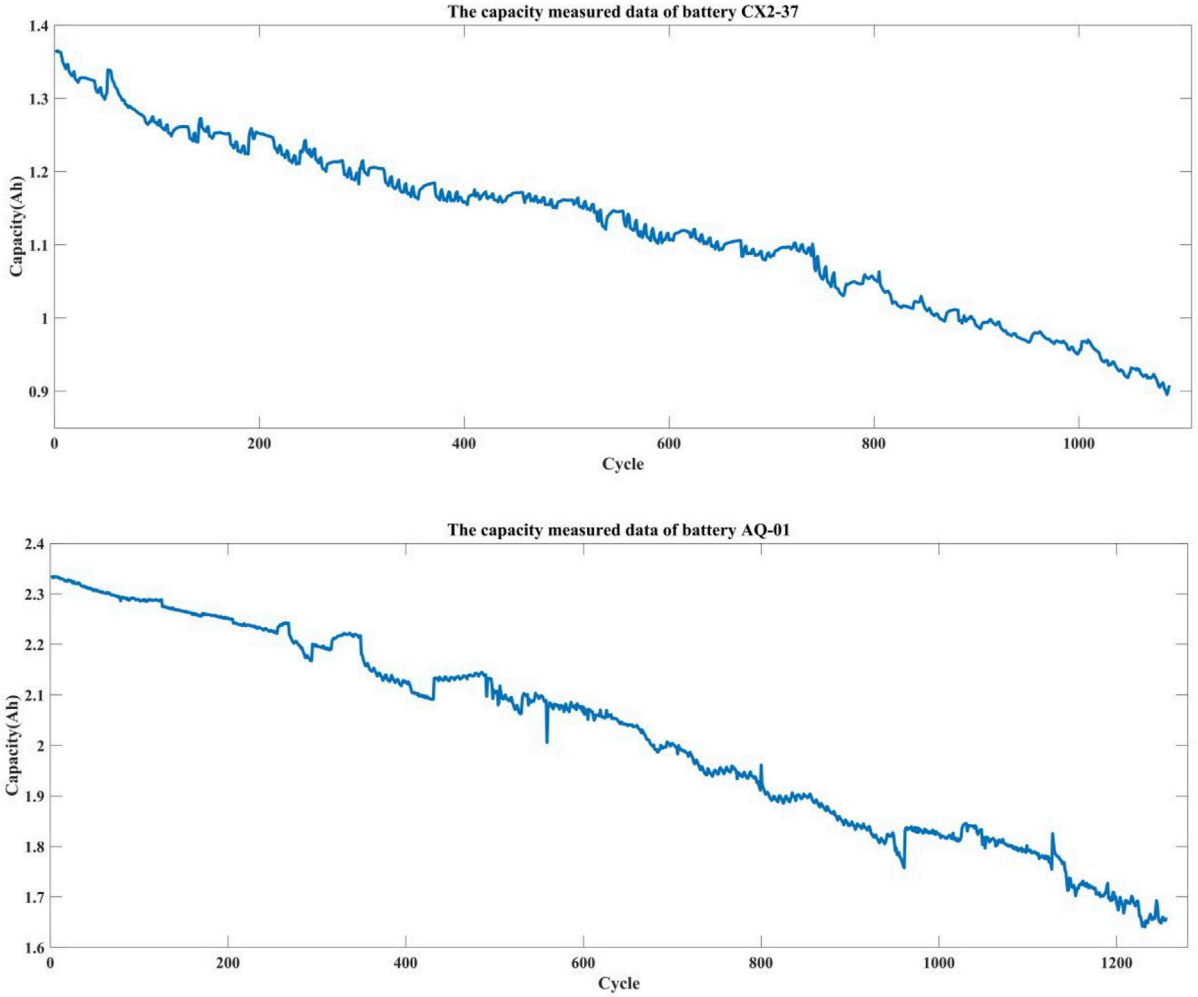

FIGURE 5
Measured capacity data of CX2-37 and AQ-01.

the standard constant current/voltage protocol, charged at 0.5C constant current (C is the measurement of the charging–discharging current to the nominal capacity) until the terminal voltage reached 4.2 V, then charged at the constant voltage of 4.2 V until the charging current dropped below 0.05 A. Discharging was operated at a 1C constant current until the battery terminal voltage of CX2-37 dropped to 2.7 V.

The second set of lithium-ion battery aging data was measured in the laboratory of AQNU university based on the high-performance battery test system (Zhang et al., 2021). Experimental equipment is shown in Figure 4. For simplicity, this lithium-ion battery capacity data is named AQ-01 in this study. Table 1 presents the summary of its specifications.

The validity of the proposed prediction method is verified by using two groups of battery degradation data of CX2-37 and AQ-01. According to the international standard, the lithium-ion battery performance test stipulates that it shall be kept in a normal working state at a normal temperature (25 ± 2) °C. When the actual capacity of the battery drops below 70–80% of the rated capacity, the lithium-ion battery is considered to be invalid. In order to ensure the safety and reliability of the system operation, the EOL threshold of all the used batteries is both set to about 70% of the rated capacity when the experiments will be terminated. Therefore, the rated capacity of battery CX2-37 is 1.33 Ah, and the EOL threshold configuration is 0.93 Ah. The rated capacity of AQ-01 battery is 2.4 Ah, and the EOL threshold is set to 1.68 Ah. The measured capacity data of CX2-37 and AQ-01 batteries are listed in Figure 5.

3.2 Experimental procedure

In order to better reflect the generalization of the proposed method. Experimental verification of transformer method is made with the selected two groups of the lithium-ion battery

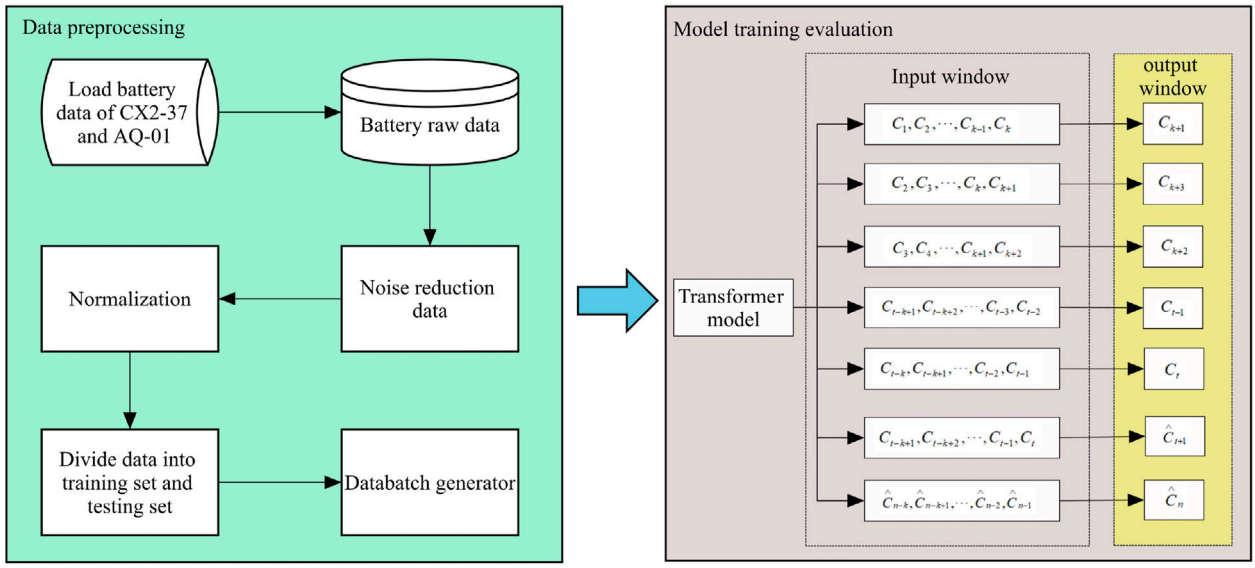

FIGURE 6
RUL prediction method's framework.

capacity data from CALCE and AQNU laboratory. The framework of the RUL prediction method proposed in this study is shown in Figure 6.

More specifically, there are five steps to realize the goal prediction.

Step 1: Select the discharging capacity as the health indicator reflecting the degradation trend of RUL, remove the noise signal of the raw data by wavelet threshold denoising method, and obtain the capacity series with a relatively stable degradation trend.

Step 2: Standardize the capacity data after denoising and smoothing.

Step 3: Divide the first 50% of the battery capacity data equally as the training set and the last 50% as the testing set. Build the transformer model in Pytorch and train the capacity series data to obtain the RUL prediction model.

Step 4: Use the transformer model to establish the mapping relationship between the early and late stages of the capacity, iteratively predicts the unknown discharging capacity of each charging–discharging cycle, then calculate the RUL of the lithium-ion battery.

Step 5: Apply different evaluation indexes to evaluate the prediction results.

3.3 Model evaluation indexes

The lithium-ion battery RUL is defined as the number of remaining useful cycles from the beginning of prediction to the end of battery life. When the actual capacity of the battery degrades to the failure threshold, the battery life is considered to be over. The RUL calculation formula of the battery is as follows:

$$T_{rul} = T_{eol} - T_{cur} \tag{9}$$

The calculation formula of the battery's RUL prediction value can be expressed in Eq. 10.

$$\widehat{T}_{rul} = \widehat{T}_{eol} - \widehat{T}_{cur} \tag{10}$$

Absolute error (AE), mean absolute error (MAE), and root mean square error (RMSE) are adopted as the evaluation criteria of the prediction model. Their calculation formulas are as follows:

$$AE = \left| T_{rul} - \widehat{T}_{rul} \right| \tag{11}$$

$$MAE = \frac{1}{n}\sum_{i=1}^{n}\left| x(i) - \widehat{x}(i) \right| \tag{12}$$

$$RMSE = \sqrt{\frac{1}{n}\sum_{i=1}^{n}\left[x(i) - \widehat{x}(i) \right]^2} \tag{13}$$

where T_{rul} is the number of remaining useful cycles at the end of the actual battery life; T_{cur} represents the cycle's starting position, while T_{eol} is the number of cycles at the end of the battery life in the actual state; $\widehat{T}_{rul}$ indicates the number of remaining useful cycles at the end of the battery life in the predicted case; $\widehat{T}_{eol}$ refers to the number of cycles at the end of the battery life in the predicted case; $x(i)$ is the real value of capacity, and $\widehat{x}(i)$ stands for the predicted capacity.

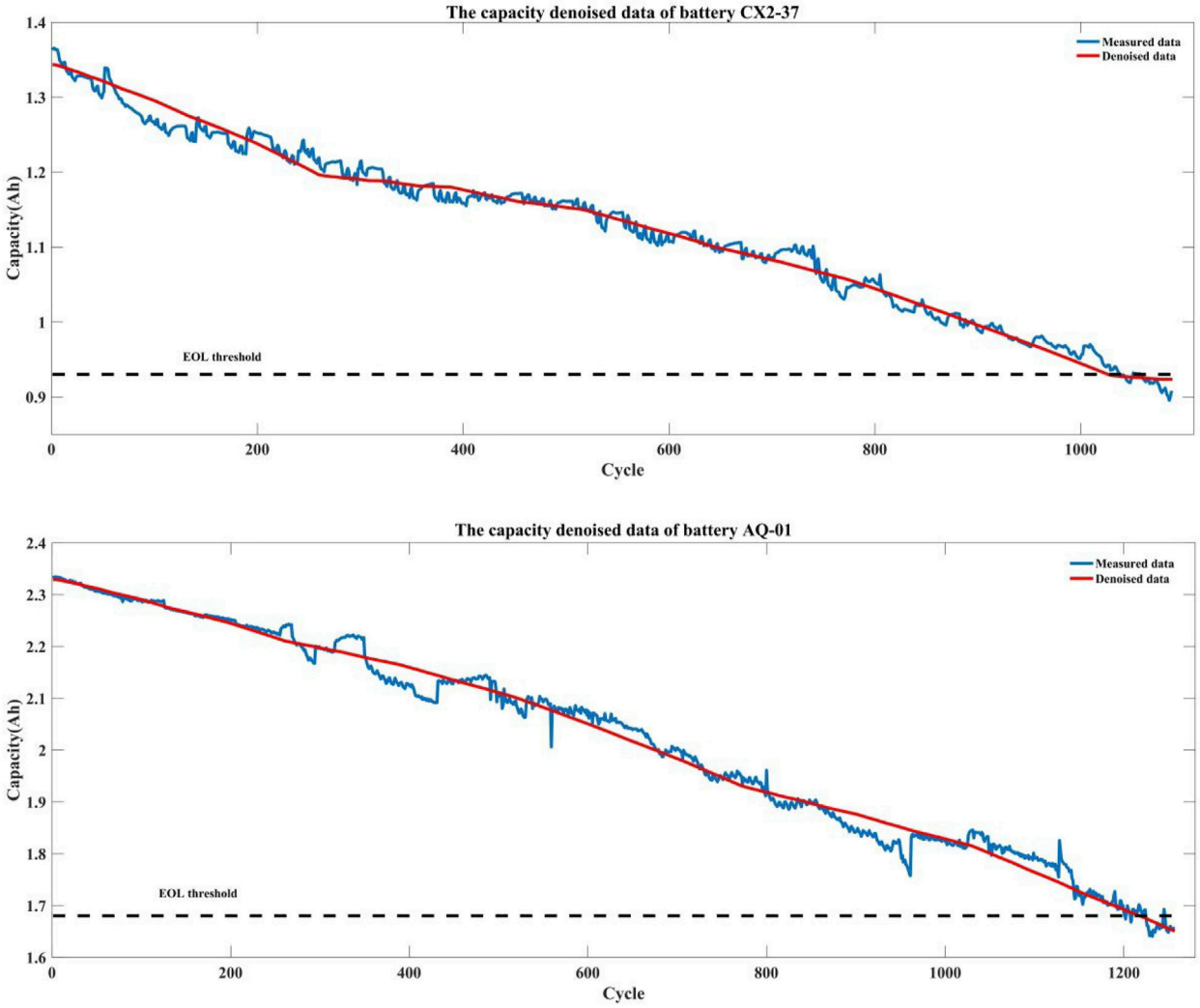

FIGURE 7
Capacity data of CX2-37 and AQ-01 batteries processed by wavelet threshold denoising.

It should be noticed that RMSE is the most comprehensive evaluation index, which can measure the fitness between the prediction curve and the actual degradation trend. The closer RMSE is to 0, the better the prediction effect.

4 Experimental results and discussions

4.1 Denoising results

Due to an irreversible chemical reaction, the discharging capacity of the lithium-ion battery will show a detailed downward trend owing to the repeated charging and discharging. The capacity data measurement process is affected by electromagnetic interference, instrument error, and changes in the external environment. The nonlinear capacity data is mixed with noise signals, and the capacity regeneration phenomenon makes the degradation track rise rapidly, briefly, and irregularly in an uncertain period, which adds difficulty to the training process of the model.

In order to remove the irregular fluctuations in the capacity curve and retain the original characteristics of the data, it helps the model achieve better learning results in the training stage. The raw data of battery capacity of CX2-37 and AQ-01 are smoothed by the wavelet threshold denoising method, and the large and small noise signals are eliminated. The effect of processed battery capacity data is shown in Figure 7.

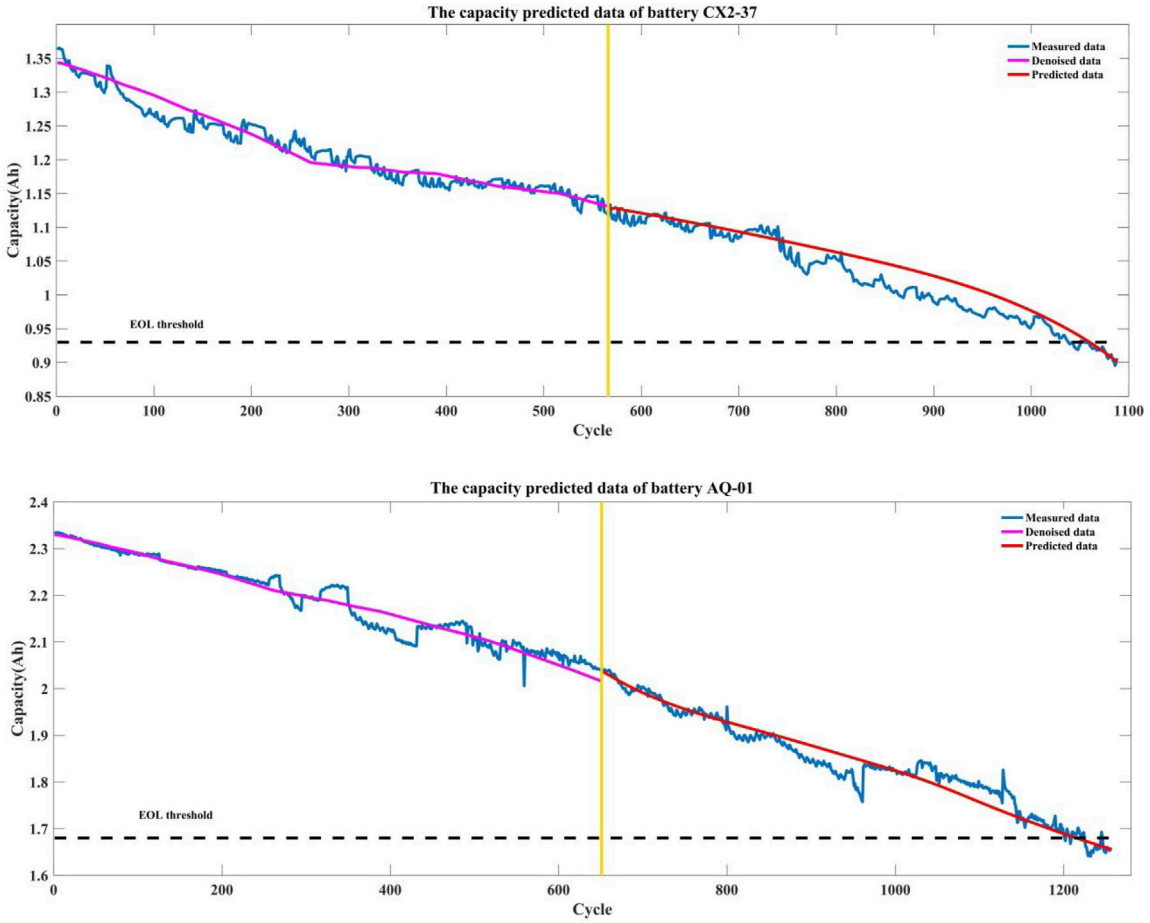

FIGURE 8
Transformer model's capacity prediction results.

TABLE 2 Statistical errors of the transformer algorithm.

Battery	Actual RUL	Predicted RUL	AE	MAE (%)	RMSE (%)
CX2-37	493	494	1	1.81	2.19
AQ-01	556	555	1	1.81	2.39

4.2 Prediction results

AE, MAE, and RMSE methods are individually adopted to evaluate the accuracy of the capacity data predicted by the RUL of lithium-ion batteries. Experiments are carried out through two groups of battery degradation data of CX2-37 and AQ-01. Both groups of capacity data set 50% of the series length as the prediction starting point, and the established transformer neural network model is employed to conduct the capacity prediction experiment. The prediction results are shown in Figure 8 and Table 2 gives the statistical errors of the above experimental results.

The prediction results of both CX2-37 and AQ-01 batteries both illustrate that the degradation trend can be accurately captured according to the mapping relationship between cycle and actual capacity, but the prediction results gradually deviate from the actual degradation curve with the increase of cycle times. From the capacity degradation trend line shown in Figure 8 and the data analysis in Table 2, the RUL prediction accuracy of CX2-37 battery based on the

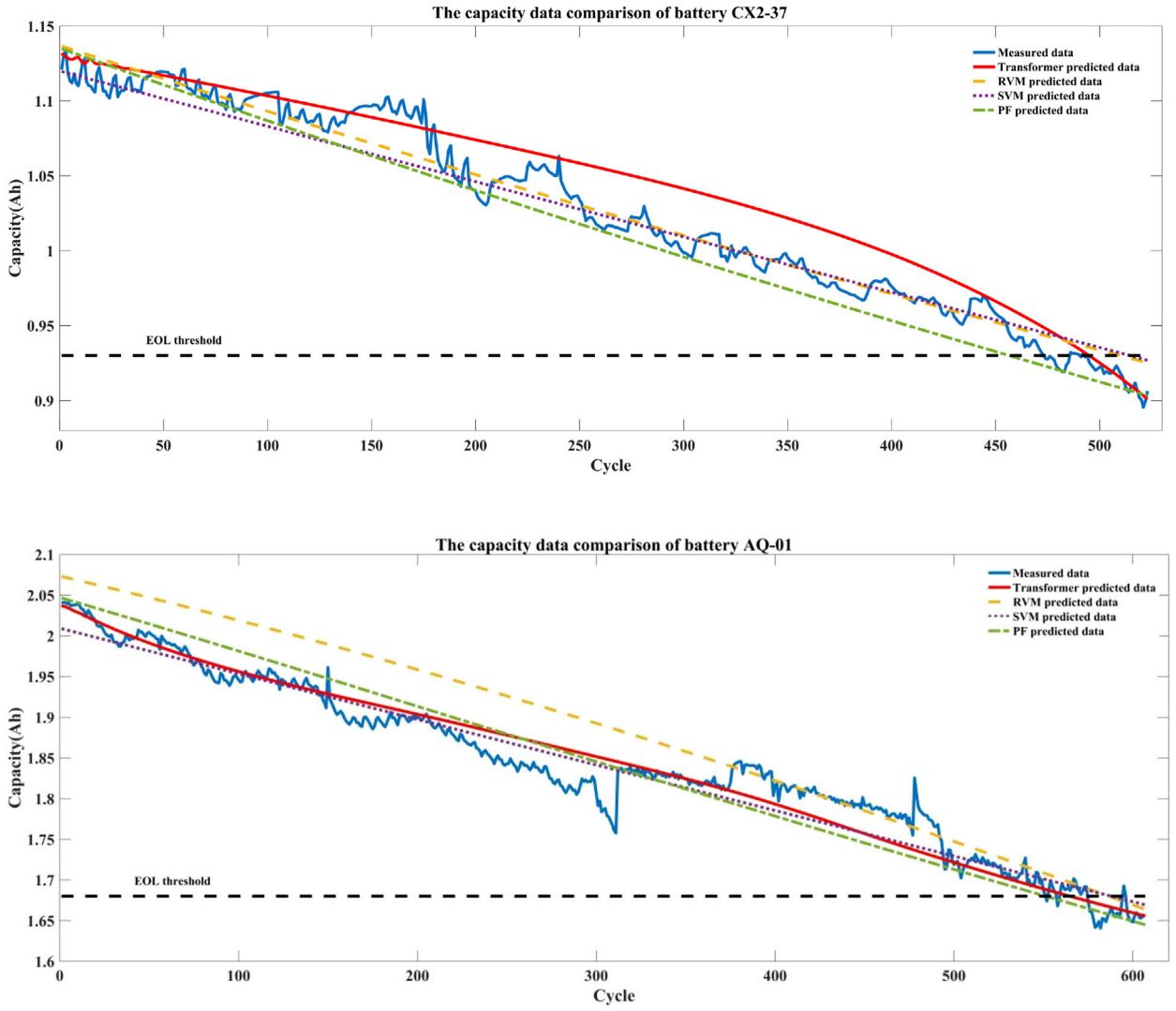

FIGURE 9
Compared experiment results between different prediction methods for CX2-37 and AQ-01 batteries.

transformer model is 494, and 1 cycle later than the true RUL, which MAE is 1.81% and RMSE is 2.19%. The RUL prediction accuracy of AQ-01 battery is 556, and 1 cycle earlier than the true RUL, in which MAE is 1.81% and RMSE is 2.39%. It demonstrates that this method has an accurate RUL prediction effect. It also shows the degradation trend prediction curve of AQ-01 battery is closer to the original curve than that of CX2-37 battery. A possible reason is transformer model mines the correlation from the global relationship and the accuracy highly depends on data, which needs a lot of training to build a better RUL prediction model. It reflects that AQ-01 battery has the best prediction results due to its long sequence length of data and better training effect.

4.3 Compared experiment

To further verify the reliability of the wavelet threshold denoising and transformer model RUL prediction methods proposed in this study, the relevance vector machine (RVM), support vector regression (SVR), and particle filter (PF) methods are separately adopted to compare and analyze with the transformer model prediction method, for proving the transformer model's accuracy and superiority in predicting the RUL. The capacity prediction results of CX2-37 and AQ-01 batteries based on the transformer, RVM, SVR, and PF methods are shown in Figure 9, while Table 3 gives the statistical errors of the above experimental results.

TABLE 3 Statistical errors of the comparison experiment.

Battery	Algorithm	Actual RUL	Predicted RUL	AE	MAE (%)	RMSE (%)
CX2-37	Transformer	493	494	1	1.81	2.19
	RVM	493	506	13	0.92	1.19
	SVM	493	511	18	1.09	1.40
	PF	493	457	36	1.46	1.74
AQ-01	Transformer	556	555	1	1.81	2.39
	RVM	556	578	22	4.33	5.24
	SVM	556	576	20	1.86	2.35
	PF	556	541	15	2.67	3.11

According to the capacity degradation trend line in Figure 9 and the errors in Table 3, this prediction method is proven to offer a better prediction accuracy. The prediction errors of CX2-37 battery based on the transformer, RVM, SVR, and PF methods are 1, 13, 18, and 36, respectively. The prediction errors of AQ-01 battery based on the transformer, RVM, SVR, and PF are 1, 22, 20, and 15, respectively. Among them, the prediction results of CX2-37 battery seriously deviate from the cycle range of the real threshold based on the PF method, but the prediction effect on AQ-01 battery is significantly better than those of the compared methods, as the effects of both MAE and RMSE are less than 2.4%.

By comparing with traditional RVM, SVR, and PF algorithms, it is found that the transformer neural network achieves the best prediction effect owing to the superior long-series data processing ability. According to Figure 9, it can also be seen that the degradation trend prediction curve of AQ-01 battery based on the PF method is close to the original curve, but the CX2-37 battery comparison prediction curve obviously deviates from the original aging curve under the same condition. This is the reason for the low accuracy of feature recognition. The transformer model has the advantage of constructing a global information interaction mechanism, which helps to establish a more sufficient feature display. At the same time, the modal data can be fused efficiently. Therefore, a better fitting trend is reflected in the two groups of experimental data and reflects that the transformer prediction method has a better generalization ability. However, the global attention mechanism also brings a large amount of computation, especially in intensive prediction tasks with facing long series of inputs. In addition, the training process of the transformer model is unstable and sensitive to parameters. Therefore, the wavelet threshold denoising method is used to smooth the original data, so as to better predict the future capacity of lithium-ion batteries and improve the prediction accuracy.

5 Conclusion

In this study, an RUL prediction method for lithium-ion batteries based on wavelet threshold denoising and transformer model has been proposed. First, the discharging capacity has been selected as the health indicator, and the wavelet threshold denoising method has been adopted to eliminate the noise signal caused by the actual measurement and instrument errors in the raw data. Second, the pre-processed data have been equally divided into the training set and testing set. Based on the training set, the transformer neural network has been used to establish the RUL prediction model of the lithium-ion battery. Moreover, two groups of experimental data from CALCE and AQNU laboratories have been chosen to verify the reliability of the proposed method. The conclusions are summarized as follows:

The onboard battery is affected by various uncertain factors during the working process, which causes the gathered data to contain noises and fluctuations. Directly using the raw data to predict the signal affects the prediction accuracy of this model. Consequently, the necessary data preprocessing method has been utilized to improve the prediction accuracy of this prediction model in this study.

Owing to the long-distance modeling ability and the feature representation ability of the series data in the transformer model, an RUL prediction framework based on the transformer neural network has been established, while a new RUL prediction method for lithium-ion batteries has been proposed and good prediction results have been achieved.

Two groups of battery capacity data from CALCE and AQNU laboratories have been employed to verify the RUL prediction method. The experimental results have shown that the prediction effect of the proposed method is superior to those of some existing calculation ones, among which the effects of MAE and RMSE are kept within 1.81 and 2.39%, respectively.

To conclude, the RUL prediction method for lithium-ion batteries consists of the data preprocessing by wavelet threshold denoising and the transformer model with a high prediction accuracy, reducing the prediction error and providing a new idea for the existing RUL prediction research of lithium-ion batteries. This method could also be applied to the prediction of other similar issues.

Data availability statement

The datasets presented in this study can be found in online repositories. The names of the repository/repositories and accession number(s) can be found in the article/supplementary material.

Author contributions

WH: methodology, software, validation, investigation, writing—original draft preparation, visualization. SZ: methodology, data curation, validation, writing—reviewing, and editing.

Funding

This study was supported by The Natural Science Research Key Project of Education Department of Anhui Province Grant No. KJ2020A0509, Anhui Provincial Natural Science Foundation Grant No. 2008085MF197, Graduate Academic Innovation Project of Anqing Normal University Grant No. 2021yjsXSCX009.

Conflict of interest

The authors declare that the research was conducted in the absence of any commercial or financial relationships that could be construed as a potential conflict of interest.

Publisher's note

All claims expressed in this article are solely those of the authors and do not necessarily represent those of their affiliated organizations, or those of the publisher, the editors, and the reviewers. Any product that may be evaluated in this article, or claim that may be made by its manufacturer, is not guaranteed or endorsed by the publisher.

References

Ahwiadi, M., and Wang, W. (2019). An enhanced mutated particle filter technique for system state estimation and battery life prediction. *IEEE Trans. Instrum. Meas.* 68 (3), 923–935. doi:10.1109/TIM.2018.2853900

Ansari, S., Ayob, A., Hossain, L., Hussain, A., and Saad, M. H. M. (2021). Multi-channel profile based artificial neural network approach for remaining useful life prediction of electric vehicle lithium-ion batteries. *Energies* 14 (22), 7521. doi:10.3390/EN14227521

Ansari, S., Ayob, A., Hossain, L., Hussain, A., and Saad, M. H. M. (2022). Multi-channel profile based artificial neural network approach for remaining useful life prediction of electric vehicle lithium-ion batteries. *Energies* 14 (22), 7521. doi:10.3390/EN14227521

Cadini, F., Sbarufatti, C., Cancelliere, F., and Giglio, M. (2019). State-of-life prognosis and diagnosis of lithium-ion batteries by data-driven particle filters. *Appl. Energy* 235, 661–672. doi:10.1016/j.apenergy.2018.10.095

Chen, Z., Shi, N., Ji, Y., Niu, M., and Wang, Y. (2021). Lithium-ion batteries remaining useful life prediction based on BLS-RVM. *Energy* 234, 121269. doi:10.1016/J.ENERGY.2021.121269

Dong, G., Yang, F., Wei, Z., Wei, J., and Tsui, K.-L. (2020). Data-driven battery health prognosis using adaptive brownian motion model. *IEEE Trans. Ind. Inf.* 16 (7), 4736–4746. doi:10.1109/TII.2019.2948018

Guha, A., and Patra, A. (2018). Online estimation of the electrochemical impedance spectrum and remaining useful life of lithium-ion batteries. *IEEE Trans. Instrum. Meas.* 67 (8), 1836–1849. doi:10.1109/TIM.2018.2809138

Guha, A., and Patra, A. (2018). State of health estimation of lithium-ion batteries using capacity fade and internal resistance growth models. *IEEE Trans. Transp. Electrific.* 4 (1), 135–146. doi:10.1109/TTE.2017.2776558

Huang, K., Ding, H., and Guo, Y. (2022). Prediction of remaining useful life of lithium-ion battery based on adaptive data preprocessing and long short-term memory networkr. *Trans. China Electrotech. Soc.* 37 (7), 57–70. doi:10.19595/j.cnki.1000-6753.tces.210860

Jiao, R., Peng, K., and Dong, J. (2020). Remaining useful life prediction of lithium-ion batteries based on conditional variational autoencoders-particle filter. *IEEE Trans. Instrum. Meas.* 99, 8831–8843. doi:10.1109/tim.2020.2996004

Jin, Y., Hou, L., and Chen, Y. (2022). A time series transformer based method for the rotating machinery fault diagnosis. *Neurocomputing* 494, 379–395. doi:10.1016/J.NEUCOM.2022.04.111

Li, X., Wang, Z., and Yan, J. (2019). Prognostic health condition for lithium battery using the partial incremental capacity and Gaussian process regression. *J. Power Sources* 421, 56–67. doi:10.1016/j.jpowsour.2019.03.008

Liu, H., Chen, F., Tong, Y., Wang, Z., Yu, X., Huang, R., et al. (2020). Impacts of driving conditions on EV battery pack life cycle. *World Electr. Veh. J.* 11, 17. doi:10.3390/wevj11010017

Liu, R., and Zhang, C. (2021). An active balancing method based on SOC and capacitance for lithium-ion batteries in electric vehicles. *Front. Energy Res.* 9, 773838. doi:10.3389/fenrg.2021.773838

Morstyn, T., Savkin, A. V., Hredzak, B., and Agelidis, V. G. (2017). Multi-agent sliding mode control for state of charge balancing between battery energy storage systems distributed in a DC microgrid. *IEEE Trans. Smart Grid* 9 (5), 4735–4743. doi:10.1109/TSG.2017.2668767

Murugan, M., Saravanan, A., Elumalai, P. V., Murali, G., Dhineshbabu, N., Kumar, P., et al. (2022). Thermal management system of lithium-ion battery packs for electric vehicles: An insight based on bibliometric study. *J. Energy Storage* 52, 104723. doi:10.1016/j.est.2022.104723

Pugalenthi, K., and Raghavan, N. (2018). A holistic comparison of the different resampling algorithms for particle filter based prognosis using lithium-ion batteries as a case study. *Microelectron. Reliab.* 91, 160–169. doi:10.1016/j.microrel.2018.08.007

Song, T., Liu, C., Wu, R., Jin, Y., and Jiang, D. (2022). A hierarchical scheme for remaining useful life prediction with long short-term memory networks. *Neurocomputing* 487, 22–33. doi:10.1016/j.neucom.2022.02.032

Tian, Y., Wang, Y., Wang, J., Wang, X., and Wang, F. (2022). Key problems and progress of vision transformers: The state of the art and prospects. *Acta Autom. Sin.* 48 (4), 957–979. doi:10.16383/j.aas.c220027

Vallés-Pérez, I., Soria-Olivas, E., Martínez-Sober, M., Serrano-Lopez, A. J., Gomez-Sanchis, J., and Mateo, F. (2022). Approaching sales forecasting using recurrent neural networks and transformers. *Expert Syst. Appl.* 201, 116993. doi:10.1016/J.ESWA.2022.116993

Wang, S., Jin, S., Deng, D., and Fernandez, C. (2021). A critical review of online battery remaining useful lifetime prediction methods. *Front. Mech. Eng.* 7 (1), 1–19. doi:10.3389/fmech.2021.719718

Xiong, R., He, H., Sun, F., and Zhao, K. (2012). Evaluation on state of charge estimation of batteries with adaptive extended kalman filter by experiment approach. *IEEE Trans. Veh. Technol.* 62 (1), 108–117. doi:10.1109/TVT.2012.2222684

Xiong, R., Li, L., Li, Z., Yu, Q., and Mu, H. (2018). An electrochemical model based degradation state identification method of lithium-ion battery for all-climate electric vehicles application. *Appl. Energy* 219, 264–275. doi:10.1016/j.apenergy.2018.03.053

Xue, Z., Zhang, Y., Cheng, C., and Ma, G. (2020). Remaining useful life prediction of lithium-ion batteries with adaptive unscented kalman filter and optimized support vector regression. *Neurocomputing* 376, 95–102. doi:10.1016/j.neucom.2019.09.074

Yuan, X., Liu, X., and Zuo, J. (2015). The development of new energy vehicles for a sustainable future: A review. *Renew. Sustain. Energy Rev.* 42, 298–305. doi:10.1016/j.rser.2014.10.016

Zhang, C., He, Y., Yuan, L., and Xiang, S. (2017). Capacity prognostics of lithium-ion batteries using EMD denoising and multiple kernel RVM. *IEEE Access* 5, 12061–12070. doi:10.1109/access.2017.2716353

Zhang, C., He, Y., Yuan, L., Xiang, S., and Wang, J. (2015). Prognostics of lithium-ion batteries based on wavelet denoising and DE-RVM. *Comput. Intell. Neurosci.* 14, 1–8. doi:10.1155/2015/918305

Zhang, C., Zhao, S., and He, Y. (2021). An integrated method of the future capacity and RUL prediction for lithium-ion battery pack. *IEEE Trans. Veh. Technol.* 71 (3), 2601–2613. doi:10.1109/TVT.2021.3138959

Zhang, D., Tan, C., Ou, T., Zhang, S., Li, L., and Ji, X. (2022a). Constructing advanced electrode materials for low-temperature lithium-ion batteries: A review. *Energy Rep.* 8, 4525–4534. doi:10.1016/J.EGYR.2022.03.130

Zhang, L., Mu, Z., and Sun, C. (2018). Remaining useful life prediction for lithium-ion batteries based on exponential model and particle filter. *IEEE Access* 6, 17729–17740. doi:10.1109/ACCESS.2018.2816684

Zhang, Q., Qin, C., Zhang, Y., Bao, F., and Liu, P. (2022b). Transformer-based attention network for stock movement prediction. *Expert Syst. Appl.* 202, 117239. doi:10.1016/J.ESWA.2022.117239

Zhao, S., Zhang, C., and Wang, Y. (2022). Lithium-ion battery capacity and remaining useful life prediction using board learning system and long short-term memory neural network. *J. Energy Storage* 52, 104901. doi:10.1016/j.est.2022.104901

frontiers | Frontiers in Energy Research

TYPE Original Research
PUBLISHED 16 August 2022
DOI 10.3389/fenrg.2022.961488

OPEN ACCESS

EDITED BY
Xiao Wang,
Wuhan University, China

REVIEWED BY
Yue Wu,
Southwest Jiaotong University, China
Wang Lina,
China Jiliang University, China
Nannan Rong,
Tianjin Polytechnic University, China

*CORRESPONDENCE
Qihe Shan,
shanqihe@163.com
Jun Zhu,
zhu_j@aliyun.com

SPECIALTY SECTION
This article was submitted to Smart Grids, a section of the journal Frontiers in Energy Research

RECEIVED 04 June 2022
ACCEPTED 28 June 2022
PUBLISHED 16 August 2022

CITATION
Wang F, Shan Q, Zhu J and Xiao G (2022), Discrete-time resilient-distributed secondary control strategy against unbounded attacks in polymorphic microgrid.
Front. Energy Res. 10:961488.
doi: 10.3389/fenrg.2022.961488

Discrete-time resilient-distributed secondary control strategy against unbounded attacks in polymorphic microgrid

Fuzhi Wang[1], Qihe Shan[1]*, Jun Zhu[2]* and Geyang Xiao[2]

[1]Navigation College, Dalian Maritime University, Dalian, China, [2]Research Institute of Intelligent Networks, Zhejiang Lab, Hangzhou, China

This study proposes a polymorphic cooperative control system for microgrid consisting of a service layer, a control layer, a data layer, and a power layer to apply a resilient-distributed secondary control strategy to distributed generators (DGs) from different manufacturers more conveniently. Due to the improvement of network openness, external cyberattacks are more likely to tamper with the neighbor information transmitted in the cooperative control system. In this study, a discrete-time resilient-distributed secondary control strategy is designed to resist potential unbounded false data injection (FDI) attacks, which introduces a virtual network layer interconnecting the control network layer to form a layered network. The strategy can maintain the stability of voltage and frequency under unbounded attacks and then greatly suppress the state estimation difference of voltage and frequency. Meanwhile, the unbounded attack depending on voltage and frequency estimation difference is suppressed to a nearly bounded attack. Finally, a microgrid consisting of six inverter-based DGs is taken as an example to validate the effectiveness of the strategy against unbounded attacks.

KEYWORDS

unbounded attack sequence, discrete-time, polymorphic network, virtual layer, resilient distributed secondary control strategy

1 Introduction

With the rapid development of power electronic devices and new energy technology, the power system has gradually transitioned to the stage of a new electric power system characterized by a high proportion of new energy and power electronic devices (Zhou et al., 2020; Tang et al., 2022). As an important part of the new electric power system, microgrid integrates geographically dispersed, intermittent and random new energy, and internal energy storage devices can adjust the flow of electric energy flexibly (Zhou J. et al., 2021; Wang et al., 2021). With the increase of the proportion of new energy, a large number of power electronic devices, such as rectifiers and inverters, have

appeared in the microgrid to replace original generators with the rotor to generate power. Since power electronic devices cannot provide the inertia from generators with rotors, the frequency of microgrids is more susceptible to be disturbed. For microgrids with a high proportion of new energy and power electronic devices, distributed secondary control (Bidram et al., 2014) has attracted wide attention as an effective strategy to maintain voltage and frequency stability.

The distributed secondary control strategy relies on advanced communication facilities and network structure to exchange neighbor information. The development of the communication network structure of microgrid mainly includes three stages, i.e., IP-based network, software-defined network (SDN) (Nunes et al., 2014; Kreutz et al., 2015), and a polymorphic network with full-dimensional definition (Hu et al., 2020, 2022; Zhang et al., 2022). The IP-based network combines the function of the control layer and the data layer in the forwarding devices, which makes it difficult for researchers to test advanced control methods and hinders the innovation of network structure. SDN separates the function of the control layer and data layer. Network devices in the data layer only remain the function of forwarding data, and the function of calculating routes is centralized in the control layer. Due to the function separation, the control layer of SDN provides more programmable ports for microgrid managers to design and implement advanced control methods. In order to make the network requirements of various DGs produced by different manufacturers in microgrids can be realized on the same communication facilities in the data layer, a polymorphic network has been established which supports various network technology. A polymorphic network is integrated into a service layer, a control layer, and a data layer, where the control layer and the data layer still maintain the separated functions. A polymorphic network is an advanced network structure that can support a resilient distributed secondary control strategy applied in the microgrid. Neighbor information of various DGs can be exchanged on the same communication facilities, which benefits improving consensus performance of cooperative control among the DGs, and even microgrids.

The more advanced the network structure, the more open it will be. Both communication links and terminals are possibly subject to potential cyberattacks (Gao et al., 2022). Common attacks in the microgrid include denial of service (DoS) and FDI attacks. DoS attacks send a large number of packets to block the communication network to prevent information exchange between the neighbor DGs. Technologies such as firewalls (Salah et al., 2012) and gates (Condry and Nelson, 2016) can effectively defend against the threat of DoS attacks launched in the communication network of the microgrid. FDI attacks are characterized by tampering with the exchanged information between the neighbor DGs. The DG receives the tampered neighbor information but does not know it, and then transmits the tampered information to other neighboring DGs. In fact, it is difficult for us to defend FDI attacks by methods against DoS attacks because of their strong stealth. Therefore, how to design a proper distributed secondary control strategy against FDI attacks has been a noteworthy topic for researchers. At present, the solution to FDI attacks in the distributed secondary strategy mainly includes two scheme types. The first scheme is to design detection algorithms to isolate the attacked communication channels. The second scheme is to design resilient distributed secondary control strategies to mitigate the impact of FDI attacks in the microgrid. In such resilient strategies, FDI attacks exist together with the microgrid, and resilient distributed control strategies aim to minimize or even eliminate the impact of FDI attacks on consensus performance as much as possible. Liu et al. defined FDI attacks in state estimation of centralized power systems (Liu et al., 2009, 2011). After this, many algorithms emerged to detect FDI attacks in the microgrid. The work in Manandhar et al. (2014) shows that although the χ^2 detector can detect faults and DoS attacks, it cannot detect well-designed FDI attacks. In order to overcome this limitation, a Euclidean detector that can effectively detect FDI attacks is proposed. Yang et al. (2022) proposed a method for detecting bad data in power transformers based on artificial intelligence. Fawzi et al. (2014) studied the estimation problem of linear systems when some sensors or actuators are destroyed by attackers, and especially pointed out that if more than half of the sensors are attacked, it is impossible to accurately reconstruct the state of the system. Wang et al. (2020) proposed a local detection and isolation algorithm which can solve the problem of undetectable attacks through the combination of observable PMU or smart sensors. Chen et al. (2021) proposed an aperiodic intermittent control strategy with random switching frequency to detect and isolate the attacked communication channels. Hu et al. (2018) and Pang et al. (2022) studied the impact of stealthy FDI attacks on the communication channels and points out that if some key communication channels are well protected, the attack behaviors will be detected.

Such detection algorithms can effectively detect FDI attacks launched in the communication channels. When the DG exchanges information with its neighbors, detection algorithms will reduce the range of the attacked DGs through time iteration, and finally determine which DG has been attacked. The process is called computation response time that often requires the microgrid system to allocate resources to complete. Therefore, isolation measures will be delayed accordingly. The impact which FDI attacks can cause is serious during the detection time between attacks launched and eliminated. Researchers have become more interested in developing resilient distributed secondary control strategies against FDI attacks to address this problem. Zeng and Chow (2014) proposed a trust-based resilient distributed secondary control strategy, which embeds a recovery mechanism in the distributed control process and enhances the resilience against FDI attacks.

Abhinav et al. (2018) designed a trust-based resilient distributed secondary control strategy against FDI attacks launched in sensors, actuators, and communication channels. Under the condition that at least half of the neighbors of each DG are secure, this strategy can defend against time-independent constant FDI attacks. Gharesifard and Başar (2012) introduced a virtual network interconnecting with the original control network to make the overall dynamic network resilient against FDI attacks with linear dynamics by designing appropriate interconnection matrices. Gusrialdi et al. (2014) extended the work of Gharesifard and Başar (2012) to the case of strongly connected directed graphs. Abhinav et al. (2018) studied the case of directed graphs and attacks with nonlinear dynamics based on the work of Gharesifard and Başar (2012) and Gusrialdi et al. (2014).

Researchers introduced the layered network theory proposed by some studies (Gharesifard and Başar, 2012; Gusrialdi et al., 2014; Abhinav et al., 2018) to the FDI attack problem of networked microgrids, and Zhou Q. et al. (2021) and Chen et al. (2021) introduced the layered network theory into distributed secondary control strategy to deal with FDI attacks launched in the communication network. Liu et al. (2022) proposed a resilient distributed optimal frequency control scheme to deal with the impact of FDI attacks by introducing the layered network theory. Zuo et al. (2020) proposed a novel concept of the cooperative and adversarial multigroup system consisting of leaders, followers, and adversaries. Zuo and Yue (2022) designed a resilient containment control method against the unbounded FDI attacks occurring in the communication network of the multigroup system proposed by Zuo et al. (2020), and it is worth mentioning that the unbounded FDI attack in this study is modeled as a proportional function of time. Unbounded attacks modeled in this way are very destructive but can be easily perceived by detectors. A more realistic attack design method is to generate a destructive and stealthy attack sequence based on the matrix parameters of the microgrid (Hu et al., 2018). The attack sequence can make the state estimation difference of the microgrid go to ∞ without being perceived by the χ^2 detector. As mentioned previously, detection and isolation measures can cause a high computational burden for the microgrid. During the calculation process of detection and isolation measures, external FDI attacks will still cause irreparable impacts on the microgrid. Therefore, how to resist this kind of destructive and stealthy unbounded attack sequence has been a novel problem.

In this study, a discrete-time resilient distributed secondary control strategy is designed to resist the impact of unbounded attack sequences on the microgrid. The main contributions of this study are as follows.

1) A polymorphic cooperative control system for microgrids consisting of a service layer, a control layer, a data layer, and a power layer is established in this study, which can apply the resilient distributed secondary control strategy to DGs from different manufacturers.
2) Considering potential unbounded FDI attacks in the polymorphic cooperative control system, a discrete-time resilient distributed secondary control strategy is designed to maintain voltage and frequency stable against unbounded attacks.
3) The state estimation difference of voltage and frequency are suppressed by a large margin. Sufficient time is provided for the deployment of detection and isolation measures before the service layer of the polymorphic cooperative control system makes wrong decisions. Meanwhile, the unbounded attack depending on voltage and frequency estimation difference is suppressed to a nearly bounded attack, which is less threat to the microgrid.

The rest of this study is organized as follows. **Section 2** introduces the microgrid polymorphic cooperative control system and the function of each layer. **Section 3** describes the influence of unbounded FDI attack on the microgrid, then designs a resilient distributed secondary control strategy against attacks, and finally uses Lyapunov theory to prove the stability of the strategy. **Section 4** validates the effectiveness of the proposed strategy by a test microgrid with six inverter-based DGs. Finally, **Section 5** presents the summary of this study.

2 Structure of the polymorphic cooperative control system

A polymorphic network is an advanced network structure supporting the microgrid operation, which can change control strategy in real-time according to the operation characteristics of the microgrid. Moreover, various DGs produced by different manufacturers can transmit information in the data layer of the polymorphic network. The polymorphic cooperative control system established in this study is shown in **Figure 1**. The polymorphic cooperative control system consists of four layers: a service layer, a control layer, a data layer, and a power layer. The service layer, control layer, and data layer constitute the polymorphic network to support the cooperative control of DGs in the power layer. The service layer is the center of the polymorphic cooperative control system, which integrates data monitoring, resource allocation, control strategy design, and other functions; and is open to microgrid managers. Managers can design and deploy distributed secondary control strategies by obtaining matrix parameters of microgrids through the service layer. In the control layer, a polymorphic identification table is configured in the distributed controller, which supports the coexistence and collaboration of IP, content, identification, geospatial location, and other identities in the same data layer. In addition, the distributed secondary control strategy deployed through the service layer is also installed in the distributed

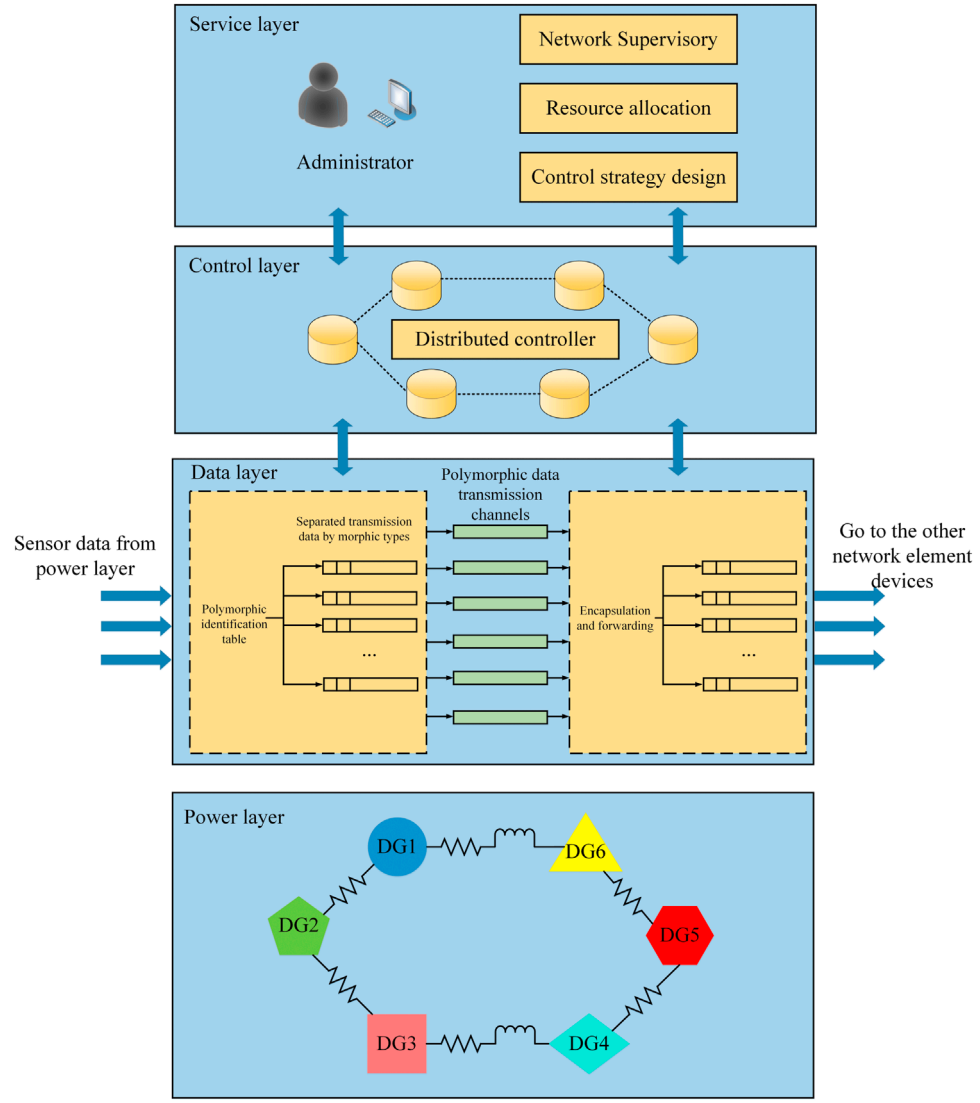

FIGURE 1
Microgrid polymorphic cooperative control system.

controller. According to the polymorphic identification table configured in the control layer, the data layer divides the polymorphic data packets uploaded through terminals in the power layer into corresponding polymorphic data transmission channels. These polymorphic packets are encapsulated and forwarded to the next network device to realize the resilient distributed secondary control strategy installed in the distributed controller. The interaction between the layers is realized through programmable ports. The upper layer transmits instructions to the lower layer, and the lower layer feeds back the collected information to the upper layer.

The service layer, control layer, and data layer of the microgrid polymorphic cooperative control system achieve the information transmission through programmable ports and separate the control function from the forwarding function. In fact, DGs in the microgrid are not provided by the same manufacturer and often support different network protocols and data package types. If a new control strategy is applied in the microgrid, managers need to manually adjust the configuration of DGs, which is undoubtedly not beneficial to the innovation of the control strategy. However, the polymorphic identification table configured in the control layer and the polymorphic data transmission channels in the data layer can make these various DGs plug and play in the same network environment. The control layer customizes the channels into processing units suitable for polymorphic data packets by programming FPGA. In this

way, the microgrid polymorphic cooperative control system can define the functions of each network layer to support the realization of distributed secondary control strategy applied in the large-scale heterogeneous DGs.

3 Resilient-distributed secondary control strategy against the unbounded FDI attack sequence

3.1 Graph preliminaries

The communication topology of microgrid discussed in this study is described as a directed graph ς including $N+m$ agents. $A_a = [a_{ij}] \in R^{N\times N}$ is the weighted adjacency matrix of ς, and a_{ij} denotes the weight value of the edge between the follower nodes, $a_{ij} > 0$ represents *DGi* that can receive information from *DGj*, otherwise $a_{ij} = 0$. $D = \mathrm{diag}(d_i) \in R^{N\times N}$ is the in-degree matrix for ς, where $d_i = \sum_{j=1}^{n} a_{ij}$. $L = D - A_a$ means the Laplace matrix of ς. Define $G_l = \mathrm{diag}(g_{li}) \in R^{nxn}, l = (1,2,\ldots,m)$, where g_{li} denotes the gain between the *l*th leader and *i*th follower. And a nomenclature containing sets, parameters, and abbreviations is shown in **Table 1**.

3.2 Problem formulation

The inherent distributed characteristics of DGs in microgrid make distributed control a more suitable secondary control strategy to adjust voltage and frequency. Microgrid managers can design proper distributed secondary control strategy to maintain voltage and frequency stable around the rated value. Only part of DGs can receive the reference information, and then complete the task in a cooperative manner through the communication network. For first-order linear multi agent systems (MASs), the distributed secondary control of microgrid with N DGs can be transformed into a synchronization problem. The local expression for the distributed secondary control strategy used to control voltage and frequency is

$$\frac{x_i(k+1)-x_i(k)}{T} = \sum_{j=1}^{n} a_{ij}\left(x_j(k)-x_i(k)\right) + \sum_{l=1}^{m} g_{li}\left(x_l(k)-x_i(k)\right), \quad (1)$$

where T is the sampling time of microgrid. $x_i(k) = \begin{bmatrix} V_i(k) \\ f_i(k) \end{bmatrix}$, $V_i(k)$ denotes the voltage of *DGi*, $f_i(k)$ denotes the frequency of *DGj*. $x_j(k) = \begin{bmatrix} V_j(k) \\ f_j(k) \end{bmatrix}$, $V_j(k)$ denotes the voltage of *DGj*, $f_j(k)$ denotes the frequency of *DGj*. $x_l(k) = \begin{bmatrix} V_l(k) \\ f_l(k) \end{bmatrix}$, $V_l(k)$ denotes the reference voltage of *DGs*, $f_l(k)$ denotes the reference frequency of *DGs*, $l = 1,2,\ldots,m$ denotes the number of leaders. Obviously, the influence caused by FDI attacks has not been considered in the distributed secondary control strategy. The neighbor information *DGi* received from *DGj* is $x_i^a(k) = x_j(k) + \Theta_{i,j}(k)$ when adversaries launched FDI attacks in the communication channels between *DGi* and *DGj*. $x_i^a(k)$ represents the neighbor information *DGi* received from *DGj* has been tampered by $\Theta_{i,j}(k)$. The local expression for the distributed secondary control strategy when the communication channels have been launched FDI attacks is

$$\frac{x_i(k+1)-x_i(k)}{T} = \sum_{j=1}^{n} a_{ij}\left(x_j(k)+\Theta_{i,j}(k)-x_i(k)\right) + \sum_{l=1}^{m} g_{li}\left(x_l(k)-x_i(k)\right). \quad (2)$$

Also, then the global form of **Eqn. 2** can be obtained as

$$\frac{x(k+1)-x(k)}{T} = \sum_{l=1}^{m}\left(G_l\otimes I_e\right)x_l^{'} - \left(\left(L\otimes I_e\right)x(k) + \sum_{l=1}^{m}\left(G_l\otimes I_e\right)x(k)\right) + \Theta(k), \quad (3)$$

where $x(k) = [x_1^T(k), x_2^T(k), \ldots, x_n^T(k)]^T$ denotes all the *DGs'* voltage and frequency state variable. Define $x_l^{'} = 1_n \otimes x_l$, and $\Theta(k) = [\Theta_1^T(k), \Theta_2^T(k), \ldots, \Theta_n^T(k)]^T$ denotes the global form of unbounded attack sequence. Define $\beta_l = 10L + G_l$, and $(L\otimes I_e)(1_n \otimes x_l) = 0$. **Eqn. 3** can be rewritten as

$$\frac{x(k+1)-x(k)}{T} = \sum_{l=1}^{m}\left(\beta_l\otimes I_e\right)x_l^{'} - \sum_{l=1}^{m}\left(\beta_l\otimes I_e\right)x(k) + \Theta(k). \quad (4)$$

TABLE 1 Nomenclature table.

Symbol	Description
Index and sets	
i,j	Index of DGs
$(\cdot)^T$	Transpose of the matrix
$\|\cdot\|$	Euclidean norm of the vector
$diag(\cdot)$	Diagonal matrix
Parameters	
N	Number of DGs
m	Number of leader DGs
a_{ij}	Gains between DGs
g_{li}	Gains between leader DGs and follower DGs
I_n	n dimensional identity matrix
$I_{N\times n}$	$N\times n$ dimensional identity matrix
I_e	Identity matrix of uncertain dimensions that aligns the dimensions of the equality matrix
$\Theta(k)$	Unbounded attack sequence
Σ_s	Control layer
Σ_h	Virtual layer
Abbreviations	
FDI	False data injection
DGs	Distributed generators
DoS	Denial of service
SDN	Software-defined network

When there exists no attacks in the communication channels, the voltage and frequency state variable $x(k)$ and measurement output $y(k)$ are shown as

$$\begin{cases} x(k+1) = \left(I_{N\times n} - T\sum_{l=1}^{m}(\beta_l \otimes I_e)\right)x(k) + T\sum_{l=1}^{m}(\beta_l \otimes I_e)x_l', \\ y(k) = Cx(k) \end{cases} \tag{5}$$

The following state estimator is proposed for voltage and frequency state variable $x(k)$:

$$\begin{cases} \hat{x}(k+1) = \left(I_{N\times n} - T\sum_{l=1}^{m}(\beta_l \otimes I_e)\right)\hat{x}(k) + T\sum_{l=1}^{m}(\beta_l \otimes I_e)x_l' + Kz(k+1), \\ z(k) = y(k+1) - CA\hat{x}(k) \end{cases} \tag{6}$$

where $A = I_{N\times n} - T\sum_{j=1}^{n}(\beta_l \otimes I_e)$ and C is the measurement matrix, and $\hat{x}(k+1) = \left[\hat{V}_1^T(k+1), \hat{f}_1^T(k+1), \ldots, \hat{V}_1^T(k+1), \hat{f}_1^T(k+1)\right]^T$ denotes the state estimation value at time $k+1$. $z(k)$ denotes the estimation residual difference at time k, which is related to whether FDI attacks can be detected. If $z(k)$ is less than a constant value, the detector will not perceive the attacks. K denotes Kalman gain, although the standard Kalman filter is time-varying, the Kalman filter can rapidly enter steady state at exponential speed from any initial conditions (Huang et al., 2020). K can be obtained from **Eqs. 7**, **8**

$$P = APA^T + Q - APC^T\left(CPC^T + R\right)^{-1}CPA, \tag{7}$$

$$K = PC^T\left(CPC^T + R\right)^{-1}, \tag{8}$$

where Q and R commonly denote the covariance of the noise in Kalman filter, and they can also be used as parameters for strategy design in noiseless environment. The application of state estimation in noiseless environment is discussed in Rapp and Nyman (2004) and Dutta et al. (2019). In principle, they can be selected as any positive definite matrices. Combine with **Eqn. 4**, when attacks have been launched in the communication channels, the voltage and frequency state variable $x(k)$ and measurement output $y(k)$ are shown as

$$\begin{cases} x^a(k+1) = \left(I_{N\times n} - T\sum_{l=1}^{m}(\beta_l \otimes I_e)\right)x^a(k) + T\left(\sum_{l=1}^{m}(\beta_l \otimes I_e)x_l' + \Theta(k)\right), \\ y^a(k) = Cx^a(k) \end{cases} \tag{9}$$

where $x^a(k+1)$ denotes the voltage and frequency state variable under attacks, and $y^a(k)$ denotes the measurement output under attacks. Accordingly, the state estimator for voltage and frequency under attacks can be shown as

$$\begin{cases} \hat{x}^a(k+1) = \left(I_{N\times n} - T\sum_{l=1}^{m}(\beta_l \otimes I_e)\right)\hat{x}^a(k) + T\sum_{l=1}^{m}(\beta_l \otimes I_e)x_l' + Kz^a(k+1), \\ z^a(k) = y^a(k+1) - C\left(I_{N\times n} - T\sum_{l=1}^{m}(\beta_l \otimes I_e)\right)\hat{x}^a(k) \end{cases} \tag{10}$$

where $\hat{x}^a(k+1) = \left[\hat{V}_1^a(k+1), \hat{f}_1^a(k+1), \ldots, \hat{V}_n^a(k+1), \hat{f}_n^a(k+1)\right]$ denotes$\hat{x}(k+1)$ under attacks at time $k+1$, and $z^a(k)$ denotes $z(k)$ under attacks at time k. Define $\Delta\hat{x}(k+1)$ and $\Delta z(k+1)$, which denote state estimation difference and the estimation residual difference, respectively. And the dynamic expression of $\Delta\hat{x}(k+1)$ and $\Delta z(k+1)$ can be obtained as

$$\begin{aligned} \Delta\hat{x}(k+1) &= \hat{x}^a(k+1) - \hat{x}(k+1) \\ &= \left(I_{N\times n} - T\sum_{l=1}^{m}(\beta_l \otimes I_e)\right)\Delta\hat{x}(k) + K\Delta z(k+1) \\ &= \left(I_{N\times n} - T\sum_{l=1}^{m}(\beta_l \otimes I_e)\right)\Delta\hat{x}(k) \\ &\quad - KC\left(I_n - T\sum_{l=1}^{m}(\beta_l \otimes I_e)\right)\Delta\hat{x}(k) \\ &\quad + KC(x^a(k+1) - x(k+1)) \\ &= (I_{N\times n} - KC)\left(I_{N\times n} - T\sum_{l=1}^{m}(\beta_l \otimes I_e)\right)\Delta\hat{x}(k) \\ &\quad + KC(x^a(k+1) - x(k+1)) \end{aligned}, \tag{11}$$

$$\begin{aligned} \Delta z(k+1) &= z^a(k+1) - z(k+1) \\ &= -C\left(I_{N\times n} - T\sum_{l=1}^{m}(\beta_l \otimes I_e)\right)\hat{x}^a(k) \\ &\quad + C\left(I_{N\times n} - T\sum_{l=1}^{m}(\beta_l \otimes I_e)\right)\hat{x}(k) \\ &\quad + y^a(k+1) - y(k+1) \\ &= -C\left(I_{N\times n} - T\sum_{l=1}^{m}(\beta_l \otimes I_e)\right)\Delta\hat{x}(k) \\ &\quad + C(x^a(k+1) - x(k+1)) \end{aligned}, \tag{12}$$

where $\hat{x}(k+1) = \left[\hat{V}_1^T(k+1), \hat{f}_1^T(k+1), \ldots, \hat{V}_1^T(k+1), \hat{f}_1^T(k+1)\right]^T$, and $x^a(k+1) - x(k+1) \neq 0$ represents the iteration process of $\Delta\hat{x}(k+1)$ and $\Delta z(k+1)$ has been affected by the unbounded attack sequence $\Theta(k)$. The attack sequence $\Theta(k)$ that depends on $\Delta\hat{x}(k)$ can satisfy $\lim_{k\to\infty}\|\Delta\hat{x}(k)\| \to \infty$ and $\lim_{k\to\infty}\|\Delta z(k)\| \leq M$ simultaneously, where M is a positive predetermined detection threshold. $\lim_{k\to\infty}\|\Delta\hat{x}(k)\| \to \infty$ represents that with the iteration of discrete time k, the voltage and frequency state estimation under unbounded attacks gradually deviates from the normal value. Since $\lim_{k\to\infty}\|\Delta\hat{x}(k)\| \to \infty$ and the generation process of $\Theta(k)$ depend upon $\Delta\hat{x}(k)$, $\lim_{k\to\infty}\|\Theta(k)\| \to \infty$ can be achieved. This study considers that $\Theta(0) = 0$ and the attack generation algorithm will be proposed later. $\lim_{k\to\infty}\|\Delta z(k)\| \leq M$ represents $\lim_{k\to\infty}\|\Delta\hat{x}(k)\| \to \infty$, the unbounded attack sequence $\Theta(k)$ will not trigger the traditional χ^2 detection.

The work of Hu et al. (2018) also inspires that protecting key communication channels can detect this stealthy unbounded attack sequence. Currently, phase measurement units (PMUs) are the most common equipment to protect communication channels (Mabaning et al., 2017; Tahabilder et al., 2017; Pei et al., 2020), which are more reliable than detectors. Algorithms detecting and isolating attacks often need to

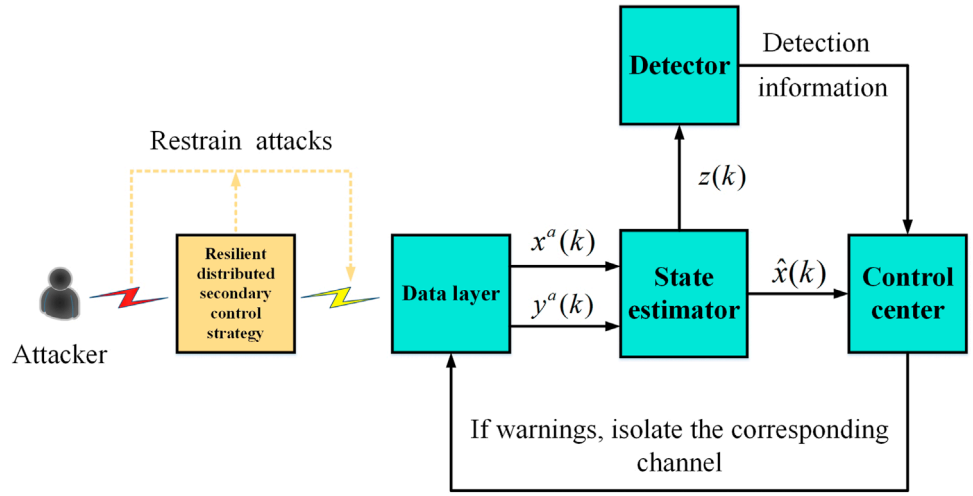

FIGURE 2
Function of the resilient-distributed control method proposed in this study in the process of unbounded attacks generation, state estimation, and detection.

consume a lot of computing resources, and the detection and isolation process that relies on the limited number of PMUs always has a certain time delay. The unbounded attack sequence which depends on $\Delta\hat{x}(k)$ will cause irreversible damage to the microgrid during the process. This study proposes a discrete-time resilient distributed secondary control strategy based on a layered network to greatly suppress the divergence degree of $\Delta\hat{x}(k)$ during the process, and the impact $\Theta(k)$ can cause will be equal to a bounded attack sequence accordingly. It can be seen from Eqn. 11 that although $x^a(k+1)$ and $x(k+1)$ are extremely close under the strategy proposed in this study, $x^a(k+1)-x(k+1)$ keeps accumulating during the iteration process of $\Delta\hat{x}(k+1)$, and $\Delta\hat{x}(k+1)$ still will tend to diverge after a long enough time. As shown in Figure 2, the strategy proposed in this study plays an essential role in the period from the beginning of FDI attack generation to the end of detection and isolation measures to enhance the resilience of the microgrid against attacks.

The following assumptions are made in this study:

Assumption 1: This monotonous unbounded attack sequence can generate at a limited rate, in other words, $\left\|\frac{a(k+1)-a(k)}{T}\right\| \le c$, where c is a positive scalar.

Assumption 2: FDI attacks cannot be launched on sensor devices directly, but only in sensor communication networks.

Assumption 3: The attacker has perfect knowledge about the system model, that is, information the attacks generation algorithm requires can be obtained by the attacker.

3.3 Resilient-distributed secondary strategy based on the layered communication network

This section introduces a virtual layer Σ_h based on the layered network (Gusrialdi et al., 2018) to interconnect with the original control layer Σ_s to form a layered communication network to enhance the resilience of the control layer Σ_s against unbounded FDI attacks, the layered network is shown in Figure 3, where the virtual layer Σ_h has no physical meaning, and it would be difficult for adversaries to associate the information in the virtual layer Σ_h with the measurements of voltage and frequency in the control layer Σ_s. There exist studies that have investigated attacks in the virtual layer Σ_h, but it is obvious that adversaries need more computing resources to launch attacks in the virtual layer Σ_h. Therefore, most work based on the layered network prefer to study attacks in the control layer Σ_s. The discrete-time resilient distributed secondary control strategy proposed in this study considers the unbounded attack sequence launched in the control layer Σ_s, and Lyapunov theory is used to validate the stability of the strategy in this section.

The layered network consisting of the control layer Σ_s and the virtual layer Σ_h can be shown in Figure 3. The control layer Σ_s and the virtual layer Σ_h have the same number of nodes, and the reference information is transmitted to the nodes in the control layer Σ_s and virtual layer Σ_h at the same time. After the unbounded attack sequence is launched in the control layer Σ_s, the layered network will generate a compensation sequence through the observer constituted by Eqs. 14, 15 so that the

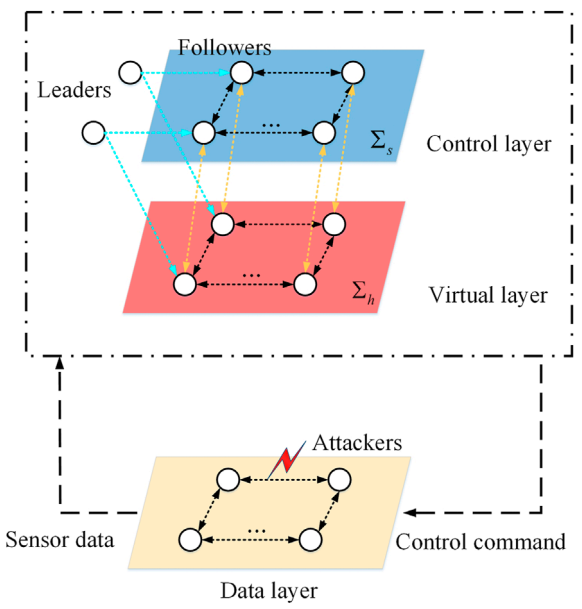

FIGURE 3
Structure of the layered communication network formed by introducing a virtual network layer.

control layer Σ_s as shown in Eqn. 13 can resist the impact of the unbounded attack sequence $\Theta(k)$.

$$x(k+1) = \left(I_{N\times n} - T\sum_{l=1}^{m}(\beta_l \otimes I_e)\right)x(k) + T\left(\sum_{l=1}^{m}(\beta_l \otimes I_e)x_l' + \Theta(k) - \hat{\Theta}(k)\right), \quad (13)$$

$$\eta(k+1) = \left(I_{N\times n} - T\sum_{l=1}^{m}(\beta_l \otimes I_e)\right)\eta(k) + T\left(\sum_{l=1}^{m}(\beta_l \otimes I_e)x_l'\right), \quad (14)$$

$$\hat{\Theta}(k+1) = T\left(\sum_{l=1}^{m}(\beta_l \otimes I_e)v(k) + \hat{\Theta}(k)\right), \quad (15)$$

where $\eta(k) = [\eta_1^T(k), \eta_2^T(k), \ldots, \eta_n^T(k)]^T$ denotes the state of nodes in the virtual network layer Σ_h, $v(k) = x(k) - \eta(k)$ denotes the difference between the control layer Σ_s and the virtual layer Σ_h at time k, and $\hat{\Theta}(k) = [\hat{\Theta}_1^T(k), \hat{\Theta}_2^T(k), \ldots, \hat{\Theta}_n^T(k)]^T$ denotes the compensation sequence. It can be seen that Eqs. 14, 15 together form an observer to generate a compensation sequence through which the impact of unbounded attack sequence in the control layer can be eliminated. Define errors between information in the leader node and that in the nodes of control layer Σ_s and virtual layer Σ_h as (16) and (17) respectively:

$$e_1(k) = x(k) - \left(\sum_{l=1}^{m}(\beta_l \otimes I_e)\right)^{-1}\sum_{l=1}^{m}(\beta_l \otimes I_e)x_l', \quad (16)$$

$$e_2(k) = \eta(k) - \left(\sum_{l=1}^{m}(\beta_l \otimes I_e)\right)^{-1}\sum_{l=1}^{m}(\beta_l \otimes I_e)x_l'. \quad (17)$$

Theorem 1: When the unbounded attack sequence $\Theta(k)$ which depends on state estimation difference satisfying assumption 1 has been launched in the communication network of microgrid as shown in Eqn. 5, the resilient distributed secondary control strategy based on the layered network as shown in Eqs. 13–15 is designed to resist the impact $\Theta(k)$ can cause. If $e_1(k)$ in Eqn. 16 is stable, it can be said that the control layer Σ_s shown in Eqn. 13 can resist the unbounded attack sequence $\Theta(k)$ and maintain voltage and frequency stable.

Proof: Define $\tilde{\Theta}(k) = \Theta(k) - \hat{\Theta}(k) = [\tilde{\Theta}_1^T(k), \tilde{\Theta}_2^T(k), \ldots, \tilde{\Theta}_N^T(k)]^T$, and make the difference between Eqs. 13, 14 to obtain Eqn. 18:

$$v(k+1) = \left(I_{N\times n} - T\sum_{l=1}^{m}(\beta_l \otimes I_e)\right)v(k) + T\tilde{\Theta}(k). \quad (18)$$

Eqn. 19 can be obtained from Eqn. 15:

$$\begin{aligned}\frac{\tilde{\Theta}(k+1) - \tilde{\Theta}(k)}{T} &= \frac{\Theta(k+1) - \Theta(k)}{T} - \frac{\hat{\Theta}(k+1) - \hat{\Theta}(k)}{T} \\ &= -\sum_{l=1}^{m}(\beta_l \otimes I_e)v(k) + \hat{\Theta}(k+1) - \hat{\Theta}(k) \\ \tilde{\Theta}(k+1) - \tilde{\Theta}(k) &= \left(I_{N\times n} - T\sum_{l=1}^{m}(\beta_l \otimes I_e)\right)v(k) \\ &\quad + T\left(\hat{\Theta}(k+1) - \hat{\Theta}(k)\right)\end{aligned}. \quad (19)$$

Rewriting Eqs. 18, 19 in the following compact form yields

$$\begin{bmatrix} v(k+1) \\ \tilde{\Theta}(k+1) \end{bmatrix} = \begin{bmatrix} I_{N\times n} - T\sum_{l=1}^{m}(\beta_l \otimes I_e) & I_{N\times n} \\ I_{N\times n} - T\sum_{l=1}^{m}(\beta_l \otimes I_e) & 0_{N\times n} \end{bmatrix}\begin{bmatrix} v(k) \\ \tilde{\Theta}(k) \end{bmatrix} + \begin{bmatrix} 0_{(N\times n)\times 1} \\ T(\Theta(k+1) - \Theta(k)) \end{bmatrix}. \quad (20)$$

Define $m(k) = \begin{bmatrix}\tilde{\Theta}^T(k) & v^T(k)\end{bmatrix}^T$, $m(k+1) = \begin{bmatrix}\tilde{\Theta}^T(k+1) & v^T(k+1)\end{bmatrix}^T$, and $m(k+1) = A_2 m(k)$, where $A_2 = \begin{bmatrix} I_{N\times n} - T\sum_{l=1}^{m}(\beta_l \otimes I_e) & I_{N\times n} \\ I_{N\times n} - T\sum_{l=1}^{m}(\beta_l \otimes I_e) & 0_{N\times n} \end{bmatrix}$. Choose a Lyapunov function candidate as

$$V_d(k) = [T(\Theta(k+1) - \Theta(k))]^T[T(\Theta(k+1) - \Theta(k))]. \quad (21)$$

Given assumption 1, $\lim_{k\to\infty}\Theta(k) = \infty$ is a monotonous and limited-growth unbounded attack sequence, and $\Theta(0) = 0$. Therefore, $V_d(k) = T^2\|(\Theta(k+1) - \Theta(k))\|^2$ is positive-definite at arbitrary time k. Next, choose a Lyapunov function candidate to prove the stability of Eqn. 20:

$$V(k) = m^T(k) P_s m(k) + V_d(k). \tag{22}$$

where $P_s > 0$ is an arbitrary symmetric and positive-definite matrix, and $V_d(k) > 0$ is known from Eqn. 21. Therefore, $V(k)$ is positive-definite at arbitrary time k. The difference form of Eqn. 22 is can be obtained as

$$\begin{aligned} &V(k+1) - V(k) \\ &\quad = m^T(k+1) P_s m(k+1) - m^T(k) P_s m(k) \\ &\qquad + V_d(k+1) - V_d(k) \\ &\quad = (A_2 m(k))^T P_s (A_2 m(k)) - m^T(k) P_s m(k) \\ &\qquad + T^2 \|\Theta(k+2) - \Theta(k+1)\| - T^2 \|\Theta(k+1) - \Theta(k)\|. \\ &\quad = m^T(k) \left(A_2^T P_s A_2 - P_s\right) m(k) \\ &\qquad + T^2 \|\Theta(k+2) - \Theta(k+1)\| - T^2 \|\Theta(k+1) - \Theta(k)\| \\ &\quad = -m^T(k) Q m(k) + T^2 \left(\|\Theta(k+2) - \Theta(k+1)\|^2 \right. \\ &\qquad \left. - \|\Theta(k+1) - \Theta(k)\|^2\right) \end{aligned} \tag{23}$$

There exists a symmetric and positive-definite matrix P_s such that $A_2^T P_s A_2 - P_s < 0$ for an arbitrary symmetric and positive-definite matrix Q. Given assumption 1, $\|\Theta(k+2) - \Theta(k+1)\|^2 \le \|\Theta(k+1) - \Theta(k)\|^2$ can be obtained, that is, $\|\Theta(k+2) - \Theta(k+1)\|^2 - \|\Theta(k+1) - \Theta(k)\|^2 \le 0$. Through the aforementioned analysis, $V(k+1) - V(k) < 0$ can be obtained at arbitrary time k. Therefore, $v(k)$ and $\tilde{\Theta}(k)$ are stable. From Eqs. 16, 17, $e_1(k) = v(k) + e_2(k)$ can be obtained. In order to prove the stability of $e_1(k)$, the stability of $e_2(k)$ also should be proved. Combine with Eqn. 14, the difference form of Eqn. 17 can be obtained as

$$\begin{aligned} &\frac{e_2(k+1) - e_2(k)}{T} \\ &\quad = \frac{\eta(k+1) - \eta(k)}{T} - 0 \\ &\quad = -\sum_{l=1}^{m} (\beta_l \otimes I_e) \eta(k) + \sum_{l=1}^{m} (\beta_l \otimes I_e) x_l^{'} \\ &\quad = \left(\sum_{l=1}^{m} (\beta_l \otimes I_e)\right) \\ &\qquad \left(-\eta(k) + \left(\sum_{l=1}^{m} (\beta_l \otimes I_e)\right)^{-1} \sum_{l=1}^{m} (\beta_l \otimes I_e) x_l^{'}\right) \\ &\quad = -\sum_{l=1}^{m} (\beta_l \otimes I_e) e_2(k) \\ &e_2(k+1) = \left(I_{N\times n} - T\sum_{l=1}^{m} (\beta_l \otimes I_e)\right) e_2(k) \end{aligned} \tag{24}$$

Choose a Lyapunov function candidate as $V^{'}(k) = e_2^T(k) P_h e_2(k)$, its difference form can be shown as

$$\begin{aligned} &V^{'}(k+1) - V^{'}(k) \\ &\quad = e_2^T(k+1) P_h e_2(k+1) - e_2^T(k) P_h e_2(k) \\ &\quad = e_2^T(k) \left(I_{N\times n} - T\sum_{l=1}^{m} (\beta_l \otimes I_e)\right)^T \\ &\qquad P_h \left(I_{N\times n} - T\sum_{l=1}^{m} (\beta_l \otimes I_e)\right) e_2(k) - e_2^T(k) P_h e_2(k) \\ &\quad = e_2^T(k) \left(\left(I_{N\times n} - T\sum_{l=1}^{m} (\beta_l \otimes I_e)\right)^T \right. \\ &\qquad \left. P_h \left(I_{N\times n} - T\sum_{l=1}^{m} (\beta_l \otimes I_e)\right) - P_h\right) e_2(k) \\ &\quad = -e_2^T(k) Q^{'} e_2(k) \end{aligned} \tag{25}$$

There exists a symmetric and positive-definite matrix Q' such that $(I_{N\times n} - T\sum_{l=1}^{m} (\beta_l \otimes I_e))^T P_h (I_{N\times n} - T\sum_{l=1}^{m} (\beta_l \otimes I_e)) - P_h = -Q^{'} < 0$, that is, $V'(k+1) - V'(k) < 0$. Therefore, $e_2(k)$ is stable. Since $e_1(k) = v(k) + e_2(k)$, the stability of $e_1(k)$ can be proved. The proof of Theorem 1 has completed here, which indicates the distributed secondary strategy proposed in this study can defend attacks to maintain the voltage and frequency stable.

3.4 Design of the unbounded attack sequence

This section will introduce the generation process of the unbounded attack sequence $\Theta(k)$, and how it destroys the state estimation of microgrid. The specific design principle of parameters required in algorithm is shown in Hu et al. (2018), The generation algorithm of unbounded attack sequence is shown in Table 2. where the length of $I^s_{N\times n}$ is $N \times n$, and all its elements equal to 0 except the *sth* element equal to 1. How to select s can only be determined after the matrix parameters of microgrid are selected, which will be given in the next section. The unbounded attack sequence $\Theta(k) = \frac{1}{T}[(I_{N\times n} - T\sum_{l=1}^{m} (\beta_l \otimes I_e))\Delta\hat{x}(k) + \varphi(k) M I^s_{N\times n}]$ depends on the state estimation difference $\Delta\hat{x}(k)$ at time k, and $\varphi(k) M I^s_{N\times n}$ is a constant

TABLE 2 Algorithm for generating an unbounded attack sequence.

Algorithm for generating an unbounded attack sequence

Initialization parameter
Define $\Delta\hat{x}(0) = \hat{x}^a(0) - \hat{x}(0)$
Choose a arbitrary $\varphi \in (0,1)$, and the detection threshold $M = 2$
while $k \ge 0$ **do**
Set $\Delta\hat{x}(0) = 0$, $\varphi(0) = 0$
Calculate $\Theta(k) = \frac{1}{T}[(I_{N\times n} - T\sum_{l=1}^{m} (\beta_l \otimes I_e))\Delta\hat{x}(k) + \varphi(k) M I^s_{N\times n}]$
Calculate $\Delta\hat{x}(k+1) = [(I_{N\times n} - KC)(I_{N\times n} - T\sum_{l=1}^{m} (\beta_l \otimes I_e))\Delta\hat{x}(k)$
$+KC(x^a(k+1) - x(k+1))]$
$k = k + 1$
$\varphi(k) = \varphi$
end while

column vector. Since the existence of $\varphi(k)MI^s_{N\times n}$, $\Theta(k)$ will make $\|\Delta\hat{x}(k+1)\|$ be continuously increasing after time $k=1$, and $\Delta\hat{x}(k+1)$ will make $\|\Theta(k)\|$ be continuously increasing in turn. Finally, when $\lim_{k\to\infty}\|\Theta(k)\|=\infty$, $\lim_{k\to\infty}\|\Delta\hat{x}(k+1)\|=\infty$. The resilient distributed secondary control strategy proposed in this study, mitigating attacks rather than eliminating them, can restore $x^a(k+1)$ to $x(k+1)$, so that $x^a(k+1)-x(k+1)$ is close to 0. In this way, compared with the distributed secondary control strategy, the resilient strategy proposed in this study can suppress $\Delta\hat{x}(k+1)$ in **Eqn. 11** and $\Delta z(k+1)$ in **Eqn. 12**. Since the unbounded attack sequence $\Theta(k)$ depends on $\Delta\hat{x}(k)$ which is greatly suppressed before detection and isolation mearsures completed, the divergence trend of $\Theta(k)$ is also greatly suppressed. The impact of $\Theta(k)$ can be equaled to that caused by a bounded attack sequence, which greatly alleviates the threat to the microgrid. The resilient distributed secondary strategy proposed in this study only plays a role in the suppression process of $\Theta(k)$ and $\Delta\hat{x}(k)$, but cannot eliminate them completely. To eliminate the impact of this kind of unbounded attack sequence on microgrid, one should find a way to detect and isolate attacks is essential. How to protect key communication channels to detect stealthy unbounded attacks is an interesting topic, and authors will think about how to realize the idea in future research.

4 Case study

In this section, a test microgrid consisting of six inverter-based *DGs* is used to verify the effectiveness of the method proposed in this study against unbounded attack sequence $\Theta(k)$ (Bidram et al., 2013; Xu et al., 2019; Ge et al., 2021). The effectiveness of a resilient distributed secondary control strategy against unbounded attacks is that the voltage and frequency of each DG can still operate within the allowable fluctuation range near the rated value when the neighbor information has tampered. The influence of unbounded attack sequence on microgrids is analyzed by simulation when the elastic distributed secondary control strategy proposed in this study is adopted.

The power layer structure consisting of six inverter-based DGs illustrated in this study is shown in **Figure 4**. And the microgrid parameters are as follows:

$T=0.001s$, $a_{ij}=10$, $g_{li}=0.001$, $N=6$, $n=2,\mathrm{m}=2$, $C=I_{N\times n}=I_{12}$,

$Q=\mathrm{diag}\,(0.01,0.01,0.01,0.001,0.001,0.001,0.01,0.01,0.01,0.001,0.001,0.001)$,

$R=\mathrm{diag}(0.1,0.1,0.1,0.1,0.1,0.1,0.1,0.1,0.1,0.1,0.1,0.1)$,

In the unbounded attack generation algorithm, $\varphi=0.1$, $I^s_{N\times n}=[0,0,1,0,0,0,0,0,0,0,0,0]^T$. Define the reference information vector $x_1=x_2=\begin{bmatrix}380V\\50Hz\end{bmatrix}$, which represents all the DGs need to follow the reference voltage $380V$ and frequency $50Hz$.

First, the distributed secondary control strategy as shown in **Eqn. 4** is used to maintain voltage and frequency stability. Next, the unbounded attack sequence is launched into the communication channels. As shown in **Eqn. 9**, $\Theta(k)$ destroys the iterative process in the form of $T\Theta(k)$. As shown in **Figure 5A**, the unbounded attack sequence given by algorithm 1 can destroy the iterative process of $V_2(k)$, $V_3(k)$, $V_5(k)$, and $V_6(k)$, that is, the voltage consensus performance of DG2, DG3, DG5, and DG6 is destroyed. Information exchange under attacks will make all the DGs' voltage tend to ∞ with the iteration of the sampling time T. **Figure 5B** shows that the frequency of DGs has not been destroyed. Combine with **Figure 5A** and **Figure 5B**, the distributed secondary control strategy is still effective in the absence of $\Theta(k)$, but the voltage consensus performance will be destroyed under $\Theta(k)$.

Figure 6A shows the generation process of $\Theta(k)$ launched in **Figure 5A**. **Figure 6B** shows the voltage estimation difference of DGs under $\Theta(k)$. Since frequency has not been tampered, $\Theta_{i2}(k)=\Delta\hat{f}(k)=0$.

$T\Theta_{ex1}(k)$ denotes $T\Theta_1(k)$ and $T\Theta_4(k)$, and $\Delta\hat{V}_{\mathrm{ex1}}(k)$ denotes $\Delta\hat{V}_1(k)$ and $\Delta\hat{V}_4(k)$. **Figure 6** indicates the generation process of $\Theta_{i1}(k)$ depends on $\Delta\hat{V}(k)$ indeed. Also, then $\Theta_{i1}(k)$ will increase $\Delta\hat{V}(k)$ in turn. However, this phenomenon is profitless for voltage stability. During the period between the initialization of $\Theta(k)$ and completion of detection and isolation measures, the $\Theta(k)$ which diverges rapidly will cause irreversible effects on the microgrid. When the voltage exceeds the rated range allowed by the microgrid, the power circuit breakers inside the microgrid will act to disconnect the main circuit and stop operation. The renewable energy equipment inside the microgrid is expensive, which cannot stand the permanent damage such sudden breakdown causes. Obviously, it is not a wise choice to let such attacks diverge rapidly and put all hope in detection and isolation measures. The resilient distributed secondary control strategy proposed in this study can greatly suppress the divergence of $\Theta(k)$, and prevent the microgrid from being attacked to the point of crash before the completion of the whole process of detection and isolation measures.

It can be seen that $\Theta(k)$ is approximated into an attack sequence with minimal growth rate. Before completion of detection and isolation algorithms, relative to the original divergence, the impact of the suppressed $\Theta(k)$ can cause equal to a bounded attack sequence.

Figure 7 shows the performance of the resilient distributed secondary control strategy proposed in this study against the unbounded attack sequence $\Theta(k)$. It can be seen from **Figure 7A** that the voltage of DGs can still converge to the allowable range of the reference value 380 V under the impact of the unbounded attack sequence $\Theta(k)$. Moreover, **Figure 7B** shows the frequency of DGs can maintain stability, which indicates the resilient distributed secondary control strategy proposed in this study can also achieve the desired control objectives

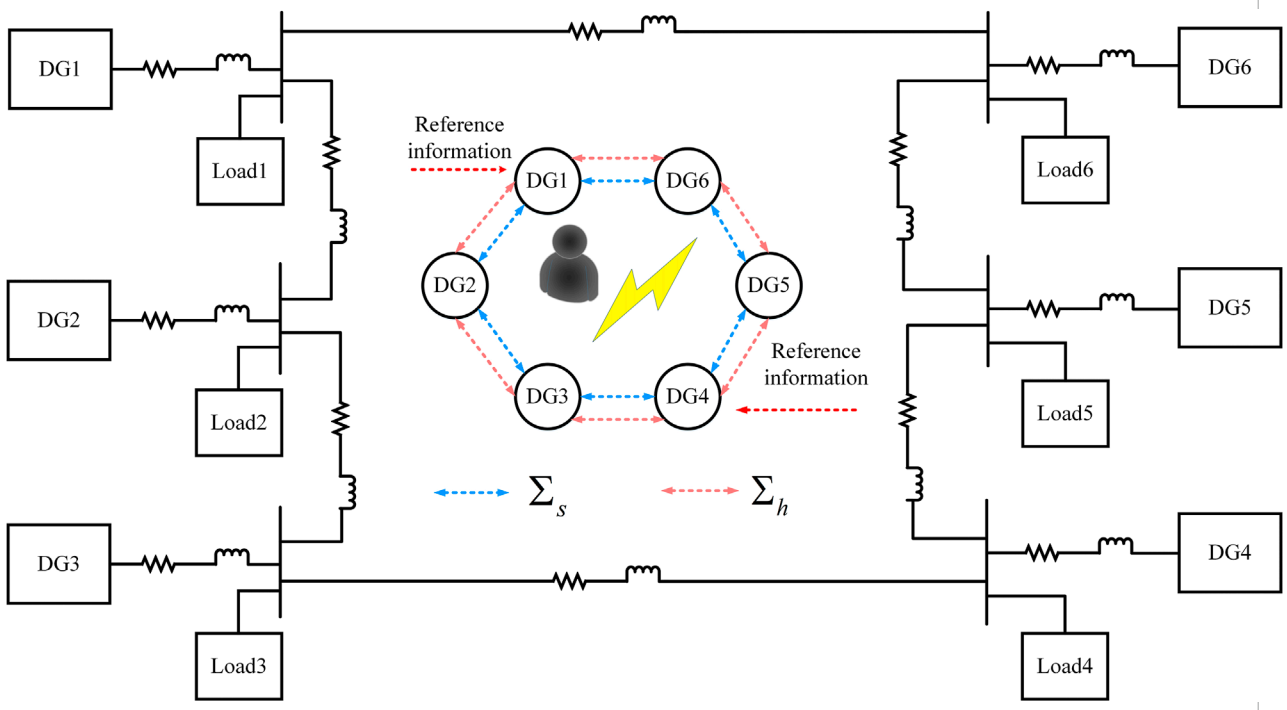

FIGURE 4
Physical structure and communication network topology of the microgrid illustrated in this study.

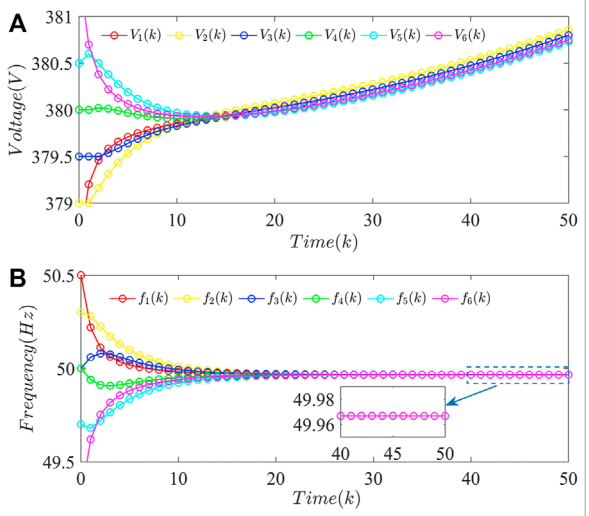

FIGURE 5
Performance of the distributed secondary control strategy against unbounded attack sequence $\Theta(k)$: **(A)** voltage; **(B)** frequency.

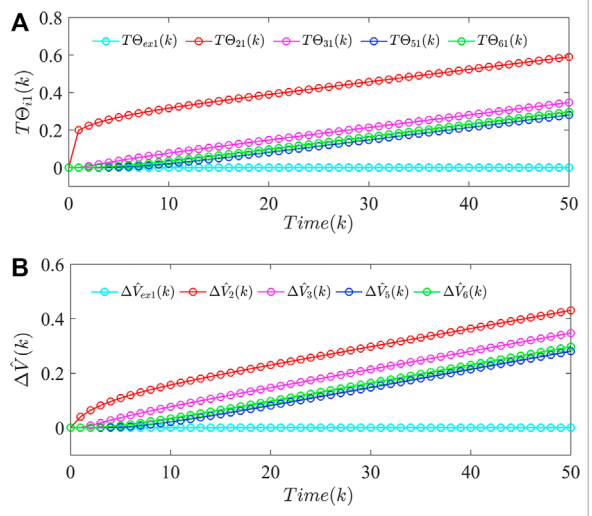

FIGURE 6
(A) Generation process of $\Theta(k)$ in **Figure 5**; **(B)** voltage estimation difference of DGs.

when there exist no attacks. It is worth mentioning that this strategy can make voltage under attacks $V^a(k)$ close to that without attacks $V(k)$, that is, $V^a(k) - V(k)$ is close to 0. Given Algorithm 1, if $\Delta\hat{x}(k)$ can be suppressed, and then $\Theta(k)$ also will be extremely suppressed. **Figure 8** shows the voltage estimation difference $\Delta\hat{V}(k)$ of DGs using the resilient distributed secondary control strategy proposed in this study. Combine with **Figure 6** and **Figure 8**, it is obvious that $\Delta\hat{V}(k)$ can be suppressed by

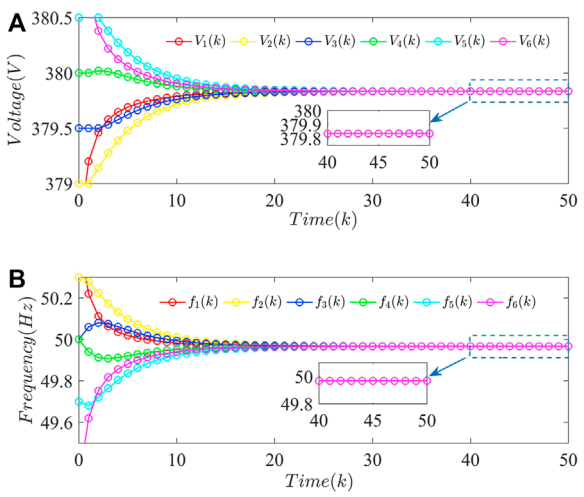

FIGURE 7
Performance of the resilient-distributed secondary control strategy proposed in this study against the unbounded attack sequence $\Theta(k)$: **(A)** voltage; **(B)** frequency.

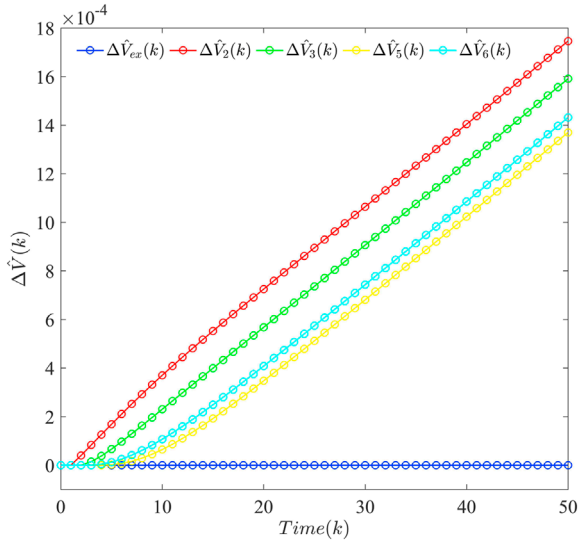

FIGURE 8
Voltage estimation difference using the resilient-distributed secondary control strategy proposed in this study.

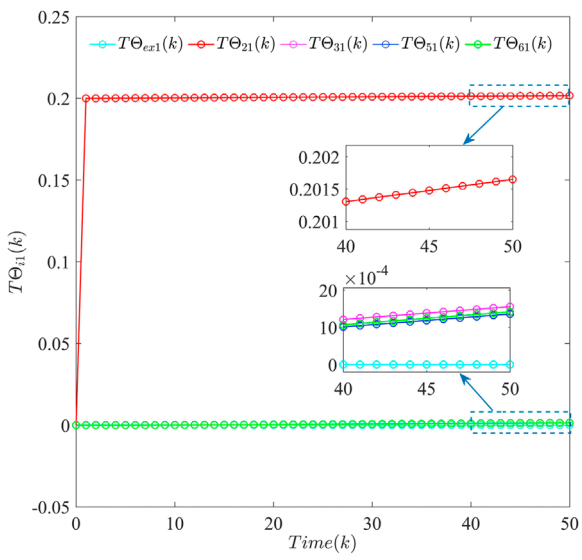

FIGURE 9
Unbounded attack sequence $\Theta(k)$ suppressed by the resilient-distributed secondary control strategy proposed in this study.

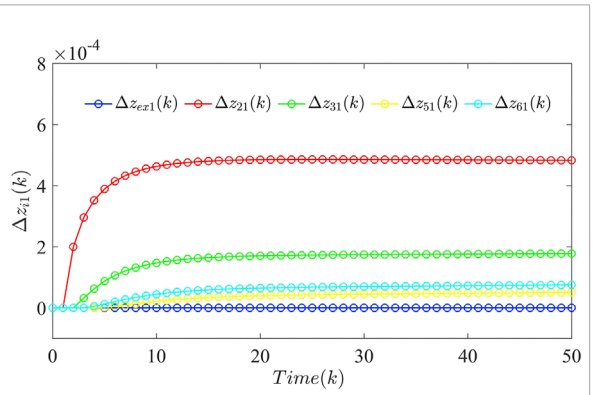

FIGURE 10
Voltage estimation residual difference $\Delta z_{i1}(k)$ of DGs using the resilient-distributed secondary control strategy proposed in this study.

the distributed secondary control strategy proposed in this study.

Figure 9 shows performance of the generation process of $\Theta(k)$ which depends on $\Delta\hat{V}(k)$ after the voltage estimation difference $\Delta\hat{V}(k)$ has been suppressed. As shown in Figure 9, the unbounded attack sequence $\Theta(k)$ is approximated into an bounded attack sequence with minimal growth rate under the resilient distributed secondary control strategy. From Eqn. 12, $\|\Delta z_{i1}(k+1)\| = \left\|-C(I_{N\times n} - T\sum_{l=1}^{m}(\beta_l \otimes I_e))\Delta\hat{x}(k) + C(x^a(k+1) - x(k+1))\right\|$ can be obtained. The resilient distributed secondary control strategy suppresses $\Delta\hat{x}(k)$ and $x^a(k+1) - x(k+1)$, which leads to $\|\Delta z_{i1}(k+1)\| < M$ as shown in Figure 10. However, it does not violate the original intention of the resilient distributed secondary control strategy, which is designed to mitigate attacks rather than detect them. It is acceptable to gain greater resilience against unbounded attack sequence at the cost of reducing $\|\Delta z_{i1}(k+1)\|$. The detection and isolation measures, such PMUs, will replace the traditional detectors by protecting key communication channels in the Σ_s to detect $\Theta(k)$. Face to well-designed unbounded attack sequence, how to deploy protection

devices in the minimum number of key communication channels has become an important topic in future research. One of authors' future work is how to integrate mitigation and detection processes to solve the problem of such unbounded attack sequence $\Theta(k)$ completely.

5 Conclusion

This study has studied the impact of a class of unbounded attack sequence $\Theta(k)$ launched in the polymorphic cooperative control system. A discrete-time resilient distributed secondary control strategy based on the layered network has been used to restore the voltage and frequency under attacks and suppress the divergence of state estimation difference. At the same time, $\Theta(k)$ depending on state estimation difference has also been suppressed, and its destructiveness has been limited to the level of a bounded attack sequence. The strategy proposed in this study is suitable for the process between the initialization of generating attacks and completion of detection and isolation measures to alleviate the irreversible impact on the microgrid. The effectiveness of a resilient distributed secondary control strategy against unbounded attacks has been validated by a test microgrid consisting of six inverter-based DGs. The authors will focus on how to integrate mitigation, detection, and isolation processes into a more complete and effective strategy against unbounded attacks.

Data availability statement

The raw data supporting the conclusion of this article will be made available by the authors, without undue reservation.

Author contributions

FW and QS designed the experiments and research methods. QS performed the format analysis. The tools analysis, data processing, and writing the original draft were carried out by JZ. GX solved the application problem of research methods. GX performed the writing—review on references. JZ and QS contributed to proofreading and organization management.

Funding

This work is supported in part by the National Key R&D Program of China (2019YFB1802501), the Key Research Project of Zhejiang Lab (2021LE0AC02), the High-Level Talents Innovation Support Plan of Dalian (Young Science and Technology Star Project) (under Grant No. 2021RQ058), the National Natural Science Foundation of China (under Grant Nos. 51939001, 61803064, 61751202, 61903092, 61976033, and U1813203), the Science and Technology Innovation Funds of Dalian (under Grant No. 2018J11CY022), the Liaoning Revitalization Talents Program (under Grant Nos. XLYC1908018 and XLYC1807046), the Natural Science Foundation of Liaoning (2019-ZD-0151 and 20170540098), and the Fundamental Research Funds for the Central Universities (under Grant Nos. 3132019345, 3132020103, and 3132020125).

Conflict of interest

The authors declare that the research was conducted in the absence of any commercial or financial relationships that could be construed as a potential conflict of interest.

Publisher's note

All claims expressed in this article are solely those of the authors and do not necessarily represent those of their affiliated organizations, or those of the publisher, the editors, and the reviewers. Any product that may be evaluated in this article, or claim that may be made by its manufacturer, is not guaranteed or endorsed by the publisher.

References

Abhinav, S., Modares, H., Lewis, F. L., Ferrese, F., and Davoudi, A. (2018). Synchrony in networked microgrids under attacks. *IEEE Trans. Smart Grid* 9, 6731–6741. doi:10.1109/TSG.2017.2721382

Bidram, A., Davoudi, A., Lewis, F. L., and Guerrero, J. M. (2013). Distributed cooperative secondary control of microgrids using feedback linearization. *IEEE Trans. Power Syst.* 28, 3462–3470. doi:10.1109/TPWRS.2013.2247071

Bidram, A., Lewis, F. L., and Davoudi, A. (2014). Distributed control systems for small-scale power networks: Using multiagent cooperative control theory. *IEEE Control Syst. Mag.* 34, 56–77. doi:10.1109/MCS.2014.2350571

Chen, Y., Qi, D., Dong, H., Li, C., Li, Z., Zhang, J., et al. (2021). A fdi attack-resilient distributed secondary control strategy for islanded microgrids. *IEEE Trans. Smart Grid* 12, 1929–1938. doi:10.1109/TSG.2020.3047949

Condry, M. W., and Nelson, C. B. (2016). Using smart edge iot devices for safer, rapid response with industry iot control operations. *Proc. IEEE* 104, 938–946. doi:10.1109/JPROC.2015.2513672

Dutta, R. G., Zhang, T., and Jin, Y. (2019). "Resilient distributed filter for state estimation of cyber-physical systems under attack," in 2019 American Control Conference (ACC), 5141–5147. doi:10.23919/ACC.2019.8815298

Fawzi, H., Tabuada, P., and Diggavi, S. (2014). Secure estimation and control for cyber-physical systems under adversarial attacks. *IEEE Trans. Autom. Contr.* 59, 1454–1467. doi:10.1109/TAC.2014.2303233

Gao, S., Peng, Z., Liu, L., Wang, D., and Han, Q.-L. (2022). Fixed-time resilient edge-triggered estimation and control of surface vehicles for cooperative target tracking under attacks. *IEEE Trans. Intell. Veh.* 1, 1–10. doi:10.1109/TIV.2022.3184076

Ge, P., Zhu, Y., Green, T. C., and Teng, F. (2021). Resilient secondary voltage control of islanded microgrids: An eskbf-based distributed fast terminal sliding mode control approach. *IEEE Trans. Power Syst.* 36, 1059–1070. doi:10.1109/TPWRS.2020.3012026

Gharesifard, B., and Başar, T. (2012). Resilience in consensus dynamics via competitive interconnections. *IFAC Proc. Vol.* 45, 234–239. doi:10.3182/20120914-2-US-4030.00018

Gusrialdi, A., Qu, Z., and Simaan, M. A. (2018). Competitive interaction design of cooperative systems against attacks. *IEEE Trans. Autom. Contr.* 63, 3159–3166. doi:10.1109/TAC.2018.2793164

Gusrialdi, A., Qu, Z., and Simaan, M. A. (2014). "Robust design of cooperative systems against attacks," in 2014 American Control Conference, 1456–1462. doi:10.1109/ACC.2014.6858789

Hu, L., Wang, Z., Han, Q.-L., and Liu, X. (2018). State estimation under false data injection attacks: Security analysis and system protection. *Automatica* 87, 176–183. doi:10.1016/j.automatica.2017.09.028

Hu, Y., Cui, Z., Li, Z., Dong, Y., Cui, P., and Wu, J. (2022). Construction technologies of polymorphic network environment based on codesign of domain-specific software/hardware. *J. Commun.* 43, 3–13. doi:10.11959/j.issn.1000436x.2022086

Hu, Y., Li, D., Sun, P., Yi, P., and Wu, J. (2020). Polymorphic smart network: An open, flexible and universal architecture for future heterogeneous networks. *IEEE Trans. Netw. Sci. Eng.* 7, 2515–2525. doi:10.1109/TNSE.2020.3006249

Huang, J., Ho, D. W., Li, F., Yang, W., and Tang, Y. (2020). Secure remote state estimation against linear man-in-the-middle attacks using watermarking. *Automatica* 121, 109182. doi:10.1016/j.automatica.2020.109182

Kreutz, D., Ramos, F. M. V., Veríssimo, P. E., Rothenberg, C. E., Azodolmolky, S., Uhlig, S., et al. (2015). Software-defined networking: A comprehensive survey. *Proc. IEEE* 103, 14–76. doi:10.1109/JPROC.2014.2371999

Liu, Y., Li, Y., Wang, Y., Zhang, X., Gooi, H. B., Xin, H., et al. (2022). Robust and resilient distributed optimal frequency control for microgrids against cyber attacks. *IEEE Trans. Ind. Inf.* 18, 375–386. doi:10.1109/TII.2021.3071753

Liu, Y., Ning, P., and Reiter, M. K. (2009). "False data injection attacks against state estimation in electric power grids," in Proceedings of the 16th ACM Conference on Computer and Communications Security, 21–32. doi:10.1145/1653662.1653666

Liu, Y., Ning, P., and Reiter, M. K. (2011). False data injection attacks against state estimation in electric power grids. *ACM Trans. Inf. Syst. Secur.* 14, 1–33. doi:10.1145/1952982.1952995

Mabaning, A. A. G., Orillaza, J. R. C., and von Meier, A. (2017). "Optimal pmu placement for distribution networks," in 2017 IEEE Innovative Smart Grid Technologies - Asia (ISGT-Asia), 1–6. doi:10.1109/ISGT-Asia.2017.8378415

Manandhar, K., Cao, X., Hu, F., and Liu, Y. (2014). Detection of faults and attacks including false data injection attack in smart grid using kalman filter. *IEEE Trans. Control Netw. Syst.* 1, 370–379. doi:10.1109/TCNS.2014.2357531

Nunes, B. A. A., Mendonca, M., Nguyen, X.-N., Obraczka, K., and Turletti, T. (2014). A survey of software-defined networking: Past, present, and future of programmable networks. *IEEE Commun. Surv. Tutorials* 16, 1617–1634. doi:10.1109/SURV.2014.012214.00180

Pang, Z.-H., Fan, L.-Z., Dong, Z., Han, Q.-L., and Liu, G.-P. (2022). False data injection attacks against partial sensor measurements of networked control systems. *IEEE Trans. Circuits Syst. Ii.* 69, 149–153. doi:10.1109/TCSII.2021.3073724

Pei, C., Xiao, Y., Liang, W., and Han, X. (2020). Pmu placement protection against coordinated false data injection attacks in smart grid. *IEEE Trans. Ind. Appl.* 56, 4381. doi:10.1109/TIA.2020.2979793

Rapp, K., and Nyman, P.-O. (2004). Stability properties of the discrete-time extended kalman filter. *IFAC Proc. Vol.* 37, 1377–1382. doi:10.1016/S1474-6670(17)31420-9

Salah, K., Elbadawi, K., and Boutaba, R. (2012). Performance modeling and analysis of network firewalls. *IEEE Trans. Netw. Serv. Manage.* 9, 12–21. doi:10.1109/TNSM.2011.122011.110151

Tahabilder, A., Ghosh, P. K., Chatterjee, S., and Rahman, N. (2017). "Distribution system monitoring by using micro-pmu in graph-theoretic way," in 2017 4th International Conference on Advances in Electrical Engineering (ICAEE), 159–163. doi:10.1109/ICAEE.2017.8255346

Tang, Z., Yang, Y., and Blaabjerg, F. (2022). Power electronics: The enabling technology for renewable energy integration. *CSEE J. Power Energy Syst.* 8, 39–52. doi:10.17775/CSEEJPES.2021.02850

Wang, X., Luo, X., Zhang, M., Jiang, Z., and Guan, X. (2020). Detection and isolation of false data injection attacks in smart grid via unknown input interval observer. *IEEE Internet Things J.* 7, 3214–3229. doi:10.1109/JIOT.2020.2966221

Wang, R., Sun, Q., Sun, C., Zhang, H., Gui, Y., and Wang, P. (2021). Vehicle-Vehicle Energy Interaction Converter of Electric Vehicles: A Disturbance Observer Based Sliding Mode Control Algorithm. *IEEE Trans. Veh. Technol* 70, 9910–9921. doi:10.1109/TVT.2021.3105433

Xu, Y., Guo, Q., Sun, H., and Fei, Z. (2019). Distributed discrete robust secondary cooperative control for islanded microgrids. *IEEE Trans. Smart Grid* 10, 3620–3629. doi:10.1109/TSG.2018.2833100

Yang, D., Qin, J., Pang, Y., and Huang, T. (2022). A novel double-stacked autoencoder for power transformers dga signals with an imbalanced data structure. *IEEE Trans. Ind. Electron.* 69, 1977–1987. doi:10.1109/TIE.2021.3059543

Zeng, W., and Chow, M.-Y. (2014). Resilient distributed control in the presence of misbehaving agents in networked control systems. *IEEE Trans. Cybern.* 44, 2038–2049. doi:10.1109/TCYB.2014.2301434

Zhang, R., Xiao, G., Shan, Q., Zou, T., Li, D., and Teng, F. (2022). Communication topology reconstruction method for multi-agent cooperative control in polymorphic networks. *J. Commun.* 43, 50–59. doi:10.11959/j.issn.1000436x.2022077

Zhou, J., Sun, H., Xu, Y., Han, R., Yi, Z., Wang, L., et al. (2021a). Distributed power sharing control for islanded single-/three-phase microgrids with admissible voltage and energy storage constraints. *IEEE Trans. Smart Grid* 12, 2760–2775. doi:10.1109/TSG.2021.3057899

Zhou, J., Xu, Y., Sun, H., Li, Y., and Chow, M.-Y. (2020). Distributed power management for networked ac–dc microgrids with unbalanced microgrids. *IEEE Trans. Ind. Inf.* 16, 1655–1667. doi:10.1109/TII.2019.2925133

Zhou, Q., Shahidehpour, M., Alabdulwahab, A., Abusorrah, A., Che, L., Liu, X., et al. (2021b). Cross-layer distributed control strategy for cyber resilient microgrids. *IEEE Trans. Smart Grid* 12, 3705–3717. doi:10.1109/TSG.2021.3069331

Zuo, S., and Yue, D. (2022). Resilient containment of multigroup systems against unknown unbounded fdi attacks. *IEEE Trans. Ind. Electron.* 69, 2864–2873. doi:10.1109/TIE.2021.3066941

Zuo, S., Lewis, F. L., and Davoudi, A. (2020). Resilient output containment of heterogeneous cooperative and adversarial multigroup systems. *IEEE Trans. Autom. Contr.* 65, 3104–3111. doi:10.1109/TAC.2019.2947620

frontiers | Frontiers in Energy Research

TYPE Original Research
PUBLISHED 17 August 2022
DOI 10.3389/fenrg.2022.962361

OPEN ACCESS

EDITED BY
Xiao Wang,
Wuhan University, China

REVIEWED BY
Hua bao,
Anhui University, China
Jiaqiang Tian,
Xi'an University of Technology, China
Ping Yang,
Southwest Jiaotong University, China

*CORRESPONDENCE
Hongming Yang,
yhm5218@163.com

SPECIALTY SECTION
This article was submitted to Smart Grids,
a section of the journal
Frontiers in Energy Research

RECEIVED 06 June 2022
ACCEPTED 12 July 2022
PUBLISHED 17 August 2022

CITATION
Xiang S, Yang H and Cao B (2022), An evaluation of domestic electric water heaters for frequency control.
Front. Energy Res. 10:962361.
doi: 10.3389/fenrg.2022.962361

An evaluation of domestic electric water heaters for frequency control

Sheng Xiang[1], Hongming Yang[1]* and Bo Cao[2]

[1]International Joint Laboratory of Energy Internet Operation and Planning Based on Distributionally Photovoltaic Storage Energy, Hunan International Joint Laboratory of Internet-based Energy Storage, Hunan Provincial Engineering Research Center of Electric Transportation and Smart Distribution Network, School of Electrical and Information Engineering, Changsha University of Science and Technology, Changsha, China, [2]Department of Electrical and Computer Engineering, University of New Brunswick, Fredericton, NB, Canada

Maintaining the frequency of a power system close to its nominal value (50 Hz or 60 Hz) is critical, which comes mainly from generators and flexible loads in traditional power systems. Direct load control (DLC) is a method to control controllable loads for power system optimization. In general, it is used to reduce or shave peak demand. Nonetheless, DLC also can be used to provide frequency control services. Domestic electric water heater (DEWH) is an important kind of controllable load, which takes a high percentage of domestic electric power consumption and has a large thermal energy storage capacity. Hence, DEWH can be a prime candidate for DLC. This study proposes a framework to provide frequency control service with DEWHs. A virtual battery pack system (VBPS) is introduced to be equivalent to the capacity of DEWHs, and a series of measurable indicators are proposed to show the capacity of the VBPS when providing frequency control services. An adaptive criterion is applied to classify controllable DEWHs, which helps to maintain end-user comfort. The performances of the proposed frequency control method during normal and contingency conditions are verified through case studies in CYME.

KEYWORDS

frequency control, direct load control, domestic electric water heater, virtual battery pack system, end-user comfort

1 Introduction

With the development of technology, more and more electrical devices are being applied to improve our daily life. However, the total electric power demand and demand variations are increasing, and the pressure on power systems is increasing too. At the same time, renewable energy plants are increasing, e.g., the U.S. will generate 20% of the nation's electricity from wind energy by 2030 (Lindenberg et al., 2008). The large-scale utilization of renewable energy benefits power systems and the environment. However, the fluctuation of renewable energy occurs frequently, which will increase the pressure on power systems. Hence, more ancillary services are required in power systems, which are

necessary to support the transmission of capacity and energy from resources to loads while maintaining reliable operation.

There are many kinds of ancillary services, such as the regulation reserve, load following, spinning reserve, and nonspinning reserve, (Hao et al., 2013; Liu et al., 2000; Meyn et al., 2015; Zhang et al., 2022). These ancillary services can be divided into two groups: the first group contains ancillary services for normal conditions, such as the regulation reserve and load following, and the second group contains ancillary services for contingency conditions, such as the spinning reserve, nonspinning reserve, and replacement reserve.

Power system frequency reflects the balance between the generation and demand, it will keep the nominal value (50 Hz or 60 Hz) when the balance is maintained. The frequency will drop when the generation becomes lower than the load demand, and vice versa. In normal conditions, the balance between generation and demand is maintained, and the frequency is close to its nominal value. The frequency should be recovered to its nominal value after contingency events with frequency control.

In traditional power systems, the frequency control services are provided by generators and flexible loads, and it requires additional costs for these services. In practice, generators are not working under full-power output, the residue capacity is used to provide these reserves. With a fixed number of generators, the total rated output power is fixed; when power demand is increasing, the generation should be increasing accordingly. Hence, the residue capacity is decreasing; in other words, the capacity of frequency control service is decreasing. However, when power demand is increasing, the required reserve capacity is increasing too. As a result, more generators are required, which will increase the construction, operation, and maintenance costs. Moreover, due to the demand variations, we cannot take full advantage of all generators, which will cause a lot of waste. Furthermore, generators provide frequency control services, and more capacity is required than the generation requirement. For example, when power systems make a generation schedule, the total capacity of online generators should meet the peak demand when the maximum generator is lost. This is a constraint that limits the capacity of online generators. As a result, there are some drawbacks to conventional generator frequency control services.

When frequency control services are provided by flexible loads, the loads in power systems can be divided into three levels: The first level is the most important load; outages will cause serious accidents and losses. The second level is less important, but outages will cause some economic losses. The third level, such as residential loads, is the first to be reduced when power system generation cannot meet the load demand, but it will have an impact on the comfort of the end-user. Overall, traditional frequency control resources have extra economic costs or affect the comfort of the end-user, and then, new resources are required.

Direct load control (DLC) regulates power demand by remotely activating or shutting down controllable loads/devices (Ericson, 2009; Gomes et al., 2007; Zhang et al., 2017; Zhang et al., 2018). It can be used not only to reduce or alter peak demand but also to provide ancillary services (Wang et al., 2017; Solanki et al., 2017; Al-jabery et al., 2017). Controllable loads should have energy storage capacity so that end-user comfort can be maintained when these loads are interrupted. These controllable loads are frequently used, and they occupy a large part of the demand for supply systems. Domestic electric water heater (DEWH) is a kind of important component of controllable loads. It has a large energy storage capacity, and it also takes up a large part of overall power consumption: 18% in the U.S. (Government of Canada, 2018), 19% in Canada (Nehrir et al., 1999), and approximately 30% domestically (Kondoh et al., 2011). The mechanism of DEWH is as follows: when the temperature of the DEWH meets its lower limit, the local thermostat turns on, and the DEWH turns on; when the temperature of the DEWH meets its upper limit, the local thermostat turns off, and the DEWH turns off; for other situations, the local thermostat maintains its previous state. A remotely controllable relay is used to control a DEWH. It can be turned off to turn off the DEWH when it is on, and the DEWH will be turned on again when the remote relay turns back; the relay cannot turn on the DEWH when its thermostat is off. Hence, the control method is called off-control. It is easy to realize in practice; we had applied it in our lab and projects.

There has some literature about controllable loads to provide ancillary services. As Lu (2012) described the potential for regulation service by water heaters, the characteristics of water heaters are not considered. In Hao et al. (2013) and Kirby et al. (2008), ancillary services are provided by heating ventilation air conditioning systems. A hotel load response for the spinning reserve is introduced in (Mathieu et al., 2015). The benefits potential of residential loads to provide ancillary services in California is shown in Vrettos (2016). Fridges and freezers were employed to collectively provide second-by-second electricity balancing (Webborn, 2019). In Biegel et al. (2013), these on-off loads were controlled when the frequency thresholds were exceeded and then the primary frequency control services were provided. Literature (Kasis et al., 2020) proved that secondary frequency control services could be provided too. Overall, DLC provides additional ancillary services, which may be an attractive option for power systems. However, obtaining end-user permission will require maintaining their comfort during DLC, which is not described in those studies. The main objective of this research is to propose a framework to provide frequency control services with DEWHs and maintain end-user comfort without temperature information.

The contributions of this study can be summarized as follows:

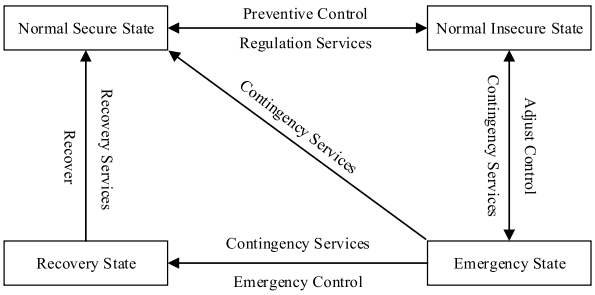

FIGURE 1
Power systems operation states and required services.

1) A virtual battery pack system (VBPS) is introduced as a centralized controller for DEWHs, and several indicators are employed to show the frequency control ability of the VBPS. DEWHs in the VBPS can be divided into four groups. Different groups are selected for control in different cases based on the estimated controllable abilities of DEWHs.
2) An adaptive parameter, AEL_{adapt}, is proposed to make the average temperature of DEWHs close to the lower limit: a). For ramp-up, the AEL_{adapt} is increased from the tolerance value to 0, which helps to make the DEWHs whose temperatures are lower than their lower limits can be heated as much as possible, following the increasing order of their estimated available energy levels. b). For ramp-down, the AEL_{adapt} is decreased from 0 to the tolerance value, which helps to keep more DEWHs on heating, following the decreasing order of their estimated available energy levels.
3) The end-user comfort is maintained in the proposed control method; whenever the estimated AEL is lower than the tolerance value, the DEWH is turned on and cannot be turned off until the AEL reaches 0.

The article is made up of five sections. Detailed analysis of the frequency control is provided in Section II. Section III presents the VBPS and objective functions for frequency control. Some case studies are provided in Section IV. Some conclusions, finally, are shown in Section V.

2 Frequency control

When all loads in a power system can be supplied by existing generators without violating any operation constraints, the power system is operated in a normal state. When the system remains in a normal state after critical unforeseen events, the power system is secure and operates in a normal safe state. Otherwise, when the balance between generation and demand is maintained, all operating inequality constraints are satisfied. However, the response to some considered contingencies is vulnerable, the power system is operating in a normal insecure state. Preventive control is required to prevent the power system from going into an emergency state. If there has a violation of any operating constraints in the power system, the power system is operating in an emergency state, and contingency services are required to correct and bring the power system into a normal state immediately. As the result of corrective control measures on the power system to avoid system collapse, the operating limit violations may be eliminated, and the system may recover stability with reconfigured topology and restore the balance between generation and demand, the power system is operating in a recovery state. The state diagram in Figure 1 illustrates the transitions between different states and necessary services.

Frequency control services are required to maintain the frequency throughout the power systems to its nominal value in all the states. The frequency is affected by active power. There are three kinds of frequency control services in the power system: primary, secondary, and tertiary control (Hui et al., 2017). Considering the communication delays, only the secondary frequency control is provided in this study. The secondary frequency control is a centralized controller that restores the frequency to its nominal value and maintains the desired exchanges between neighboring control areas. It is activated from 30 s to 15 min (Hui et al., 2017; Stephen, 2012). In this study, the frequency controls services are provided in 1 min.

The ancillary services for frequency control can be divided into two groups: for normal conditions, such as the regulation service and load following; for contingency conditions, such as spinning, nonspinning reserve, and replacement reserve (Meyn et al., 2015; Hui et al., 2017).

2.1 Frequency control during normal conditions

When the balance between generation and demand is maintained, and the inequality constraints are afforded, the power system is in its normal state. Regulation reserve is automatically provided by online resources (generators or flexible loads), and its goal is to correct the minute-to-minute deviations between the generation and demand, under normal conditions. The minimum bid size in Pennsylvania, Jersey, and Maryland Power Market is 100 kW (Hui et al., 2017; PJM Manual, 2019) and is typically in the range of 1–10 MW (Webborn, 2019; Nousios and Aebi, 2022). The control signal is typically the output of a proportional-integral controller with the area control error as an input.

Load following is similar to the regulation service, but it has a slower ramp rate and fewer sign changes per unit time. It is used

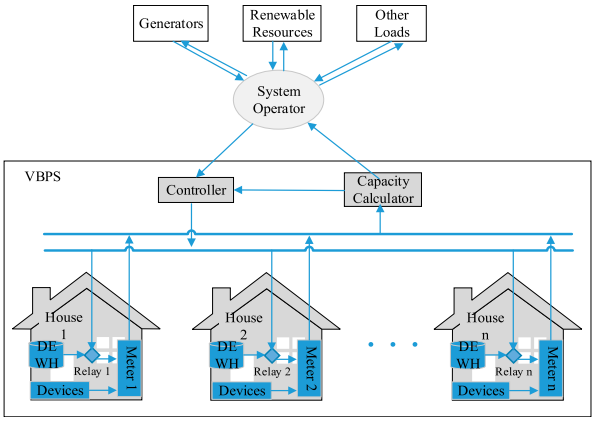

FIGURE 2
Framework of the virtual battery pack system (VBPS) that provides frequency control in the power system.

to bridge the gap between the hourly energy markets and frequency regulation. It is still under normal conditions, and it can be manually activated. When a power system with load follows, the frequency regulation signal is usually unrelated and crosses zero frequently (NERC, 2011).

2.2 Frequency control during contingency conditions

When there are some disturbances in power systems, such as transmission faults, and generator losses, the stability of power systems will be affected. Contingency services are required to keep power systems stable under those situations.

Spinning reserve is provided by online generators that are not fully loaded or online loads in response to the disturbances immediately. In other words, it changes the generation or loads to response disturbances. As per the North America Reliability Corporation (NERC) disturbance standard, Spinning reserve is available within 10 min and can be maintained for 10–120 min (Pijnenburg et al., 2016). It is typically activated automatically using an automatic generation control (AGC) signal.

The nonspinning reserve is similar to the spinning reserve. The main difference is that the nonspinning reserve does not need to respond immediately. The resources can be offline but still must be capable of reaching full output within the required 10 min (Paull et al., 2010). Nonspinning reserve is typically dispatched using an AGC signal.

Some regions specify a third contingency reserve called replacement reserve. Online generators, offline generators, and responsive loads can provide this kind of reserve, which can be capable of sustaining response for 2–4 h. It is a type of tertiary control reserve.

Of course, load shedding is the last choice for power systems when the frequency decline cannot be arrested through the above actions. Loads are tripped off to maintain power system stability.

No matter what kind of contingency services resources, the required response speed is from seconds to no more than 10 min. All in all, contingency services restore the generation/load balance after a short time when the sudden unexpected loss by change generation or loads.

3 Virtual battery pack system for frequency control

It is obvious that decreasing the loads is equivalent to increasing generation, and vice versa. This is the basic theory for DLC to provide ancillary services. A DEWH is similar to a battery. When the DEWH gets energy from power systems, it is equivalent to the charging process of the battery. When the DEWH is controlled to reduce its electricity consumption, it is equivalent to the discharging process of the battery. The difference between a DEWH and a battery is the thermal energy stored in the DEWH can be consumed through hot water consumption. In this study, we use a VBPS to represent a DEWHs system. Figure 2 shows the framework of the VBPS to provide frequency control services for the power system.

DEWHs' states can be identified from smart meters. When the power ramp-up/down value is equal to the rated power of the DEWH, the state of the DEWH turns on/off respectively (Xiang et al., 2020; DeOreo and Mayer, 2000). All the control actions are applied through additional relays; it is called off-control. Considering the available control actions require communication times, it is not realistic to provide the primary frequency control. Hence, we discuss the VBPS providing the secondary frequency control in this study. The capacity of the VBPS is sent to the system operator (SO). Then, an objective will send to the controller to select control actions.

Based on the continuous-time state space model of air conditioners (Lu, 2012), the DEWH can be written as follows:

$$\dot{T}(t) = AT(t) + BU(t) + CU_1(t) \tag{1}$$

$$A = -\frac{A_s}{c\rho V_{tank} R}$$

$$B = \begin{bmatrix} \frac{T_{in}}{V_{tank}} & \frac{A_s}{c\rho V_{tank} R} & m(t)P \end{bmatrix}$$

$$C = -\frac{1}{V_{tank}} \tag{2}$$

$$U(t) = \begin{bmatrix} V(t) \\ T_{am}(t) \\ m(t) \end{bmatrix}$$

$$U_1(t) = V(t)$$

TABLE 1 Available control signals.

Condition	Signal	Thermostat	Relay	$T \geq T_{tole}$
1	On	Off	On	Y
2	On/Off	On	On	Y
3	On	On	On	N
4	On/Off	On	Off	Y
5	On	On	Off	N

Y means true, N means false, and T_{tole} is the tolerance temperature to maintain end-user comfort.

where $T(t)$ is the temperature of DEWH, A_S is the surface area of DEWH, R is the thermal resistance of the insulation material, c is the specific heat capacity of water, ρ is the density of water, V_{tank} is the tank volume, T_{in} is the temperature of inlet cold water, p is the rated power of DEWH, $V(t)$ is the volume of consumed hot water, T_{am} is the ambient temperature around DEWH, and $m(t)$ is the state of DEWH, $m(t) \in [0, 1]$.

The state of DEWH is decided by its internal thermostat state ($Thm\ (t)$) and relay state ($R\ (t)$).

$$m(t) = R(t) \cdot Thm(t) \tag{3}$$

The relay state is controlled by control actions. The internal thermostat state follows a mechanical mechanism: if the temperature reaches its upper limit (TH), the thermostat state turns "*off*"; if the temperature reaches its lower limit (TL), the thermostat turns "*on*"; otherwise, the previous state is maintained. The thermostat state can be written as follows:

$$Thm(t) = \begin{cases} 1, & T(t) < TL \\ 0, & T(t) > TH \\ Thm(t-1), & otherwise \end{cases} \tag{4}$$

The input for the DEWH is its relay state $R(t)$, then rewrite 1) as follows:

$$\dot{T}(t) = A'(t) \cdot T(t) + B' \cdot U'(t) + C'(t) \cdot D'(t) \tag{5}$$

where the state is $T(t)$, the input is $U(t)$, and $D(t)$ is the disturbance as follows:

$$\begin{cases} A'(t) = -\dfrac{A_S}{c\rho V_{tank} R} - \dfrac{1}{V_{tank}} V(t) \\ B'(t) = Thm(t) P \\ U'(t) = R(t) \\ C'(t) = \begin{bmatrix} \dfrac{T_{in}}{V_{tank}} & \dfrac{A_S}{c\rho V_{tank} R} \end{bmatrix} \\ D'(t) = \begin{bmatrix} V(t) \\ T_{am}(t) \end{bmatrix} \end{cases} \tag{6}$$

With a first-order Euler discretization, the discrete time model maintains the structure of the continuous-time matrices and can be written as follows:

$$T_{k+1} = \left(I + \Delta t A'(t)\right) T_k + \Delta t B' U'(t) + \Delta t C'(t) D'(t) \tag{7}$$

where Δt is the time interval.

Furthermore, the output of the state space model is the total consumed electric power as follows:

$$Y(k) = Pm(k) \tag{8}$$

To maintain end-user comfort, these available control actions are shown in Table 1. It is obvious that when DEWHs in condition 2 get "*off*" signals, the demand is reduced; it is equivalent to the discharging process of the VBPS. Nevertheless, these DEWHs in condition 5 should be turned back and increase demand. The available discharging rate of the VBPS is decided by the number of DEWHs in conditions 2 and 5. The discharging rate should be as follows:

$$\begin{aligned} &0 \leq P_{dis}(t) \leq maxP_{dis}(t) \\ &maxP_{dis}(t) = \sum_{j=1}^{k2(t)} P_{j,rated} - \sum_{i=1}^{k5(t)} P_{i,rated} \end{aligned} \tag{9}$$

where $k_2(t)$ and $k_5(t)$ are the total number of DEWHs in conditions 2 and 5 at time t, respectively.

The available charging rate of the VBPS is decided by the number of DEWHs, the thermostats of which are "*on*." The charging rate can be as follows:

$$\begin{aligned} &0 \leq P_{cha}(t) \leq maxP_{cha}(t) \\ &maxP_{cha}(t) = \sum_{i=1}^{N} P_{i,rated}(t) Thm_i(t) - P_{base}(t) \end{aligned} \tag{10}$$

where N is the total number of DEWHs in the VBPS and P_{base} is the demand of the baseline.

In practice, it is hard to measure the DEWH's temperature. In our previous control algorithm (Xiang et al., 2020), we can control DEWHs without temperature measurements and maintain end-user comfort. In Eqs. 6 and 7, it is clear that the disturbances that affect the DEWH's temperature are the ambient temperature and draw-out hot water. With the analysis of hot water consumption activities and their probabilities, the disturbances in the worst cases can be easily presented as that in Xiang et al. (2020). Then, the estimated temperature of the DEWH in the worst case will be calculated. The available energy level, AEL, was employed to show the control ability of the DEWH, which can be expressed as follows:

$$AEL = \frac{T - TL}{TH - TL} \tag{11}$$

where T is the temperature of the DEWH (estimated by Eq. 7) and TH and TL are the upper and lower limits. $AEL > 0$ indicates the DEWH's temperature is higher than the lower limit and vice versa. The tolerance value of the available energy level can be obtained by letting the tolerance temperature into Eq. 11.

It is obvious that the maximum discharging rate and the maximum charging rate vary with the number of DEWHs in each condition, which is decided by the tolerance temperature;

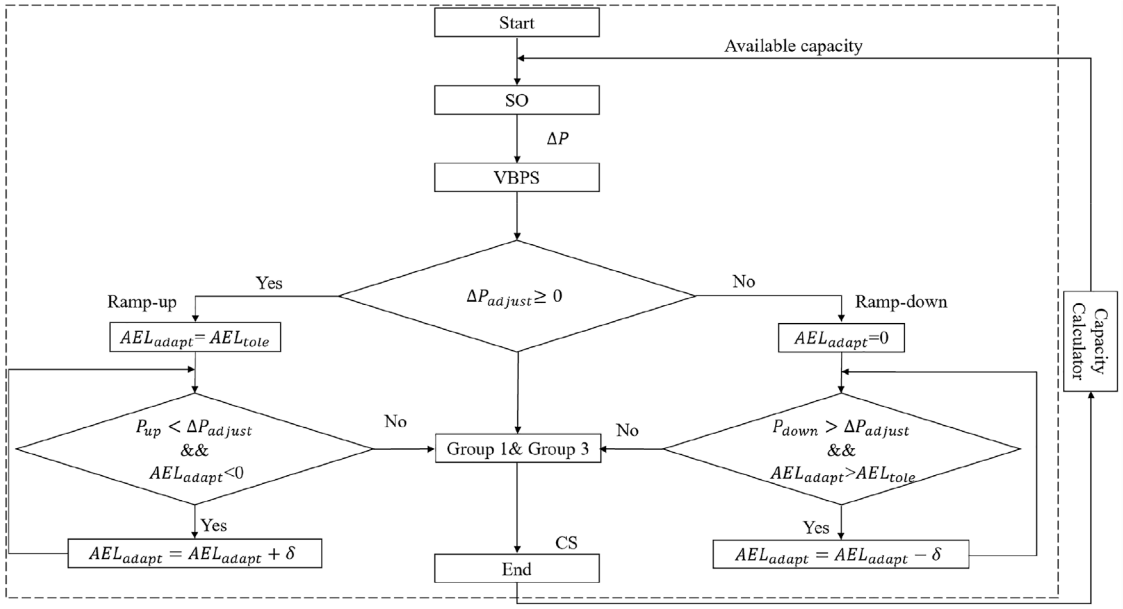

FIGURE 3
Schematic representation of the VBPS that provides ancillary services.

Algorithm

Do

Step 1: Get the desired correcting power $\Delta P(t)$ from the SO.

Step 2: Adjust the adjusted power $\Delta P_{adjust}(t)$.

Step 3: If $\Delta P_{adjust}(t) \geq 0$, go to Step 3.1; else, go to Step 3.2.

Step 3.1: Set initial AEL_{adapt} as AEL_{tole}.

a). Calculate the increased power, P_{up}.

b). If $P_{up} < \Delta P_{adjust}(t)$ & $AEL_{adapt} < 0$, update AEL_{adapt}, repeat a); else, go to c).

c). Generate control signals for these DEWHs with $AEL \leq AEL_{adapt}$, then go to Step 4.

Step 3.2: Set initial AEL_{adapt} as zero.

a). Calculate the decreased power, P_{down}.

b). If $P_{down} > \Delta P_{adjust}(t)$ & $AEL_{adapt} > AEL_{tole}$, update AEL_{adapt}, go to a); else, go to c).

c). Generate control signals for these DEWHs with $AEL \leq AEL_{adapt}$, then go to Step 4.

Step 4: Select DEWHs for control.

Step 5: Apply control actions to the VBPS; calculate and send the available capacities.

End

FIGURE 4
Pseudocode of proposed algorithm.

hence, with the changing of the tolerance temperature, the two parameters can be changed.

Similar to the description above, the primary frequency control will let the frequency be in an acceptable range; then, the secondary frequency control through VBPS will let the frequency be maintained at its nominal value. The flow chart of the proposed method is shown in Figures 3 and 4, which is the pseudocode. The details are as follows:

Step 1. Get $\Delta P(t)$ from the SO;

Step 2. Generate $\Delta P_{VBPS}(t)$

$$\Delta P_{adjust}(t) = -\Delta P(t) - \sum_{j=1}^{k3(t)} P_{j,rate} \tag{12}$$

where $k_3(t)$ is the total number of DEWHs in condition 3.

Then, adjust it with the constraint of the VBPS:

$$\Delta P_{adjust}(t) = \begin{cases} -maxP_{dis}(t), \ when\ \Delta P_{adjust}(t) < -maxP_{dis}(t) \\ maxP_{cha}(t), \ when\ \Delta P_{adjust}(t) > maxP_{cha}(t) \\ \Delta P_{adjust}(t) \end{cases} \tag{13}$$

Step 3. If $\Delta P_{adjust} \geq 0$, the VBPS power should be increased, and the VBPS should match the unbalance by charging. Then, proceed to Step 3.1; otherwise, if the VBPS should be discharged, proceed to Step 3.2.

Step 3.1. Set the initial value of the adaptive AEL_{adapt} as the tolerance value AEL_{tole}.

a) Calculate the increased power, P_{up}, which is the total demand of DEWHs with relays that are off and $AEL_{tole} \leq AEL \leq AEL_{adapt}$.

$$P_{up} = sum\Big(\boldsymbol{P}.*\big((\boldsymbol{AEL} \geq AEL_{tole})\&\big(\boldsymbol{AEL} \leq AEL_{adapt}\big)\&(\boldsymbol{RS} == 0)\big)\Big) \tag{14}$$

where $\boldsymbol{P} = [P_{rate,1}, P_{rate,2}, \ldots, P_{rate,N}]^T$ is the set of the rated powers of each DEWH and N is the number of DEWHs in the VBPS; $\boldsymbol{RS} = [RS_1, RS_2, \ldots, RS_N]^T$ is the set of the relay state of each DEWH; $\boldsymbol{AEL} = [AEL_1, AEL_2, \ldots, AEL_N]^T$ shows the AEL of each DEWH.

b) If $P_{up} < \Delta P_{adjust}(t)$ and $AEL_{adapt} < 0$, update AEL_{adapt} to increase P_{up}.

$$AEL_{adapt} = AEL_{adapt} + \delta \tag{15}$$

where δ is a default value.

If $P_{up} \geq \Delta P_{adjust}(t)$ or $AEL_{adapt} = 0$, go to c).

c) Select the DEWHs of which relays are off and their $AELs$ between AEL_{tole} and AEL_{adapt}. These DEWHs are candidates for on signals. Two kinds of controllable DEWHs are classified: 1). DEWHs in which relays are off and AELs are higher than AEL_{adapt}, and 2). DEWHs of which relays are on and AELs between *0* and *1* (Group 1). An objective for the two kinds of DEWHs is calculated using Eq. 16 and then go to Step 4

$$P_{obj}(t) = \Delta P_{adjust}(t) - P_{up} \tag{16}$$

Step 3.2. Decrease the VBPS power to respond to a negative $\Delta P_{adjust}(t)$. At first, the initial value of the adaptive AEL_{adapt} is set as 0.

a) Calculate the decreased power P_{down}, which consists of two parts and can be written as follows:

$$P_{down} = -P_1 + P_{up} \tag{17}$$

where P_1 is the power of these DEWHs with relays that are on and AELs that are not negative (Group 1). It can be expressed as follows:

$$P_1 = sum(\boldsymbol{P}.*((\boldsymbol{AEL} \geq 0)\&(\boldsymbol{AEL} < 1)\&(\boldsymbol{RS} == 1))) \tag{18}$$

b) If $P_{down} > \Delta P_{adjust}(t)$ and $AEL_{adapt} > AEL_{tole}$, decrease the AEL_{adapt} to reduce the increased power P_1 with the following:

$$AEL_{adapt} = AEL_{adapt} - \delta \tag{19}$$

If $P_{down} \leq \Delta P_{adjust}(t)$ or $AEL_{adapt} = AEL_{tole}$, proceed to 3.1. c).

Step 4. Generate control signals for the controllable DEWHs. If $P_{obj}(t) \geq 0$, the power of these DEWHs should be increased; proceed to Step 4.1; otherwise, if the power should be decreased, proceed to Step 4.2.

Step 4.1. If $P_{obj}(t) \geq 0$, more DEWHs should be sent on signals to increase the VBPS power. These DEWHs with relays that are off and AELs are higher than AEL_{adapt} are sorted in descending order by their AELs. The objective function is as follows:

$$\begin{aligned} &min\left|P_{obj}(t) - \sum_{i=1}^{w1(t)} P_{rate,i} CS_i\right| \\ &s.t. \begin{cases} if\ CS_{i-1} = 1,\ CS_i = 1 \\ if\ CS_{i-1} = 0,\ CS_i = 0\ or\ 1 \end{cases} \end{aligned} \tag{20}$$

where *w1* is the number of DEWHs in the descending order and *i* means the i^{th} DEWHs and *CS* are the control signals for the DEWHs in the VBPS.

Step 4.2. If $P_{obj} < 0$, more DEWHs should receive off-signals to decrease the VBPS power. These DEWHs with relays that are on and $AEL > 0$ are selected for control (DEWHs in condition 1) are sorted in ascending order by their AELs.

$$min\left|P_{obj}(t) + \sum_{j=1}^{k1(t)} P_{rate,i}(1 - CS_i)\right|$$
$$s.t.\begin{cases} if\ CS_{i-1} = 0,\ CS_i = 0 \\ if\ CS_{i-1} = 1,\ CS_i = 0\ or\ 1 \end{cases} \quad (21)$$

where $k1$ is the number of DEWHs in the ascending order.

Step 5. Execute control signals on the VBPS.

In this control algorithm, the *AEL* of each DEWH is generated by the estimated temperature. The temperature is estimated based on the disturbances under the worst cases, which ensures that the estimated temperature is lower than the actual temperature. The DEWH with *AEL* lower than the tolerance value is kept heating to avoid its *AEL* dropping too low, which ensures that the temperature is not too low to affect the end-user comfort. Furthermore, the AEL_{adapt} allows more DEWHs with *AELs* that are negative to be turned on and DEWHs with *AELs* that are positive and large to be turned off. Therefore, the temperature of DEWHs should be closer to the lower limit to maintain end-user comfort.

3.1 Virtual battery pack system provides frequency control services during normal condition

When the VBPS provides regulation service, its demand can be as follows:

$$\Delta P(t) = P_{base}(t) + w_t P_{reg}(t) \quad (22)$$

where $w_t \in [-1, 1]$ is the normalized regulation control signal and P_{reg} is the regulation capacity of the VBPS.

The regulation capacity P_{reg} cannot be a boundless, arbitrary value. It is based on the baseline, and it is expected that the regulation capacity is at its maximum value to obtain the highest income. In general, the up/down capacity should be equal, and the regulatory capacity of an hour can be written as follows:

$$P_{reg}(t) = \min(maxP_{dis}(t), maxP_{cha}(t)) \quad (23)$$

As the hourly regulation reserve bid for the power market is preprovided, the maximum charging and maximum discharging rate should be forecasted. In the discrete time model (5), the disturbance parameters include hot water consumption *V(t)* and ambient temperature $T_{am}(t)$. The ambient temperature can select the temperature of the same time on the similar weather of the same season. The hot water consumption can use the average value of the hot water consumption patterns, which can be obtained by using statistical data (Mayer and DeOreo et al., 1999; Zhao et al., 2022). Then, taking the baseline as an objective with our previous control algorithm, the maximum charging, and discharging rate can be generated, with (13), selecting the hourly regulation reserve to bid in the power market.

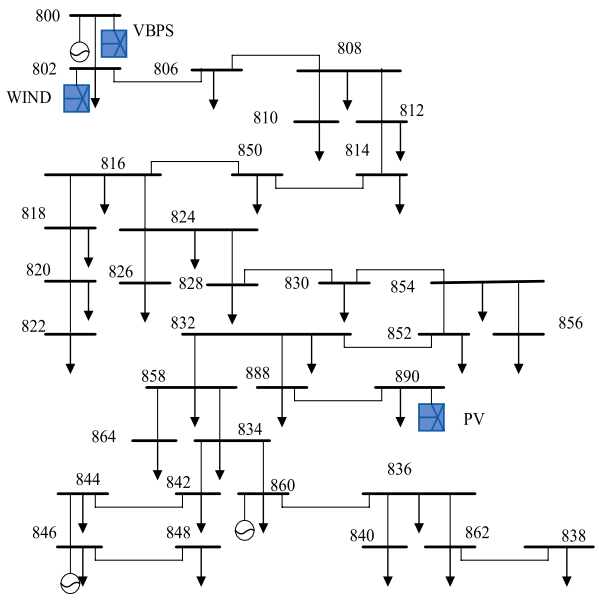

FIGURE 5
Diagram of IEEE 34-bus system.

Nowadays, the increasing use of renewable energy as an alternative to fossil fuels is a general trend that has a benefit for the environment. However, due to the randomness of weather, cloud, wind, etc., the generation from renewable resources is varied, which will increase the pressure on power systems to maintain the balance between generation and demand. In general, it can be defended by storage devices or regulation reserves (Chau et al., 2018; Mahdavi et al., 2017). Through charging and discharging, the VBPS can match the fluctuation and maintain the balance between generation and demand.

3.2 Virtual battery pack system provides contingency reserve

When a disturbance is occurring, generation or demand will be changed, and the VBPS will provide the capacity to match the variation. When generators are lost due to the disturbance, the VBPS will be discharged to match the generation decrease; when loads are lost due to the disturbance, the VBPS will be charged to match the load decrease. The contingency reserve can be provided before the VBPS capacity is used up; with our previous control method, the sustainable time is long enough to meet the requirement of the contingency reserve.

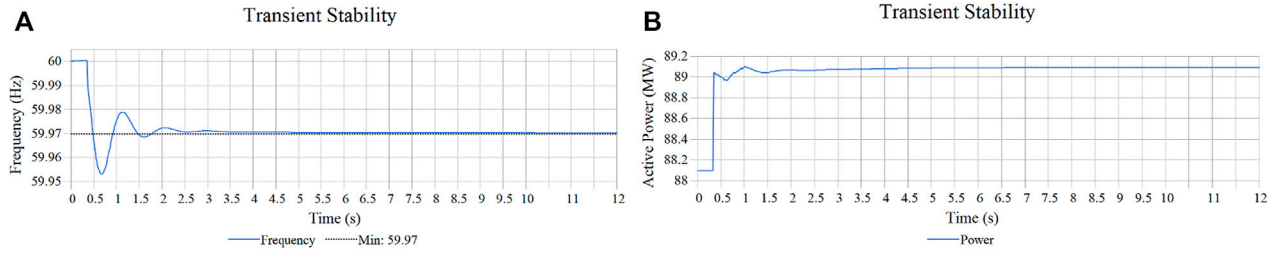

FIGURE 6
(A) Frequency without the VBPS in CYME, **(B)** Power generation without the VBPS in CYME.

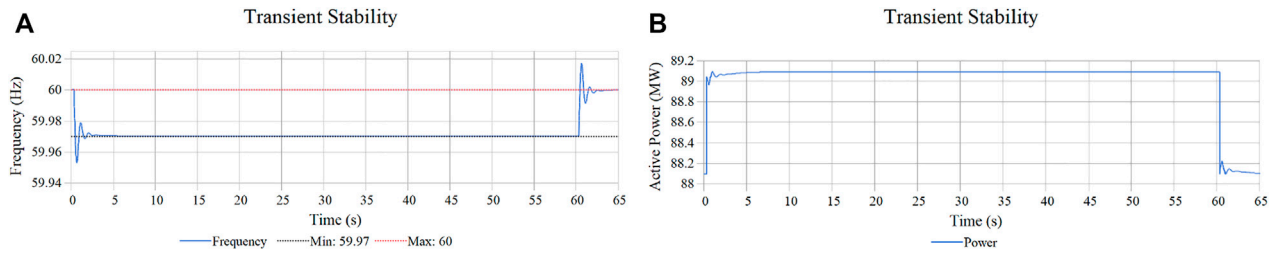

FIGURE 7
(A) Frequency with the VBPS in CYME, **(B)** Power generation with the VBPS in CYME.

When the capacities are used up, the VBPS loses the ability for frequency control services. However, with the varying tolerance temperature, the available capacity will increase. With the increasing number of DEWHs in the systems, the capacity can be increased. Moreover, because of the installation of DEWHs diffusely in North America, the expandable capacity is substantial enough. Hence, there is enough available capacity of the VBPS to provide frequency control services.

4 Case studies

A VBPS consists of 20,000 DEWHs, the hot water consumptions are generated from CREST_Demand_Model v2.2 (Richardson et al., 2008). Some case studies are implemented to prove the ability of the VBPS to provide frequency control services with CYME. The test model structure is an IEEE 34-node test feeder (Schneider et al., 2017). It is shown in Figure 5, and load data are 30-min uncertain data downloaded from PJM. The electricity consumption of the VBPS takes 6.4% of the total electricity consumption of the whole test system and approximately the maximum demand of 20% (morning peak). The transient stability analysis tool of CYME power engineering software is used to show the frequency variations, the simulation time step is 0.0167 s. The CYME power engineering software is a suite of applications composed of a network editor, analysis modules, and user-customizable model libraries from which you can choose to get the most powerful solution.

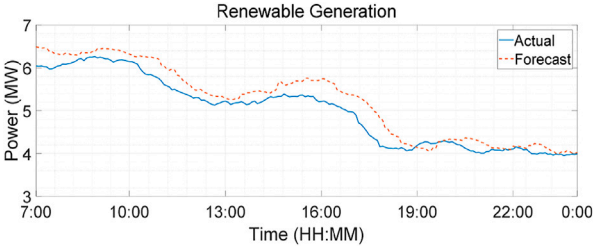

FIGURE 8
Actual and forecast renewable generation.

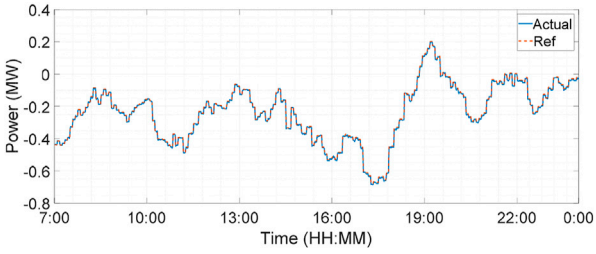

FIGURE 9
Charge/discharge rate of the VBPS.

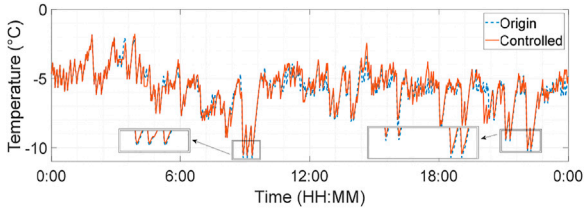

FIGURE 11
Minimum temperature.

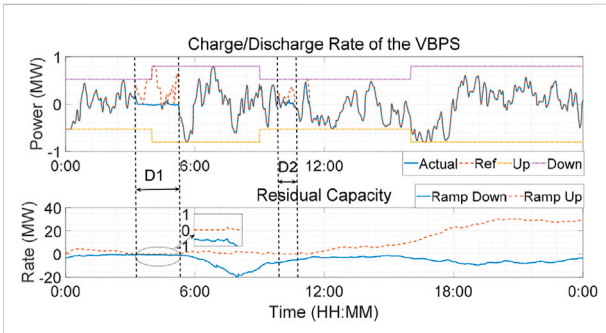

FIGURE 10
Regulation services.

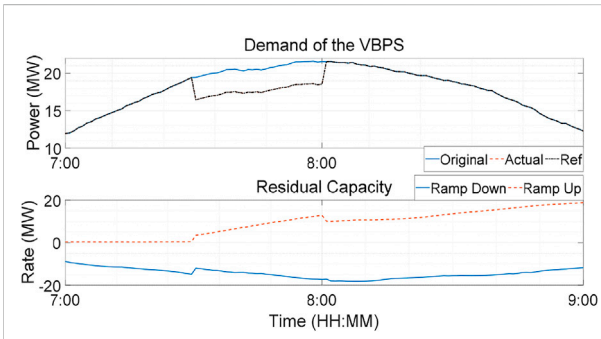

FIGURE 12
Contingency frequency control.

4.1 Normal condition services

4.1.1 Renewable generation variations

When building a generating schedule for generators, the loads and renewable generations will be forecasted. However, there are differences between forecasting values and actual values. Some reserve capacity should be used to match these differences. Figure 6A shows the frequency drop of 0.03 Hz because of a lack of 1 MW renewable generation when there is no secondary frequency control. The generators in the test model will increase generation to recover the lack of renewable generation, which is shown in Figure 6B. In this case, a 1-MW reserve of online generators is used to match the lack of renewable generation, and the power system is still stable. However, the frequency is not at its nominal value.

With the VBPS providing the secondary frequency control services 1-min after the unbalance, the frequency and generation are shown in Figure 7. It is clear that the system frequency is recovered to its nominal value as shown in Figure 7A, B, and the spinning reserve of online generators is recovered too.

Hence, with the VBPS providing the secondary frequency control, the frequency can be maintained at its nominal value, and the capacity of generators can be restored, which will increase the stability for another unbalance.

The VBPS provides the secondary frequency control to match the differences between actual and forecasted renewable generation from 7:00 a.m. to 0:00 a.m. The renewable generation is shown in Figure 8, the actual and forecast generation is not matched, which is normal in practice. With the VBPS to provide secondary frequency control, when the actual generation is less than the forecast value, the VBPS will be discharged, and vice versa. The Ref line in Figure 9 is the objective of the VBPS charge/discharge to defend the frequency variations, and the solid line is the actual charge/discharge rate of the VBPS. The two lines are approximately coinciding.

A metric is selected to present the tracking performance, the root-mean-square (RMS) power tracking error as a percentage of the total steady-state power consumption (Mathieu et al., 2013).

$$RMS = \frac{\sqrt{\frac{1}{L}\sum_{i=1}^{L}\left(P_{actual,i} - P_{Ref,i}\right)^2}}{P_{avg}} \tag{24}$$

where L is the length of the following duration, $P_{actual,i}$ is the actual power demand, $P_{Ref,i}$ is the reference power demand, and P_{avg} is the average actual power demand of this duration. The

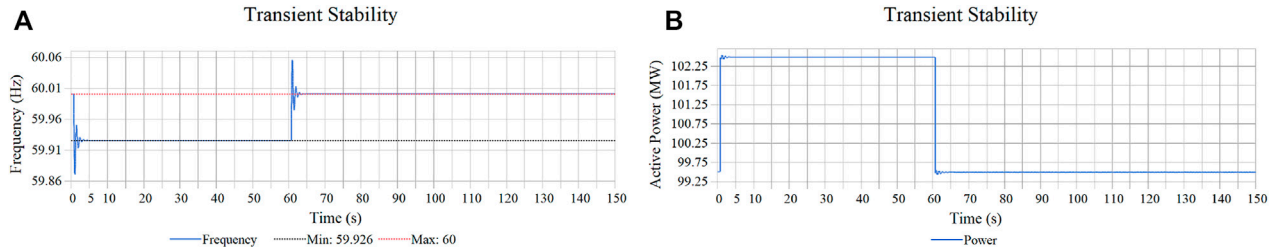

FIGURE 13
(A) Frequency in CYME with a generator loss with the VBPS, **(B)** Power generation in CYME with a generator loss with the VBPS.

RMS is 0.069% in this case; in other words, the error is very small, and the performance is good.

The average price ($/MWh) of regulation services is $15.5/MWh (Hummon et al., 2013); in this case, the VBPS provides approximately 4.2 MWh, and the benefit is approximately 65 $.

4.1.2 Regulation

In general, regulation services are required to correct the minute-to-minute deviations between the generation and demand. For this model, the required regulation service capacities of the test model are 800 kW (4–8 a.m. and 4 p.m. to 0 a.m.) and 525 kW (besides time), as the up and down lines in Figure 10. The case study of the VBPS provides regulation services is carried out, and the regulation test signals are downloaded from PJM.

From Figure 10, for 24 h, besides these durations (D1 and D2 in the figure) when the ramp-up capacity (charging) is used up, the VBPS provides regulation services with a good performance, and the RMS value is 2.1%. The durations D1 and D2 when the ramp-up capacity is used up are because the number of DEWHs in conditions 4 and 5 is 0, and all the relays are on; hence, the available ramp-up capacity is used up. The durations are, fortunately, short, and the available capacity can be extended through increase the capacity of the VBPS. In Figure 10, there still has a lot of available capacity during the evening peak.

The minimum temperatures of the VBPS under the original case and with the proposed method are shown in Figure 11. The adaptive criterion helps to increase the minimum temperature, which benefits the end-user comfort.

The available capacity calculator in Figure 2 is used to send the available capacity to the SO, the SO cannot send the requirement that exceeds the available capacity.

4.2 Contingency response services

As DEWHs can be turned off immediately, the VBPS can be used to respond to contingency events quickly; then, the balance can be maintained.

In general, the start time of generators is approximately 30 min; hence, contingency response resources should provide services for at least 30 min.

The generator on Bus 846 is lost, and the generation loss is 3 MW at 7:30 a.m., with the discharging of the VBPS to maintain the contingency event in 30 min; the VBPS will keep discharging and maintain the system frequency at its nominal value. Figure 12 shows the total demand of the VBPS; during the 30 min, the VBPS discharge in 3 MW matches the lost generation, and the RMS value is 0.01%. The residual available charge/discharge capacity is also shown in Figure 12. It is clear that the VBPS still has enough capacity.

Figure 13A shows the frequency drop of 0.074 Hz when the generation is lost; then, with the VBPS discharge in 3 MW, the balance is recovered, and the frequency backs to its nominal value. Figure 13B shows that the total generation besides the lost generation increases to defend the contingency event with the primary frequency control, and a 3 MW spinning reserve is used. With the VBPS providing secondary frequency control 1 min later, the generation backs to its previous value and the spinning reserve is recovered.

With all the case studies above, the ability of the VBPS to provide frequency control service is excellent, and the benefit is attractive. With the expansion of the VBPS, the available capacity will be more and more. It could be an important frequency control service resource in the future.

5 Conclusion

As an important component of controllable load, DEWHs can be used for peak shaving. It also has a great capacity for ancillary services. In this study, a VBPS is proposed to represent the state and available capacity of DEHWs systems, which will be a virtual unit in power systems. When the system frequency is shifted from its nominal value, a charge or discharge requirement will be sent to the VBPS, then some relays will be turned on or off to respond to the requirement. An IEEE 34 nodes test model is selected to test the performances of the VBPS that provides secondary frequency control services in CYME. Case studies show that with the VBPS providing secondary frequency control services, the system frequency can be maintained at its nominal value. It is obvious that with the VBPS, the reserve capacity of online generators is not consumed, which will increase the stability of power systems or reduce the requirement of these reserves to save money.

The advantages of taking the VBPS as a frequency control services resource include the following: a). The available capacity is large, which is because the thermal storage in a DEWH is large, and it can be turned off without affecting end-user comfort for a long duration; the time duration is related to hot water consumption. b). The system expansion is very easy, which is due to the widespread implementation of DEWHs in North America; the more DEWHs in the VBPS, the more the available capacity. c). The energy stored in the VBPS will be directly used by hot water consumption, which is different from other energy storage devices, such as a battery or flywheel; it does not need to convert the stored energy back into power systems, and the energy loss is less than other storage devices. d). The state of the VBPS can be directly controlled by control signals, and the response speed is quick. Hence, the DEWH system providing frequency control services is a feasible method, and the ability of DEWHs is further excavated.

Data availability statement

The original contributions presented in the study are included in the article/supplementary material; further inquiries can be directed to the corresponding author.

Author contributions

SX designed and wrote this manuscript HY revised this manuscript and will provide the payment BC revised this manuscript.

Acknowledgments

This work was supported in part by the National Natural Science Foundation of China (No. 71931003, No. 72061147004, and No. 72171026), the Science and Technology Projects of Hunan Province under (No. 2019GK5015, No. 2020GK1014, and No. 2021WK2002), the University Industry Collaborative Education Program (No. 202102574001 and No. 202102574005), the Young Talent Project of the Provincial Education Department of Hunan Province (No. 21B0334), the Hunan International Scientific and Technological Cooperation Base of Energy Storage Interconnection (No. 2018WK4010), the Big Data-driven Energy Internet International Science and Technology Cooperation Based of the Ministry of Science and Technology (No.2017D01011).

Conflict of Interest

The authors declare that the research was conducted in the absence of any commercial or financial relationships that could be construed as a potential conflict of interest.

Publisher's note

References

Al-jabery, K., Xu, Z., Yu, W., Wunsch, D. C., Xiong, J., Shi, Y., et al. (2017). Demand-side management of domestic electric water heaters using approximate dynamic programming. *IEEE Trans. Comput. -Aided. Des. Integr. Circuits Syst.* 36 (5), 775–788. doi:10.1109/tcad.2016.2598563

Nousios, D., and Aebi, S. (2022). *Basic Principles of ancillary service products*. Switzerland: Swissgrid Ltd.

Biegel, B., Hansen, L., Andersen, P., and Stoustrup, J. (2013). Primary control by ON/OFF demand-side devices. *IEEE Trans. Smart Grid* 4 (4), 2061–2071. doi:10.1109/tsg.2013.2257892

Chau, T. K., Yu, S. S., Fernando, T., and Iu, H. H. (2018). Demand-side regulation provision from industrial loads integrated with solar PV panels and energy storage system for ancillary services. *IEEE Trans. Ind. Inf.* 14 (11), 5038–5049. doi:10.1109/tii.2017.2782244

DeOreo, W. B., and Mayer, P. W. (2000). *The end uses of hot water in single family homes from flow trace analysis*. California, Hayward: Aquacraft Inc Rep. Undated.

Goverment of Canada (2018). *Energy Use Handbook 1990 to, 2018*. Ottawa, Canada: Natural Resources Canada.

Ericson, T. (2009). Direct load control of residential water heaters. *Energy Policy* 37 (9), 3502–3512. doi:10.1016/j.enpol.2009.03.063

Gomes, A., Antunes, C. H., and Martins, A. G. (2007). A multiple objective approach to direct load control using an interactive evolutionary algorithm. *IEEE Trans. Power Syst.* 22 (3), 1004–1011. doi:10.1109/tpwrs.2007.901468

Hao, H., Kowli, A., Lin, Y., Barooah, P., and Meyn, S. (2013). "Ancillary service for the grid via control of commercial building HVAC systems," in 2013 American Control Conference, Washington, DC, USA, 17-19 June 2013, 467–472.

Hui, H., Ding, Y., Liu, W., Lin, Y., and Song, Y. (2017). Operating reserve evaluation of aggregated air conditioners. *Appl. Energy* 196, 218–228. doi:10.1016/j.apenergy.2016.12.004

Hummon, M., Denholm, P., Jorgenson, J., and Palchak, D. (2013). *Fundamental drivers of the cost and price of operating reserves*. Golden, Colorado: National Renewable Energy Lab.

Kasis, A., Monshizadeh, N., and Lestas, L. (2020). Secondary frequency control with on-off load side participation in power networks. *IEEE Trans. Control Netw. Syst.* 7 (2), 603–613. doi:10.1109/tcns.2019.2934386

Kirby, B., Kueck, J., Laughner, T., and Morris, K. (2008). Spinning reserve from hotel load response. *Electr. J.* 21 (10), 59–66. doi:10.1016/j.tej.2008.11.004

Kondoh, J., Lu, N., and Hammerstrom, D. J. (2011). "An evaluation of the water heater load potential for providing regulation service," in 2011 IEEE Power and Energy Society General Meeting, Detroit, MI, USA, 24-28 July 2011,

Lindenberg, S., Smith, B., and O'Dell, K. (2008). *20% wind energy by 2030*. Denver, Colorado: Natl. Renew. Energy Lab. NREL US Dep. Energy Renew. Energy Consult. Serv. Energy. Inc.

Liu, Y., Alaywan, Z., Rothleder, M., Liu, S., and Assadian, M. (2000). "A rational buyer's algorithm used for ancillary service procurement," in 2000 IEEE Power Engineering Society Winter Meeting. Conference Proceedings (Cat. No.00CH37077), Singapore, 23-27 January 2000, 855.

Lu, N. (2012). An evaluation of the HVAC load potential for providing load balancing service. *IEEE Trans. Smart Grid* 3 (3), 1263–1270. doi:10.1109/tsg.2012.2183649

Mahdavi, N., Braslavsky, J. H., Seron, M. M., and West, S. R. (2017). Model predictive control of distributed air-conditioning loads to compensate fluctuations in solar power. *IEEE Trans. Smart Grid* 8 (6), 3055–3065. doi:10.1109/TSG.2017.2717447

Mathieu, J. L., Dyson, M. E. H., and Callaway, D. S. (2015). Resource and revenue potential of california residential load participation in ancillary services. *Energy Policy* 80, 76–87. doi:10.1016/j.enpol.2015.01.033

Mathieu, J. L., Koch, S., and Callaway, D. S. (2013). State estimation and control of electric loads to manage real-time energy imbalance. *IEEE Trans. Power Syst.* 28 (1), 430–440. doi:10.1109/tpwrs.2012.2204074

Mayer, P. W., and DeOreo, W. B. (1999). *Residential end uses of water*. Denver, Colorado, United States: Amer Water Works Assn.

Meyn, S. P., Barooah, P., Bušić, A., Chen, Y., and Ehren, J. (2015). Ancillary service to the grid using intelligent deferrable loads. *IEEE Trans. Autom. Contr.* 60 (11), 2847–2862. doi:10.1109/tac.2015.2414772

Nehrir, M. H., LaMeres, B. J., and Gerez, V. (1999). "A customer-interactive electric water heater demand-side management strategy using fuzzy logic," in Power Engineering Society 1999 Winter Meeting IEEE, New York, NY, USA, 31 January 1999 - 04 February 1999, 433.

NERC (2011). *IVGTF task 2.4 report, operating practices, procedures, and tools*. Atlanta, Georgia, United States: North American Electric Reliability Cop.

Paull, L., Li, H., and Chang, L. (2010). A novel domestic electric water heater model for a multi-objective demand side management program. *Electr. Power Syst. Res.* 80 (12), 1446–1451. doi:10.1016/j.epsr.2010.06.013

Pijnenburg, P., Saleh, S. A., and McGaw, P. (2016). Performance evaluation of the ZIP model-phaselet frame approach for identifying appliances in residential loads. *IEEE Trans. Ind. Appl.* 52 (4), 3408–3421. doi:10.1109/tia.2016.2535268

PJM Manual (2019). *PJM, manual 11: energy & ancillary services market operations revision: 106*, 30. Norristown, Pennsylvania, United States: PJM.

PJM (2019). Available at: https://www.pjm.com/.

Richardson, I., Thomson, M., and Infield, D. (2008). A high-resolution domestic building occupancy model for energy demand simulations. *Energy Build.* 40 (8), 1560–1566. doi:10.1016/j.enbuild.2008.02.006

Schneider, K. P., Mather, B. A., Pal, B. C., Ten, C. W., Shirek, G. J., Zhu, H., et al. (2017). Analytic considerations and design basis for the IEEE distribution test feeders. *IEEE Trans. Power Syst.* 33 (3), 3181–3188. doi:10.1109/tpwrs.2017.2760011

Solanki, B. V., Raghurajan, A., Bhattacharya, K., and Cañizares, C. A. (2017). Including smart loads for optimal demand response in integrated energy management systems for isolated microgrids. *IEEE Trans. Smart Grid* 8 (4), 1739–1748. doi:10.1109/tsg.2015.2506152

Stephen, Koch. (2012). "*Demand response methods for ancillary services and renewable energy integration in electric power systems*," (Stuttgart, Germany: Dipl. -Ing. Univ. Stuttgart). Ph.D. dissertation.

Vrettos, E. (2016). *Control of residential and commercial loads for power system Ancillary services*. Zürich, Switzerland: ETH Zurich.

Wang, J., Zhang, H., and Zhou, Y. (2017). Intelligent under frequency and under voltage load shedding method based on the active participation of smart appliances. *IEEE Trans. Smart Grid* 8 (1), 353–361. doi:10.1109/tsg.2016.2582902

Webborn, E. (2019). Natural heterogeneity prevents synchronization of fridges with deterministic frequency control. *IEEE Access* 7, 130206–130214. doi:10.1109/access.2019.2923158

Xiang, S., Chang, L., Cao, B., He, Y., and Zhang, C. (2020). A novel domestic electric water heater control method. *IEEE Trans. Smart Grid* 11 (4), 3246–3256. doi:10.1109/TSG.2019.2961214

Zhang, C., He, Y., Yuan, L., and Xiang, S. (2017). Capacity prognostics of lithium-ion batteries using EMD denoising and multiple kernel RVM. *IEEE Access* 5, 12061–12070. doi:10.1109/access.2017.2716353

Zhang, C., Zhao, S., and He, Y. (2022). An integrated method of the future capacity and RUL prediction for lithium-ion battery pack. *IEEE Trans. Veh. Technol.* 71 (3), 2601–2613. doi:10.1109/tvt.2021.3138959

Zhang, X., Hug, G., Kolter, J. Z., and Harjunkoski, I. (2018). Demand response of ancillary service from industrial loads coordinated with energy storage. *IEEE Trans. Power Syst.* 33 (1), 951–961. doi:10.1109/tpwrs.2017.2704524

Zhao, S., Zhang, C., and Wang, Y. (2022). Lithium-ion battery capacity and remaining useful life prediction using board learning system and long short-term memory neural network. *J. Energy Storage* 52, 104901. doi:10.1016/j.est.2022.104901

frontiers | Frontiers in Energy Research

TYPE Original Research
PUBLISHED 31 August 2022
DOI 10.3389/fenrg.2022.985316

OPEN ACCESS

EDITED BY
Chaolong Zhang,
Anqing Normal University, China

REVIEWED BY
Chuan-Ke Zhang,
China University of Geosciences Wuhan, China
Pengfei Tu,
Nanyang Technological University, Singapore
Wang Xiang,
Huazhong University of Science and Technology, China

*CORRESPONDENCE
Aihong Tang,
tah@whut.edu.cn

SPECIALTY SECTION
This article was submitted to Smart Grids,
a section of the journal
Frontiers in Energy Research

RECEIVED 03 July 2022
ACCEPTED 13 July 2022
PUBLISHED 31 August 2022

CITATION
Chen X, Tang A, Xiong B and Zhou W (2022), Research on the output coordinated strategy of a DPFC considering device fault probability. *Front. Energy Res.* 10:985316. doi: 10.3389/fenrg.2022.985316

Research on the output coordinated strategy of a DPFC considering device fault probability

Xiaogang Chen[1], Aihong Tang[2]*, Binyu Xiong[2] and Wei Zhou[2]

[1]State Grid Zhejiang Electric Power Co., Ltd., Hangzhou, China, [2]Automation School, Wuhan University of Technology, Wuhan, China

A distributed power flow controller (DPFC) can control the line power flow in a flexible and fast way to meet the requirements of a new power system. However, the output of DPFC sub-units is generally distributed by the even distribution method or proportional distribution method at present. The internal health status and output capacity of the device are not taken into account, which affects the efficiency and service life of the device. In this article, a reliability description method of DPFC based on fault probability is proposed. The coordination strategy of output voltage capability and the number of input sub-units is proposed, and the process of the proposed coordinated strategy for device output is presented. The simulation results show that the proposed coordinated output strategy can address the issue of rapid reliability decline caused by the long-term work of some sub-units and improve the overall reliability of the DPFC.

KEYWORDS

power systems, distributed power flow controller, fault probability, output voltage capability, number of switching sub-units

Introduction

Under the background of 'dual carbon,' China proposes the goal of building a new power system based on renewable energy. A large scale of renewable energy, such as wind and solar energy, will be connected to the transmission network or distribution network in a centralized or distributed manner. The volatility and intermittency nature of renewable energy output and the insufficient transmission capacity of lines may lead to overload and bidirectional power flow problems of transmission lines (Kang and Yao, 2017; Huang et al., 2019a; Zhang et al., 2022). At the same time, uncontrolled power flow will cause problems such as insufficient power supply in some regions, large transmission loss of lines, and even reduced stability and reliability of the system (Rashed et al., 2020; Liu et al., 2021).

Distributed power flow controller changes transmission line parameters by generating or absorbing reactive power so as to achieve flexible and fast line power flow regulation (Brissette et al., 2015; Shen et al., 2021; Song et al., 2022).

In 2019, in order to solve the problem of system congestion caused by the high penetration of renewable energy, IPTO of Greek transmission company installed a full control mode power flow regulator (hereafter referred to as DPFC in this article) (Gaigowal and Renge, 2016) developed by Smart Wires company in Peloponnesian, Greece. Inductance–capacitance smooth transition full control distributed power flow controller was successfully put into operation in Huzhou and Hangzhou in 2020, which is led by Zhejiang Electric Power Company, and participated by State Grid of China and NR Electric Company (Zhan et al., 2019).

The abovementioned engineering application results show that (Gaigowal and Renge, 2016; Zhan et al., 2019) the failure of a certain phase or a group of units of DSSC does not affect the operation of other units, and the overall reliability is much higher than that of the conventional centralized flexible AC transmission system(FACTS). However, hundreds of DPFC sub-units are installed along the overhead transmission line in groups, and in different phases, the operation environment is poor. The health status of a single sub-unit is easily affected, which affects the output capacity of the device, changes the normal dynamic response characteristics of the DPFC sub-unit, and directly affects the response characteristics and output capability of other DPFC sub-units through power line coupling. The health status of a single sub-unit has a great impact on the achievement of the expected goal of power flow regulation and restricts the speed of the popularization and application of DPFC.

Research studies on DPFC of references (Gaigowal and Renge, 2016; Ke et al., 2019; Guan et al., 2021; Xiong et al., 2022; Zhao et al., 2022) have adopted an even distribution method (all the sub-units in operation have equivalent output) and proportional distribution method (the output of each sub-unit is distributed proportionally by capacity) in the control strategy to distribute the output of each sub-unit in a centralized manner. In the study by Gaigowal and Renge (2016), a centralized management and optimal allocation scheme for DPFC is proposed, which completes the optimal allocation test of DPFC master unit based on RTDS. In the study by Guan et al. (2021), the impedance and power equivalent models of the DPFC system are proposed to analyze the relationship between voltage, impedance, and power of DPFC. In the study by Zhao et al. (2022), a real-time optimal allocation method for the output of DPFC sub-units based on centralized control is proposed, which is based on the idea of 'state classification - prioritized by regulation performance'. However, the optimization methods proposed in studies by Gaigowal and Renge (2016); Guan et al. (2021); and Zhao et al. (2022) are all in need of multiple rounds of debugging, the regulation speed is slow, and the priority of the sub-unit is only determined by the adjustable capacity of each unit, the DPFC will have a large overall operation loss when the regulation target is relatively small, for the sub-unit with large capacity will stay in operation for a long time and the sub-unit with small capacity will have a low utilization rate. The economic benefits and reliability of the device are low. In the study by Xiong et al. (2022), a cluster control strategy is proposed so that the distributed flexible AC transmission equipment can work stably with a high compensation efficiency in the whole operation range, but the difference in device capacity and device operation loss is not considered. By dispatching and configuring the available resources in a centralized control method, a switching control strategy for DPFC sub-unit is proposed by Ke et al. (2019), which can enrich the application scenarios of DPFC and enhance the application flexibility of DPFC, but it is essentially an even distribution method. When the even distribution method is used, if the capacity of the sub-unit is inconsistent, the utilization rate of the sub-unit with large capacity is low, and the economic effect is poor. The regulation range of the whole system is restricted by the sub-unit with the smallest capacity, and the sub-unit with a small capacity will be prone to overload and heat, which will bring damage to the health of DPFC. When the proportional distribution method is used, the output will be determined in proportion according to the capacity of each sub-unit. But if the regulation need is small, all the sub-units will be charged and put into operation, the overall utilization rate of the device is low, the device loss is large, and it also affects the health status of the device indirectly (Mao et al., 2017). In the study by Tang et al. (2022), the proposed optimal output power coordinated control strategy of DPFC considers the total loss of DPFC device. But it is based on the optimal algorithm, which leads to the high complexity of this method. Moreover, we can learn from the abovementioned literature that all the sub-units of DPFC are assumed to be healthy in the current even distribution method and proportional distribution method, and their output distribution is on the basis of the rated capacity of the device, which is defaulted to the maximum available of all the sub-units. However, as mentioned in the existing demonstration projects (Gaigowal and Renge, 2016; Zhan et al., 2019) and references (Liu et al., 2016; Qian et al., 2018; Elgebaly, 2019; Saeed et al., 2019), if the device is not in a healthy status, the maximum capacity of DPFC can be used will no longer be its rated capacity. It can be concluded that whether the proportional distribution method is adopted or the even distribution method is used, the sub-unit cannot operate as expected in the control so DPFC will fail to achieve the expected power flow control target, which affects the safe and stable operation of the power system.

In this article, a coordinated output control method considering the health status of the device is proposed to improve the utilization efficiency of the device capacity, reduce the device loss, and give full play to the economic and efficient power flow function of DPFC.

Basic principle

The primary equipment of DPFC sub-unit is a H-bridge voltage source converter consists of IGBT (Peddakapu et al., 2020). Its basic structure is shown is shown in Figure 1.

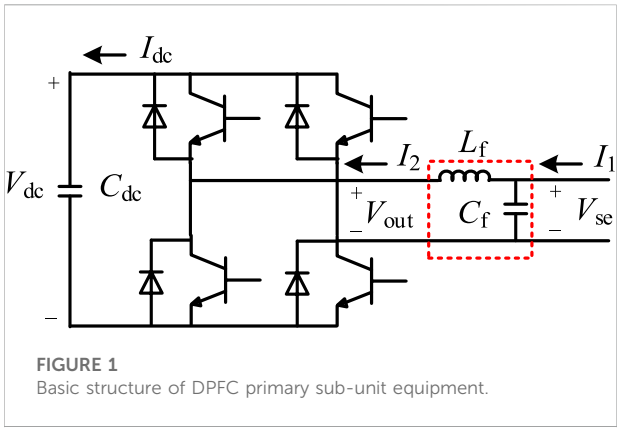

FIGURE 1
Basic structure of DPFC primary sub-unit equipment.

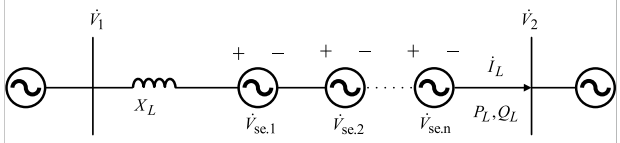

FIGURE 2
Equivalent controllable voltage source model of DPFC System.

It is of note that V_{dc} is the DC capacitor voltage of DPFC sub-unit, I_{dc} is the current flows through the DC capacitor of DPFC sub-unit, I_1 is the current flows between DPFC sub-unit and power grid, I_2 is the current flows through the filter of DPFC sub-unit, V_{out} is the voltage output by the voltage source converter, and V_{se} is the voltage at the filter of DPFC sub-unit and it is the voltage injected into the grid-side at the same time. C_{dc} is the DC-side capacitor, and C_f and L_f are the parameters of the filter capacitor and filter inductor, respectively. The filter link in DPFC sub-unit primary structure can be configured according to different application scenarios, which is circled in Figure 1. The control strategy of DPFC with or without filter link will be slightly different.

When filter link is included in the DPFC sub-unit, the following equations can be obtained according to the circuit equation of DPFC sub-unit:

$$V_{out} = V_c - L_f \frac{dI_2}{dt}, \tag{1}$$

$$I_2 = I_1 - C_f \frac{dV_{se}}{dt}. \tag{2}$$

When filter link is not configured in the DPFC sub-unit, V_{out} is exactly the voltage V_{se} injected into the grid-side by DPFC sub-unit.

The whole DPFC system is composed of multiple DPFC sub-units. These sub-units are all connected to the power system in series. Each sub-unit can be viewed as a controllable voltage source. The equivalent model of the whole DPFC system in power system is shown in Figure 2.

In Figure 2, $\dot{V}_1$ and $\dot{V}_2$ are voltages at the sending and receiving end of the line where the DPFC system is installed, respectively. X_L is the equivalent impedance of the line, $\dot{I}_L$ is the current flows in this single line system, and P_L and Q_L are the active power flow and reactive power flow at the receiving end of the line, respectively. $\dot{V}_{se.i}$ (where i = 1, 2, ...n) is the equivalent voltage injected into the line by the *i*th DPFC sub-unit. According to the equivalent model in Figure 2, the current and power flow of the line satisfy the following equations:

$$\dot{I}_L = \frac{\left(\dot{V}_1 - \dot{V}_2 - \sum_i^n \dot{V}_{se,i}\right)}{jX_L}, \tag{3}$$

$$P_L = \mathrm{RE}\left(\dot{V}_2 \dot{I}_L^*\right), \tag{4}$$

$$Q_L = \mathrm{IM}\left(\dot{V}_2 \dot{I}_L^*\right). \tag{5}$$

It is of note that the injection voltage is the voltage injected into the line by DPFC sub-unit, the output voltage is voltage at the AC-side of the converter. In order to further analyze the impact of the injection voltage of the DPFC sub-unit on active power flow of the line, the active power flow is expressed in detail and rewritten as follows:

$$P_L = \frac{V_1 V_2}{X_L}\left(1 \pm \frac{\sum_{i=1}^n V_{se,i}}{\sqrt{V_1^2 + V_2^2 - 2V_1 V_2 \cos\theta_{12}}}\right). \tag{6}$$

It can be obtained from Eq. 6 that if the active power flow reference value of DPFC system is determined, the line impedance parameters need to be compensated by DPFC system can be derived as follows:

$$X_{se.sum} = \frac{V_1 V_2 \sin\delta_{12}}{P_{L.ref}} - X_L, \tag{7}$$

where δ_{12} is the phase difference between $\dot{V}_1$ and $\dot{V}_2$, and $P_{L.ref}$ is the reference value of P_L. The effective value of line current I_L is obtained as follows:

$$|I_L| = \frac{\sqrt{(V_1 - V_2\cos\delta_{12})^2 + (V_2\sin\delta_{12})^2}}{X_L + X_{se.sum}}. \tag{8}$$

The total voltage injected by all the DPFC sub-units in operation can be written as shown in Eq. 9:

$$V_{se.sum} = |I_L| X_{se.sum}. \tag{9}$$

Control for a single DPFC sub-unit is essentially the control of the output voltage of DPFC sub-unit. The DPFC sub-unit is acting on the line through the injection voltage V_{se}. The output voltage is transformed into dq coordinate system by park transformation in this paper, to realize the decoupling control of the dq axis component of output voltage.

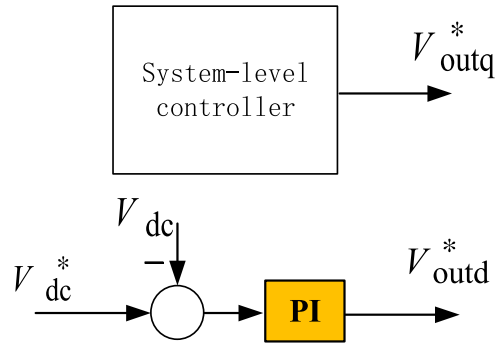

FIGURE 3
Simplified control strategy of DPFC sub-unit.

Considering that if the LC link is not included in the primary equipment of the DPFC sub-unit, the injection voltage will be the output voltage to be controlled. The control strategy can be simplified, as shown in Figure 3.

In the control strategy mentioned in Figure 3, V^*_{dc}, the reference value of the DC capacitor in DPFC sub-unit is subtracted with its corresponding feedback first. Then, the result of this subtraction operation will be the driving signal of the PI controller to output the d-axis component of the modulation signal. The q-axis component of the modulated signal is given by the upper system-level controller.

The system-level controller of DPFC consists of the calculation module, the mode control module (DPFC can work in several different modes (Lou et al., 2021)), and the output voltage distribution module. It is described in detail in Figure 4.

It can be seen from Figure 4 that for DPFC working in all the modes, the output distribution of DPFC sub-units concentrates on the q-axis component of the output voltage, and that is the output of the output voltage distribution module. So, in the following, the distribution method for the q-axis component of the output voltage will be mainly analyzed to realize the optimal output distribution of multiple DPFC sub-units.

Output distribution method of DPFC

When the even distribution method is adopted for the output of DPFC, if the output voltage need is small, the actual output of each sub-unit is very small, and the utilization rate of the DC voltage is low (which means a low modulation ratio). When the converter used in DPFC is a voltage source converter, if the modulation ratio is very low, there will be a large proportion of harmonics in the output voltage, the waveform distortion of the output voltage will be serious, and the device efficiency will not be high. Therefore, in order to improve the working efficiency of each DPFC sub-unit, it is better to ensure that the output voltage of each DPFC sub-unit is higher than 80% of the rated voltage.

At the same time, before selecting the DPFC sub-unit to operate, if the sub-unit with high reliability are selected as the power flow controller to track the reference, the reliability of the whole system will be greatly improved (Huang et al., 2019b; Chen et al., 2019; Huang and Gao, 2019; Zhu et al., 2020). In order to express the reliability index of DPFC sub-unit, a control strategy is proposed in this study as follows:

The DPFC sub-unit is a kind of power electronic device consisting of IGBT, if the average fault-free operation time of the sub-unit is 1/λ, then the service life of the sub-unit matches the exponential distribution with parameter λ, and its failure probability is written as follows:

$$F(t) = P\{X \le t\} = 1 - e^{-\lambda t}, t \ge 0. \tag{10}$$

So, the reliability of DPFC sub-unit can be expressed as a function related to the total operation time of the converter.

$$\rho(t) = 1 - F(t) = e^{-\lambda t}. \tag{11}$$

With the constraint of this function, the fault probability will increase as the operation time past, which means that the DPFC sub-unit with a long term of operation will be exposed to a greater failure risk. If the output distribution of DPFC is divided into multiple steps, when the distribution for the next step is needed, the DPFC sub-unit with a larger cumulative working time is more difficult to assign into operation, which can make DPFC sub-unit with less operation time is much easier to work. It not only ensures the relative average utilization rate of all DPFC sub-units installed on the line but also reduces the fault probability of a single DPFC sub-unit. In order to realize the abovementioned function, an output coordinated control strategy which can work autonomously and alternately for DPFC is proposed in this paper. It mainly consists of two steps to determine the output of DPFC sub-unit:

1) The output distribution module receives the voltage injection instructions $V_{se.sum}$ from DPFC mode control module, assuming that the rated output voltage of each DPFC sub-unit is $V_{se.nom}$, to ensure the voltage inverted by every sub-unit is higher than 80% of the rated voltage, the number of DPFC sub-units in need to be invested is

$$n = \left[\frac{V_{se.sum}}{0.8 \times V_{se.nom}}\right], \tag{12}$$

where the following relation should be satisfied:

$$V_{se.sum} - n \times V_{se.nom} \le 0. \tag{13}$$

The abovementioned equation indicates that the total output voltage of DPFC, $V_{se.sum}$, should be less than the sum of the rated output voltage of invested DPFC sub-units. The output voltage of

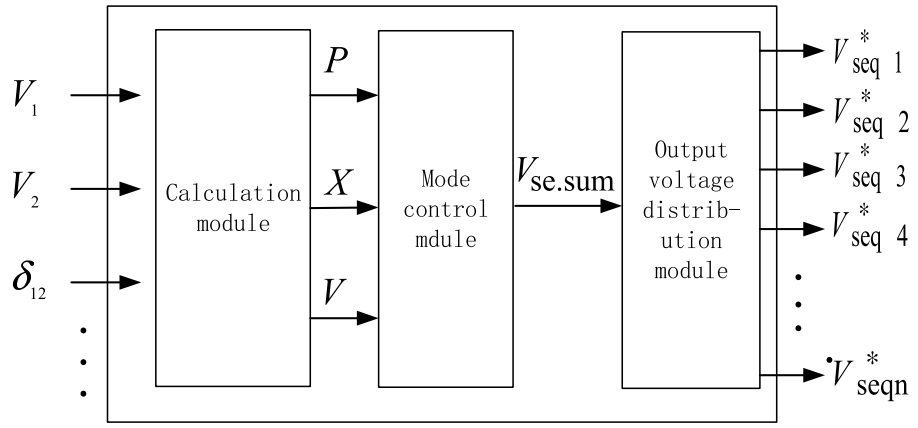

FIGURE 4
System-level controller diagram of DPFC.

each DPFC sub-unit (which is expressed as modulation depth here) can be obtained subsequently as follows:

$$V_{seqi} = \left(\frac{V_{se.sum} - 0.8 \times n \times V_{se.nom}}{n} + 0.8 \times V_{se.nom}\right)/V_{se.nom}. \tag{14}$$

If the result of Eq. 14 satisfies that $V_{seqi} > 1$. It will be out of the modulation range of DPFC sub-unit. In this case, extra DPFC sub-unit (which is not included in the number of n) should be added to achieve the compensation target. The output of these extra sub-units is as follows:

$$V_{seqi} = (V_{seqi} - 1)^* n. \tag{15}$$

The modified output of each DPFC sub-unit can be obtained by Eq. 15,

$$V_{seqi} = (V_{se.sum} - V_{seqi})/n. \tag{16}$$

2) After the number of sub-units required for operation, n, and the output of each sub-unit, V_{seqi}, are obtained. The DPFC sub-unit with operation time less than a working cycle T (24 h are noted as a working cycle in this article) in the previous step is selected, the quantity of these sub-units is noted as m. And the number these sub-units are formed into a set M. Considering that if the total running time t_{run} of each DPFC sub-unit is small, the result calculated by Eq. 12 will be very small. It is difficult to accurately express this result even using double-precision data types. Therefore, the total operation time of DPFC sub-units t_{run} is directly used as an indicator to judge the reliability of DPFC in this study.

① It is of note that the quantity of the DPFC sub-unit put into operation in the previous step as n_0. When $n \geq n\_0$, first, the DPFC sub-units not included in the set M are ranked according to their total running time. n_real ($n\_real = n - m$) DPFC sub-units with smaller total running time are selected as the supplementary sub-units, and then, the output instructions V_{seqi} are given to these n DPFC sub-units.

② When $n < n\_0$, if $m \geq n$, only n DPFC sub-units with smaller total running time are selected from the set M to operate in the next step. If $m < n$, the DPFC sub-units not included in the set M should be ranked according to their total running time, and n_real ($n\_real = n - m$)DPFC sub-units with smaller total running time are selected as the supplementary sub-units. Finally, the output instructions V_{seqi} are given to these n DPFC sub-units. The flow chart of the specific output distribution strategy is shown in Figure 5.

Simulation analysis of the DPFC output control strategy

In order to verify the correctness and effectiveness of the proposed DPFC output control strategy, the verification environment of the output allocation strategy is constructed based on the m code of Matlab, i.e., to make the rated output voltage of each DPFC sub-unit V_o = 1kV, the total number of the sub-units is 10, and the total running time of each DPFC unit (within 744 h) and the working time of the

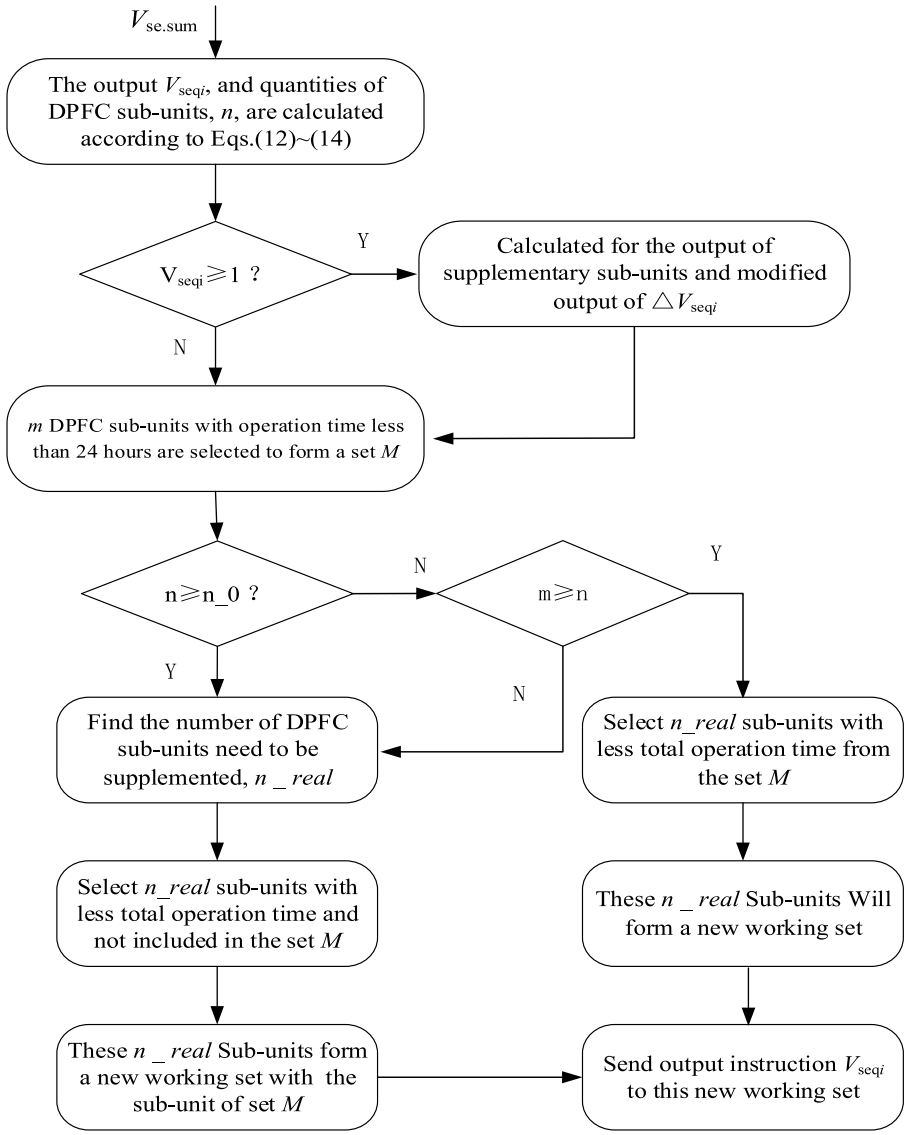

FIGURE 5
Flow chart of output distribution strategy.

previous step (within 24 h) are randomly generated. The simulation time is 1 month (i.e., 744 h), and the simulation step length is 1 h $V_{se.sum}$ was set to 2.2, 3.0, 3.8, 4.6, and 5.4 kV at 1, 181, 361, 541, and 721 h, respectively. The simulation results are shown in Figure 6.

As shown in Figure 6A, the total operation time of all DPFC sub-units is different from the initial value of operation time in the last step. However, as the simulation time passes, the total running time of each DPFC sub-unit is gradually consistent, and the working time of each DPFC sub-unit in the previous step is limited to within 24 h. This is because the sub-unit with a smaller total running time will operate for a longer time to ensure that each DPFC sub-unit is fully utilized and that the total running time of each DPFC unit is most balanced. As shown in Figure 6B, the output of DPFC sub-unit is generally maintained at full rated output between 1h–360 h, and the number of working sub-units changes from 2 to 3. However, in 1–180 h, due to the obtained DPFC unit output instructions $V_{seqi} > 1$, additional DPFC sub-units are required to work, and the output of these DPFC sub-units is 0.2 times the rated capacity. During 360–744 h, the output of each DPFC sub-unit is

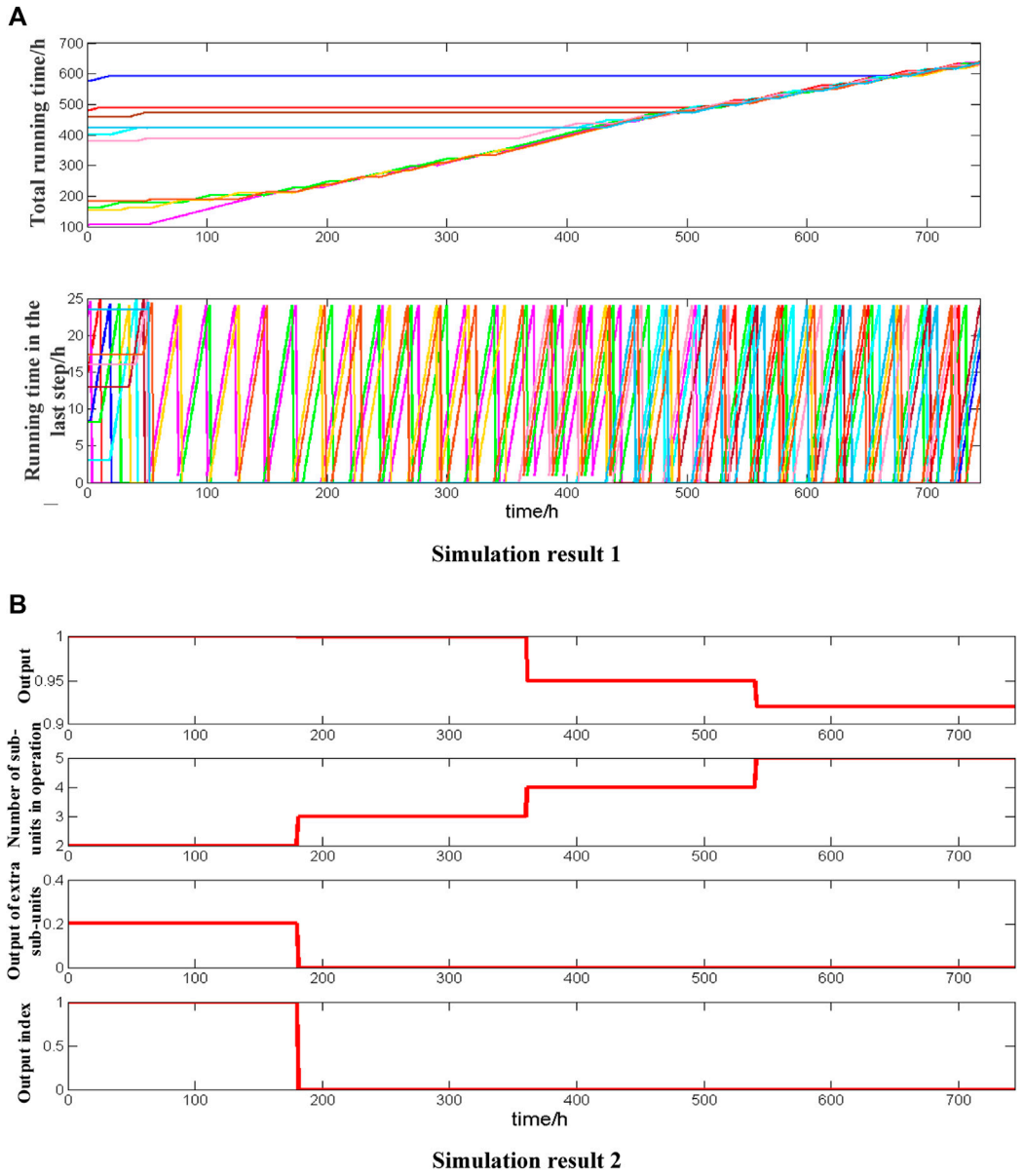

FIGURE 6
Simulation results of DPFC output distribution: **(A)** simulation result 1 and **(B)** simulation result 2.

maintained above 0.8 times the rated capacity, and the number of working units is gradually changed from 4 to 5 without supplementary units.

Conclusion

The disadvantages of the existing output control strategy are analyzed in this article. In addition, a coordination strategy of output voltage capability and the number of input sub-units is proposed. The simulation results are as follows:

1) The output distribution strategy proposed in this article can ensure that all DPFC sub-units in operation are maintained at a high output state (excluding supplementary units) all along the operation time, and the capacity of DPFC units in operation is fully utilized.
2) The shift mechanism of the proposed output distribution strategy can ensure that all DPFC sub-units are involved in

the power flow control task, which is a good solution to the rapid decline of reliability caused by the long-term work of some DPFC units, so as to improve the overall reliability of DPFC device and its service life.

Data availability statement

The raw data supporting the conclusion of this article will be made available by the authors, without undue reservation.

Author contributions

AT and XC contributed to the conception and design of the study. WZ and BX organized the database. XC performed the statistical analysis. XC contributed to the validation of the study. AT and BX contributed to the resources of the study. XC wrote the first draft of the manuscript. WZ, AT, and BX wrote sections of the manuscript. All authors contributed to manuscript revision and read and approved the submitted version.

Conflict of interest

The authors declare that this study received funding from State Grid Zhejiang Electric Power Co., Ltd. The funder had the following involvement in the study: study design, data collection and analysis, decision to publish, preparation of the manuscript.

Publisher's note

References

Brissette, A., Maksimovic, D., and Levron, Y. (2015). Distributed series static compensator deployment using a linearized transmission system model. *IEEE Trans. Power Deliv.* 30 (03), 1269–1277. doi:10.1109/tpwrd.2014.2362764

Chen, S., Lin, Q., Chen, S., Cai, F., and Wang, W. (2019). Review on intelligence fault diagnosis in power electronic converters[J]. *Electr. Eng.* 20 (03), 6–12.

Elgebaly, Ahmed E. (2019). "Optimized design of single tum transformer of distributed static series compensators using fem based on ga[C]," in 2019 21st International Middle East Power Systems Conference, 1133–1138.

Gaigowal, S. R., and Renge, M. M. (2016). "Distributed power flow controller using single phase DSSC to realize active power flow control through transmission line[C]," in 2016 International Conference on Computation of Power, Energy Information and Commuincation, 747–751.

Guan, Minyuan, Shen, Jianliang, Lou, Ping, Jin, Guoliang, and Wu, Guoqiang (2021). Equivalence analysis of voltage, impedance and power relationships of distributed power flow controller based on cascaded H-bridge converter[J]. *Adv. Technol. Electr. Eng. Energy* 40 (07), 40–47.

Huang, J., and Gao, Y. (2019). "Converter fault diagnosis method based on principal component analysis combined with improved similarity classifier[C]," in 2019 Chinese Automation Congress, 5051–5054.

Huang, W., Zhang, N., Yang, J., Wang, Y., and Kang, C. (2019a). Optimal configuration planning of multi-energy systems considering distributed renewable energy. *IEEE Trans. Smart Grid* 10 (02), 1452–1464. doi:10.1109/tsg.2017.2767860

Huang, X., Qi, L., and Pan, J. (2019b). A new protection scheme for MMC-based MVdc distribution systems with complete converter fault current handling capability. *IEEE Trans. Ind. Appl.* 55 (05), 4515–4523. doi:10.1109/tia.2019.2917360

Kang, C., and Yao, L. (2017). Key scientific issues and theoretical research framework for power systems with high proportion of renewable energy[J]. *Automation Electr. Power Syst.* 41 (09), 2–11.

Ke, M., Marco, L., Frede, L., and Tamas, K. (2019). Thermal loading and lifetime estimation for power device considering mission profiles in wind power converter. *IEEE Trans. Power Electron.* 30, 590–602. doi:10.1109/TPEL.2014.2312335

Liu, Bin, Liu, Jun, Xiong, Yong, and Lu, Xiongwei (2016). Technology of power proportionally distributed for paralleled inverters in microgrid[J]. *Power Electron.* 50 (01), 49–52.

Liu, B., Yang, Q., Zhang, H., and Wu, H. (2021). An interior-point solver for AC optimal power flow considering variable impedance-based FACTS devices. *IEEE Access* 9, 154460–154470. doi:10.1109/access.2021.3128035

Lou, W., Xiang, Z., Pan, W., Tang, A., Zhou, W., and Zhai, X. (2021). "Reserch on multi-mode operation of distributed power flow controller[C]," in 2021 IEEE 4th International Electrical and Energy Conference, 1–6.

Mao, Wenjin, Li, Hongwei, and Chao, Li (2017). A distribution system reconfiguration method considering the optimal active power dispatching of DGs[J]. *Power Syst. Prot. Control* 45 (13), 57–63.

Peddakapu, K., Mohamed, M. R., Sulaiman, M. H., Srinivasarao, P., Veerendra, A. S., and Leung, P. K. (2020). Performance analysis of distributed power flow controller with ultra-capacitor for regulating the frequency deviations in restructured power system[J]. *J. Energy Storage* 31 31. doi:10.1016/j.est.2020.101676

Qian, M., Zhao, D., Ma, J., Jiang, D., Ding, M., and Xiang, L. (2018). "A centralized frequency regulation strategy of PV power plant based equal adjustable capacity proportion mode[C]," in 2018 China International Conference on Electricity Distribution, 1797–1801.

Rashed, G. I., Haider, H., and Shafik, M. B. (2020). Enhancing energy utilization efficiency of Pakistani system considering FACTS devices and distributed generation: Feasibility study. *Chin. J. Electr. Eng.* 6 (2), 66–82. doi:10.23919/cjee.2020.000012

Saeed, P., Wang, Z., and Frede, B. (2019). "Reliability modeling of power electronic converters: A general approach[C]," in 2019 IEEE 20th Workshop on Control and Modeling for Power Electronics, 1–7.

Shen, C., Cao, J., Tang, M., Wu, M., Lin, C., and Bai, J. (2021). Research on real-time control optimization application function of DPFC[J]. *Zhejiang Electr. Power* 40 (09), 55–61. doi:10.19585/j.zjdl.202109008

Song, Jingen, Xu, Hua, Zhang, Dianqing, and Xu, Ting (2022). Design and application of control system for distributed power flow controller[J]. *Power Electron.* 56 (05), 93–96.

Tang, A., Zhou, W., Song, J., Qiu, P., Chen, Q., Zhai, X., et al. (2022). Optimal output power coordinated control strategy of distributed power flow controller[J]. *Int. J. Electr. Power & Energy Syst.* 140, 140. doi:10.1016/j.ijepes.2022.108075

Xiong, B., Tang, J., Li, Y., Xie, C., Wang, Z., Zhang, X., et al. (2022). Design of A Two-Stage control strategy of vanadium redox flow battery energy storage systems for grid application. *IEEE Trans. Sustain. Energy*. doi:10.1109/TSTE.2022.3181751

Zhan, X., Wang, Y., Zhao, G., and Zhu, N. (2019). Research and design of distributed static synchronous series compensator[J]. *Power Electron.* 53 (03), 95–98.

Zhang, C., Zhao, S., and He, Y. (2022). An integrated method of the future capacity and RUL prediction for lithium-ion battery pack. *IEEE Trans. Veh. Technol.* 71 (3), 2601–2613. doi:10.1109/tvt.2021.3138959

Zhao, S., Zhang, C., and Wang, Y. (2022). Lithium-ion battery capacity and remaining useful life prediction using board learning system and long short-term memory neural network. *J. Energy Storage* 52, 104901. doi:10.1016/j.est.2022.104901

Zhu, Y., Xu, S., and Zhang, J. (2020). Reliability modeling and analysis of multilevel converter systems[J]. *Chin. J. Sci. Instrum.* 41 (03), 70–78.

frontiers | Frontiers in Energy Research

TYPE Original Research
PUBLISHED 07 September 2022
DOI 10.3389/fenrg.2022.994629

OPEN ACCESS

EDITED BY
Chaolong Zhang,
Anqing Normal University, China

REVIEWED BY
Xun Wu,
Central South University, China
Meng Zhang,
Xi'an Jiaotong University, China
Zhao Dongdong,
Northwestern Polytechnic University, United States

*CORRESPONDENCE
Youmin Zhang,
ymzhang@encs.concordia.ca

SPECIALTY SECTION
This article was submitted to Smart Grids, a section of the journal Frontiers in Energy Research

RECEIVED 15 July 2022
ACCEPTED 02 August 2022
PUBLISHED 07 September 2022

CITATION
Chen C, Song Y, Zhang Y, Tian J, Gao S and Lang B (2022), Adaptive fault-tolerant control of five-phase permanent magnet synchronous motor current using chaotic-particle swarm optimization. *Front. Energy Res.* 10:994629.
doi: 10.3389/fenrg.2022.994629

Adaptive fault-tolerant control of five-phase permanent magnet synchronous motor current using chaotic-particle swarm optimization

Chaobo Chen[1,2], Ye Song[2], Youmin Zhang[1,3]*, Jiaqiang Tian[4], Song Gao[2] and Baohua Lang[2]

[1]School of Automation and Information Engineering, Xi'an University of Technology, Xi'an, China, [2]School of Electronic Information Engineering, Xi'an Technological University, Xi'an, China, [3]Department of Mechanical, Industrial and Aerospace Engineering, Concordia University, Montreal, QC, Canada, [4]School of Electrical Engineering, Xi'an University of Technology, Xi'an, China

Both torque ripple and current harmonics are enlarged due to single-phase open-circuit fault of five-phase permanent magnet synchronous motor (FPMSM). Based on chaotic-particle swarm, an adaptive optimization fault tolerant control algorithm is proposed for the FPMSM current. First, Park and Clarke matrices are modified in coordinate transformation process. A reduced-order decoupling matrix is obtained under the open-circuit fault of FPMSM stator winding. Second, the fault-tolerant current is generated with the principle of constant magnetomotive force. Third, the current is adaptively optimized using chaotic-particle swarm algorithm. Hence, motor torque and motor current keep uniform steady state and dynamic performance with them in regular operation. Finally, numerical simulations are carried out to verify the effectiveness of the developed method.

KEYWORDS

five-phase permanent magnet synchronous motors, chaos-particle swarm optimization algorithm, open-circuit fault, fault-tolerant control strategy, minimal torque ripple

Introduction

The five-phase permanent magnet synchronous motor has the advantages of low torque ripple, multiple control degrees of freedom, and high efficiency (Liu et al. (2022); Zhang et al. (2021); Zhao et al. (2022)). It can achieve fault-tolerant operation without additional hardware support. Hence, it is widely used in industrial applications requiring high efficiency and reliability, such as systems in aerospace, energy conversion (Okedu Kenneth and Barghash, 2021), electric vehicle drive, etc. (Tao et al. (2019)). Among main body faults of a motor, the winding fault happens mostly. The faults include the winding open-circuit fault and the interturn short circuit fault. In particular, the winding open-circuit fault is the most common (Salehifar et al. (2014)).

The open-circuit fault of the motor winding will generate a large torque ripple. The heat generated by a large current usually causes irreversible demagnetization of permanent magnet (Huang et al. (2021)). These phenomena lead to a fast drop of control performance. Besides, the function of whole system is seriously affected. Therefore, it is necessary and critical to adopt an appropriate fault-tolerant control (FTC) strategy under fault conditions.

Field-oriented control (FOC) and direct torque control (DTC) are widely used in motor control strategies. At present, many advanced control strategies have been employed for fault-tolerant control of motors, including fuzzy control, adaptive control, model predictive control, etc. The principle of constant instantaneous torque was employed in (Zhao et al. (2011)). Lagrangian multiplication was used to obtain the expression of the fault-tolerant reference current. The ripple component was eliminated in output torque. However, the process is complicated. In addition, the method cannot work in the online case. A new coordinate transformation was developed in (Zhou et al. (2019)). The d-q axis current keeps unchanged before and after the phase failure. The torque remains intact at the moment of phase failure. However, it cannot guarantee the effect of suppressing the subsequent torque ripple. In (Gaeta et al. (2013)), three new coordinate transformations were proposed. A mathematical model was deduced for embedded PMSM after phase failure. Nevertheless, the influence of the third harmonic current is ignored. The effectiveness of the algorithm should be improved. Reference (Wu et al. (2019)) introduced a method of virtual voltage vector based on DTC. By optimizing its duty cycle and distributing the vector action time, it effectively suppressed the low-order harmonic current. Besides, it improved the utilization rate of the DC bus voltage, and widened the speed regulation range of the motor. Reference (Liu (2020)) designed a new direct torque control strategy based on matrix converter and DTC theory of PMSM. The developed method effectively suppressed torque fluctuations and made the system more robust. However, the above methods (Wu et al. (2019); Liu (2020)) lead to large ripple, due to the interaction of the fundamental current and the third harmonic back EMF in the FT-DTC method. Reference (Chen et al. (2021)) proposed a fault-tolerant control method combining quasi-proportional resonance and sliding mode observer. The method is suitable for the non-fault state of a motor. It can also accurately estimate the rotor position and motor speed in the event of a motor fault. In (Chen et al. (2019)), a model predictive torque control strategy was proposed, based on the voltage vector pre-screening. This method determined the sector position of the stator flux linkage and combined the transformation of torque and flux linkage amplitude. The corresponding voltage vector set was selected as the candidate vector of a prediction model by the look-up table method. The method effectively reduced the traversal times based on satisfying the control performance. However, the selection of the weight coefficient reduced the adaptability of the algorithm. In (Fnaiech et al. (2010)), the fuzzy reasoning and sliding mode control theory was employed for the fault-tolerant control of winding phase-missing faults of six-phase induction motors. The system had robust stability. Besides, the tracking accuracy was improved. Unfortunately, the selection of fuzzy control parameters relied on expert experience and was highly subjective. Meanwhile, there was also the defect of high-frequency switching of sliding mode. Based on this, this paper proposes an adaptive fault-tolerant control of five-phase permanent magnet synchronous motor current using chaotic-particle swarm optimization.

The rest of the paper is arranged as follows: *FOC and coordinate transformation* Section corrects the Park and Clarke transformation matrices of FPMSM in the process of coordinate transformation. *Optimizing the reference current with the adjustment factor* Section solves the problem of phase loss of the motor in the FOC control framework, and at the same time, adaptively optimizes the solved fault-tolerant current using the adjustment factor. *Simulation and verification* Section builds a simulation in MATLAB/Simulink, and verifies the algorithm's feasibility through the simulation results and data. The conclusion of the thesis is given in *Conclusion* Section.

FOC and coordinate transformation

Both the air gap magnetic field and the stator magnetic field have a coupling phenomenon in the flux linkage relationship, which leads to the vector control structure more complicated. **Figure 1** shows the schematic diagram of the system based on field-oriented control, where the motor is working normally, FOC is also known as vector control. The rotor field orientation is modeled on the control method of a DC motor. It uses coordinate transformation to decompose the stator current of an AC motor into a magnetic field component current and a torque component current, which are separately controlled. The magnetic flux current component and the torque current component are completely decoupled, to obtain the dynamic performance similar to the DC speed control system. The permanent magnet synchronous motor, established by coordinate transformation, can analyze the steady-state operation of the motor when the sine wave is input. The motor's instantaneous performance can also be analyzed.

Mathematical model of five-phase permanent magnet synchronous motor

The basic idea of coordinate transformation is to convert relevant variables into the five-phase static coordinate system to the d-q rotating coordinate system for mathematical operations.

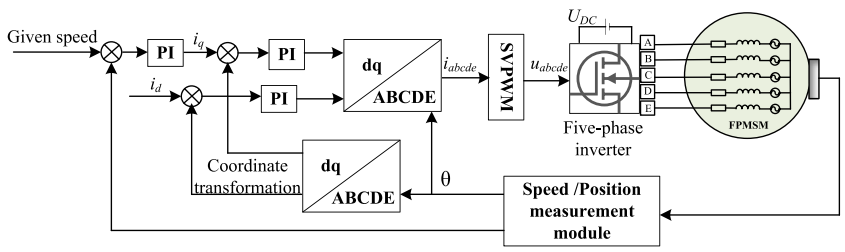

FIGURE 1
Block diagram of motor control system based on FOC.

The d-q axis is a rotating coordinate system with synchronous rotational speed established by the synchronous rotation of the stator and rotor magnetic fields of the motor during coordinate transformation. The controller changes the voltage of the d-q axis to control the current of the d-q axis. However, in the end, the five-phase voltage of the motor can only be the voltage in the static coordinate system. Therefore, the corresponding inverse transformation must be performed again in the control algorithm, to convert the voltage of the d-q axis into a five-phase voltage for the drive bridge.

For the five-phase PMSM, the design, processing, and installation of permanent magnets will make the air-gap magnetic field become non-ideal sinusoidal, with a certain amount of 3rd harmonic components. In addition, some research works artificially inject the 3rd harmonic magnetic potential to improve the power and torque ripple of the motor (Gao et al. (2013); Chen Q. et al. (2022)). Therefore, there will be a non-zero third harmonic current. It is beneficial to consider both the fundamental current and the third harmonic current in the modeling process for the subsequent work.

$$\boldsymbol{I}_{dq} = \boldsymbol{T}\boldsymbol{I}_{\mathrm{s}} = \boldsymbol{T}_{\mathrm{Park}}\boldsymbol{T}_{\mathrm{Clarke}}\boldsymbol{I}_{\mathrm{s}} \tag{1}$$

where $\boldsymbol{T} = \boldsymbol{T}_{\mathrm{Park}}\boldsymbol{T}_{\mathrm{Clarke}}$, $\boldsymbol{I}_{dq} = \left[i_{d1}\ i_{q1}\ i_{d3}\ i_{q3}\ i_n\right]^{\mathrm{T}}$, $\boldsymbol{I}_{\mathrm{s}} = \left[i_a\ i_b\ i_c\ i_d\ i_e\right]^{\mathrm{T}}$.

The five-phase motor is a coordinate transformation from the natural coordinate system (*abcde*) to the rotational phase ($d_1q_1d_3q_{3n}$). This transformation extends the $abc \rightarrow dqn$ transformation and is used for three-phase to the five-phase case. Usually, the coordinate transformation is divided into two parts: Clarke (*abcde* to $\alpha_1\beta_1\alpha_3\beta_3 z$) and Park ($\alpha_1\beta_1\alpha_3\beta_3 z$ to $d_1q_1d_3q_3n$) transformation. Under normal working conditions, the five-phase PMSM extended Clarke transformation matrix is:

$$\boldsymbol{T}_{\mathrm{Clarke}} = \begin{bmatrix} 1 & \cos\theta & \cos2\theta & \cos2\theta & \cos\theta \\ 0 & \sin\theta & \sin2\theta & -\sin2\theta & -\sin\theta \\ 1 & \cos2\theta & \cos\theta & \cos\theta & \cos2\theta \\ 0 & -\sin2\theta & \sin\theta & -\sin\theta & \sin2\theta \\ 1 & 1 & 1 & 1 & 1 \end{bmatrix} \tag{2}$$

In the normal working state of the motor, the Park transformation matrix is:

$$\boldsymbol{T}_{\mathrm{Park}} = \begin{bmatrix} \cos\theta & \sin\theta & 0 & 0 & 0 \\ -\sin\theta & \cos\theta & 0 & 0 & 0 \\ 0 & 0 & \cos3\theta & \sin3\theta & 0 \\ 0 & 0 & -\sin3\theta & \cos3\theta & 0 \\ 0 & 0 & 0 & 0 & 1 \end{bmatrix} \tag{3}$$

The stator voltage equation of the five-phase PMSM in natural coordinates is (Tian et al. (2018)):

$$\boldsymbol{U}_{\mathrm{s}} = \boldsymbol{R}_{\mathrm{s}}\boldsymbol{I}_{\mathrm{s}} + \frac{\mathrm{d}\left(\boldsymbol{L}_{\mathrm{s}}\boldsymbol{I}_{\mathrm{s}} + \boldsymbol{\Lambda}_{\mathrm{m}}\right)}{\mathrm{d}t} \tag{4}$$

where $\boldsymbol{U}_{\mathrm{s}}$ and $\boldsymbol{I}_{\mathrm{s}}$ are the stator voltage and current vectors, respectively. $\boldsymbol{R}_{\mathrm{s}}$ and $\boldsymbol{L}_{\mathrm{s}}$ are the stator resistance and stator inductance matrices, respectively. $\boldsymbol{\Lambda}_{\mathrm{m}}$ is the permanent magnet flux linkage vector represented by its first and third space harmonics, as shown in the following **Formula 5**.

$$\boldsymbol{\Lambda}_{\mathrm{m}}^{abcde} = \boldsymbol{\Lambda}_1 \begin{bmatrix} \cos\theta \\ \cos\left(\theta - \delta\right) \\ \cos\left(\theta - 2\delta\right) \\ \cos\left(\theta + 2\delta\right) \\ \cos\left(\theta + \delta\right) \end{bmatrix} + \boldsymbol{\Lambda}_3 \begin{bmatrix} \cos3\theta \\ \cos3\left(\theta - \delta\right) \\ \cos3\left(\theta - 2\delta\right) \\ \cos3\left(\theta + 2\delta\right) \\ \cos3\left(\theta + \delta\right) \end{bmatrix} \tag{5}$$

The electromagnetic torque expression for the five-phase PMSM can be found in (Ge et al. (2018)). Due to the space-time decoupling characteristics of the fundamental wave and 3rd harmonic, the fundamental symmetrical current cannot cause torque ripple. Therefore, the electromagnetic motor torque is given by **Equation 6** (Tian et al. (2018)) under the normal state of the motor.

$$\boldsymbol{T}_{\mathrm{em}} = \frac{5\boldsymbol{P}_p}{2}\left(\boldsymbol{\Lambda}_1\boldsymbol{i}_{q1} + 3\boldsymbol{\Lambda}_3\boldsymbol{i}_{q3}\right) \tag{6}$$

where $\boldsymbol{P}_p$ is the number of pole pairs. The contribution of the third harmonic $\boldsymbol{\Lambda}_3\boldsymbol{i}_{q3}$ to the total torque is about 1% (Tian et al. (2018)). In summary, we can control the torque by adjusting $\boldsymbol{i}_{q1}$.

Corrected motor model under fault conditions

If a normal motor model is used in the *dq* axis under a single-phase fault, the remaining four-phase currents are unbalanced and distorted. The back EMF will cause fluctuations in speed and torque. The A-phase open-circuit fault can be taken as an example for analysis. Once the A-phase is opened, the five-phase motor is reduced from a five-dimensional symmetrical system to a four-dimensional asymmetrical system. **Equation 7** shows the decoupling transformation modified Clarke matrix (Dwari and Parsa (2011)). The derivation of (7) is based on following steps. First, removing the first column element corresponding to A. Second, removing the elements corresponding to the third row of $\boldsymbol{i}_{d3}$. Third, modifying the elements to make each row orthogonal to each other.

$$\boldsymbol{T}'_{\text{Clarke}} = \begin{bmatrix} \cos\theta - 1 & \cos 2\theta - 1 & \cos 2\theta - 1 & \cos\theta - 1 \\ \sin\theta & \sin 2\theta & -\sin 2\theta & -\sin\theta \\ -\sin 2\theta & \sin\theta & -\sin\theta & \sin 2\theta \\ 1 & 1 & 1 & 1 \end{bmatrix} \tag{7}$$

Here, the motor current expression is:

$$\boldsymbol{I}^{\alpha_1\beta_1\beta_3 n} = \boldsymbol{T}'_{\text{Clarke}}\boldsymbol{I}^{bcde} \tag{8}$$

For the faulty motor, the third row is deleted in order to correct the Clarke transformation matrix, resulting in the lack of $\boldsymbol{i}_{\alpha_3}$ component. Therefore, it is not applicable to apply the previous Park transformation only to the $\boldsymbol{i}_{\beta_3}$ current component. Combining with the modified Clarke transformation, the Park transformation is modified as:

$$\boldsymbol{T}'_{\text{Park}} = \begin{bmatrix} \cos\theta & \sin\theta & 0 & 0 \\ -\sin\theta & \cos\theta & 0 & 0 \\ 0 & 0 & 1 & 0 \\ 0 & 0 & 0 & 1 \end{bmatrix} \tag{9}$$

The expression form of the stator voltage remains unchanged. Once an open-circuit motor fault occurs in a certain phase of winding, the system dimension decreases. Moreover, the fundamental wave and the third harmonic are no longer decoupled. At this time, the fundamental wave current will interact with the third harmonic magnetic potential to generate torque ripple. The permanent magnet flux linkage can be expressed as:

$$\boldsymbol{\Lambda}_{\text{m}}^{'bcde} = \boldsymbol{\Lambda}_1 \begin{bmatrix} \cos(\theta - \delta) \\ \cos(\theta - 2\delta) \\ \cos(\theta + 2\delta) \\ \cos(\theta + \delta) \end{bmatrix} + \boldsymbol{\Lambda}_3 \begin{bmatrix} \cos 3(\theta - \delta) \\ \cos 3(\theta - 2\delta) \\ \cos 3(\theta + 2\delta) \\ \cos 3(\theta + \delta) \end{bmatrix} \tag{10}$$

The electromagnetic torque equation under fault conditions can also be obtained (Tian et al. (2018)):

$$\boldsymbol{T}_{\text{em}} = \frac{5\boldsymbol{P}_{\text{p}}}{2}\boldsymbol{\Lambda}_1\boldsymbol{i}_q\left[1 + \frac{3\boldsymbol{\Lambda}_3}{2\boldsymbol{\Lambda}_1}(-\cos(2\theta) + \cos(4\theta))\right] \tag{11}$$

When an open-circuit fault occurs in the winding, the winding structure of the stator is no longer symmetrical. Now, the circular rotating magnetic field can be reconstructed by adjusting the amplitude and phase of the residual phase current. Hence, the motor torque is smooth before and after the fault. The system reliability is also improved.

It can be seen that the basic torque component in **Equation 11** is the same as the basic torque component in **Equation 6** for normal operation of the motor. According to **Equation 11**, the existence of the 3rd harmonic magnetic potential after the fault will cause the 2nd and 4th torque ripples. In many cases, due to the small $\left(\frac{\boldsymbol{\Lambda}_3}{\boldsymbol{\Lambda}_1}\right)$ ratio, these ripples are acceptable. Let the 2nd and 4th torque ripple caused by the 3rd harmonic magnetic potential be 0, $\boldsymbol{i}_q = C$, and substitute it into the **Formula 1** to obtain the residual phase current. The new reference current enables the system to achieve bumpless operation with minimal torque ripple under fault conditions.

Optimizing the reference current with the adjustment factor

Simulation results indicate that the system can realize the minimum torque fluctuation and even undisturbed operation under single-phase conditions with open-circuit fault. First, the coordinate transformation matrix is modified. Then, the reset reference current is obtained under the constraint of instantaneous power balance. FTC is theoretically realized, but the amplitude of the fault-tolerant current obtained in this way is seriously unbalanced. Simulation results also show that the residual phase current fluctuates greatly and even doubles the motor's rated current. In practical applications, such a reference current will generate high heat for a long time. It is a big hidden danger to permanent magnets and other working parts. It may cause more secondary severe damage to the motor drive system than an open-circuit fault.

For the above problem of large fluctuation range of residual phase current. Using the idea of vector synthesis, the objective function is to minimize the current fluctuation. The torque fluctuation fluctuates within a small allowable range. The phase current balance is used as the constraint condition. Finally, the adjustment factor α is optimized. **Figure 2** shows the control block diagram of the control system. In **Figure 2**, the reference current of the motor without faults and the fault-tolerant reference current under the optimal torque is vector synthesized under the α adjustment factor. Besides, the fault-tolerant reference current is considered. This approach considers the torque ripple under fault and considers the optimal current for motor operation under fault.

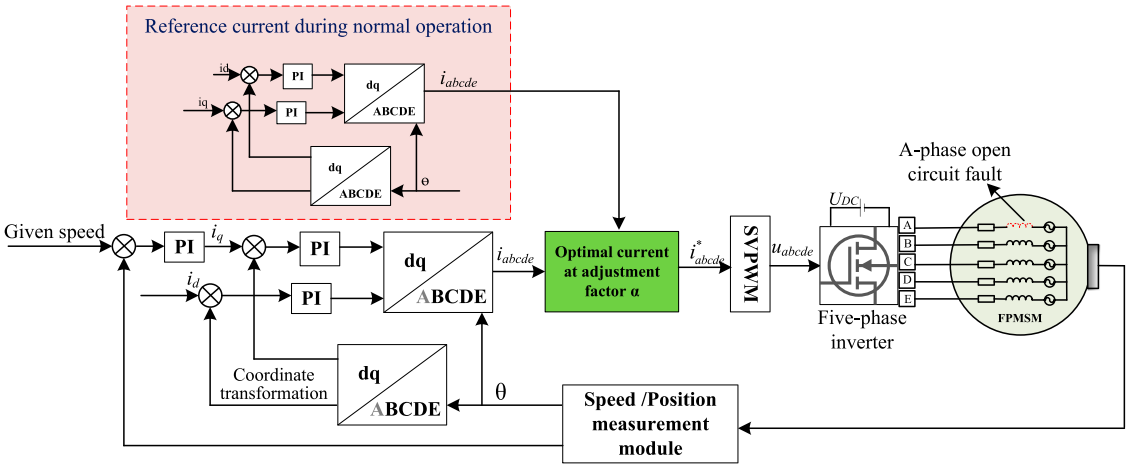

FIGURE 2
Block diagram of system control applying fault-tolerant control strategy.

Chaotic particle swarm optimization algorithm

The chaotic particle swarm optimization (CPSO) algorithm (Wang et al. (2021)) has the following characteristics. The adaptive inertia weight is used to accelerate the convergence speed, which is improved based on the particle swarm optimization (PSO) algorithm. The system is avoided falling into local optimum by performing chaotic searches in the neighborhood. CPSO can be used to solve parameter optimization problems. The traditional PSO algorithm is prone to premature phenomenon in the solution process. To avoid this shortcoming, CPSO was based on a logistic equation. When the particle falls into the local optimum, a chaotic disturbance is used to jump out of the local optimum.

Fault-tolerant reference current of fusion chaotic particle swarm optimization algorithm

The above CPSO is applied to optimize the reference current. The optimization idea of CPSO is followed. Once a fault is detected, the system can smoothly switch from the normal working mode to the fault-tolerant running mode without changing the hardware form. The A-phase open-circuit fault is an example. The reference current is optimized by adding adjustment factors in CPSO. The reference current is divided into the current reference $\boldsymbol{i}_{abcde}$ of the system's normal operation before the fault and the fault-tolerant reference current $\boldsymbol{i}'_{bcde}$ obtained under the electro-magnetic power balance method. An adjustment factor is set as α, and optimized reference current $\boldsymbol{i}^*_{bcde}$ can be expressed as:

$$\boldsymbol{i}^*_{bcde} = \alpha \boldsymbol{i}'_{bcde} + (1-\alpha)\,\boldsymbol{i}_{bcde} \tag{12}$$

The chaotic particle swarm is used to adaptively optimize α, taking the minimum torque fluctuation as the optimization goal, and the optimal torque state corresponds to an optimal α. The particle swarm variables are:

1) Decision variables α;
2) The minimum torque ripple change is defined as $\Delta \boldsymbol{T}_{em}$, then the objective function is:

$$\Delta \boldsymbol{T}_{em} = \min \int_0^T \left| \frac{\mathrm{d}\boldsymbol{T}_{em}}{\mathrm{d}t} \right| \mathrm{d}t \tag{13}$$

The torque fluctuation after fault tolerance is optimized by using the reference current under the fault and the reference current under the normal operation of the motor under the adjustment factor α.

3) Constraints:

$$s.t. \begin{cases} \boldsymbol{G}_j(\boldsymbol{I}^*) = \sum_{j=2}^{5} \boldsymbol{I}^* = 0 \\ \boldsymbol{T}_{em} \geq \boldsymbol{T}_L \\ \boldsymbol{i}_{abcde} < \boldsymbol{i}'_{bcde} \end{cases} \tag{14}$$

In (14), the first equation denotes that the obtained reference current must meet and be zero (Chen Z. et al. (2022)). The second inequality is the electromagnetic torque of the motor is greater than the load torque (Li et al. (2014)). The third inequality denotes that the current fluctuation range is smaller than that without fault tolerance after the fault.

The adjustment factor α is optimized under the above constraints to minimize the torque ripple. This approach

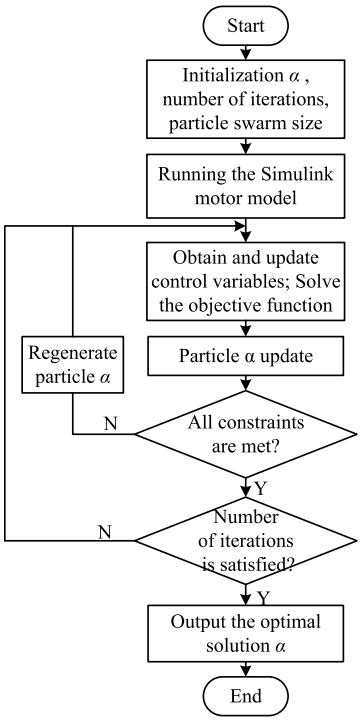

FIGURE 3
Flow chart of chaotic particle swarm optimization α.

TABLE 1 Parameters of five-phase permanent magnet synchronous motor.

Parameters	Symbol	Value
Pole pairs	P_p	4
Fundamental PM flux linkage	Ψ_{m1}	0.505 Wb
Third harmonic flux linkage	Ψ_{m3}	0.024 Wb
Stator resistance	R_s	0.12 Ω
Stator inductance	L_s	1.35 mH
Given speed	n	1,500 r/min

considers both the torque fluctuation and the current fluctuation range, which is a dual consideration for the safe operation of the motor. Figure 3 presents the flow chart of alpha optimization.

Simulation and verification

In order to verify the feasibility of the FT-FOC strategy proposed in this paper, it is used for the normal and single phase open-circuit fault conditions of the motor respectively. Comparisons are carried out with the fault-tolerant reference current based on different adjustment factors α. The five-phase PMSM parameters are shown in Table 1.

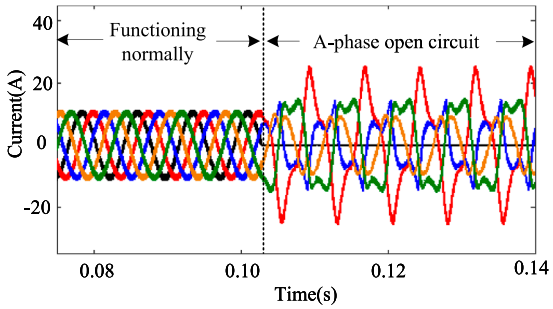

FIGURE 4
Motor current under normal and open-circuit fault conditions.

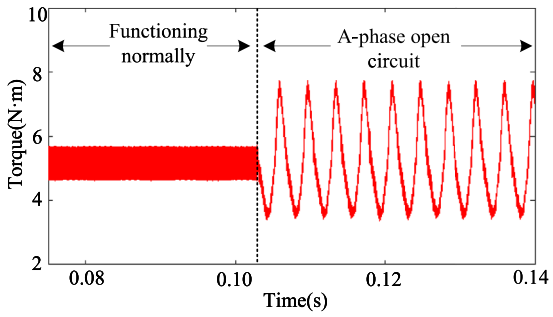

FIGURE 5
Torque of the motor under normal and open-circuit fault conditions.

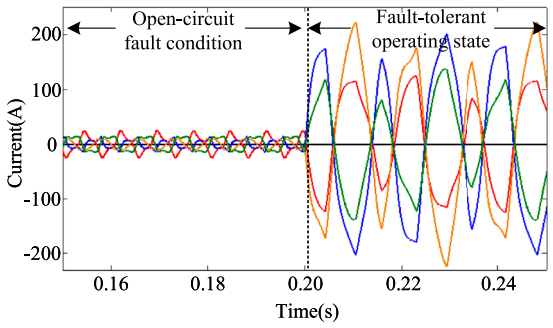

FIGURE 6
Motor current in fault and fault tolerant state.

The current, electromagnetic torque and rotational speed curves of the motor under normal and A-phase open-circuit fault states are shown in Figure 4 and Figure 5 respectively.

When the coordinate transformation is used, the current electromagnetic torque waveforms of the motor in the fault and fault-tolerant operation state are shown in Figure 6 and Figure 7, where $\alpha = 0$.

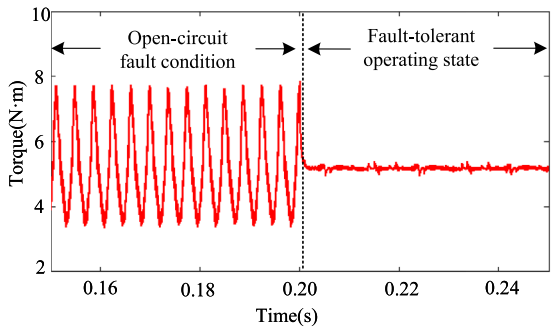

FIGURE 7
Torque in fault and fault tolerant state.

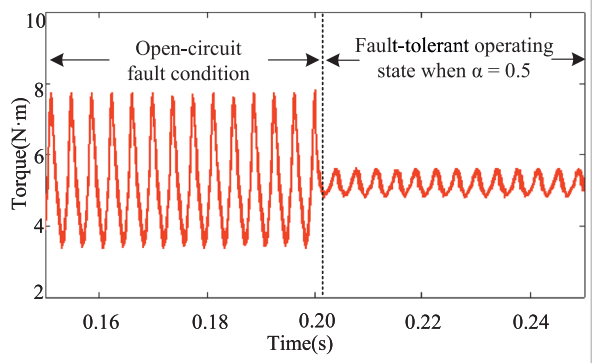

FIGURE 9
Torque under the condition of motor fault and FT when $\alpha = 0.5$.

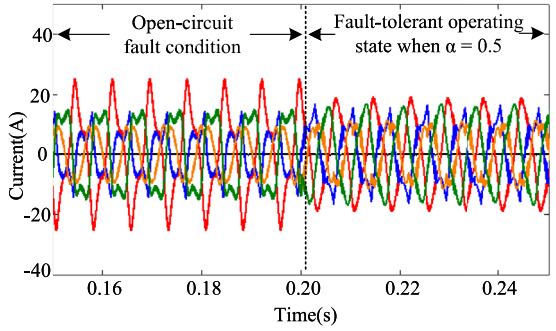

FIGURE 8
Current under the condition of motor fault and FT when $\alpha = 0.5$.

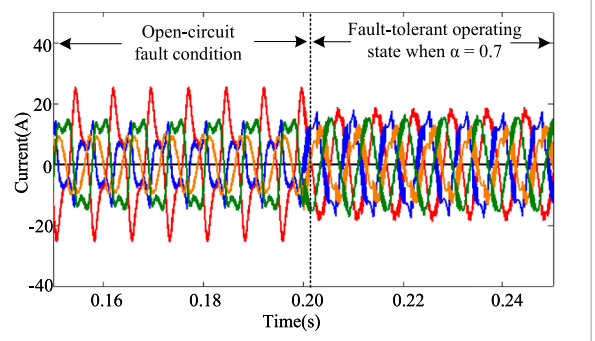

FIGURE 10
Current under the condition of motor fault and FT when $\alpha = 0.7$.

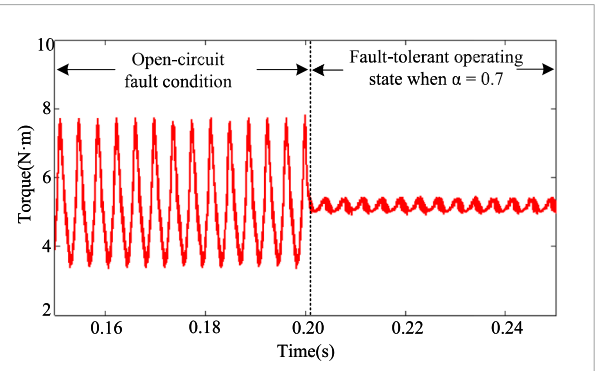

FIGURE 11
Torque under the condition of motor fault and FT when $\alpha = 0.7$.

In the normal operation state of the motor, the torque fluctuation range of the motor is 1N·m. After the open-circuit fault of phase A occurs, the torque fluctuation range is 4N·m, which is 4 times that of normal operation. When the fault-tolerant current is used as the reference current, the torque fluctuation range is 0.5N·m, where the optimization effect is remarkable. However, because of the imbalance of the effective value of each phase current, the current fluctuates greatly. The chaotic particle swarm optimization algorithm is used to optimize the current adaptively under the adjustment factor α equal to 0.5 and 0.7, respectively. The simulation results of the current and electromagnetic torque of the motor operation are shown in Figures 8–11.

In order to further illustrate the current fluctuation of the motor under different adjustment factors, the relationship is obtained between the adjustment factor and the current range from the simulation experiment. The relationship is shown in Table 2.

It can be seen from the table that in different applications, the safe operation range of the open-circuit fault and the corresponding torque fluctuation can be selected to meet the safe operation of the motor. Meanwhile, the motor runs reliably and smoothly under acceptable conditions for fluctuations after a fault occurs.

TABLE 2 Relationship between different adjustment factors and current range and torque ripple.

α	Current range(A)	Torque range (N· m)
0.1	±23	4.0∼6.5
0.2	±20	4.4∼6.1
0.3	±20	4.5∼5.9
0.4	±18	4.9∼5.5
0.5	±18	4.8∼5.4
0.6	±18	4.8∼5.5
0.7	±18	4.8∼5.4
0.8	±19	4.9∼5.4
0.9	±25	4.9∼5.4
0	±223	4.5∼5.5
1.0	±25	3.5∼7.5

Conclusion

Compared with the previous related research, the main contributions of this paper are as follows. First, the fault-tolerant current is adaptively optimized by the chaotic particle swarm optimization algorithm. The current fluctuation is also considered on the premise of considering the torque fluctuation. The adaptive optimization of the current by the CPSO achieves the effect of filtering and reducing the amplitude of the fault-tolerant current after a fault. From the current point of view, the dimension of the safe operation of the motor is increased. Second, the proposed FT-FOC control strategy has the advantage of maintaining the exact same control structure before and after failure. This ensures a very smooth transition of the system to fault-tolerant mode. Finally, simulation verified that the proposed FTC strategy could reduce the torque pulsation when a fault occurs and ensure that the dynamic performance reaches the normal state level. It can also ensure that the fault-tolerant current range is basically the same as the current range before the fault, which enhances the robustness of the system against external interference.

To sum up, the field-oriented FTC strategy adopted in this paper considers the two motor operating parameters of torque and current simultaneously, which broadens the dimension of reliable operation of the system.

Data availability statement

The original contributions presented in the study are included in the article/Supplementary Material, further inquiries can be directed to the corresponding author.

Author contributions

CC, YS, and YZ contributed to conception and design of the study. JT and SG organized the database. CC and YS performed the simulation and statistical analysis. CC wrote the first draft of the manuscript. YS and BL wrote sections of the manuscript. All authors contributed to manuscript revision, read, and approved the submitted version.

Funding

This work was supported by the Shaanxi Province Key Research and Development Program under Grant (No. 2021GY-149), Shaanxi Province Science and Technology Innovation Guidance Special (Fund) Project under Grant (No. 2022QFY01-16), the National Natural Science Foundation of China (No. 61833013), and the Natural Sciences and Engineering Research Council of Canada.

Conflict of interest

The authors declare that the research was conducted in the absence of any commercial or financial relationships that could be construed as a potential conflict of interest.

Publisher's note

All claims expressed in this article are solely those of the authors and do not necessarily represent those of their affiliated organizations, or those of the publisher, the editors and the reviewers. Any product that may be evaluated in this article, or claim that may be made by its manufacturer, is not guaranteed or endorsed by the publisher.

References

Chen, F., Hua, W., Huang, W., Zhu, J., and Tong, M. (2019). Open-circuit fault-tolerant strategies for a five-phase flux-switching permanent magnet motor based on model predictive torque control method. *Proc. CSEE* 39, 337–346. doi:10.13334/j.0258-8013.pcsee.181802

Chen, Q., Xia, Y., Zhao, W., and Liu, G. (2022a). Open-circuit fault-tolerant control for five-phase permanent magnet motors with trapezoidal back-emf by deadbeat current tracking. *Trans. China Electrotech. Soc.* 37, 368–379. doi:10.19595/j.cnki.1000-6753.tces.200897

Chen, Y., Yang, Z., Zhou, H., Ji, C., and Li, P. (2021). Pmsm open circuit fault tolerance control. *Electr. Mach. Control* 25, 11–16. doi:10.15938/j.emc.2021.09.002

Chen, Z., Zhang, X., Liu, C., Zhang, H., and Luo, G. (2022b). Research on current decoupling and harmonic suppression strategy of permanent magnet synchronous motor by proportional resonance adaptive disturbance rejection control. *Proc. CSEE* 1. doi:10.13334/j.0258-8013.pcsee.211791

Dwari, S., and Parsa, L. (2011). Fault-tolerant control of five-phase permanent-magnet motors with trapezoidal back emf. *IEEE Trans. Ind. Electron.* 58, 476–485. doi:10.1109/TIE.2010.2045322

Fnaiech, M. A., Betin, F., Capolino, G.-A., and Fnaiech, F. (2010). Fuzzy logic and sliding-mode controls applied to six-phase induction machine with open phases. *IEEE Trans. Ind. Electron.* 57, 354–364. doi:10.1109/TIE.2009.2034285

Gaeta, A., Scelba, G., and Consoli, A. (2013). Modeling and control of three-phase pmsms under open-phase fault. *IEEE Trans. Ind. Appl.* 49, 74–83. doi:10.1109/TIA.2012.2228614

Gao, H., Yang, G., Liu, J., and Zhao, P. (2013). Air-gap mmf analysis for five-phase pmsm with third harmonic injection. *Electr. Mach. Control* 17, 1–6. doi:10.15938/j.emc.2013.10.005

Ge, Q., Tian, B., Sun, L., An, Q., and Zhao, K. (2018). Unified foc of five-phase permanent magnet motor under open-circuit conditions. *Electr. Power Autom. Equip.* 38, 192–200. doi:10.16081/j.issn.1006-6047.2018.02.025

Huang, W., Du, J., Hua, W., and Fan, Q. (2021). An open-circuit fault diagnosis method for pmsm drives using symmetrical and dc components. *Chin. J. Electr. Eng.* 7, 124–135. doi:10.23919/CJEE.2021.000031

Li, Y., Lu, H., Qu, W., and Sheng, S. (2014). A permanent magnet synchronous motor current suppression method based on resonant controllers. *Proc. CSEE* 34, 423–430. doi:10.13334/j.0258-8013.pcsee.2014.03.013

Liu, X., Wang, Z., Wang, W., Lv, Y., Yuan, B., Wang, S., et al. (2022). Smo-based sensorless control of a permanent magnet synchronous motor. *Front. Energy Res.* 10, 1–10. doi:10.3389/fenrg.2022.839329

Liu, X., Zeng, Z., and Wunsch Ii, D. C. (2020). Memristor-based LSTM network with *in situ* training and its applications. *Neural Netw.* 40, 300–311. doi:10.1016/j.neunet.2020.07.035

Okedu Kenneth, E., and Barghash, H. (2021). Enhancing the transient state performance of permanent magnet synchronous generator based variable speed wind turbines using power converters excitation parameters. *Front. Energy Res.* 9, 1–10. doi:10.3389/fenrg.2021.655051

Salehifar, M., Arashloo, R., Moreno-Equilaz, J., Sala, V., and Romeral, L. (2014). Fault detection and fault tolerant operation of a five phase pm motor drive using adaptive model identification approach. *IEEE J. Emerg. Sel. Top. Power Electron.* 2, 212–223. doi:10.1109/JESTPE.2013.2293518

Tao, T., Zhao, W., Cheng, M., and Wang, Z. (2019). Overview of fault tolerant control and its key technologies for polyphase motors. *CJEE* 39, 316–326. doi:10.13334/j.0258-8013.pcsee.181589

Tian, B., Mirzaeva, G., An, Q., Sun, L., and Semenov, D. (2018). Fault-tolerant control of a five-phase permanent magnet synchronous motor for industry applications. *IEEE Trans. Ind. Appl.* 54, 3943–3952. doi:10.1109/tia.2018.2820060

Wang, X., Fu, X., Dong, J., and Jiang, J. (2021). Dynamic modified chaotic particle swarm optimization for radar signal sorting. *IEEE Access* 9, 88452–88466. –88466doi. doi:10.1109/ACCESS.2021.3091005

Wu, X., Song, W., and Xue, C. (2019). Direct torque control schemes for five-phase permanent magnet synchronous machines based on duty ratio optimization of virtual voltage vector sets. *Proc. CSEE* 39, 857–867. doi:10.13334/j.0258-8013.pcsee.170953

Zhang, C., Zhao, S., and He, Y. (2021). An integrated method of the future capacity and rul prediction for lithium-ion battery pack. *IEEE Trans. Veh. Technol.* 71, 2601–2613. doi:10.1109/TVT.2021.3138959

Zhao, S., Zhang, C., and Wang, Y. (2022). Lithium-ion battery capacity and remaining useful life prediction using board learning system and long short-term memory neural network. *J. Energy Storage* 52, 104901. doi:10.1016/j.est.2022.104901

Zhao, W., Cheng, M., Hua, W., Jia, H., and Cao, R. (2011). Back-emf harmonic analysis and fault-tolerant control of flux-switching permanent-magnet machine with redundancy. *IEEE Trans. Ind. Electron.* 58, 1926–1935. doi:10.1109/TIE.2010.2050758

Zhou, X., Sun, J., Li, H., and Song, X. (2019). High performance three-phase pmsm open-phase fault-tolerant method based on reference frame transformation. *IEEE Trans. Ind. Electron.* 66, 7571–7580. doi:10.1109/TIE.2018.2877197

frontiers | Frontiers in Energy Research

TYPE Original Research
PUBLISHED 08 September 2022
DOI 10.3389/fenrg.2022.997782

OPEN ACCESS

EDITED BY
Xiao Wang,
Wuhan University, China

REVIEWED BY
Wang Xiang,
Huazhong University of Science and Technology, China
Hengrui Ma,
Qinghai University, China
Yuan Chen,
Anhui University, China
Fei Tang,
Wuhan University, China

*CORRESPONDENCE
Tang Aihong,
tah@whut.edu.cn

SPECIALTY SECTION
This article was submitted to Smart Grids,
a section of the journal
Frontiers in Energy Research

RECEIVED 19 July 2022
ACCEPTED 16 August 2022
PUBLISHED 08 September 2022

CITATION
Peng Q, Jingen S, Qian C, Wei Z, Bingyu X and Aihong T (2022), Research on oscillation characteristics of wind farm sending system based on participation factor.
Front. Energy Res. 10:997782.
doi: 10.3389/fenrg.2022.997782

Research on oscillation characteristics of wind farm sending system based on participation factor

Qiu Peng[1], Song Jingen[1], Chen Qian[1], Zhou Wei[2], Xiong Bingyu[2] and Tang Aihong[2]*

[1]State Grid Zhejiang Electric Power Co.,Ltd., Hangzhou, China, [2]Automation School, Wuhan University of Technology, Wuhan, China

The MMC-HVDC transmission system of wind farms has a very broad application prospect, but there is gradually growing major concern that the system is prone to broadband oscillation. And the mechanism of oscillation also remains to be clarified. In this article, based on the basic principle of eigenvalue analysis, the theoretical calculation equation of the quantitative evaluation index of the participation factor is deduced. The small-signal model of the MMC-HVDC transmission system for a wind farm is established. Combining with the case of 200 wind turbines connected to the grid, the eigenvalue analysis method is used to obtain the dominant oscillation mode of the system. The participation factors of 11 oscillation modes of the system are calculated to further analyze the relationship between the oscillation modes and the state variables in the MMC-HVDC transmission system of the wind farms. And the correlation between the participation factors of each oscillation mode, wind farm, and the MMC system is investigated, which laid a foundation for the formulation of broadband oscillation suppression strategies.

KEYWORDS

wind farm sending system, oscillation characteristics, participation factor, oscillation mod, correlations

1 Introduction

The MMC-HVDC transmission system of wind farms has a very broad application prospect, but with the continuous construction of related engineering projects, the broadband oscillation problem of the system has gradually become prominent. According to relevant reports, there have been numerous wind farms connected to the actual project of MMC-HVDC in China and abroad, and the phenomenon of broadband oscillation instability appears in the system debugging or production operation stage. For instance, the grid-connected project of the VSC-HVDC system of the doubly fed wind farm in Nan'ao, Guangdong Province, China, experienced oscillation during the system commissioning, which eventually led to the outage of the system (Lu

et al., 2015). In addition, the Shanghai Nanhui demonstration project also encountered similar problems in the initial commissioning stage (Wang et al., 2017).

The oscillation problem of traditional power systems is mainly caused by the single oscillation mode of the synchronous generator, which only oscillates in the local regional power grid. The broadband oscillation problem of wind farms through the MMC-HVDC transmission system is caused by the interaction and coupling of power electronic equipment, various control links, and transmission network electrical equipment. The manifestation is the continuous oscillation of divergence in a wide frequency range, which has multimodal characteristics and shows indigenous time-varying characteristics. If the broadband oscillation problem of the MMC-HVDC transmission system of wind farms is not effectively solved, it will cause damage to the power supply side power generation equipment, which will result in the tripping of new energy stations and active power shortage of the power grid. Moreover, the generated oscillation components will be transmitted to the user side through the transmission network, which will eventually cause a large area of power outages and pose a great threat to the safe and stable operation of the power grid (Cai et al., 2021). However, the mechanism and characteristics of the oscillation are not clear (Sun et al., 2021). Therefore, analyzing the broadband oscillation mode, dynamic characteristics, and correlation with the participation factor of the MMC-HVDC transmission system of wind farms in-depth will lay the foundation for the formulation of broadband oscillation suppression strategy, which has very important theoretical and engineering significance for the safe and stable operation of the grid connecting system.

At present, there are many analysis methods of broadband oscillation mechanisms in China and abroad, which include the impedance analysis method (Rygg et al., 2016; Shah and Parsa, 2017; Wen et al., 2017), frequency scanning method (Yang et al., 2020), complex torque coefficient method, time domain simulation method, and eigenvalue analysis method.

In Liu et al. (2016), the RLC impedance circuit model is used to retain the dynamic characteristics of each part of the DFIG, and circuit parameters are used to qualitatively and quantitatively analyze the stability of the DFIG series compensated transmission system. In regard to the stability problem caused by the interaction between the DFIG and flexible transmission system, the impedance analysis method has been adopted by Sun et al. (2018), and it has been found that under certain operating conditions, the DFIG and flexible system constitute an equivalent negative resistance resonant circuit, which leads to subsynchronous oscillations of the system. However, the disadvantage of the impedance analysis method is that it cannot give the coupling relationship of various physical quantities in the system nor can it reflect the internal dynamic characteristics of the system.

Research of Tang et al. (2022) and Suriyaarachchi et al. (2013) have been based on the frequency scanning method. The stability characteristics of the doubly fed wind farm connected to the grid through series compensation have been analyzed by Tang et al. (2022), and the system oscillation characteristics and influencing factors have also been investigated. The results have shown that the increase of series compensation degree and decrease of wind speed would lead to system oscillation. In Suriyaarachchi et al. (2013), the existence of unstable points in the doubly fed wind power grid-connected system was first studied by the frequency scanning method, and the oscillation mechanism of the system was then further analyzed by other methods. It was found that the subsynchronous oscillation was caused by the state variables of the wind turbine and the grid side, and the participation of the control system was not high. However, the frequency scanning method could not reveal the mechanism of system oscillation, and the accuracy of the analysis results was greatly related to the scanning step length.

In order to make the complex torque coefficient method suitable for analyzing the interaction mechanism between the controllers of the wind power grid-connected system, there are two main development directions currently (Tang et al., 2019). One is to ignore the mechanical part of the system and only consider the electrical part of the system. The complex torque coefficient of the electrical system is used to assess whether the system has the risk of oscillation. Research by Tang et al. (2021) is an example in this direction, in which the equivalent model of the DFIG converter is constructed by ignoring the mechanical part of the system. And then based on the compound torque coefficient method, the influence of system structure parameters and control parameters on electrical damping is studied. The other is to divide the system into parts to be studied and the rest, and then represent them by two electrical subsystems respectively, so as to identify the part to be studied. This method has been adopted by Hu et al. (2017), through which the phase-locked loop control part of a doubly fed induction generator is formed into a subsystem, and the influence of the phase-locked loop control parameters on the small signal stability of the wind farm is analyzed. However, this method is only suitable for analyzing the stability of the single-input single-output system and is difficult to be applied in large-scale wind power grid-connected systems.

The time-domain simulation method can not only directly observe whether there is an oscillation phenomenon in the system but also exhibit the ability to simulate the stability change of the system under disturbance or fault conditions. However, it is difficult to analyze the generation mechanism and influencing factors of oscillation (Xie et al., 2017; Chen et al., 2022).

In Wang et al. (2015) and Huang et al. (2019), the eigenvalue analysis method is used to study the stability of wind power grid-connected systems. And the influence of wind speed, number of wind turbines, and control system parameters on system stability

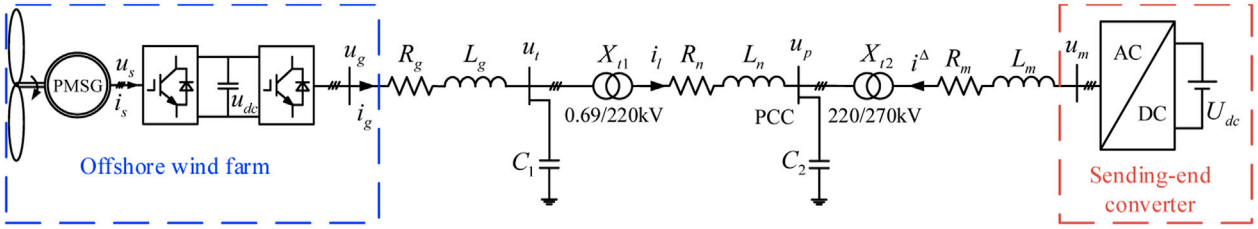

FIGURE 1
Structure diagram of a simplified system.

and oscillation frequency are analyzed. In Kunjumuhammed et al. (2017), Chen et al. (2018), Shao et al. (2019), and Guo et al. (2020), the small-signal model of the wind farm sending out through a flexible transmission system is established, the dominant participation factors of each oscillation mode of the system are investigated, and the corresponding oscillation suppression strategy is proposed. The eigenvalue analysis based on the small-signal model can not only obtain the system oscillation mode and its participation factor but also be combined with the classical or modern control theory to guide the design of the oscillation suppression controller, which is an important method for system stability analysis.

In this article, based on the basic principle of eigenvalue analysis, the theoretical calculation method of the quantitative evaluation index of participation factors is investigated. Based on the small-signal model of the wind farm sending out through the MMC-HVDC transmission system, the eigenvalue analysis method is used to obtain the dominant oscillation mode of the system. And the correlation in-between the participation factors of each oscillation mode and the wind farm and the MMC system is analyzed, which provides the basis for the oscillation suppression method.

2 Mathematical model of system of wind farm sending out through direct current transmission

2.1 Equivalent circuit of system of wind farm sending out through direct current transmission

The system of wind farm sending out through DC transmission consists of the wind farm, boost transformer, AC cable, and the MMC-HVDC system, in which the MMC-HVDC system includes matching transformer, sending-end converter (SEC), DC submarine cable, and receiving-end converter (REC).

Assuming that the AC power grid on the coast is a robust power grid, that is, when the MMC-HVDC system runs steadily, the receiving-end converter can almost completely track the reference value of the DC voltage. The influence of the REC side on the SEC side is so small that it can be ignored. Therefore, in order to simplify the analysis, the DC side of the SEC can be replaced by a constant DC voltage source to simulate the DC voltage control effect of the REC. In addition, in order to improve the simulation efficiency, the stand-alone equivalent method is adopted in this article to model the wind farm equivalently (An et al., 2018). And the equivalent circuit of the DC transmission system of the wind farm is presented in Figure 1.

In Figure 1, the wind farm is simplified as a single typhoon. u_s and i_s are the port voltage and current of the permanent magnet synchronous generator, respectively. u_g and i_g are the output voltage and current of the grid-side converter in the wind farm, respectively. (R_g, L_g), (R_n, L_n), and (R_m, L_m) are the resistance and inductance of simplified lines. X_{t1} is the equivalent boost transformer, X_{t2} is the matching transformer, and L_{t1} and L_{t2} are the leakage inductance of X_{t1} and X_{t2}, respectively. C_1 is the capacitance of the collector line, and C_2 is the filter capacitance of the SEC in the MMC-HVDC system.

2.2 Small-signal model of system of wind farm sending out through direct current transmission

Combined with the dynamic model of the wind turbine (Gao, 2021) and MMC system (Bergna-Diaz et al., 2018), and based on the interface model of the wind farm and MMC system (Liu et al., et al.), a complete system dynamic model of the wind farm sending out through MMC-HVDC can be obtained. After linearization of the overall dynamic model at the steady-state equilibrium point, the small-signal model of the system of the wind farm sending out through MMC-HVDC can be described as follows:

$$\frac{d\Delta \boldsymbol{x}}{dt} = \boldsymbol{A}\Delta \boldsymbol{x} + \boldsymbol{B}\Delta \boldsymbol{u}. \tag{1}$$

where matrix A is the state matrix of the small-signal model of the system, and the small signal stability of the system is related to the eigenvalue of A; matrix B is the input matrix of the system. $\Delta \boldsymbol{x}$

TABLE 1 Classification and meaning of wind turbine state variables.

Module	State variables
Actuating system	Mechanical speed of wind turbine ω_s
PMSG	d-axis and q-axis component of stator current i_{sd}, i_{sq}
Back-to-back converter	Capacitor voltage of DC-side u_{dc}
	Machine-side converter control system x_{w1}, x_{w2}, x_{w3}
	Grid-side converter control system x_{w4}, x_{w5}, x_{w6}
AC-side transmission line	d-axis and q-axis component of grid-side converter output current i_{gd}, i_{gq}
	d-axis and q-axis component of grid-side converter output voltage u_{td}, u_{tq}
	d-axis and q-axis current of collector line i_{ld}, i_{lq}
PLL	Intermediate variables, x_{pll}, and phase angles, θ_g

TABLE 2 Classification and meaning of state variables of the MMC system.

Module	State variables
Main circuit	d-axis and q-axis voltage u_{pd}, u_{pq}
	d-axis and q-axis current at AC-side i_d^{Δ}, i_q^{Δ}
	Internal circulation of MMC i_d^{Σ}, i_q^{Σ}, i_0^{Σ}
	Differential mode equivalent capacitance voltage u_{Cd}^{Δ}, u_{Cq}^{Δ}, $u_{C0_d}^{\Delta}$, $u_{C0_q}^{\Delta}$
	Common-mode equivalent capacitor voltage u_{Cd}^{Σ}, u_{Cq}^{Σ}, u_{C0}^{Σ}
Control system	Intermediate variable of voltage control system x_{m1}, x_{m2}, x_{m3}, x_{m4}
	Intermediate variables of circulation suppression controller x_{m5}, x_{m6}

is the state variable of the linearized system of the wind farm sending out through MMC-HVDC, $\boldsymbol{x} = [\boldsymbol{x_w}, \boldsymbol{x_m}]^T$, in which $\boldsymbol{x_w}$ is the state variable of the wind turbine after stand-alone equivalence and $\boldsymbol{x_m}$ is the state variable of the MMC system. $\Delta\boldsymbol{u}$ is the input variable of the linearized system of the wind farm sending out through MMC-HVDC, $\boldsymbol{u} = [\boldsymbol{u_w}, \boldsymbol{u_m}]^T$, in which $\boldsymbol{u_w}$ represents the input variable of the wind turbine after stand-alone equivalent and $\boldsymbol{u_m}$ represents the input variable of the MMC system.

The state variables of the wind turbines can be written as $\boldsymbol{x_w} = [\omega_s, i_{sd}, i_{sq}, u_{dc}, i_{gd}, i_{gq}, u_{td}, u_{tq}, i_{ld}, i_{lq}, x_{pll}, \theta_g, x_{w1}, x_{w2}, x_{w3}, x_{w4}$, and the input variable of the wind turbines can be written as $\boldsymbol{u_w} = [\omega_{sref}, i_{sdref}, u_{dcref}, i_{gqref}]^T$. The state variables of the MMC system is $\boldsymbol{x_m} = [u_{pd}, u_{pq}, i_d^{\Delta}, i_q^{\Delta}, i_d^{\Sigma}, i_q^{\Sigma}, i_0^{\Sigma}, u_{Cd}^{\Delta}, u_{Cq}^{\Delta}, u_{C0_d}^{\Delta}, u_{C0_q}^{\Delta}, u_{Cd}^{\Sigma}, u_{Cq}^{\Sigma}, u_{C0}^{\Sigma}$, and the input variables of the MMC system is $\boldsymbol{u_m} = [u_{pdref}, u_{pqref}, i_{dref}^{\Sigma}, i_{qref}^{\Sigma}]^T$.

In order to distinguish the meaning of each state variable, the state variables are clarified according to each module of the wind turbine in this article, and the classification results are shown in Table 1. At the same time, the state variables are classified according to each module of the MMC system, and the classification results are shown in Table 2.

3 Participation factor of broadband oscillation quantitative evaluation index

The eigenvalue analysis method can find out the main oscillation mode of the system, and it can also obtain the participation factor of the oscillation mode and the eigenvalue sensitivity of the system parameters. The calculation method of the quantitative evaluation index of the participation factor is investigated below.

For any eigenvalue λ_i of state matrix $\boldsymbol{A}$, if the non-zero vector $U_i \in R^{n\times 1}$, the following relationship should be satisfied:

$$AU_i = \lambda_i U_i \quad i = 1, 2, \cdots, n. \tag{2}$$

TABLE 3 Parameters of PMSG wind power system.

Module	Parameters and corresponding symbols	Reference value
Wind turbine	Wind turbine radius R	63 m
	Air density ρ	1.225 kg/m^3
	Self-damping coefficient B_m	0.002
PMSG	Number of pole-pairs N_p	48
	Stator equivalent resistance R_s	0.006 Ω
	Stator equivalent inductance ($L_d = L_q$)	3.95 mH
	Rotor permanent magnet flux linkage ψ_f	1.48 W b
DC-side	DC-side capacitor C_{dc}	50 mF
Machine-side control system	Speed reference value ω_{sref}	1 p.u.
	Reference value of stator d-axis current i_{sdref}	0 p.u.
	Speed outer loop controller coefficient (k_{wp1}、 k_{wi1})	0.25, 5
	Controller coefficient of q-axis current inner loop (k_{wp2}、 k_{wi2})	1, 50
	Controller coefficient of d-axis current inner loop (k_{wp3}, k_{wi3})	1, 50
Grid-side control system	Reference value of DC-side capacitor voltage u_{dcref}	1 kV
	Reference value of q-axis component of grid-side converter output current i_{gqref}	0 p.u.
	Coefficient of capacitor voltage outer loop controller (k_{wp4}, k_{wi4})	4, 50
	Controller coefficient of d-axis current inner loop (k_{wp5}, k_{wi5})	3, 100
	Controller coefficient of q-axis current inner loop (k_{wp6}, k_{wi6})	3、100
PLL	Coefficient of PLL controller (k_{p_pll}, k_{i_pll})	50, 100
AC-side transmission line	Filter resistance R_g	0.0005 Ω
	Filter inductance L_g	0.2 mH
	Collector line resistance R_l	0.05 Ω/km
	Collector line inductance L_l	0.38 mH/km
	Collector line capacitanceC_1	0.187 μF/km
	Transformer ratio of X_{t1}	0.69/220 kV
	Leakage inductance of transformerX_{t1} L_{t1}	0.1 p.u.

Then the vector U_i is called the right eigenvector corresponding to the eigenvalues λ_i. In the same way, if the non-zero vector $V_i \in R^{n\times 1}$, the following relationship would be satisfied:

$$V_i^T A = \lambda_i V_i^T \quad i = 1, 2, \cdots, n. \tag{3}$$

The vector V_i is called the left eigenvector corresponding to the eigenvalues λ_i. With the aim of quantitatively analyzing the impact of each state variable in different oscillation modes, the following participation matrix p is defined:

$$P = \begin{bmatrix} p_{11} & p_{12} & \cdots & p_{1n} \\ p_{21} & p_{22} & \cdots & p_{2n} \\ \vdots & \vdots & \ddots & \vdots \\ p_{n1} & p_{n2} & \cdots & p_{mn} \end{bmatrix}, \tag{4}$$

where the participation factor p_{ki} can quantitatively reflect the correlation between the oscillation mode and the system state variables, which means the influence of the system state variables x_k on the oscillation mode λ_i. The calculation expression is as follows:

TABLE 4 MMC system parameters.

Module	Parameters and corresponding symbols	Reference value
AC-side transmission line	Filter capacitance C_2	5 μF
	Resistance of AC-side line R_f	0.5 Ω
	Inductance of AC-side line L_f	46.12 mH
	Transformer ratio of X_{t2}	220/270 kV
	Leakage inductance of transformerX_{t2} L_{t2}	0.1 p.u.
Sending-end converter	Number of sub-modules	400
	Bridge arm resistance R_{arm}	1 Ω
	Bridge arm inductance L_{arm}	50 mH
	Equivalent capacitance of bridge arm C_{arm}	36.84 μF
Voltage control system	Reference value of d-axis voltage of PCC u_{pdref}	1 p.u.
	Reference value of q-axis voltage of PCC u_{pqref}	0 p.u.
	Controller coefficient of d-axis voltage outer loop (k_{mp1}, k_{mi1})	1, 10
	Controller coefficient of q-axis voltage outer loop (k_{mp3}, k_{mi3})	1, 10
	Controller coefficient of d-axis current inner loop (k_{mp2}, k_{mi2})	10, 200
	Controller coefficient of 1-axis current inner loop (k_{mp4}, k_{mi4})	10, 200
Circulation suppression controller	Reference value of internal circulation d-axis component i^{Σ}_{dref}	0 p.u.
	Reference value of internal circulation q-axis component i^{Σ}_{qref}	0 p.u.
	Controller coefficient of d-axis circulation (k_{mp5}, k_{mi5})	40, 400
	Controller coefficient of q-axis circulation (k_{mp6}, k_{mi6})	40, 400

TABLE 5 Main oscillation modes of the system of the wind farm sending out *via* MMC-HVDC.

Oscillation modes	Number of grid-connected wind farm, n = 100	Number of grid-connected wind farm, n = 200		
	Eigenvalue	Eigenvalue	Oscillation frequency/Hz	Damping ratio
$\lambda_{1,2}$	−36.32±j8613.73	−44.25±j7752.84	1233.90	0.00571
$\lambda_{3,4}$	−41.04±j8120.56	−50.64±j7290.74	1160.36	0.00695
$\lambda_{5,6}$	−50.53±j3961.32	−42.84±j4396.20	699.68	0.00974
$\lambda_{7,8}$	−51.31±j3517.22	−41.60±j3920.24	623.93	0.01061
$\lambda_{9,10}$	−14.47±j668.28	10.23±j648.47	103.21	−0.01578
$\lambda_{11,12}$	−97.42±j794.77	−98.29±j786.40	125.16	0.12403
$\lambda_{13,14}$	−58.05±j970.91	−57.66±j971.23	154.58	0.05925
$\lambda_{15,16}$	−666.78±j157.34	−666.65±j154.86	24.65	0.97406
$\lambda_{17,18}$	−356.01±j118.35	−303.76±j163.67	26.05	0.88034
$\lambda_{19,20}$	−1.31±j52.31	0.20±j51.84	8.25	−0.00377
$\lambda_{21,22}$	−51.19±j327.59	−66.745±j342.42	54.50	0.19133

$$p_{ki} = \frac{V_{ki}U_{ki}}{V_i^T U_i}. \quad (5)$$

V_{ki} and U_{ki} mentioned above are the elements of column i and row k in the eigenvector matrices $\boldsymbol{V}$ and $\boldsymbol{U}$, respectively.

The greater the value of the participation factor p_{ki}, indicating that the higher the correlation between the oscillation mode λ_i and the state variables x_k, the greater the impact of x_k.

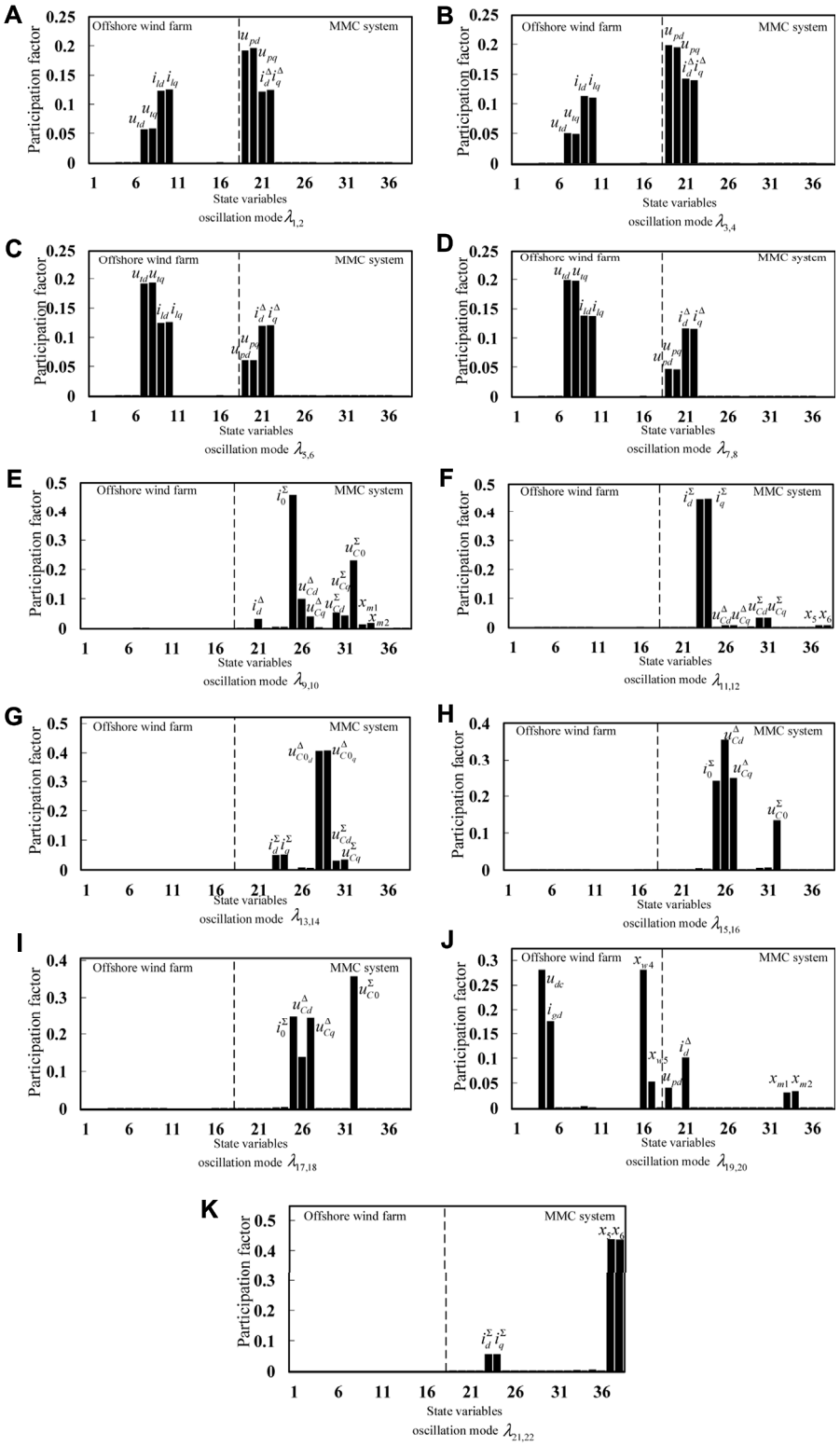

FIGURE 2
Participation factors of 11 oscillation modes of the system. The part label **(A–K)** is used for the distinction between results of 11 oscillation modes, there is no additional description needed.

4 Analysis of oscillation characteristics

4.1 System oscillation mode

The research results of Xie et al. (2016) show that with the increase in the number of grid-connected direct-drive fans, the damping level of the system shows a downward trend, which increases the risk of oscillation of the system. In this article, the number of grid-connected direct-drive fans is set to 100, and then the number is increased to 200. The specific parameters of direct-drive fans are shown in Table 3, and the parameters of the MMC system are shown in Table 4.

Based on the small-signal model of the system of the wind farm sending out through MMC-HVDC established above, the initial values of each state variable in the small-signal model are obtained by power flow calculation, and then the main oscillation modes of the system are calculated by the eigenvalue analysis method. The final results are shown in Table 5.

It can be concluded from Table 1 that there are 11 main oscillation modes in the system of the wind farm sending out *via* MMC-HVDC, which includes 4 sub/super synchronous oscillation modes, $\lambda_{15,16}$, $\lambda_{17,18}$, $\lambda_{19,20}$, and $\lambda_{21,22}$; 5 intermediate frequency oscillation modes, namely, $\lambda_{5,6}$, $\lambda_{7,8}$, $\lambda_{9,10}$, $\lambda_{11,12}$, and $\lambda_{13,14}$; and 2 high-frequency oscillation modes $\lambda_{1,2}$ and $\lambda_{3,4}$. In addition, it can be seen from the table above that when the number of direct drive fans connected to the grid is 200, the damping ratio of oscillation modes $\lambda_{1,2}$ and $\lambda_{3,4}$ in the system is negative, and the damping ratio of other oscillation modes is still positive. In addition, it can be seen from Table 1 that when the number of direct drive fans connected to the grid is 200. According to the former analysis, these two oscillation modes with a negative damping state will lead to the oscillation operation of the system of wind farm sending out *via* MMC-HVDC, which has the greatest impact on the stability of the system. The damping ratio of other oscillation modes in the system is positive, and the damping ratio of these oscillation modes is large, which is not easy to cause a negative damping state.

4.2 Analysis of the correlation between participation factors and state variables under different oscillation modes

In order to further analyze the relationship between the oscillation modes and the state variables in the system of the wind farm sending out *via* MMC-HVDC, the participation factors of 11 oscillation modes of the system are calculated and normalized. The results are shown in Figure 2.

It can be seen from Figure 2 that the participation variables of the oscillation modes $\lambda_{1,2}$, $\lambda_{3,4}$, $\lambda_{5,6}$, and $\lambda_{7,8}$ are the same, and they are all dominated by state variables u_{td}, u_{tq}, i_{ld}, i_{lq}, u_{pd}, u_{pq}, i_d^{Δ}, and i_q^{Δ}. It is related to the state variables of AC cable connecting the wind farm system, but the dominant participation factors of each oscillation mode are not the same. Oscillation modes $\lambda_{1,2}$ and $\lambda_{3,4}$ are dominated by state variables u_{pd} and u_{pq} of the MMC system, while oscillation modes $\lambda_{5,6}$ and $\lambda_{7,8}$ are dominated by state variables u_{td} and u_{tq} of the wind farm system.

State variables related to oscillation modes $\lambda_{9,10}$ are mainly variables i_0^{Σ} and u_{C0}^{Σ} of the MMC system, and their participation factors are 0.4627 and 0.2312, respectively. It can be seen that this oscillation mode is generated within the MMC system and is not much related to the wind farm. In addition, because the damping ratio of the oscillation mode is negative, the stability of the system is greatly affected.

The oscillation mode $\lambda_{11,12}$ is mainly related to i_d^{Σ}, i_q^{Σ}, u_{Cd}^{Σ}, and u_{Cq}^{Σ}. They are state variables of the MMC system. The dominant participation factors are i_d^{Σ} and i_q^{Σ}. The oscillation mode $\lambda_{13,14}$ is mainly related to i_d^{Σ}, i_q^{Σ}, $u_{C0_d}^{\Delta}$, $u_{C0_q}^{\Delta}$, u_{Cd}^{Σ}, and u_{Cq}^{Σ}. They are state variables of the MMC system. The dominant participation factors are u_{Cd}^{Σ} and u_{Cq}^{Σ}.

The participation variables of the oscillation modes $\lambda_{15,16}$ and $\lambda_{17,18}$ are all the same. They are all related to the state variables of the MMC system, which includes i_0^{Σ}, u_{Cd}^{Δ}, u_{Cq}^{Δ}, and u_{C0}^{Σ}. The participation factors of oscillation mode $\lambda_{15,16}$ can be ranked in the descending order as follows: u_{Cd}^{Δ}, u_{Cq}^{Δ}, i_0^{Σ}, and u_{C0}^{Σ}. The participation factors of the oscillation mode $\lambda_{17,18}$ can be ranked in the descending order as follows: u_{C0}^{Σ}, i_0^{Σ}, u_{Cq}^{Δ}, and u_{Cd}^{Δ}, which is the opposite to that of the oscillation modes $\lambda_{15,16}$.

The state variables related to the oscillation mode $\lambda_{19,20}$ mainly include u_{dc}, i_{gd}, x_{w4}, and x_{w5} of the wind farm system and u_{pd}, i_d^{Δ}, x_{m1}, and x_{m2} of the MMC system. It can be seen that the oscillation mode $\lambda_{19,20}$ is not only related to the constant DC voltage control link of the grid-side converter control system of the wind farm but also related to the constant d-axis AC voltage control link of the SEC. In addition, since the damping ratio of the oscillation mode is also negative, it has a great impact on the stability of the system.

The main participation variables of the oscillation mode $\lambda_{21,22}$ are i_d^{Σ}, i_q^{Σ}, x_{m5}, and x_{m6}. And their participation factors are 0.05585, 0.05584, 0.43757, and 0.43651, respectively.

Therefore, the oscillation modes can be classified according to the correlation between the participation factors of each oscillation mode and the wind farm and MMC system, as is shown in Table 6.

It can be seen from Table 6 that the oscillation modes $\lambda_{1,2}$, $\lambda_{3,4}$, $\lambda_{5,6}$, $\lambda_{7,8}$, and $\lambda_{19,20}$ are related to the wind farm and MMC system. While the oscillation modes $\lambda_{9,10}$, $\lambda_{11,12}$, $\lambda_{13,14}$, $\lambda_{15,16}$, $\lambda_{17,18}$, and $\lambda_{21,22}$ are generated within the MMC system, and there is no obvious correlation with the wind farm. In addition, the oscillation modes $\lambda_{9,10}$ and $\lambda_{19,20}$ are in a negative damping state, in which the oscillation mode $\lambda_{9,10}$ is mainly related to the state variables i_0^{Σ} and u_{C0}^{Σ}, and the oscillation mode $\lambda_{19,20}$ is generated by the coupling between the wind farm control system and the SEC voltage control system.

TABLE 6 The main participation factors and subsystems of each oscillation mode.

Oscillation mode	Main participation factors	Participation subsystems
$\lambda_{1,2}$	u_{pd}, u_{pq}, i_{ld}, i_{lq}, i_d^{Δ}, i_q^{Δ}, u_{td}, u_{tq}	Wind farm + MMC system
$\lambda_{3,4}$	u_{pd}, u_{pq}, i_{ld}, i_{lq}, i_d^{Δ}, i_q^{Δ}, u_{td}, u_{tq}	Wind farm + MMC system
$\lambda_{5,6}$	u_{td}, u_{tq}, i_{ld}, i_{lq}, i_d^{Δ}, i_q^{Δ}, u_{pd}, u_{pq}	Wind farm + MMC system
$\lambda_{7,8}$	u_{td}, u_{tq}, i_{ld}, i_{lq}, i_d^{Δ}, i_q^{Δ}, u_{pd}, u_{pq}	Wind farm + MMC system
$\lambda_{9,10}$	i_0^{Σ}, u_{C0}^{Σ}, u_{Cd}^{Δ}, u_{Cq}^{Δ}, u_{Cd}^{Σ}, u_{Cq}^{Σ}, i_d^{Δ}	MMC system
$\lambda_{11,12}$	i_d^{Σ}, i_q^{Σ}, u_{Cd}^{Σ}, u_{Cq}^{Σ}	MMC system
$\lambda_{13,14}$	u_{Cd}^{Σ}, u_{Cq}^{Σ}, i_d^{Σ}, i_q^{Σ}	MMC system
$\lambda_{15,16}$	u_{Cd}^{Δ}, u_{Cq}^{Δ}, i_0^{Σ}, u_{C0}^{Σ}	MMC system
$\lambda_{17,18}$	u_{C0}^{Σ}, i_0^{Σ}, u_{Cq}^{Δ}, u_{Cd}^{Δ}	MMC system
$\lambda_{19,20}$	u_{dc}, x_{w4}, i_{gd}, i_d^{Δ}, x_{w5}, u_{pd}, x_{m1}, x_{m2}	Wind farm + MMC system
$\lambda_{21,22}$	x_{m5}, x_{m6}, i_d^{Σ}, i_q^{Σ}	MMC system

5 Conclusion

In this article, the theoretical calculation equations of the quantitative evaluation index of the participation factor are derived, and the small-signal model of the system of the wind farm sending out through MMC-HVDC is constructed. Taking the equivalent circuit of the simplified DC transmission system of the wind farm with 200 direct-drive wind turbines connected to the grid as an example, the oscillation mode of the system was analyzed by using the eigenvalue analysis method based on the quantification of the participation factor. The contribution is summarized below:

1) When the number of wind turbines connected to the grid increases, the oscillation modes $\lambda_{9,10}$ and $\lambda_{19,20}$ with a negative damping state appear in the system. It is verified that with the increase in the number of grid-connected direct-drive fans, the damping level of the system will decrease and the risk of oscillation of the system will increase.
2) The oscillation modes $\lambda_{9,10}$ and $\lambda_{19,20}$ will lead to the oscillation operation of the system of the wind farm sending out *via* MMC-HVDC, which has the greatest impact on the stability of the system. The damping ratio of the other oscillation modes in the system is positive, and the damping ratio of these oscillation modes is large, which has a small effect on the stability of the system.
3) By calculating the participation factors of the two oscillation instability modes, it was found that the oscillation mode $\lambda_{9,10}$ is caused by the zero-sequence current i_0^{Σ} inside the MMC system, which is not much related to the wind farm. While the oscillation mode $\lambda_{19,20}$ is caused by the interaction and coupling between the wind farm and the MMC system.

Data availability statement

The raw data supporting the conclusions of this article will be made available by the authors, without undue reservation.

Author contributions

QP, SJ, and CQ contributed to conception and design of the study. QP organized the database. SJ and CQ performed the statistical analysis. QP wrote the first draft of the manuscript. SJ, CQ, TA, XB, and WZ wrote sections of the manuscript. All authors contributed to manuscript revision, read, and approved the submitted version.

Conflict of interest

QP, SJ, and CQ, were employed by State Grid Zhejiang Electric Power Co., Ltd.

The authors declare that this study received funding from State Grid Zhejiang Electric Power Co., Ltd. The funder had the following involvement in the study: study design, data collection and analysis, decision to publish, preparation of the manuscript.

Publisher's note

References

An, Z., Shen, C., Zheng, Z., Wang, Z., and Wei, W. (2018). Assessment method for equivalent models of wind farms based on direct-driven wind generators considering randomness. *Proc. CSEE* 38 (22), 6511–6520. doi:10.13334/j.0258-8013.pcsee.180617

Bergna-Diaz, G., Freytes, J., Guillaud, X., D' Arco, S., and Suul, J. A. (2018). Generalized voltage-based state-space modelling of modular multilevel converters with constant equilibrium in steady-state. *IEEE J. Emerg. Sel. Top. Power Electron.* 6 (2), 707–725. doi:10.1109/JESTPE.2018.2793159

Cai, X., Yang, R., Zhou, J., Fang, Z., Yang, M., Shi, X., et al. (2021). Review on offshore wind power integration via DC transmission. *Automation Electr. Power Syst.* 45 (21), 2–22.

Chen, B., Lin, T., Chen, R., Guo, Z., Sheng, Y., and Xu, X. (2018). Characteristics of multi-band oscillation for direct drive wind farm interfaced with VSC-hvdc system. *Trans. China Electrotech. Soc.* 33 (S1), 176–184. doi:10.19595/j.cnki.1000-6753.tces.180954

Chen, S., Cao, Q., and Jia, M. (2022). Concepts, characteristics and prospects of application of digital twin in power system. *Proc. CSEE* 42 (02), 487–499. doi:10.13334/j.0258-8013.pcsee.211594

Gao, M. (2021). *Study on parameter identification of doubly-fed wind turbine and dynamic equivalent method of wind farm*. Beijing: North China Electric Power University.

Guo, X., Li, Y., Xie, X., Hou, Y., and Zhang, D. (2020). Sub-synchronous oscillation characteristics caused by PMSG-based wind plant farm integrated via flexible HVDC system. *Proc. CSEE* 40 (04), 1149–1160+1407. doi:10.13334/j.0258-8013.pcsee.182540

Hu, J., Wang, B., Wang, W., Tang, H., Chi, Y., and Hu, Q. (2017). Small signal dynamics of DFIG-based wind turbines during riding through symmetrical faults in weak AC grid. *IEEE Trans. Energy Convers.* 32 (2), 720–730. doi:10.1109/tec.2017.2655540

Huang, B., Sun, H., Liu, Y., Wang, L., and Chen, Y. (2019). Study on subsynchronous oscillation in D-PMSGs-based wind farm integrated to power system. *IET Renew. Power Gener.* 13 (1), 16–26. doi:10.1049/iet-rpg.2018.5051

Kunjumuhammed, L. P., Bikash, C. P., Gupta, R., and Dyke, K. J. (2017). Stability analysis of a PMSG-based large offshore wind farm connected to a VSC-hvdc. *IEEE Trans. Energy Convers.* 32 (3), 1166–1176. doi:10.1109/tec.2017.2705801

Liu, H., Xie, X., Zhang, C., Li, Y., and Hu, Y. (2016). Quantitative SSR analysis of series-compensated DFIG-based wind farms using aggregated RLC circuit model. *IEEE Trans. Power Syst.* 32 (1), 474–483. doi:10.1109/tpwrs.2016.2558840

Liu, Y., Wang, J., Wang, Z., Chen, W., Ye, Y., Fu, C., et al. Research on AC admittance matrix modeling and frequency coupling effect of MMCHVDC under power control. *Proc. CSEE*, 1–14.

Lu, J., Dong, P., Shi, G., Cai, X., and Li, X. (2015). Subsynchronous oscillation and its mitigation of MMC-based HVDC with large doubly-fed induction generator-based wind farm integration. *Proc. CSEE* 35 (19), 4852–4860. doi:10.13334/j.0258-8013.pcsee.2015.19.002

Rygg, A., Molinas, M., Zhang, C., and Cai, X. (2016). A modified sequence-domain impedance definition and its equivalence to the dq-domain impedance definition for the stability analysis of AC power electronic systems. *IEEE J. Emerg. Sel. Top. Power Electron.* 4 (4), 1383–1396. doi:10.1109/jestpe.2016.2588733

Shah, S., and Parsa, L. (2017). Impedance modeling of three-phase voltage source converters in DQ, sequence, and phasor domains. *IEEE Trans. Energy Convers.* 32 (3), 1139–1150. doi:10.1109/tec.2017.2698202

Shao, B., Zhao, S., Pei, J., Li, R., and Song, S. (2019). Subsynchronous oscillation characteristic analysis of grid-connected DDWFs via VSC-HVDC system. *Power Syst. Technol.* 43 (09), 3344–3355. doi:10.13335/j.1000-3673.pst.2018.2567

Sun, K., Yao, W., Cai, Y., and Wen, J. (2021). Impedance modeling and analysis of medium-frequency oscillation caused by VSC-hvdc connected to local weak grid and DFIG-based wind farms. *Front. Energy Res.* 9. doi:10.3389/fenrg.2021.693903

Sun, K., Yao, W., and Wen, J. (2018). Mechanism and characteristics analysis of subsynchronous oscillation caused by DFIG-based wind farm integrated into grid through VSC-hvdc system. *Proc. CSEE* 38 (22), 6520–6533. doi:10.13334/j.0258-8013.pcsee.172415

Suriyaarachchi, D., Annakkage, U. D., Karawita, C., and Jacobson, D. A. (2013). A procedure to study sub-synchronous interactions in wind integrated power systems. *IEEE Trans. Power Syst.* 28 (1), 377–384. doi:10.1109/tpwrs.2012.2204283

Tang, A., Lu, Z., Yang, H., Zou, X., Huang, Y., and Zheng, X. (2021). Digital/analog hybrid simulation platform of distributed power flow controller based on ADPSS and dspace. *CSEE J. Power Energy Syst.* 7 (1), 181–189. doi:10.17775/CSEEJPES.2020.02210

Tang, A., Shao, Y., Xu, Q., Zheng, X., Zhao, H., and Xu, D. (2019). Multi-objective coordination control of distributed power flow controller. *CSEE J. Power Energy Syst.* 5 (03), 348–354. doi:10.17775/CSEEJPES.2018.01450

Tang, A., Zhou, W., Song, J., Qiu, P., Chen, Q., Zhai, X., et al. (2022). Optimal output power coordinated control strategy of distributed power flow controller. *Int. J. Electr. Power & Energy Syst.* 140, 108075. doi:10.1016/j.ijepes.2022.108075

Wang, L., Xie, X., Jiang, Q., Liu, H., Li, Y., and Liu, H. (2015). Investigation of SSR in practical DFIG-based wind farms connected to a series-compensated power system. *IEEE Trans. Power Syst.* 30 (5), 2772–2779. doi:10.1109/tpwrs.2014.2365197

Wang, L., Xie, X., Liu, H., Zhan, Y., He, J., and Wang, C. (2017). Review of emerging SSR/SSO issues and their classifications. *J. Eng.* 2017 (13), 1666–1670. doi:10.1049/joe.2017.0615

Wen, B., Burgos, R., Boroyevich, D., Mattavelli, P., and Shen, Z. (2017). AC stability analysis and dq frame impedance specifications in power-electronics-based distributed power systems. *IEEE J. Emerg. Sel. Top. Power Electron.* 5 (4), 1455–1465. doi:10.1109/jestpe.2017.2728640

Xie, X., Liu, H., He, J., Zhang, C., and Qiao, Y. (2016). Mechanism and characteristics of subsynchronous oscillation caused by the interaction between full-converter wind turbines and AC systems. *Proc. CSEE* 36 (09), 2366–2372. doi:10.13334/j.0258-8013.pcsee.2016.09.007

Xie, X., Zhang, X., Liu, H., Li, Y., and Zhang, C. (2017). Characteristic analysis of subsynchronous resonance in practical wind farms connected to series-compensated transmissions. *IEEE Trans. Energy Convers.* 32 (3), 1117–1126. doi:10.1109/tec.2017.2676024

Yang, L., Xu, Z., Wang, X., Xing, F., Xu, Z., and Yang, L. (2020). Analysis on harmonic resonance of offshore wind farm transmitted by VSC - HVDC system. *Guangdong Electr. Power* 33 (07), 1–10.

frontiers | Frontiers in Energy Research

TYPE Original Research
PUBLISHED 13 September 2022
DOI 10.3389/fenrg.2022.1013696

OPEN ACCESS

EDITED BY
Chaolong Zhang,
Anqing Normal University, China

REVIEWED BY
Shuo Zhang,
Shandong University, China
Rui Li,
University of Strathclyde,
United Kingdom
Bhaskar Mitra,
Pacific Northwest National Laboratory (DOE), United States
Xiuyan Wei,
Shandong University, China

*CORRESPONDENCE
Yanxun Guo,
guoyanxun@zzu.edu.cn

SPECIALTY SECTION
This article was submitted to Smart Grids, a section of the journal Frontiers in Energy Research

RECEIVED 07 August 2022
ACCEPTED 25 August 2022
PUBLISHED 13 September 2022

CITATION
Xu Z, Liang J, Guo Y and Wang Y (2022), A capacitor-based DC circuit breaker for HVDC power grid.
Front. Energy Res. 10:1013696.
doi: 10.3389/fenrg.2022.1013696

A capacitor-based DC circuit breaker for HVDC power grid

Zhuang Xu[1], Jun Liang[1,2], Yanxun Guo[1]* and Yaoqiang Wang[1]

[1]School of Electrical Engineering, Zhengzhou University, Zhengzhou, China, [2]School of Engineering, Cardiff University, Cardiff, United Kingdom

DC circuit breakers (DCCBs) are the critical equipment to isolate faults in high-voltage DC grids. The improvement of interruption performances of capacitor-based DCCBs (C-DCCBs) has been widely researched. However, in previous papers, the adaptive reclosing of C-DCCBs is less considered and requires further research. In this paper, a novel C-DCCB with adaptive reclosing ability is proposed. The interruption and adaptive reclosing processes of the proposed C-DCCB are presented. The fault current is interrupted by charging the internal capacitor to a voltage higher than the system voltage. The fault property identification is key to adaptive reclosing and is achieved using the capacitor discharge characteristic. The parameter designs are analyzed to guarantee successful interruptions, and the identification criteria are proposed to serve the adaptive reclosing. On the one hand, the proposed C-DCCB has good interruption performances; on the other hand, an adaptive reclosing strategy is designed for the proposed C-DCCB to restore the power transmission whereas avoiding a second fault shock, which is the main contribution of this paper. Finally, the interruption and adaptive reclosing performances of the proposed C-DCCB are validated using PSCAD/EMTDC simulations.

KEYWORDS

adaptive reclosing, dc circuit breaker, fault property identification, HVDC grid, thevenin equivalent circuits

1 Introduction

High-voltage DC (HVDC) grids have great application potential in renewable energy integration, island power supply and AC grid interconnection (Hertem and Ghandhari, 2010)- (An et al., 2017). However, after a DC fault occurs, the DC fault current quickly increases and the DC voltage rapidly drops, which seriously affects the safe and stable operation of HVDC grids. DC circuit breakers (DCCBs) can soon isolate the fault area and maintain the normal operation of the nonfault area. Traditionally, DCCBs are divided into mechanical, solid-state and hybrid DCCBs (Bucher and Franck, 2016)- (Chen et al., 2021). Several mechanical DCCBs use semiconductors such as thyristors to improve the interruption performance, obscuring the boundary between mechanical and hybrid DCCBs (Wen et al., 2018)- (Wu et al., 2020a). In this paper, DCCBs that interrupt the fault current by semiconductors with turn-off ability are called semiconductor-based DCCBs (S-DCCBs); DCCBs that interrupt the fault current by charging the internal capacitor to a voltage higher than the system voltage are called capacitor-based DCCBs (C-DCCBs).

In S-DCCBs, the main breaker (MB), which is composed of insulated-gate bipolar transistors (IGBTs) or integrated gate commutated thyristors (IGCTs), can interrupt the fault current. In (Hafner and Jacobson, 2011; Hassanpoor et al., 2015; Wen et al., 2016; Jovcic et al., 2019), S-DCCBs conduct the system current with small conduction losses during a normal state. During interruptions, the system current is commutated into the MB and then interrupted by the MB. S-DCCBs have attracted considerable attention because of good interruption performances. In China, S-DCCBs with different topologies have been applied to the Zhoushan DC project and Zhangbei DC grid project, respectively (Jovcic et al., 2019). However, the interruption capacity of S-DCCBs is limited by the turn-off capacity of IGBT and IGCT, and IGBT and IGCT bring high construction costs.

For C-DCCBs, the system current is commutated into the internal capacitor during the interruption. It gradually decreases to 0 after the capacitor is charged to a voltage higher than the system voltage. C-DCCBs usually use semiconductors without turn-off ability to save the construction cost, such as thyristors and diodes. C-DCCBs with different topologies in China have been applied to the Zhangbei DC grid project and the Nan'ao DC grid project, respectively (Liu, 2019)- (Chen et al., 2018). Many topologies have been proposed to improve the C-DCCB performances regarding bidirectional interruption, interruption speed, pre-activation ability, etc. The C-DCCB in (Wu et al., 2020b) achieves bidirectional current commutation using bridge-type branches. In (Jamshidifar and Jovcic, 2018), the C-DCCB uses fast thyristors to quickly interrupt large fault currents. In (Sima et al., 2019), the capacitor is inserted into a bridge composed of spark gap switches, and this topology guarantees that the C-DCCB can consecutively interrupt the fault current. The pre-activation of DCCB achieves that the DCCB operation time overlaps with the protection time, which effectively reduces the fault interruption time (Hafner and Jacobson, 2011). However, the C-DCCBs in (Chen et al., 2018; Jamshidifar and Jovcic, 2018; Liu, 2019; Sima et al., 2019; Wu et al., 2020b) do not have the pre-activation ability. For C-DCCBs in (Wu et al., 2019) and (Guo et al., 2020), the thyristors in the MB can temporarily conduct the load current, thus achieving the pre-activation ability. In (Augustin et al., 2021), a C-DCCB family consisting of one unidirectional and six bidirectional concepts is presented, and all concepts have the pre-activation ability. Nevertheless, the reclosing of C-DCCBs is not considered in (Liu, 2019)- (Augustin et al., 2021).

Considering that most overhead line faults are transient, the DCCB should reclose in time to restore the power transmission after isolating (Wang et al., 2203). However, in case of a permanent fault, the direct reclosing will bring a second fault shock, which is harmful to the HVDC grid. To solve this problem, the permanent and transient faults should be discriminated, and the DCCB only reconnects the HVDC grid to the isolated line when the fault is transient, which is called adaptive reclosing.

The fault property identification is key to the adaptive reclosing strategy. Because the permanent and transient faults result in different boundary conditions, the fault property can be identified according to the traveling wave characteristics (Wang et al., 2203)- (Mei et al., 2021). In (Wang et al., 2203), the voltage pulse is produced by the hybrid MMC on the healthy pole. However, considering the construction and conduction cost, the half-bridge MMC is more attractive than the hybrid MMC for HVDC grids. In (Song et al., 2019)- (Zhang et al., 2020), the voltage pulse is injected into the fault line by controlling the MB of S-DCCBs. The MMC and S-DCCB are simultaneously controlled to produce the voltage pulse in (Yang et al., 1123). In (Mei et al., 2021), the voltage pulse comes from the energy absorption module of S-DCCB. In (Li et al., 2020), the HVDC grid charges the fault line through the arrester of S-DCCB, and the fault property is identified using the fault line voltage. In (Pei et al., 2019), the fault property can be identified using the fault current, and the fault current is limited because the MB modules are sequentially turned on. However, the methods in (Wang et al., 2203)- (Pei et al., 2019) do not consider the C-DCCBs.

For C-DCCBs, most previous papers consider the direct reclosing and the consecutive interruption ability rather than the fault property identification is focused on. For example (Sima et al., 2019),- (Augustin et al., 2021) use different methods to quickly restore the interruption ability of C-DCCBs before the direct reclosing. Nevertheless, the fault property identification and adaptive reclosing of C-DCCBs are worth studying to improve the reclosing performance. In (Wen et al., 2021), for HVDC grids adopting C-DCCBs, the fault property is identified by comparing the residual voltages at two ends of the isolated fault line. However, this method only applies to symmetrical monopole DC systems and requires long-distance communication. In (Torwelle et al., 2021), a grounded branch is added to the C-DCCB, which enables the internal capacitor charges the fault line, and the fault property is identified using the line voltage. However, the capacitor may need to charge the fault line multiple times, which obviously increases the reclosing time.

Although several C-DCCBs with good interruption performances have been proposed, the C-DCCB with adaptive reclosing ability needs further research. In this paper, a novel C-DCCB is proposed to serve HVDC grids. On the one hand, the proposed C-DCCB achieves good interruption performances; on the other hand, it has the ability of adaptive reclosing, which is the main contribution of this paper. The adaptive reclosing ability avoids the second fault shock in case of permanent faults and the voltage oscillations in case of transient faults. The paper is structured as follows. Section 2 describes the

topology and operation of the proposed C-DCCB. Section 3 analyzes the parameter design and fault property identification. Section 4 shows the simulation results, which validate the performance of the proposed C-DCCB. Finally, Section 5 concludes this paper.

2 Proposed DC circuit breaker

2.1 Topology of the proposed C-DCCB

As shown in Figure 1, the proposed C-DCCB contains the main conductor (MC), MB, energy absorber (EA) and precharge branch. The MC is composed of a fast disconnector (FD) and a load commutation switch (LCS), and the LCS only endures the commutation voltage. The MB is composed of an inductor L, capacitor C, diodes D_1–D_2, and thyristors T_1–T_4. The EA is composed of an arrester and diode D_3. The precharge branch is composed of a resistor R_1 and thyristor T_5. Both sides of the C-DCCB are equipped with residual current breakers (RCBs). The RCB can interrupt residual DC currents of up to 10 A, and the interruption time is 30 ms. After a current zero occurs, the FD can restore its dielectric strength within a few milliseconds to withstand the peak transient interruption voltage (TIV). In practical engineering, the FD can be composed of several vacuum circuit breakers to achieve operation performance (Shi et al., 2015).

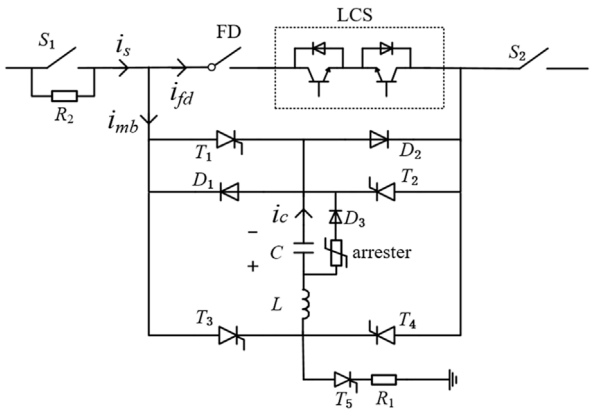

FIGURE 1
Topology of the capacitor-based DC circuit breaker.

To clarify the operation processes, the current curves in C-DCCB during interrupting fault currents and reclosing with transient faults are shown in Figure 2, where i_s, i_{mb}, i_{fd}, i_c and i_{ar} are the currents of the DC system, MB, FD, capacitor C and arrester, respectively. The reference directions of currents and capacitor voltage u_c are marked in Figure 1. During operations, the main switching events and time labels are given in Figure 2.

2.2 Operation processes of the C-DCCB

2.2.1 Capacitor precharge

Initially, the HVDC grid precharges the capacitor C by turning on T_1, T_2 and T_5, and the current path is shown in Figure 3A. After the capacitor voltage u_c is charged to the system voltage, T_1, T_2 and T_5 naturally turn off. Because of the

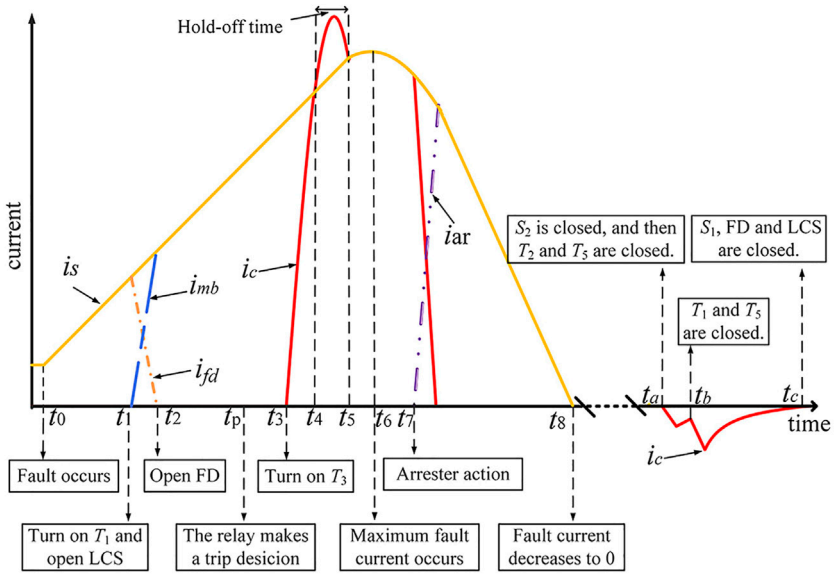

FIGURE 2
Current curves during interrupting fault currents and reclosing with a transient fault.

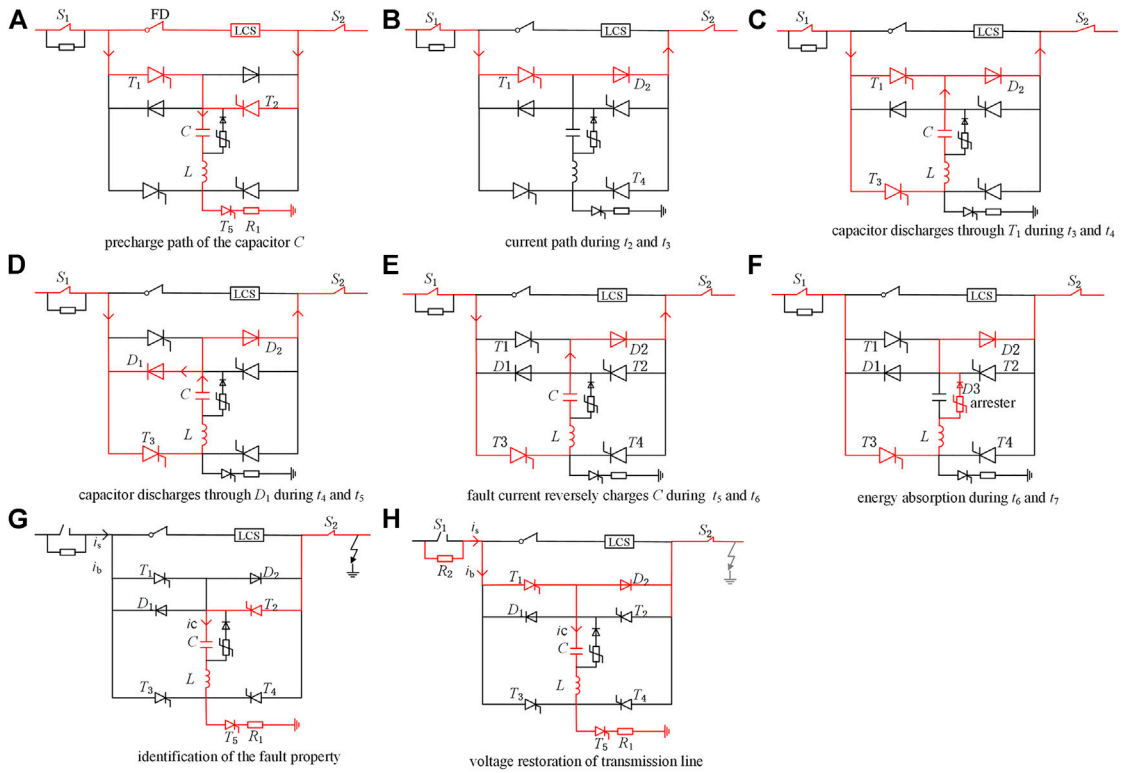

FIGURE 3
Operation procedures of the C-DCCB.

leakage discharge, u_c slowly decreases during the normal state. Once u_c decreases to a preset value, T_1, T_2 and T_5 are turned on to precharge the capacitor. Thus, u_c is always no less than the preset value during the normal state.

2.2.2 Current commutation

During the normal state, the MC conducts the load current with small conduction losses. Considering the pre-activation strategy, once the protection detects a potential fault at $t = t_1$, the C-DCCB commutates the current into the MB by turning on T_1 and turning off the LCS. At $t = t_2$, i_{fd} decreases to 0, and the FD begins to open. After that, the current path in the C-DCCB is shown in Figure 3B. If the protection decides not to interrupt the current at $t = t_p$, the C-DCCB successively closes the FD and LCS; thus, the current naturally commutates into the MC, and the thyristor T_1 turns off naturally after the current of T_1 is smaller than the holding current; Otherwise, the C-DCCB performs the following interruption operations.

During t_1–t_p, the voltage drop in the C-DCCB is equal to the on-state voltages of T_1 and D_2; thus, the disturbance caused by the pre-activation is insignificant. By pre-commutating the system current from the MC into the MB, the C-DCCB operation time overlaps with the protection time. Thus, the pre-activation effectively reduces the fault clearing time.

2.2.3 Capacitor discharge

As shown in Figure 3C, during t_3 and t_4 the system provides the fault current to the fault point through S_1, T_1, D_2 and S_2. At the same time, the capacitor discharges through the following loop: C—T_1—T_3—L. As shown in Figure 3D, after i_c exceeds the fault current at $t = t_4$, T_1 is reversely blocked, and the discharging loop is changed as: C—D_1—T_3—L. After i_c decreases to the fault current at $t = t_5$, D_1 is reversely blocked, and T_1 begins to endure the forward voltage stress, as shown in Figure 3E. To reliably turn off T_1, the time interval between t_4 and t_5, which is the reverse-bias time of T_1 and marked as t_R, should be greater than the turn-off time t_q. The turn-off time t_q, which can be found in the datasheet, is the minimum reverse-bias time to ensure the turn-off of the thyristor (Technical Information, 2012).

During t_2 and t_5, the voltage drop in the C-DCCB is rather small compared with the system voltage. After $t = t_5$, the voltage drop in the C-DCCB is approximately equal to the capacitor voltage and quickly charged to the system voltage. We mark the FD operation time as t_{FD}. The value

of t_3 should meet the following two constraints: 1) t_3 should not be earlier than t_p, and 2) the FD recovers its dielectric strength at $t = t_2 + t_{FD}$, which time instant should be earlier than t_5 to avoid the interruption failure. Considering that the interval between t_3 and t_5 is greater than t_q, these two constraints can be satisfied when t_3 is selected as:

$$t_3 = \max\left(t_p, t_2 + t_{FD} - t_q\right) \tag{1}$$

2.2.4 Energy absorption

After the capacitor is charged to the arrester reference voltage, the fault current commutates into the EA and gradually decreases, as shown in Figure 3F. The arrester releases the residual energies stored in the system, and the peak TIV usually is limited to 1.5 times the system voltage. After the fault current decreases to 10 A, S_1, and S_2 are opened to isolate the fault totally. After the isolation, the capacitor voltage u_c is opposite to its initial state.

2.2.5 Adaptive reclosing

To guarantee that the DC line recovers its insulation characteristic, the reclosing is usually hundreds of milliseconds later than the isolation (Yang et al., 1123).

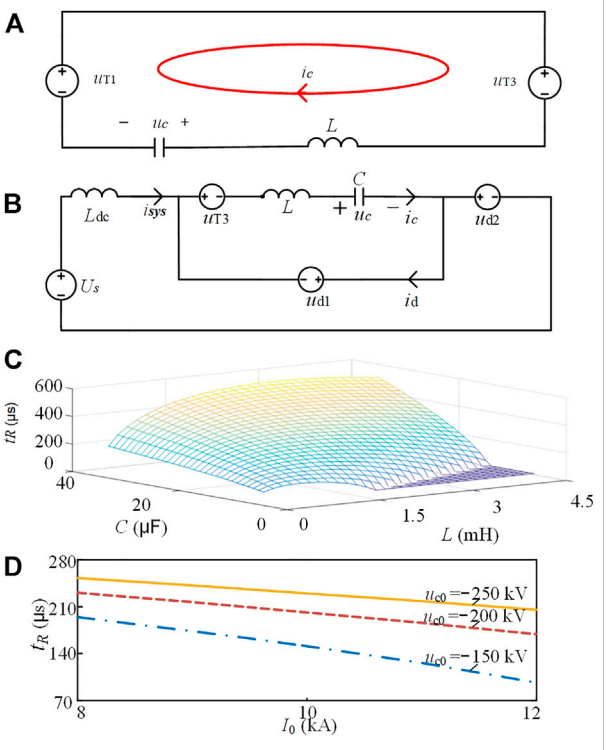

FIGURE 4
(A) Equivalent circuit of the capacitor discharging during t3 and t4. **(B)** equivalent discharge circuit of the capacitor during t4 and t5; **(C)** relations of tR, L, and C **(D)** relations of IR. Io. and uc0.

After receiving the adaptive reclosing command, the C-DCCB closes S_2 and turns on T_2 and T_5. If the fault is permanent, the capacitor C significantly discharges through the following loop: C—L—T_5—R_1—fault point—S_2—T_2, as shown in Figure 3G. If the fault is transient, the capacitor slightly discharges through the equivalent grounded capacitance of the DC line.

After identifying the permanent fault, S_2 is opened to isolate the fault when the discharging current is smaller than 10 A. After identifying the transient fault, the C-DCCB turns on T_1 and T_5; thus, the capacitor C and the DC line are charged to the system voltage, as shown in Figure 3H; after that, the C-DCCB successively closes S_1, FD and LCS, and the reclosing is completed.

After reclosing the C-DCCB located on one side of the DC line, if the fault is transient, the line voltage is close to the system voltage; otherwise, the line voltage is much less than the system voltage. Thus, the C-DCCB located on the other side of the DC line directly identifies the fault property using the line voltage.

3 Parameter design and fault property identification of the C-DCCB

3.1 Turning T_1 off

During t_3 and t_4, the capacitor discharging loop is equivalent to the circuit shown in Figure 4A, where u_{Ti} is the voltage drop in T_i, $i = 1, 2, 3, 4$. Assume that thyristors have the same voltage drops of u_T, then we can obtain:

$$\begin{bmatrix} \dot{u}_c \\ \dot{i}_c \end{bmatrix} = \begin{bmatrix} 0 & -1/C \\ -1/L & 0 \end{bmatrix} \begin{bmatrix} u_c \\ i_c \end{bmatrix} \tag{2}$$

where the initial values of i_c and u_c are 0 and u_{c0}, respectively, and u_{c0} is negative under the reference direction in Figure 1.

After a metallic fault occurs at the load side of the C-DCCB, the system side of the C-DCCB is equivalent to a voltage source connected in series with an inductor L_{dc}. The equivalent capacitor discharge circuit during t_4 and t_5 is shown in Figure 4B, where i_{sys} is the system current, i_d is the current flowing through D_1, u_{di} is the voltage drop in D_i, $i = 1, 2$. Assume that the diodes have the same voltage drop of u_d, then we can obtain:

$$\begin{bmatrix} 0 & 0 & 0 & -L \\ L_{dc} & 0 & 0 & L \\ 1 & 1 & 0 & -1 \\ 0 & 0 & 1 & 0 \end{bmatrix} \begin{bmatrix} \dot{i}_{sys} \\ \dot{i}_d \\ \dot{u}_c \\ \dot{i}_c \end{bmatrix} = \begin{bmatrix} u_c + u_T + u_d \\ U_s - u_c - u_T - u_d \\ 0 \\ i_c/C \end{bmatrix} \tag{3}$$

In Eq. 3, the initial values of u_c and i_c can be obtained from those final values in Eq. 2; i_{sys} and i_c have the same initial value, and i_d has an initial value of 0.

In this analysis, U_s = 200 kV, L_{dc} = 0.04 H, u_{c0} = −200 kV, and the fault current at t_3 has a value of I_0 = 10 kA. Substituting these parameters into (2) and (3), the relations of the reverse-bias time t_R, L and C can be obtained. As shown in Figure 4C, t_R increases with C, because the larger capacitor stores more energy to maintain the reverse-bias of T_1. When L is small, t_R increases with L. However, when L exceeds a critical value L_C, t_R decreases with L. When C is too small and L is too large, t_R is 0. When C = 9 μF and L = 1.2 mH, the relations of t_R, I_0 and u_{c0} are shown in Figure 4D. The value of t_R decreases with I_0 and increases with the absolute value of u_{c0}.

According to the relations of t_R and system parameters, the parameter design principles of the C-DCCB are as follows: 1) the values of L and C should guarantee that t_R is greater than the turn-off time t_q under the worst interruption condition, i.e., the C-DCCB interrupts the maximum fault current when the initial capacitor voltage u_{c0} has a minimum absolute value; 2) the value of L should be close to the critical value L_c to improve the utilization efficiency of L and C.

3.2 Fault property identification

3.2.1 Analysis model:

This section takes the reclosing after a positive pole fault as an example. As shown in Figure 5A, the systems on both sides of the negative pole are represented by the Thevenin equivalent circuits; U_{eq1} and U_{eq2} are Thevenin voltages; Z_{eq1} and Z_{eq2} are Thevenin impedances; u_r is the capacitor voltage at the beginning of reclosing. Taking the fault point as a boundary, the DC line is divided into two parts. If the fault is permanent, the switch k_1 is closed; otherwise, k_1 is opened. The turn-on commands of thyristors T_L and T_R represent the reclosing commands of C-DCCBs on the left and right sides, respectively.

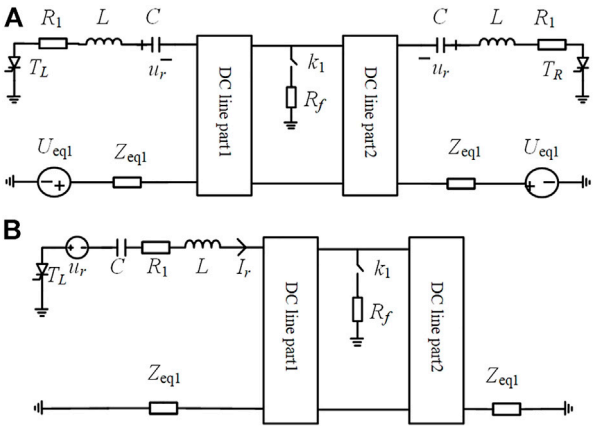

FIGURE 5
(A) Schematic of the system circuit after isolating the fault pole; **(B)**equivalent system circuit during the reclosing.

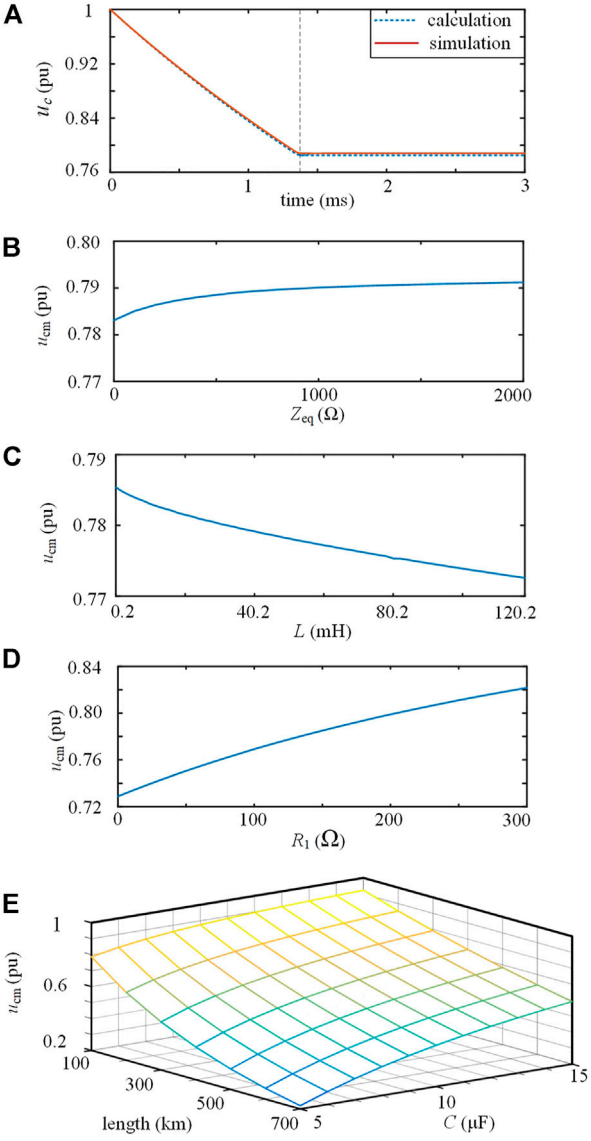

FIGURE 6
(A) Simulation and calculation values of Δu during reclosing without fault; **(B)** relation between ucm and Zeq **(C)** relation between ucm and L **(D)** relation between ucm and R1 **(E)** relations of ucm, C and line length.

We assume that the C-DCCB on the left side closes S_2, T_2 and T_5, which is equivalent to that T_L is turned on in Figure 5A. According to the superposition theorem, during the reclosing, the system response change is caused by the excitation of the voltage source u_r. Considering only the excitation of u_r, the equivalent system circuit is shown in Figure 5B.

Using the DC line's frequency-dependent parameter, the nodal admittance matrix of the DC line can be obtained, and

then the bus admittance matrix of the circuit in Figure 5B can be established. The self-impedance of the node connecting the voltage source u_r and the capacitor C is marked as Z_{self}, then the current injected into the DC line, marked as I_r, is:

$$I_r = u_r / \left(sZ_{self}\right) \tag{4}$$

where s is the Laplace operator.

During reclosing, the capacitor voltage u_c is:

$$u_c = u_r + I_r / (sC) \tag{5}$$

The value of u_c in the frequency domain can be calculated by combining (4) and (5). The value of u_c in the time domain can be obtained using the numerical inversion of the Laplace transform (Gómez and Uribe, 2009). The detailed calculation process can refer to the method in (Guo et al., 2021) and is not repeated in this paper.

3.2.2 Transient fault:

At the beginning of reclosing, the voltage source u_r generates a current traveling wave on the DC line. When the fault is transient, because the DC line end is an open circuit, the current traveling wave is totally reflected at the DC line end, and the reflection wave is in the opposite direction of the original traveling wave. When the reflection current wave transmits to the DC line head, I_r decreases to 0, and the thyristor T_L is reversely biased, causing the capacitor voltage u_c keeps unchanged.

According to the system parameters in Section 4, we take u_r = 1 pu, C = 9 μF, L = 1.2 mH, R_1 = 150 Ω, $Z_{eq1} = Z_{eq2}$ = 100 Ω. As shown in Figure 6A, the capacitor discharges through the DC line during reclosing without fault, and u_c gradually decreases. Because of the current reflection wave, the thyristor T_L is turned off and u_c keeps unchanged after 1.36 ms. The deviation between the calculation and simulation values of u_c is relatively small, which validates the accuracy of the analysis model.

During reclosing, the minimum value of u_c is marked as u_{cm}. The relations of u_{cm} and the system parameters are discussed using the above analysis model. The values of Z_{eq1} and Z_{eq2} are related to the non-fault area of the DC grid. When $Z_{eq1} = Z_{eq2} = Z_{eq}$, the relation between u_{cm} and Z_{eq} is shown in Figure 6B. When Z_{eq} increases from 0 to 2 kΩ, u_{cm} only increases by 1.0%, indicating that the non-fault area of the DC grid has little influence on u_{cm}.

As shown in Figure 6C, when L increases from 0.2 to 120.2 mH, u_{cm} only decreases by 1.6%, indicating that the influence of L on u_{cm} is not significant. As shown in Figure 6D, u_{cm} increases with increasing R_1, because R_1 limits the amplitude of the current traveling wave, thus limiting the discharge of capacitor C. As shown in Figure 6E, u_{cm} increases with the increasing C. With the DC line length increase, the arrival time of the current reflection wave increases, causing the increase in capacitor discharge time and the decrease of u_{cm}.

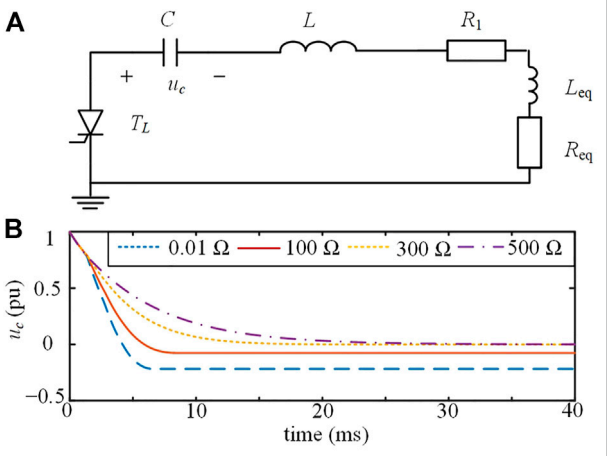

FIGURE 7
(A) Equivalent discharge circuit during reclosing with a permanent fault; **(B)** waveforms of uc, when the permanent fault has different fault resistances.

3.2.3 Permanent fault:

After reclosing the C-DCCB with a permanent fault, the current traveling wave will be reflected at the fault point. If the fault resistance is less than the line wave impedance, the current reflection wave has the same polarity as the original current traveling wave; otherwise, compared to the original current traveling wave, the current reflection wave has an opposite polarity and smaller amplitude. Therefore, the traveling wave effect will not cause the capacitor current to cross zero during reclosing with a permanent fault.

As shown in Figure 3G, the capacitor significantly discharges through R_1, L and the fault line during reclosing with a permanent fault. The equivalent parallel admittance of the DC line has little effect on the discharge. Using the lumped parameter model of the DC line, the equivalent capacitor discharge circuit is shown in Figure 7A, where R_{eq} and L_{eq} are the equivalent resistance and inductance of the DC line, respectively. For this second-order circuit, when $(R_1 + R_{eq}) > 2\sqrt{(L + L_{eq})/C}$, the discharge process is overdamped, and u_c gradually decreases to 0. When $(R_1 + R_{eq}) < 2\sqrt{(L + L_{eq})/C}$, the discharge process is underdamped, and u_c decreases to a negative value when the discharge current crosses zero. After the discharge current crosses zero, the thyristor T_L is turned off, and u_c maintains the negative value.

As shown in Figure 7B, for a permanent fault located at the DC line end, when the fault resistance is 0 and 100 Ω, the discharge is underdamped, and the minimum value of u_c is less than 0. When the fault resistance is 300 and 500 Ω, the discharge process is overdamped, and u_c decreases to 0. These results are consistent with the above analysis.

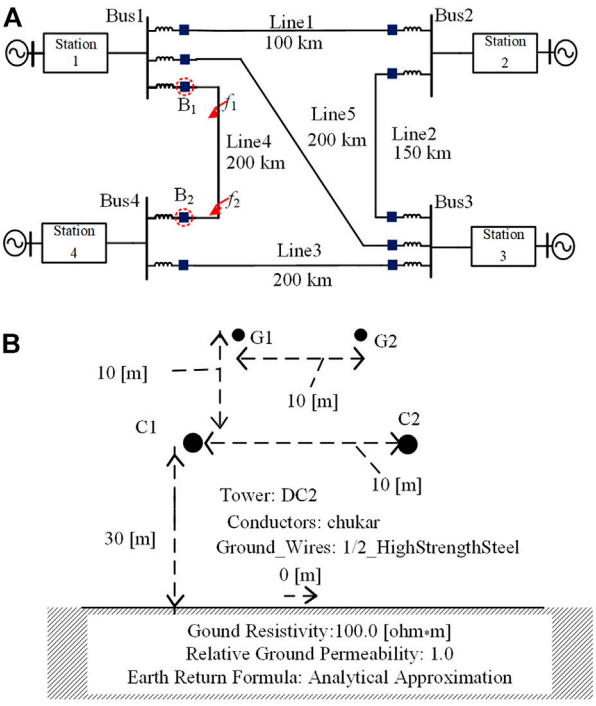

FIGURE 8
(A) Topology of the DC grid; **(B)** configuration of transmission line.

3.2.4 Criteria for identifying the fault property:

According to the above analysis, during reclosing with transient faults, u_c decreases to a positive value u_{cm}, which can be calculated using Eq. 4 and Eq. 5. During reclosing with permanent faults, u_c decreases to be no more than 0. A permanent fault is identified using the following criterion:

$$u_c(t) \le u_{th} = u_{cm} - u_{mar1} \tag{6}$$

where u_{th} is the voltage threshold, and u_{mar1} is a positive safety margin.

A transient fault is identified using the following criterion:

$$u_c(t) > u_{th} \;\; \& \;\; |u_c(t-\Delta t) - u_c(t)| < u_{error} \tag{7}$$

A slighter fault causes a slower capacitor discharge rate during reclosing with a permanent fault. The values of u_{error} and Δt should satisfy the following conditions: 1) the criterion in Eq. 7 is not true in the case of the slightest permanent fault, which occurs at the end of DC line and has the largest fault resistance; and 2) u_{error} is greater than the maximum measurement error.

In addition, to correctly identify the transient fault that lasts longer than hundreds of milliseconds, the following method is adopted: after identifying a permanent fault, the C-DCCB will perform another reclosing attempt to identify the fault property again unless the number of reclosing attempts reaches the maximum value allowed by the system.

TABLE 1 Parameters of the C-DCCB.

Parameter	Value
Interruption capacity	12 kA
Peak TIV	300 kV
FD operation time t_{FD}	2 ms
Capacitance C	9 μF
Inductance L	1.2 mH
Resistances R_1, R_2	100 Ω, 800 Ω
Preset recharge value of u_c	−180 kV
Turn-off time of T_1 and T_2	60 μs (5STF28H2060)
Voltage threshold u_{th}	140.7 kV

4 Simulation results

4.1 Simulation parameters

As shown in Figure 8A, a four-terminal bipolar DC grid is established in PSCAD/EMTDC, and the rated voltage is ±200 kV. In the DC grid, each station contains 2 MMCs, and its neutral point is directly earthed. For the equivalent model, all sub-modules in each MMC arm are equivalent to a Thevenin equivalent circuit; thus, the simulation efficiency is greatly improved. The DC grid is bipolar and has a rated voltage of ±200 kV, and the detailed equivalent model of MMC in (Cigré, 2014) is used. Both ends of the DC line are equipped with C-DCCBs and current-limiting inductors of 0.04 H. The C-DCCB located on the Bus1 side of Line 4 is marked as B_1 and taken as an example. For simplicity, only simulation results of the positive pole are shown in this paper. The parameters of the C-DCCB and simulation model

TABLE 2 Main parameters of the HVDC Grid.

Parameters	Values
Rated power of station (MW)	Station 1: −600 Station 2: 600 Station 3: −600 Station 4: 600
Length of the Overhead Lines (km)	line l_1: 100 line l_2: 150 line l_3: 200 line l_4: 200 line l_5: 200
Arm inductance L_{arm} (mH)	Station 1: 19 Station 2: 58 Station 3: 29 Station 4: 19
Capacitance of sub-module C_0 (μF)	Station 1: 450 Station 2: 150 Station 3: 300 Station 4: 450
Arm resistance r_0 (Ω)	Station 1: 0.18 Station 2: 0.55 Station 3: 0.27 Station 4: 0.18
L_{dc} (mH)	40
Number of arm sub-modules n_0	200

are shown in Table 1 and Table 2, and the design of reclosing parameters is presented as follows.

During the interruption, the internal capacitor voltage u_c is charged to the peak TIV of 300 kV. After the interruption, the capacitor C slowly discharges through the arrester and D_3. After a time delay of 300 ms, the capacitor voltage is discharged to u_r = 192 kV at the beginning of reclosing. The transmission line is based on the frequency-dependent model, and the line configuration is shown in Figure 8B. Substituting the C-DCCB and line parameters into (4) and (5), we can obtain that u_{cm} = 0.785 u_r. In this paper, the safety margin u_{mar1} is taken as 10 kV. Then, the voltage threshold u_{th} in (6) and (7) has a value of 0.785 × 192–10 = 140.7 kV.

For DC grid protections, the maximum value of fault resistance is usually hundreds of ohm. In simulations, even if the permanent fault located on the B_2 side of Line 4 has a fault resistance of up to 1 kΩ, u_c decreases to u_{th} within 3 ms during the reclosing process. Thus, as long as Δt is greater than 3 ms and u_{error} is less than (u_r–u_{th}), the permanent fault will not cause malfunctions of criterion in Eq. 7. We assume that the capacitor voltmeter has a voltage range of 350 kV and an accuracy ratio of 0.1%; thus, the maximum measurement error of the voltmeter is 0.35 kV. Considering these above conditions, we select u_{error} and Δt as 0.5 kV and 5 ms, respectively.

4.2 Interruption of fault current

As shown in Figure 8A, considering the most serious fault condition, a metallic fault occurs at the line side of B_1 at t = 0 ms, and the initial capacitor voltage is −180 kV. After the fault is detected at t = 1 ms, the interruption results are shown in Figure 9, where i_{dc}, i_{T1}, i_c and i_{ar} are the currents flowing through Line 4, T_1, C and arrester, respectively.

We assume that the protection detects the fault at t = 1 ms. As shown in Figure 9, after t = 1 ms, T_1 is turned on and then the LCS is turned off. At t = 1.16 ms, i_{dc} is commutated into the MB, and the FD is opened without arc. Substituting system parameters into (1), T_3 is turned on at t = 3.1 ms. After that, i_c rapidly exceeds the fault current; thus, T_1 is reversely biased. The reverse-bias of T_1 continues until i_{dc} exceeds i_c. The reverse-bias time is 120 μs and two times t_q, which is sufficient to turn off T_1. With the charging of the capacitor, i_{dc} reaches the maximum value of 11.7 kA at t = 3.29 ms and then gradually decreases. At t = 3.42 ms, i_{dc} is commutated into the arrester. At t = 10.3 ms, i_{dc} falls to below 10 A.

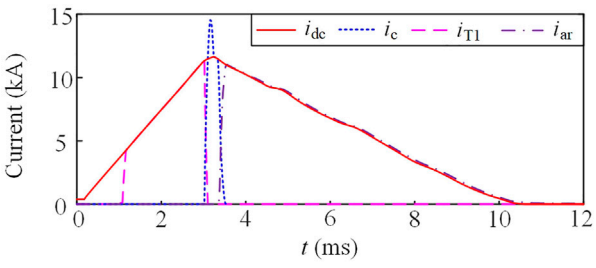

FIGURE 9
Current waveforms during the interruption.

For the typical hybrid DCCB in (Hafner and Jacobson, 2011), the fault current decreases almost immediately after the FD recovers the dielectric strength. For the C-DCCB, the fault current begins to fall at t = 3.29 ms, which is only 0.13 ms later than the instant that the FD recovers the dielectric strength at t = 3.16 ms. The time interval from the fault inception to the moment that the fault current begins to decrease is defined as the fault neutralization time. The fault neutralization time of C-DCCB is only a few hundred microseconds longer than that of typical hybrid DCCB, indicating a quick interruption speed.

4.3 Reclosing with a permanent fault

4.3.1 Permanent metallic fault

We set a permanent fault at the midpoint of Line 4 at t = 0 ms, and the fault resistance is 0.01 Ω. At t = 300 ms, B_1 begins to reclose, i.e., T_2 and T_5 are turned on. As shown in Figure 10A, u_c gradually decreases during reclosing and is smaller than u_{th} = 140.7 kV after t = 301.08 ms. Thus, B_1 identifies the permanent fault. During reclosing, the capacitor discharges through R_1, L and the fault line, and this second-order discharge circuit is underdamped because the fault resistance is small. As shown in Figure 10A, when i_c crosses 0 at t = 305.08 ms, u_c decreases to a negative value, and T_2 and T_5 are turned off. After that, S_2 is opened to isolate the permanent fault.

At the initial stage of reclosing, i_c undergoes multiple abrupt changes because of the traveling wave effect. The traveling impact

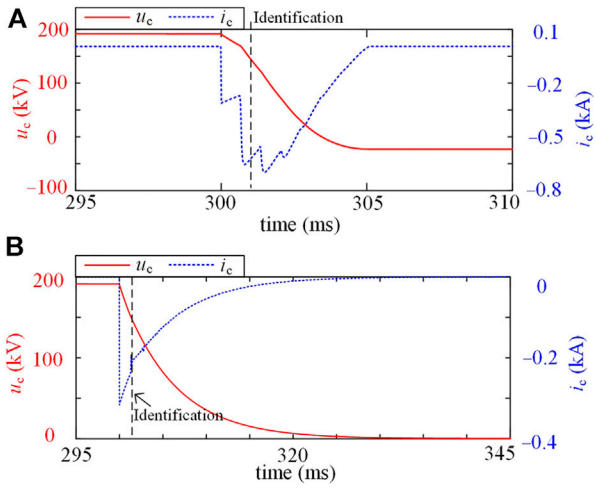

FIGURE 10
Simulation results during reclosing: **(A)** permanent metallic fault: **(B)** permanent high resistance fault.

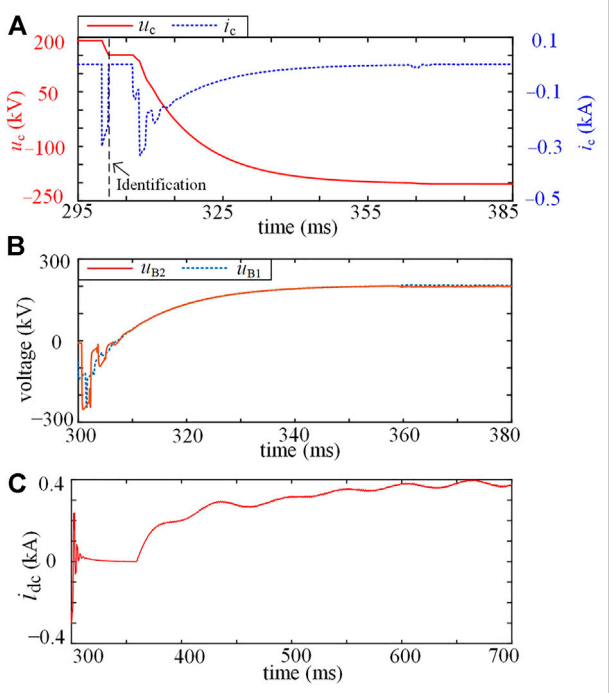

FIGURE 11
Simulation results during reclosing with a transient fault: **(A)** the value of uc and ic; **(B)** line voltages uB1 and uB2; **(C)** line current idc.

decreases over time and is not significant after 302.5 ms. At t = 305.08 ms, the zero crossing of i_c is caused by the underdamped discharge process rather than the traveling effect, which is consistent with the analysis in Section 3.2.

4.3.2 Permanent high-resistance fault

We set a permanent fault at the B_2 side of Line 4, and the fault resistance is 500 Ω. After the interruption, B_1 begins to reclose at t = 300 ms. As shown in Figure 10B, u_c decreases to u_{th} = 140.7 kV at t = 301.76 ms; thus, the permanent fault is identified. Because the fault resistance is large, the capacitor discharge process is overdamped. At t = 320 ms, u_c decreases to 6.7 kV and i_c is smaller than 10 A. Then, S_2 begins to be opened, and the fault is totally isolated at t = 340 ms.

4.4 Reclosing with a transient fault

After isolating a transient fault on Line 4, B_1 begins to reclose at t = 300 ms; thus, a current traveling wave is injected into Line 4. The current traveling wave transmits along Line 4 and is totally reflected at the end of Line 4. As shown in Figure 11A, at t = 301.40 ms, the current reflection wave arrives at the head of Line 4 and causes i_c to cross 0, because the reflected wave is in the opposite polarity of the original traveling wave. After that, u_c maintains at 151 kV. At t = 306.36 ms, the criterion in Eq. 7 is activated, indicating that the fault on Line 4 has disappeared. After that, B_1 turns on T_1 and T_5; thus, the DC grid charges the capacitor C and Line 4 through the resistor R_2. Finally, the capacitor C is charged to the system voltage.

As shown in Figure 11B, the voltage of Line 4 on B_1 side, marked as u_{B1}, increases to 190 kV at t = 339.20 ms, and B_1 begins to close S_1. At t = 339.24 ms, the voltage of Line 4 on B_2 side, marked as u_{B2}, increases to 190 kV; thus, B_2 directly identifies that the line fault has disappeared, and S_1, S_2, FD and LCS in B_2 are successively closed. After that, u_{B1} and u_{B2} gradually recover to close to 200 kV.

During the reclosing process, the discharging of the capacitor and charging of Line 4 cause negative and positive abrupt changes in i_{dc}, respectively, as shown in Figure 11C. After t = 360 ms, MCs of B_1 and B_2 have been closed; thus, i_{dc} begins to restore to the normal value. Line 4 begins to restore the power transmission. This restoration process takes hundreds of milliseconds. A special control strategy can be used to improve the restoration speed, which will be considered in future work.

4.5 Comparisons

In this section, the C-DCCBs in (Liu, 2019), (Wu et al., 2019) and (Guo et al., 2020) are compared with the proposed C-DCCB.

4.5.1 Interruption performance

In these C-DCCBs, only the C-DCCB in (Liu, 2019) opens the FD with arcing, which increases the FD operation time. Thus, when the same FD is used, the C-DCCB in (Liu, 2019) has a longer interruption time than the other three C-DCCBs. For the other three C-DCCBs, the fault current decreases within a few hundred microseconds after the FD recovers the dielectric strength, indicating a quick interruption speed.

Except for the MC, the C-DCCB in (Liu, 2019) cannot provide another current path to conduct the load current, whereas the other three C-DCCBs can conduct the load current using the thyristors in the MB. Therefore, the C-DCCB in (Liu, 2019) does not have the pre-activation ability, whereas the other three C-DCCBs have the pre-activation ability. Combining the protection and pre-activation, these three C-DCCBs can further reduce the interruption time.

During the interruption of backward direction currents, the C-DCCB in (Liu, 2019) cannot decrease the FD current to 0 until the capacitor discharge current is reversed, causing a larger interruption time. In (Wu et al., 2019), the C-DCCB interrupts only the forward direction currents and cannot interrupt the backward direction fault currents. Because of the symmetry of topology, the proposed C-DCCB can interrupt bidirectional currents with the same performance, and the C-DCCB in (Guo et al., 2020) also has this interruption characteristic.

4.5.2 Semiconductor cost

The peak TIV of these C-DCCBs, marked as U_p, is selected as 300 kV to compare the semiconductor cost. For the proposed C-DCCB, T_1 and T_2 are turned off during the interruption of the

TABLE 3 Semiconductor costs of C-DCCBs.

C-DCCB	N2825 TE400	5STF 28H2060 (¥)	W3082MC450(¥)	Total cost (¥)
In (Liu, 2019)	558,450 (¥)	0 (¥)	215,740 (¥)	774,190 (¥)
In (Wu et al., 2019)	558,450 (¥)	2,479,500 (¥)	0 (¥)	3,037,950 (¥)
In (Guo et al., 2020)	2,792,250 (¥)	826,500 (¥)	1,078,700 (¥)	4,697,450 (¥)
Our	1,675,350 (¥)	1,653,000 (¥)	647,220 (¥)	3,975,570 (¥)

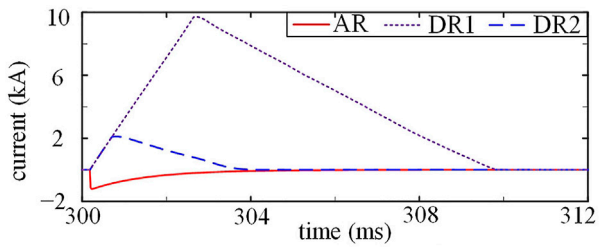

FIGURE 12
Waveforms of idc when the C-DCCB recloses with a permanent fault using different reclosing strategies.

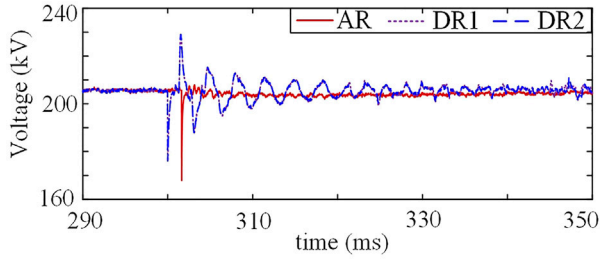

FIGURE 13
Waveforms of ubus1 when the C-DCCB recloses with a transient fault using different reclosing strategies.

forward direction and backward direction currents, respectively. They should be composed of fast thyristor modules to maintain a short interruption time. The thyristors T_3 and T_4 are naturally turned off after the interruption, and the thyristor T_5 is naturally turned off after the precharge process; thus, thyristors T_3, T_4 and T_5 can be composed of phase-control thyristor modules. Then, the proposed C-DCCB contains phase-control thyristor modules with a voltage rating of $3U_p$, fast thyristor modules with a voltage rating of $2U_p$, and diode modules of $3U_p$.

For the C-DCCB in (Liu, 2019), a triggered spark gap or reverse-conducting thyristor can be used to trigger the capacitor discharge during the interruption. The reverse-conducting thyristor comprises phase-control thyristor modules with a voltage rating of U_p and diode modules with a voltage rating of U_p. In (Wu et al., 2019), three thyristors need to be turned off during the interruption process. They should be composed of fast thyristor modules with a voltage rating of $3U_p$; one thyristor is naturally turned off after the interruption and can be composed of phase-control thyristor modules with a voltage rating of U_p. In (Guo et al., 2020), one thyristor is turned off during the interruption process and composed of fast thyristor modules with a voltage rating of U_p. In addition, phase-control thyristor modules with a voltage rating of $5U_p$ and diode modules with a voltage rating of $5U_p$ are also needed in (Guo et al., 2020).

We assume that the thyristor module N2825TE400 (4 kV, ¥ 3,723 (findic and digikey, 2021)), fast thyristor module 5STF 28H2060 (2 kV, ¥ 2,755 (findic and digikey, 2021)) and diode module W3082MC450 (4.5 kV, ¥ 1,610 (findic and digikey, 2021)) are used, and a safety voltage margin of 2 is maintained. Then, the device costs of these C-DCCBs are given in Table 3, and the unit of device costs is RMB. The C-DCCBs in (Liu, 2019) and (Guo et al., 2020) have the smallest and largest semiconductor costs, respectively, and the proposed C-DCCB has a higher semiconductor cost than the C-DCCB in (Wu et al., 2019).

According to the evaluation method in (Evans et al., 2019), the capacitor C of 9 μF in the proposed C-DCCB has a cost of ¥ 2,231,323, which is more than half of the total semiconductor cost of ¥ 3,975,570. Thus, the capacitor cost is vital for evaluating the construction cost of C-DCCBs. For C-DCCBs, the capacitor value is related to the interruption conditions, such as voltage rating and interruption capacity. Comparing capacitor costs of C-DCCBs should be based on the same interruption conditions. Considering that the capacitor values in (Liu, 2019), (Wu et al., 2019), (Guo et al., 2020) and this paper are selected based on different interruption conditions, the capacitor costs are not compared to avoid injustice.

4.5.3 Reclosing performance

For the C-DCCB in (Liu, 2019), the polarities of the capacitor voltage are in the opposite directions before and after the interruption. The C-DCCB in (Liu, 2019) requires additional circuits to restore the normal state of the capacitor before reclosing, which increases the construction cost and is not conducive to fast reclosing. The C-DCCB in (Wu et al., 2019) has the same polarity of capacitor voltage before and after the interruption, and the C-DCCB in (Guo et al., 2020) can quickly restore the initial capacitor voltage using the grounded branch. Thus, these two C-DCCBs have a fast reclosing ability.

However, direct reclosing rather than adaptive reclosing is considered in previous papers. The direct reclosing strategy

directly recloses the C-DCCB to reconnect the HVDC grid to the isolated line, and the C-DCCB interrupts the fault current in case of permanent faults. Considering that these C-DCCBs have similar performances during the direct reclosing, the proposed C-DCCB is used to perform the direct reclosing to validate the advantage of the proposed adaptive reclosing strategy.

For the first direct reclosing method, which is marked as DR1, the proposed C-DCCB successively closes S_1, S_2 and FD. For the second direct reclosing method, which uses the pre-activation ability and is marked as DR2, the proposed C-DCCB successively closes S_1—S_2 and turns on T_1—T_2, and then the system current is commutated into the MC by closing FD and turning on LCS. Compared with the DR1, the DR2 effectively reduces the interruption time during the permanent fault because the process of commutating the fault current from MC into MB is avoided. The proposed adaptive reclosing strategy is marked as AR.

We set a permanent metallic fault at the head of Line 4. For DR1 and DR2, we assume that the fault detection time is only 0.2 ms. As shown in Figure 12, compared with DR1, DR2 reduces the maximum value of i_{dc} from 9.73 to 2.11 kA because DR2 has a much shorter interruption time. For the proposed adaptive reclosing strategy, the maximum absolute value of i_{dc} is only 1.22 kA. Therefore, compared with direct reclosing strategies, the proposed adaptive reclosing strategy effectively limits the fault current during the permanent fault.

We set a transient fault at Line 4, and B_1 recloses using different reclosing strategies. The simulation results are shown in Figure 13. For DR1 and DR2, the HVDC grid directly charges the positive pole of Line 4, causing oscillations in the Bus1 voltage u_{bus1}, and DR1 and DR2 almost have the same waveforms of u_{bus1}. For the adaptive reclosing strategy, the HVDC grid charges the positive pole of Line 4 and the internal capacitor of C-DCCB through the resistor R_2 at 301.6 ms; thus, u_{bus1} drops to 168 kV and then quickly returns to the normal value without significant oscillations. Compared with direct reclosing strategies, the adaptive reclosing strategy effectively reduces the voltage oscillations in HVDC grids.

5 Conclusion

This paper proposes a novel C-DCCB with adaptive reclosing ability. The parameter design is analyzed to ensure the reliable turn-off of the thyristor, which is key to the successful interruption. The transient process during adaptive reclosing is analyzed to identify the fault property. The semiconductor cost, interruption and reclosing performances of the proposed C-DCCB are compared with those of previous C-DCCBs. The main conclusions are summarized as follows.

1) The proposed C-DCCB achieves good interruption performances, such as quick interruption speed and pre-activation ability. During interruptions, the fault current decreases within a few hundred microseconds after the FD restores the dielectric strength. Using the pre-activation, the fault current is commutated into the MB during the protection time, thus effectively reducing the interruption time.
2) During the adaptive reclosing, the internal capacitor has a large initial voltage and discharges through the grounded branch. The capacitor voltage decreases to a positive value when the fault is transient, and the capacitor voltage is no more than 0 when the fault is permanent; thus, the fault property is identified using the capacitor voltage.
3) The adaptive reclosing of C-DCCBs is less considered in previous papers. An adaptive reclosing strategy is designed for the proposed C-DCCB, which is the main contribution of this paper. Using the adaptive reclosing strategy, the proposed C-DCCB avoids the second fault shock in case of permanent faults, and the power transmission is restored without significant voltage oscillations in transient faults.

Data availability statement

The original contributions presented in the study are included in the article/Supplementary Material, further inquiries can be directed to the corresponding author.

Author contributions

ZX: Writing-Original Draft, Visualization. JL: Writing–Review and Editing, Supervision. YG: Conceptualization, Methodology, Writing-Original Draft. YW: Supervision.

Funding

This work is supported by the National Natural Science Foundation of China (52107130).

Acknowledgments

This is a brief acknowledgement of the contributions of individual colleagues, institutions, or agencies that assisted the writers' efforts in the writing of this article.

Conflict of interest

The authors declare that the research was conducted in the absence of any commercial or financial relationships that could be construed as a potential conflict of interest.

Publisher's note

References

An, T., Tang, G., and Wang, W. (2017). Research and application on multi-terminal and DC grids based on VSC-HVDC technology in China. *High. Volt.* 2, 1–10. doi:10.1049/hve.2017.0010

Augustin, T., Becerra, M., and Nee, H.-P. (2021). Enhanced active resonant DC circuit breakers based on discharge closing switches. *IEEE Trans. Power Deliv.* 36 (3), 1735–1743. doi:10.1109/tpwrd.2020.3014084

Bucher, M. K., and Franck, C. M. (2016). fault current interruption in multiterminal HVDC networks. *IEEE Trans. Power Deliv.* 31 (1), 87–95. doi:10.1109/tpwrd.2015.2448761

Chen, M., Xu, H., and Zhang, Z. (2018). Design and simulation of coupling mechanical high voltage DC circuit breaker. *High. Volt. Eng.* 44 (2), 380–387.

Chen, W., Zeng, R., He, J., Wu, Y., Wei, X., Fang, T., et al. (2021). Development and prospect of direct-current circuit breaker in China. *High. Volt.* 6, 1–15. doi:10.1049/hve2.12077

Cigré (2014). *TB604—guide for the development of models for HVDC converters in a HVDC grid joint working group B4.57*.

Evans, N., Dworakowski, P., Al-Kharaz, M., Hegde, S., Perez, E., and Morel, F. (2019). "Cost-performance framework for the assessment of Modular Multilevel Converter in HVDC transmission applications," in *IECON 2019- 45th annual conference of the* (Lisbon, Portugal: IEEE Industrial Electronics Society), 4793–4798.

findic and digikey (2021). *findic digikey*. Available: https://www.findic.com/ https://www.digikey.com/(accessed on Aug. 19, 2021).

Gómez, P., and Uribe, F. A. (2009). The numerical Laplace transform: An accurate technique for analyzing electromagnetic transients on power system devices. *Int. J. Electr. Power & Energy Syst.* 31 (2–3), 116–123. doi:10.1016/j.ijepes.2008.10.006

Guo, Y., Li, H., Liang, Y., and Wang, G. (2021). A method to calculate short-circuit faults in high-voltage DC grids. *IEEE Trans. Power Deliv.* 36 (1), 267–279. doi:10.1109/tpwrd.2020.2978625

Guo, Y., Wang, G., Zeng, D., Li, H., and Chao, H. (2020). A thyristor full-bridge-based DC circuit breaker. *IEEE Trans. Power Electron.* 35 (1), 1111–1123. doi:10.1109/tpel.2019.2915808

Hafner, J., and Jacobson, B. (2011). "Proactive hybrid HVDC breakers—a key innovation for reliable HVDC grids," in *CIGRE bologna conf*, 1–8.

Hassanpoor, A., Hafner, J., and Jacobson, B. (2015). Technical assessment of load commutation switch in hybrid HVDC breaker. *IEEE Trans. Power Electron.* 30 (10), 5393–5400. doi:10.1109/tpel.2014.2372815

Hertem, V., and Ghandhari, M. (2010). "Multi-terminal VSC HVDC for the European supergrid: Obstacles. *Renew. Sustain. Energy Rev.* 14, 3156–3163.

Jamshidifar, A., and Jovcic, D. (2018). Design, modeling and control of hybrid DC circuit breaker based on fast thyristors. *IEEE Trans. Power Deliv.* 33 (2), 919–927. doi:10.1109/tpwrd.2017.2761022

Jovcic, D., Tang, G., and Pang, H. (2019). Adopting circuit breakers for high-voltage dc networks: Appropriating the vast advantages of dc transmission grids. *IEEE Power Energy Mag.* 17 (3), 82–93. doi:10.1109/mpe.2019.2897408

Li, B., He, J., Li, Y., and Wen, W. (2020). A novel DCCB reclosing strategy for the flexible HVDC grid. *IEEE Trans. Power Deliv.* 35 (1), 244–257. doi:10.1109/tpwrd.2019.2938594

Liu, C., (2019). "535kV high voltage DC circuit breaker insulation test analysis," in *2019 5th international conference on electric power equipment - switching technology* (Kitakyushu, Japan: ICEPE-ST), 580–584.

Mei, J., Ge, R., Zhu, P., Fan, G., Wang, B., and Yan, L. (2021). An adaptive reclosing scheme for MMC-HVDC systems based on pulse injection from parallel energy absorption module. *IEEE Trans. Power Deliv.* 36 (3) 1809–1818. doi:10.1109/tpwrd.2020.3015311

Pei, X., Tang, G., and Zhang, S. (2019). Sequential auto-reclosing strategy for hybrid HVDC breakers in VSC-based DC grids. *J. Mod. Power Syst. Clean. Energy* 7 (3), 633–643. doi:10.1007/s40565-018-0486-1

Shi, Z., Zhang, Y., Jia, S., Song, X., Wang, L., and Chen, M. (2015). Design and numerical investigation of a HVDC vacuum switch based on artificial current zero. *IEEE Trans. Dielectr. Electr. Insul.* 22 (1), 135–141. doi:10.1109/tdei.2014.004533

Sima, W., Fu, Z., Yang, M., Yuan, T., Sun, P., Han, X., et al. (2019). A novel active mechanical HVDC breaker with consecutive interruption capability for fault clearances in MMC-HVDC systems. *IEEE Trans. Ind. Electron.* 66 (9), 6979–6989. doi:10.1109/tie.2018.2878115

Song, G., Wang, T., and Hussain, K. S. T. (2019). DC line fault identification based on pulse injection from hybrid HVDC breaker. *IEEE Trans. Power Deliv.* 34 (1), 271–280. doi:10.1109/tpwrd.2018.2865226

Technical Information (2012). *Bipolar semiconductors*. Infineon. Available: https://www.infineon.com/cms/de/product/power/high-power-diodes-thyristors/thyristor-diode-discs/?redirId=28573#! documents.

Torwelle, P., Bertinato, A., Grieshaber, W., Yang, Y., Raison, B., Le, T. D., et al. (2021). Pre-energization concept for overhead lines in MTDC grids using DCCB internal capacitor. *IEEE Trans. Power Deliv.* 37 (1–1), 155–164. doi:10.1109/tpwrd.2021.3054599

Wang, T., Song, G., and Hussain, K. S. T. (22032019). Adaptive single-Pole auto-reclosing scheme for hybrid MMC-HVDC systems. *IEEE Trans. Power Deliv.* 34 (6), 2194–2203. doi:10.1109/tpwrd.2019.2921674

Wen, W., Huang, Y., Sun, Y., Wu, J., Al-Dweikat, M., and Liu, W. (2016). Research on current commutation measures for hybrid DC circuit breakers. *IEEE Trans. Power Deliv.* 31 (4), 1456–1463. doi:10.1109/tpwrd.2016.2535397

Wen, W., Liu, H., Li, B., Li, P., Zhang, N., Gao, C., et al. (41332021). Novel reclosing strategy based on transient operating voltage in pseudobipolar DC system with mechanical DCCB. *IEEE Trans. Power Electron.* 36 (4), 4125–4133. doi:10.1109/tpel.2020.3022070

Wen, W., Wang, Y., Li, B., Huang, Y., Li, R., and Wang, Q. (94312018). Transient current interruption characteristics of a novel mechanical DC circuit breaker. *IEEE Trans. Power Electron.* 33 (11), 1. doi:10.1109/tpel.2018.2797243

Wu, Y., Wu, Y., Rong, M., and Yang, F. (2019). Development of a novel HVdc circuit breaker combining liquid metal load commutation switch and two-stage commutation circuit. *IEEE Trans. Ind. Electron.* 66 (8), 6055–6064. doi:10.1109/tie.2018.2870387

Wu, Y., Wu, Y., Yang, F., Rong, M., and Hu, Y. (2020). A novel current injection DC circuit breaker integrating current commutation and energy dissipation. *IEEE J. Emerg. Sel. Top. Power Electron.* 8 (3), 2861–2869. doi:10.1109/jestpe.2019.2911103

Wu, Y., Wu, Y., Yang, F., Rong, M., and Hu, Y. (2020). Bidirectional current injection MVDC circuit breaker: Principle and analysis. *IEEE J. Emerg. Sel. Top. Power Electron.* 8 (2), 1536–1546. doi:10.1109/jestpe.2018.2888590

Yang, S., Xiang, W., Lu, X., Zuo, W., and Wen, J. (11232020). An adaptive reclosing strategy for MMC-HVDC systems with hybrid DC circuit breakers. *IEEE Trans. Power Deliv.* 35 (3), 1111–1123. doi:10.1109/tpwrd.2019.2935311

Zhang, S., Zou, G., Xu, C., and Sun, W. (2020). A reclosing scheme of hybrid DC circuit breaker for MMC-HVDC systems. *IEEE J. Emerg. Sel. Top. Power Electron.* 9, 7126–7137. doi:10.1109/jestpe.2020.3025598

frontiers | Frontiers in Energy Research

TYPE Original Research
PUBLISHED 29 September 2022
DOI 10.3389/fenrg.2022.1009545

OPEN ACCESS

EDITED BY
Chaolong Zhang,
Anqing Normal University, China

REVIEWED BY
Weihang Yan,
National Renewable Energy Laboratory (DOE), United States
Jun Hao,
University of Denver, United States
Juan Wei,
Hunan University, China

*CORRESPONDENCE
Jun Zhang,
jun.zhang.ee@whu.edu.cn

SPECIALTY SECTION
This article was submitted to Smart Grids,
a section of the journal
Frontiers in Energy Research

RECEIVED 02 August 2022
ACCEPTED 22 August 2022
PUBLISHED 29 September 2022

CITATION
Xu P, Zhang J, Lu J, Zhang H, Gao T and Chen S (2022), A prior knowledge-embedded reinforcement learning method for real-time active power corrective control in complex power systems.
Front. Energy Res. 10:1009545.
doi: 10.3389/fenrg.2022.1009545

A prior knowledge-embedded reinforcement learning method for real-time active power corrective control in complex power systems

Peidong Xu[1], Jun Zhang[1]*, Jixiang Lu[2], Haoran Zhang[1], Tianlu Gao[1] and Siyuan Chen[1]

[1]School of Electrical Engineering and Automation, Wuhan University, Wuhan, China, [2]Technology Research Center, State Key Laboratory of Intelligent Power Grid Protection and Operation Control, NARI Group Corporation, Nanjing, China

With the increasing uncertainty and complexity of modern power grids, the real-time active power corrective control problem becomes intractable, bringing significant challenges to the stable operation of future power systems. To promote effective and efficient active power corrective control, a prior knowledge-embedded reinforcement learning method is proposed in this paper, to improve the performance of the deep reinforcement learning agent while maintaining the real-time control manner. The system-level feature is first established based on prior knowledge and cooperating with the equipment-level features, to provide a thorough description of the power network states. A global-local network structure is then constructed to integrate the two-level information accordingly by introducing the graph pooling method. Based on the multi-level representation of power system states, the Deep Q-learning from Demonstrations method is adopted to guide the deep reinforcement learning agent to learn from the expert policy along with the interactive improving process. Considering the infrequent corrective control actions in practice, the double-prioritized training mechanism combined with the λ-return is further developed to help the agent lay emphasis on learning from critical control experience. Simulation results demonstrate that the proposed method prevails over the conventional deep reinforcement learning methods in training efficiency and control effects, and has the potential to solve the complex active power corrective control problem in the future.

KEYWORDS

active power corrective control, deep Q-learning from demonstrations, graph pooling, power system, prior knowledge

1 Introduction

Security control is a critical method to ensure the safe and reliable operation of power systems. The blackouts in recent years show that successive outages of transmission lines are the main cause of cascading failures and even system crashes. Therefore, it is of great significance to perform real-time and effective active power corrective control in the complex power system, to efficiently eliminate line overloads, prevent cascading failures and ensure the stable operation of the power grid.

Scholars have conducted extensive research on this topic. In the early days, generation rescheduling and load shedding are carried out to mitigate the transmission line congestion based on the sensitivity matrices (Talukdar et al., 2005). Fuzzy logic control is also utilized to alleviate the line overloads (Lenoir et al., 2009). As the power system becomes increasingly complex, the security-constrained optimal power flow (SCOPF) approaches considering N-1 contingencies are widely adopted. Based on linear network compression, a preventive SCOPF problem is solved to avoid all possible overloads by pre-schedule (Karbalaei et al., 2018). Considering the large cost to satisfy all N-1 constraints in the preventive control method, corrective control is introduced in the SCOPF approach to mitigate overloads in contingencies. A corrective SCOPF approach is proposed in (Cao et al., 2015) with the help of multi-terminal VSC-HVDC. By introducing the unified power flow controller as the fast corrective control measure, a three-stage corrective SCOPF approach is proposed in (Yan et al., 2020a) based on Benders decomposition and sequential cone programming. A real-time distributed OPF approach is also proposed to perform robust corrective control (Ding et al., 2020). Efforts are also made to make full use of the preventive method and the corrective method. In (Waseem and Manshadi, 2021), contingencies are filtered and divided for preventive actions and corrective actions, and the SCOPF problem is solved based on a decomposed convex relaxation algorithm. The combination of preventive SCOPF and corrective SCOPF is proposed in (Xu et al., 2013) to promote system security, while the evolutionary algorithm and the interior-point method are adopted for optimal solutions. Besides, considering the open-loop feature of the OPF-based methods, the model-predictive control method is also developed to alleviate overloads based on the model-based linear power flow model (Martin and Hiskens, 2016).

The existing methods provide enlightening solutions to realize the effective corrective control of power systems. However, with the high penetration of renewable energy and the wide interconnection of power grids, the power system's operation mode and stability characteristics become more complex (Yan et al., 2019; Yan et al., 2020b; Yan et al., 2021). The strong complexity and uncertainty of the new-type power system aggravate the modeling difficulty of the active power corrective control problem. Correspondingly, the model-based methods will face great challenges in promoting the effectiveness and efficiency of the corrective control strategy. Meanwhile, the swiftly developed deep reinforcement learning (DRL) method can deal with complicated problems in a model-free manner with high computational efficiency. These features make the DRL method suitable for the real-time active power corrective control problem. In our previous work, by introducing the simulation assistance, graph neural networks, and the multi-agent framework, we have proposed basic methods for the application of deep reinforcement learning in modern power system corrective control and verified the efficiency, feasibility, and adaptability of the DRL method (Xu et al., 2020; Chen et al., 2021; Xu et al., 2021).

However, the active power corrective control in new-type power systems demands the efficient and accurate alleviation of line overloads under the highly dynamic and strongly uncertain network operation states, which is of great complexity. The interactive learning of the conventional DRL method usually requires a lot of time, and the performance of the final strategy explored in the complex power system with massive constraints can be difficult to guarantee. At the same time, as aforementioned, there are plenty of model-based methods, as well as human experience, in the field of active power corrective control. If we can make full use of the prior knowledge, it will be of great help to apply the DRL method to active power corrective control more efficiently and effectively. In recent years, researchers begin to study the fusion of prior knowledge in DRL methods. A deep Q-learning from demonstrations (DQfD) method is proposed in (Hester et al., 2018), where human experience is collected as demonstration data to pre-train the DRL agent and further join its interactive learning process. Based on this idea, some researchers focus on improving the performance of the DQfD method by introducing soft expert guidance or behavioral cloning (Gao et al., 2018; Li et al., 2022a). Most recently, attempts of applying the prior knowledge guided DRL in power systems have been made, where the emergency voltage control is conducted (Li et al., 2022b).

Enlightened by the above work, a prior knowledge-embedded reinforcement learning (PKE-RL) method for active power corrective control is proposed in this paper, to improve the exploration efficiency and control performance of DRL methods in complex corrective control problems. The contributions of this paper are as follows:

1) According to the multi-level characteristics of the power system, the differential integration method of the real-time power grid state based on graph convolution and graph pooling is proposed, to fully represent and fuse the system operation indexes and fine-grained equipment features at global and local levels.
2) Based on the idea of Deep Q-learning from Demonstrations, the prior experience is introduced to the initial strategy optimization and whole-process guidance of the agent

training. Considering the sparsity of the corrective control action, a double-prioritized DQfD(λ) training mechanism is further developed to focus the training process on critical control trajectories.

3) The simulation results in the modified 36-bus system demonstrate that the proposed method can effectively utilize the prior knowledge to further improve the DRL training performance and optimize the operation stability of power grids.

The remainder of this paper is organized as follows: Section 2 describes the active power corrective problem and formulates it as a Markov decision process (MDP). Section 3 illustrates the proposed prior knowledge-embedded reinforcement learning method. In Section 4, case studies are given to verify the proposed method. Section 5 summarizes our work and provides future directions for our research.

2 Problem formulation

2.1 Objective and constraints

The goal of the conventional active power corrective control is generally described as:

$$\begin{cases} \min f\left(|\Delta \mathbf{P_G}|, \Delta \mathbf{P_L}, \Delta \mathrm{N}\right) \\ \text{s.t.} \left|P_{ij}\right| \le \bar{P}_{ij} \end{cases} \tag{1}$$

where $f(\cdot)$ denotes the function related to the control cost, $\Delta \mathbf{P_G}$ and $\Delta \mathbf{P_L}$ represent the amount of generator redispatch and load shedding, respectively. ΔN represents the adjustment of the topology, such as line switching or bus-bar splitting. Notably, topological changes are assumed to be cost-free in this paper. P_{ij} and $\bar{P}_{ij}$ denote the current power and capacity of the transmission line l_{ij}.

Along with the traditional constraints, to guide the corrective control actions to the feasible region and minimize their disturbance to the power grid, the number of topological control actions and redispatch amounts of generators are also restricted.

$$X_{line} + X_{bus} \le N_{\text{limit}} \tag{2}$$

$$\begin{cases} |\Delta \mathbf{P_G}| \le \min\left(\mathbf{P_{G\,max}} - \mathbf{P_G}, \mathbf{R_{up}}\right) \\ |\Delta \mathbf{P_G}| \le \min\left(\mathbf{P_G} - \mathbf{P_{G\,min}}, \mathbf{R_{down}}\right) \end{cases} \tag{3}$$

where X_{line}, X_{bus}, N_{limit} represent the number of line switching actions, bus-bar switching actions, and the limited topological actions, respectively. $\mathbf{P_{G\,max}}$, $\mathbf{P_{G\,min}}$, $\mathbf{R_{up}}$, $\mathbf{R_{down}}$ denote the upper and lower bounds of the generator outputs, as well as the bidirectional ramping rates of the generators.

As the active power corrective control aims to avoid cascading failures by mitigating overloads, same as (Xu et al., 2021), the problem is extended to a time-series control problem as illustrated in Eq. 4. The goal can transform into securing the system operation while minimizing the overall cost during the control period, where corrective actions are carried out to alleviate overloads, preventive actions can also be considered to promote the system stability in advance:

$$\min \sum_{t=0}^{T} \left[f\left(|\Delta \boldsymbol{P_G}(t)|, \Delta \boldsymbol{P_L}(t), t\right) + f_{net}(t) + E_{loss}(t) \cdot p(t) \right] \tag{4}$$

where T denotes the control duration, $f_{net}(t)$ represents the network loss cost, which can reflect the economic influence of corrective actions. $E_{loss}(t)$ symbolizes the energy loss at time t when a blackout strikes and $p(t)$ represents the marginal price of the generators' outputs.

Furthermore, considering the practical constraints, the reaction time and the recovery time of power equipment are adopted, to reflect the available time for mitigating the overloads and the time requirements for reactivating the power equipment.

2.2 Problem formulated as MDP

According to the objective function presented in Eq. 4, the active power corrective control can be modeled as MDP in the form of a 5-element tuple $= \{\mathcal{S}, \mathcal{A}, \mathcal{P}, \mathcal{R}, \gamma\}$. Where γ symbolizes the discounting factor and $\mathcal{P}$ represents the state transition probability matrix. The details of other elements are elaborated as follows:

State space $\mathcal{S}$: The state $s_t \in \mathcal{S}$ represents the observation collected by the dispatch center from the power grid. As topological adjustments and node injections are addressed to mitigate line overloads, the features of generators, loads, and transmission lines are considered. Thus, the state is consisted of the active power status of power equipment and the load ratio of each line, i.e.,

$$s_t = (\mathbf{P}, \boldsymbol{\rho}) \tag{5}$$

where $\mathbf{P}$ denote the active power status of the power equipment, including outputs of generators, consumption of loads, and power flow at both ends of the lines. $\boldsymbol{\rho}$ represents the load ratio of each transmission line, i.e., the current flow divided by the thermal limit of each line.

Action space $\mathcal{A}$: To avoid damaging the interest of consumers, the action space comprises generator redispatch, line switching, bus-bar switching, and do-nothing actions. Notably, the line switching and bus-bar switching actions change the topology of the power grid in different ways. The bus-bar switching intervenes in the bus selection of the connected power equipment in one substation, while the line switching action alters the operating status of lines.

Reward function $\mathcal{R}$: As the control agent aims to secure the long-term operation of the power grid under strong uncertainties, the available transmission capacity (ATC) must be maintained to promote the flexibility of the power system with

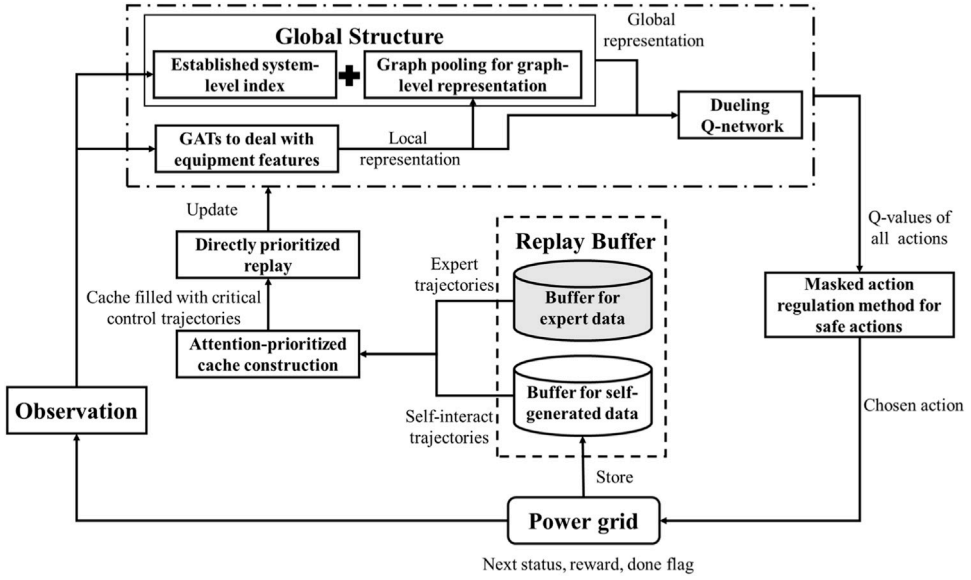

FIGURE 1
The overall architecture of the proposed PKE-RL method.

considering the risks brought by the heavy-loaded lines and overload lines. Thus, the modified available transmission capacity is introduced to represent the flexibility of the grid (Nacional de Colombia, Universidad, 2020):

$$o_t = \sum_{i=1}^{N_L} [max(0, (1-\rho_i^2)) - \alpha \cdot max(0, \rho_i - 1) - \beta \cdot max(0, \rho_i - 0.9)) \quad (6)$$

where N_L denotes the number of lines, α and β represent the penalty factors of overload and heavy load, respectively.

Based on MDP, the current system flexibility reflects the immediate effect of the action at the last time step, then the reward r_t can be defined as:

$$r_t = sign(o_{t+1}) \log(1 + |o_{t+1}|) \quad (7)$$

where $sign(\cdot)$ produces a plus or minus sign according to the positive elements or the negative elements. Equation 7 can maintain the reward over a reasonable scale for the DRL agent to learn (Hester et al., 2018).

3 The prior knowledge-embedded reinforcement learning method

Although the deep reinforcement learning method can handle various problems with high computation efficiency, the effectiveness of the learned policy depends on its interaction with the environment. For the active power corrective control in new-type power systems, the existence of massive constraints, the strong uncertainty of power grid disturbances, and the selection of the proper measure from huge candidate strategies should be considered simultaneously. Thus, it can be challenging for the self-evolving reinforcement learning method to learn a high-quality corrective control strategy in such complex power networks.

To promote the effectiveness of the reinforcement learning method in active power corrective control problems, a prior knowledge-embedded reinforcement learning method is developed in this paper. The architecture is illustrated in Figure 1. The system-level power network feature is constructed to merge domain knowledge into the observation of the DRL agent. Based on the graph pooling method, a global-local network structure is established to assist the agent deal with the system-level information and equipment-level features accordingly. Then, with the perception ability enhanced, the deep Q-learning from demonstrations method is introduced to improve the DRL agent's capability with the guidance of expert knowledge. Besides, a double-prioritized DQN(λ) algorithm is utilized to facilitate the training process by focusing on the evaluation of key corrective control trajectories. The dueling deep Q-network is utilized as the basic DRL framework.

3.1 The multi-level differential integration of environment features

As the power grid is a high-dimensional dynamic system with strong complexity, a multi-level differential integration approach for environment features is proposed to aid the agent to realize a better perception of the status.

In the bulk power system, there are plenty of features provided for the agent at the moment of decision, and the key information can be difficult to extract since the features are from various equipment in a wide area. Hence, the global-level feature is established on the current modified ATC of the grid to provide an additional holistic perspective as in Eq. 8:

$$s_{t,global} = o_t \tag{8}$$

According to Eq. 7 and Eq. 8, it can be easily found that the global-level feature represents r_{t-1} in another form.

To coordinate with the multi-level features, in our network architecture, a differential integration strategy for global and local features is proposed. For the local features, graph attention networks (GATs) are introduced to perform representation learning due to the network-structure data format. The power equipment can be regarded as nodes of a graph. Thus, the adjacency matrix can be constructed based on the connections between the power equipment, i.e., the origin and extremity of lines, generators, and loads. The feature matrix is formed by combining the common and the unique features of the above equipment. The details of graph formulation for local features are shown in (Xu et al., 2021). Thus, the adjacency matrix and feature matrix in this problem can be elaborated as:

$$\mathbf{A}_{ij} = \begin{cases} 1, & \text{if equipment } i \text{ and } j \text{ on same bus or same line} \\ 0, & \text{otherwise} \end{cases} \tag{9}$$

$$\mathbf{X}_{equipment-type} \begin{cases} \text{Origin} \\ \text{Extremity} \\ \text{Load} \\ \text{Generator} \end{cases} \begin{bmatrix} P_{OR} & \rho \\ P_{EX} & \rho \\ P_L & 0 \\ P_G & 0 \end{bmatrix} \tag{10}$$

where P_{OR} and P_{EX} denote the active power flow at the origin and the extremity of the transmission line, respectively. P_L represents the active consumption value of the load, and P_G stands for the active power output of the generator. ρ denotes the load ratio of the transmission line.

Then, GATs can be utilized to conduct graph convolution. The graph attention layer with multi-head attention for transformed features of the ith node $\boldsymbol{h}_i$ can be defined in Eq. 11 as (Veličković et al., 2017):

$$\boldsymbol{h}_i^{'} = \sigma\left(\frac{1}{K}\sum_{k=1}^{K}\sum_{j\in\mathcal{N}_i}\alpha_{ij}^{k}\mathbf{W}^{k}\boldsymbol{h}_j\right) \tag{11}$$

Where σ symbolizes the non-linear activation function, $\mathcal{N}_i$ denotes the neighboring node set of the ith node, K represents the number of independent attention mechanisms, α_{ij}^{k} symbolizes the normalized attention coefficients computed by the kth attention mechanism (Vaswani et al., 2017), and $\mathbf{W}^{k}$ is the kth weight matrix. Notably, the initial transformed features of nodes $\mathbf{H}^{0}$ equals the feature matrix $\mathbf{X}$.

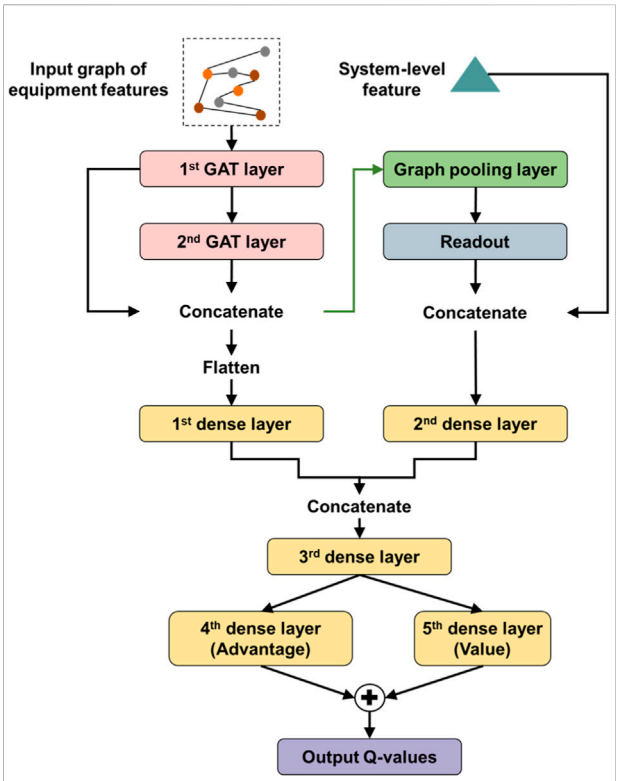

FIGURE 2
The proposed network architecture.

After the graph convolution, the transformed node-level vectors of the local features are obtained to serve as the concrete representation of the current status. To get a comprehensive environment perception, a self-learning graph-level representation is acquired by introducing graph pooling on the transformed node-level vectors. Specifically, a self-attention graph pooling method is adopted to efficiently extract important information from node-level vectors, while nodal features and graph topology are both considered. In (Lee et al., 2019), the attention score of each node is obtained by adopting graph convolution:

$$V = \delta\left(GAT\left(\mathbf{H}, \mathbf{A}\right)\right) \tag{12}$$

where δ represents the activation function and $GAT(\cdot)$ denotes the graph attention layer with multi-head attention as shown in Eq. 11.

Then, the most important nodes based on the attention score will be preserved as in Eq. 13.

$$\mathrm{id} = top - rank\left(V, |\zeta N|\right) \tag{13}$$

where id denotes the indexes of the preserved nodes, $top-rank$ represents the function of obtaining those indexes, ζ controls the ratio of preserved nodes, and N denotes the number of nodes.

The graph pooling can then be realized according to Eq. 14:

$$\begin{cases} \mathbf{H}_{out} = \mathbf{H}_{\mathrm{id}} \odot V\mathrm{id} \\ \mathbf{A}_{out} = \mathbf{A}_{\mathrm{id,id}} \end{cases} \tag{14}$$

Thus, the important nodes are preserved to assist the agent address on fewer nodes with critical information maintained, which can prevent the distraction from the redundant signals in the bulk power system. Based on features of the important nodes, a readout layer is further adopted to aggregate the critical information and make graph-level representation as shown in Eq. 15 (Cangea et al., 2018):

$$\boldsymbol{G} = \frac{\sum_{i=1}^{N_C} \boldsymbol{g}_i}{N_C} \parallel \max_{i=1}^{N_c} \mathbf{g}_i \tag{15}$$

where $\mathbf{g}_i$ represents the features of the ith important node, N_C represents the number of the important nodes, and $\parallel$ is the concatenation function.

Finally, the self-learning graph-level representation and the prior-designed global-level feature are concatenated as the global representation. The global representation is then combined with the concrete representation via trainable weights and the multi-level differential integration of environment features is realized. The overall architecture of the adopted neural network is illustrated in Figure 2.

3.2 Deep Q-learning from demonstrations focusing on key corrective control trajectories

In many decision-making problems, the typical reinforcement learning method usually converges into a good policy from scratch after massive interactions with the environment. However, the diverse scenarios, few feasible solutions, and the complex electrical relation between power flow and node injection or topology in the active power corrective control problem make it challenging for DRL agents to learn an effective strategy by pure interaction, even with the help of simulation software. Additional work should be done to further promote the agent's performance.

In power system corrective control, there always exists expert data like dispatcher operation records or model-based control strategies. This kind of data contains prior knowledge and usually performs well in alleviating overloads. Thus, in this paper, the deep Q-learning from demonstrations method is introduced to make full use of the expert knowledge. The domain knowledge is first utilized to pre-train the agent and then guide the agent during the rest of the training process, to improve the effectiveness of the learned corrective control policy.

In general, the DQfD method realizes merging prior knowledge into standard deep Q-learning by constructing a comprehensive loss function with four losses considered (Hester et al., 2018):

$$L(\theta) = L_{DQ}(\theta) + \alpha_1 L_n(\theta) + \alpha_2 L_E(\theta) + \alpha_3 L_{L2}(\theta) \tag{16}$$

where θ denote the Q-network parameters. $L_{DQ}(\theta), L_n(\theta), L_E(\theta), L_{L2}(\theta)$ denote the 1-step deep Q-learning loss, the n-step deep Q-learning loss, the expert loss, and the L2 regularization loss, respectively. α parameters represent the weights between different losses.

Among the losses, the deep Q-learning losses ensure the agent improves itself from temporal-difference (TD) learning, the expert loss is designed to guide the agent to follow the action strategy of the demonstrator, while the L2 regularization loss promotes the generalization ability of the agent by restricting the network parameters.

Specifically, considering the credit assignment problem, the n-step deep Q-learning loss is introduced to help better evaluate the actions' long-term benefits and promote the entire training process. The n-step loss is computed based on the n-step return:

$$L_n(\theta) = \mathbb{E}_{(s,a,R^n)\sim U(\mathcal{D})}\left[(R^n - Q(s,a;\theta))^2\right] \tag{17}$$

$$R_t^n = r_t + \gamma r_{t+1} + \cdots + \gamma^n \max_{a' \in \mathcal{A}} Q\left(s_{t+n}, a'\right) \tag{18}$$

where a is the agent action, $\mathcal{D}$ symbolizes the replay buffer, and R^n denotes the n-step return.

As the most important part of all four losses, the expert loss is established under the assumption that the expert's action prevails over other available actions in each scenario selected from demonstration data, as shown in Eq. 19. In the corresponding scenario, a large margin supervised loss is introduced to measure the equality between the greedy action and expert's action (Piot et al., 2014). The supervised loss is 0 while the greedy action is the same as the expert's action, and the supervised loss is a positive constant otherwise. Under this setting, the Q-values of other actions are at least a margin lower than the Q-value of the expert's action, allowing the agent to imitate the expert while satisfying the Bellman equation and evaluating the unseen actions reasonably.

$$L_E(\theta) = \max_{a \in \mathcal{A}} [Q(s,a) + l(a_E, a)] - Q(s, a_E) \tag{19}$$

where $l(a_E, a)$ represents the large margin supervised loss, a_E denotes the expert's action.

Based on the comprehensive loss function, the DQfD method merges the domain knowledge in the pre-training stage and formal training stage. During the pre-training phase, the DRL agent performs batch training by sampling from the collected demonstration data. Then, the pre-trained agent starts interacting with the environment and storing the self-generated data into the replay buffer $\mathcal{D}$. The self-generated data is updated continuously, while the

demonstration data keeps unchanged to provide persistent guidance. And the proportion of demonstration data in experience replay is controlled to maintain the self-improving ability of the agent. Notably, when the sampled transition comes from the self-generated data, the expert loss doesn't work and equals 0.

In the DRL-based active power corrective control architecture, the conducted action, e.g., switching the bus-bar or modifying the generator's output, can alleviate the current heavy loads or overloads, as well as change the future operation point of the power grid. Thus, the long-term effect of the action must be precisely evaluated. The n-step return can help reduce the estimation bias to some extent, but in our problem, the proper selection of "n" can be challenging since the power system is highly complex. Meanwhile, despite the strong uncertainties of system disturbances, the power system can maintain stable operation at most times without additional actions. Thus, the proportion of preventive or corrective actions can be relatively low in the replay buffer, which may lead to the lack of sampling and training of these important control actions, even with tricks like the prioritized replay. The above two issues can hamper the training performance of the agent.

To further enable the DRL-based method in active power corrective control problems, based on our previous work (Xu et al., 2022), a double-prioritized DQfD(λ) training mechanism is introduced and developed in this paper. The critical corrective control trajectories are particularly analyzed with the ratio of the demonstration data and self-generated data carefully controlled.

Along with the experience replay, the λ-return is first introduced to estimate the long-term benefit of agent actions instead of the n-step return. The λ-return is defined as the exponential average of every n-step return (Watkins, 1989) as in Eq. 20, so the accurate evaluation of the actions can be realized without the selection of "n".

$$R_t^\lambda = (1-\lambda)\sum_{n=1}^{T-t-1}\lambda^{n-1}R_t^n + \lambda^{T-t-1}R_t^{T-t} \tag{20}$$

where $\lambda \in [0,1]$ controls the decay rate of future returns.

In this way, the deep Q-learning losses can be replaced by the λ-discounted deep Q-learning loss as the λ-return considers every n-step return, $n = 1, 2, \cdots, T-t$. The comprehensive loss function can be expressed as in Eq. 21.

$$\begin{cases} L(\theta) = L_\lambda(\theta) + \alpha_2 L_E(\theta) + \alpha_3 L_{L2}(\theta) \\ L_\lambda(\theta) = \mathbb{E}_{(s,a,R^\lambda)\sim U(\mathcal{D})}\left[\left(R^\lambda - Q(s,a;\theta)\right)^2\right] \end{cases} \tag{21}$$

Practically, the λ-return can be computed recursively based on the trajectory of transitions as in (Daley and Amato, 2019), as illustrated in Eq. 22. The λ-returns of transitions from trajectories are stored into the replay buffer $\mathcal{D}$ and serve as the target network. The batch training based on experience replay can then be realized according to the new comprehensive loss function.

$$R_t^\lambda = R_t^l + \gamma\lambda\left[R_{t+1}^\lambda - \max_{a'\in\mathcal{A}} Q\left(s_{t+1}, a'\right)\right] \tag{22}$$

As the calculation of the λ-return can be resource-consuming, when integrating the λ-return with the experience replay, a dynamic small cache $\mathcal{H}$ is constructed by sampling short trajectories of transitions from the repay buffer $\mathcal{D}$, to refresh and store the corresponding λ-returns. Specifically, during the entire training process, periodically, C/B blocks, i.e., short trajectories containing neighboring transitions, are sampled to form the small cache $\mathcal{H}$. Different from the random sampling policy in (Daley and Amato, 2019), a demonstration-ratio-constraint attention-prioritized cache construction method is developed to improve the number of effective control transitions in the cache, with the ratio of the expert experience and the interaction experience restricted.

In the DQfD method, the repay buffer $\mathcal{D}$ is composed of two parts: the demonstration buffer $\mathcal{D}_{demo}$ and the interaction buffer $\mathcal{D}_{self}$. To restrict the ratio of the expert experience within a certain range from the cache construction stage, the number of sampled blocks from the demonstration buffer $\mathcal{D}_{demo}$ is defined as:

$$N_{demo} = \frac{C}{B}\varepsilon_d \tag{23}$$

where ε_d denotes the expected demonstration ratio in the batch training.

Therefore, N_{demo} and $N_{self} = (C/B)\cdot(1-\varepsilon_d)$ blocks are sampled from the demonstration buffer $\mathcal{D}_{demo}$ and the interaction buffer $\mathcal{D}_{self}$, respectively. For the demonstration buffer $\mathcal{D}_{demo}$ with size U_{demo}, the number of candidate blocks is $U_{demo} - B + 1$. We define the attention degree of each block as the diversity of the effective control actions within it, as illustrated in Eq. 24.

$$\varphi_i = \frac{\|set(\boldsymbol{a}_i)\| - 1}{B} \tag{24}$$

where $\boldsymbol{a}_i$ represents the agent's action trajectory in the ith block, where the "do nothing" action is included. $set(\cdot)$ denotes the function that selects non-repeatable elements to form a set. $\|\cdot\|$ calculates the number of elements. Thus, the blocks containing more kinds of effective control actions will have higher attention degrees.

Then, the N_{demo} blocks are sampled from the demonstration buffer $\mathcal{D}_{demo}$ according to their attention degrees, the sampling probability of the ith block is illustrated as:

$$P(i) = \frac{\varphi_i}{\sum_{k=1}^{U_{demo}-B+1}\varphi_k} \tag{25}$$

The methodology of sampling blocks from the interaction buffer $\mathcal{D}_{self}$ is the same as the demonstration method. Based on the proposed attention-prioritized blocks sampling strategy, we can promote a better evaluation of the action set as the

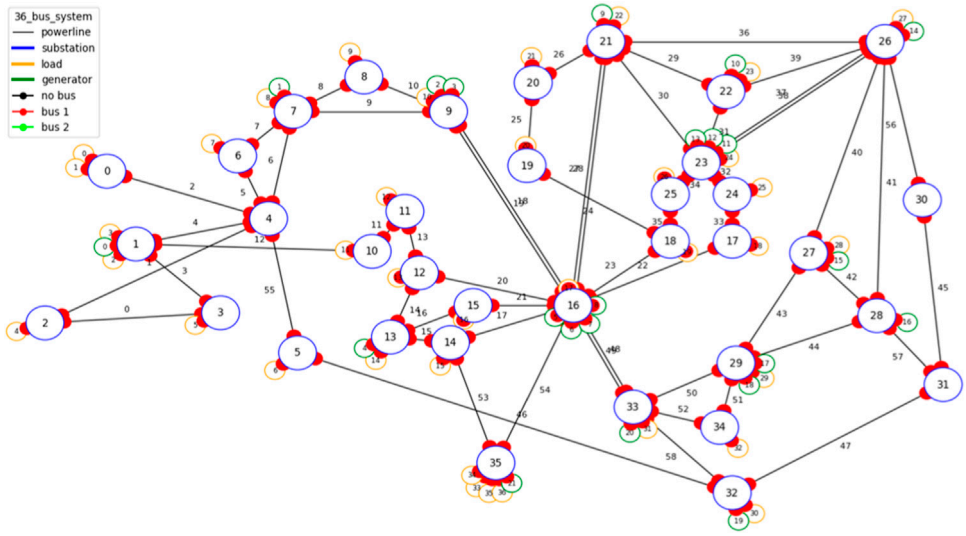

FIGURE 3
The modified 36-bus system.

established cache always contains various effective control experience, while the expert-imitation ability and the self-learning ability is controlled from the source.

Based on the cache, the computation of the λ-return is performed in each block. A directly prioritized replay policy is adopted to improve the transition sampling and batch training process. The transitions are sampled from the cache with the TD error-based probabilities:

$$p(e_j) = \begin{cases} \dfrac{(1+\mu)}{C}, & \text{if } |\delta_j| > \delta_{median} \\ \dfrac{1}{C}, & \text{if } |\delta_j| = \delta_{median} \\ \dfrac{(1-\mu)}{C}, & \text{if } |\delta_j| < \delta_{median} \end{cases} \tag{26}$$

where e_j and δ_j denote the jth transition and its TD error, respectively. $\mu \in [0, 1]$ controls the prioritized degree of sampling. δ_{median} represents the median TD error value of the cache.

Based on the double-prioritized DQfD(λ) training mechanism, the important corrective control experience can be emphasized during the entire training process.

Meanwhile, considering the massive restrictions presented in the dynamic operation, during the training and deployment process, a masked action regulation method is developed to prevent the DRL agent from taking actions violating the constraints. The greedy action can be selected as in Eq. 27:

$$a_{greedy} = \text{argmax}\mathbf{a}_{mask}Q(s_t, \forall a) \tag{27}$$

where $\mathbf{a}_{mask}$ is a 0–1 action mask vector with the size of action space, while the ith action violates the constraints according to the simple prior knowledge based on the observation, the action is masked with $\mathbf{a}_{mask}$ set to 0, otherwise set to 1.

4 Case study

4.1 Experiment setup

Same as our previous work (Xu et al., 2021), a modified 36-bus system originated from the IEEE 118-bus system is selected to verify the proposed method. The power grid consists of 59 transmission lines, 22 generators, and 37 loads, all the elements are connected to the bus-bars of the 36 substations, as illustrated in Figure 3. Among the generators, there are four wind farms and eight photovoltaic power plants, which will cause power fluctuations due to the uncertainties of their outputs. Besides, there can be at most two random "N-1" events occurring in the system within 1 day to reflect the strong system disturbance in future power networks.

The corresponding strategies are deployed on the open-source platform Grid2Op (RTE-France, 2021) to perform active power corrective control every 5 min a day. The topological actions are considered in our action set with the number of simultaneous actions restricted to 1, avoiding too many changes to the network topology. Considering the reality of power grids, the cooldown time of each topological action is set to 15 min 245 effective topological control actions and 1 "do nothing" action compose the action set by pre-selection with the help of simulation (L2RPN, 2020).

In the following experiments, all the DRL-based agents are trained on a Linux server with 4 11 GB GPUs.

TABLE 1 The details of the pke-rl agent.

Parameters	Value
1st GAT layer dimension	8
2nd GAT layer dimension	8
Number of attention heads	4
Dense layers dimension	[128, 128, 512, 246, 1]
Graph pooling ratio	0.5
Readout layer output dimension	32

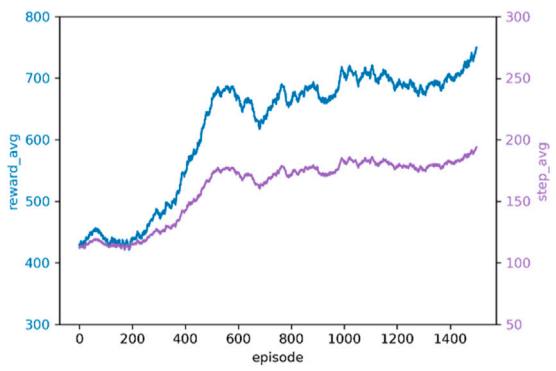

FIGURE 4
The training performance of the PKE-RL agent.

4.2 Performance of the proposed method

In this section, the performance of the proposed prior knowledge-embedded reinforcement learning method is evaluated by various operation scenarios. A dueling DQN structure as shown in Figure 2 is utilized to represent our agent, i.e., the PKE-RL agent. The details of the agent are illustrated in Table 1. 12,288-timestep active power corrective control trajectories are selected from the expert policy's demonstrations (L2RPN, 2020) to serve as prior knowledge. The lambda value λ, replay buffer size U, cache size C, block size B, expected demonstration ratio ε_d, and refresh frequency are set to 0.5, 32,768, 8,192, 128, 0.2, and 2048, respectively.

The PKE-RL agent is pre-trained with expert knowledge for 500 steps and then trained in the modified 36-bus system for 1,500 episodes. The averaged cumulative rewards curve and the averaged operation steps curve are shown in Figure 4.

As shown in Figure 4, despite the complexity of the scenarios, our agent keeps swiftly improving itself during the first 500 episodes and maintains a slow uptrend till the end of the training process, indicating the good learning ability of the proposed method.

To further evaluate the effectiveness of the proposed PKE-RL method, 100 random unseen scenarios containing renewable energy fluctuation and system disturbance are generated to serve as the test set. The aforementioned expert policy is adopted as the baseline method, where a simulation-based action enumeration strategy and a predefined empirical action selection strategy are combined to provide a thorough corrective control strategy. The trained PKE-RL model is deployed in a simulation-assisted manner: the top-3 actions with the largest Q-values are verified by the simulation software, and the action with the best estimated overload alleviating effect is chosen to execute. The related metrics of the two methods deployed on the test set are illustrated in Table 2.

According to Table 2, we can observe that the expert policy prevails over the proposed PKE-RL method in the operation-related metrics. As the expert policy is the combination of an empirical strategy and a simulation-based strategy, the projection from the power state to the control action can be complex for the proposed method to handle in a relatively short time. Besides, with only 12 trajectories sampled from the expert policy, the proposed method can achieve around 70% of the performance of the complicated demonstration policy, with only 18.5% of the time consumption to make corrective control decisions. More representative demonstration data may help the proposed method perform better. Specifically, the expert policy often demands over 200 DC power flow based-simulations to generate the decision, which will be more time-consuming when adopting accurate AC power flow or more actions are taken into consideration. The results indicate that the proposed method has the potential to effectively perform real-time active power corrective control in highly dynamic power systems with strong complexity.

Two evaluation scenarios are selected to investigate the corrective control process of two methods in detail, namely Scenario I and Scenario II. The "N-1" contingencies, the max line load ratio in the grid, and the agents' control actions in Scenario I are illustrated in Figure 5.

In Scenario I, both two methods maintain the daylong operation with 2 "N-1" events strike. One overload and three overloads occur during the control of the expert policy and the PKE-RL method, respectively. Particularly, it can be seen from Figure 5 that an overload occurs after the second "N-1" event strike at time step 66, both two methods perform the corresponding corrective control action immediately, and the overload is eliminated in both scenarios. Notably, the expert policy yields the decision based on 209 simulations, while the PKE-RL method only needs a nearly computation-free deep network inference and three simulations. The above results indicate that the PKE-RL method can learn an efficient corrective control strategy with fair performance in maintaining the power girds stable operation.

The system operation status in Scenario II is illustrated in Figure 6.

TABLE 2 performance comparison between the pke-rl method and expert policy.

Method	Average operating steps	Completed episodes	Overloads elimination rate (%)	Average control action time(s)
PKE-RL method	209.11	53	60.14	**0.079**
Expert policy	**242.48**	**73**	**86.90**	0.426

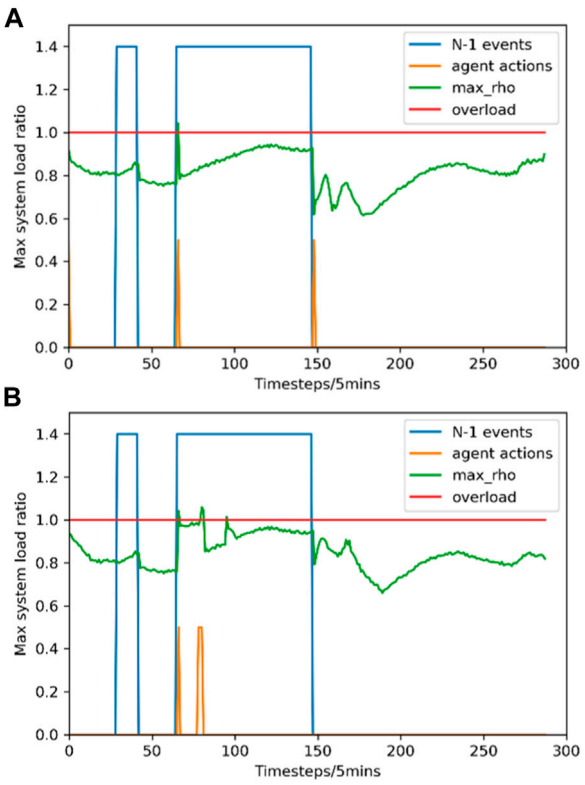

FIGURE 5
System operation status comparison between two methods in Scenario I. **(A)** Expert policy; **(B)** PKE-RL method.

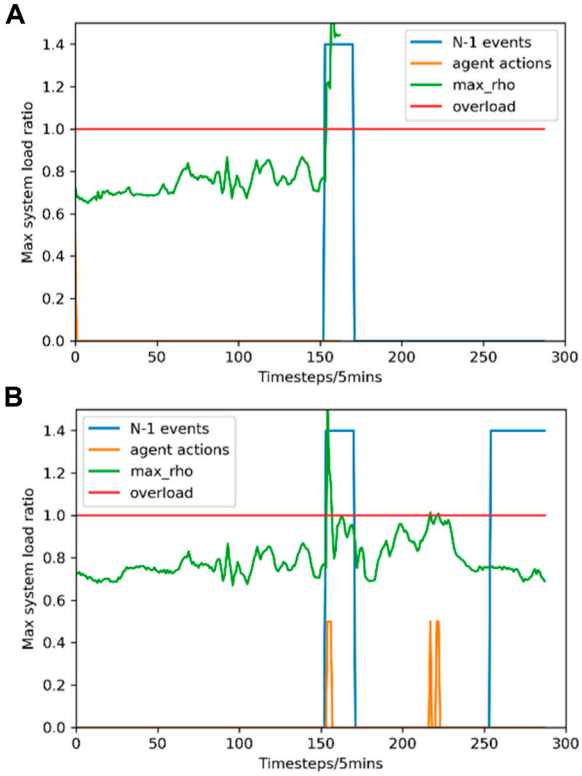

FIGURE 6
System operation status comparison between two methods in Scenario II. **(A)** Expert policy; **(B)** PKE-RL method.

In Figure 6, it is clear that the proposed method realizes a successful daylong control with 2 "N-1" events attacks, while the expert policy fails to survive the first "N-1" event. It can be seen from Figure 6 that a severe overload occurs after the first "N-1" event strikes at time step 154, the expert policy cannot produce an effective strategy based on the initial preventive action, while the PKE-RL method performs the corresponding corrective control actions, alleviating the load ratio effectively to prevent the system collapse. Although two normal overloads occur in the following time steps due to power fluctuation, both overloads are eliminated swiftly under the proposed method. The conclusion may be drawn that the PKE-RL method has the capability of converging into a corrective control strategy exceeding the expert policy by combining the imitation ability and the self-learning ability.

4.3 Efficacy of the proposed double-prioritized DQfD (λ) training mechanism

As merging the demonstration data into deep Q-learning plays a critical role in prior knowledge enhancement, the DQN-based model, the standard DQfD-based model, and the double-prioritized DQfD(λ)-based model are evaluated to demonstrate the proposed method. The three models share the same parameters apart from training hyperparameters, i.e., the

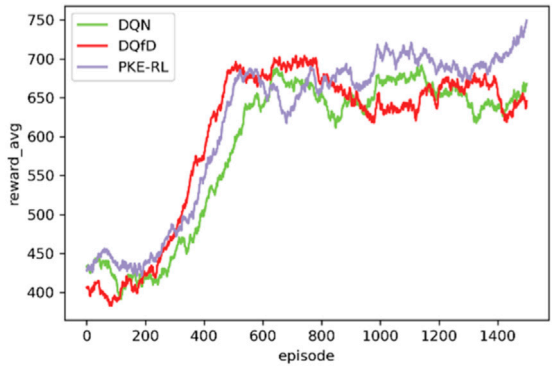

FIGURE 7
The training performance of the DRL agents.

weights between different losses. The DQfD(λ)-based model originates from Section 4.2, the standard DQfD-based model is pre-trained with the same demonstration data for 500 steps and is also trained for 1,500 episodes with the DQN-based model. The averaged cumulative rewards curves of the above three models are shown in Figure 7.

As illustrated in Figure 7, the performance of demonstration data enhanced models prevails over the DQN-based model at the initial learning phase at both speed and range. Besides, the demonstration data enhanced models show better operation promoting ability most time during the training. The results indicate that the introduction of expert knowledge can accelerate the learning process and improve the capability of the DRL agent in complex corrective control problems. Furthermore, the performance of the standard DQfD-based model suffers fluctuations after the middle of training, while the DQfD(λ)-based model keeps improving persistently. The conclusion can be drawn that the proposed double-prioritized DQfD(λ) training mechanism can better guide the agent to learn from the demonstration and interaction.

To further evaluate the effectiveness of the proposed training mechanism, The 100 random unseen scenarios mentioned in Section 4.2 are also utilized to demonstrate the feasibility of the proposed training mechanism. All the models are deployed in the same simulation-assisted manner as in Section 4.2. The models of the early training process, i.e., after 250 episodes of training, are also evaluated with the well-trained models. The related metrics of the three methods deployed on the test set are summarized in Table 3.

According to Table 3, one can observe that the DQfD class models exhibit fair performance after the short-term training, indicating the merging of expert data can assist the DRL agent in efficiently gaining adequate corrective control knowledge without too much exploration within complex power systems. Meanwhile, the DQfD class models can still make progress and prevail over the DQN-based model at the end of the training, showing the ability of the DQfD class method to guide the agent to optimize its policy persistently. Specifically, the DQfD(λ)-based model performs satisfying from the start to the end, the related agent can alleviate the overloads with fewer control actions and maintain the long-term operation of the grids. Thus, we can infer that the proposed double-prioritized DQfD(λ) training mechanism can improve the DRL agent's training efficiency and effectiveness in active power corrective control.

Similar to Section 4.2, two scenarios are selected to inspect the effectiveness of three well-trained DRL models in detail. Firstly, scenario II is selected again to evaluate the performance of the DQN-based model and the DQfD-based model in handling the severe post-contingency overload, the results are illustrated in Figure 8.

According to Figure 8, although the two models manage to alleviate the load ratio to some extent, specifically the DQfD-based model conducts more powerful corrective actions and realizes a larger reduction in the load ratio, they all fail to survive the first "N-1" event. The results demonstrate the feasibility of the proposed training mechanism.

A new scenario, namely scenario III, is chosen to evaluate the performance of the three models in handling the simpler situation. The system operation status in Scenario III is illustrated in Figure 9.

In Scenario III, all three models maintain the daylong operation with 1 "N-1" event strikes. However, there are six overloads, six overloads, and three overloads that occur during the control of the DQN-based model, the DQfD-based model, and the DQfD(λ)-based model, respectively. Besides, we can easily find that multiple severe overloads happen between time step 100 to time step 200 under the two basic DRL models' control, while the overload situation is

TABLE 3 performance comparison between the DRL models.

Model	Average operating steps	Completed episodes	Overloads elimination rate (%)	Average overload time steps	Average control actions
DQN early	185.06	39	46.10	4.06	4.43
DQfD early	**200.33**	**47**	52.59	3.98	4.37
DQfD(λ) early	200.14	**47**	**54.86**	**3.96**	**4.29**
DQN final	205.39	50	58.09	4.5	4.96
DQfD final	**209.48**	50	55.7	3.89	4.2
DQfD(λ) final	209.11	**53**	**60.14**	**3.5**	**3.91**

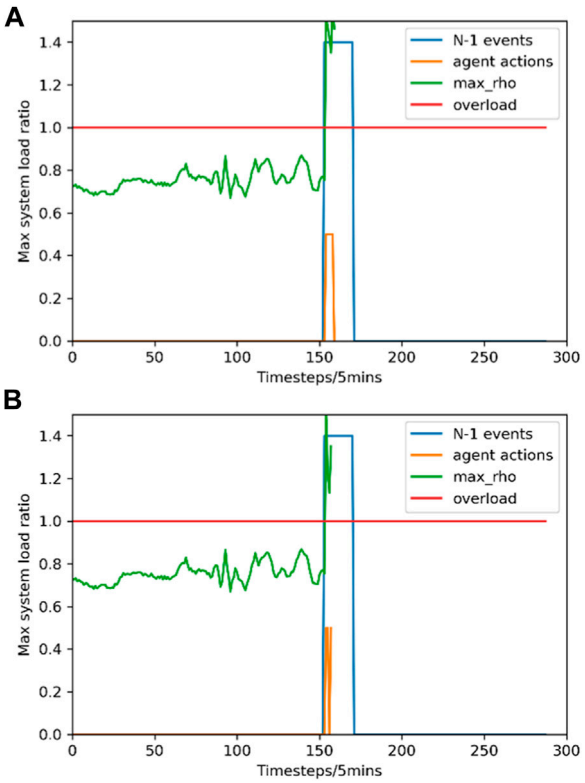

FIGURE 8
System operation status comparison between two basic DRL models in Scenario II. **(A)** DQN-based model; **(B)** DQfD-based model.

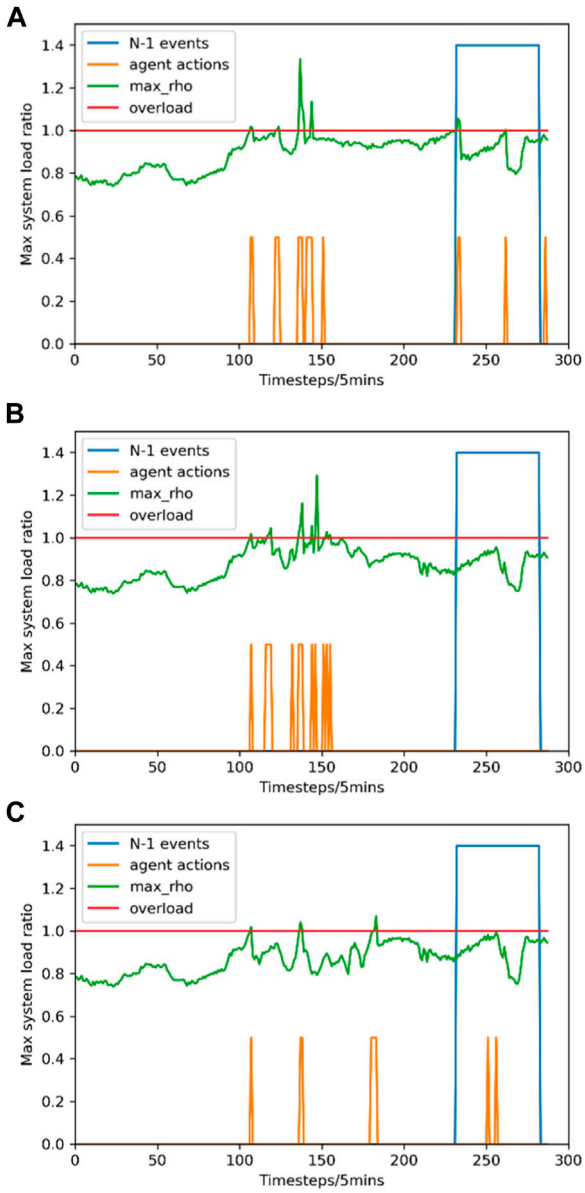

FIGURE 9
System operation status comparison between three DRL models in Scenario III. **(A)** DQN-based model; **(B)** DQfD-based model; **(C)** DQfD(λ)-based model.

much better under the control of the enhanced DRL model. Meanwhile, to alleviate the overloads, 17 and 14 corrective control actions are conducted by the DQN-based model and the DQfD-based model, respectively. The DQfD(λ)-based model only conducts five actions to deal with overloads. The results further demonstrate the effectiveness of the proposed double-prioritized DQfD(λ) training mechanism, where the trained model can promote the long-term stable operation of power grids by learning a simple but powerful corrective control strategy.

4.4 Performance comparison of different expected demonstration ratios

The expected demonstration ratio controls the agent's imitation preference to the expert policy by altering the number of demonstration data in the cache. Thus, to evaluate the impact of this hyperparameter, three models with the expected demonstration ratios set to 0.1, 0.2, and 0.3 are trained by the proposed PKE-RL method with other parameters same as those in IV.2. The averaged cumulative rewards curves of the above three models are shown in Figure 10.

As illustrated in Figure 10, in this problem, the agent with the highest expected demonstration ratio (simplified as "demo-ratio") improves itself faster than other agents but maintains a stable but relatively poor performance for the rest of the training process, indicating that strong expert policy intervention can

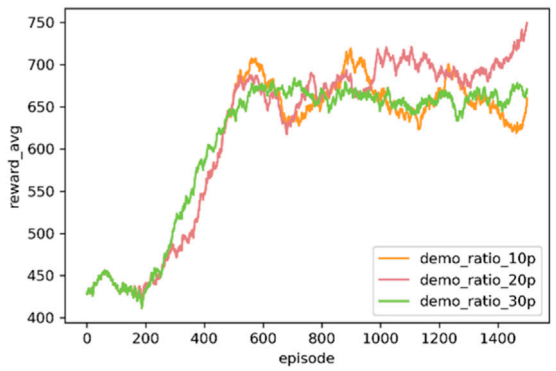

FIGURE 10
The training performance of the PKE-RL agents under different expected demonstration ratios.

limit the further improvement of the agent. In contrast, the agent with the lowest demo-ratio learns a better policy first but suffers from frequent large fluctuations like the DQN agent in Figure 7, showing the unstableness brought by the weighted self-exploration process. Finally, the agent with the middle demo-ratio performs best during the entire training process. Based on the above results, the assumption can be made that a best demo-ratio point may exist to balance the imitation process and the self-exploration process.

5 Conclusion

In this paper, a prior knowledge-embedded reinforcement learning method is proposed to provide a solution to solve the complex active power corrective control problem with effectiveness and efficiency. Specifically, the differential integration method of the real-time power grid state based on graph convolution and graph pooling, as well as the double-prioritized DQfD(λ) training mechanism, are proposed to enhance the perception and the training efficiency of the DRL agent in complex power grids. Results show that the proposed method can learn from the complicated expert policy with fair performance without excessive demonstration data and deployed in a real-time manner. Besides, embedding the prior knowledge can promote a good initial control ability of the agent and alleviate the overall overloads with fewer actions than conventional DRL methods.

As we mainly verify the basic feasibility of the proposed method, the effectiveness of our method should be further improved. In our future works, the accurate selection of representative demonstration data, the delicate fusion of various expert policies, and the efficient utilization of the imperfect demonstration data are going to be studied to make our method applicable for the real-world active power corrective control problem.

Data availability statement

Publicly available datasets were analyzed in this study. This data can be found here: https://competitions.codalab.org/competitions/33121#learn_the_details-instructions.

Author contributions

PX implemented numerical simulation and wrote the manuscript. JZ proposed the idea and revised the manuscript. JL revised the manuscript. HZ helped conduct experiments. TG and SC assisted in data collection.

Funding

The work is supported by the National Key R&D Program of China under Grant 2018AAA0101504 and the Science and technology project of SGCC (State Grid Corporation of China): fundamental theory of human in-the-loop hybrid augmented intelligence for power grid dispatch and control. The funder was not involved in the study design, collection, analysis, interpretation of data, the writing of this article, or the decision to submit it for publication.

Conflict of interest

Author JL was employed by NARI Group Corporation.

The remaining authors declare that the research was conducted in the absence of any commercial or financial relationships that could be construed as a potential conflict of interest.

Publisher's note

References

Cangea, C., Veličković, P., Jovanović, N., Kipf, T., and Liò, P. (2018). Towards sparse hierarchical graph classifiers. arXiv preprint Available at: https://arXiv/org/abs/1811.01287 (Accessed February 22, 2022).

Cao, J., Du, W., and Wang, H. F. (2015). An improved corrective security constrained OPF for meshed AC/DC grids with multi-terminal VSC-HVDC. *IEEE Trans. Power Syst.* 31 (1), 485–495. doi:10.1109/tpwrs.2015.2396523

Chen, S., Duan, J., Bai, Y., Zhang, J., Shi, D., and Sun, Y. (2021). Active power correction strategies based on deep reinforcement learning—part II: A distributed solution for adaptability. *CSEE J. Power Energy Syst.*8, 2096–0042.doi:10.17775/CSEEJPES.2020.07070

Daley, B., and Amato, C. (2019). Reconciling λ-returns with experience replay. *Adv. Neural Inf. Process. Syst.* 32.

Ding, L., Hu, P., Liu, Z. W., and Wen, G. (2020). Transmission lines overload alleviation: Distributed online optimization approach. *IEEE Trans. Ind. Inf.* 17 (5), 3197–3208. doi:10.1109/tii.2020.3009749

Gao, Y., Xu, H., Lin, J., Yu, F., Levine, S., and Darrell, T. (2018). Reinforcement learning from imperfect demonstrations. arXiv preprint Available at: http://arXiv/org/abs/1802.05313 (Accessed March 5, 2022).

Hester, T., Vecerik, M., Pietquin, O., Lanctot, M., Schaul, T., Piot, B., et al. (2018). Deep Q-learning from demonstrations." in Proceedings of the AAAI Conference on Artificial Intelligence, New Orleans, LA, USA, February 2–7, 2018. Columbia Canada: PKP Publishing Services Network. 32, doi:10.1609/aaai.v32i1.11757

Karbalaei, F., Shahbazi, H., and Mahdavi, M. (2018). A new method for solving preventive security-constrained optimal power flow based on linear network compression. *Int. J. Electr. Power & Energy Syst.* 96, 23–29. doi:10.1016/j.ijepes.2017.09.023

L2RPN (2020). HoracioMartinez. Available at: https://github.com/horacioMartinez/L2RPN (Accessed April 8, 2022).

Lee, J., Lee, I., and Kang, J. (2019). "Self-attention graph pooling," in Proceeding International conference on machine learning, Vancouver, Canada, December 8–14, 2019. (PMLR), 3734–3743.

Lenoir, L., Kamwa, I., and Dessaint, L. A. (2009). Overload alleviation with preventive-corrective static security using fuzzy logic. *IEEE Trans. Power Syst.* 24 (1), 134–145. doi:10.1109/tpwrs.2008.2008678

Li, X., Wang, X., Zheng, X., Dai, Y., Yu, Z., Zhang, J. J., et al. (2022). Supervised assisted deep reinforcement learning for emergency voltage control of power systems. *Neurocomputing* 475, 69–79. doi:10.1016/j.neucom.2021.12.043

Li, X., Wang, X., Zheng, X., Jin, J., Huang, Y., Zhang, J. J., et al. (2022). Sadrl: Merging human experience with machine intelligence via supervised assisted deep reinforcement learning. *Neurocomputing* 467, 300–309. doi:10.1016/j.neucom.2021.09.064

Martin, J. A., and Hiskens, I. A. (2016). Corrective model-predictive control in large electric power systems. *IEEE Trans. Power Syst.* 32 (2), 1651–1662. doi:10.1109/tpwrs.2016.2598548

Nacional de Colombia, Universidad. (2020). L2RPN-NEURIPS-2020. Available at: https://github.com/unaioperator/l2rpn-neurips-2020 (Accessed April 15, 2022).

Piot, B., Geist, M., and Pietquin, O. (2014). "Boosted bellman residual minimization handling expert demonstrations," in Proceeding Joint European Conference on machine learning and knowledge discovery in databases (Berlin, Heidelberg: Springer Nancy, France), September 15–19, 2014 8725 549.

Rte-France. (2021). Grid2Op. Available at: https://github.com/rte-france/Grid2Op (Accessed March 23, 2022).

Talukdar, B. K., Sinha, A. K., Mukhopadhyay, S., and Bose, A. (2005). A computationally simple method for cost-efficient generation rescheduling and load shedding for congestion management. *Int. J. Electr. Power & Energy Syst.* 27 (5-6), 379–388. doi:10.1016/j.ijepes.2005.02.003

Vaswani, A., Shazeer, N., Parmar, N., Uszkoreit, J., Jones, L., and Polosukhin, I. (2017). Attention is all you need. *Adv. neural Inf. Process. Syst.* 30.

Veličković, P., Cucurull, G., Casanova, A., Romero, A., Lio, P., and Bengio, Y. (2017). Graph attention networks. arXiv preprint Available at: http://arXiv/org/abs.1710.10903 (Accessed March 17, 2022).

Waseem, M., and Manshadi, S. D. (2021). Decomposing convexified security-constrained AC optimal power flow problem with automatic generation control reformulation. *Int. Trans. Electr. Energy Syst.* 31 (9), e13027. doi:10.1002/2050-7038.13027

Xu, P., Duan, J., Zhang, J., Pei, Y., Shi, D., and Sun, Y. (2021). Active power correction strategies based on deep reinforcement learning-part I: A simulation-driven solution for robustness. *CSEE J. Power Energy Syst.*8.1122–1133. 10.17775/CSEEJPES.2020.07090.

Xu, P., Pei, Y., Zheng, X., and Zhang, J. (2020). "A simulation-constraint graph reinforcement learning method for line flow control," in Proceeding 2020 IEEE 4th Conference on Energy Internet and Energy System Integration (EI2), Wuhan, China, October 30–Novermber 1, 2020, (Wuhan China: IEEE), 319–324. doi:10.1109/EI250167.2020.9347305

Xu, P., Zhang, J., Gao, T., Chen, S., Wang, X., Jiang, H., et al. (2022). Real-time fast charging station recommendation for electric vehicles in coupled power-transportation networks: A graph reinforcement learning method. *Int. J. Electr. Power. Energy Syst.* 141, 108030. doi:10.1016/j.ijepes.2022.108030

Xu, Y., Dong, Z. Y., Zhang, R., Wong, K. P., and Lai, M. (2013). Solving preventive-corrective SCOPF by a hybrid computational strategy. *IEEE Trans. Power Syst.* 29 (3), 1345–1355. doi:10.1109/tpwrs.2013.2293150

Yan, M., Shahidehpour, M., Paaso, A., Zhang, L., Alabdulwahab, A., and Abusorrah, A. (2020). A convex three-stage SCOPF approach to power system flexibility with unified power flow controllers. *IEEE Trans. Power Syst.* 36 (3), 1947–1960. doi:10.1109/tpwrs.2020.3036653

Yan, W., Cheng, L., Yan, S., Gao, W., and Gao, D. W. (2019). Enabling and evaluation of inertial control for PMSG-WTG using synchronverter with multiple virtual rotating masses in microgrid. *IEEE Trans. Sustain. Energy* 11 (2), 1078–1088. doi:10.1109/tste.2019.2918744

Yan, W., Shah, S., Gevorgian, V., and Gao, D. W. (2021). "Sequence impedance modeling of grid-forming inverters," in Proceeding2021 IEEE Power & Energy Society General Meeting (PESGM), Washington DC USA: IEEE, 1–5. doi:10.1109/PESGM46819.2021.9638001

Yan, W., Wang, X., Gao, W., and Gevorgian, V. (2020). Electro-mechanical modeling of wind turbine and energy storage systems with enhanced inertial response. *J. Mod. Power Syst. Clean Energy* 8 (5), 820–830. doi:10.35833/mpce.2020.000272

Watkins, C. J. C. H. (1989). *Learning from delayed rewards*. Surrey United Kingdom: Royal Holloway University of London

Nomenclature

$\Delta\mathbf{P_G}$, $\Delta\mathbf{P_L}$ Amount of generator redispatch and load shedding

$\Delta\mathbf{N}$ Adjustment of the topology

$P_{ij}, \bar{P}_{ij}$ Current power and capacity of the transmission line l_{ij}.

X_{line}, X_{bus}, $N_{\mathbf{limit}}$ Number of line switching actions, bus-bar switching actions, and the limited topological actions, respectively

$\mathbf{P}_{\mathbf{G}\max}$, $\mathbf{P}_{\mathbf{G}\min}$ Upper and lower bounds of the generator outputs

$\mathbf{R_{up}}$, $\mathbf{R_{down}}$ Bidirectional ramping rates of the generators

$\boldsymbol{T}$ Control duration

$f_{net}(t)$ Network loss cost

$E_{loss}(t)$ Energy loss at time t when a blackout strikes

$p(t)$ Marginal price of the generators' outputs

$\mathbf{P}$ Active power status of the power equipment

$\boldsymbol{\rho}$ Load ratio of each transmission line

N_L Number of lines

α , β Penalty factors of overload and heavy load

P_{OR} , P_{EX} Active power flow at the origin and the extremity of the transmission line, respectively.

P_L Active consumption value of the load

P_G Active power output of the generator

$\boldsymbol{K}$ Number of independent attention mechanisms

$\mathcal{N}_i$ Neighboring node set of the ith node

α_{ij}^k Normalized attention coefficients computed by the kth attention mechanism

$\mathbf{W}^k$ kth weight matrix

$\mathbf{g}_i$ Features of the ith important node

N_C Number of the important nodes

$L_{DQ}(\theta), L_n(\theta), L_E(\theta), L_{L2}(\theta)$ 1-step deep Q-learning loss, n-step deep Q-learning loss, expert loss, and L2 regularization loss

R^n n-step return

ε_d Expected demonstration ratio in the batch training.

frontiers | Frontiers in Energy Research

TYPE Original Research
PUBLISHED 24 January 2023
DOI 10.3389/fenrg.2022.1033066

OPEN ACCESS

EDITED BY
Chaolong Zhang,
Jinling Institute of Technology, China

REVIEWED BY
Sennai Mesfun,
Research Institutes of Sweden (RISE), Sweden
Johan Tallgren,
VTT Technical Research Centre of Finland Ltd., Finland
Gurpreet Kaur,
Commonwealth Scientific and Industrial Research Organisation (CSIRO), Australia
Paul Okonkwo,
Dhofar University, Oman

*CORRESPONDENCE
Jun Zhou,
zhoujun@mail.xjtu.edu.cn

SPECIALTY SECTION
This article was submitted to Smart Grids, a section of the journal Frontiers in Energy Research

RECEIVED 31 August 2022
ACCEPTED 05 December 2022
PUBLISHED 24 January 2023

CITATION
Mao H, Nie D, Chen X, Cai Y, Zhao J, Zhang X, Yu H, Ma W, Lv Z and Zhou J (2023), Innovative technology for large-scale photovoltaic consumption using reversible solid oxide cells.
Front. Energy Res. 10:1033066.
doi: 10.3389/fenrg.2022.1033066

Innovative technology for large-scale photovoltaic consumption using reversible solid oxide cells

Hongtao Mao[1], Dong Nie[1], Xi Chen[1], Yanan Cai[1], Jie Zhao[1], Xuzheng Zhang[2], Haoyu Yu[2], Wanli Ma[2], Zepeng Lv[2] and Jun Zhou[2]*

[1]Baoding Power Supply Company, State Grid Corporation of China, China, [2]State Key Laboratory of Electrical Insulation and Power Equipment, Xi'an Jiaotong University, Xi'an, China

It is inevitable that renewable energy consumption will increase as installed capacity continues to increase, primarily wind and photovoltaic power generation. Power to Gas (P2G) technology can store electrical energy in the form of chemical energy on a large scale. Reversible solid oxide cell (RSOC) has a very high conversion efficiency in both electrolytic gas production and fuel cell power generation compared with traditional electricity-to-gas devices. For the future integrated energy system, Reversible solid oxide cells are expected to play a significant role in integrating power generation and energy storage. This work proposes a new integrated energy system based on Reversible solid oxide cell for photovoltaic (PV) consumption. The Integrated Electricity-Gas System (IEGS) considers the two modes of electrolysis and power generation of Reversible solid oxide cell in the model. The model takes the minimum running cost as the objective function to linearize part of the model to generate a mixed integer linearization problem and solve it in GAMS. The case study shows that wind power is maximized, and the gas mixture can be transported in natural gas pipelines, improving the economics and stability of Integrated Electricity-Gas System. This work not only can reduce the operating cost of the system but also increase the high penetration of photovoltaic power generation. A quantitative assessment of the impact of hydrogen injection ratio and renewable energy penetration was also carried out.

KEYWORDS

electric-to-gas, reversible solid oxide cells, photovoltaic consumption, renewable energy, hydrogen

1 Introduction

The rapid and disorderly development of renewable energy has raised some related issues (Zhang et al., 2022; Zhao S, et al., 2022). First of all, renewable energy power generation is mainly wind power generation and photovoltaic power generation, which naturally have the characteristics of intermittent fluctuation. The integration of renewable energy into the grid is a huge challenge for the power network that requires stability and security (Denholm and Hand, 2011; Brouwer et al., 2014; Ahmed and Khalid, 2019). Secondly, most of the areas rich in renewable energy are located at the terminal stations of the power grid. Although the installed capacity is large, it cannot be fully absorbed on site. Due to the rapid and unbalanced development of renewable energy and regional environmental impacts, the surrounding facilities of some large-scale new energy power plants that have been built are not perfect, which may easily lead to waste of renewable resources. A promising solution to these problems is to convert it into other energy for consumption (Fang et al., 2018; Wang et al., 2019; Martínez Ceseña et al., 2020). Power to gas (P2G) technology produces hydrogen by hydrolysis of water using renewable energy power, which can supply power during peak power demand of the grid, and store surplus energy when renewable energy power generation is more than power demand. Paul C. Okonkwo has studied Proton exchange membrane fuel cells (PEMFCs), which converted power to gas through hydrolysis of water (Okonkwo et al., 2021a; Okonkwo et al., 2021b; Okonkwo and Otor, 2021; Okonkwo et al., 2022). Reversible Solid Oxide Cells (RSOC) can achieve an energy conversion efficiency of more than 85% for electrolysis mode, which is far above other methods in forms of energy storage, and have the advantages of bidirectional conversion, low preparation cost, and easy realization of cogeneration (Zhang et al., 2010; Laguna-Bercero, 2012). RSOC stands out among many P2G processes (Mogensen et al., 2019a). The RSOC can consist of the integrated operation of both positive and negative modes of co-electrolysis and co-generation (Luo et al., 2017). In addition to producing hydrogen, RSOC can also convert hydrogen into part of synthetic natural gas (SNG) through co-electrolysis. The produced hydrogen is mixed with natural gas and injected into the natural gas pipeline to form Hydrogen-Enriched Compressed Natural Gas (HCNG). Current experimental and simulation studies have demonstrated that it is feasible to inject hydrogen in the range of 10%–20% without changing the natural gas pipeline and natural gas equipment used by users (Abeysekera et al., 2016; Lapo et al., 2021; Zhao et al., 2021). Such a high proportion of hydrogen injection enables the natural gas network to store large amounts of renewable energy. Through P2G technology, the natural gas network and the power network are coupled, which greatly improves the flexibility of the power system and promotes the ability of the entire system to absorb renewable energy, such as photovoltaic power generation.

The operation mode of the electric P2G part of the integrated energy includes the injection and utilization of hydrogen (Schiebahn et al., 2015; Manuel et al., 2016). Aiming at the difficult problem of transmission of a large number of wind power equipment installed in different regions to the demand center, the literature (Qadrdan et al., 2015) studied an operation optimization model of the combined natural gas and power network in the United Kingdom. Reference (Stephen and Pierluigi, 2015a) considers the amount of hydrogen that can be mixed with natural gas under different natural gas network conditions and develops a two-stage optimization method for integrated power and natural gas networks. The impact of P2G technology on natural gas prices and seasonal gas storage utilization was assessed. Reference (Gao et al., 2018) linearized the non-linear electric-gas hybrid integrated energy system model to construct an integrated energy system model with linear power flow distribution characteristics. Under the condition of satisfying the demand for electric load and heat load, the economical and reliable indicators of the system are analyzed, and the economic benefits of P2G technology absorbing wind power are evaluated.

RSOC has become more and more popular due to its high energy conversion efficiency in both hydrogen production and cogeneration (Singhal, 2012; Barelli et al., 2017). RSOC stacks can not only be used as distributed power generation devices but also can be grouped and integrated into large-scale stationary power generation/P2G power plants. In the integrated energy system, it is possible to switch freely between working modes, making the use and storage of hydrogen more flexible. In recent research work, solid oxide cells (SOFCs) have been thermodynamically modeled. Several studies have provided insight into the dynamic performance of the co-electrolysis/generation process (Becker et al., 2012; Foit et al., 2017; Yu et al., 2017). In addition, the electrochemical performance and durability of RSOC were studied, and the internal electrolytic reduction process was analyzed in detail (Azra et al., 2005; Mogensen et al., 2019b). RSOC-based energy systems have also been extensively studied. Previous work modeled fuel cells in microgrid-scale analysis but did not consider the co-electrolysis process. In the modeling of energy systems with power-to-gas relationships, the research mainly focuses on the planning and operation of networks. Fuel cells are generally used as devices with fixed energy conversion efficiency, and P2G technology is generally directly modeled as input/output components (Stephen and Pierluigi, 2015b; Haifei and Yibo, 2018; Luo et al., 2018).

In this work, a new type of RSOC electricity-gas integrated energy system hub station is constructed, which is able to inject hydrogen produced by electrolysis into the existing natural gas network for storage of renewable energy and utilization of mixed gas. The modes of co-electrolysis and power generation are considered in the RSOC modeling. The time start-up cost of RSOC is also considered. Combining the DC power flow model with the gas power flow model realizes the network optimization

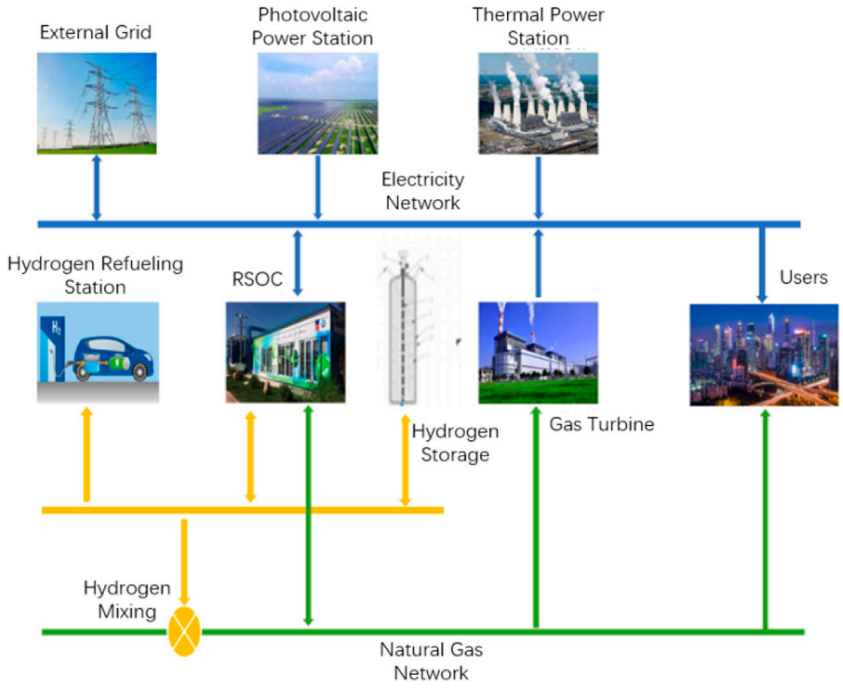

FIGURE 1
The IEGS including RSOC and H_2 injection.

of the electrical integrated energy system. A mixed integer linear programming problem can be obtained by linearizing the Weymouth gas flow function incrementally. In terms of case studies, the above model is tested using an improved RTS-24 busbar grid combined with a 20-node natural gas network. The benefits and impacts of H_2 injection, storage and utilization and natural gas blending throughout the natural gas pipeline are quantitatively analyzed. The effects of different renewable energy levels and H_2 injection limitations on integrated energy systems with P2G were investigated. The research results show that RSOC combined with P2G and H_2/SNG injection can increase the consumption of new energy through the energy system, and improve economic and environmental benefits.

2 Conception

The RSOC of integrated electricity-gas energy system studied in this work aims to provide multiple energy carriers such as electricity, natural gas, and hydrogen and their mixtures on the basis of the transmission network, and has a considerable renewable penetration rate. The advantage of this system is that it reduces the capacity of the hydrogen storage facility and saves the transportation losses of compressed hydrogen. As shown in Figure 1, RSOC stacks are considered multi-stackable and can be grouped into large stationary power plants. RSOC system consists of SOEC part and methanation part, which are combined in one reactor with different temperature gradient zones (Zhou et al., 2020). When the photovoltaic power generation is insufficient, the RSOC will operate in fuel cell mode and provide power together with a conventional heat set and a gas turbine (GT). During sufficient PV availability, the RSOC will operate in electrolyser mode, generating H_2 with SNG that can be injected, stored and utilized, and passed through the storage unit and NG network. The injected H_2 can be mixed in the NG pipeline and sent to the downstream natural gas terminal. The mixed gas can be utilized by traditional gas-consuming units such as gas turbines and household stoves, as long as the mixed hydrogen does not exceed a safe mixing percentage. The mathematical model of the energy system includes a power network model and a gas pipeline network model that injects a certain proportion of hydrogen mixed with natural gas.

3 Mathematical formulation of IEGS

3.1 Objective function

The goal of IEGS is to minimize the overall operating cost while meeting the user's electricity and gas needs. Its objective function is shown in Eq. 1. The first item represents the power

10.3389/fenrg.2022.1033066

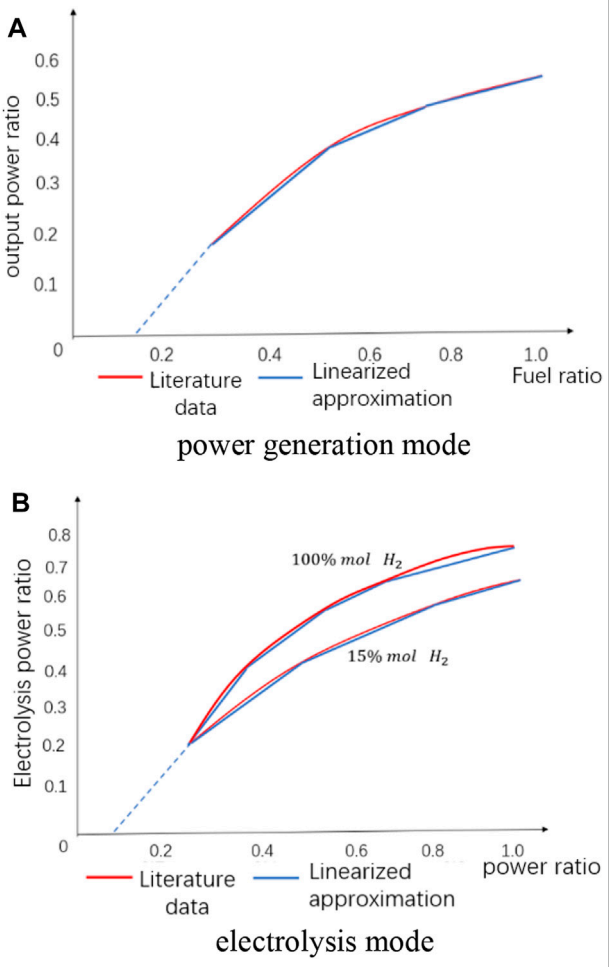

FIGURE 2
Linearization of the characteristic curve of RSOC during steady-state operation. **(A)** power generation mode, **(B)** electrolysis mode.

generation cost of the generator set; the second item is the natural gas cost provided by the natural gas source; the third item is the photovoltaic curtailment cost. The fourth item is the cost of power abandonment.

$$C = \sum_{g\in\Omega_{T,t}} b_g P_{g,t} + \sum_{n,t} c_n Sg_{n,t} + \sum_{i,t} VOLV \times P_{i,t}^{vc} + \sum_{i,t} VOLL \times LS_{i,t}, \quad (1)$$

where $P_{g,t}$ is the power generation of the generator set g at time t, $Sg_{n,t}$ is the gas production at the gas source n at time t, $LS_{i,t}$ is the load shedding amount at the bus i, and $P_{i,t}^{vc}$ is the power of the abandoned photovoltaic. The constants are: b_g the power generation price of the thermal unit g, C_n the natural gas price at the gas source point n, $VOLL$ the price required to reduce the load of the system, and $VOLV$ the price of the abandoned light.

3.2 Modeling of RSOC

The RSOC station model proposed in this work adopts the method of lumped functions and considers several properties of RSOC in the hour time frame. Part-load performance of power generation and co-electrolysis, operating schedule for RSOC, and time-varying start-up costs are calculated as mixed integer linear programming (MILP). Fitted curves for the part-load performance of power generation and co-electrolysis at steady-state RSOC are given in Figure 2. Since the C=O bond is not easily broken, the co-electrolysis efficiency decreases with the increase of the volume fraction of the prepared SNG. Figure 2B depicts the operating curves for 15% (mol) H_2 and 100% (mol) H_2. Part-load performance can be expressed as a non-linear function in Eqs 2, 3. It is assumed that the effect of the production fraction of SNG on the co-electrolysis efficiency is linear, that is, a coefficient χ is added in front of the electrolysed natural gas in Eq. 3. Equation 4 expresses the constraint of natural gas production. β is the maximum gas production fraction. Carbon dioxide converted or captured during RSOC operation can be inferred from the natural gas produced.

$$P_{r,t} = f\left(E_{r,t}^{in}\right), \quad (2)$$

$$E_{r,t}^{H_2} + \chi E_{r,t}^{SNG} = F\left(P_{r,t}^{P2G}\right), \quad (3)$$

$$\frac{E_{r,t}^{SNG}}{H_{NG}} \le \beta \cdot \left(\frac{E_{r,t}^{SNG}}{H_{NG}} + \frac{E_{r,t}^{H_2}}{H_{H_2}}\right), \quad (4)$$

$$E_{r,t}^{CO_2} = \eta^{CO_2} E_{r,t}^{SNG}. \quad (5)$$

In the above formula, the subscript r represents each RSOC. $E_{i,t}^{in}$ is the input energy of the gas; $E_{r,t}^{H_2}$ and $E_{r,t}^{SNG}$ is the electrolysis of hydrogen and natural gas. $P_{r,t}^{P2G}$ is the input power supply for the common electrolysis process. H_{NG} and H_{H_2} is calorific value of natural gas and hydrogen. The non-linear function $f(x)$ can be linearized piece by piece by incremental linearization techniques, as expressed by Eqs 6–8 (Li and Yu, 1999).

$$f(x) = f(x_1) + \sum_{s=1}^{N-1} \left[f(x_{s+1}) - f(x_s)\right] \cdot \xi_s, \quad (6)$$

$$x = x_1 + \sum_{s=1}^{N} (x_{s+1} - x_s) \cdot \xi_s, \quad (7)$$

$$\xi_{s+1} \le SC_s, \quad SC_s \le \xi_s, \quad 0 \le \xi_s \le 1. \quad (8)$$

ξ_S represents the position of the number s segment; $f(x_s)$ is the starting position of the number SC_S segment; is a binary variable.

RSOC is limited by physical conditions and cannot be started and stopped frequently. The device needs to consider the start and stop time constraints, as represented by Eqs 9, 10.

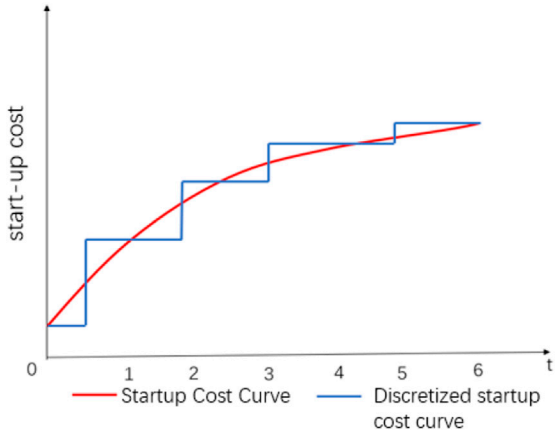

FIGURE 3
The relationship between startup cost and offline time.

$$Y(t,j)+\sum_{s} Z(t+s,j)\le 1, \tag{9}$$

$$Z(t,j)+\sum_{s} Y(t+s,j)\le 1, \tag{10}$$

where $Y(t, j)$ and $Z(t, j)$ represent the start and stop states of the number j fuel cell during t, respectively. They are both binary variables. 0 means the battery is off, 1 means the battery is on. The logical relationship between the switch states of the electrolysis and power generation modes of the fuel cell is shown in Eqs 11–14.

$$U_{r,t}^{gen}-U_{r,t-1}^{gen}=Y_{r,t}^{gen}-Z_{r,t}^{gen}, \tag{11}$$

$$U_{r,t}^{ele}-U_{r,t-1}^{ele}=Y_{r,t}^{ele}-Z_{r,t}^{ele}, \tag{12}$$

$$Y_{r,t}^{gen}+Z_{r,t}^{gen}\le 1, \tag{13}$$

$$Y_{r,t}^{ele}+Z_{r,t}^{ele}\le 1. \tag{14}$$

The response of the SOFC is relatively slow when it switches from one thermal equilibrium state to another, so it is necessary to consider its ramping power when the solid oxide fuel cell works. The relationship between the minimum operating power and the rise/fall power is determined by Eqs 15, 16.

$$P_r^{rd,gen}\le P_{r,t}^{gen}-P_{r,t-1\le}^{gen}P_r^{ru,gen}, \tag{15}$$

$$P_r^{rd,ele}\le P_{r,t}^{P2G}-P_{r,t-1}^{P2G}\le P_r^{ru,ele}. \tag{16}$$

$P_{r,t}^{gen}$ represents the generated power of the RSOC at time t; $P_{r,t}^{P2G}$ represents the electrolysis power of the RSOC at time t; $P_r^{ru,gen}$, $P_r^{rd,gen}$ represent the uphill and downhill power in the fuel cell power generation mode; and $P_r^{ru,ele}$, $P_r^{rd,ele}$ represent the uphill and downhill power in the electrolysis mode.

As the operating hub of the entire integrated energy system, the RSOC's start-up and shutdown costs cannot be ignored. As a thermal unit, the start-up cost of an RSOC is considerable. A 1 kWh SOC stack requires approximately 1.3 kWh of energy to cold start (Peksen, 2018). In an energy system, the RSOC can be taken offline for a short period of time and then connected to the grid before it is fully cooled, so that the start-up cost of the RSOC is much lower than when it is fully cooled. The start-up cost of the RSOC is measured by the input gas energy and depends on how long the RSOC is offline before start-up. A typical time-dependent start-up cost function can be found in (Carrion and Arroyo, 2006). The start-up cost is discretized, as shown in Figure 3 and Eqs 17, 18.

$$E_{r,t-1}^{sl}\ge K_r^l\left(U_{r,t}^{ele}+U_{r,t}^{gen}\right)-\sum_{n=1}^{l}\left(K_r^l-K_r^{n-1}\right)\cdot\left(U_{r,t-n}^{ele}+U_{r,t-n}^{gen}\right), \tag{17}$$

$$K_r^l=V_r^{sl}\left(1-e^{-(1/\tau)}\right)+F_r^{sl}, \tag{18}$$

Among them, l is the length of the RSOC offline, K_r^l is the start-up cost of fuel cell after the offline time length, V_r^{sl} is the maximum start-up cost variable, F_r^{sl} is the fixed start-up cost, and τ is the cooling time constant. So the start-up cost when the RSOC is fully cooled is $V_r^{sl}+F_r^{sl}$.

3.3 Electricity network

The integrated energy system adopts the transmission network and adopts the DC power flow transmission model. Equations 19–23 represent the constraints of the transmission network.

$$\sum_{g\in\Omega_G^i}\left(P_{g,t}-P_{g,t}^{P2G}\right)+LS_{i,t}+P_{i,t}^{v}-L_{i,t}=\sum_{j\in\Omega_l^i}P_{ij,t}, \tag{19}$$

$$P_{ij,t}=\frac{\delta_{i,t}-\delta_{j,t}}{x_{ij}}, \tag{20}$$

$$-P_{ij}^{\max}\le P_{ij,t}\le P_{ij}^{\max}, \tag{21}$$

$$P_t^{pv}=p_i^{v}+p_t^{vc}, \tag{22}$$

$$0\le LS_{i,t}\le L_{i,t}. \tag{23}$$

In the formula, $L_{i,t}$ is the power load, $\delta_{i,t}$ is the included angle of the busbar i, x_{ij} is the reactance of the transmission line between the busbar i and j, P_t^{pv} is the predicted photovoltaic power generation, P_i^{v} is the photovoltaic power generation included in the power grid, and P_t^{vc} is the amount of abandoned light.

3.4 Gas network

Gas network constraints include pressure boundary constraints and gas flow equilibrium constraints. For a pipeline node, the gas coming in from the node mainly comes from the terminal gas supply, storage facilities, gas supply from pipelines (transmitted from other nodes), and hydrogen produced by P2G, and the gas going out mainly goes to

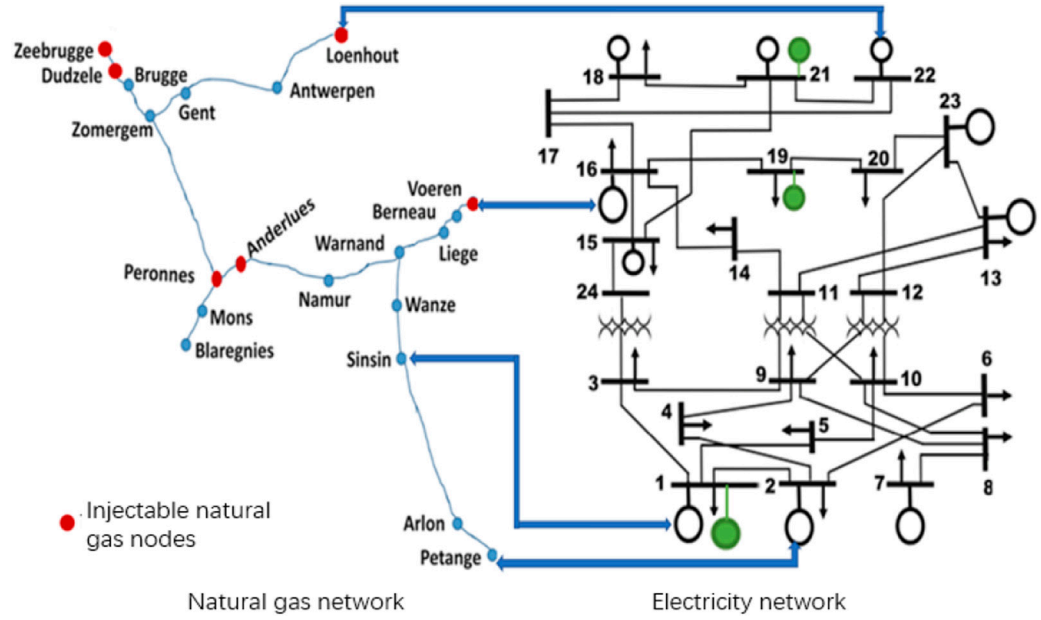

FIGURE 4
The IEGS network test system.

another pipeline or is consumed by utilization. For network optimization, the volume of injected H_2 is converted to the volume of natural gas. Equations 24–26 further constrain the gas source output and gas flow.

$$\sum_m Q_{n,m,t} + GL_{n,t} + \sum_{g\in\Omega_G^n} \frac{E_{g,t}^{in} + E_{r,t}^{sl} + E_{r,t}^{CO_2}}{H_{NG}} = \sum_m Q_{m,n,t} + \sum_{r\in\Omega_R^n} \frac{E_{r,t}^{H_2} + E_{r,t}^{SNG}}{H_{NG}} + Sg_{n,t}, \tag{24}$$

$$Sg_n^{\min} \le Sg_{n,t} \le Sg_n^{\max}, \tag{25}$$

$$Q_{n,m}^{\min} \le Q_{n,m,t} \le Q_{n,m}^{\max}, \tag{26}$$

Among them, $Q_{n,m,t}$ is the gas volume flow rate from node n to node m, and $GL_{n,t}$ is the gas load at node n. The nodal pressure constraints follow the Weymouth formula:

$$Q_{m,n,t}|Q_{m,n,t}| = C_{mn}^2 \cdot \left(p_{m,t}^2 - p_{n,t}^2\right), \tag{27}$$

$$p_n^{\min} \le p_{n,t} \le p_n^{\max}. \tag{28}$$

Linearize the Weymouth formula in order to make the entire optimization system a mixed integer linear programming model. In the Weymouth formula, it can be linearized by the incremental linearization technique mentioned in the previous section.

$$Q_{m,n,t}|Q_{m,n,t}| = Q_1|Q_1| + \sum_{\kappa=1}^{N-1} \left(Q_{k+1}|Q_{k+1}| - Q_k|Q_k|\right) \cdot \xi_k, \tag{29}$$

$$Q_{m,n,t} = Q_1 + \sum_{\kappa=1}^{N-1} \left(Q_{k+1} - Q_k\right) \cdot \xi_k, \tag{30}$$

$$\xi_{k+1} \le SG_k \le \xi_k \tag{31}$$

$$0 \le \xi_k \le 1. \tag{32}$$

In order to ensure a safe mixing ratio of the hydrogen mixture, the limit of the mixture of hydrogen and natural gas must be limited. The risks and hazards of mixing high proportions of hydrogen with natural gas have been evaluated in many projects (Azra et al., 2005). In this paper, the mixing constraint of H_2 can be expressed as:

$$\frac{Q_{n,t}^{H_2}}{Q_{n,t}^{H_2} + Q_{n,t}^{SNG} + Sg_{n,t}} \le MI. \tag{33}$$

The MI is the maximum mix limit percentage. $Q_{n,t}^{H_2}$ and $Q_{n,t}^{SNG}$ are the quantities of hydrogen and natural gas injected at node n, and $Sg_{n,t}$ is the quantities of natural gas supplied by the node.

4 Case studies

4.1 Tested system

As shown in Figure 4, the tested electric-gas integrated energy system network consists of a 20-node gas system and a modified IEEE RTS-24-bus power system. In the following

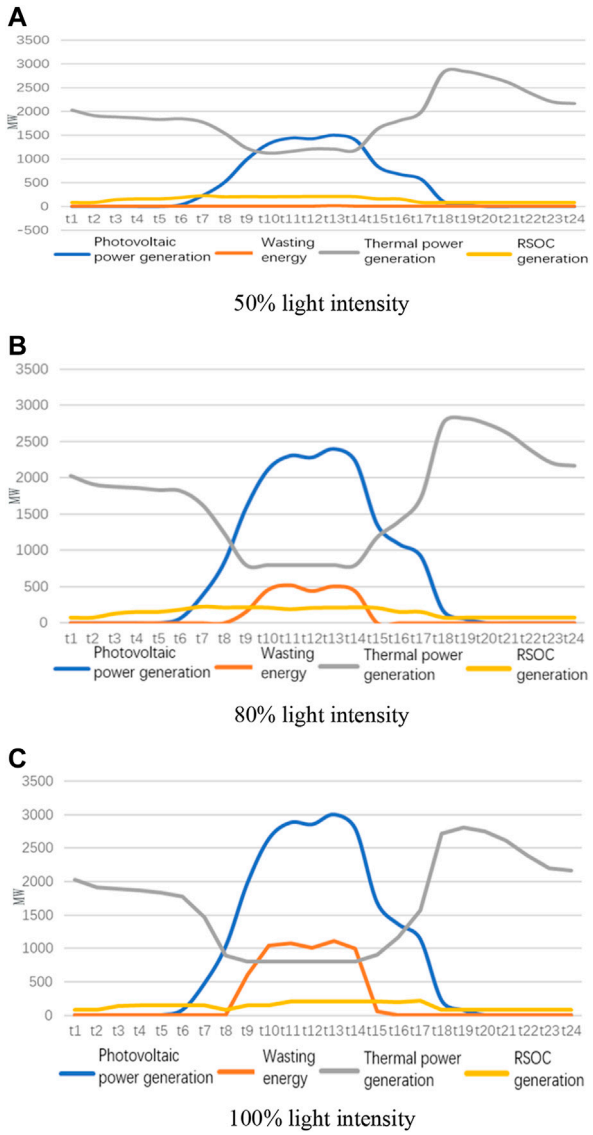

FIGURE 5
Scheduling results for hydrogen injection with a maximum concentration of 20%. **(A)** 50% light intensity, **(B)** 80% light intensity, **(C)** 100% light intensity.

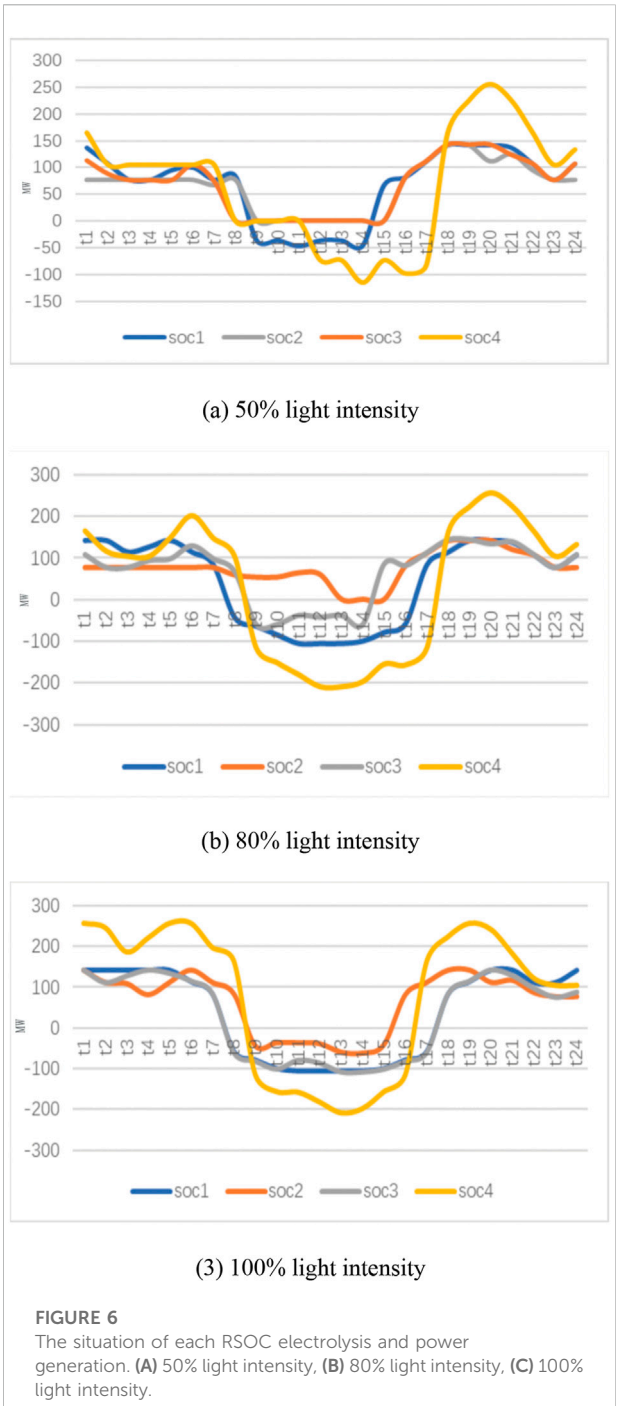

FIGURE 6
The situation of each RSOC electrolysis and power generation. **(A)** 50% light intensity, **(B)** 80% light intensity, **(C)** 100% light intensity.

example, we demonstrate the behavior of the proposed model during hourly optimization of the day. There are three photovoltaic power plants on Lines 1, 19 and 21 with capacities of 750, 1,000, and 1,250 MW respectively. When the sunlight is sufficient during the day, the excess photovoltaic power generation of the power system can be used by the reversible solid oxide fuel cell to participate in the P2G process. RSOC1, RSOC2, RSOC3, and RSOC4 are installed on bus bars 1, 2, 16 and 22 with capacities of 152, 152, 155, and 300 MW respectively. The technical data of RSOC refer to literature (Peksen, 2018; Mogensen et al., 2019b), which are uniformly adjusted to all RSOC units. The performance of power generation and co-electrolysis is shown in Figure 2. The power generation efficiency of each fixed RSOC is 52%, and the electrolysis efficiency of pure H_2 is 76%. The maximum gas production is 85%, and the total electrolysis efficiency is 69%. Start-up fees vary over time, as shown in Figure 3. The electricity demand data, natural gas demand data, and photovoltaic power generation forecast data are shown in Figure 5. User natural gas

TABLE 1 Operating results of the system under different hydrogen doping concentrations and light intensities.

H_2 injection concentration (%)	Light intensity (%)	System cost ($10^3$$)	PV cuts (MWh)	H_2 produc-tion (10^6M^3)	SNG produc-tion (10^6M^3)
0%	50%	289	26	0	0
0%	80%	3055	3756	0	0
0%	100%	3216	7141	0	0
5%	50%	2841	15	0.944	0
5%	80%	2979	3299	0.944	0
5%	100%	3135	6608	0.944	0
20%	50%	2835	23	0.988	0.194
20%	80%	2931	2518	0.984	0.216
20%	100%	3091	5902	0.981	0.187

demand is measured by the volume of natural gas, which adds up to 36.4×10^6 SCM per day. The rest of the system data can be obtained from literature [38].

Because photovoltaic power plants fluctuate greatly on a daily basis, they have been chosen as the renewable energy source of this integrated energy system. This indicates a system's ability to absorb renewable energy more clearly in a fluctuating renewable energy environment. In order to evaluate the impact of different levels of renewable energy and different hydrogen injection limitations on the established integrated energy system, three different light levels were used: 1) low light (50%) light intensity, 2) medium light (80%) light intensity, 3) strong light (100%) light intensity, three hydrogen injection limits: 1) 5% maximum hydrogen injection concentration; 2) 20% maximum hydrogen injection concentration; 3) 0% hydrogen injection concentration. In order to operate the system at different light intensities, the system will increase/decrease the input predicted photovoltaic power generation power for each time period, while the light intensity changes hourly way does not change. In order to reflect the changes in the system when the hydrogen injection limit values are different, the injection percentage parameter MI in Eq. 33 for the maximum hydrogen injection concentration is adjusted to adjust the maximum hydrogen injection concentration that can be safely injected into the natural gas pipeline.

4.2 20% H_2 injection limit

Figure 5 shows the scheduling results for a maximum H_2 injection concentration of 20%. We can observe that as light intensity increases, fossil fuel power generation decreases, and electrolysis power increases. When the light intensity increases to 80%, the power generation of fossil fuels is lower at the time of t9–t14. This is because the light intensity at noon is large, the power supplied to the grid is sufficient, and a part can be used for electricity to gas conversion. When the light intensity is 100%, the power generation of fossil fuels and the power of electricity to gas does not change greatly, which is caused by the power limitation of fuel cell electricity to gas and the limitation of the maximum hydrogen concentration. The electricity-to-gas process can still generate fossil fuel power at night, even when there is no light. This is because the lines are congested, and in order to balance supply and demand, part of the electricity is converted into natural gas or hydrogen.

The operating state of the RSOC is shown in Figure 6 and Table 1. As light intensity increases, the P2G process's operating power increases. At 50% light intensity, RSOC1 and RSOC4 operate in electrolysis mode at noon, and the rest of the time is to provide power to the power system. The start-up costs for RSOC1, RSOC2 and RSOC4 are 183, 206, and 408 MWh, respectively, because PV generation is not sufficient to maintain the minimum P2G operating power of these units. At 80% light intensity, all RSOCs can operate in electrolysis and power generation modes, except for all-day RSOC2 in power generation mode. At 100% light intensity, all RSOC will participate in the electrolysis and power generation process. Under 50% light intensity, although the efficiency of converting electricity to natural gas is relatively low, the gas production is still considerable. SNG production balances hydrogen and natural gas mixing ratios. The production of electricity to natural gas and hydrogen increased continuously with the increase of light intensity, but the increase was not obvious at more than 80% light intensity. To integrate more unconsumed photovoltaic power generation, more natural gas needs to be mixed with hydrogen injection pipelines. In addition, due to the limitation of the transmission capacity of the circuit line, when the light intensity is relatively high, a part of the renewable energy cannot be converted into hydrogen and natural gas in time through the RSOC for storage.

4.3 System operation results under different maximum hydrogen injection concentrations

Under the framework of energy dispatch, the benefit of mixing different concentrations of hydrogen 0%, 5% and 20% maximum hydrogen injection concentration scenarios is discussed. Among them, the total optimal cost includes source gas cost, photovoltaic reduction penalty, and load reduction.

It can be concluded from Table 2 that when the highest hydrogen doping concentration is 20%, the system cost and photovoltaic reduction are relatively reduced, while the production of hydrogen and natural gas increases correspondingly. In spite of this, the cost of the system did not decrease significantly after the light intensity gradually increased. This is because when calculating the cost of the system, its light penalty is taken into account. The cost of the system will increase significantly when the light intensity is high, and the load demand is low. It is found that when the highest hydrogen doping concentration is 5%, the natural gas production is 0 when the highest hydrogen doping concentration is 20%. When the highest hydrogen doping concentration is 20%, the system will generate natural gas, which reduces the supplement of external natural gas and reduces the cost. The intake of hydrogen gas is higher.

5 Conclusion

In this work, we presented a power-to-gas integrated energy system based on RSOC in order to promote the development of multi-energy complementary systems. By dividing the electricity-to-gas process in the RSOC into electricity-to-hydrogen and electricity-to-natural gas, we investigated the system characteristics and the time-varying law of start-up costs under different RSOC operating modes (electrolysis and power generation). Based on the DC power flow power system model and the linearized gas pipeline model, the optimal scheduling problem of the integrated energy system is established. In addition, we also evaluated the amount of energy generated from renewable sources, such as photovoltaics, and the effect of the maximum concentration of hydrogen injection on the energy system. This work also quantified the economic benefits of power-to-gas in renewable energy integration. With the continuous improvement and progress of electricity-to-gas technology, reversible solid oxide fuel cells may ultimately contribute significantly to carbon neutrality.

Data availability statement

The original contributions presented in the study are included in the article/Supplementary Material, further inquiries can be directed to the corresponding author.

Author contributions

All authors listed have made a substantial, direct, and intellectual contribution to the work and approved it for publication.

Funding

This work was supported by State Key Laboratory of Electrical Insulation and Power Equipment (EIPE22314).

Conflict of interest

Authors HM, DN, XC, YC, and JZ were employed by Baoding Power Supply Company.

The remaining authors declare that the research was conducted in the absence of any commercial or financial relationships that could be construed as a potential conflict of interest.

Publisher's note

All claims expressed in this article are solely those of the authors and do not necessarily represent those of their affiliated organizations, or those of the publisher, the editors and the reviewers. Any product that may be evaluated in this article, or claim that may be made by its manufacturer, is not guaranteed or endorsed by the publisher.

References

Abeysekera, M., Wu, J., Jenkins, N., and Rees, M. (2016). Steady state analysis of gas networks with distributed injection of alternative gas. *Appl. Energy* 164 (15), 991–1002. doi:10.1016/j.apenergy.2015.05.099

Ahmed, A., and Khalid, M. (2019). A review on the selected applications of forecasting models in renewable power systems. *Renew. Sustain. Energy Rev.* 100, 9–21. doi:10.1016/j.rser.2018.09.046

Azra, S., Miriam, K., Tord, T., and Assadi, M. (2005). Steady state and transient thermal stress analysis in planar solid oxide fuel cells. *J. Power Sources* 145 (2), 463–469. doi:10.1016/j.jpowsour.2004.11.073

Barelli, L., Bidini, G., Cinti, G., and Ottaviano, A. (2017). Study of SOFC-SOE transition on a RSOFC stack. *Int. J. Hydrogen Energy* 42 (41), 26037–26047. doi:10.1016/j.ijhydene.2017.08.159

Becker, W. L., Braun, R. J., Penev, M., and Melaina, M. (2012). Production of Fischer–Tropsch liquid fuels from high temperature solid oxide co-electrolysis units. *Energy* 47, 99–115. doi:10.1016/j.energy.2012.08.047

Brouwer, A. S., Broek, M., Seebregts, A., and Faaij, A. (2014). Impacts of large-scale Intermittent Renewable Energy Sources on electricity systems, and how these can be modeled. *Renew. Sustain. Energy Rev.* 33, 443–466. doi:10.1016/j.rser.2014.01.076

Carrion, M., and Arroyo, J. M. (2006). A computationally efficient mixed-integer linear formulation for the thermal unit commitment problem. *IEEE Trans. Power Syst.* 21 (3), 1371–1378. doi:10.1109/tpwrs.2006.876672

Denholm, P., and Hand, M. (2011). Grid flexibility and storage required to achieve very high penetration of variable renewable electricity. *Energy Policy* 39 (3), 1817–1830. doi:10.1016/j.enpol.2011.01.019

Fang, J., Zeng, Q., Ai, X., Chen, Z., and Wen, J. (2018). Dynamic optimal energy flow in the integrated natural gas and electrical power systems. *IEEE Trans. Sustain. Energy* 9 (1), 188–198. doi:10.1109/tste.2017.2717600

Foit, S. R., Vinke, I. C., De, L. G., and Eichel, R. A., (2017). Power to syngas an enabling technology for the transition of the energy system[J]. *Energy Storage Convers.* 56 (20), 5488–5498.doi:10.1002/anie.201607552

Gao, Y., Wang, P., Xue, Y., Wen, F., Zhang, L., Sun, K., et al. (2018). Collaborative planning of integrated electricity-gas energy systems considering demand side management[J]. *Autom. Electr. Power Syst.* 42 (13), 3–11. doi:10.7500/AEPS20180223002

Haifei, Z., and Yibo, W. (2018). Distributed optimal energy flow of electricity-gas integrated energy system considering P2G[J]. *Electr. Meas. Instrum.* 55 (21), 61–67.doi:10.1109/TPWRS.2019.2929685

Laguna-Bercero, M. A. (2012). Recent advances in high temperature electrolysis using solid oxide fuel cells: A review. *J. Power Sources* 203, 4–16. doi:10.1016/j.jpowsour.2011.12.019

Lapo, C., Gabriele, G., Dominique, A., and Carcasci, C. (2021). Steady-state analysis of a natural gas distribution network with hydrogen injection to absorb excess renewable electricity. *Int. J. Hydrogen Energy* 46 (50), 25562–25577. doi:10.1016/j.ijhydene.2021.05.100

Li, H. L., and Yu, C. S. (1999). A global optimization method for nonconvex separable programming problems. *Eur. J. Operational Res.* 117 (2), 275–292. doi:10.1016/s0377-2217(98)00243-4

Luo, Y., Shi, Y, Zheng, Y., and Cai, N. (2017). Reversible solid oxide fuel cell for natural gas/renewable hybrid power generation systems. *J. Power Sources* 340, 60–70. doi:10.1016/j.jpowsour.2016.11.057

Luo, Y., Wu, X., Shi, Y., Ghoniem, A. F., and Cai, N. (2018). Exergy analysis of an integrated solid oxide electrolysis cell-methanation reactor for renewable energy storage. *Appl. Energy* 215, 371–383. doi:10.1016/j.apenergy.2018.02.022

Manuel, G., Jonathan, L., Friedemann, M., McDaniel Koch, A., Graf, F., Bajohr, S., et al. (2016). Renewable power-to-gas: A technological and economic review. *Renew. Energy* 85, 1371–1390. doi:10.1016/j.renene.2015.07.066

Martínez Ceseña, E. A., Loukarakis, E., Good, N., and Mancarella, P. (2020). Integrated electricity– heat–gas systems: Techno–economic modeling, optimization, and application to multienergy districts. *Proc. IEEE* 108 (9), 1392–1410. doi:10.1109/jproc.2020.2989382

Mogensen, M. B., Chen, M., Frandsen, H. L., Graves, C., Hansen, J. B., Hansen, K. V., et al. (2019). Reversible solid-oxide cells for clean and sustainable energy. *Clean. Energy* 3 (3), 175–201. doi:10.1093/ce/zkz023

Mogensen, M. B., Chen, M., Frandsen, H. L., Graves, C., Hansen, J. B., Hansen, K. V., et al. (2019). Reversible solid-oxide cells for clean and sustainable energy. *Clean. Energy* 3 (3), 175–201. doi:10.1093/ce/zkz023

Okonkwo, P. C., Belgacem, I. B., Emori, W., and Uzoma, P. C. (2021). Nafion degradation mechanisms in proton exchange membrane fuel cell (pemfc) system: A review. *Int. J. hydrogen energy* 46 (55), 27956–27973. doi:10.1016/j.ijhydene.2021.06.032

Okonkwo, P. C., Emori, W., Uzoma, P. C., Mansir, I. B., Radwan, A. B., Ige, O. O., et al. (2022). A review of bipolar plates materials and graphene coating degradation mechanism in proton exchange membrane fuel cell. *Int. J. Energy Res.* 46 (4), 3766–3781. doi:10.1002/er.7428

Okonkwo, P. C., Ige, O. O., Uzoma, P. C., Emori, W., Benamor, A., et al. (2021). Platinum degradation mechanisms in proton exchange membrane fuel cell (pemfc) system: A review. *Int. J. Hydrogen Energy* 46 (29), 15850–15865. doi:10.1016/j.ijhydene.2021.02.078

Okonkwo, P. C., and Otor, C. (2021). A review of gas diffusion layer properties and water management in proton exchange membrane fuel cell system. *Int. J. Energy Res.* 45 (3), 3780–3800. doi:10.1002/er.6227

Peksen, M. (2018). Safe heating-up of a full scale SOFC system using 3D multiphysics modelling optimisation. *Int. J. Hydrogen Energy* 43 (1), 354–362. doi:10.1016/j.ijhydene.2017.11.026

Qadrdan, M., Abeysekera, M., Chaudry, M., Wu, J., and Jenkins, N. (2015). Role of power-to-gas in an integrated gas and electricity system in Great Britain. *Int. J. Hydrogen Energy* 40 (17), 5763–5775. doi:10.1016/j.ijhydene.2015.03.004

Schiebahn, S., Grube, T., Robinius, M., Tietze, V., Kumar, B., Stolten, D., et al. (2015). Power to gas: Technological overview, systems analysis and economic assessment for a case study in Germany. *Int. J. Hydrogen Energy* 40 (12), 4285–4294. doi:10.1016/j.ijhydene.2015.01.123

Singhal, S. C. (2012). Solid oxide fuel cells: Past, present and future[J]. *Solid Oxide Fuels Cells Facts Figures*, 1–23.

Stephen, C., and Pierluigi, M. (2015). Integrated modeling and assessment of the operational impact of power-to-gas (P2G) on electrical and gas transmission networks. *IEEE Trans. Sustain. Energy* 6 (4), 1234–1244. doi:10.1109/tste.2015.2424885

Stephen, C., and Pierluigi, M. (2015). Storing renewables in the gas network: Modelling of power-to-gas seasonal storage flexibility in low-carbon power systems [J]. *IET generation Transm. Distribution* 10 (3), 566–575.

Wang, C., Dong, S., Xu, S., Yang, M., Dong, X., and Liang, J., (2019). Impact of power-to-gas cost characteristics on power-gas-heating integrated system scheduling. *IEEE Access* 7, 17654–17662. doi:10.1109/access.2019.2894866

Yu, L., Shi, Y., Yi, Z., and Cai, N. (2017). Reversible solid oxide fuel cell for natural gas/renewable hybrid power generation systems. *J. Power Sources* 340, 60–70. doi:10.1016/j.jpowsour.2016.11.057

Zhang, X., Chan, S. H., Li, G., Ho, H. K., Li, J., and Feng, Z. (2010). A review of integration strategies for solid oxide fuel cells. *J. Power Sources* 195 (3), 685–702. doi:10.1016/j.jpowsour.2009.07.045

Zhang, Z., Zhou, J., Zong, Z., Chen, Q., Zhang, P., and Wu, K. (2019). Development and modelling of a novel electricity-hydrogen energy system based on reversible solid oxide cells and power to gas technology. *Int. J. Hydrog. Energy* 44, 28305–28315. doi:10.1016/j.ijhydene.2019.09.028

Zhao, P., Gu, C., Hu, Z., Xie, D., Hernando-Gil, I., and Shen, Y. (2021). Distributionally robust hydrogen optimization with ensured security and multi-energy couplings. *IEEE Trans. Power Syst.* 36 (1), 504–513. doi:10.1109/tpwrs.2020.3005991

Zhang, C., Zhao, S., and He, Y., (2022). An integrated method of the future capacity and RUL prediction for lithium-ion battery pack[J]. *IEEE Trans. Veh. Technol.* 71 (3), 2601–2613. doi:10.1109/TVT.2021.3138959

Zhou, S., Sun, K., Wu, Z., Gu, W., Wu, G., Li, Z., et al., (2020). Optimized operation method of small and medium-sized integrated energy system for P2G equipment under strong uncertainty[J]. *Energy* 199 (15), 117269. doi:10.1016/j.energy.2020.117269

Zhao, S., Zhang, C., and Wang, Y., (2022). Lithium-ion battery capacity and remaining useful life prediction using board learning system and long short-term memory neural network[J]. *J. of Energy Storage* 52, 104901. doi:10.1016/j.est.2022.104901

Nomenclature

Abbrevations

HCNG Hydrogen-Enriched Compressed Natural Gas

IEGS Integrated Electricity-Gas System

P2G Power to Gas

PV Photovoltaic

RSOC Reversible solid oxide cell

SNG Synthetic natural gas

SOFCs Solid oxide cells

English letter

$GL_{n,t}$ the gas load at node n

$LS_{i,t}$ load shedding amount at the bus i

SC_S binary variable

$Sg_{n,t}$ gas production at the gas source n at time t

b_g the power generation price of the thermal unit

c_n the natural gas price at the gas source point n

$delta_{i,t}$ the included angle of the busbar i

$E_{r,t}^{H_2}$ the electrolysis of hydrogen

$E_{r,t}^{in}$ the input energy of the gas

$E_{r,t}^{SNG}$ the electrolysis of natural gas

F_r^{sl} fixed start-up cost

H_{H_2} calorific value of hydrogen

H_{NG} calorific value of natural gas

K_r^l start-up cost of fuel cell after the offline time length

l length of the ROSC offline

$L_{i,t}$ power load

$P_{g,t}$ power generation of the generator set g at time t

$P_{i,t}^{vc}$ power of the abandoned photovoltaic

$P_{r,t}^{gen}$ generated power of the RSOC at time t

$P_{r,t}^{P2G}$ input power supply for the common electrolysis process

P_i^v the photovoltaic power generation included in the power grid

$P_r^{rd,ele}$ downhill power in the electrolysis mode

$P_r^{rd,gen}$ downhill power in the fuel cell power generation mode

$P_r^{ru,ele}$ uphill power in the electrolysis mode

$P_r^{ru,gen}$ uphill power in the fuel cell power generation mode

P_t^{pv} the predicted photovoltaic power generation

P_t^{vc} the amount of abandoned light

$Q_{n,m,t}$ the gas volume flow rate from node n to node m

$Q_{n,t}^{H_2}$ the quantities of hydrogen injected at node n

$Q_{n,t}^{SNG}$ the quantities of natural gas injected at node n

tau cooling time constant

V_r^{sl} the maximum start-up cost variable

VOLL the price required to reduce the load of the system

VOLV the price of the abandoned light

x_{ij} the reactance of the transmission line between the busbar i and j

Y (t, j) binary variable indicating start state

Z (t, j) binary variable indicating stop state

Frontiers in
Energy Research

Advances and innovation in sustainable, reliable and affordable energy

Explores sustainable and environmental developments in energy. It focuses on technological advances supporting Sustainable Development Goal 7: access to affordable, reliable, sustainable and modern energy for all.

Discover the latest Research Topics

See more →

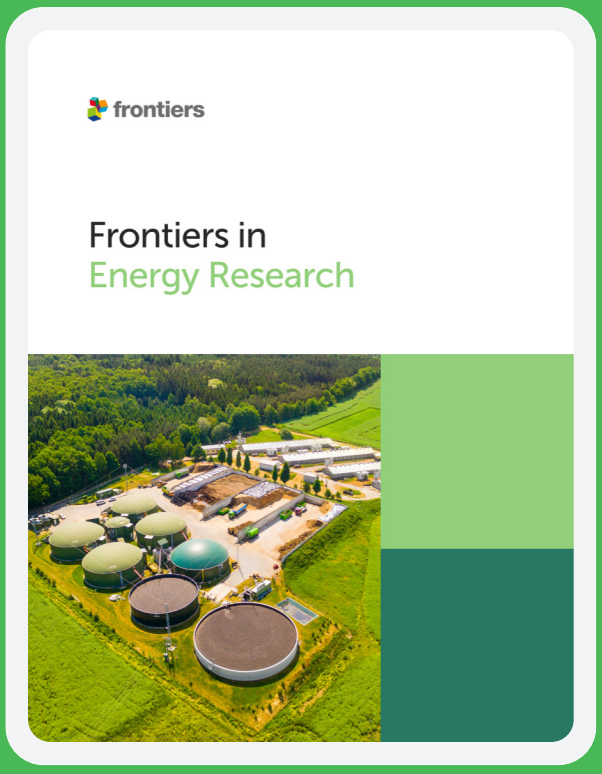

Frontiers

Avenue du Tribunal-Fédéral 34
1005 Lausanne, Switzerland
frontiersin.org

Contact us

+41 (0)21 510 17 00
frontiersin.org/about/contact